

**NASA Contractor Report 3758**

**Free Jet Feasibility Study of a  
Thermal Acoustic Shield Concept  
for AST/VCE Application**

*Single Stream Nozzles*

**R. K. Majjigi, J. F. Brausch,  
B. A. Janardan, T. F. Balsa,  
P. R. Knott, and N. Pickup**

CONTRACT NAS3-22137  
JULY 1984

**NASA**

NASA Contractor Report 3758

**Free Jet Feasibility Study of a  
Thermal Acoustic Shield Concept  
for AST/VCE Application**

*Single Stream Nozzles*

**R. K. Majjigi, J. F. Brausch,  
B. A. Janardan, T. F. Balsa,  
P. R. Knott, and N. Pickup**  
*General Electric Company  
Cincinnati, Ohio*

**Prepared for  
Lewis Research Center  
under Contract NAS3-22137**



**National Aeronautics  
and Space Administration**

**Scientific and Technical  
Information Branch**

1984

## TABLE OF CONTENTS

<u>SECTION</u>	<u>Page</u>
FOREWORD	vii
1.0 SUMMARY	1
2.0 INTRODUCTION	2
3.0 SCALE MODEL NOZZLE DESCRIPTION AND SCOPE OF TESTING	5
3.1 Single Stream Scale Model Nozzle Description	5
3.2 Scope of Testing	15
3.2.1 Acoustic Tests	15
3.2.2 Laser Velocimeter Tests	42
3.2.3 Aerodynamic Calibration and Diagnostic Tests	42
4.0 TEST RESULTS AND DISCUSSION	53
4.1 Acoustic Test Results	53
4.1.1 Influence of Thermal Acoustic Shields on Unsuppressed Annular Plug Nozzle	54
4.1.2 Influence of Thermal Acoustic Shields on a 32 Chute Mechanical Suppressor Nozzle	84
4.1.3 Comparison of Acoustic Influence of Thermal Acoustic Shields on Unsuppressed Annular Plug and 32 Chute Suppressor Nozzles	109
4.2 Laser Velocimeter Test Results	140
4.2.1 Plume Characteristics of Unsuppressed Annular Plug Nozzle With Thermal Acoustic Shield Under Static and Simulated Flight Conditions	147
4.2.2 Plume Characteristics of 32 Chute Suppressor Nozzle With Thermal Acoustic Shield Under Static and Simulated Flight Conditions	157
4.3 Aerodynamic Calibration and Diagnostic Test Results	171
4.3.1 Stagnation Pressure Calibration of Full and Partial Thermal Acoustic Shield Streams	171
4.3.2 Measured and Predicted Pressure Field Interactions of Core and Shield Streams	176

TABLE OF CONTENTS (Continued)

<u>SECTION</u>	<u>Page</u>
4.3.3 Influence of Thermal Acoustic Shields on the Base Drag of the 32 Chute Suppressor Nozzle Under Heated, Simulated Flight and Static Conditions	189
4.3.4 Aerodynamic and Acoustic Performance Evaluation of the Thermal Acoustic Shield on the 32 Chute Suppressor Nozzle	199
5.0 THEORETICAL AEROACOUSTIC PREDICTION METHOD FOR THERMAL ACOUSTIC SHIELDS	212
5.1 Background	212
5.2 Methodologies for Axially Asymmetric Thermal Acoustic Shields	213
5.2.1 A Theory for Planar (2-D) Thermal Acoustic Shields	213
5.2.2 Analytical/Computational Modifications of the M*G*B Method for Partial Thermal Acoustic Shields and Selective Data Theory Comparisons	250
6.0 AN INSTALLED NOISE ANALYSIS OF THERMAL ACOUSTIC SHIELD DATA	268
6.1 Introduction	268
6.2 Data Sources	270
6.2.1 Jet Noise Test Data	270
6.2.2 Flight Profiles	271
6.2.3 Non-Jet Noise Components	271
6.3 Method of Analysis	276
6.3.1 General Description	276
6.3.2 Rescale of Jet Test Data	279
6.4 Results of Analysis	285
6.4.1 TAS Obtained by a Bleed System	286
6.4.2 TAS Obtained from an Independent Source	295
6.4.3 Other Analysis Results	303
6.5 Conclusions and Recommendations	309
7.0 CONCLUSIONS AND RECOMMENDATIONS	312

TABLE OF CONTENTS (Concluded)

<u>SECTION</u>	<u>Page</u>
8.0 REFERENCES	317
9.0 NOMENCLATURE	322
APPENDIX A-I - ACOUSTIC TEST MATRICES OF CONFIGURATIONS TAS-1 THRU TAS-9 IN SI UNITS	325

## FOREWORD

The Boeing Airplane Company was subcontracted by General Electric during this project. The technical comments from Jack O'Keefe and Rudolph Mangiarotty of the Boeing Company during the course of the project were very helpful.

The numerous technical discussions with Philip Gliebe and Robert Lee of the General Electric Company during the analysis and theoretical modeling phases of the project have helped this project considerably.

The authors would like to thank Don Hoerst and Ann Price for their help in data reduction and report preparation.

## 1.0 SUMMARY

The objective of this investigation is to develop a technology base for the thermal acoustic shield concept as a noise suppression device for single stream exhaust nozzles. Acoustic data for 314 test points for 9 scale model nozzle configurations were obtained. Five of these configurations employed an unsuppressed annular plug core jet and the remaining four nozzles employed a 32 chute suppressor core nozzle. Influence of simulated flight and selected geometric and aerodynamic flow variables on the acoustic behavior of the thermal acoustic shield was determined. Laser velocimeter and aerodynamic measurements were employed to yield valuable diagnostic information regarding the flow field characteristics of these nozzles. An existing theoretical aeroacoustic prediction method was modified to predict the acoustic characteristics of partial thermal acoustic shields.

From the results of this investigation, it was found that: the three significant physical influences of a thermal acoustic shield are: 1) mid and high frequency noise reduction at shallow angles to the jet axis due to total internal reflection; 2) mid and high frequency noise reduction in the front quadrant and at  $\theta_1 = 90^\circ$  due to source strength reduction; and 3) low frequency noise amplification due to an elongation of the jet plume. Due to the larger high frequency noise content of the 32 chute suppressor nozzle, the thermal acoustic shield yields larger PNL and EPNL reductions for the 32 chute nozzle compared to the unsuppressed annular plug nozzle. PNL and EPNL reductions due to the thermal acoustic shield are dependent on the observer sideline distance, and hence appropriate sideline distances must be utilized in determining the noise suppression at takeoff, cutback and approach cycle conditions. The shield thickness has a significant bearing on the noise reduction potential of a thermal acoustic shield. Partial thermal acoustic shields create significant amount of acoustic and flow asymmetry which is confirmed by the theoretical predictions. An increase in base drag of the 32 chute suppressor nozzle due to the shields was observed, but is smaller for the simulated flight case than the static case.

## 2.0 INTRODUCTION

A future Advanced Supersonic Transport (AST) has to be fuel efficient and environmentally acceptable (noise and pollution wise) to be a viable candidate for commercial aeronautical applications. Significant advancements in jet noise reduction technology on test bed vehicles have been made since the introduction of the first generation supersonic transport (SST), the Anglo-French Concorde, into the commercial airline service. These advancements include the variable cycle engine (VCE) employing an inverted velocity profile coannular plug nozzle (Reference 2.1), and a mechanical suppressor nozzle employing a combination of lobe and tube elements and a treated ejector (Reference 2.2).

In the past, the major concentration of research and design efforts for obtaining a large amount of jet noise reduction has been through mechanical suppressor concepts. Although progress with this classical approach has been rewarding (References 2.3 and 2.4), there is a need to find and develop alternative and/or complementary methods. New approaches have to be developed which focus not only on the usual rapid jet mixing concepts, but on the fluid shielding, reflection/refraction properties of the exhaust streams. Utilization of a high temperature low velocity gas stream surrounding the main jet (henceforth referred to as Thermal Acoustic Shield [TAS]) to refract the noise of the main jet is such an alternative method. A ray acoustics analysis of the shielding of the noise emitted from a high speed conic jet by a hot, subsonic semi-circular shield jet (Reference 2.5) evaluated the effectiveness of shielding by the semi-circular shield jet. Experimental studies of thermal acoustic shields utilizing scale model nozzles by Ahuja and Dosanjh (Reference 2.6), Goodykoontz (Reference 2.7) and Pickup, Mangiarotty and O'Keefe (Reference 2.8) have shown impressive reduction in spectral sound pressure levels by the thermal acoustic shields on mechanically unsuppressed nozzles.



The primary objective of this investigation is to develop a technology base for the thermal acoustic shield concept as a noise suppression device for mechanically suppressed and unsuppressed plug nozzles employing a single core flow. Effects of simulated flight velocity, and selected geometric and aerodynamic flow variables on the acoustic behavior of the thermal acoustic shield were to be determined by this investigation. Laser velocimeter diagnostic data in terms of mean and turbulent velocities were obtained to aid in understanding of the underlying aerodynamic mechanisms of the jet plumes of the nozzles with thermal acoustic shields. The impact of the thermal acoustic shield on the base drag of mechanically suppressed nozzles and the static pressure field interactions between the core and thermal acoustic shield streams were evaluated in this study. Finally, an existing theoretical aeroacoustic prediction method (M\*G\*B model) was extended to predict the acoustic characteristics of partial thermal acoustic shields.

This final report summarizes the research effort required as part of Contract NAS3-22137 and includes all the pertinent information regarding the prime results from the testing and analytical studies. References 2.9 and 2.10 constitute the Comprehensive Data Report required as part of the contract. Reference 2.9 includes detailed schematics of the nine model nozzle configurations and tabulation of aerodynamic test conditions and measured basic acoustic data. Reference 2.10 contains the laser velocimeter plume data and base pressure data for a 32 chute annular plug suppressor nozzle. The model hardware design report, a description of the General Electric Anechoic Free Jet Facility, and details of the data acquisition and reduction procedures are provided in the appendices of Reference 2.10.

#### REFERENCES FOR SECTION 2.0

- 2.1 Vdoviak, J.W., Knott, P.R. and Ebacker, J.J., "Aerodynamic/Acoustic Performance of YJ101/Double Bypass VCE with Coannular Plug Nozzle", NASA CR-159869, January 1981.
- 2.2 Fitzsimmons, R.D., McKinnon, R.A., Johnson, E.S. and Brooks, J.R., "Flight and Wind Tunnel Test Results of a Mechanical Jet Noise Suppressor Nozzle", AIAA Paper Number 80-0165, January 1980.

- 2.3 Stringas, E.J., Clapper, W.S., Brausch, J.F., et al, "High Velocity Jet Noise Source Location and Reduction, Task 3 - Experimental Investigation of Suppression Principles, Volume II - Parametric Testing and Source Measurements", General Electric Company Contractor Final Report Number FAA-RD-76-79, III-II, December 1978.
- 2.4 Knott, P.R., Janardan, B.A. and Majjigi, R.K., "Free-Jet Investigation of Mechanically Suppressed, High-Radius-Ratio Coannular Plug Model Nozzles", Final Report Draft for Contract NAS3-21608, October 1981.
- 2.5 Vijayaraghavan, A. and Parthasarathy, S.P., "Noise Shielding by a Hot Subsonic Jet", AIAA Paper Number 81-2018, October 1981.
- 2.6 Ahuja, K.K. and Dosanjh, D.S., "Heated Fluid Shroud as an Acoustic Shield for Noise Reduction - An Experimental Study", AIAA Paper Number 77-1286, October 1977.
- 2.7 Goodykoontz, J., "Effect of a Semi-Annular Thermal Acoustic Shield on Jet Exhaust Noise", NASA TM 81615, Prepared for the One-Hundredth Meeting of the Acoustical Society of America, November 1980.
- 2.8 Pickup, N., Mangiarotty, R.A. and O'Keefe, J.V., "Tests of a Thermal Acoustic Shield with a Supersonic Jet", AIAA Paper Number 81-2021, October 1981.
- 2.9 Majjigi, R.K., Janardan, B.A., Brausch, J.F., Hoerst, D.J., Price, A.O., and Knott, P.R., "Free-Jet Feasibility Study of a Thermal Acoustic Shield Concept for AST/VCE Application - Single Flow," General Electric Technical Information Series Report Number R82AEB493, Vol. I, also, NASA CR-168302, July 1983.
- 2.10 Majjigi, R.K., Janardan, B.A., Brausch, J.F., Hoerst, D.J., Price, A.O., and Knott, P.R., "Free-Jet Feasibility Study of a Thermal Acoustic Shield Concept for AST/VCE Application - Single Flow," General Electric Technical Information Series Report Number R82AEB493, Vol. II, also, NASA CR-168303, July 1983.

### 3.0 SCALE MODEL NOZZLE DESCRIPTION AND SCOPE OF TESTING

A brief description of the nine (9) scale model nozzles which have been tested in this program and the scope of testing including the rationale for the acoustic, laser velocimeter and aerodynamic diagnostic and calibration tests performed, are discussed in this section.

#### 3.1 SINGLE STREAM SCALE MODEL NOZZLE DESCRIPTION

A set of nine (9) configurations which employ single flow primary nozzles were tested during the course of this program, and are as follows:

<u>CONFIGURATION</u>	<u>DESCRIPTION</u>
TAS-1	Baseline unshielded, unsuppressed annular plug nozzle
TAS-2	Unsuppressed annular plug nozzle with 180° thermal acoustic shield of 0.48" thickness
TAS-3	Unsuppressed annular plug nozzle with 180° thermal acoustic shield of 0.97" thickness
TAS-4	Unsuppressed annular plug nozzle with 360° thermal acoustic shield of 0.48" thickness
TAS-5	Convergent-divergent annular plug nozzle with 180° thermal acoustic shield of 0.48" thickness
TAS-6	Unshielded 32-chute annular plug suppressor nozzle
TAS-7	32-chute annular plug suppressor nozzle with 180° thermal acoustic shield of 0.48" thickness
TAS-8	32-Chute annular plug suppressor nozzle with 180° thermal acoustic shield of 0.97" thickness
TAS-9	32-Chute annular plug suppressor nozzle with 360° thermal acoustic shield of 0.48" thickness

Table 3-I lists the above configurations along with sketches. For a complete description of these model hardware designs, see Reference 3.1. Table 3-II lists the geometric parameters of the nine (9) TAS Nozzle Configurations and Figure 3.1 shows a schematic sketch of a TAS Nozzle Configuration along with definition of salient geometric parameters.

The baseline unshielded, unsuppressed annular plug nozzle (Configuration TAS-1) serves as a reference nozzle to evaluate the acoustic benefit of the different thermal acoustic shields. Configuration TAS-2 employs a partial (180°) shield of 0.48" thickness on the annular plug nozzle. Configuration TAS-3 employs a partial shield of 0.97" thickness on the annular plug nozzle to study the effect of doubling the shield thickness on the acoustic performance of the thermal acoustic shield. Configuration TAS-4 employs a full (360°) shield of 0.48" thickness on the annular plug nozzle. Acoustic comparison of configurations TAS-2 and TAS-4 will indicate the relative merits of the partial vs. full shields of the same thickness. Acoustic comparisons of configurations TAS-3 and TAS-4 indicate the relative merits of partial and full shields of approximately equal flow areas. Configuration TAS-5 employs a primary nozzle which has a convergent-divergent flowpath designed for an exit Mach number of 1.4 and a 180° shield nozzle of 0.48" thickness. The convergent-divergent core nozzle was tested in Reference 3.2. Configuration TAS-6 is the unshielded 32-chute annular plug suppressor nozzle and will serve as the baseline nozzle to evaluate the acoustic benefit of different thermal acoustic shields on a mechanical suppressor nozzle (see Figure 3.2). The shields (viz., 180° shields of 0.48" and 0.97" thickness and 360° shield of 0.48" thickness) were so designed as to be applicable for both the annular plug nozzle (Configuration TAS-1) and the 32-chute suppressor nozzle (Configuration TAS-6). The objectives of such a design were:

- A. To determine the relative merits of the selected thermal acoustic shields on a mechanical suppressor nozzle and an unsuppressed nozzle.
- B. To keep hardware commonality as a means of cost reduction.

TABLE 3-1. SINGLE PRIMARY SHIELDING MODELS/EXPERIMENT, SEMI-ANALYTICAL, ACOUSTIC SHIELDING

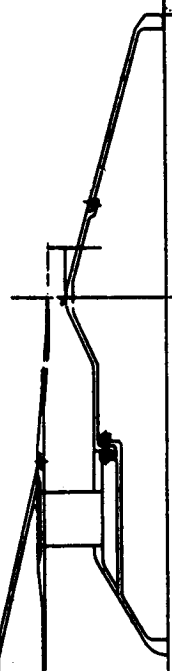
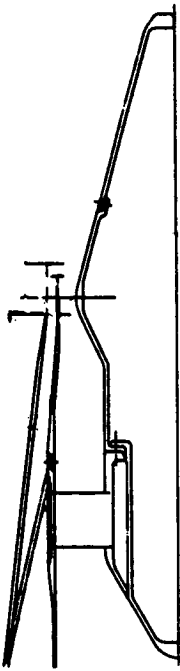
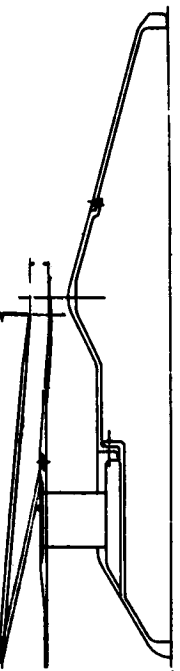
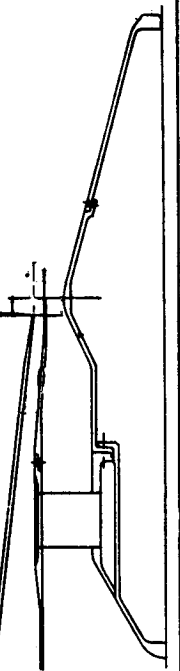
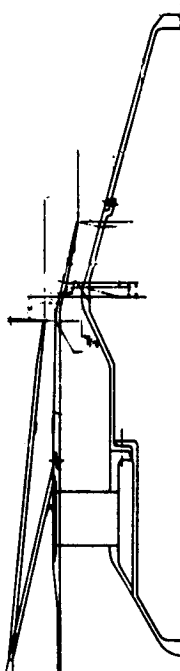
CONFIG. IDENT.	DESCRIPTION	RELATIVE
TAB-1	Baseline unshielded unpressured annular plug nozzle	
TAB-2	Unpressured annular plug nozzle with 180° thermal acoustic shield of 0.48" thickness	
TAB-3	Unpressured annular plug nozzle with 180° thermal acoustic shield of 0.97" thickness	
TAB-4	Unpressured annular plug nozzle with 360° thermal acoustic shield of 0.48" thickness	
TAB-5	Convergent-Divergent annular plug nozzle with 180° thermal acoustic shield of 0.48" thickness	

TABLE 3-1 (CONT'D). SINGLE PRIMARY NOZZLE WITH/WITHOUT THERMAL ACOUSTIC SHIELD

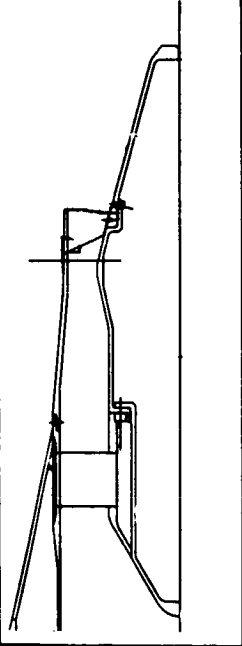
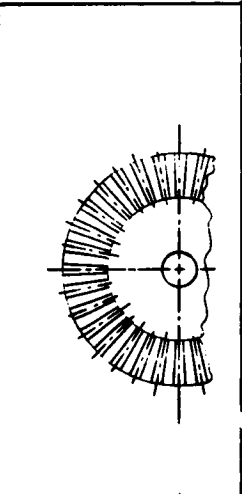
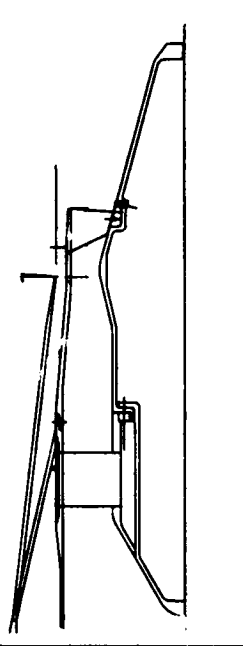
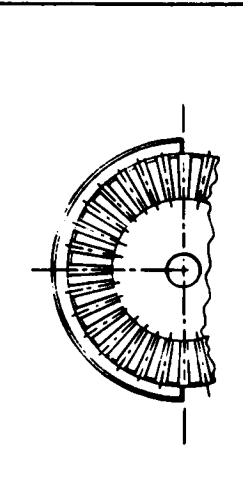
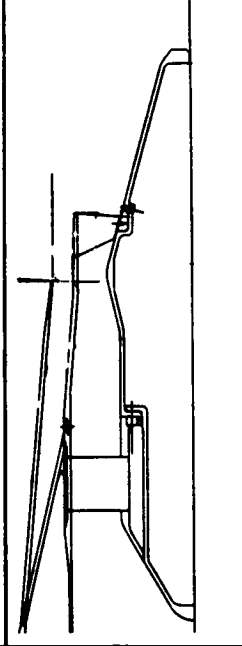
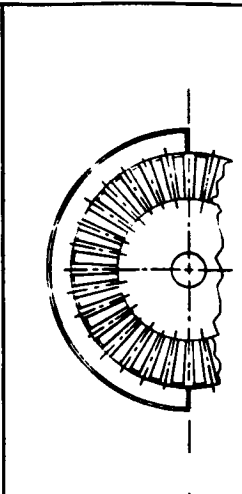
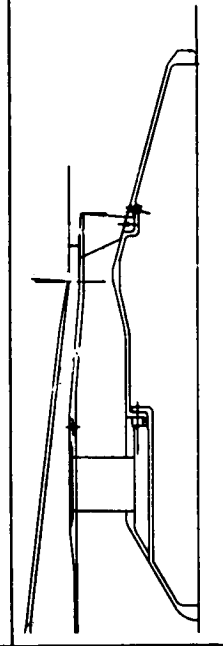
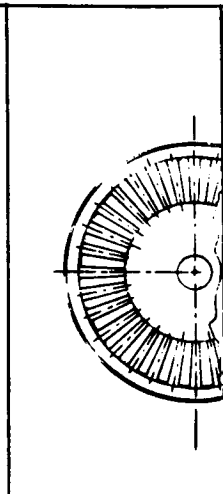
CONFIG. IDENT.	DESCRIPTION	SECTION	
TAS-6	Unshielded 32-chute annular plug suppressor nozzle		
TAS-7 C	32-chute annular plug suppressor nozzle with 180° thermal acoustic shield of 0.48" thickness		
TAS-8	32-chute annular plug suppressor nozzle with 180° thermal acoustic shield of 0.97" thickness		
TAS-9	32-chute annular plug suppressor nozzle with 360° thermal acoustic shield of 0.48" thickness		

TABLE 3-II. GEOMETRIC PARAMETERS OF SINGLE FLOW THERMAL ACOUSTIC SHIELD NOZZLES.

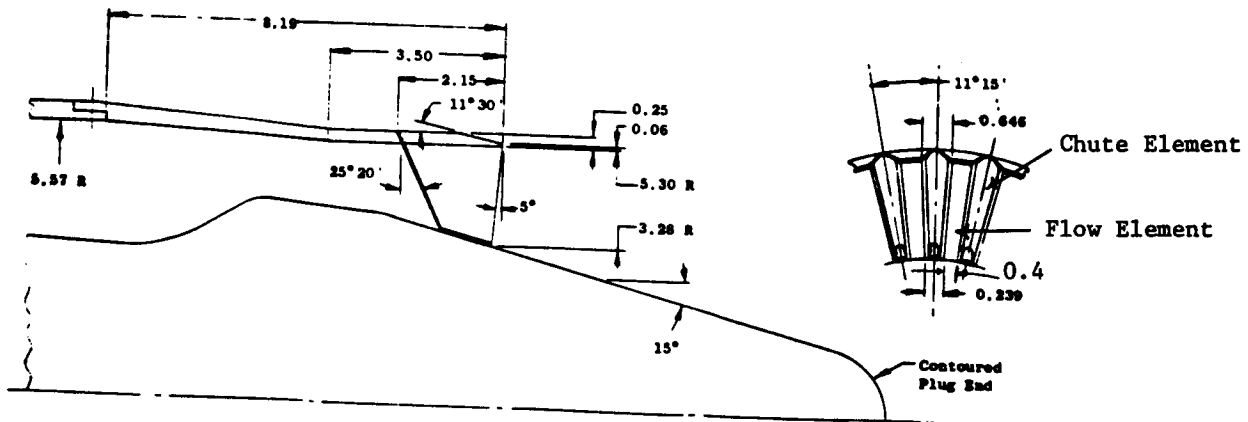
P A R A M E T E R S	C O N F I G U R A T I O N #								
	TAS-1	TAS-2	TAS-3	TAS-4	TAS-5	TAS-6	TAS-7	TAS-8	TAS-9
Unsuppressed/32-Chute	Unsup.	Unsup.	Unsup.	Unsup.	Unsup.	32-Ch.	32-Ch.	32-Ch.	32-Ch.
Throat Height, $h_{th}$ , in	0.8	0.8	0.8	0.8	0.8	2.021	2.021	2.021	2.021
Phys. Throat Area, $A_{th}$ , in <sup>2</sup>	25.28	25.28	25.28	25.28	25.28	26.15	26.15	26.15	26.15
Assumed Discharge Coeff., $C_D$	0.98	0.98	0.98	0.98	0.98	0.977	0.977	0.977	0.977
Effective Throat Area, $A_{th}^e$ , in <sup>2</sup>	24.77	24.77	24.77	24.77	24.77	25.55	25.55	25.55	25.55
$D_{eq}$ based on $A_{th}$ , in	5.67	5.67	5.67	5.67	5.67	5.77	5.77	5.77	5.77
$D_{eq}$ based on $A_{th}^e$ , in	5.62	5.62	5.62	5.62	5.62	5.70	5.70	5.70	5.70
Hub Radius @ Throat, $R_{th}^h$ , in	4.64	4.64	4.64	4.64	4.64	4.64	3.28	3.28	3.28
Tip Radius @ Throat, $R_{th}^t$ , in	5.44	5.44	5.44	5.44	5.44	5.44	5.30	5.30	5.30
Throat Radius Ratio, $R_r^{th}$	0.85	0.85	0.85	0.85	0.85	0.85	0.62	0.62	0.62
C-D or Conv. Termination	Conv.	Conv.	Conv.	Conv.	Conv.	C-D	Conv.	Conv.	Conv.
Exit Height, $h_e$ , in	0.8	0.8	0.8	0.8	1.024	2.021	2.021	2.021	2.021
Phys. Exit Area, $A_e$ , in <sup>2</sup>	25.28	25.28	25.28	25.28	28.28	26.15	26.15	26.15	26.15
Effective Exit Area, $A_e^e$ , in <sup>2</sup>	24.77	24.77	24.77	24.77	27.71	25.55	25.55	25.55	25.55
$D_{eq}$ based on $A_e$ , in	5.67	5.67	5.67	5.67	6.00	5.77	5.77	5.77	5.77
$D_{eq}$ based on $A_e^e$ , in	5.62	5.62	5.62	5.62	5.94	5.70	5.70	5.70	5.70
Hub Radius @ Exit, $R_e^h$ , in	4.64	4.64	4.64	4.64	3.88	3.28	3.28	3.28	3.28
Tip Radius @ Exit, $R_e^t$ , in	5.44	5.44	5.44	5.44	4.90	5.30	5.30	5.30	5.30
Exit Radius Ratio, $R_r^e$	0.85	0.85	0.85	0.85	0.79	0.62	0.62	0.62	0.62
Exit/Throat Height Ratio	1.00	1.00	1.00	1.00	1.28	1.00	1.00	1.00	1.00
Exit/Throat Area Ratio	1.00	1.00	1.00	1.00	1.12	1.00	1.00	1.00	1.00

TABLE 3-II (CONT'D). GEOMETRIC PARAMETERS OF SINGLE FLOW THERMAL ACOUSTIC SHIELD NOZZLES.

B. 32-CHUTE TURBOJET SUPPRESSOR GEOMETRY

Parameter	Value
Number of Elements	32
Suppressor Area Ratio	2.1 (Annulus Area/Flow Area)
Exit Plane Cant Angle, deg	5°
Primary Flow Width Ratio	1.0 (i.e., parallel sided flow elements)
Flow Element Width @ Hub, in	0.4
Flow Element Width @ Tip, in	0.4
Chute Width @ Hub, in	0.24
Chute Width @ Tip, in	0.65
Chute Depth @ Hub, in	1.00
Chute Depth @ Tip, in	2.00

ALL DIMENSIONS IN INCHES



32-Chute, AR = 2.1,  $R_T^e = 0.62$  Turbojet Suppressor.



TABLE 3-II (CONT'D). GEOMETRIC PARAMETERS OF SINGLE FLOW THERMAL ACOUSTIC SHIELD NOZZLES.

P A R A M E T E R	C O N F I G U R A T I O N #								
	TAS-1	TAS-2	TAS-3	TAS-4	TAS-5	TAS-6	TAS-7	TAS-8	TAS-9
Shield Arc, deg.	--	180°	180°	360°	180°	--	180°	180°	360°
Shield Thickness, $h_{TAS}$ , in	--	0.48	0.97	0.48	0.48	--	0.48	0.97	0.48
Inner Radius @ Throat, $R_I^{TAS}$ , in	--	5.50	5.50	5.50	5.89	--	5.50	5.50	5.50
Outer Radius @ Throat, $R_O^{TAS}$ , in	--	5.99	6.47	5.99	6.38	--	5.99	6.47	5.99
Radius Ratio @ Throat, $R_I^{TAS}$	--	0.92	0.85	0.92	0.92	--	0.92	0.85	0.92
Phys. Throat Area, $A_{TAS}$ , in <sup>2</sup>	--	8.75	18.21	17.49	9.33	--	8.75	18.21	17.49
Assumed Discharge Coeff., $C_D$	--	0.92	0.92	0.92	0.92	--	0.92	0.92	0.92
Effective Throat Area, $A_{TAS}^e$ , in <sup>2</sup>	--	8.05	16.76	16.09	8.58	--	8.05	16.76	16.09
$D_{eq}$ based on $A_{TAS}$ , in	--	3.34	4.82	4.72	3.45	--	3.34	4.82	4.72
$D_{eq}$ based on $A_{TAS}^e$ , in	--	3.20	4.62	4.53	3.31	--	3.20	4.62	4.53
Shield Inner Flowpath Angle @ Throat, $\theta_1$ , deg.	--	1°	1°	1°	1°	--	1°	1°	1°
Shield Outer Flowpath Angle @ Throat, $\theta_0$ , deg.	--	6°40'	5°	6°40'	5°20'	--	6°40'	5°	6°40'
Shield Throat Angle, $\theta_{th}$ , deg.	--	3.8°	3.0°	3.8°	3.2°	--	3.8°	3.0°	3.8°
Approx. Axial Distance to Primary Nozzle Exit Plane, $X_e$ , in	--	0.80	0.80	0.80	4.60	--	3.21	3.21	3.21

TABLE 3-II (CONCLUDED). GEOMETRIC PARAMETERS OF SINGLE FLOW THERMAL ACOUSTIC SHIELD NOZZLES.

D. TOTAL EXHAUST PARAMETERS

PARAMETERS	C O N F I G U R A T I O N #								
	TAS-1	TAS-2	TAS-3	TAS-4	TAS-5	TAS-6	TAS-7	TAS-8	TAS-9
Total Throat Area, $A_{th}^T$ , in <sup>2</sup>	25.28	34.03	43.49	42.77	34.61	26.15	34.90	44.36	43.64
$D_{eq}$ based on $A_{th}^T$ , $D_{eq}^{th}$ , in	5.67	6.58	7.44	7.38	6.64	5.77	6.67	7.52	7.45
Total Exit Area, $A_e^T$ , in <sup>2</sup>	25.28	34.03	43.49	42.77	37.61	26.15	34.90	44.36	43.64
$D_{eq}$ based on $A_e^T$ , $D_{eq}^e$ , in	5.67	6.58	7.44	7.38	6.92	5.77	6.67	7.52	7.45
Plug Half Angle, deg.	15°	15°	15°	15°	15°	15°	15°	15°	15°

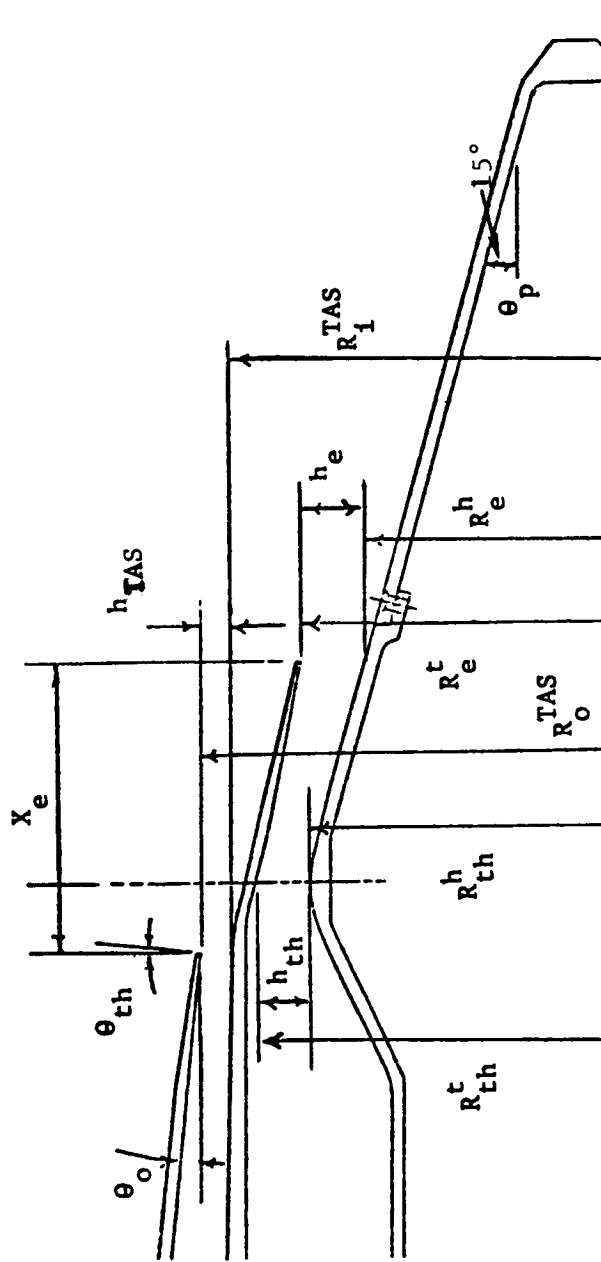


FIGURE 3.1. A SCHEMATIC SKETCH OF A TYPICAL THERMAL ACOUSTIC SHIELD NOZZLE WITH DEFINITION OF SALIENT GEOMETRIC PARAMETERS.



**FIGURE 3.2.** 32 CHUTE TURBOJET SUPPRESSOR WITH STATIC PRESSURE INSTRUMENTATION FOR BASE PRESSURE MEASUREMENT.

### 3.2 SCOPE OF TESTING

The scope of testing can be summarized under:

- A. Acoustic Tests
- B. Laser Velocimeter Tests
- C. Aerodynamic Calibration and Diagnostic Tests

The following subsections contain the salient details and a brief discussion of the rationale for the testing performed under each of the above categories.

#### 3.2.1 ACOUSTIC TESTS

In order to develop a technology base for the thermal acoustic shield concept for nozzles with single flow primary nozzles, data for a total of 314 acoustic test points were obtained for the nine (9) configurations (see Reference 3.4). Table 3-III shows the breakdown of the acoustic test points for each configuration. The aerodynamic flow conditions corresponding to the acoustic test points of each of the configurations along with the rationale for the testing are included in this subsection. Sample sheets specifying the variables listed in the tables that summarize the aerodynamic flow conditions are presented in Table 3-IV. In addition to the core and shield jet parameters, the tabulated data contain the mixed conditions that are calculated on a mass-averaged basis for velocity and total temperature. The mass-averaged velocity ( $V^{\text{mix}}$ ) and the mass-averaged total temperature ( $T_T^{\text{mix}}$ ) are calculated using the following expressions:

$$V^{\text{mix}} = \frac{\dot{w}^j V^j + \dot{w}^{\text{sj}} V^{\text{sj}}}{\dot{w}^j + \dot{w}^{\text{sj}}} \quad (3.1)$$

and

$$T_T^{\text{mix}} = \frac{\dot{w}^j T_T^j + \dot{w}^{\text{sj}} T_T^{\text{sj}}}{\dot{w}^j + \dot{w}^{\text{sj}}} \quad (3.2)$$

Table 3-III Breakdown of the Acoustic Test Points for Single Primary Flow Nozzles With/ Without Thermal Acoustic Shield.

Config.	Description of the Configuration	Orientation	Acous. Test Pts		Comments
			Static	Flight	
TAS-1	Baseline unshielded un-suppressed annular plug nozzle	See Note 1	8	8	Simulate an engine operating line
TAS-2	Un-suppressed annular plug nozzle with 180° TAS of 0.48" thickness	Sideline <sup>(2)</sup>	6	6	" " " " "
"	"	Community <sup>(2)</sup>	6	6	" " " " "
"	"	Opposite <sup>(2)</sup>	6	6	" " " " "
"	"	Sideline <sup>(2)</sup>	11	11	V <sub>r</sub> , CV <sub>r</sub> , T <sub>r</sub> <sup>2</sup> parametric study at Takeoff condition
"	"	Community <sup>(2)</sup>	13	12	V <sub>r</sub> , CV <sub>r</sub> , T <sub>r</sub> <sup>2</sup> parametric study at Cutback condition
TAS-3	Un-suppressed annular plug nozzle with 180° TAS of 0.97" thickness	Sideline <sup>(2)</sup>	8	8	Simulate an engine operating line
"	"	Community <sup>(2)</sup>	8	8	" " " " "
TAS-4	Un-suppressed annular plug nozzle with 360° TAS of 0.48" thickness	See Note 1	8	8	" " " " "
TAS-5	Convergent-Divergent annular plug nozzle with 180° TAS of 0.48" thickness	Sideline <sup>(2)</sup>	9	9	Evaluate T.A.S. effectiveness on a C-D annular plug nozzle
TAS-6	Unshielded 32-chute annular plug suppressor nozzle	See Note 1	8	8	Simulate an engine operating line
TAS-7	32-chute annular plug suppressor nozzle with 180° TAS of 0.48" thickness	Sideline <sup>(2)</sup>	6	6	" " " " "
"	"	Community <sup>(2)</sup>	6	6	" " " " "
"	"	Sideline <sup>(2)</sup>	11	11	V <sub>r</sub> , CV <sub>r</sub> , T <sub>r</sub> <sup>2</sup> , parametric study at Takeoff condition
"	"	Community <sup>(2)</sup>	11	11	V <sub>r</sub> , CV <sub>r</sub> , T <sub>r</sub> <sup>2</sup> , parametric study at Cutback condition
TAS-8	32-chute annular plug suppressor nozzle with 180° TAS of 0.97" thickness	Sideline <sup>(2)</sup>	8	8	Simulate an engine operating line
"	"	Community <sup>(2)</sup>	8	8	" " " " "
"	"	Sideline <sup>(2)</sup>	-	8	V <sub>r</sub> , CV <sub>r</sub> , T <sub>r</sub> <sup>2</sup> , parametric study at Takeoff condition
"	"	Community <sup>(2)</sup>	-	9	V <sub>r</sub> , CV <sub>r</sub> , T <sub>r</sub> <sup>2</sup> , parametric study at Cutback condition
TAS-9	32-chute annular plug suppressor nozzle with 360° TAS of 0.48" thickness	See Note 1	8	8	Simulate an engine operating line
Total Acoustic Test Points			149	165	Grand Total of 314 Acoustic Test Points

**NOTES:**

- (1) Due to geometric axisymmetry the choice of orientation does not arise,
- (2) For partial shields, the azimuthal locations for sideline, community and opposite community are indicated in the sketch below.

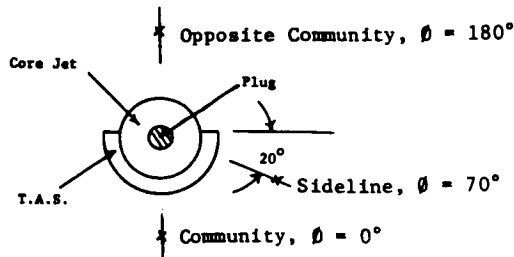
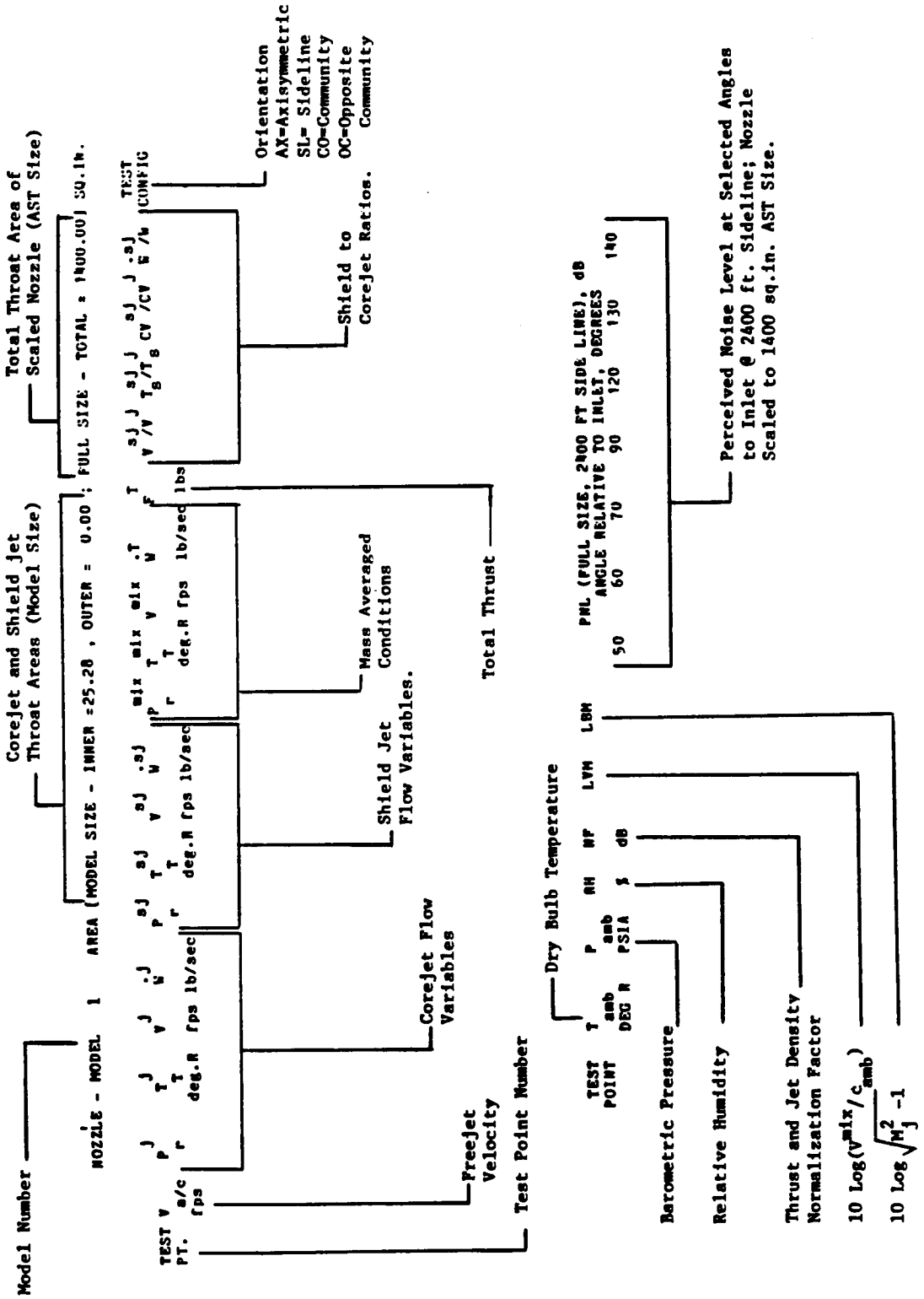


TABLE 3-IV DESCRIPTION OF AERODYNAMIC DATA SHEET



where

- $W^j$  = weight flow through the core jet  
 $W^{sj}$  = weight flow through the shield jet  
 $V^j$  = ideally expanded core jet velocity  
 $V^{sj}$  = ideally expanded shield jet velocity  
 $T_T^j$  = stagnation temperature of the core jet  
 $T_T^{sj}$  = stagnation temperature of the shield jet

One may note that  $V^{mix}$  can also be referred to as specific ideal gross thrust since it is defined as (total thrust/total weight flow) and  $T_T^{mix}$  can also be referred to as specific stagnation enthalpy since it is defined as (total stagnation enthalpy/total weight flow). From the known  $V^{mix}$  and  $T_T^{mix}$  other mixed flow parameters have been calculated by using standard isentropic relations. The weight flows tabulated correspond to scaled up area of the nozzles. Certain key aerodynamic ratios are defined below:

$$V_r = \frac{V^{sj}}{V^j} \quad (3.3)$$

$$CV_r = CV^{sj}/CV^j = \frac{C^{sj} + V^{sj}}{C^j + V^j} \quad (3.4)$$

where

$C^{sj}$  = sonic velocity of shield jet based on shield jet exit condition

$C^j$  = sonic velocity of core jet based on core jet exit condition

$$T_r^s = \frac{T_S^{sj}}{T_S^j} \quad (3.5)$$

where

$T_S^{sj}$  = is the static temperature of shield jet based on shield jet exit condition

$T_S^j$  = is the static temperature of core jet based on core jet exit condition



$CV_r$  is a measure of the discontinuity of the phase velocity at the core jet and shield jet interface and serves as an indicator of the extent of noise transmission loss due to such a discontinuity.

The thermal acoustic shield weight flow ratio is defined as:

$$W_r = \frac{.sj}{W} \quad (3.6)$$

$$W_r = \frac{.j \quad .sj}{W + W}$$

The ambient pressure and temperature, along with the relative humidity in the General Electric Anechoic Facility at the time of the test, are presented in the aerodynamic data tables. In addition, the measured far-field PNL data extrapolated to a 731.5 m (2400 ft.) distance and scaled to an AST product size of  $0.903m^2$  ( $1400 \text{ in.}^2$ ) also are presented in the tables. The selected data correspond to microphone locations of  $\theta_1 = 50^\circ, 60^\circ, 70^\circ, 90^\circ, 120^\circ, 130^\circ$  and  $140^\circ$ .

The normalization factor (NF) found in these tables is employed to normalize the measured perceived noise level (PNL) on a reference thrust and jet density basis as follows:

$$PNLN = \text{Normalized PNL} = PNL + NF \quad (3.7)$$

$$\text{where } NF = -10 \log \left[ \frac{F^T}{F_{ref}} \left( \frac{\rho_{mix}}{\rho_{amb}} \right)^{\omega-1} \right] \quad (3.8)$$

and where

- $F^T$  = total ideal gross thrust
- $F_{ref}$  = reference thrust (5130 lbs)
- $\rho_{mix}$  = density based on mass-averaged conditions
- $\rho_{amb}$  = ambient air density
- $\omega$  = density exponent

Table 3-V gives the test matrix for configuration TAS-1 simulating an engine operating line which has been constructed utilizing the cycle information on the General Electric YJ101 Engine (see Reference 3.3) and staying within facility temperature limits (see Reference 3.5).



An alternate engine operating line was constructed for configuration TAS-2 keeping the total temperature of the core and shield jets approximately the same. In a practical application of the thermal acoustic shield, the shield jet flow could be obtained from the core jet flow through a choke plate flow conditioning device, in which case, the total temperature of the shield jet would equal that of the core jet and the pressure ratio of the shield jet will be lower compared to that of the core jet due to losses in the choke plate device. The shield to core jet velocity ratio was set at a nominal value of 0.6. Table 3-VI constitutes the test matrix for configuration TAS-2 simulating an engine operating line in sideline, community and opposite community orientations. The objectives for measuring the acoustic data at the three (3) azimuthal locations were to determine the azimuthal variation of the acoustic field for a partial shield and also to determine the reflective and refractive characteristics of the partial shield.

Parametric studies were also conducted by keeping the core jet conditions constant and varying the shield jet conditions to determine the influence of  $V_r$ ,  $CV_r$ , and  $T_r^S$  on the acoustic behavior of the thermal acoustic shield. A typical takeoff case (the core jet condition corresponding to test point 209 in Table 3-VI) and a typical cutback case (the core jet condition corresponding to test point 221 in Table 3-VI) were selected. Tables 3-VII and 3-VIII respectively list the aerodynamic conditions for the takeoff and cutback parametric studies conducted. The takeoff parametric study has been conducted in sideline orientation and the cutback parametric study has been conducted in community orientation.

Figures 3.3 and 3.4 respectively show plots of the various test points for the takeoff and cutback cases for  $V_r$ ,  $CV_r$  and  $T_r^S$  parametric study. The constraints on the selection of the test points were:

- A. The maximum shield total temperature that could be achieved in the facility is  $\approx 1730^\circ\text{R}$ .
- B. The minimum shield total temperature that could be achieved in the facility without causing burner instability is  $\approx 800^\circ\text{R}$ .



TABLE 3-VI. (CONT'D) TEST MATRIX FOR CONFIGURATION TAS-2 SIMULATING ENGINE OPERATING LINE IN SIDELINE, COMMUNITY, AND OPPOSITE COMMUNITY ORIENTATIONS.

\*\*\*\*\* BRITISH UNITS \*\*\*\*\*

TEST POINT	T amb DEC R	P amb PSIA	RH %	MF dB	LVM	LBM	50	PML (FULL SIZE, 2400 FT SIDE LINE), dB ANGLE RELATIVE TO INLET, DEGREES					140	SIDELINE	COMMUNITY	OPPOSITE COMMUNITY
								60	70	90	120	130				
205	487.6	14.52	36	-3.3	2.12	-10.00	86.5	87.9	91.2	93.5	98.9	101.2	101.1			
206	492.9	14.52	82	-3.2	2.10	-10.00	87.8	88.4	91.0	91.7	94.6	96.3	95.5			
207	487.4	14.51	36	-4.0	2.56	-3.34	91.0	92.9	95.9	97.7	103.3	106.5	106.4			
208	493.5	14.52	82	-3.9	2.54	-3.42	93.1	93.8	96.4	96.1	99.0	101.2	101.8			
209	488.8	14.48	36	-4.6	2.85	-2.03	92.2	94.2	98.1	99.7	105.0	109.4	107.4			
210	490.4	14.41	86	-4.6	2.89	-2.00	95.5	97.0	99.8	98.7	102.3	105.2	106.2			
211	488.3	14.48	36	-5.1	3.08	-1.41	93.3	95.5	99.5	101.2	106.7	111.9	108.9			
212	493.6	14.52	82	-5.0	3.10	-1.43	97.8	99.0	101.6	101.1	103.8	108.0	107.6			
213	488.1	14.48	36	-5.9	3.34	-0.64	97.0	98.9	102.7	104.1	109.0	114.9	110.5			
214	495.2	14.53	82	-5.9	3.32	-0.64	102.4	102.9	105.9	104.8	106.3	111.0	110.6			
215	486.5	14.48	34	-6.8	3.57	-0.01	99.9	102.0	105.9	107.3	111.5	117.8	112.6			
216	498.5	14.50	82	-6.9	3.57	0.03	105.7	105.5	108.9	108.4	109.7	114.8	112.5			
221	485.1	14.58	88	-3.1	1.98	-10.00	85.5	87.5	89.0	90.5	97.9	101.2	100.8			
222	487.2	14.52	49	-3.4	2.08	-10.00	86.2	88.0	89.0	87.9	93.5	95.4	95.1			
223	487.2	14.52	74	-4.0	2.46	-3.54	90.0	92.5	93.6	93.8	101.2	106.2	107.7			
224	488.8	14.52	49	-3.9	2.54	-3.42	91.6	93.4	93.9	93.8	98.0	101.1	101.4			
225	488.2	14.51	74	-4.8	2.79	-2.03	92.1	94.9	96.4	99.0	104.4	109.7	106.8			
226	487.4	14.51	49	-4.7	2.81	-2.04	95.5	97.1	97.5	98.0	100.8	104.8	105.8			
227	487.3	14.57	74	-5.0	3.06	-1.48	93.1	95.8	97.7	100.6	106.8	112.1	109.7			
228	487.7	14.52	74	-5.1	3.02	-1.48	97.2	99.2	99.6	100.6	102.6	107.4	107.9			
229	487.6	14.57	74	-5.9	3.33	-0.67	97.0	99.6	101.3	104.2	109.1	114.6	109.4			
230	488.0	14.52	74	-5.9	3.27	-0.68	101.2	103.0	103.5	103.7	105.8	111.0	110.6			
231	488.1	14.51	74	-6.9	3.51	-0.03	99.5	102.6	104.4	107.3	111.4	117.3	112.5			
232	488.3	14.52	74	-6.8	3.52	-0.04	104.7	106.7	107.7	107.9	109.9	114.5	112.1			
287	478.0	14.63	52	-3.1	2.13	-10.00	86.2	89.1	91.9	94.9	100.2	102.0	102.1			
288	478.3	14.63	52	-3.0	2.09	-10.00	86.2	89.7	92.1	93.0	95.5	97.3	95.5			
289	478.0	14.63	52	-3.9	2.59	-3.47	90.9	93.8	96.9	98.6	103.4	106.7	109.1			
290	481.1	14.63	52	-3.9	2.57	-3.47	94.3	95.8	97.7	97.7	100.3	102.2	101.7			
291	478.3	14.63	52	-4.6	2.92	-2.02	92.8	95.9	99.1	101.0	105.4	109.8	105.8			
292	483.3	14.64	52	-4.2	2.80	-2.53	96.7	98.6	101.0	100.7	103.2	106.3	105.8			
293	477.4	14.62	52	-4.9	3.15	-1.45	94.0	97.2	100.6	102.5	106.8	112.4	111.1			
294	482.4	14.63	52	-4.9	3.12	-1.45	99.2	100.8	102.4	102.4	104.9	108.4	108.0			
295	476.2	14.62	52	-5.8	3.40	-0.65	98.0	100.5	103.7	105.6	109.6	115.4	112.1			
296	479.7	14.63	52	-5.9	3.39	-0.62	102.8	105.3	106.9	106.1	107.8	112.2	110.3			
297	476.9	14.62	52	-6.8	3.65	0.03	101.0	103.8	106.9	108.5	111.8	117.8	112.3			
298	478.5	14.63	52	-6.7	3.65	0.02	106.3	108.5	110.4	109.4	110.4	115.0	112.1			

TABLE 3-VII. TEST MATRIX FOR CONFIGURATION TAS-2 FOR V, CV, AND T<sup>S</sup> PARAMETRIC STUDY FOR A TAKEOFF CASE IN SIDELINE ORIENTATION

\*\*\*\*\* BRITISH UNITS\*\*\*\*\*

NOZZLE - MODEL TAS-2 CONTINUED

TEST PT.	V a/c	P r	T deg.R	J T	J W	J W	P r	T deg.R	V aj	V aj	V aj	W .aj	P r	T deg.R	mix T	mix V	mix W	T F	V /V <sub>T<sup>S</sup></sub>	aj J T <sub>S</sub>	aj J CV	aj J W /M	TEST CONFIG
237	0	2.722	1655	1676	2237	528.0	1.616	913	1185	145.4	2.419	1495	2010	673.	42085				0.53	0.62	0.65	0.22	SL
238	400	2.718	1676	1676	2250	522.6	1.577	904	1152	141.4	2.406	1512	2016	664.	41613				0.51	0.61	0.64	0.21	SL
239	0	2.792	1647	1647	2256	543.4	1.395	1138	1115	104.9	2.452	1565	2071	648.	41746				0.49	0.83	0.68	0.16	SL
240	400	2.706	1673	1673	2244	518.4	1.419	1166	1156	105.8	2.389	1587	2059	624.	39957				0.52	0.82	0.69	0.17	SL
241	0	2.712	1649	1649	2229	527.5	1.311	1358	1104	85.3	2.387	1608	2073	613.	39483				0.50	1.00	0.71	0.14	SL
242	400	2.705	1659	1659	2234	521.8	1.308	1389	1112	83.5	2.382	1622	2079	605.	39123				0.50	1.01	0.72	0.14	SL
243	0	2.696	1657	1657	2230	523.0	1.264	1627	1126	71.8	2.373	1654	2096	595.	38765				0.50	1.20	0.76	0.12	SL
244	400	2.693	1639	1639	2216	522.9	1.267	1594	1121	72.6	2.371	1634	2082	596.	38552				0.51	1.19	0.76	0.12	SL
245	0	2.736	1646	1646	2236	532.9	1.398	1664	1355	86.6	2.418	1648	2112	620.	40681				0.61	1.21	0.82	0.14	SL
246	400	2.692	1667	1667	2235	518.1	1.408	1620	1351	88.4	2.385	1660	2106	606.	39703				0.60	1.15	0.81	0.15	SL
247	0	2.718	1648	1648	2231	529.0	1.504	1415	1371	105.4	2.420	1609	2088	634.	41174				0.61	1.00	0.78	0.17	SL
248	400	2.681	1676	1676	2237	519.2	1.486	1474	1380	101.8	2.389	1643	2096	621.	40469				0.62	1.03	0.79	0.16	SL
249	0	2.661	1676	1676	2230	513.2	1.605	1172	1336	126.8	2.389	1576	2053	640.	40833				0.60	0.79	0.73	0.20	SL
250	400	2.705	1673	1673	2243	519.5	1.613	1186	1352	126.2	2.425	1577	2069	646.	41524				0.60	0.81	0.73	0.20	SL
251	0	2.759	1642	1642	2241	537.7	1.879	920	1350	171.8	2.505	1467	2025	709.	44674				0.60	0.61	0.69	0.24	SL
252	400	2.654	1680	1680	2230	509.7	1.897	933	1369	171.7	2.430	1492	2013	681.	42634				0.61	0.60	0.69	0.25	SL

TEST POINT	T amb DEG R	P amb PSIA	RH %	NF dB	LVH	LBM	PWL (FULL SIZE, 2400 FT SIDE LINE), dB						
							50	60	70				
237	481.2	14.47	34	-5.2	2.72	-1.73	92.2	94.2	98.3	99.7	105.9	110.1	109.8
238	491.1	14.44	86	-5.2	2.69	-1.79	96.1	97.1	100.1	99.9	102.5	105.4	106.5
239	482.3	14.49	34	-5.0	2.84	-1.75	92.8	94.6	98.3	99.8	105.6	110.4	110.0
240	492.4	14.38	86	-4.8	2.77	-1.98	96.2	97.2	100.5	99.6	102.2	105.2	105.9
241	484.5	14.49	34	-4.6	2.84	-2.08	92.6	94.5	98.3	99.7	105.7	110.2	109.1
242	490.9	14.41	86	-4.6	2.82	-2.10	96.1	96.9	100.0	99.1	102.1	105.2	105.5
243	483.8	14.49	34	-4.4	2.89	-2.19	92.6	94.4	98.2	99.9	105.2	109.3	109.2
244	493.7	14.42	86	-4.5	2.82	-2.19	95.4	96.6	100.1	98.9	102.2	105.6	106.4
245	486.3	14.49	34	-4.7	2.91	-1.91	92.3	94.1	98.1	99.8	105.0	109.2	108.7
246	492.9	14.42	86	-4.6	2.87	-2.03	95.4	97.5	100.1	99.4	102.0	105.0	106.0
247	483.5	14.49	34	-4.8	2.87	-1.86	92.6	94.4	98.2	99.7	105.6	110.0	109.3
248	492.7	14.55	86	-4.7	2.85	-1.99	95.9	96.9	100.1	99.3	102.0	105.2	106.0
249	482.0	14.49	34	-4.9	2.81	-1.92	92.2	94.1	98.0	99.8	105.7	110.5	109.8
250	491.3	14.41	86	-5.0	2.80	-1.79	95.7	97.1	100.1	99.7	102.0	105.3	106.0
251	481.8	14.48	34	-5.6	2.75	-1.42	91.9	93.7	97.5	98.4	105.7	110.2	109.7
252	492.6	14.44	86	-5.4	2.67,	-1.66	95.5	96.6	99.7	98.9	102.2	105.7	106.1









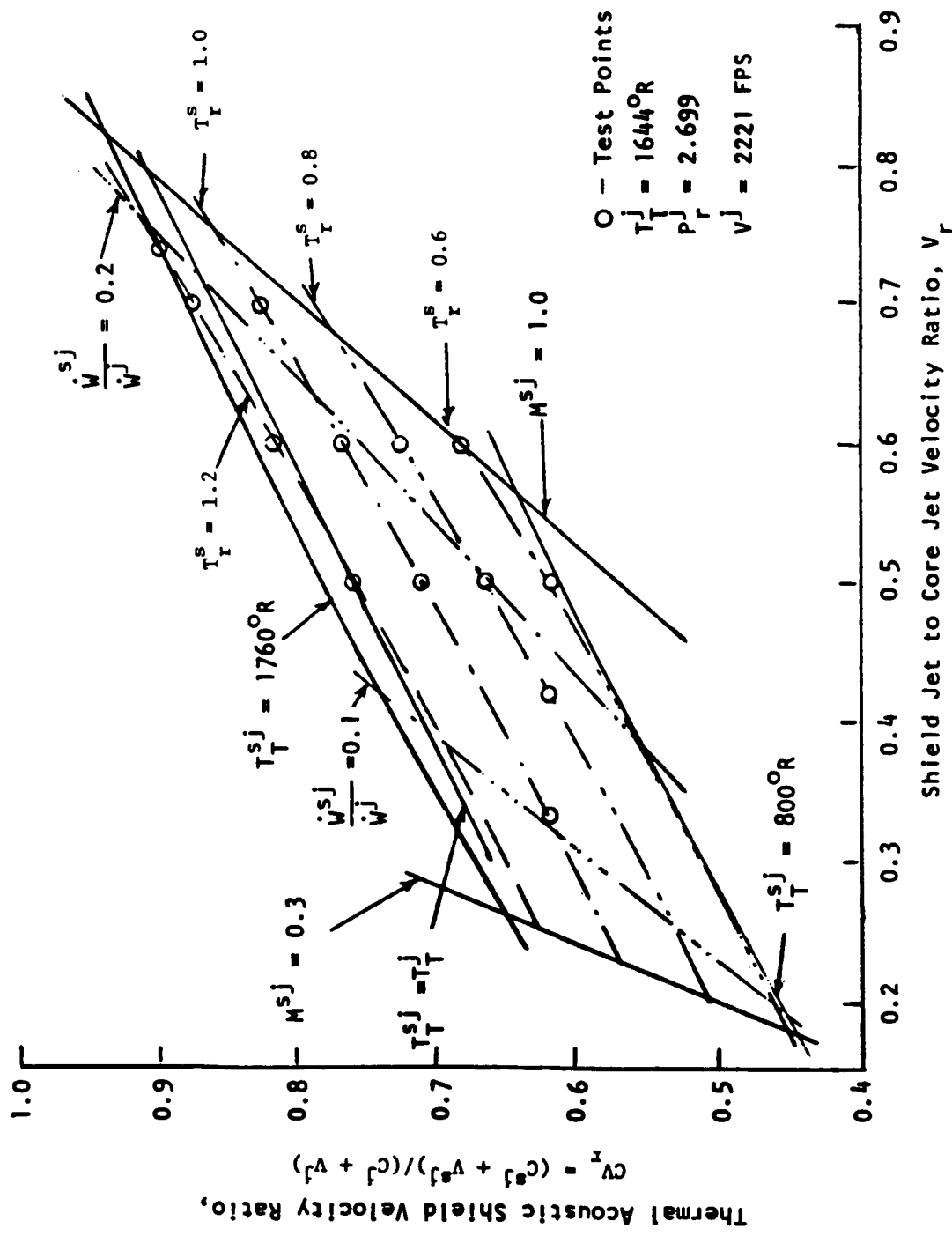


FIGURE 3.3. SELECTION OF TEST POINTS FOR A PARAMETRIC STUDY OF  $V_r$ ,  $CV_r$ , and  $T_r^S$  FOR A TAKEOFF CASE.

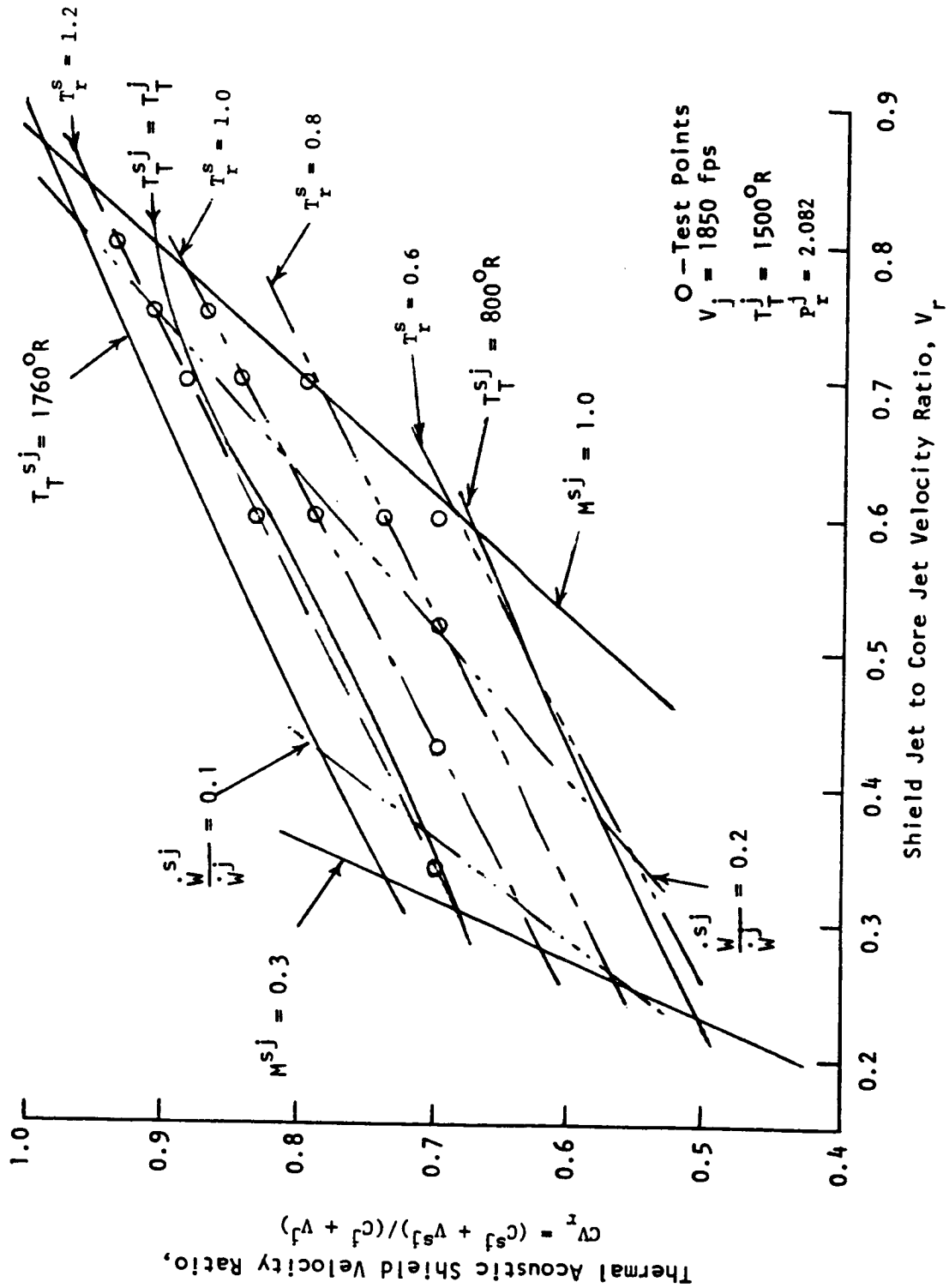


FIGURE 3.4. SELECTION OF TEST POINTS FOR A PARAMETRIC STUDY OF  $V_r$ ,  $CV_r$ , and  $T_r^s$  FOR A CUTBACK CASE.

- C. To avoid any shock noise contributions from the shield, the maximum exit Mach number of the shield is restricted to 1.0.
- D. The minimum value of the Mach number of the shield is chosen to be 0.3 so that reasonable values of velocity ratio could be obtained.

The above four (4) constraints bounded the domain of parametric variations. Lines of constant static temperature ratio (i.e.,  $T_S^{sj}/T_S^j = T_r^s$ ) are shown in Figures 3.3 and 3.4, as well as lines of constant weight flow ratios (viz,  $W^{sj}/W^j = 0.1$  and  $0.2$ ). Next, lines of equal total temperatures (i.e.  $T_T^{sj} = T_T^j$ ) are shown in the same figures. The equations which were utilized in evolving the above parametric study are listed below:

$$V_r = \frac{v^{sj}}{v^j} = \frac{M^{sj}}{M^j} \sqrt{\frac{T_S^{sj}}{T_S^j}} \quad (3.9)$$

$$CV_r = \frac{C^{sj} + v^{sj}}{C^j + v^j} = \frac{T_S^{sj}}{T_S^j} \times \left[ \frac{1 + M^{sj}}{1 + M^j} \right] \quad (3.10)$$

$$\frac{W^{sj}}{W^j} = \frac{A^{sj}}{A^j} \frac{M^{sj}}{M^j} \sqrt{\frac{T_S^j}{T_S^{sj}}} \quad (3.11)$$

$$\frac{T_T^{sj}}{T_S^{sj}} = 1 + \frac{\gamma-1}{2} (M^{sj})^2 \quad (3.12)$$

where

- $M^{sj}$  = Ideally expanded shield jet Mach number  
 $M^j$  = Ideally expanded core jet Mach number  
 $A^{sj}$  = Shield jet exit area  
 $A^j$  = Core jet area  
 $\gamma$  = Ratio of specific heats

The engine operating line for configurations TAS-3 and TAS-4 were constructed as in the case of configuration TAS-2, that is, by keeping the total temperature of the shield and core jets approximately the same and by setting the shield to core jet velocity ratio at a nominal value of 0.6. Configuration TAS-3 was tested both in sideline and community orientations whereas the question of orientation does not arise for configuration TAS-4. Tables 3-IX and 3-X respectively contain the test matrices for configurations TAS-3 and TAS-4.

The effect of the partial thermal acoustic shield on a convergent-divergent annular plug nozzle designed for an exit Mach number of 1.4 (i.e., a design pressure ratio = 3.1) was tested according to the test matrix shown in Table 3-XI, in the sideline orientation. The core nozzle was maintained at the design condition, an underexpanded condition and an overexpanded condition. At each of the above core jet conditions, the shield to core jet velocity ratios were nominally set 0.5, 0.6 and 0.7, keeping the total temperatures of the shield and core jets approximately the same, to diagnose the influence of velocity ratio.

The test matrices for the 32-chute annular plug suppressor nozzle with and without the thermal acoustic shields were constructed in a similar fashion to that of the unsuppressed annular plug nozzle with and without the thermal acoustic shields. The test matrix for configuration TAS-6 shown in Table 3-XII was intended to simulate an identical engine operating line as that of configuration TAS-1. The minor differences are due to experimental variations.

Table 3-XIII shows the test matrix for configuration TAS-7 simulating engine operating line in sideline and community orientations, keeping the total temperatures of the shield and core jet approximately the same and setting the shield to core jet velocity ratio nominally at 0.6. Tables 3-XIV show the test matrix for configuration TAS-7, for  $V_r$ ,  $CV_r$  and  $T_r^s$  parametric studies for a takeoff case in sideline orientation and is similar to Table 3-VII. Table 3-XV is the test matrix for  $V_r$ ,  $CV_r$  and  $T_r^s$  parametric studies for a cutback case in community orientation for configuration TAS-7 and is similar in scope to Table 3-VIII.















TABLE 3-XIII (CONT'D) TEST MATRIX FOR CONFIGURATION TAS-7 SIMULATING ENGINE OPERATING LINE IN SIDELINE AND COMMUNITY ORIENTATIONS

\*\*\*\*\* BRITISH UNITS \*\*\*\*\*

TEST POINT	T amb DEG R	P amb PSIA	RH %	MF dB	LVM	LBM	PWL (FULL SIZE, 2400 FT SIDE LINE), dB							
							ANGLE RELATIVE TO INLET, DEGREES	60	70	80	90	120	130	140
705	512.0	14.49	64	-3.5	1.97	-10.00	84.8	85.8	90.4	94.4	94.4	98.5	96.6	94.4
706	514.8	14.52	64	-3.6	1.97	-10.00	89.8	89.8	92.9	94.5	94.5	96.6	92.7	87.7
707	511.9	14.49	64	-4.2	2.42	-3.44	87.6	88.2	92.6	96.1	96.1	100.7	99.2	97.4
708	516.1	14.52	64	-4.3	2.41	-3.39	91.3	91.0	94.5	96.5	96.5	99.5	96.2	91.7
709	511.7	14.48	64	-4.8	2.77	-2.00	90.5	90.8	95.2	98.0	98.0	102.9	101.7	101.4
710	514.9	14.52	49	-4.8	2.77	-2.03	93.0	92.8	96.2	98.4	98.4	101.6	99.3	95.5
711	508.3	14.48	45	-5.1	3.01	-1.42	94.1	93.2	97.4	99.5	99.5	104.7	103.8	104.2
712	515.7	14.51	49	-5.2	2.99	-1.42	94.1	94.3	97.3	99.3	99.3	103.6	100.7	97.9
713	508.6	14.48	45	-6.2	3.22	-0.60	95.2	95.9	100.0	101.4	101.4	106.4	106.3	107.8
714	514.7	14.52	49	-6.1	3.22	-0.63	97.0	97.0	99.9	101.0	101.0	105.1	102.8	101.1
715	506.6	14.48	45	-7.1	3.45	0.05	96.5	97.6	101.4	103.2	103.2	108.7	110.3	110.8
716	514.8	14.52	49	-7.1	3.46	0.02	99.6	99.7	102.3	103.8	103.8	107.3	105.6	105.6
721	501.5	14.41	82	-3.4	1.99	-10.00	85.7	86.5	90.8	94.7	94.7	98.1	97.2	93.9
722	497.6	14.40	63	-3.3	2.05	-10.00	90.1	90.1	93.2	94.9	94.9	97.4	93.4	88.7
723	498.3	14.37	84	-3.9	2.51	-3.50	88.1	88.8	93.3	97.2	97.2	100.3	100.2	96.7
724	501.1	14.40	88	-4.0	2.48	-3.46	93.0	92.0	95.0	97.0	97.0	99.4	96.6	92.0
725	497.8	14.32	84	-4.7	2.83	-1.98	91.1	91.4	96.1	98.7	98.7	102.1	102.1	100.4
726	499.4	14.41	88	-4.7	2.82	-2.05	94.4	93.7	96.3	98.7	98.7	101.6	99.8	95.9
727	497.9	14.33	84	-5.0	3.02	-1.46	92.5	93.1	97.5	99.9	99.9	103.6	104.0	103.2
728	499.9	14.40	88	-5.1	3.03	-1.44	95.1	94.5	97.2	99.5	99.5	103.3	101.2	98.5
729	497.1	14.31	84	-5.9	3.28	-0.63	95.4	95.6	100.0	101.6	101.6	105.8	106.9	106.7
730	499.8	14.40	88	-6.0	3.28	-0.62	98.2	97.9	100.6	101.9	101.9	105.7	104.1	102.1
731	498.6	14.30	84	-6.8	3.47	-0.08	96.6	97.3	101.3	102.9	102.9	107.6	109.3	110.2
732	501.9	14.43	88	-7.0	3.50	0.04	100.4	100.3	103.1	103.5	103.5	107.1	106.7	106.5

SIDELINE

COMMUNITY

TABLE 3-XIV. TEST MATRIX FOR CONFIGURATION TAS-7 FOR V, CV, AND T<sub>r</sub> PARAMETRIC STUDY FOR A TAKEOFF CASE IN SIDELINE ORIENTATION

\*\*\*\*\* BRITISH UNITS \*\*\*\*\*

NOZZLE - MODEL TAS-7 CONTINUED

TEST POINT	V	a/c	P	J	T	deg. R	fpa	lb/sec	R	deg. R	V	deg. R	fpa	lb/sec	W	.sj	P	mix	T	V	mix	V	mix	T	F	T	lb/sec	T	V/V <sub>r</sub>	T <sub>s</sub> /T <sub>r</sub>	CV	/CV	W	/W	T	TEST CONFIG
737	0	2.694	1647	1647	1647	1.575	917	1150	137.0	2.398	1496	2003	666.	41453	0.52	0.63	0.65	0.21	SL																	
738	0	2.692	1655	1655	1655	1.552	911	1137	134.2	2.391	1503	2004	659.	41035	0.51	0.63	0.64	0.20	SL																	
739	0	2.701	1639	1639	1639	1.399	1137	1120	102.8	2.390	1557	2040	634.	40230	0.50	0.62	0.68	0.16	SL																	
740	0	2.710	1656	1656	1656	1.423	1142	1148	105.0	2.400	1571	2054	633.	40417	0.51	0.61	0.69	0.17	SL																	
741	0	2.701	1652	1652	1652	1.300	1439	1119	79.3	2.370	1624	2083	609.	39413	0.50	1.05	0.73	0.13	SL																	
742	0	2.680	1678	1678	1678	1.309	1441	1135	80.1	2.370	1646	2090	599.	38890	0.51	1.03	0.73	0.13	SL																	
743	0	2.701	1645	1645	1645	1.252	1659	1116	67.8	2.386	1647	2097	598.	38996	0.50	1.24	0.76	0.11	SL																	
744	0	2.698	1656	1656	1656	1.265	1619	1126	70.5	2.384	1652	2100	600.	39134	0.50	1.19	0.76	0.12	SL																	
745	0	2.694	1651	1651	1651	1.386	1662	1338	83.3	2.391	1653	2104	612.	39999	0.60	1.20	0.81	0.14	SL																	
746	0	2.694	1655	1655	1655	1.417	1580	1345	88.8	2.394	1645	2100	617.	40219	0.60	1.13	0.80	0.14	SL																	
747	0	2.695	1648	1648	1648	1.502	1406	1335	105.1	2.409	1598	2076	634.	40910	0.60	0.95	0.76	0.17	SL																	
748	0	2.703	1654	1654	1654	1.502	1406	1335	102.4	2.416	1614	2089	629.	40844	0.61	0.99	0.76	0.16	SL																	
749	0	2.694	1642	1642	1642	1.610	1200	1356	122.6	2.424	1559	2056	653.	41699	0.61	0.83	0.75	0.19	SL																	
750	0	2.698	1666	1666	1666	1.623	1195	1364	123.5	2.430	1576	2070	647.	41651	0.61	0.81	0.74	0.19	SL																	
751	0	2.691	1639	1639	1639	1.885	926	1350	167.4	2.463	1468	2009	697.	43515	0.61	0.61	0.69	0.24	SL																	
752	0	2.684	1668	1668	1668	1.886	946	1373	165.0	2.458	1494	2026	686.	43206	0.61	0.61	0.69	0.24	SL																	
753	0	2.695	1647	1647	1647	1.547	1731	1567	96.2	2.420	1660	2121	625.	41205	0.71	1.22	0.88	0.15	SL																	
754	0	2.686	1665	1665	1665	1.543	1743	1560	95.8	2.412	1677	2129	621.	41100	0.70	1.21	0.87	0.15	SL																	
755	0	2.700	1640	1640	1640	1.659	1502	1563	113.2	2.447	1616	2104	645.	42152	0.70	1.04	0.84	0.18	SL																	
756	0	2.697	1657	1657	1657	1.662	1492	1561	113.2	2.445	1627	2111	638.	41882	0.70	1.02	0.84	0.18	SL																	
757	0	2.694	1643	1643	1643	1.615	1757	1650	100.9	2.433	1661	2128	630.	41698	0.74	1.23	0.80	0.16	SL																	
758	0	2.685	1670	1670	1670	1.620	1763	1650	101.4	2.427	1685	2141	626.	41643	0.74	1.21	0.90	0.16	SL																	

TEST POINT	P	amb	PSIA	deg. R	LVM	LFM	LBW	deg. R	50	60	70	90	120	130	140
737	508.6	14.48	45	-5.4	2.58	-1.83	90.5	91.4	95.3	98.4	102.8	101.0	99.4		
738	512.1	14.41	41	-5.4	2.57	-1.85	93.5	93.4	96.4	98.2	101.7	98.8	95.3		
739	507.8	14.48	45	-5.1	2.66	-1.98	90.5	91.2	95.4	98.2	102.9	101.8	99.7		
740	513.1	14.42	44	-5.1	2.67	-1.93	94.1	93.6	97.3	99.0	103.2	99.1	95.2		
741	509.1	14.48	45	-4.8	2.75	-2.09	90.4	91.2	95.4	98.4	103.2	102.5	100.9		
742	514.0	14.42	44	-4.7	2.74	-2.15	93.7	92.8	95.9	98.2	101.5	99.3	95.1		
743	511.4	14.48	44	-4.7	2.77	-2.14	90.1	90.6	94.9	98.0	102.9	101.7	100.2		
744	514.2	14.51	49	-4.7	2.76	-2.14	93.4	93.4	96.3	98.4	101.6	99.1	95.4		
745	512.5	14.49	44	-4.8	2.78	-2.02	90.8	91.0	95.4	98.4	102.9	101.6	101.7		
746	518.4	14.52	49	-4.9	2.75	-1.99	92.9	92.7	96.1	98.2	101.9	99.1	95.5		
747	509.8	14.49	45	-5.1	2.73	-1.89	90.4	91.2	95.3	98.3	102.8	101.4	101.2		
748	515.2	14.41	44	-5.1	2.74	-1.87	93.8	93.8	96.2	98.5	101.9	99.3	95.3		
749	509.6	14.49	45	-5.3	2.69	-1.79	90.3	91.1	95.3	98.3	101.9	101.5	101.2		
750	514.5	14.41	44	-5.2	2.70	-1.77	93.2	93.1	96.4	98.3	101.9	99.4	95.5		
751	507.6	14.48	45	-5.7	2.60	-1.56	89.9	90.7	95.3	97.9	102.8	101.6	100.4		
752	514.6	14.42	41	-5.7	2.61	-1.57	93.7	93.2	96.1	98.4	101.1	98.7	95.2		
753	512.2	14.47	44	-4.9	2.81	-1.85	90.6	91.1	95.1	98.0	103.0	101.9	102.3		
754	513.9	14.51	49	-4.9	2.82	-1.88	92.7	92.6	96.1	97.8	101.5	99.1	95.5		
755	509.4	14.49	45	-5.1	2.79	-1.73	90.5	91.1	95.3	98.2	103.2	101.7	101.3		
756	515.2	14.41	44	-5.1	2.78	-1.74	93.3	92.9	96.2	98.4	101.6	99.1	95.5		
757	510.2	14.49	44	-5.0	2.84	-1.79	90.4	91.0	95.3	98.2	103.3	102.1	102.4		
758	518.2	14.52	49	-5.0	2.83	-1.81	93.2	92.5	95.6	98.1	101.9	99.5	95.6		

TABLE 3-XV. TEST MATRIX FOR CONFIGURATION TAS-7 FOR V, CV, AND T<sub>r</sub> PARAMETRIC STUDY FOR A CUTBACK CASE IN COMMUNITY ORIENTATION

\*\*\*\*\* BRITISH UNITS \*\*\*\*\*

NOZZLE - MODEL TAS-7 CONTINUED

TEST PT.	V a/c	P	J	T	J	V	J	P	R	T	deg.R		V		F	T	V/W	T <sub>S</sub> /T <sub>S</sub>	CV	CV/W	J	T	TEST CONFIG
											deg.R	lb/sec	deg.R	lb/sec									
763	0	2.072	1503	1503	1023	973	97.5	1.890	1414	1686	522.	27340	0.53	0.76	0.70	0.19	CO						
764	400	2.068	1520	1058	1092	969	90.3	1.885	1444	1701	511.	27038	0.52	0.81	0.71	0.18	CO						
765	0	2.069	1504	1049	938	1139	129.8	1.926	1371	1682	553.	28927	0.62	0.67	0.72	0.23	CO						
766	400	2.075	1502	1050	943	1130	127.8	1.927	1373	1684	553.	28923	0.61	0.68	0.72	0.20	CO						
767	0	2.070	1507	1050	1125	1127	104.3	1.907	1431	1707	528.	28000	0.61	0.82	0.75	0.20	CO						
768	400	2.073	1509	1054	1155	1113	99.6	1.905	1442	1713	523.	27844	0.60	0.85	0.76	0.19	CO						
769	0	2.079	1504	1054	1339	1327	1131	87.2	1.904	1474	513.	27577	0.61	0.99	0.79	0.17	CO						
770	400	2.077	1515	1060	1320	1107	85.6	1.899	1482	1733	509.	27420	0.60	0.98	0.78	0.17	CO						
771	0	2.069	1506	1050	1262	1584	1109	69.9	1.885	1517	490.	26597	0.60	1.20	0.83	0.14	CO						
772	400	2.073	1507	1052	1261	1571	1102	70.5	1.888	1516	494.	26825	0.59	1.19	0.83	0.14	CO						
773	0	2.064	1507	1047	1392	1593	1317	84.7	1.902	1522	504.	27554	0.71	1.17	0.89	0.17	CO						
774	400	2.073	1509	1054	1402	1574	1323	86.8	1.911	1520	510.	27969	0.71	1.16	0.88	0.17	CO						
775	0	2.075	1503	1051	1480	1324	1301	103.3	1.929	1468	528.	28634	0.70	0.96	0.84	0.20	CO						
776	400	2.076	1516	1060	1473	1338	1300	102.1	1.928	1481	526.	28607	0.70	0.96	0.83	0.19	CO						

TEST POINT T amb DEG R P amb PSIA RH MF LFV LBM PML (FULL SIZE, 2400 FT SIDE LINE), dB

TEST POINT	T amb DEG R	P amb PSIA	RH	MF	LFV	LBM	ANGLE RELATIVE TO INLET, DEGREES						
							50	60	70	140			
763	500.2	14.40	88	-3.9	1.87	-10.00	85.6	86.7	90.7	94.9	98.4	97.3	93.9
764	501.1	14.40	88	-3.7	1.91	-10.00	90.7	90.0	93.3	95.3	97.3	93.8	88.4
765	500.3	14.40	88	-4.3	1.86	-7.11	86.4	86.9	91.2	94.9	98.6	97.2	93.6
766	500.1	14.40	88	-4.3	1.86	-7.09	90.3	90.1	93.6	95.4	97.0	93.5	88.3
767	499.3	14.40	88	-3.8	1.93	-9.88	86.0	86.8	91.2	94.7	98.1	97.6	92.6
768	500.7	14.39	88	-3.8	1.94	-10.00	89.6	89.5	92.4	94.8	96.7	93.5	88.4
769	499.3	14.39	88	-3.6	1.99	-10.00	85.7	86.6	91.2	94.7	99.0	97.0	93.4
770	496.7	14.40	63	-3.5	2.00	-10.00	89.7	90.0	93.3	95.1	97.3	93.8	88.2
771	497.3	14.31	84	-3.2	2.03	-10.00	85.2	86.1	90.8	94.7	96.3	95.2	92.1
772	497.2	14.40	63	-3.3	2.03	-10.00	90.0	90.3	93.2	94.4	96.5	93.7	88.3
773	498.6	14.32	84	-3.3	2.06	-10.00	85.6	86.4	91.0	94.7	96.7	96.8	91.6
774	497.5	14.40	63	-3.4	2.08	-9.88	89.3	89.6	92.8	94.9	96.5	93.5	88.0
775	498.9	14.40	82	-3.7	2.02	-7.52	86.0	86.7	91.0	94.8	97.8	96.5	93.5
776	496.7	14.41	63	-3.6	2.05	-7.71	90.1	90.5	93.7	95.4	96.6	93.7	88.6



Table 3-XVI is the test matrix for configuration TAS-8 simulating engine operating line in sideline and community orientations. Since the 0.97" thick 180° shield showed significant noise suppression, a limited amount of  $V_r$ ,  $CV_r$  and  $T_r^S$  parametric testing for both a takeoff case in sideline orientation and a cutback case in community orientation was conducted and the corresponding test matrices are shown respectively in Tables 3-XVII and 3-XVIII.

Table 3-XIX is the test matrix for Configuration TAS-9 simulating engine operating line.

Appendix A-I contains the test matrices of configurations TAS-1 thru TAS-9 in SI units.

### 3.2.2 LASER VELOCIMETER TESTS

The laser velocimeter, a noninvasive diagnostic tool for flow field measurements, was employed to measure the mean and turbulent velocity distributions in the jet plumes of selected unsuppressed and mechanically suppressed nozzles with partial and full thermal acoustic shields. Table 3-XX shows the breakdown of the laser velocimeter (LV) test points, scope of the plume measurements and the aerodynamic conditions at which the plume surveys were conducted. LV measurements were conducted for the takeoff cycle under both static and simulated flight conditions for all the four (4) selected single primary flow nozzles with thermal acoustic shield (viz., configurations TAS-2, TAS-4, TAS-8 and TAS-9). LV measurements for the cutback cycle under static and simulated flight conditions were conducted only for configuration TAS-2, to study the plume characteristics at another cycle condition. The complete details of the LV measurements are contained in Reference 3.5.

### 3.2.3 AERODYNAMIC CALIBRATION AND DIAGNOSTIC TESTS

The thermal acoustic shield flow for the partial shields is obtained by a gradual transitioning from a full 360° annular test facility duct to the 180° arc fluid shield nozzle. Sealing techniques were incorporated to prevent leakage from the 180° nozzle segment to the outer ambient atmosphere





TABLE 3-XVI (CONT'D) TEST MATRIX FOR CONFIGURATION TAS-8 SIMULATING ENGINE OPERATING LINE IN SIDELINE AND COMMUNITY ORIENTATIONS

\*\*\*\*\* BRITISH UNITS \*\*\*\*\*

TEST POINT	T amb DEC R	P amb PSIA	RH %	MF dB	LVM	LBM	PWL (FULL SIZE, 2400 FT SIDE LINE), dB ANGLE RELATIVE TO INLET, DEGREES	SIDELINE					COMMUNITY				
								50	60	70	90	120	130	140	50	60	70
801	501.1	14.29	85	-4.3	0.29	-10.00	77.2	78.3	82.9	86.2	86.5	85.2	82.3				
802	488.8	14.43	70	-4.1	0.38	-10.00	80.2	80.2	83.9	85.9	85.9	81.3	74.9				
803	500.5	14.28	85	-3.3	1.36	-10.00	82.4	83.3	88.1	91.5	93.2	81.3	89.5				
804	487.8	14.43	70	-3.0	1.45	-10.00	86.6	86.3	90.6	91.2	91.8	88.4	83.5				
805	503.6	14.29	85	3.1	1.73	-10.00	84.3	85.3	89.8	93.4	95.3	95.7	93.3				
806	489.1	14.43	70	-2.8	1.84	-10.00	88.5	87.8	91.7	92.8	93.9	91.0	87.0				
807	504.8	14.27	86	-3.4	2.22	-6.13	86.1	87.1	91.6	95.1	98.0	98.3	97.2				
808	489.3	14.43	70	-3.2	2.30	-6.24	88.9	88.3	92.1	94.2	96.5	94.4	90.3				
809	505.3	14.27	86	-4.0	2.57	-3.23	88.6	89.0	93.3	96.7	100.0	101.3	101.6				
810	487.2	14.43	70	-3.9	2.64	-3.23	91.5	90.2	94.4	95.9	99.1	97.1	95.1				
811	506.2	14.26	86	-4.4	2.80	-2.39	90.1	90.3	94.7	97.9	102.2	103.6	104.4				
812	488.6	14.42	70	-4.2	2.87	-2.39	93.0	91.7	95.6	97.2	100.5	99.1	98.0				
813	508.8	14.26	81	-5.3	3.02	-1.32	93.7	93.9	97.4	99.5	105.0	106.9	108.1				
814	494.5	14.43	70	-5.1	3.09	-1.35	95.1	93.8	97.2	99.0	103.0	102.4	102.1				
815	510.6	14.25	81	-6.2	3.27	-0.53	96.3	96.6	100.2	101.1	107.1	110.0	111.7				
816	489.3	14.42	70	-6.2	3.34	-0.51	98.2	97.6	101.0	100.9	105.2	105.7	106.4				
817	496.5	14.52	46	-4.3	0.32	-10.00	75.1	77.1	81.4	85.2	85.7	83.1	78.3				
818	505.6	14.52	68	-4.2	0.34	-10.00	78.6	79.0	82.8	84.8	83.7	78.3	71.9				
819	498.3	14.53	46	-3.3	1.37	-10.00	79.7	81.3	86.0	89.6	91.2	90.2	85.7				
820	505.8	14.52	68	-3.3	1.38	-10.00	84.1	84.4	88.5	89.3	88.9	85.4	80.6				
821	499.0	14.52	46	-3.1	1.77	-10.00	81.9	83.3	88.2	91.5	94.2	93.3	90.7				
822	505.6	14.52	68	-3.1	1.77	-10.00	85.9	85.9	89.7	90.9	91.2	88.2	84.3				
823	500.3	14.51	46	-3.4	2.24	-6.12	84.2	85.5	90.3	93.5	97.6	96.3	95.5				
824	505.8	14.52	60	-3.3	2.24	-6.27	87.9	88.1	91.6	93.1	94.1	92.3	89.1				
825	499.9	14.51	46	-4.0	2.59	-3.20	86.6	87.6	92.1	95.6	100.2	100.6	100.6				
826	507.7	14.52	60	-4.1	2.56	-3.18	89.3	89.7	93.1	94.5	96.4	95.4	94.3				
827	534.5	14.51	38	-4.6	2.67	-2.37	88.5	89.4	93.8	96.7	102.0	102.4	103.3				
828	506.6	14.51	60	-4.4	2.80	-2.37	90.3	90.7	94.0	95.4	98.5	97.8	97.4				
829	501.1	14.50	38	-5.2	3.06	-1.35	91.6	92.4	96.1	98.4	104.8	106.7	106.9				
830	507.0	14.52	60	-5.3	3.05	-1.34	92.9	92.8	96.2	97.2	100.6	101.4	102.2				
831	502.6	14.50	38	-6.2	3.30	-0.53	94.3	95.2	99.1	100.4	107.3	109.9	109.4				
832	505.3	14.52	60	-6.3	3.29	-0.54	96.0	95.9	98.9	100.0	103.4	105.5	107.0				

TABLE 3-XVII.  
 TEST MATRIX FOR CONFIGURATION TAS-8 FOR V, CV, AND T<sub>r</sub><sup>s</sup> PARAMETRIC  
 STUDY FOR A TAKEOFF CASE IN SIDELINE ORIENTATION

\*\*\*\*\* BRITISH UNITS \*\*\*\*\*

NOZZLE - MODEL TAS-8 CONTINUED

TEST PT.	V		J		P		J		T		P		J		T		P		J		T		P		J		T		TEST CONFIG																																																																																																																																	
	a/o		lb/sec		deg. R		lb/sec		deg. R		lb/sec		deg. R		lb/sec		deg. R		lb/sec		deg. R		lb/sec		deg. R		lb/sec																																																																																																																																			
	400	800	1620	2200	1.714	1408	717	82.4	2.178	1585	1558	504	30701	0.33	1.10	0.64	0.16																																																																																																																																													
834	800	2.688	1620	2200	1.714	1408	717	82.4	2.178	1585	1558	504	30701	0.33	1.10	0.64	0.16	SL	836	800	2.689	1639	2214	420.0	1.276	1091	939	144.9	2.148	1498	1887	565	33140	0.42	0.81	0.63	0.26	SL	838	800	2.697	1638	2216	421.1	1.572	862	1120	232.7	2.208	1361	1826	654	37117	0.51	0.60	0.63	0.36	SL	842	800	2.695	1629	2209	416.9	1.316	1351	1108	137.0	2.168	1560	1937	554	33350	0.50	1.00	0.72	0.25	SL	844	800	2.686	1618	2198	417.1	1.253	1602	1098	112.8	2.155	1615	1964	530	32358	0.50	1.21	0.76	0.21	SL	848	800	2.676	1630	2204	413.2	1.493	1336	1320	170.6	2.205	1544	1945	584	35309	0.60	0.95	0.76	0.29	SL	856	800	2.686	1660	2228	416.3	1.657	1473	1547	188.5	2.272	1602	2015	605	37891	0.69	1.01	0.83	0.31	SL	858	800	2.689	1629	2207	416.1	1.621	1710	1634	167.8	2.262	1652	2042	584	37072	0.74	1.20	0.89	0.29	SL

\*\*\*\*\* BRITISH UNITS \*\*\*\*\*

\*\*\*\*\* BRITISH UNITS \*\*\*\*\*

\*\*\*\*\* BRITISH UNITS \*\*\*\*\*

\*\*\*\*\* BRITISH UNITS \*\*\*\*\*

\*\*\*\*\* BRITISH UNITS \*\*\*\*\*

\*\*\*\*\* BRITISH UNITS \*\*\*\*\*

\*\*\*\*\* BRITISH UNITS \*\*\*\*\*

\*\*\*\*\* BRITISH UNITS \*\*\*\*\*

\*\*\*\*\* BRITISH UNITS \*\*\*\*\*

\*\*\*\*\* BRITISH UNITS \*\*\*\*\*

\*\*\*\*\* BRITISH UNITS \*\*\*\*\*

TABLE 3-XVIII. TEST MATRIX FOR CONFIGURATION TAS-8 FOR V<sub>r</sub>, CV<sub>r</sub>, AND T<sub>r</sub><sup>S</sup> PARAMETRIC STUDY FOR A CUTBACK CASE IN COMMUNITY ORIENTATION

\*\*\*\*\* BRITISH UNITS \*\*\*\*\*

NOZZLE - MODEL TAS-8 CONCLUDED

TEST PT.	V a/c	J T	J T	J W	J W	J P	s j T	s j T	- s j V	- s j W	s j W	mix T	mix V	mix W	T F	s j J	s j J	s j J	T <sub>6</sub> /T <sub>8</sub>	CV	CV	W/W	T TEST CONFIG	
																								deg.R
860	400	2.071	1511	1854	335.3	1.108	1333	681	82.1	1.749	1476	1623	417.	21064	0.37	1.04	0.68	0.20	0.20	0.20	0.20	0.20	0.20	CO
862	400	2.065	1505	1847	335.0	1.155	1314	799	98.7	1.740	1462	1608	434.	21686	0.43	1.02	0.71	0.23	0.23	0.23	0.23	0.23	0.23	CO
864	400	2.070	1511	1853	335.4	1.328	1046	990	160.1	1.772	1361	1574	496.	24253	0.53	0.77	0.70	0.32	0.32	0.32	0.32	0.32	0.32	CO
866	400	2.066	1522	1858	333.4	1.502	954	1122	206.3	1.824	1305	1577	548.	26455	0.60	0.68	0.71	0.38	0.38	0.38	0.38	0.38	0.38	CO
872	400	2.073	1513	1856	335.3	1.257	1651	1122	112.5	1.761	1548	1672	448.	23279	0.60	1.25	0.85	0.25	0.25	0.25	0.25	0.25	0.25	CO
874	400	2.071	1511	1854	335.4	1.373	1635	1307	135.4	1.794	1546	1696	471.	24829	0.70	1.21	0.89	0.29	0.29	0.29	0.29	0.29	0.29	CO
880	400	2.075	1513	1858	335.9	1.461	1565	1393	153.3	1.828	1529	1712	489.	26033	0.75	1.14	0.90	0.31	0.31	0.31	0.31	0.31	0.31	CO
884	400	2.066	1513	1853	334.4	1.502	1654	1481	155.3	1.838	1558	1735	490.	26407	0.80	1.19	0.94	0.32	0.32	0.32	0.32	0.32	0.32	CO
886	400	2.070	1514	1855	335.0	1.097	1285	635	79.2	1.751	1470	1622	414.	20882	0.34	1.00	0.66	0.19	0.19	0.19	0.19	0.19	0.19	CO

TEST POINT	T amb DEG R	P amb PSIA	RH %	MF dB	LVH	LBM	PNL (FULL SIZE, 2400 FT SIDE LINE), dB						
							50	60	70				
860	508.5	14.52	80	-2.9	1.67	-10.00	85.9	86.6	90.2	91.2	93.1	90.1	85.5
							85.4	86.1	89.8	91.0	92.2	89.5	84.8
862	504.9	14.51	83	-3.1	1.65	-10.00	85.5	86.7	90.2	91.4	92.0	88.5	83.7
							86.6	87.2	90.6	92.4	91.3	87.6	83.0
864	508.3	14.52	80	-4.6	1.54	-10.00	86.6	87.2	90.6	92.4	91.3	87.6	83.0
							85.5	86.3	89.7	90.5	90.8	84.0	84.0
872	506.1	14.51	83	-2.9	1.81	-10.00	84.7	85.7	89.5	90.7	90.6	88.0	84.2
							85.3	86.5	89.5	91.0	90.7	88.4	84.5
874	505.3	14.51	83	-3.3	1.91	-10.00	86.1	86.4	90.3	91.5	91.3	89.0	85.5
							86.1	86.4	90.3	91.5	91.3	89.0	85.5
880	506.8	14.52	83	-3.2	1.97	-10.00	86.2	86.9	90.1	91.6	93.6	90.7	86.2
							86.2	86.9	90.1	91.6	93.6	90.7	86.2

TABLE 3-XIX. TEST MATRIX FOR CONFIGURATION TAS-9 SIMULATING ENGINE OPERATING LINE

\*\*\*\*\* BRITISH UNITS \*\*\*\*\*

NOZZLE - MODEL TAS-9 AREA [MODEL SIZE - INNER = 26.15 , OUTER = 17.49 ; FULL SIZE - TOTAL = 1400.00] SQ. IN.

TEST PT.	V a/c	P	J	J	J	P	F	T	T	deg.R	T	P	mix	T	mix	V	mix	T	F	T	V/V	T <sub>B</sub> /T <sub>B</sub>	CV	W/W	TEST CONFIG
	fps	deg.R	deg.R	deg.R	deg.R	deg.R	deg.R	deg.R	deg.R	deg.R	deg.R	deg.R	deg.R	deg.R	deg.R	deg.R	deg.R	deg.R	deg.R	deg.R	deg.R	deg.R	deg.R	deg.R	deg.R
	lb/sec	lb/sec	lb/sec	lb/sec	lb/sec	lb/sec	lb/sec	lb/sec	lb/sec	lb/sec	lb/sec	lb/sec	lb/sec	lb/sec	lb/sec	lb/sec	lb/sec	lb/sec	lb/sec	lb/sec	lb/sec	lb/sec	lb/sec	lb/sec	lb/sec
901	0	1.555	1273	1349	271.9	1.164	1301	816	99.7	1.414	1281	1206	372.	13931	0.60	1.10	0.85	0.27	AX						
902	400	1.556	1264	1344	273.1	1.165	1294	815	100.0	1.414	1272	1202	373.	13947	0.61	1.11	0.85	0.27	AX						
903	0	1.887	1489	1705	317.2	1.246	1456	1033	114.6	1.648	1451	1527	432.	20494	0.61	1.12	0.83	0.26	AX						
904	400	1.879	1465	1710	314.1	1.240	1471	1029	112.7	1.642	1467	1530	427.	20298	0.60	1.12	0.83	0.26	AX						
905	0	2.076	1510	1856	341.5	1.281	1522	1119	119.5	1.777	1513	1665	461.	23863	0.60	1.15	0.82	0.27	AX						
906	400	2.070	1532	1867	337.8	1.291	1508	1131	122.0	1.776	1526	1671	460.	23889	0.61	1.11	0.82	0.27	AX						
907	0	2.391	1579	2055	384.0	1.339	1605	1245	127.4	1.992	1585	1853	511.	29465	0.61	1.19	0.82	0.25	AX						
908	400	2.382	1607	2070	379.3	1.335	1622	1246	126.0	1.986	1611	1864	505.	29284	0.60	1.18	0.82	0.25	AX						
909	0	2.701	1649	2226	424.2	1.390	1675	1348	133.3	2.205	1655	2016	558.	34937	0.61	1.21	0.82	0.24	AX						
910	400	2.693	1667	2235	420.8	1.381	1717	1352	130.2	2.197	1678	2026	551.	34698	0.60	1.23	0.82	0.24	AX						
911	0	2.909	1708	2338	447.6	1.418	1752	1419	133.9	2.352	1715	2126	581.	38432	0.61	1.25	0.82	0.23	AX						
912	400	2.917	1704	2338	447.6	1.418	1752	1419	133.9	2.352	1715	2126	581.	38432	0.61	1.25	0.82	0.23	AX						
913	0	3.327	1716	2463	510.7	1.473	1718	1476	144.4	2.631	1717	2245	655.	45723	0.60	1.26	0.82	0.22	AX						
914	400	3.327	1709	2459	509.4	1.486	1739	1500	144.3	2.638	1716	2247	654.	45675	0.61	1.26	0.82	0.22	AX						
915	0	3.855	1719	2588	591.8	1.560	1732	1582	155.6	3.007	1722	2379	747.	55261	0.61	1.29	0.81	0.21	AX						
916	400	3.882	1664	2550	603.2	1.579	1757	1614	156.1	3.030	1683	2357	759.	55644	0.63	1.35	0.84	0.21	AX						

TEST POINT	T amb DEG R	P amb PSIA	RH %	MF DB	LVM	LBM	PML (FULL SIZE, 2400 FT SIDE LINE), DB	ANGLE RELATIVE TO INLET, DEGREES	90	120	130	140
901	502.6	14.51	57	-4.2	0.40	-10.00	79.0	80.2	83.6	89.9	87.1	83.1
902	509.7	14.50	46	-4.3	0.36	-10.00	82.7	82.5	85.5	88.1	87.4	77.0
903	502.2	14.51	57	-3.3	1.43	-10.00	83.5	84.5	88.5	92.2	95.4	90.9
904	515.4	14.50	46	-3.4	1.38	-10.00	86.1	85.7	89.3	91.8	93.9	84.5
905	501.9	14.50	57	-3.1	1.81	-10.00	85.1	85.9	90.0	93.7	97.5	93.7
906	515.2	14.49	46	-3.2	1.77	-10.00	88.0	88.0	91.6	93.3	95.9	87.0
907	500.4	14.50	57	-3.4	2.28	-5.83	87.5	88.5	92.6	96.1	98.8	97.6
908	516.5	14.50	46	-3.4	2.24	-6.03	90.2	89.9	93.0	95.5	98.8	91.6
909	500.4	14.50	57	-4.0	2.65	-3.07	91.1	91.5	95.4	97.8	101.8	102.2
910	517.3	14.51	46	-4.1	2.59	-3.13	92.5	91.7	94.8	97.3	101.0	95.8
911	498.6	14.50	57	-4.4	2.88	-2.27	93.0	93.7	97.4	99.2	103.1	104.6
912	521.4	14.41	46	-4.5	2.79	-2.24	94.7	93.6	96.7	98.7	102.5	98.3
913	498.5	14.50	57	-5.2	3.12	-1.28	95.9	96.3	99.9	100.7	104.8	108.0
914	520.4	14.41	40	-5.4	3.03	-1.25	97.4	96.3	99.9	101.2	104.1	102.2
915	496.5	14.49	75	-6.2	3.38	-0.48	96.5	97.2	100.9	102.7	104.1	110.7
916	518.1	14.41	40	-6.5	3.25	-0.44	99.8	99.6	101.6	102.6	106.4	107.4

TABLE 3-XX. SCOPE OF THE LASER VELOCIMETER TESTS AND TEST CONDITIONS ON SINGLE PRIMARY FLOW NOZZLES WITH THERMAL ACOUSTIC SHIELDS

Config.	Description	LV Test Pt.	Matching Acoustic Test Pt.	V <sub>a/c</sub> fps	Core Jet		Shield Jet		Mixed Conditions		Scope of LV Testing		Comment			
					V <sub>j</sub> , fps	T <sub>pj</sub> OR Pr <sub>j</sub>	V <sub>sj</sub> , fps	T <sub>psj</sub> OR Pr <sub>sj</sub>	V <sub>mix</sub> , fps	T <sub>pmix</sub> OR P <sub>mix</sub>	Transverse Histograms					
TAB-2	Unsuppressed Annular Plug Nozzle With 180° TAS of 0.48" Thickness	1	225	0	2181	1585	2.703	1299	1580	1.383	2058	1584	2.389	17	66	Takeoff
		2	226	400	2192	1601	2.700	1310	1614	1.381	2069	1603	2.387	17	58	Takeoff
		3	221	0	1812	1490	2.020	1108	1525	1.273	1703	1496	1.844	14	54	Outback
		4	222	400	1859	1486	2.110	1128	1514	1.288	1748	1490	1.915	15	54	Outback
TAB-4	Unsuppressed Annular Plug Nozzle With 360° TAS of 0.48" Thickness	5	409	0	2211	1633	2.691	1362	1681	1.398	2002	1645	2.190	17	51	Takeoff
		6	410	400	2220	1640	2.704	1344	1629	1.401	2001	1637	2.199	21	64	Takeoff
TAB-8	32 Chute Annular Plug Suppressor Nozzle With 180° TAS of 0.97" Thickness	7	893*	0	2211	1631	2.695	1323	1619	1.388	1990	1628	2.188	14	52	Takeoff
		8	894*	400	2218	1640	2.696	1325	1606	1.394	1993	1632	2.190	14	50	Takeoff
TAB-9	32 Chute Annular Plug Suppressor Nozzle With 360° TAS of 0.48" Thickness	9	909	0	2226	1649	2.701	1348	1675	1.390	2016	1655	2.205	19	60	Takeoff
		10	910	400	2235	1667	2.693	1352	1717	1.381	2026	1678	2.197	10	45	Takeoff
Total											158	356				

\*Test conditions for test points 894 and 910 match acoustic test points 825 and 826 respectively, which had shield mounted in community orientation. However, during LV tests, shield was mounted in opposite community orientation.

(see Reference 3.1). An aerodynamic calibration of the thermal acoustic shield exit plane conditions with respect to the upstream test facility charging station conditions was conducted on the 180° shield of 0.48" thickness on configuration TAS-2 and on the 360° shield of 0.48" thickness on configuration TAS-4 to evaluate flow turning total pressure losses.

An aerodynamic analysis utilizing the Stream Tube Curvature (STC) method (see Reference 3.1) indicated a possibility of static pressure feedback from the supersonic core jet to the subsonic shield jet, which in turn could reduce the shield's effective flow area and cause a low discharge coefficient,  $C_D$ . Diagnostic tests to verify this observation were conducted on both the 180° and 360° shields. Tables 3-XXI and 3-XXII contain the aerodynamic calibration and diagnostic test matrices for configurations TAS-2 and TAS-4 respectively.

To determine the influence of the thermal acoustic shield on the chute base drag of the 32 chute suppressor, the chutes were instrumented for static pressure measurements along the base region (see Reference 3.1). The base static pressures were measured for configurations TAS-6, TAS-7, TAS-8 and TAS-9 along the engine operating line when the corresponding acoustic tests were performed. The test matrices of the engine operating line for configurations TAS-6, TAS-7, TAS-8 and TAS-9 are respectively shown in Tables 3-XII, 3-XIII, 3-XVI and 3-XIX. The complete details of the base pressure data for Configurations TAS-6, TAS-7, TAS-8 and TAS-9 are contained in Reference 3.5.

TABLE 3-XXI. AERODYNAMIC CALIBRATION AND DIAGNOSTIC TEST MATRIX FOR CONFIGURATION TAS-2

Test Point	Core Jet			Shield Jet			Comments	• Static Tests Only		
	V <sub>J</sub> , fps	T <sub>r</sub> <sup>J</sup> , OR	Pr <sup>J</sup>	v <sub>SJ</sub> , fps	T <sub>r</sub> <sup>SJ</sup> , OR	Pr <sup>SJ</sup>				
C201	828	550	1.5	421	550	1.1	Aerodynamic Calibration @ T <sub>r</sub> <sup>SJ</sup> = 550°R			
C203	828	550	1.5	691	550	1.3				
C205	828	550	1.5	828	550	1.5				
C207	828	550	1.5	964	550	1.7				
C209	828	550	1.5	1052	550	1.9				
C223	1508	1730	1.5	1168	1663	1.280			Aerodynamic Calibration @ T <sub>r</sub> <sup>SJ</sup> = 1730°R	
C225	1508	1730	1.5	1505	1701	1.504				
C227	1508	1730	1.5	1707	1710	1.698				
C229	1508	1730	1.5	1859	1694	1.905			Influence of Supersonic Core Jet on Subsonic Shield Jet	
C231	2592	1730	3.9	760	1233	1.149				
C233	2592	1730	3.9	1076	1644	1.234				
C235	2592	1730	3.9	1548	1669	1.544				
C237	2592	1730	3.9	1814	1629	1.892				



TABLE 3-XXII. AERODYNAMIC CALIBRATION AND DIAGNOSTIC TEST MATRIX FOR CONFIGURATION TAS-4

Test Point	Core Jet			Shield Jet			Comments	• Static Tests Only		
	V <sub>J</sub> , fps	T <sub>TJ</sub> , °R	Pr	v <sub>SJ</sub> , fps	T <sub>TSJ</sub> , °R	Pr <sub>SJ</sub>				
C401	828	550	1.5	421	550	1.1	Aerodynamic Calibration @ T <sub>TSJ</sub> = 550°R			
C403	828	550	1.5	691	550	1.3				
C405	828	550	1.5	828	550	1.5				
C407	828	550	1.5	964	550	1.7				
C409	828	550	1.5	1052	550	1.9				
C421	1508	1730	1.5	748	1730	1.1			Aerodynamic Calibration @ T <sub>TSJ</sub> = 1730°R	
C423	1508	1730	1.5	1228	1730	1.3				
C425	1508	1730	1.5	1508	1730	1.5				
C427	1508	1730	1.5	1718	1730	1.7				
C429	1508	1730	1.5	1876	1730	1.9				
C431	2590	1700	3.9	440	955	1.06	Influence of Supersonic Core Jet on Subsonic Shield Jet			
C437	2590	1700	3.9	730	1324	1.13				
C435	2590	1700	3.9	1500	1575	1.54				
C433	2590	1700	3.9	1800	1695	1.89				

## REFERENCES FOR SECTION 3.0

- 3.1 Brausch, J.F., Majjigi, R.K. and Bediako, E.D., "Model Hardware Design Report for a Thermal Acoustic Shield Concept for AST/VCE Application - Single Stream Nozzle Designs", General Electric Technical Information Series Report Number R81AEG575, July 1981.
- 3.2 Yamamoto, K., et al., "Experimental Investigation of Shock-Cell Noise Reduction for Single Stream Nozzles in Simulated Flight," General Electric Technical Information Series Report No. R82AEB492, September 1983.
- 3.3 Vdoviak, J.W., Knott, P.R. and Ebacker, J.J., "Aerodynamic/Acoustic Performance of YJ101/Double Bypass VCE with Coannular Plug Nozzle", NASA CR-159869, January 1981.
- 3.4 Majjigi, R.K., Janardan, B.A., Brausch, J.F., Hoerst, D.J., Price, A.O., and Knott, P.R., "Freejet Feasibility Study of a Thermal Acoustic Shield Concept for AST/VCE Application - Single Flow", General Electric Technical Information Series Report Number R82AEB493, Vol. I; also, NASA CR-168302, July 1983.
- 3.5 Majjigi, R.K., Janardan, B.A., Brausch, J.F., Hoerst, D.J., Price, A.O., and Knott, P.R., "Free-Jet Feasibility Study of a Thermal Acoustic Shield Concept for AST/VCE Application - Single Flow," General Electric Technical Information Series Report Number R82AEB493, Vol. II; also, NASA CR-168303, July 1983.

#### 4.0 TEST RESULTS AND DISCUSSION

The principal objective of this investigation was to develop a thermal acoustic shield technology data base for AST/VCE application by experimentally evaluating the influence of selected geometric and aerodynamic flow variables and simulated flight velocity on the acoustic behavior of unsuppressed and mechanically suppressed nozzles with a thermal acoustic shield. A laser velocimeter for the measurement of mean and turbulent velocities and an aerodynamic instrumentation package for the measurement of total and static pressures, have been employed as diagnostic tools in understanding the flow characteristics of selected nozzles with the thermal acoustic shield. Salient results of the experimental investigation are analyzed in this section. Subsection 4.1 deals with the analyses of the acoustic test results; subsection 4.2 deals with the analyses of the laser velocimeter test results and subsection 4.3 contains the analyses of the aerodynamic calibration and diagnostic test results.

##### 4.1 ACOUSTIC TEST RESULTS

The discussion of the acoustic test results is grouped under the following headings:

1. Influence of thermal acoustic shields on the unsuppressed annular plug nozzle
2. Influence of thermal acoustic shields on the 32 chute mechanical suppressor nozzle
3. Selective comparisons of the acoustic influence of thermal acoustic shields on unsuppressed annular plug and 32 chute suppressor nozzle.

#### 4.1.1 INFLUENCE OF THERMAL ACOUSTIC SHIELDS ON AN UNSUPPRESSED ANNULAR PLUG NOZZLE

##### 4.1.1.1 Influence of Partial Shields and Full Shield on An Unsuppressed Plug Nozzle

The acoustic influence of the 180° shields of 0.48" and 0.97" thicknesses and the 360° shield of 0.48" thickness, on the unsuppressed annular plug nozzle at typical approach, cutback and takeoff cycle conditions of AST/VCE under both static and simulated flight conditions, is analyzed in this subsection. The measured acoustic model scale data has been scaled to an AST/VCE size of  $0.9032 \text{ m}^2$  ( $1400 \text{ in}^2$ ) flow area and extrapolated to 370', 1000' and 2400' distances for the approach, cutback and takeoff conditions respectively. The above distances refer to the typical aircraft noise monitoring locations as prescribed by the FAR-Part 36 (1969) regulation (see Reference 4.1). The distance for takeoff noise measurement location (viz., 2400 ft) is derived from a ground sideline distance of 2128 ft (0.35 nautical mile) from the runway and an aircraft altitude of ~ 1100 ft, a typical altitude at which maximum takeoff sideline noise is measured. The community noise measurement location is prescribed to be 21280 ft (3.5 nautical mile) from the aircraft brake release point. Typical calculated aircraft trajectories indicate that the aircraft achieves an altitude of ~ 1000 ft at the community noise measurement location, at which point a thrust cutback is implemented. The noise measurement location for approach is prescribed to be directly beneath the aircraft when the aircraft is at an altitude of 370 ft.

Figure 4.1.1-1 compares the static PNL directivities and spectral content at three (3) angles at 370' sideline distance, of configurations TAS-1, TAS-3 and TAS-4 for an approach condition. Note the PNL reduction at all observer angles by both the 180° shield of 0.97" thickness (TAS-3) and the 360° shield of 0.48" thickness (TAS-4) on the unsuppressed annular plug nozzle. For  $\theta_i \geq 110^\circ$ , the partial shield of 0.97" thickness (TAS-3) yields larger PNL reductions compared to the full shield of 0.48" thickness (TAS-4) indicating the enhanced refractive/reflective character of a partial

Symbol	Point	Config.	Orientation
○	101	TAS-1	Axisymmetric
◇	317	TAS-3	Community
△	401	TAS-4	Axisymmetric

$T^* = 1400 \text{ In.}^2$   
 370' Flyover Distance  
 Static  
 Approach Cycle

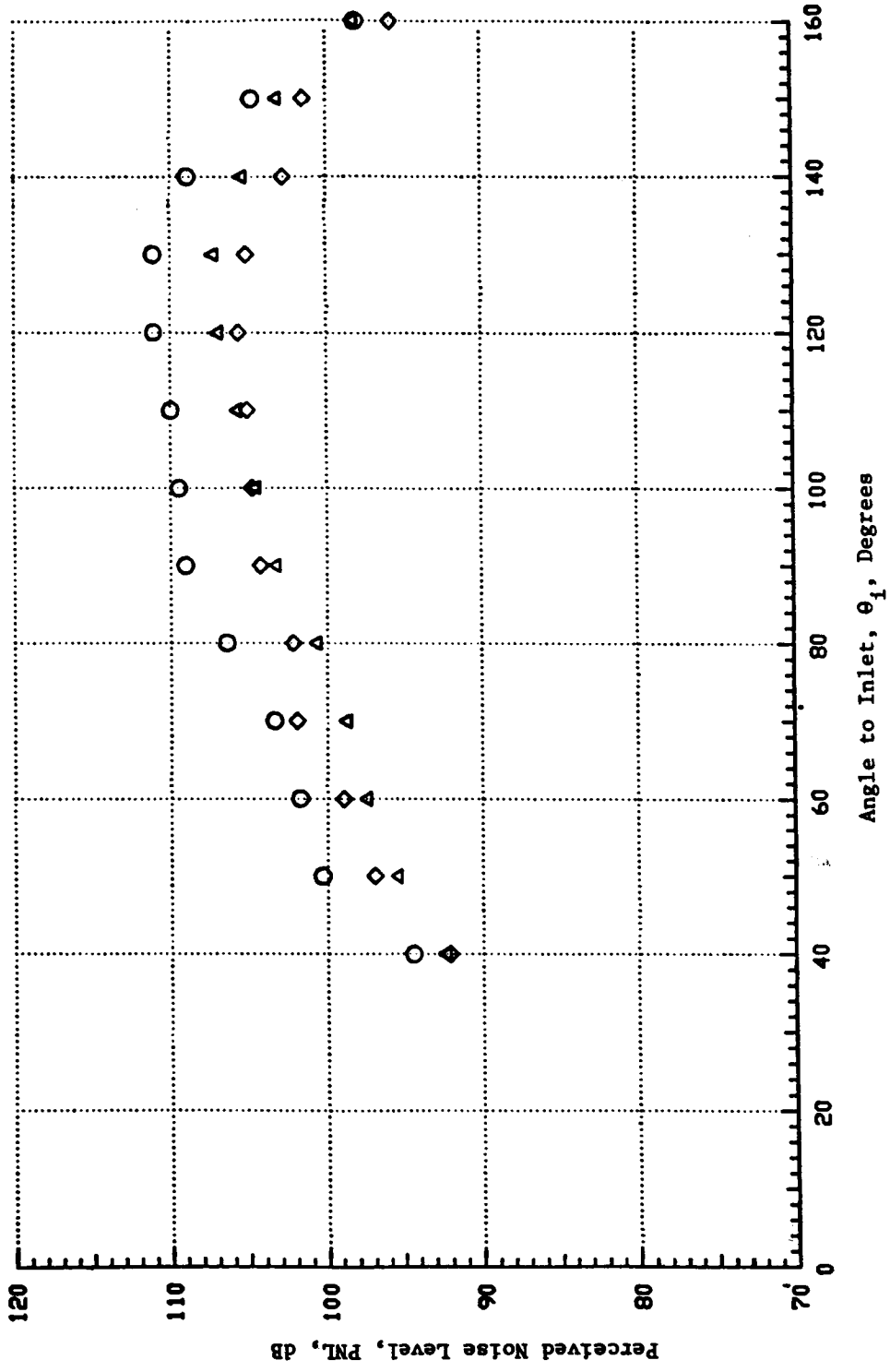
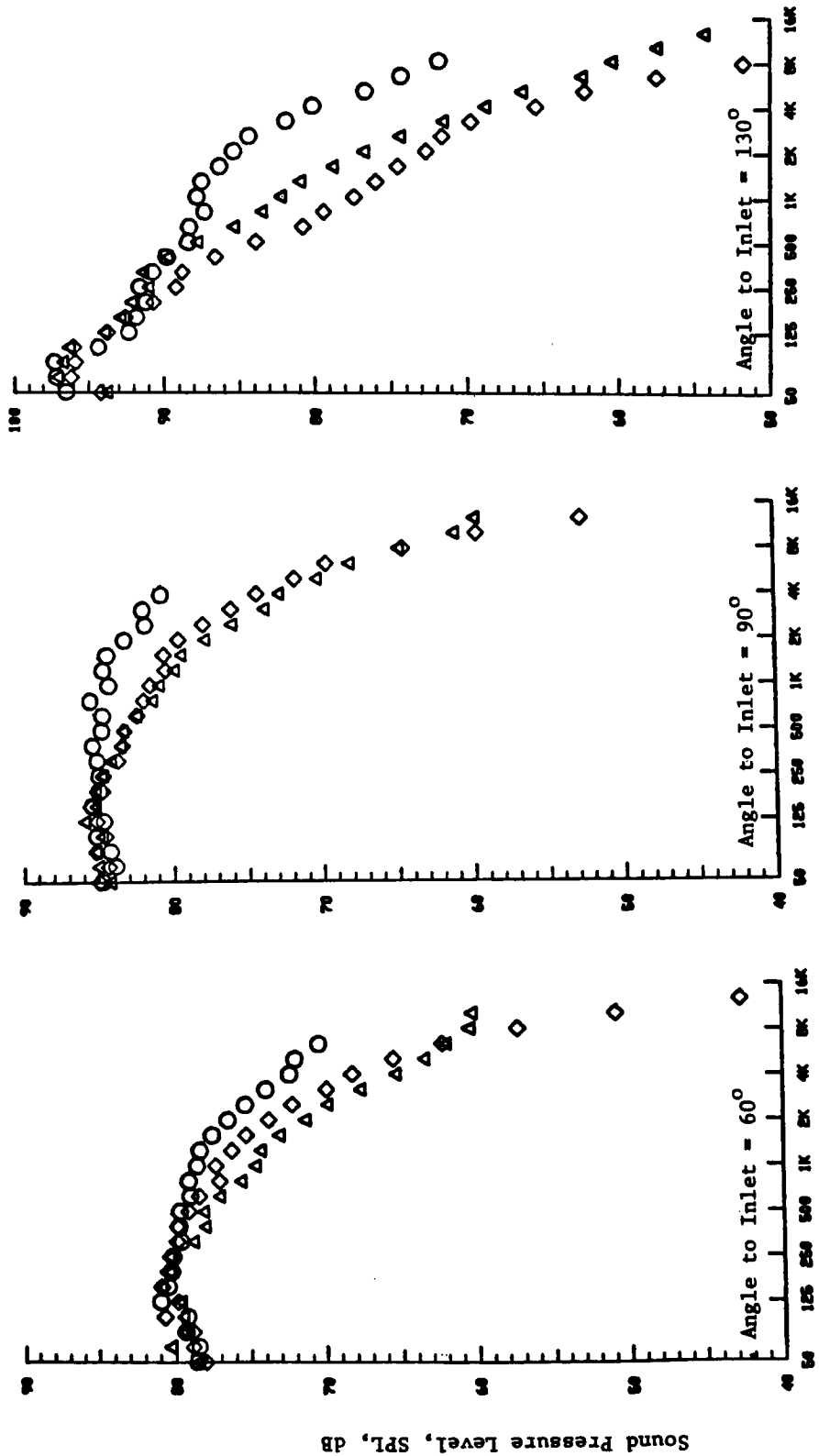


Figure 4.1.1-1a. Influence of the Thermal Acoustic Shields on PNL Directivity of Unsuppressed Annular Plug Nozzle for a Typical Approach Case (Static).

Symbol	Point	Config.	Orientation
○	101	TAS-1	Axisymmetric
◇	317	TAS-3	Community
△	401	TAS-4	Axisymmetric

$A^T = 1400 \text{ In.}^2$   
 370' Flyover Distance  
 Static  
 Approach Cycle



1/3 Octave Band Center Frequency, Hz

Figure 4.1.1-1b. Influence of the Acoustic Shields on the Spectral Content of Unsuppressed Annular Plug Nozzle for a Typical Approach Case (Static).

shield compared to the full shield carrying approximately equal shield flow rate. The spectral comparison at  $\theta_i = 130^\circ$  shows that the partial shield is able to reduce the mid and high frequencies (viz., frequencies greater than 250 HZ) more effectively than the full shield of the same flow rate. The spectral data at  $\theta_i = 60^\circ$  and  $90^\circ$  show a reduction of mid and high frequencies by both the full and partial shield to about the same extent.

Next, the acoustic influence of the thermal acoustic shields on the unsuppressed annular plug nozzle at typical thrust cutback and takeoff cycle conditions is studied. The acoustic data for the cutback cycle is extrapolated to 1000 ft flyover distance ( $\phi = 0^\circ$ ) whereas for the takeoff cycle, the data is extrapolated to 2400 ft sideline distance ( $\phi = 70^\circ$ ). Figures 4.1.1-2 and 4.1.1-3 compare the PNL directivities and spectral content of configurations TAS-1, TAS-2, TAS-3 and TAS-4 for cutback and takeoff cycle conditions respectively. For the cutback cycle, the  $360^\circ$  shield of 0.48" thickness yields the maximum PNL reduction in the front quadrant compared to the other thermal acoustic shields whereas, at the peak noise angle (viz.,  $\theta_i = 130^\circ$ ) the  $360^\circ$  shield of 0.48" thickness (TAS-4) yields the same PNL reduction as the  $180^\circ$  shield of 0.97" thickness (TAS-3) (see Figure 4.1.1-2a). At angles aft of  $130^\circ$ , the  $180^\circ$  shield of 0.97" thickness (TAS-3) yields the maximum noise reduction among the three (3) thermal acoustic shields being compared.

The  $180^\circ$  shield of 0.48" thickness shows noise reduction at almost all the observer angles, and exhibits a slight amplification at the peak noise angle (compared to the baseline annular plug nozzle, configuration TAS-1). This can be explained by examining the spectral composition at  $\theta_i = 130^\circ$  (see Figure 4.1.1-2b). Note the low frequency amplification compared to the baseline annular plug nozzle by both the partial shields. The reflective/refractive effect of the  $180^\circ$  shield of 0.48" thickness in reducing the high frequency noise is noted for frequencies greater than 1,000 HZ at  $\theta_i = 130^\circ$ . Since the SPL of the baseline nozzle at 1,000 HZ is about 10 dB lower than the peak SPL, the effect of high frequency noise reduction by the shield on PNL is not noticed. In fact, the PNL of configuration TAS-2 is slightly higher than that of configuration TAS-1 due to the amplification of the low frequency noise. However, the  $180^\circ$  shield of 0.97" thickness is seen to

Symbol	Point	Config.	Shield Config.	Peak $\Delta$ PNL, dB
○	105	TAS-1	No Shield	0.0
□	221	TAS-2	180 Thin Shield	-0.2
◇	321	TAS-3	180 Thick Shield	2.4
△	405	TAS-4	360 Thin Shield	2.4

$A^T = 1400 \text{ In.}^2$   
 1000' Flyover Distance  
 Static  
 Outback Cycle

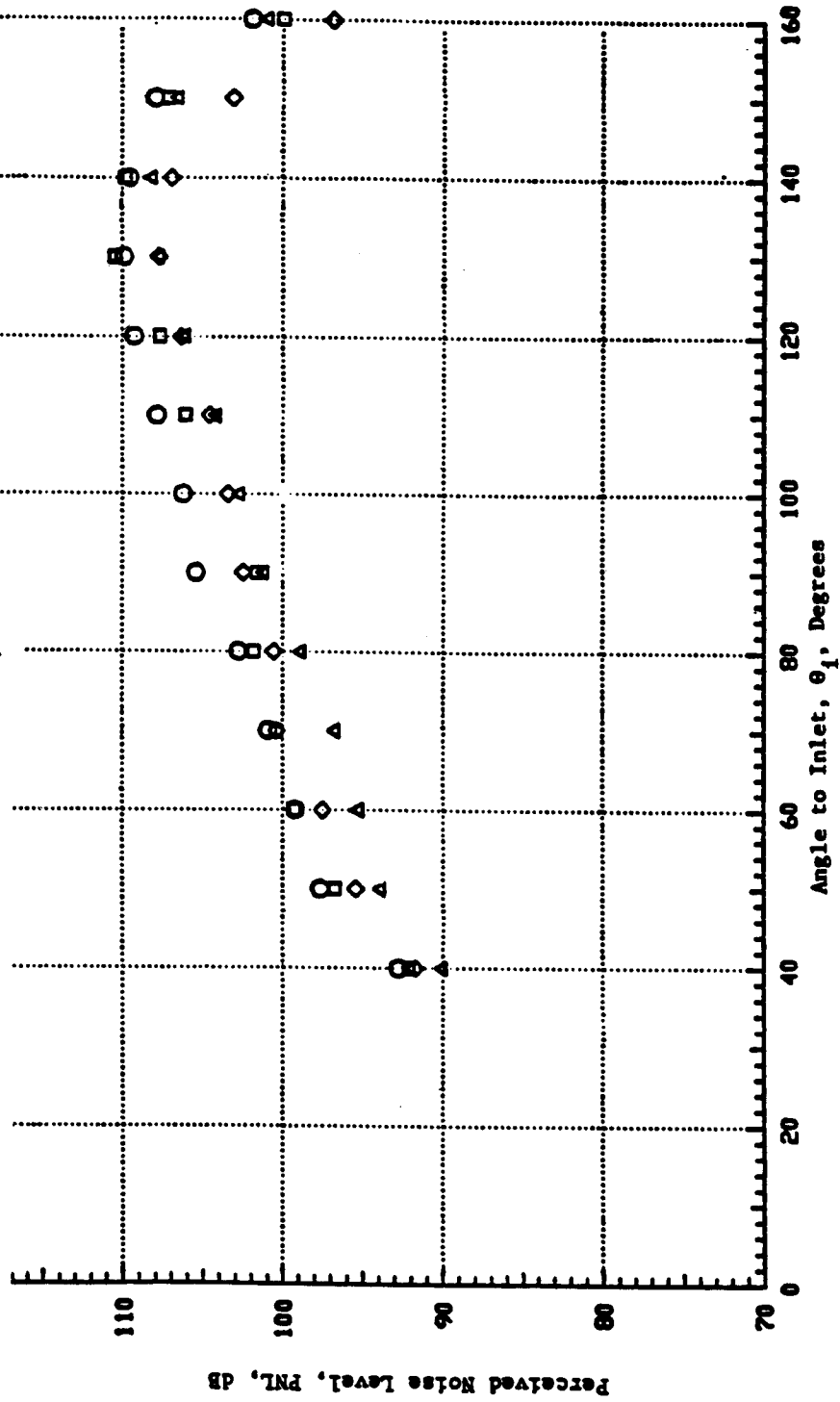
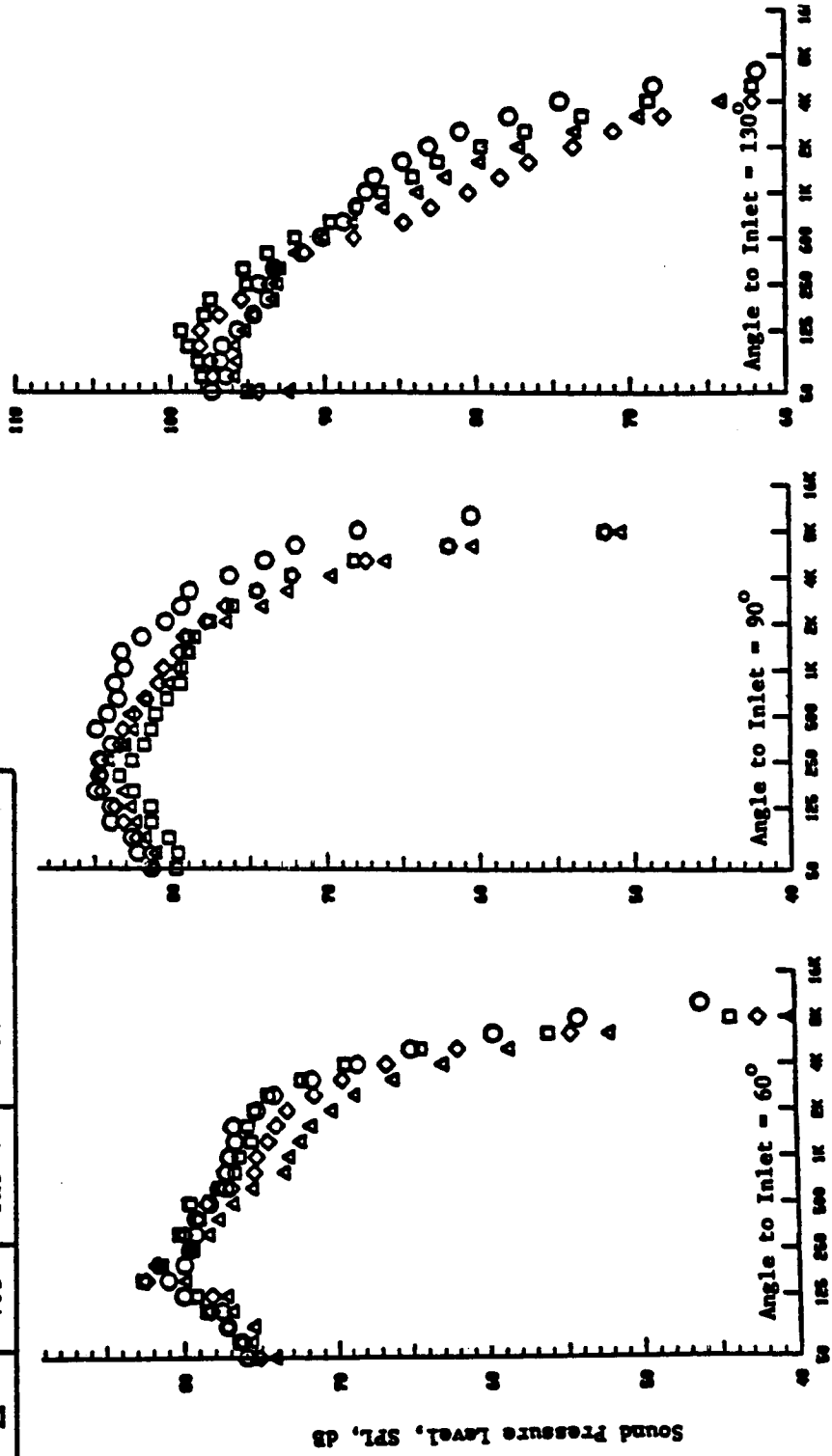


Figure 4.1.1-2a. Influence of the Thermal Acoustic Shields on PNL Directivity of Unsuppressed Annular Plug Nozzle at a Typical Outback Cycle (Static).



Symbol	Point	Config.	Shield Config.
○	105	TAS-1	No Shield
□	221	TAS-2	180 Thin Shield
◇	321	TAS-3	180 Thick Shield
△	405	TAS-4	360 Thin Shield

$A^T = 1400 \text{ In.}^2$   
 1000' Flyover Distance  
 Static  
 Outback Cycle



1/3 Octave Band Center Frequency, Hz

Figure 4.1.1-2b. Influence of the Thermal Acoustic Shields on the Spectral Content of Unsuppressed Annular Plug Nozzle at a Typical Outback Cycle (Static).

Symbol	Point	Config.	Orientation
○	109	TAS-1	Axisymmetric
□	209	TAS-2	Sideline
◇	309	TAS-3	Sideline
△	409	TAS-4	Axisymmetric

$T = 1400 \text{ In.}^2$   
 2400' Sideline,  $\phi = 70^\circ$   
 Static  
 Takeoff Cycle

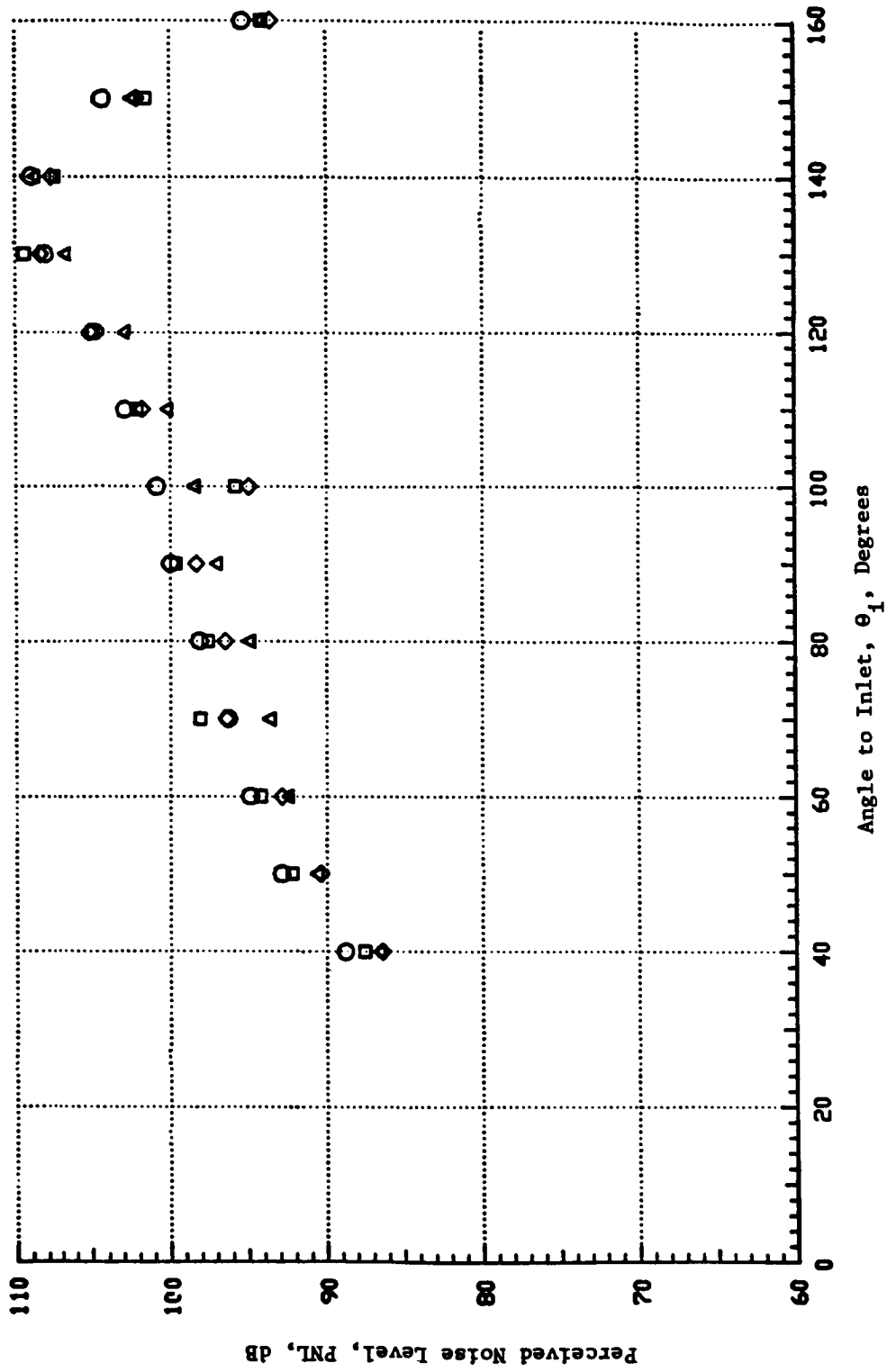
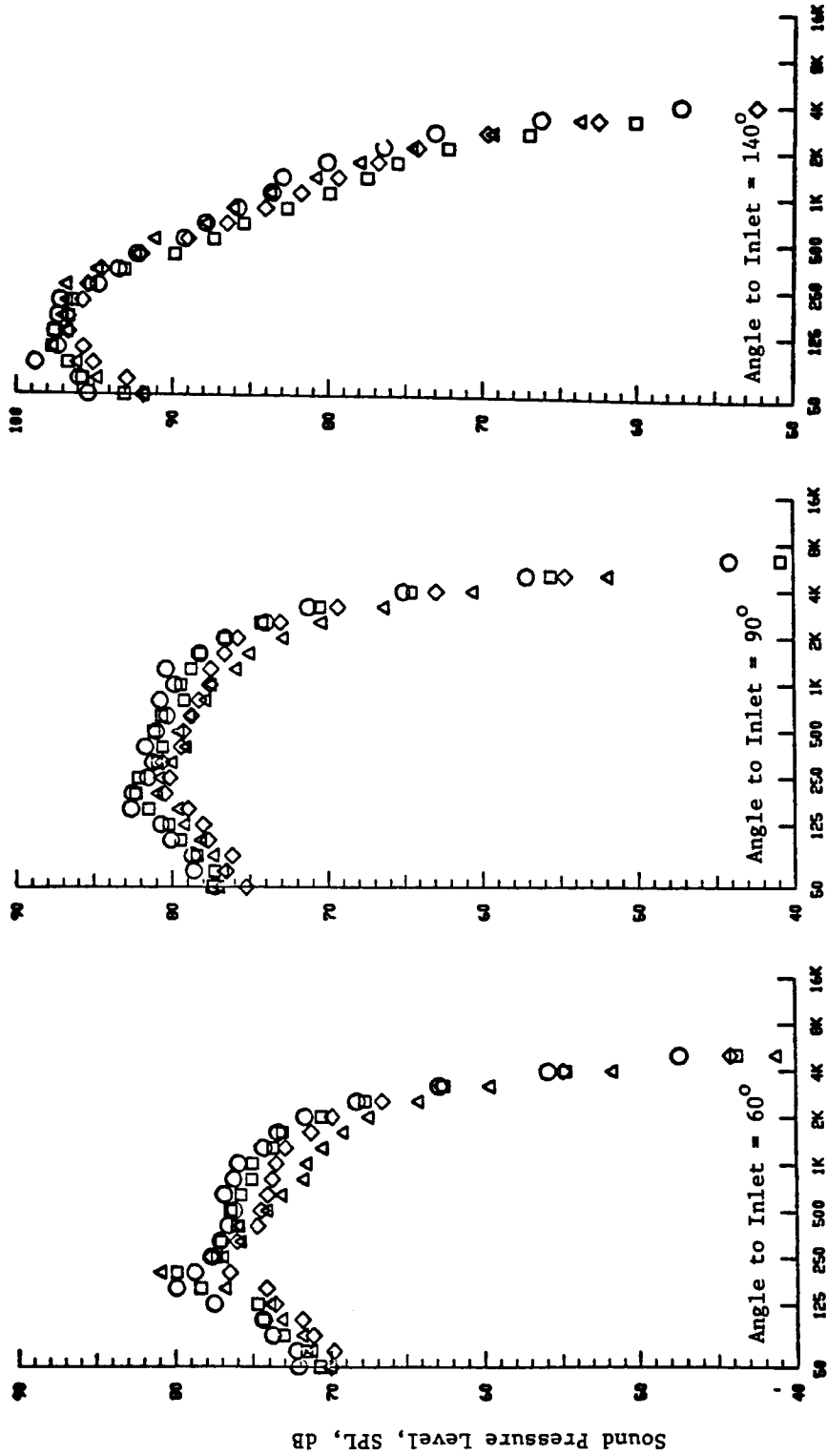


Figure 4.1.1-3a. Influence of the Thermal Acoustic Shields on PNL Directivity of Unsuppressed Annular Plug Nozzle at a Typical Takeoff Cycle (Static).

Symbol	Point	Config.	Orientation
○	109	TAS-1	Axisymmetric
□	209	TAS-2	Sideline
◇	309	TAS-3	Sideline
△	409	TAS-4	Axisymmetric

$T = 1400 \text{ In.}^2$   
 $A = 2400' \text{ Sideline, } \phi = 70^\circ$   
 Static  
 Takeoff Cycle



1/3 Octave Band Center Frequency, Hz

Figure 4.1.1-3b. Influence of the Thermal Acoustic Shields on the Spectral Content of Unsuppressed Annular Plug Nozzle at a Typical Takeoff Cycle (Static).

reduce the noise for frequencies > 250HZ indicating that the thickness of the partial shield is an important parameter in determining the reflective properties of the partial shields. The 360° shield of 0.48" thickness does not show low frequency noise amplification at  $\theta_i = 130^\circ$  and is seen to reduce the noise for frequencies > 500 HZ. The high frequency noise reduction effectiveness of the full shield of 0.48" thickness is in between those of the two partial shields. At the 4,000 HZ one-third octave band, the SPL reductions for the 180° shield of 0.97" thickness, the 360° shield of 0.48" thickness and the 180° shield of 0.48" thickness at  $\theta_i = 130^\circ$  are respectively 12.5 dB, 10.5 dB and 5.9 dB indicating the effective high frequency noise reduction by the shields.

Next, the spectral data at  $\theta_i = 90^\circ$  are examined. The low frequency noise amplification is not observed for any of the shields, and the high frequency noise reduction shows a different character compared to  $\theta_i = 130^\circ$ . The 360° shield of 0.48" thickness is seen to be more effective at  $\theta_i = 90^\circ$  in reducing the high frequency noise, compared to the partial shields. The spectral comparison at  $\theta_i = 60^\circ$  (see Figure 4.1.1-2b) shows low frequency amplification by all three (3) shields and similar spectral characteristics as at  $\theta_i = 90^\circ$  indicating source strength reduction is a more significant factor in the front quadrant and at  $\theta_i = 90^\circ$  rather than the reflective/refractive character of the thermal acoustic shields.

Figure 4.1.1-3 contains the static PNL directivity and spectral comparisons of configurations TAS-1, TAS-2, TAS-3 and TAS-4 at 2400 ft sideline distance at a takeoff cycle condition. At the peak noise angle ( $\theta_i = 140^\circ$ ) both the partial shields yield a PNL reduction of 2 dB and the 360° shield hardly yields any reduction. The spectral data at  $\theta_i = 140^\circ$  (see Figure 4.1.1-3b) shows high frequency noise reduction by the shields. However, the contribution of the high frequency noise to PNL is very small due to the large air attenuation at 2400 ft sideline distance under consideration. The spectral data at  $\theta_i = 60^\circ$  clearly shows the presence of shock noise contribution by the supersonic core jet at the takeoff cycle. The 360° shield yields the maximum high frequency noise reduction compared to the partial shields. At  $\theta_i = 90^\circ$ , the spectral data does not very clearly show the dominance of shock cell noise indicating that jet noise is equally significant at  $\theta_i = 90^\circ$ .

#### 4.1.1.2 Azimuthally Asymmetric Acoustic Field Characteristics of Partial Shield on Unsuppressed Annular Plug Nozzle

Azimuthal asymmetry of the partial shield acoustics is an important feature whose determination will help in diagnosing the range of frequencies and observer angles affected by the partial shields. Figure 4.1.1-4 compares the PNL directivities and spectra at two (2) angles to inlet axis of configuration TAS-2 in community, sideline and opposite community orientations. One notes that the PNL values increase with an increase in azimuthal angle,  $\phi$ . The spectral data at  $\theta_i = 130^\circ$  shows that the low frequency noise of all the three (3) orientations is insensitive to shield orientation (i.e., for frequencies  $< 250$  Hz). At mid and high frequencies, there is a definite trend showing that the shield is able to reflect the noise to the opposite community orientation. The high frequency noise in sideline orientation is in between that of the community and opposite community orientations indicating a gradual variation with the azimuthal angle,  $\phi$ . The spectral data at  $\theta_i = 60^\circ$  again shows that the low frequency noise is insensitive to shield orientation. However, the mid and high frequency noise does not show the variation with azimuthal angle as was observed in the aft quadrant indicating that the reflective/refractive effects of the partial shield are not dominant in the front quadrant. The dominant mechanism in the front quadrant is possibly the source strength reduction due to the shield and also eddy convection effects.

Next, to highlight the reflective character of the partial shield, acoustic data of configuration TAS-2 in community and opposite community orientations will be compared with those of the baseline annular plug nozzle, configuration TAS-1.

Figure 4.1.1-5 compares the PNL directivities and spectral content at  $\theta_i = 130^\circ$  and  $60^\circ$  of the baseline annular plug nozzle (TAS-1) and the annular plug nozzle with  $180^\circ$  TAS of 0.48" thickness (TAS-2) in community and opposite community orientations at a typical cutback case in flight. One notes that the partial shield gives noise reduction at all observer locations in community orientation compared to the baseline plug nozzle. The PNL's in the opposite community orientation are higher than those of the baseline plug nozzle, indicating the reflective character of the partial shield. The

Sym.	Point	Orientation	Azimuthal Angle, $\phi$ , Degrees
□	205	Sideline	70
○	221	Community	0
◇	287	Opp. Community	180

$T = 1400 \text{ In.}^2$   
 1000' Distance  
 Static  
 Cutback Cycle

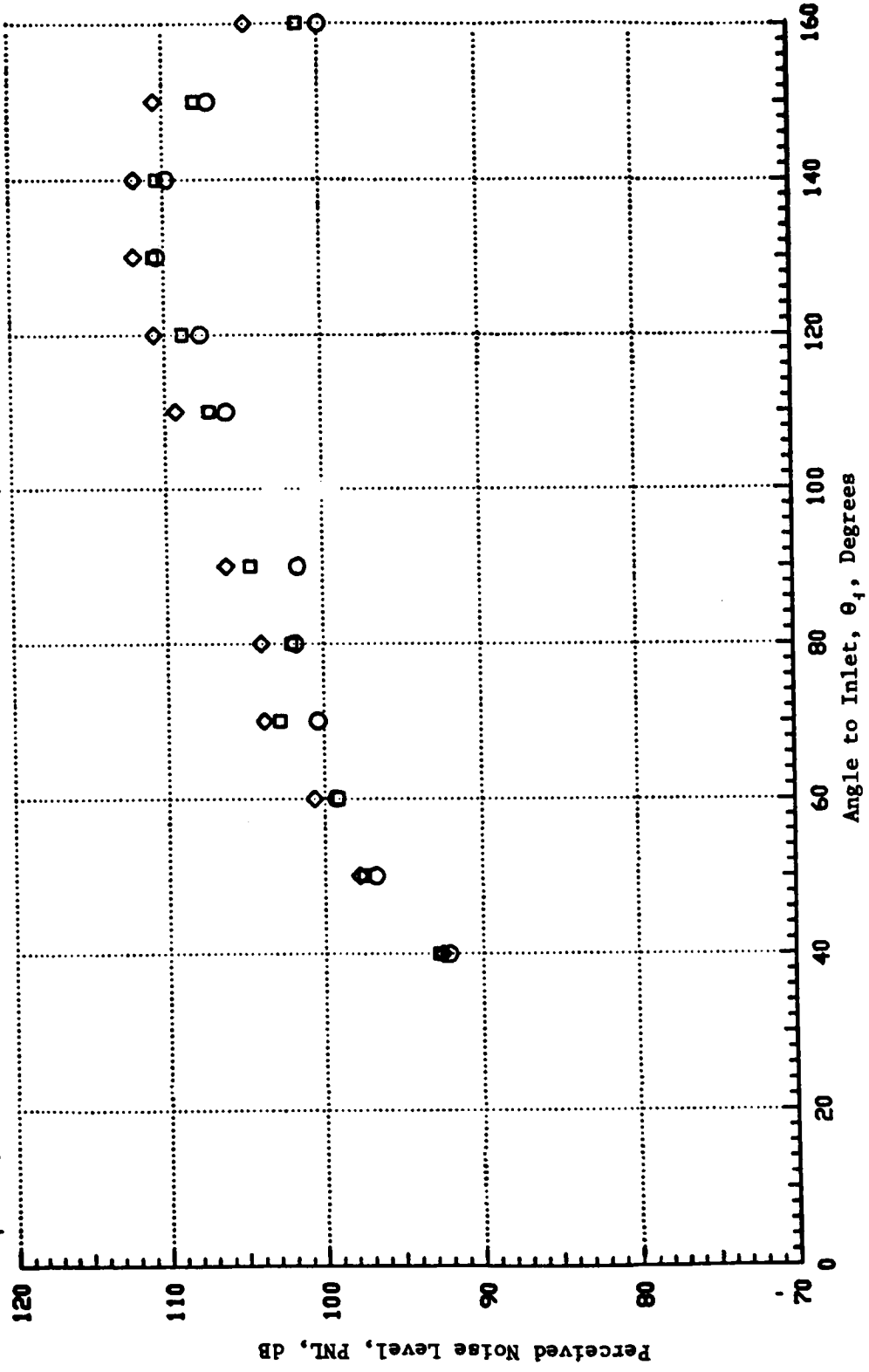
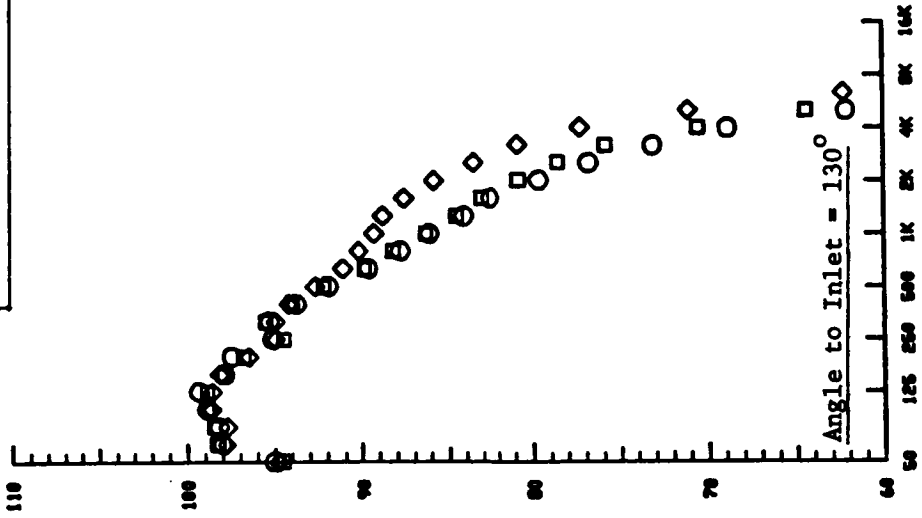
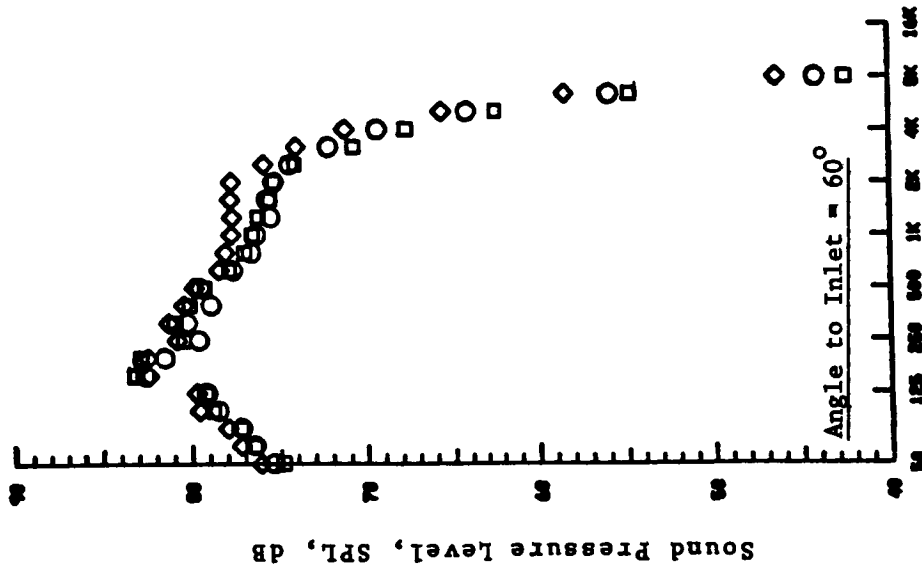


Figure 4.1.1.-4a. Azimuthal Variation of PNL Directivities of the Unsuppressed Annular Plug Nozzle with 180° Thermal Acoustic Shield at a Typical Cutback Cycle (Static).

Sym. Point	Orientation	Azimuthal Angle, $\phi$ , Degrees
□	Sideline	70
○	Community	0
◇	Opp. Community	180



$A^T = 1400 \text{ In.}^2$   
 1000' Distance  
 Static  
 Cutback Cycle

1/3 Octave Band Center Frequency, Hz

Figure 4.1.1-4b. Azimuthally Asymmetric Spectral Content of the Unsuppressed Annular Plug Nozzle with 180° Thermal Acoustic Shield at a Typical Cutback Cycle (Static).

Config.	Orient.	Test Point	Core Jet			Shield Jet			Mixed Conditions		
			$V^j$ , fps	$T_T^j$ , °R	$P_r^j$	$V^{sj}$ , fps	$T_T^{sj}$ , °R	$P_r^{sj}$	$V^{mix}$ , fps	$T_T^{mix}$ , °R	$P_r^{mix}$
TAS-1	Axisymm.	106	1874	1529	2.086	←----- NO SHIELD	-----→	1874	1529	2.086	
TAS-2	Community	222	1859	1486	2.110			1748	1490	1.915	
TAS-2	Opposite Community	288	1847	1516	2.052			1733	1516	1.869	

- $V_{a/c} = 400$  fps
- 1000' Distance
- Cutback Cycle
- $A_T = 1400$  in<sup>2</sup>

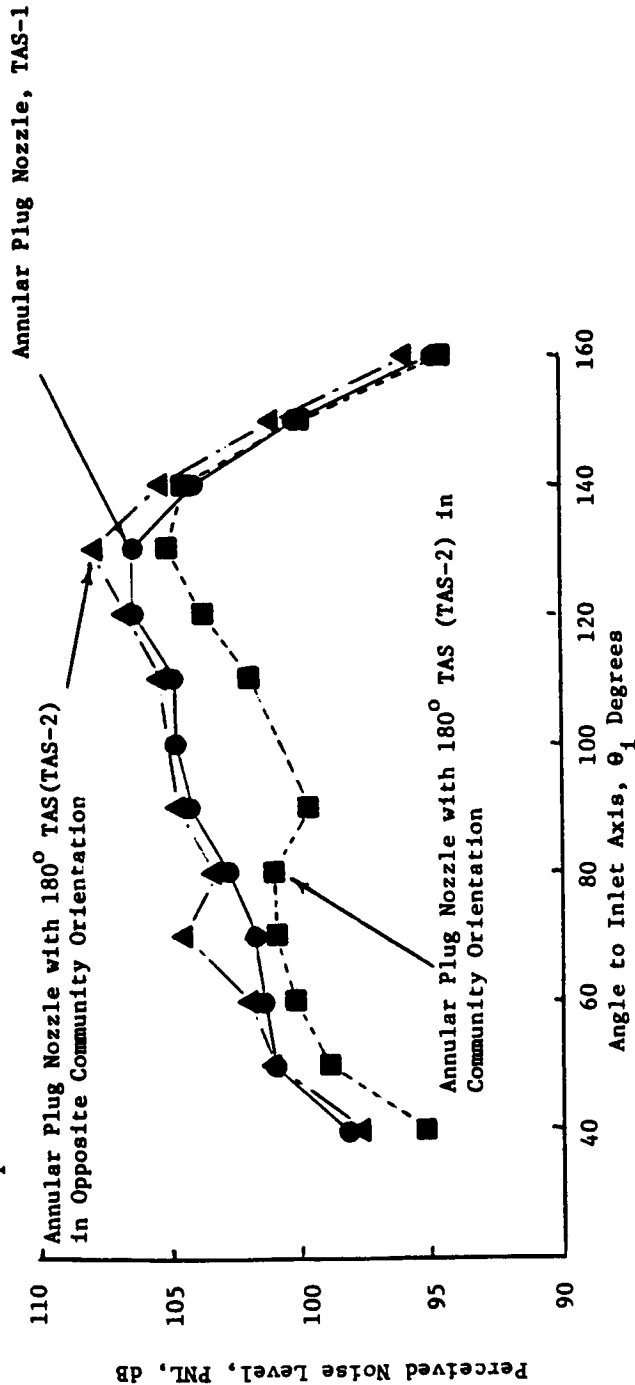
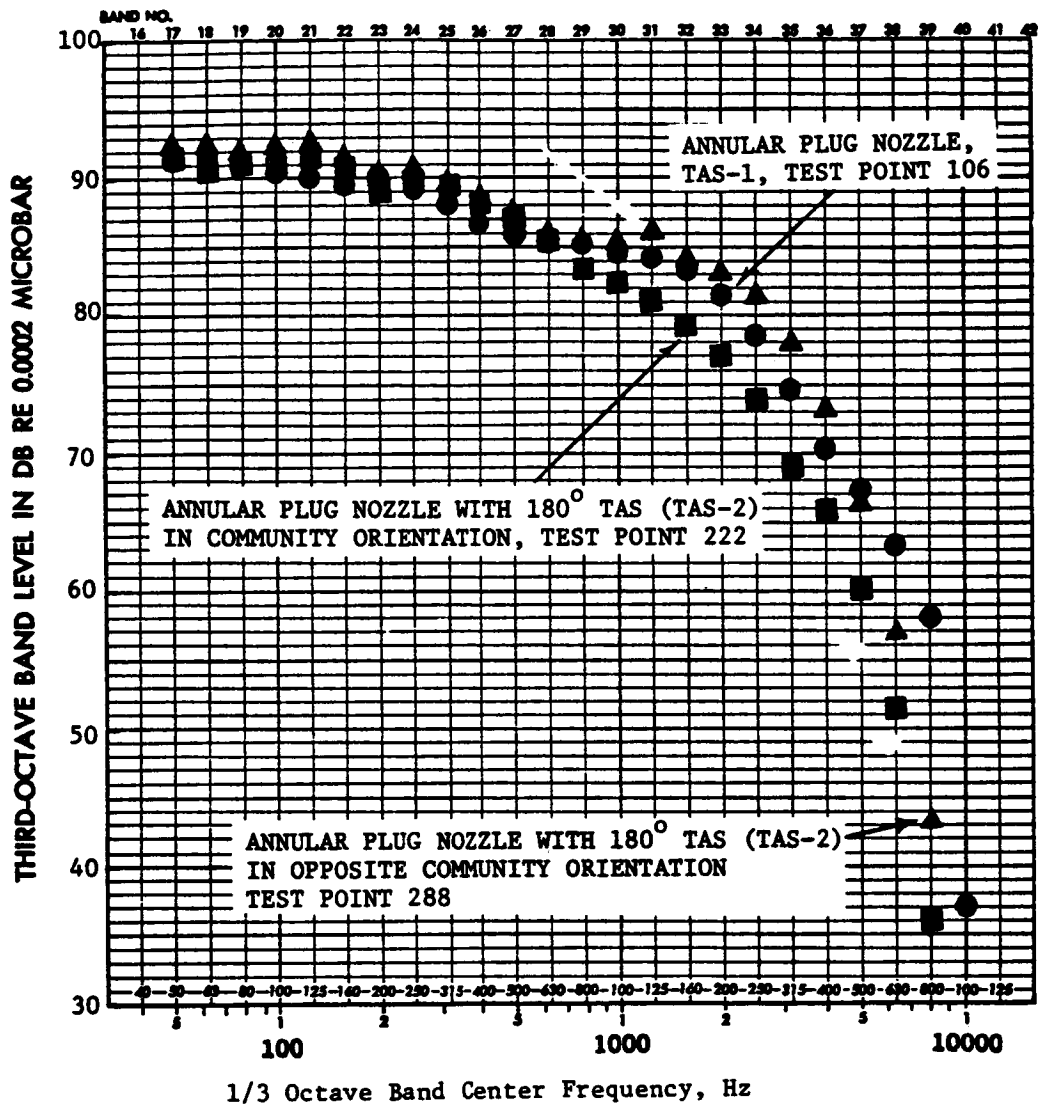


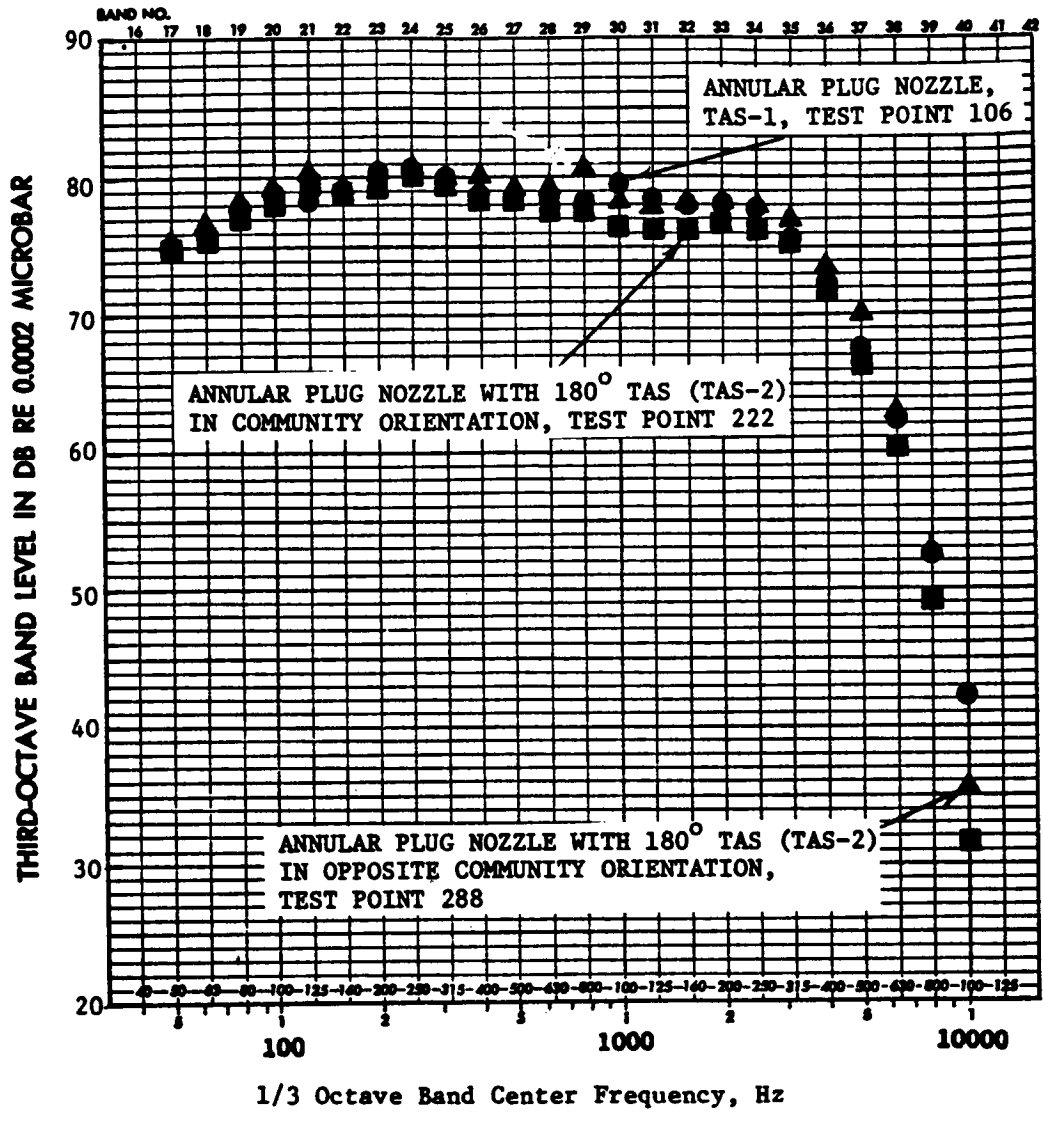
FIGURE 4.1.1-5a. AZIMUTHALLY ASSYMETRIC PNL DIRECTIVITIES OF A PLUG NOZZLE WITH THE PARTIAL SHIELD IN COMPARISON WITH THAT OF THE PLUG NOZZLE WITHOUT THE SHIELD AT A TYPICAL CUTBACK CONDITION IN FLIGHT.





- Angle to Inlet = 130°
- $V_{a/c}$  = 400 fps
- 1000' Distance
- CUTBACK CYCLE
- $A_T$  = 1400 in<sup>2</sup>

FIGURE 4.1.1-5b. AZIMUTHALLY ASSYMETRIC SPECTRAL CONTENT OF A PLUG NOZZLE WITH THE PARTIAL SHIELD AT  $\theta_i = 130^\circ$  IN COMPARISON WITH THAT OF THE PLUG NOZZLE WITHOUT THE SHIELD AT A TYPICAL CUTBACK CONDITION IN FLIGHT.



- Angle to Inlet = 60°
- $V_{a/c} = 400$  fps
- 1000' Distance
- CUTBACK CYCLE<sub>2</sub>
- $A_T = 1400$  in.<sup>2</sup>

FIGURE 4.1.1-5c. AZIMUTHALLY ASSYMETRIC SPECTRAL CONTENT OF A PLUG NOZZLE WITH THE PARTIAL SHIELD AT  $\theta_1 = 60^\circ$  IN COMPARISON WITH THAT OF THE PLUG NOZZLE WITHOUT THE SHIELD AT A TYPICAL CUTBACK CONDITION IN FLIGHT

spectral distribution at  $\theta_i = 130^\circ$  (see Figure 4.4.1-5b) shows that the partial shield has noticeably reduced the mid and high frequency noise of the baseline plug nozzle in the community orientation and has increased the mid frequency noise in the opposite community orientation. The low frequency noise is not affected by the partial shield indicating that the shield might have mixed with the core jet at locations where low frequency noise is generated. The spectral data at  $\theta_i = 60^\circ$  shows a slight reflective character at mid-frequencies in the sense that the data of the nozzle with  $180^\circ$  shield in community and opposite community orientations are on either side of the data of baseline annular plug nozzle.

#### 4.1.1.3 Influence of the Kinematic Ratios ( $V_r$ , $CV_r$ and $T_r^S$ ) on Acoustic Characteristics of Unsuppressed Annular Plug Nozzle

Typical results of the parametric variation of the partial thermal acoustic shield's aerodynamic conditions, keeping the core conditions of the unsuppressed plug nozzle reasonably constant, are presented in this subsection. For this study, the core jet of configuration TAS-2 is maintained at a typical cutback condition and the partial shield aerodynamic conditions are varied within the domain of practical interest (see Subsection 3.2.1 and Figure 3.3). Velocity ratio ( $V_r$ ) determines the shearing gradient between the core and shield jets. The thermal acoustic shield velocity ratio ( $CV_r$ ) is a ratio of the phase velocity of the shield jet to the core jet, which determines the refraction characteristics of the shield jet.

Figure 4.1.1-6 shows the influence of varying the velocity ratio ( $V_r$ ) of the shield, keeping the thermal acoustic shield velocity ratio ( $CV_r$ ) constant, on the PNL directivity and spectral content at  $\theta_i = 60^\circ$  and  $140^\circ$ . Note that over the limited range of variation of the velocity ratio, there is no noticeable variation of the PNL directivity or spectrum at  $\theta_i = 60^\circ$ . Only at very high frequencies at  $\theta_i = 140^\circ$  does  $V_r \approx 0.6$  yield lower SPL's than  $V_r = 0.7$ . Figure 4.1.1-7 shows the influence of varying the thermal acoustic shield velocity ratio ( $CV_r$ ) keeping the shield to core jet velocity ( $V_r$ ) reasonably constant, on the PNL directivity and spectra at  $\theta_i = 60^\circ$  and  $150^\circ$ . One again detects the influence of  $CV_r$  only at very high frequencies. From ray acoustics

SYMBOL	POINT	$V_r$	$CV_r$	$T_r^s$
○	269	0.58	0.79	1.05
□	277	0.70	0.80	0.81

Configuration TAS-2  
Community Orientation

$A^T = 1400 \text{ In.}^2$   
1000' Flyover Distance  
Static  
Cutback Cycle

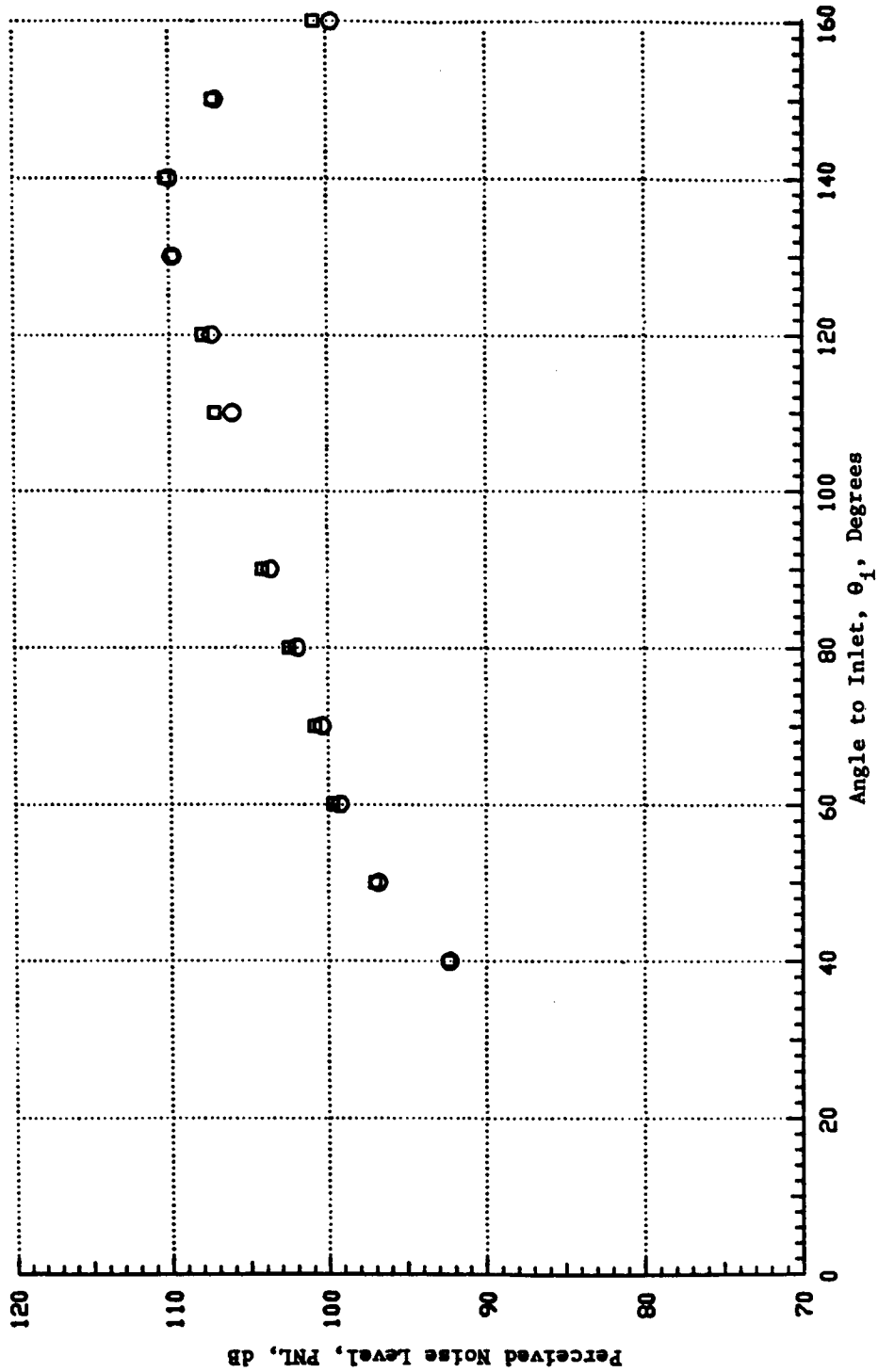


Figure 4.1.1-6a. Influence of the Velocity Ratio ( $V_r$ ) on the PNL Directivity of Configuration TAS-2, Keeping the Thermal Acoustic Shield Velocity Ratio ( $CV_r$ ) Constant for a Typical Cutback Cycle (Static).

SYMBOL	$V_r$	$CV_r$	$T_r^S$	Configuration TAS-2
○	0.58	0.79	1.05	Community Orientation
□	0.70	0.80	0.81	

$A^T = 1400 \text{ In.}^2$   
 1000' Flyover Distance  
 Static  
 Outback Cycle

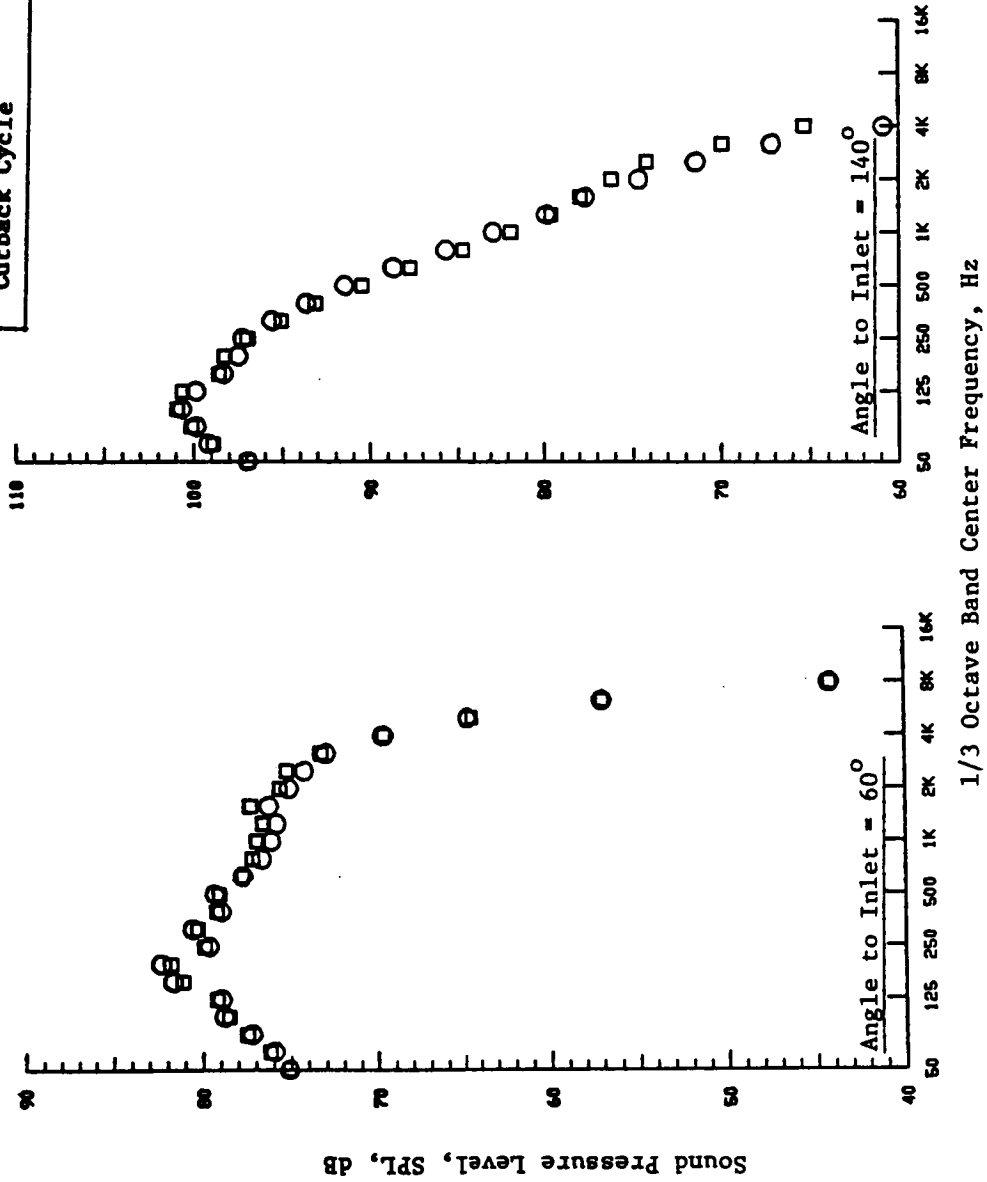


Figure 4.1.1-6b. Influence of the Velocity Ratio on the Spectral Content of Configuration TAS-2, Keeping  $CV_r$  Constant for a Typical Outback Cycle (Static).

SYMBOL	POINT	$V_r$	$CV_r$	$T_r^S$
○	265	0.60	0.71	0.66
□	271	0.59	0.83	1.22

Configuration TAS-2  
Community Orientation

$A^T = 1400 \text{ In.}^2$   
1000' Flyover Distance  
Static  
Outback Cycle

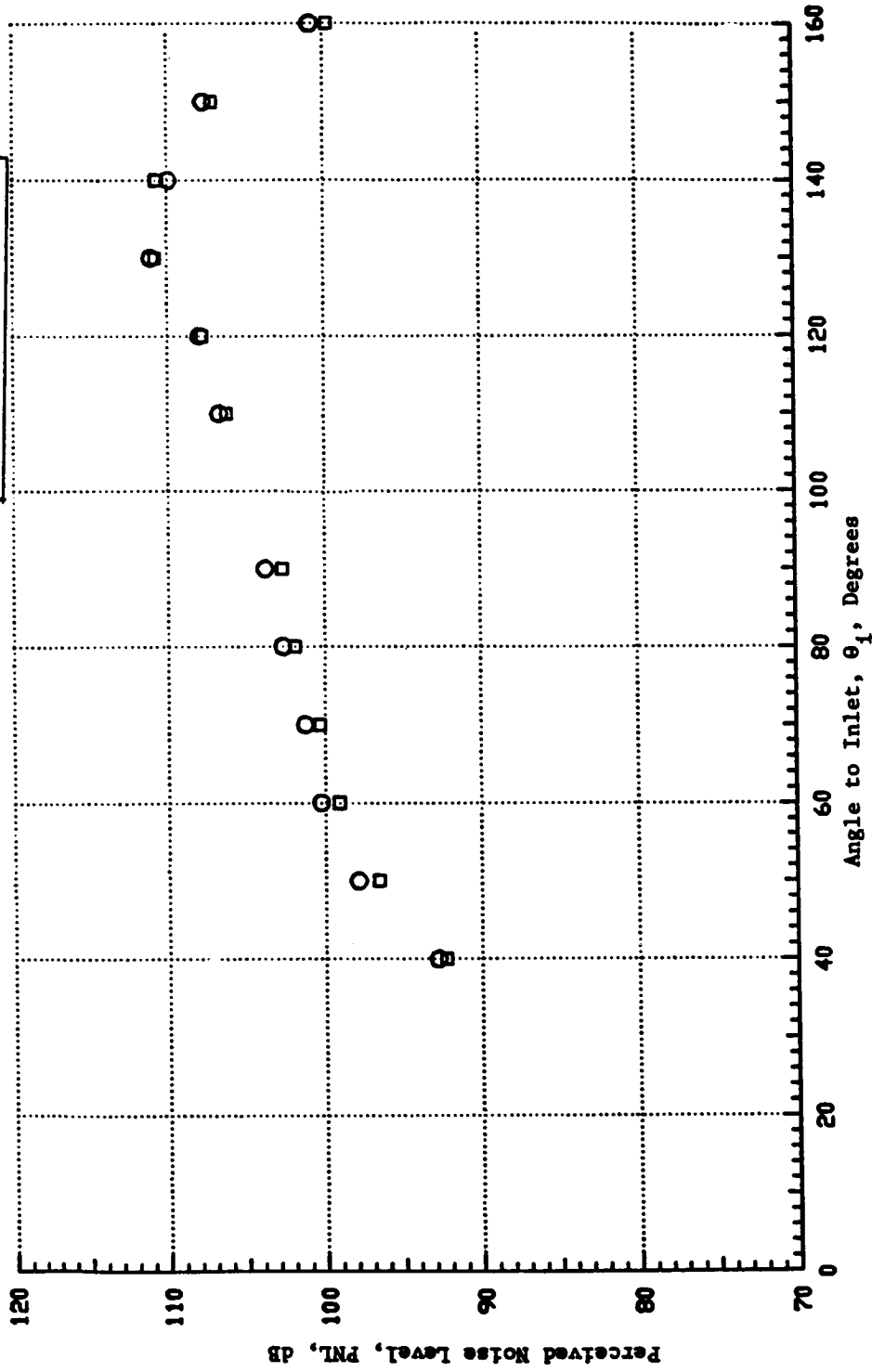


Figure 4.1.1-7a. Influence of the Thermal Acoustic Shield Velocity Ratio ( $CV_r$ ) on the PNL Directivity of Configuration TAS-2, Keeping the Velocity Ratio ( $V_r$ ) Constant for a Typical Outback Cycle (Static).

$A^T = 1400 \text{ In.}^2$   
 1000' Flyover Distance  
 Static  
 Outback Cycle

Configuration TAS-2  
 Community Orientation

POINT	$V_r$	$CV_r$	$T_r^S$
265	0.60	0.71	0.66
271	0.59	0.83	1.22

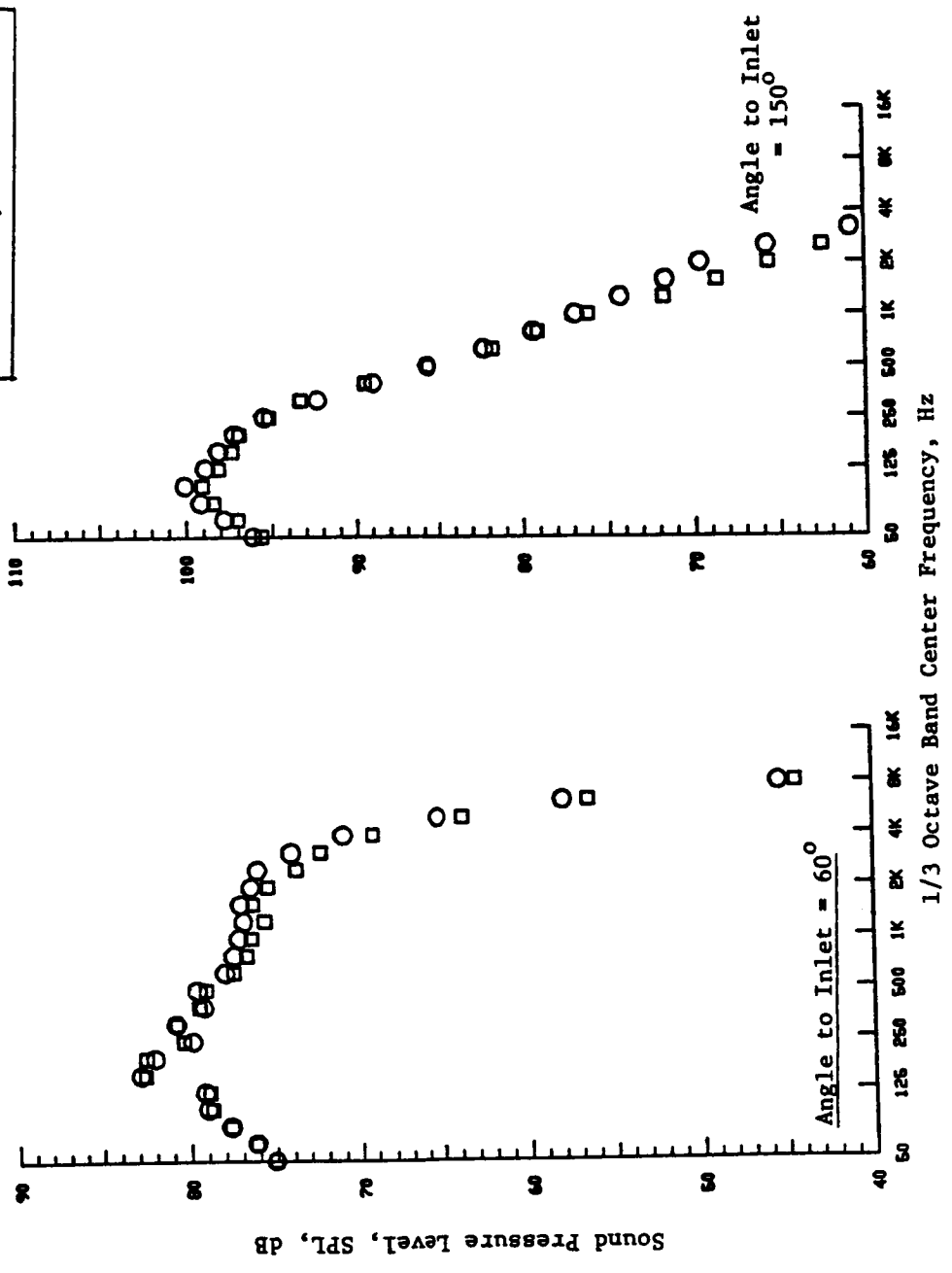


Figure 4.1.1-7b. Influence of  $CV_r$  on the Spectral Content of Configuration TAS-2, Keeping the  $V_r$  Constant for a Typical Outback Cycle (Static).

considerations, a higher value of  $CV_r$  yields higher refraction capabilities. Since the contribution of high frequencies to PNL is negligible for the case under study, there are no noticeable differences in PNL.

Next, the combined influence of varying  $V_r$  and  $CV_r$ , keeping the static temperature ratio ( $T_r^S$ ) reasonably constant, on the PNL directivity and spectral content at  $\theta_i = 60^\circ$  and  $140^\circ$  is shown in Figure 4.1.1-8. As with the variation of  $V_r$  keeping  $CV_r$  constant and vice versa, the combined influence of varying  $V_r$  and  $CV_r$  keeping  $T_r^S$  constant is not significant on the PNL directivity of the unsuppressed annular plug nozzle with a partial shield, over the range of conditions tested. The spectral data in the aft quadrant shows some influence of  $V_r$  and  $CV_r$  in the high frequency region only.

#### 4.1.1.4 Influence of the Partial Shield on Unsuppressed Annular Plug Nozzle With a Convergent-Divergent Flowpath for the Core Nozzle

The application of a convergent-divergent flowpath to guide a supersonic stream for complete expansion at the design Mach number to ambient pressure for a plug nozzle has been shown to give shock cell noise reduction (see Reference 4.3). The shock cell noise reduction is attributed to the absence of a strong shock cell structure on the plug surface due to the convergent-divergent flowpath. The core nozzle of configuration TAS-5 employs a convergent-divergent flowpath designed for an exit Mach number of 1.4 and a  $180^\circ$  shield of 0.48" thickness. The convergent-divergent core nozzle alone (Configuration SC-4) was tested under a separate contract. The objective of this subsection is to evaluate the acoustic effect of the partial shield on the convergent-divergent annular plug nozzle.

Figure 4.1.1-9 compares the PNL directivities and spectral composition at four (4) angles to observer of configurations TAS-5 and SC-4 with the core at the design condition (viz.,  $M^j = 1.4$ ,  $V^j = 2420$  fps,  $p_r^j = 3.12$ ,  $T_T^j = 1730^\circ R$ ). The partial thermal acoustic shield was maintained at a velocity ratio (i.e.  $v^{sj}/v^j$ ) of 0.6, keeping the total temperature of the shield at  $1730^\circ R$ . Configuration TAS-5 was tested in a sideline orientation ( $\phi = 70^\circ$ ). The TAS has no influence on the front quadrant perceived noise



SYMBOL	POINT	$V_r$	$CV_r$	$T_r^S$
○	271	.59	.83	1.22
□	283	.80	.93	1.19

Configuration TAS-2  
Community Orientation

$A^T = 1400 \text{ In.}^2$   
1000' Flyover Distance  
Static  
Outback Cycle

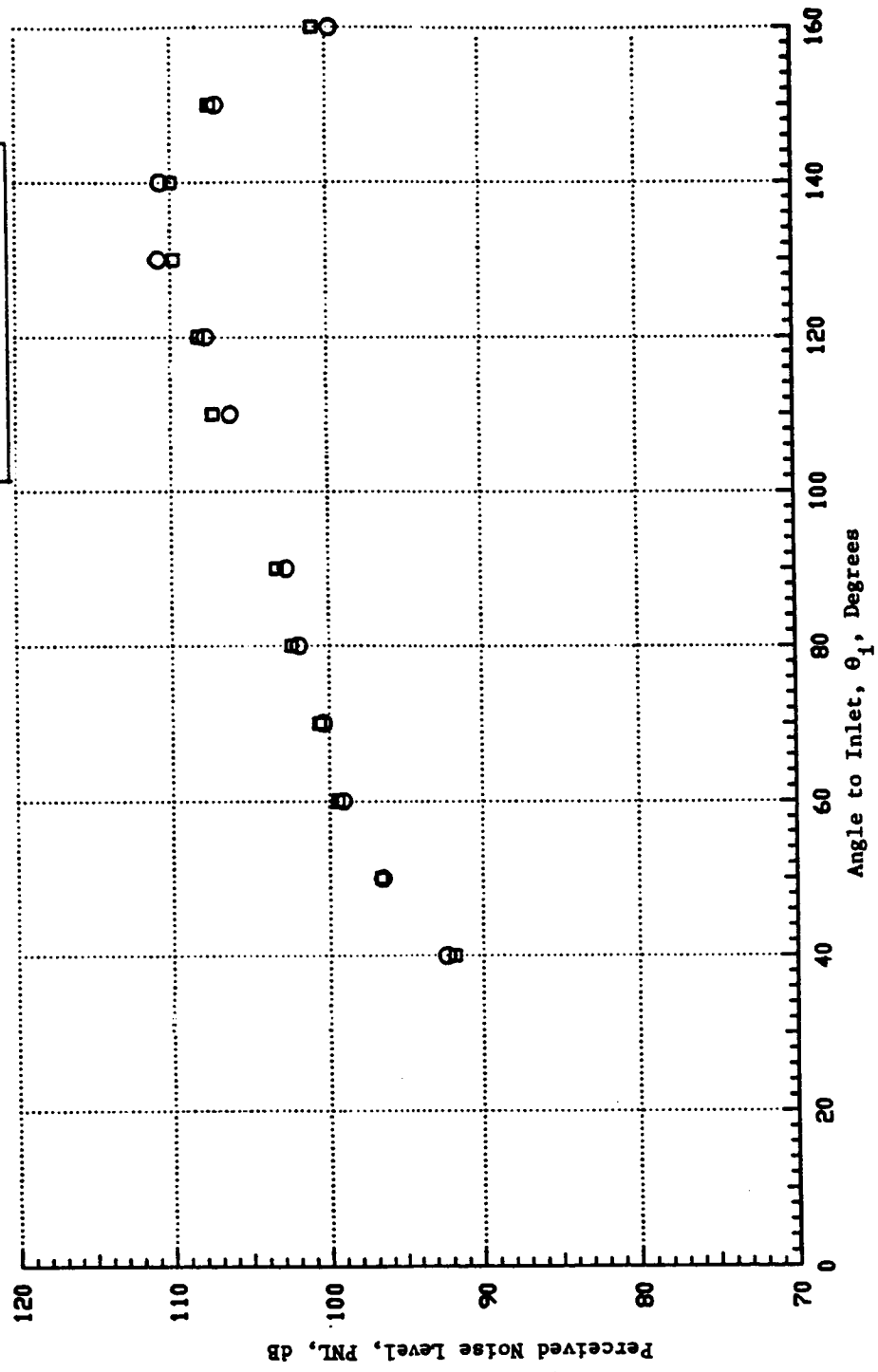


Figure 4.1.1-8a. Combined Influence of  $V_r$  and  $CV_r$  on the PNL Directivity of Configuration TAS-2, Keeping the Static Temperature Ratio ( $T_r^S$ ) Constant for a Typical Outback Cycle (Static).

SYMBOL	POINT	$V_r$	$CV_r$	$T_r^S$
○	271	.59	.83	1.22
□	283	.80	.93	1.19

Configuration TAS-2  
Community Orientation

$A^T = 1400 \text{ In.}^2$   
1000' Flyover Distance  
Static  
Cutback Cycle

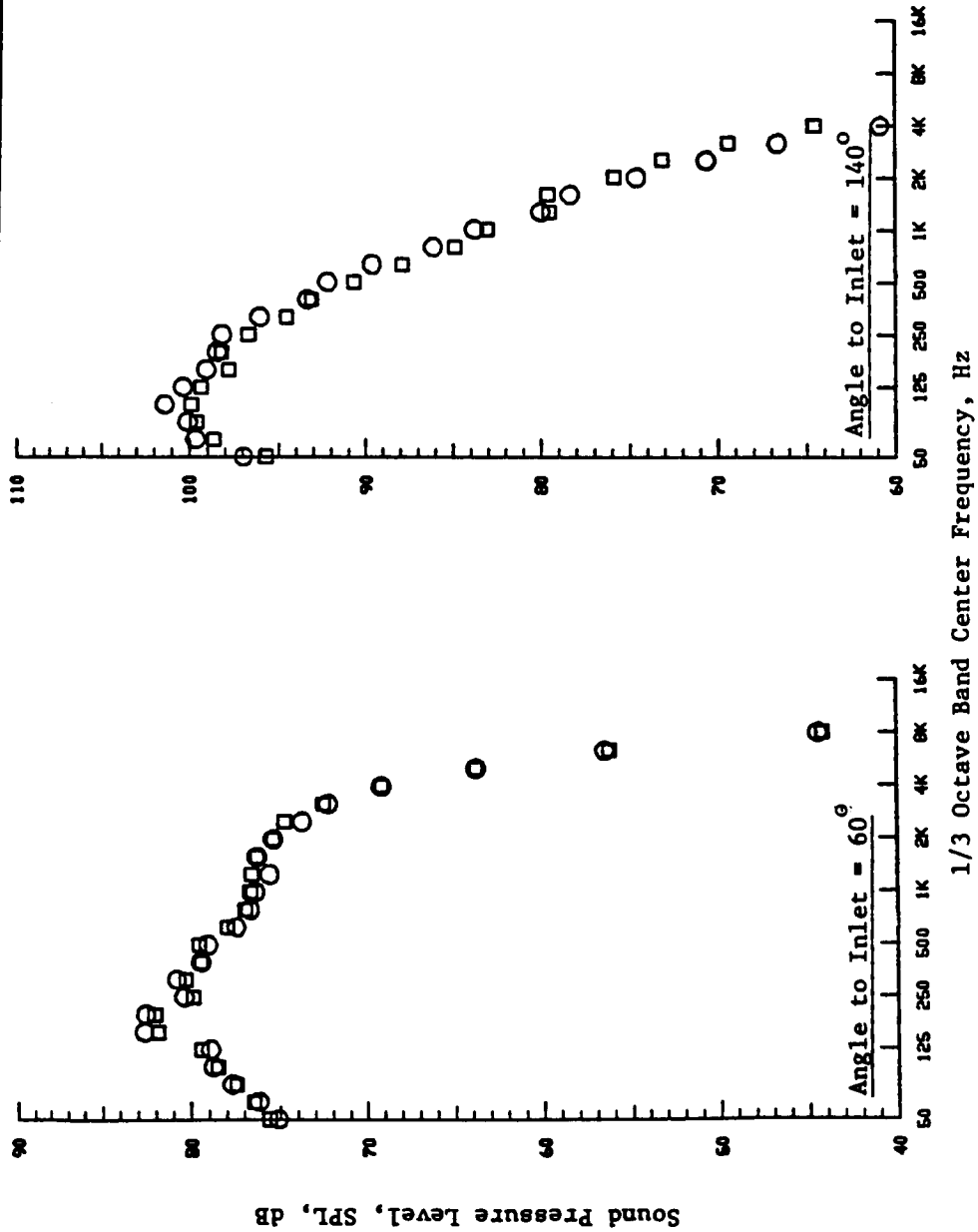


Figure 4.1.1-8b. Combined Influence of  $V_r$  and  $CV_r$  on the Spectral Content of Configuration TAS-2, Keeping the  $T_r^S$  Constant for a Typical Cutback Cycle (Static).

Sym.	Point	Config.	Orientation
O	413	SC-4	Axisymmetric
□	509	TAS-5	Sideline

$A^* = 1400 \text{ in.}^2$   
 2400' Sideline,  $\phi = 70^\circ$   
 Static

C-D Nozzle at Design Condition

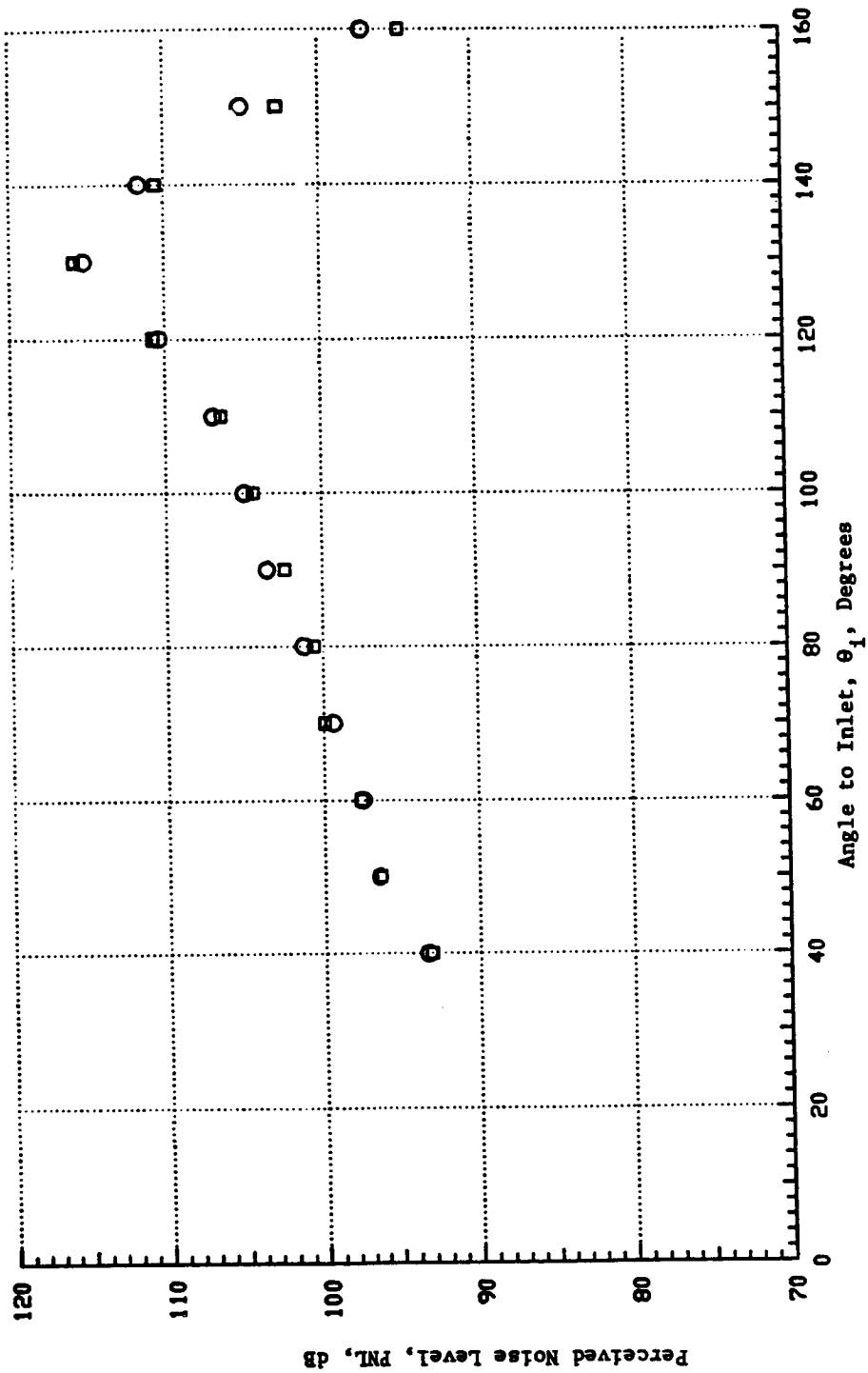


Figure 4.1.1-9a. Influence of the Partial Thermal Acoustic Shield on PNL Directivity of Unsuppressed Annular Plug Nozzle with a Convergent-Divergent Flowpath Operating at the Design Mach Number of 1.4 (Static).

Sym.	Point	Config.	Orientation
○	413	SC-4	Axiallysymmetric
□	509	TAS-5	Sideline

$A^* = 1400 \text{ In.}^2$   
 2400' Sideline,  $\phi = 70^\circ$   
 Static

C-D Nozzle at Design Condition

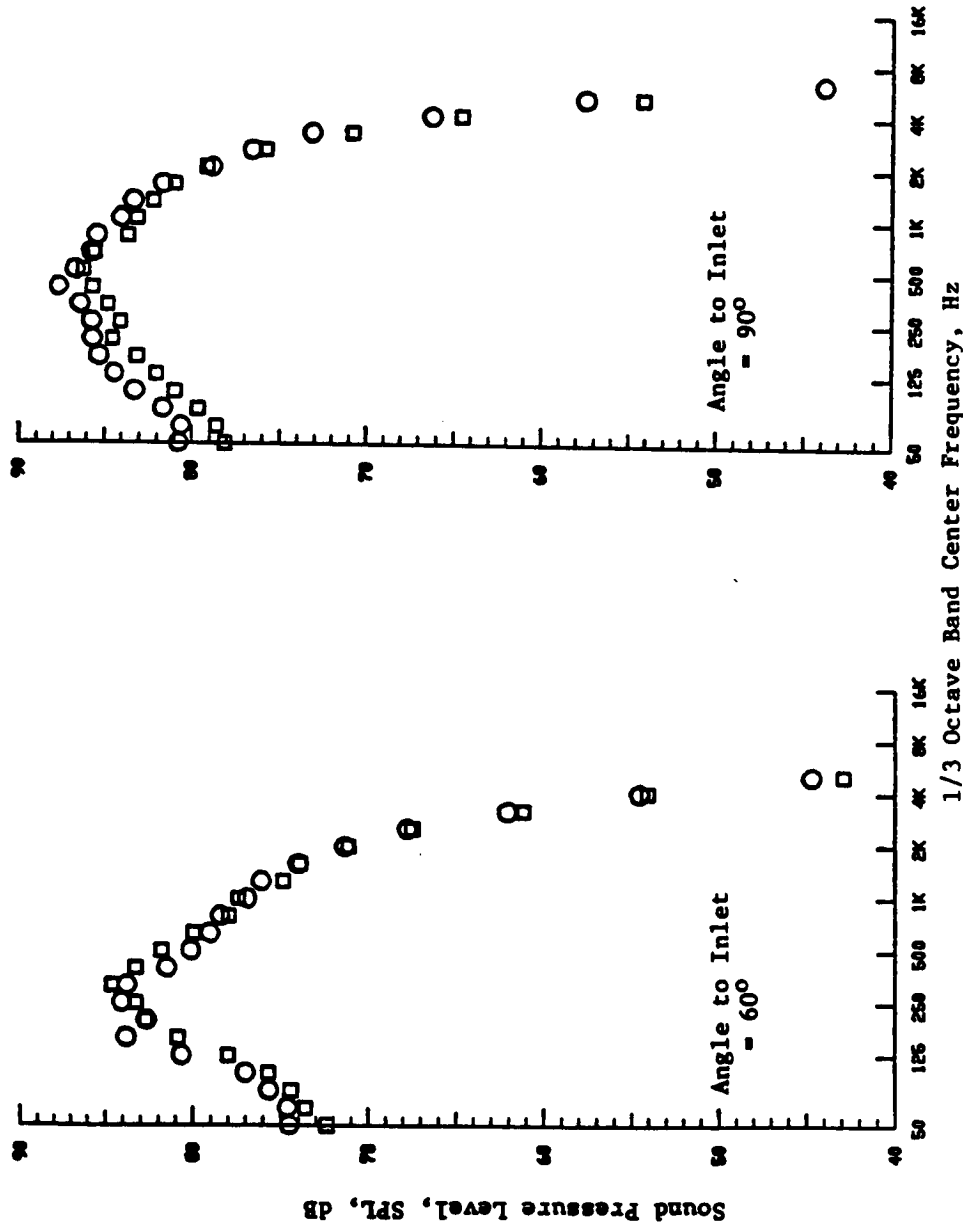


Figure 4.1.1-9b. Influence of the Partial Thermal Acoustic Shield on the Spectral Content of the Unsuppressed Annular Plug Nozzle with a Convergent-Divergent Flowpath Operating at the Design Mach Number of 1.4 (Static).

Sym.	Point	Config.	Orientation
○	413	SC-4	Axisymmetric
□	509	TAS-5	Sideline

C-D Nozzle at Design Condition

$T^* = 1400 \text{ In.}^2$   
 $A^* = 2400'$  Sideline,  $\phi = 70^\circ$   
 Static

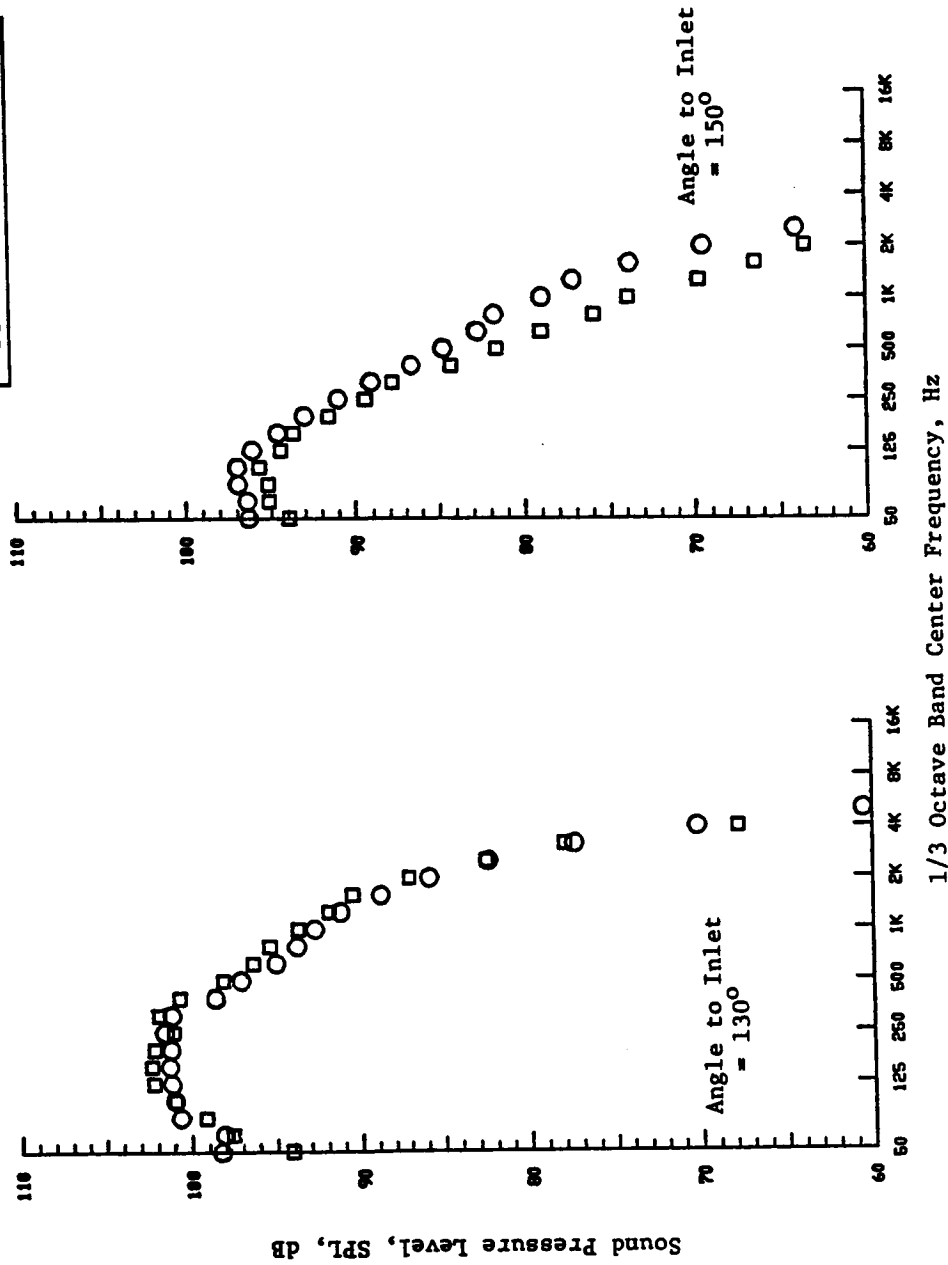


Figure 4.1.1-9c. Influence of the Partial Thermal Acoustic Shield on the Spectral Content of the Unsuppressed Annular Plug Nozzle with a Convergent-Divergent Flowpath at the Design Mach Number of 1.4 (Static).

levels. There is a slight PNL increase at the peak noise angle (viz.,  $\theta_i = 130^\circ$ ) and a noise reduction at shallow angles to the jet axis (viz.,  $\theta_i = 140^\circ, 150^\circ$  and  $160^\circ$ ). The spectral data at  $\theta_i = 60^\circ, 90^\circ$  and  $130^\circ$  indicates a minor or negligible influence of the partial shield. At  $\theta_i = 130^\circ$ , the slight amplification of PNL by the shield can be ascribed to the low frequency noise amplification by the shield. However, at  $\theta_i = 150^\circ$  one notices significant reductions in the high frequency noise by the partial shield.

It will be shown in Subsection 4.1.3 that for an unsuppressed annular plug nozzle, the thermal acoustic shield becomes ineffective in yielding any PNL reductions as the core jet velocity increases due to the dominance of the low frequency noise of the very high velocity core jets and the ability of the thermal acoustic shield to suppress mainly the mid and high frequency noise. The core jet velocity of configuration TAS-5 at the design condition is in the domain of very high core jet velocities where the thermal shield was not effective in yielding PNL reductions at many observer locations.

For the purpose of comparison, the influence of the  $180^\circ$  shield of 0.48" thickness on the unsuppressed annular plug with a convergent termination at the cycle condition similar to that of configuration TAS-5 was analyzed. Figure 4.1.1-10 compares the PNL directivities and spectral composition of configurations TAS-2 and TAS-1. The partial thermal acoustic shield of configuration TAS-2 was maintained at a velocity ratio (i.e.,  $V^{sj}/V^j$ ) of 0.6, and was tested in sideline orientation. Again, one notes that the partial shield gives PNL reductions only at very shallow angles (viz.,  $\theta_i = 140^\circ, 150^\circ$  and  $160^\circ$ ) and yields a slight amplification of PNL at the peak noise angle. The spectral composition at  $\theta_i = 60^\circ, 90^\circ, 130^\circ$  and  $150^\circ$  of configurations TAS-1 and TAS-2 bear similar relationships as those of configurations SC-4 and TAS-5.

One significant geometric difference between the  $180^\circ$  shields on unsuppressed annular plug nozzle with convergent termination and on unsuppressed annular plug nozzle with convergent-divergent termination is the axial stagger between the core and shield streams. In the case of configuration TAS-2, the axial stagger between the shield and core jets is 0.8" whereas in the case of configuration TAS-5, the axial stagger is 4.60"

Sym.	Point	Config.	Orientation
○	113	TAS-1	Axisymmetric
□	213	TAS-2	Sideline

Core Nozzle at C-D Design Condition

$A^* = 1400 \text{ In.}^2$   
 2400' Sideline,  $\phi = 70^\circ$   
 Static

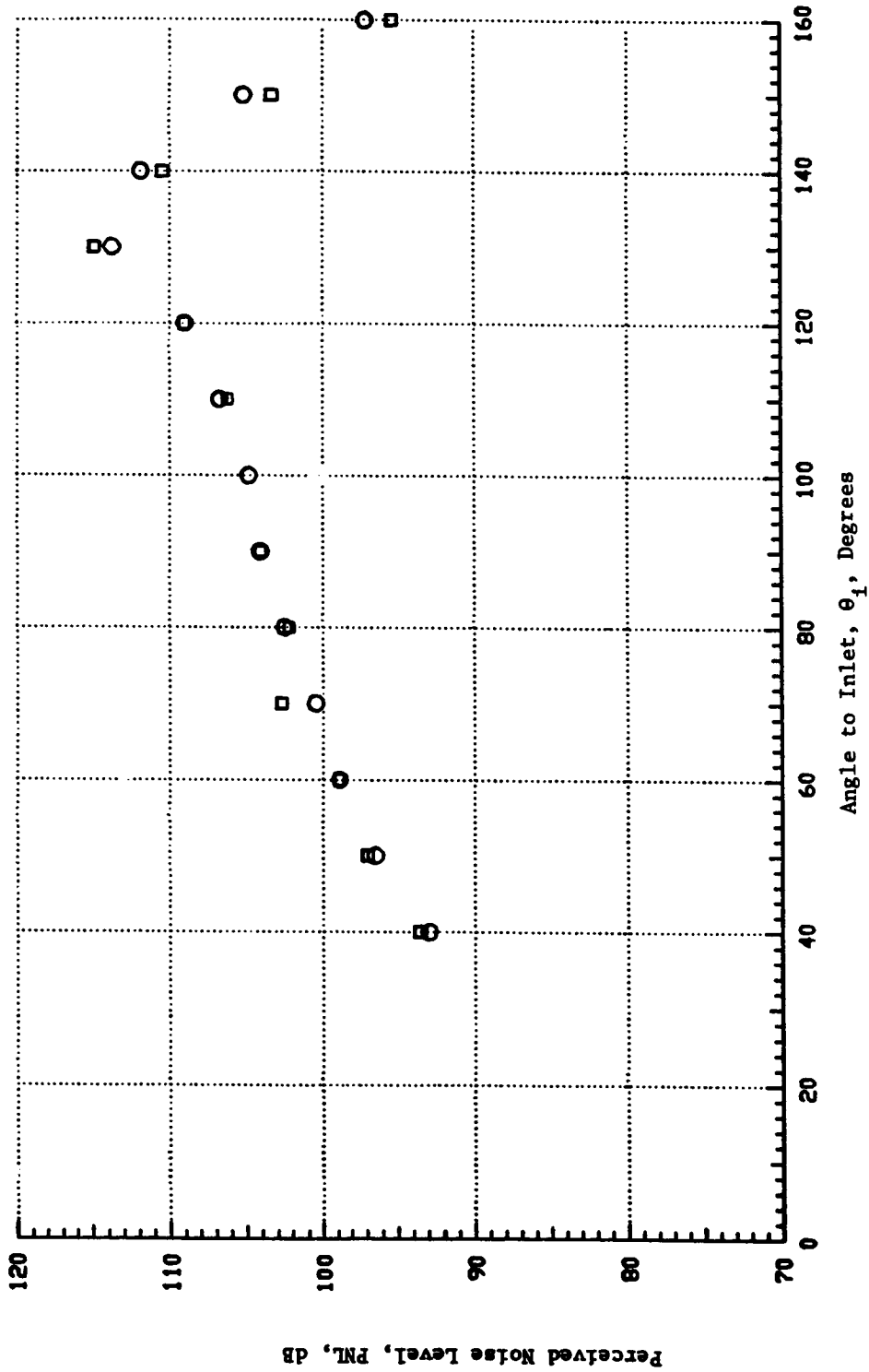


Figure 4.1.1-10a. Influence of the Partial Thermal Acoustic Shield on PNL Directivity of Unsuppressed Annular Plug Nozzle with a Convergent Flowpath Operating approximately at the C-D Nozzle Design Mach Number of 1.4 (Static).

Sym.	Point	Config.	Orientation
○	113	TAS-1	Axisymmetric
□	213	TAS-2	Sideline

$A^* = 1400 \text{ In.}^2$   
 2400° Sideline,  $\phi = 70^\circ$   
 Static

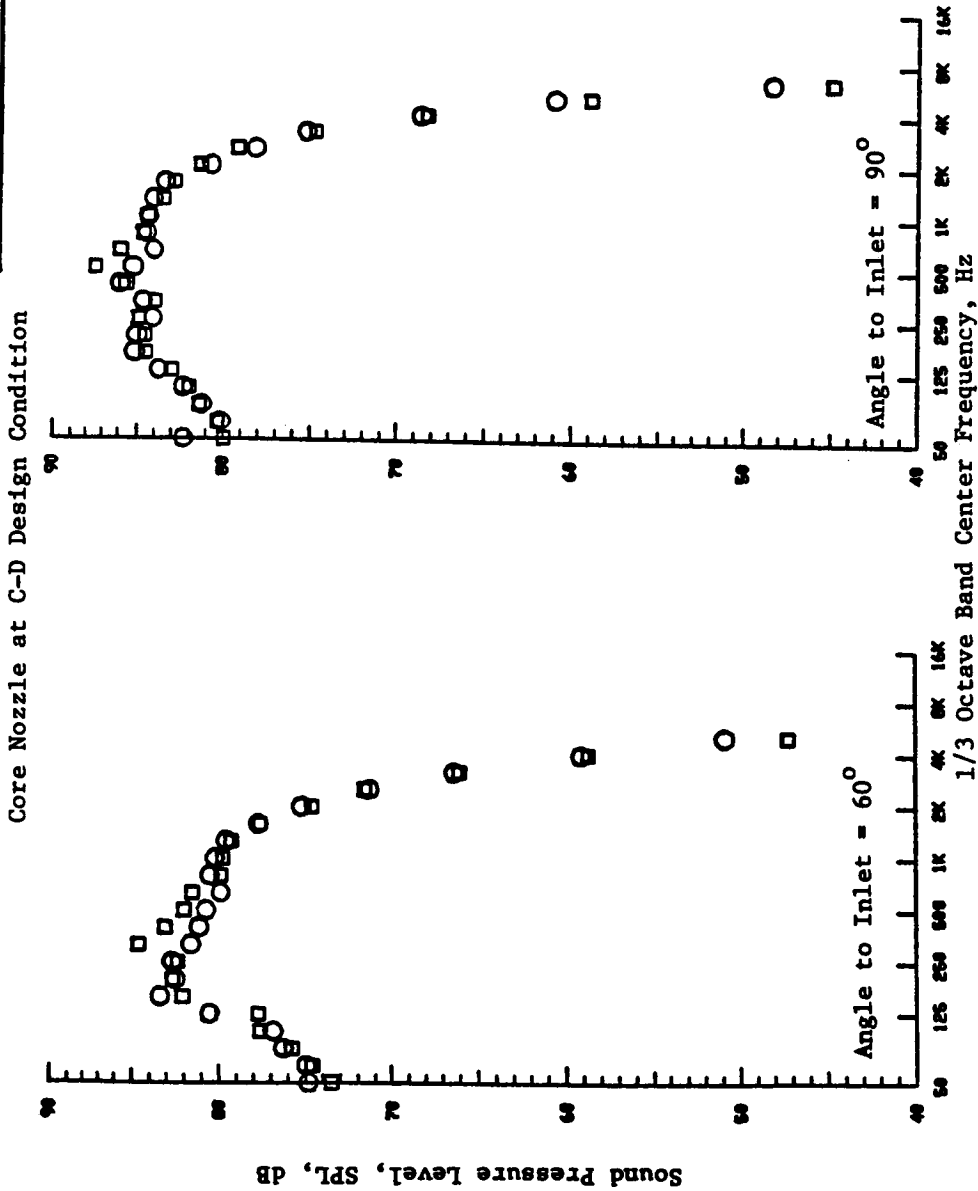


Figure 4.1.1-10b. Influence of the Partial Thermal Acoustic Shield on Spectral Content of Unsuppressed Annular Plug Nozzle with a Convergent Flowpath Operating Approximately at the C-D Nozzle Design Mach Number of 1.4 (Static).



Sym.	Point	Config.	Orientation
○	113	TAS-1	Axisymmetric
□	213	TAS-2	Sideline

Core Nozzle at C-D  
Design Condition

$A^* = 1400 \text{ In.}^2$   
2400' Sideline,  $\phi = 70^\circ$   
Static

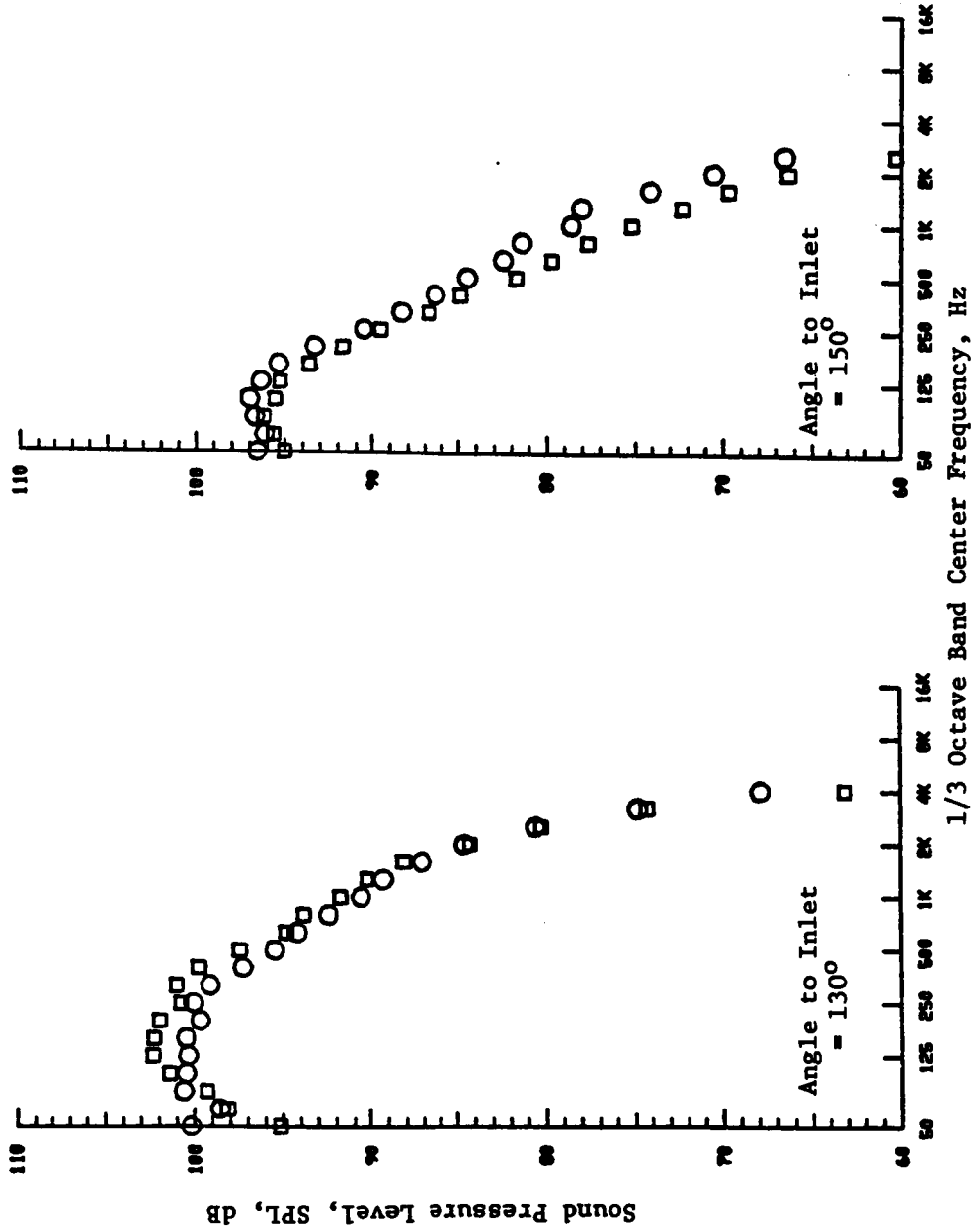


Figure 4.1.1-10c. Influence of the Partial Thermal Acoustic Shield on Spectral Content of Unsuppressed Annular Plug Nozzle with a Convergent Flowpath Operating Approximately at the C-D Design Mach Number of 1.4 (Static).

(see Table 3-II). However, the acoustic comparisons of configuration SC-4 with TAS-5 and of configuration TAS-1 with TAS-2 indicate a similar influence of the partial thermal acoustic shields, implying that the axial stagger between the shield and core streams does not significantly influence the acoustic behavior of the shields, at high core jet velocities.

#### 4.1.2 INFLUENCE OF THERMAL ACOUSTIC SHIELDS ON 32 CHUTE MECHANICAL SUPPRESSOR NOZZLE

##### 4.1.2.1 Influence of Partial Shields and Full Shield on 32 Chute Suppressor Nozzle

The acoustic influence of the 180° shields of 0.48" and 0.97" thicknesses and the 360° shield of 0.48" thickness on the 32 chute suppressor nozzle at typical approach, cutback and takeoff cycle conditions at appropriate sideline distances is discussed in this subsection.

Figures 4.1.2-1 and 4.1.2-2 respectively show the PNL and spectral data of configurations TAS-6, TAS-8 and TAS-9 at an approach cycle at a sideline distance of 370 ft for static condition. The PNL directivities indicate that the 180° shield of 0.97" thickness gives excellent noise suppression at all observer angles. At the peak noise angle ( $\theta_i = 120^\circ$ ), a PNL reduction of 8.0 dB is obtained by the 180° shield of 0.97" thickness. The PNL reduction at  $\theta_i = 90^\circ$  by the 180° shield of 0.97" thickness is 4.5 dB. The PNL reductions in the front quadrant by the partial shield are about the same as at  $\theta_i = 90^\circ$ , whereas the PNL reductions in the aft quadrant by the partial shield are noticeably larger. The 360° shield of 0.48" thickness carries about the same amount of shield flow rate as the 180° shield of 0.97" thickness, but yields lesser amount of the PNL reductions compared to the partial shield.

Figures 4.1.2-2a and 4.1.2-2b compare configurations TAS-6, TAS-8 and TAS-9 at four (4) observer angles ( $\theta_i = 60^\circ, 90^\circ, 120^\circ$  and  $140^\circ$ ) for the approach cycle static condition. The pronounced high frequency content of the 32 chute mechanical suppressor nozzle is noticeable at all the four (4) observer angles. At  $\theta_i = 90^\circ$ , the SPL reductions by the shields are due to source modifications. The partial shield of 0.97" thickness and the 360°

Sym.	Point	Config.	Orientation
○	601	TAS-6	Axisymmetric
◇	817	TAS-8	Community
△	901	TAS-9	Axisymmetric

$A^T = 1400 \text{ In.}^2$   
 370' Flyover Distance  
 Static  
 Approach Cycle

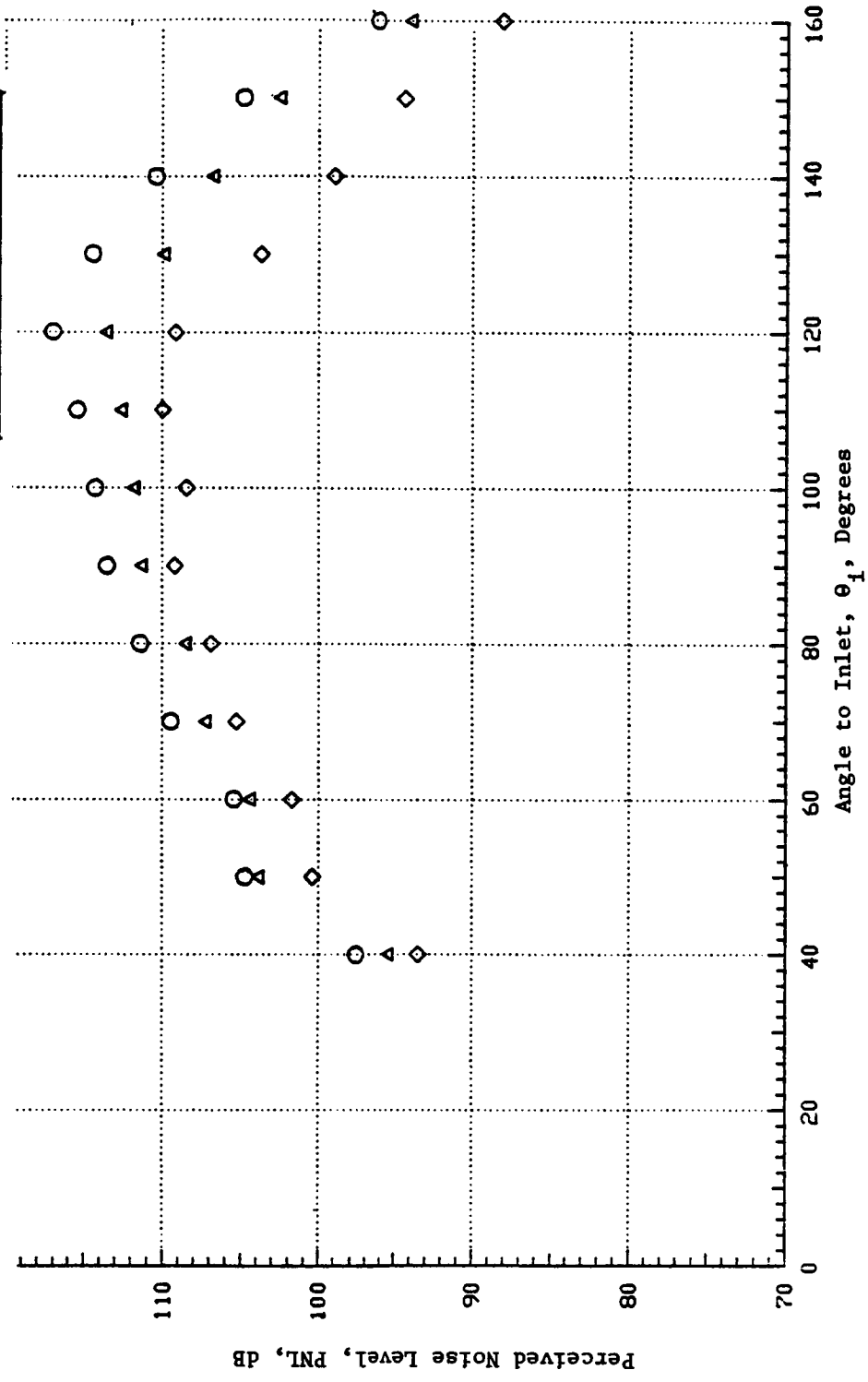


Figure 4.1.2-1. Influence of the Thermal Acoustic Shields on PNL Directivity of a 32 Chute Suppressor Nozzle at a Typical Approach Case (Static).

Sym.	Point	Config.	Orientation
○	601	TAS-6	Axisymmetric
◇	817	TAS-8	Community
△	901	TAS-9	Axisymmetric

$T = 1400 \text{ In.}^2$   
 370' Flyover Distance  
 Static  
 Approach Cycle

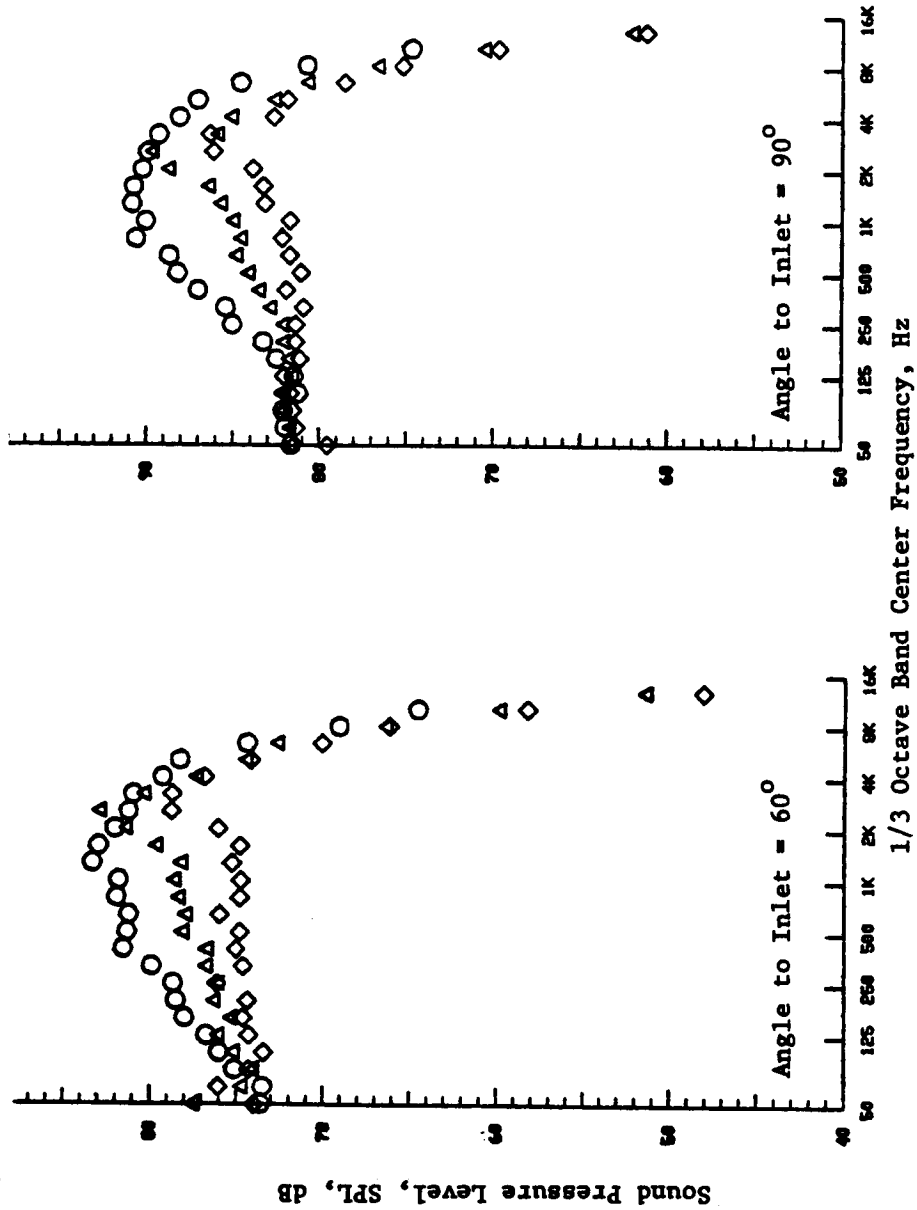


Figure 4.1.2-2a. Influence of the Thermal Acoustic Shields on the Spectral Content of 32 Chute Suppressor Nozzle at a Typical Approach Case (Static).

Sym.	Point	Config.	Orientation
○	601	TAS-6	Axisymmetric
◇	817	TAS-8	Community
△	901	TAS-9	Axisymmetric

$T = 1400 \text{ In.}^2$   
 370' Flyover Distance  
 Static  
 Approach Cycle

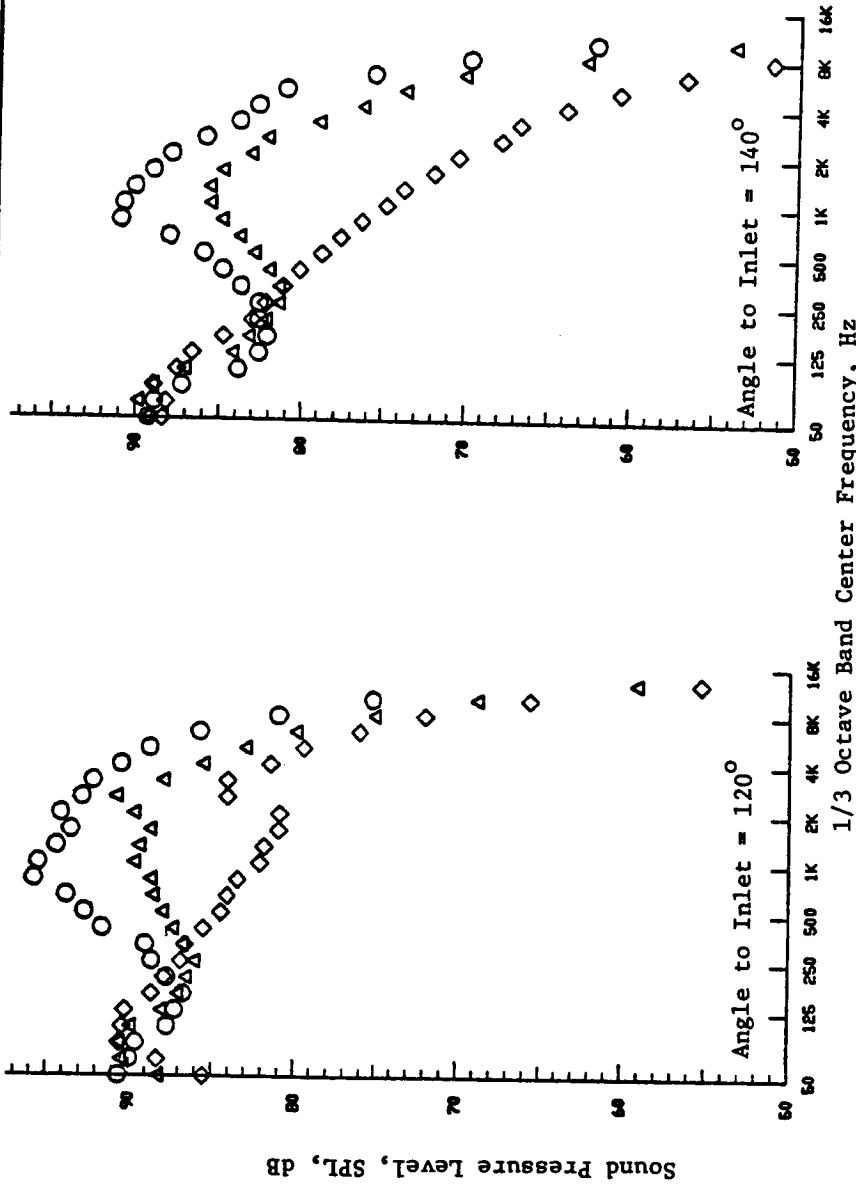


Figure 4.1.2-2b. Influence of the Thermal Acoustic Shields on the Spectral Content of 32 Chute Suppressor Nozzle at a Typical Approach Cycle (Static).

shield of 0.48" thickness are seen to reduce the noise of the suppressor for frequencies greater than 160 HZ. Significant spectral differences between the partial and the full shield occur at mid-frequencies (between 500 HZ to 2500 HZ), but no significant differences between the two shields are observed at very high frequencies at  $\theta_i = 90^\circ$ .

Similar observations can be made by examining the spectra at  $\theta_i = 60^\circ$ . The spectral shapes of the two shielded configurations exhibit a similar relationship to the unshielded configuration spectrum at  $\theta_i = 60^\circ$  as was observed at  $90^\circ$ , indicating that the speculated source modification by the shields noted at  $\theta_i = 90^\circ$  is the significant effect at a forward quadrant angle such as  $60^\circ$ . The changes between  $\theta_i = 60^\circ$  and  $90^\circ$  can be attributed to the eddy convection effects which exist at  $\theta_i = 60^\circ$  and which are minimal at  $\theta_i = 90^\circ$ . Since both the shield and core jets are subsonic for the approach cycle, there is no shock cell noise to contend with in the front quadrant.

Next, the spectral data at  $\theta_i = 120^\circ$  and  $140^\circ$  are analyzed. A large noise reduction was obtained by the  $180^\circ$  shield of 0.97" thickness for frequencies greater than 250 HZ. The maximum SPL reduction by the partial shield at  $\theta_i = 120^\circ$  equals 13.7 dB at 1000 HZ and the maximum SPL reduction at  $\theta_i = 140^\circ$  equals 20.3 dB at 5000 HZ, indicating that the partial shield effectively suppresses the high frequency noise in the aft quadrant. In contrast, the maximum SPL reduction by the full shield of 0.48" thickness at  $\theta_i = 120^\circ$  equals 7.3 dB at 1000 HZ and the maximum SPL reduction at  $\theta_i = 140^\circ$  equals 8.5 dB at 10,000 HZ. Also, the partial shield is able to suppress significantly better than the full shield for frequencies greater than 315 HZ implying that for a given shield flow rate, a partial shield is a better high and mid frequency noise suppressor than the full shield. It should also be pointed out that at  $\theta_i = 120^\circ$  and  $140^\circ$ , there is an amplification of the low frequency noise (i.e., for frequencies less than 250 HZ) by the thermal acoustic shields which is attributed to the stretching of the jets by the shields due to a reduction of the shear stresses.

Next, the influence of the  $180^\circ$  shields of 0.48" thickness, and 0.97" thickness and the  $360^\circ$  shield of 0.48" thickness on the 32 chute suppressor at cutback and takeoff cycle conditions are discussed.

Figures 4.1.2-3 and 4.1.2-4 respectively show the PNL directivity and spectral content of configurations TAS-6, TAS-7, TAS-8 and TAS-9 at a typical thrust cutback case at a 1000 ft sideline distance. The partial shields are in community orientation. As in the approach case, the 180° shield of 0.97" thickness has yielded maximum PNL reduction. At the peak noise angle of  $\theta_i = 120^\circ$ , the 180° shield of 0.97" thickness has yielded 8.0 dB reduction, the 180° shield of 0.48" thickness has yielded 2.5 dB reduction and the 360° shield of 0.48" thickness has yielded 3.0 dB reduction. At all the observer angles, there are no significant differences in the perceived noise levels of configurations TAS-7 and TAS-9 indicating that the full and partial shield of same thickness do not exhibit different directivity patterns. However, doubling the shield thickness of the partial shield has yielded significantly higher noise reductions for the 32 chute suppressor nozzle at all observer locations, indicating that the thickness of the shield is a significant parameter in determining the effectiveness of the shield.

The spectral content of configurations TAS-6, TAS-7, TAS-8 and TAS-9 are analyzed next. The spectral comparison at  $\theta_i = 90^\circ$  indicates no significant differences in the spectral content of configurations TAS-7 and TAS-9. Configuration TAS-8 shows the maximum suppression for frequencies greater than 250 HZ. There is no noticeable amplification of the low frequency noise at  $\theta_i = 90^\circ$ .

The 32 chute suppressor nozzle generates a large amount of high frequency noise, whose sources are located close to the jet exit plane. The partial shield of 0.97" thickness (TAS-8) is seen to modify the high frequency portion of the spectrum considerably compared to the partial shield and full shield of 0.48" thickness (TAS-7 and TAS-9, respectively), indicating that the thicker partial shield (TAS-8) is able to alter the source characteristics to a greater extent. The differences in spectral character at  $\theta_i = 60^\circ$  for the four configurations are similar to those at  $\theta_i = 90^\circ$ .

Significantly different trends are exhibited in the aft quadrant. At the three aft angles considered (viz.,  $\theta_i = 120^\circ$ ,  $140^\circ$  and  $150^\circ$ ) one notices that the partial shield of 0.97" thickness (TAS-8) is able to effectively suppress the dominant mid and high frequency content of the 32 chute suppressor and has eliminated the characteristic suppressor nozzle high

Sym	Point	Config.	Shield Config.	Peak $\Delta$ PNL, dB
○	605	TAS-6	No Shield	0
□	721	TAS-7	180 Thin Shield	2.5
◇	821	TAS-8	180 Thick Shield	8.0
△	905	TAS-9	360 Thin Shield	3.0

$A^T = 1400 \text{ In.}^2$   
 1000' Flyover Distance  
 Static  
 Outback Cycle

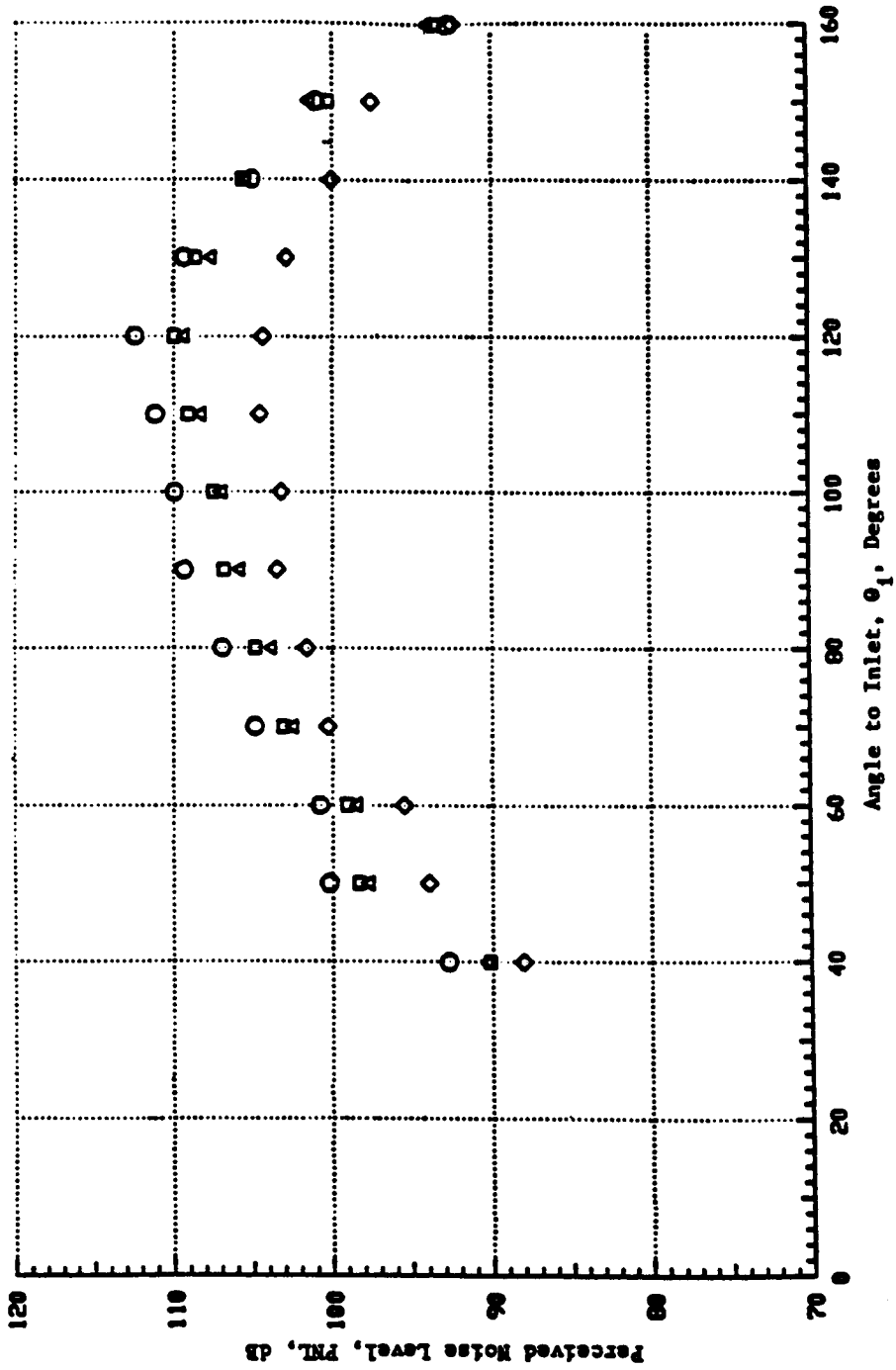


Figure 4.1.2-3. Influence of the Thermal Acoustic Shields on the PNL Directivity of the 32 Chute Suppressor Nozzle at a Typical Outback Case (Static).



Sym.	Point	Config.	Shield Config.
○	605	TAS-6	No Shield
□	721	TAS-7	180 Thin Shield
◇	821	TAS-8	180 Thick Shield
△	905	TAS-9	360 Thin Shield

$A^T = 1400 \text{ In.}^2$   
 1000' Flyover Distance  
 Static  
 Outback Cycle

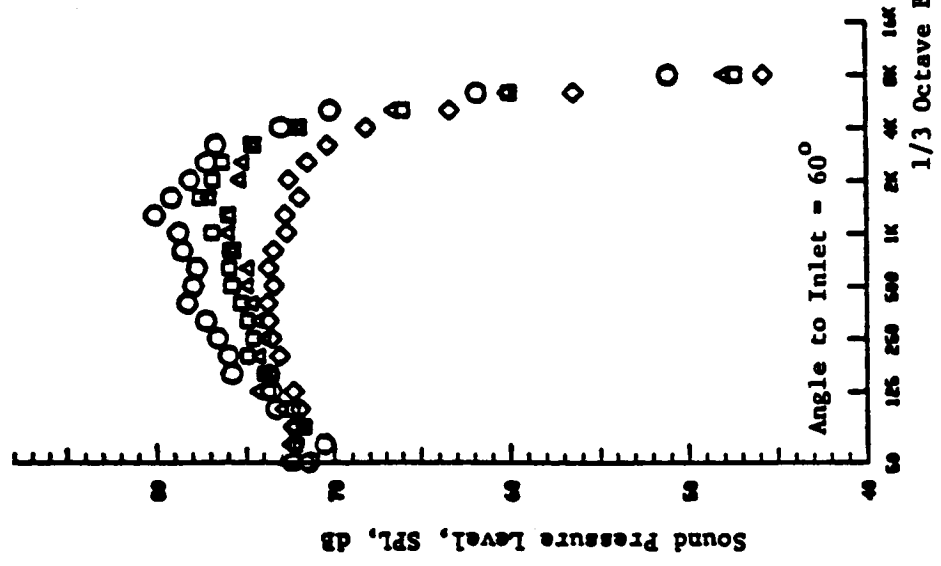
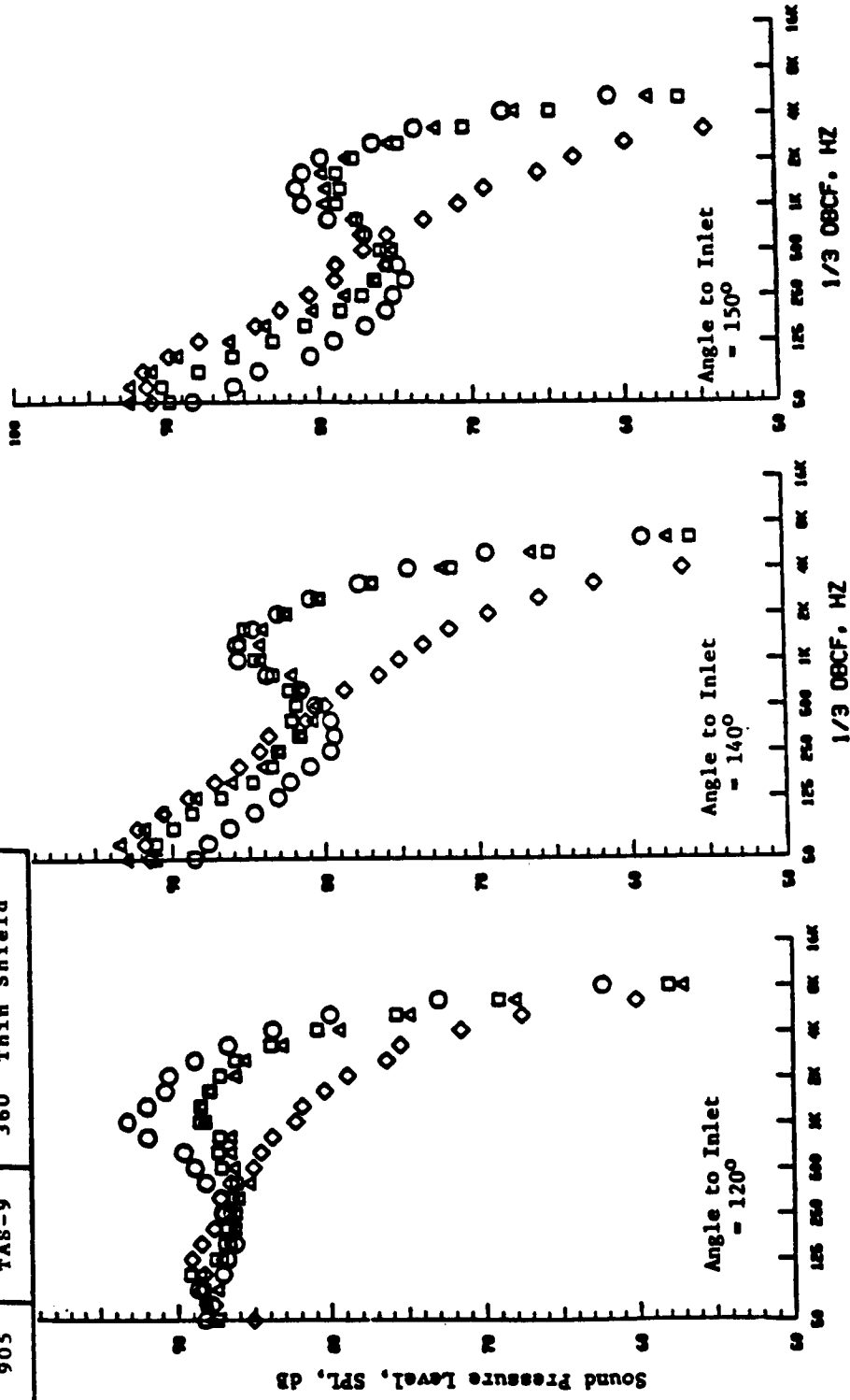


Figure 4.1.2-4a. Influence of the Thermal Acoustic Shield on the Spectral Content of the 32 Chute Suppressor Nozzle at a Typical Outback Case (Static).

Sym.	Point	Config.	Shield Config.
○	605	TAS-6	No Shield
□	721	TAS-7	180 Thin Shield
◇	821	TAS-8	180 Thick Shield
△	905	TAS-9	360 Thin Shield

$A^T = 1400 \text{ In.}^2$   
 1000' Flyover Distance  
 Static  
 Outback Cycle



1/3 Octave Band Center Frequency, Hz

Figure 4.1.2-4b. Influence of the Thermal Acoustic Shields on the Spectral Content of the 32 Chute Suppressor Nozzle at a Typical Outback Case (Static).

frequency peak. The 180° shield of 0.48" thickness (TAS-7) and the 360° shield of 0.48" thickness (TAS-9) did not eliminate the high frequency peak, again indicating that the thickness of the shield affects both the source characteristics and the reflective characteristics. No significant differences between the 180° and 360° shields of 0.48" thickness were observed at the aft angles except at very high frequencies at  $\theta_i = 140^\circ$  and  $150^\circ$ . The 180° shield of 0.48" thickness (TAS-7) is quieter than the 360° shield of 0.48" thickness (TAS-9) for frequencies greater than 4000 HZ at  $\theta_i = 140^\circ$ , and 2500 HZ at  $\theta_i = 150^\circ$ . This indicates that a partial shield is a better noise suppressor than the full shield of the same thickness only at shallow angles to jet axis and at very high frequencies where the ray acoustic considerations such as total internal reflection of partial shields and possible multiple reflections of full shields come into play. Also, at shallow angles to jet axis, there is considerable low frequency noise amplification by all the thermal acoustic shields, and such an amplification of low frequency noise is not noted at  $\theta_i = 90^\circ$ . Hence, though the shields have been able to suppress the high frequency noise, the accompanying low frequency noise amplification offsets this gain to minimize perceived noise level reductions. Also, at shallow angles to the jet axis, the distance between the observer and jet exit plane increases at a fixed sideline distance (e.g., the distance between jet exit plane and observer for  $\theta_i = 150^\circ$  and a sideline distance of 1000 ft equals 2000 ft). Hence, the high frequency components undergo larger air attenuation effects than the low frequency components, and the corresponding contribution to the perceived noise level by the high frequency noise is reduced compared to the low frequency noise.

The influence of various thermal acoustic shields on the 32 chute suppressor nozzle at a typical takeoff cycle are analyzed next. For the takeoff case, the sideline distance is chosen to be 2400 ft and the orientation of partial shields is at an azimuthal angle,  $\phi$ , of  $70^\circ$  (see Table 3-III). Figures 4.1.2-5 and 4.1.2-6 respectively show the PNL directivity and spectral content of configuration TAS-6, TAS-7, TAS-8 and TAS-9 at the takeoff cycle under static condition. Compared to the approach and cutback cases, the thermal acoustic shields are seen to give smaller PNL reductions at this takeoff cycle. In the case of cutback cycle, the 180° shield of 0.97" thickness yielded 8.1 dB PNL reduction at  $\theta_i = 120^\circ$

Sym.	Point	Config.	Orientation
○	609	TAS-6	Axisymmetric
□	709	TAS-7	Sideline
◇	809	TAS-8	Sideline
◇	909	TAS-9	Axisymmetric

$T = 1400 \text{ In.}^2$   
 2400' Sideline  
 Static  
 Takeoff Cycle

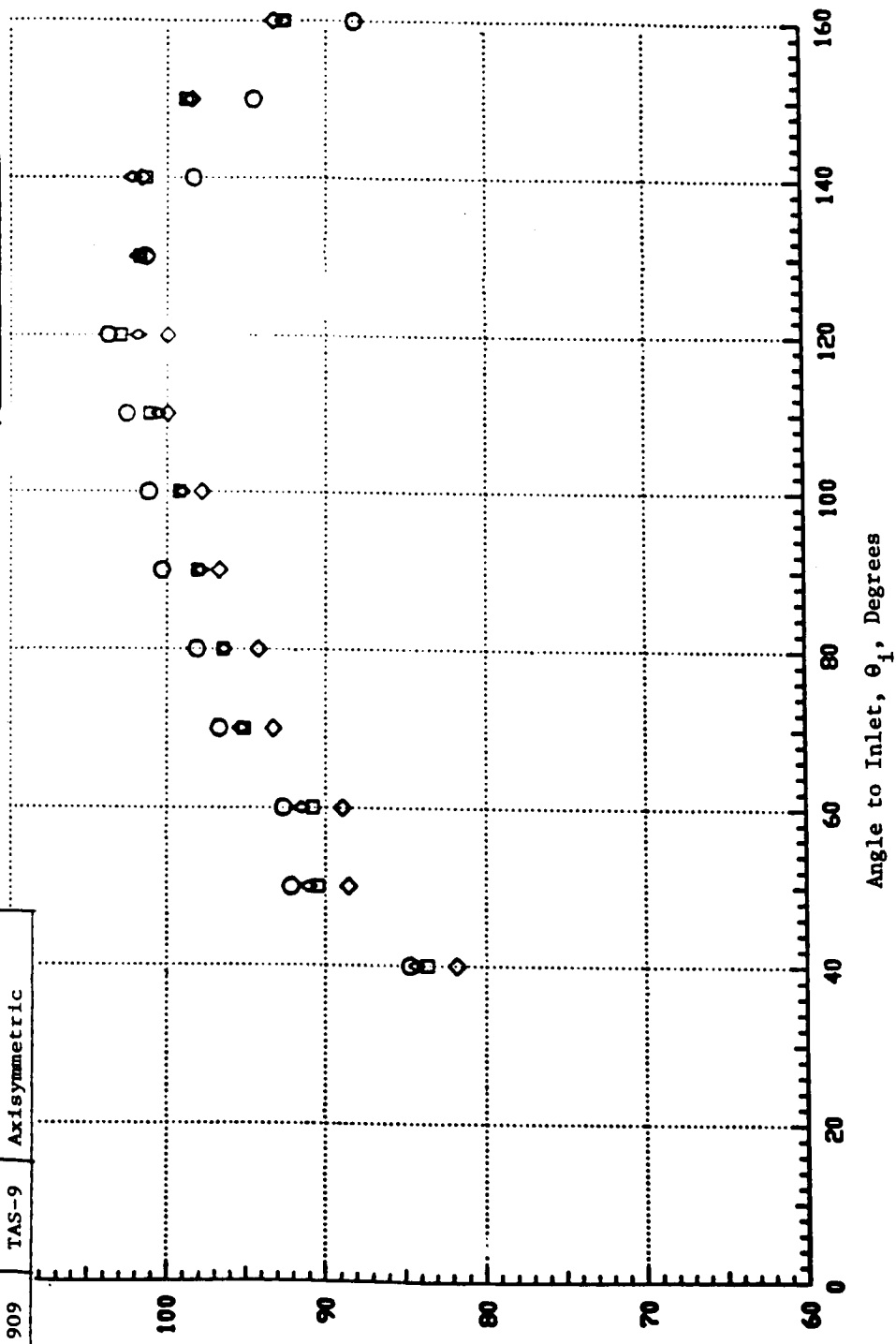


Figure 4.1.2-5. Influence of the Thermal Acoustic Shields on the PNL Directivity of the 32 Chute Suppressor Nozzle at a Typical Takeoff Case (Static).

Sym.	Point	Config.	Orientation
○	609	TAS-6	Axisymmetric
□	709	TAS-7	Sideline
◇	809	TAS-8	Sideline
◇	909	TAS-9	Axisymmetric

T = 1400 In. <sup>2</sup>  
A = 2400' Sideline  
Static  
Takeoff Cycle

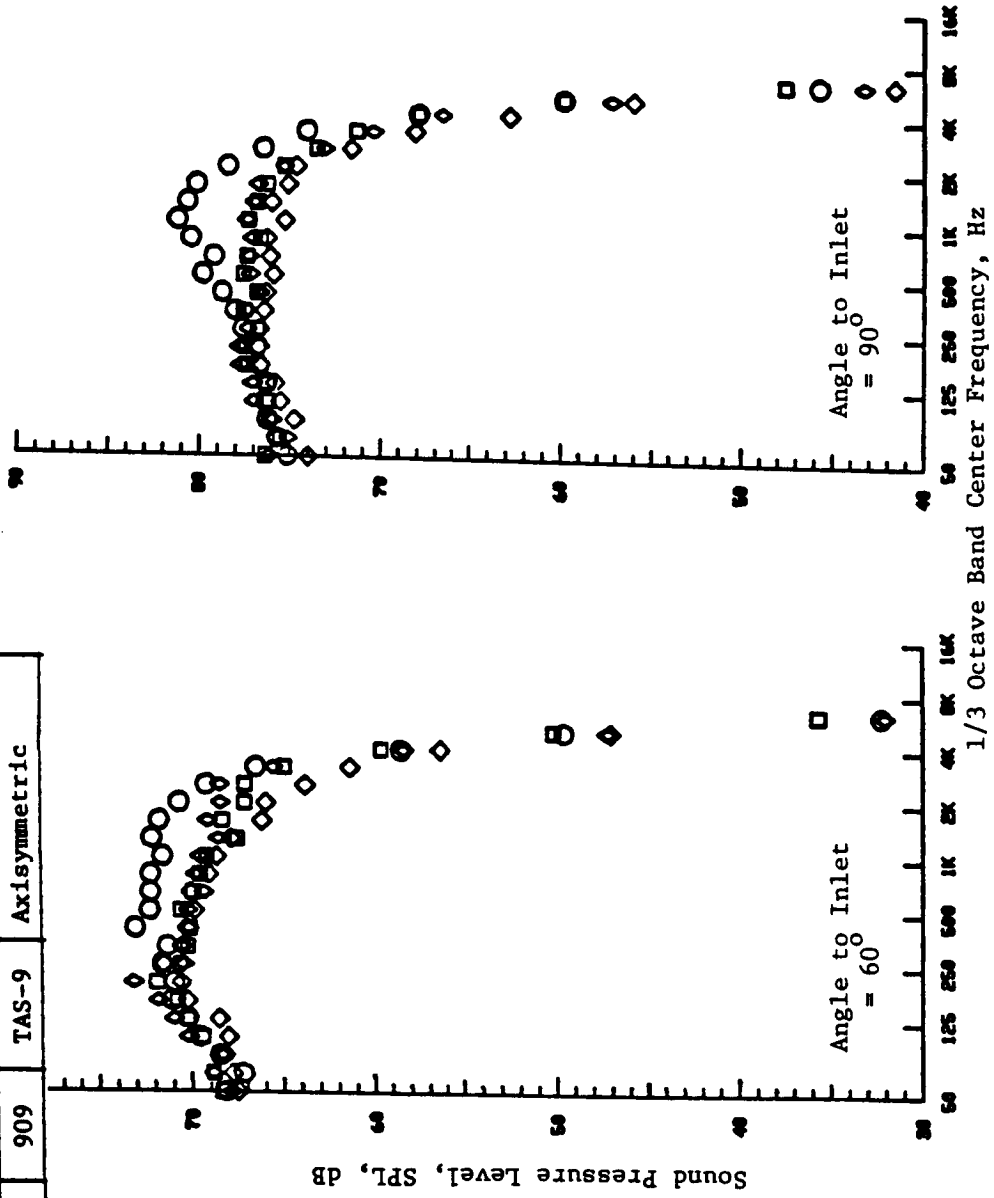
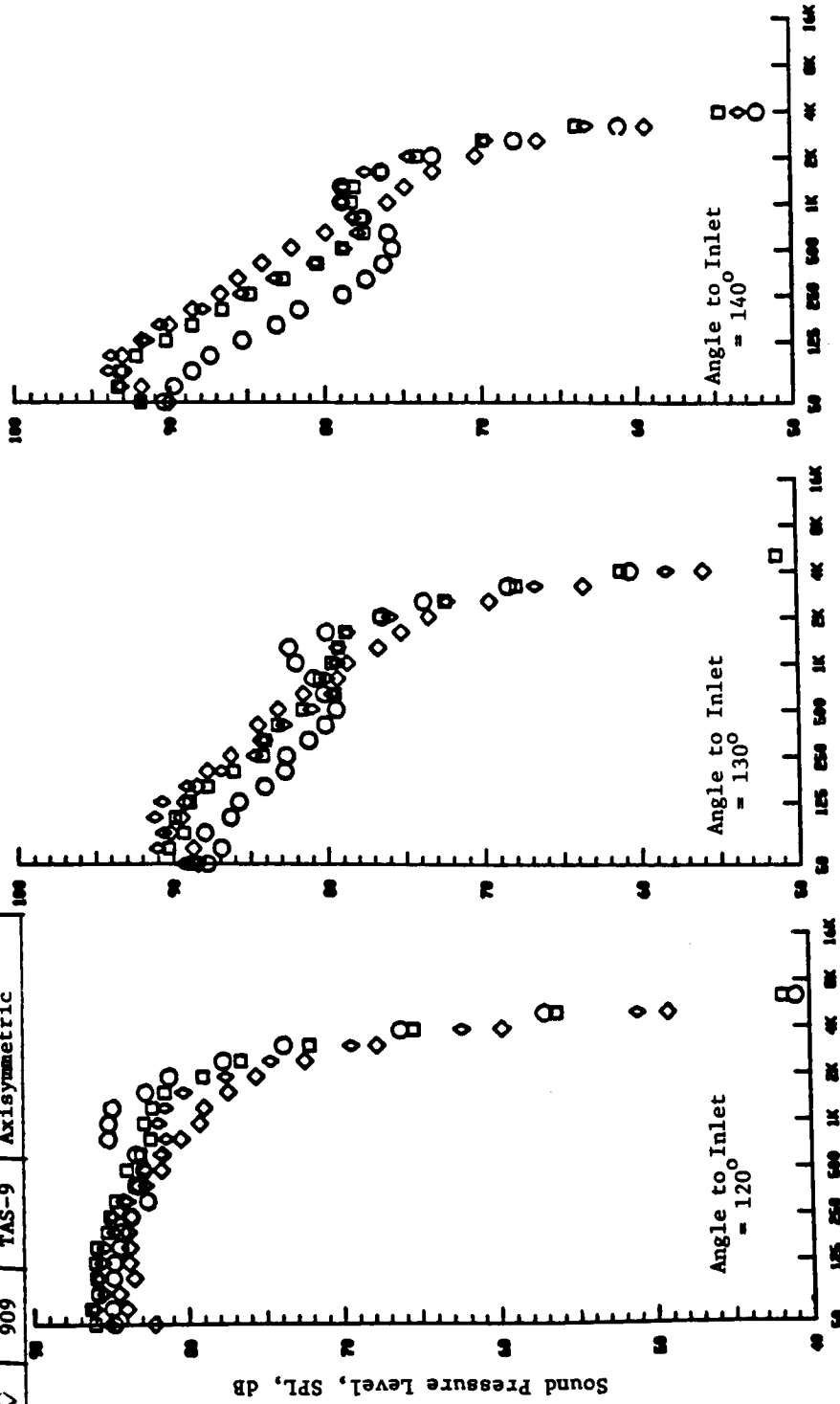


Figure 4.1.2-6a. Influence of the Thermal Acoustic Shields on the Spectral Content of the 32 Chute Suppressor Nozzle at a Typical Takeoff Case (Static).

Sym.	Point	Config.	Orientation
○	609	TAS-6	Axisymmetric
□	709	TAS-7	Sideline
◇	809	TAS-8	Sideline
◊	909	TAS-9	Axisymmetric

$A^T = 1400 \text{ In.}^2$   
 2400' Sideline  
 Static  
 Takeoff Cycle



1/3 Octave Band Center Frequency, Hz

Figure 4.1.2-6b. Influence of the Thermal Acoustic Shields on the Spectral Content of the 32 Chute Suppressor Nozzle at a Typical Takeoff Case (Static).

whereas in the takeoff case, it yielded only 4 dB PNL reduction. Also, for  $\theta_i > 130^\circ$ , one notices amplification by all the three (3) shields for the takeoff cycle.

From ray acoustic considerations, one would anticipate that the thermal acoustic shields should yield significant noise reductions at shallow angles to the jet axis owing to the total internal reflections possible for angles shallower than the critical angle for total internal reflection. (For the shield and jet velocities under consideration, the critical angle for total internal reflection as predicted by the Snell's law lies between  $110^\circ$  and  $120^\circ$  to inlet axis.) In the present case, however, the thermal acoustic shields have given perceived noise level reductions everywhere except shallow angles to the jet axis indicating that the acoustic behavior of the thermal acoustic shields over a distributed noise source such as a jet flow is governed by many factors such as the stretching of the jet flow, modification of the noise sources within the jet by the shield flow, and modified eddy convection effects.

Application of the Snell's law to model the refraction/reflection effects of the thermal acoustic shields is a simplistic approach and one has to realize the relevance of other fluid dynamic effects in understanding the behavior of the thermal acoustic shields. One notices that the  $180^\circ$  shield of 0.97" thickness yields an amplification of the noise by 5.2 dB in perceived noise level at  $\theta_i = 160^\circ$ .

An analysis of the spectral content at various observer angles will aid in understanding the observed PNL directivities. At  $\theta_i = 90^\circ$ , there is a noticeable high frequency peak of the 32 chute suppressor. However, it is not as pronounced as it was at the cutback case which is attributable to the larger sideline distance for the takeoff case and the accompanying higher air attenuation of the high frequency components. The spectral reductions by the shields are noticed to be lower at the takeoff case compared to the cutback case; for example, the  $180^\circ$  shield of 0.97" thickness yielded 8.4 dB reduction at 1000 HZ for the cutback case whereas it yielded only 5.9 dB reduction for the takeoff case at the same 1/3-octave band. This means that as the core jet velocity increases, the ability of the thermal acoustic shield to reduce the source noise is decreasing. Note again that the  $180^\circ$  and  $360^\circ$  shields of

0.48" thickness show minor differences at  $\theta_i = 90^\circ$  as in the cutback case. The front quadrant spectra at  $\theta_i = 60^\circ$  show relatively similar features as at  $\theta_i = 90^\circ$ .

Next, the spectral content at  $\theta_i = 120^\circ$ ,  $130^\circ$  and  $140^\circ$  are analyzed. At 1000 HZ frequency, the  $180^\circ$  shield of 0.97" thickness yields a reduction of 5.8 dB at the takeoff case whereas for the cutback case, it yields 11 dB reduction at the same 1/3-octave band frequency, indicating the reduced potential of the thermal acoustic shield to suppress noise at higher core jet velocities. At  $\theta_i = 130^\circ$ , configurations TAS-6, TAS-7, TAS-8 and TAS-9 have approximately the same perceived noise level, but the spectral composition of these four (4) configurations is to be studied next. The configurations with the shields suffer from low frequency amplification, as well as simultaneously yielding high frequency reductions. Configuration TAS-8 does not show any high frequency peak, whereas configuration TAS-7 and TAS-9 do show the high frequency peak, indicating that the thicker partial shield is still the best high frequency noise suppressor of the three shields. However, it also has the maximum low frequency noise content.

Because of this interplay between the high frequency suppression and the accompanying low frequency amplification, the thermal acoustic shield nozzles can have the same PNL as the 32 chute suppressor by itself. The spectral data at  $\theta_i = 140^\circ$  shows even more pronounced low frequency noise amplification by the thermal acoustic shields. At  $\theta_i = 130^\circ$ , the  $180^\circ$  shield of 0.97" thickness yielded noise reductions for frequencies greater than 630 HZ whereas at  $\theta_i = 140^\circ$ , noise reductions are noted for frequencies greater than 800 HZ indicating the increased dominance of low frequency noise at shallower angles to the jet axis, and the resulting increase in the perceived noise level due to the thermal acoustic shields.

#### 4.1.2.2 Azimuthally Asymmetric Acoustic Field Characteristics of Partial Shield on the 32 Chute Suppressor Nozzle

In this subsection, the azimuthally asymmetric acoustic field characteristics of the 32 chute suppressor with the  $180^\circ$  shield of 0.97" thickness at typical approach, cutback and takeoff cycle conditions are discussed. The acoustic measurements have been performed with microphones in



the community and typical sideline look angle of 20° orientations. The measured acoustic data has been scaled to 1400 in<sup>2</sup> and the data extrapolated to 2400 ft sideline distance for all the above three cycle conditions for this study.

Figure 4.1.2-7 shows the azimuthally asymmetric PNL directivities of configuration TAS-8 in sideline and community orientations for approach, cutback and takeoff cycle conditions. It is to be noted that at all the above conditions, the perceived noise level measured in the sideline orientation is higher than or equal to that measured in the community orientation. Also, the azimuthal asymmetry in the PNL directivity for the takeoff cycle is smaller than those for the cutback and approach cycles indicating that as the core jet velocity (and correspondingly the shield jet velocity) increases, the azimuthal asymmetric influence of the partial shield reduces.

Next, the asymmetric influence of the partial shield on the spectral content at the approach, cutback and takeoff cycles is analyzed. Figure 4.1.2-8 compares the asymmetric influence of the 180° shield of 0.97" thickness on the 32 chute suppressor at  $\theta_i = 90^\circ$  for approach, cutback and takeoff cycles. Note that azimuthal asymmetry exists for mid and high frequencies (viz., typically for frequencies greater than 630 HZ) and at low frequencies there is no noticeable azimuthal asymmetry, implying that the mid and high frequency noise sources are located in the region where the partial shield jet has not fully mixed with the core jet to yield an asymmetric flow field. Next, figure 4.1.2-9 compares the asymmetric influence of the partial shield on the 32 chute suppressor at  $\theta_i = 140^\circ$  for approach, cutback and takeoff cycles. As at  $\theta_i = 90^\circ$ , the acoustic field of frequencies less than 630 HZ does not show any notable azimuthal variation. At higher frequencies, one finds that there is a significant azimuthal variation between community and sideline orientations. The azimuthal variation at  $\theta_i = 140^\circ$  is not only caused by the asymmetric source distributions, but also by the azimuthally asymmetric reflection/scattering of the high frequency noise by the partial shield. Particularly at the sideline orientation, which has a look angle of 20°, there is a significant possibility of "spill-over" of the noise reflected by the partial shield to the observer which in turn results in higher noise levels in the sideline position. It is to be noted that at the takeoff cycle, the azimuthal variation of the spectra is smaller compared to

Configuration TAS-8

Sym	Point	Orientation
□	801	Sideline
○	817	Community

$A^T = 1400$  In.  
2400' Distance  
Static  
Approach Cycle

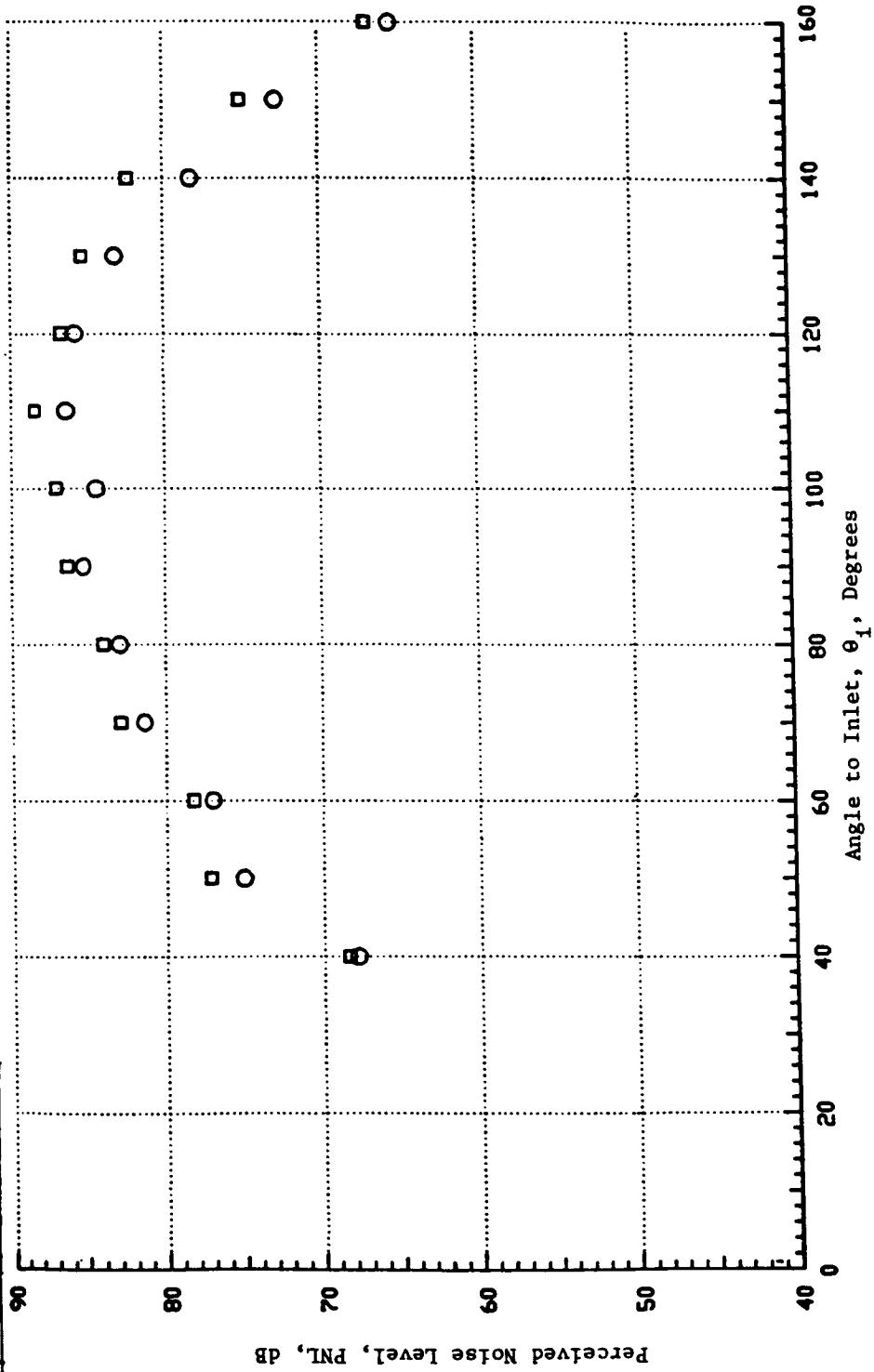


Figure 4.1.2-7a. Azimuthally Asymmetric PNL Directivity of the 32 Chute Suppressor Nozzle with 180° Shield of 0.97" Thickness at a Typical Approach Cycle (Static).

Configuration TAS-8

Sym	Point	Orientation
□	805	Sideline
○	821	Community

A<sup>T</sup> = 1400 In. 2  
 2400' Distance  
 Static  
 Cutback Cycle

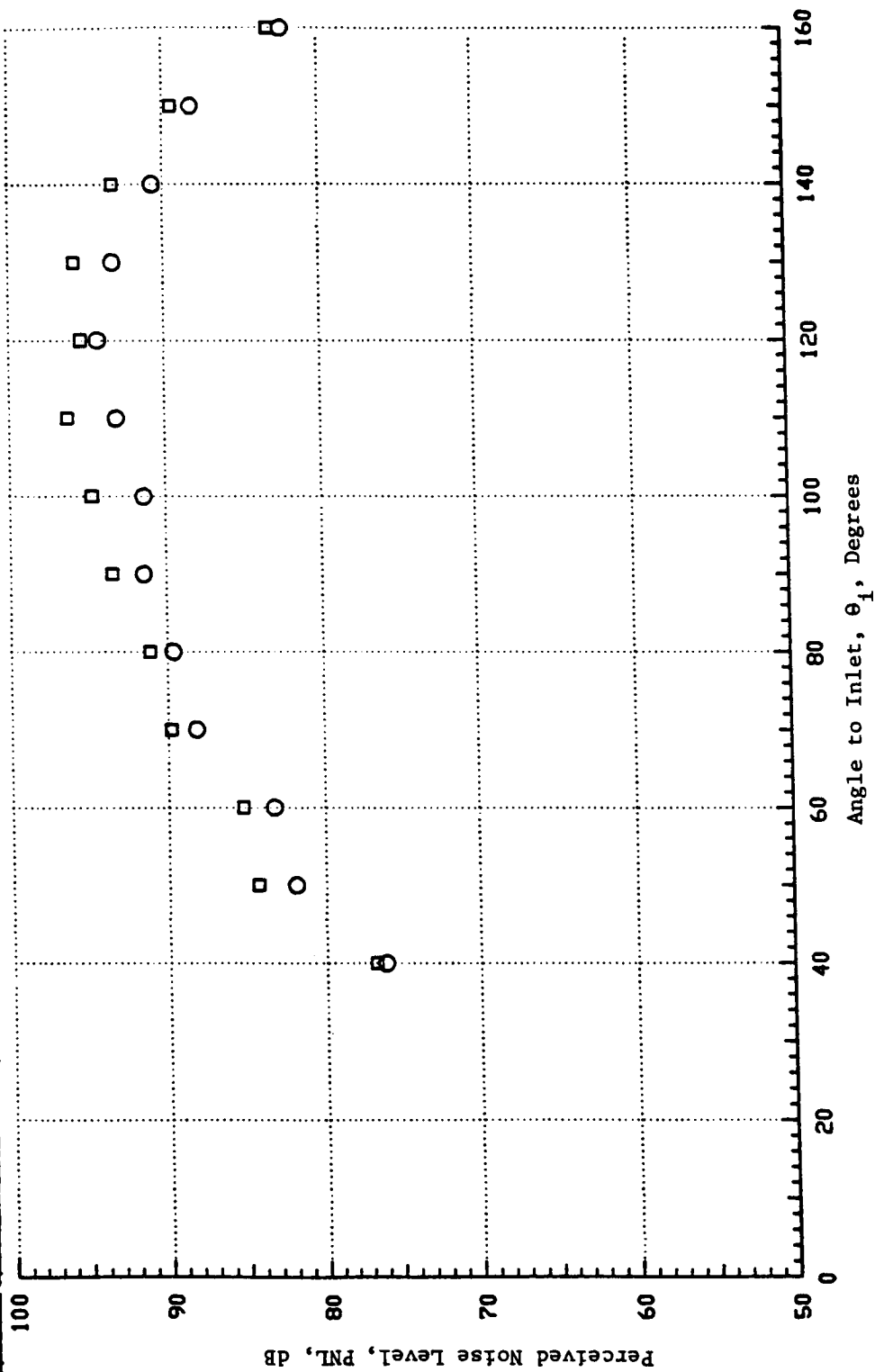


Figure 4.1.2-7b. Azimuthally Asymmetric PNL Directivity of the 32 Chute Suppressor Nozzle with 180° Shield of 0.97" Thickness at a Typical Cutback Cycle (Static).

Configuration TAS-8

Sym	Point	Orientation
□	809	Sideline
○	825	Community

$A^T = 1400 \text{ In.}^2$   
 2400' Distance  
 Static  
 Takeoff Cycle

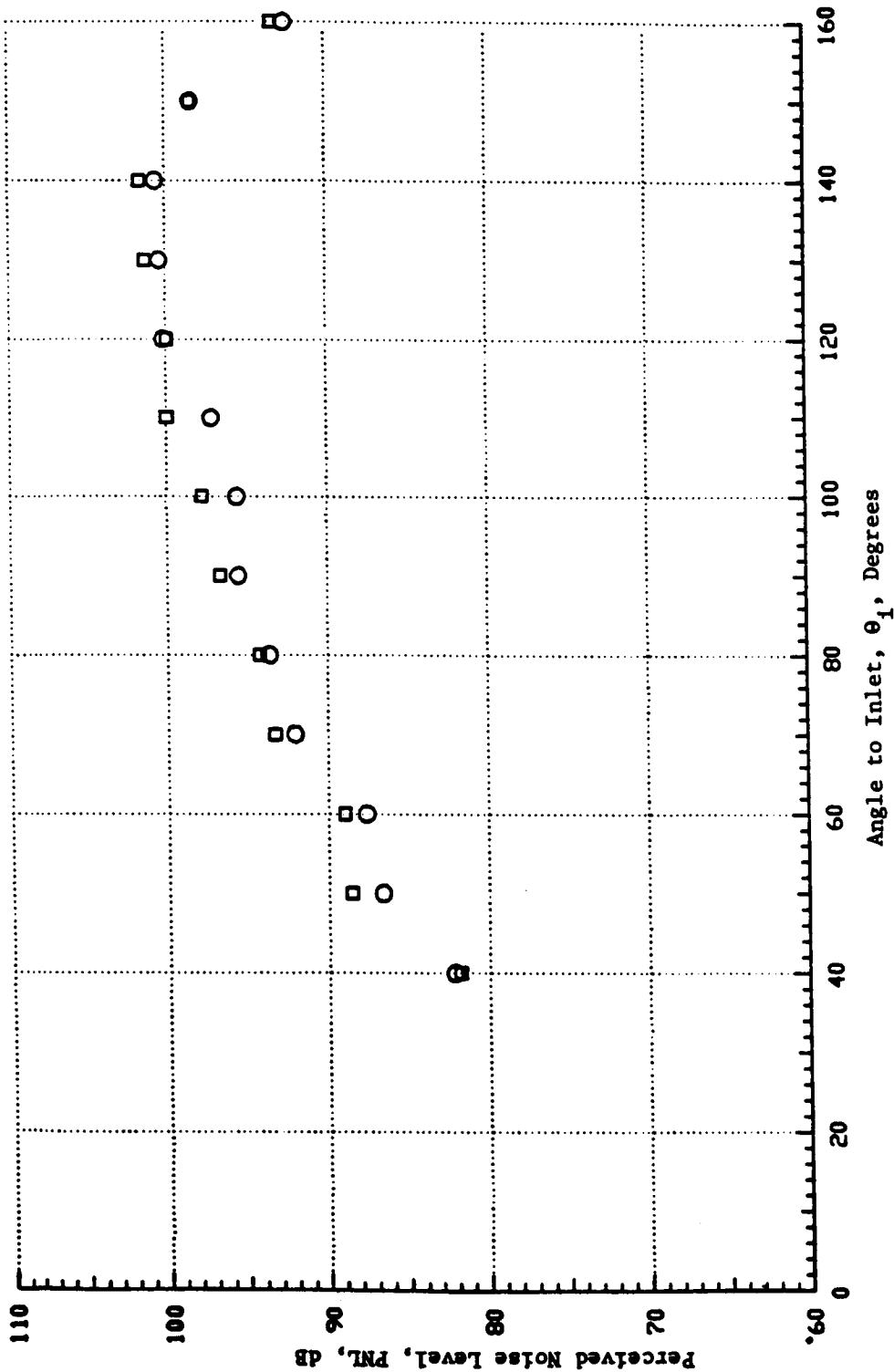


Figure 4.1.2-7c. Azimuthally Asymmetric PNL Directivity of the 32 Chute Suppressor Nozzle with 180° Shield of 0.97" Thickness at a Typical Takeoff Case (Static).

$A^T = 1400 \text{ In.}^2$   
 2400' Distance  
 Static

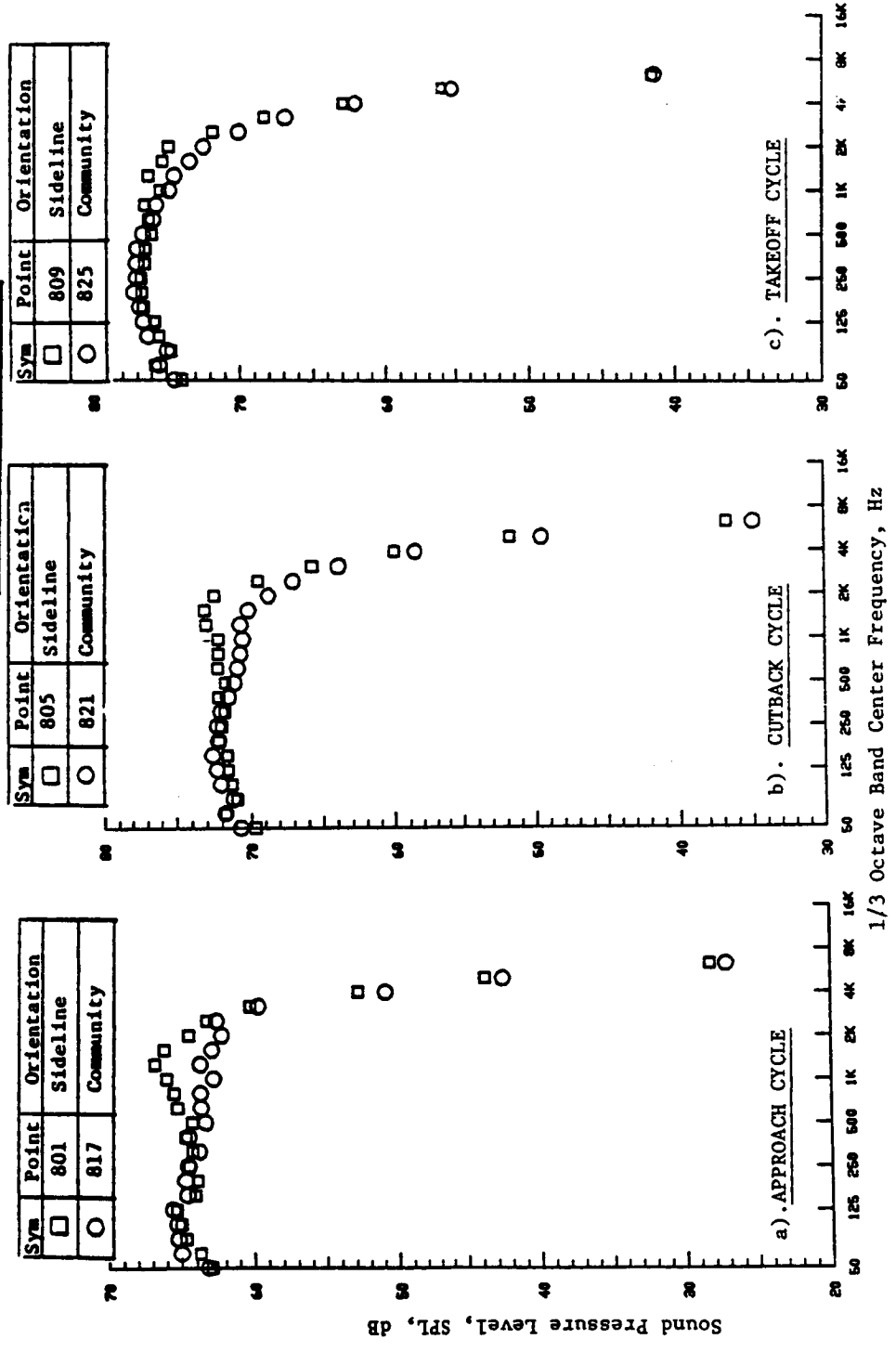
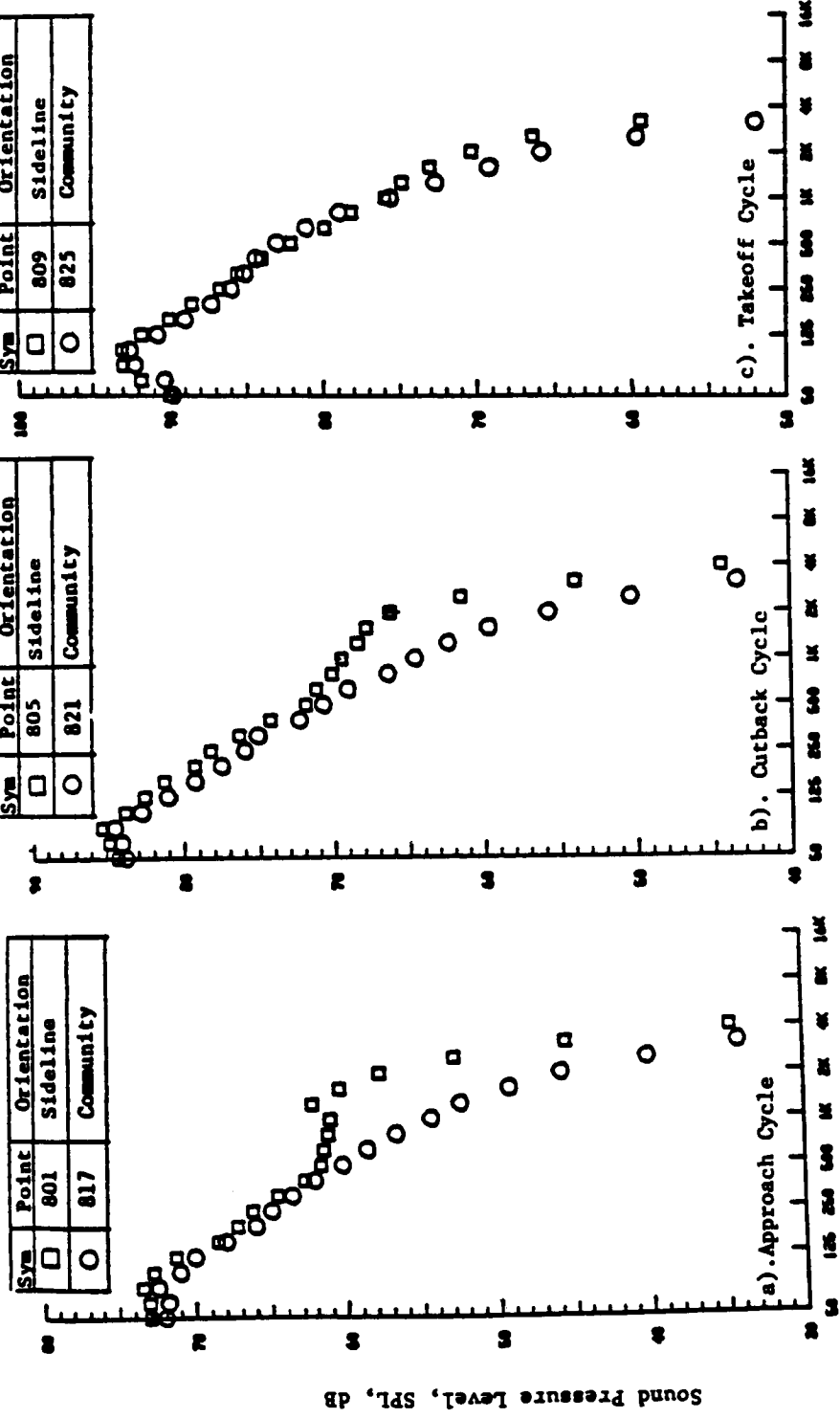


Figure 4.1.2-8. Azimuthally Asymmetric Spectral Content of the 32 Chute Suppressor Nozzle with 180° Shield of 0.97" Thickness at Approach, Cutback, and Takeoff Cycles at  $\theta_1 = 90^\circ$  (Static).

$T = 1400 \text{ In.}^2$   
 $A = 2400' \text{ Distance}$   
 Static



1/3 Octave Band Center Frequency, Hz

Figure 4.1.2-9. Azimuthally Asymmetric Spectral Content of the 32 Chute Suppressor Nozzle with 180° Shield of 0.97" Thickness at Approach, Cutback, and Takeoff Cycles at  $\theta_i = 140^\circ$  (Static).

that at cutback and approach cycles, indicating the reduced potential of the partial shield to influence the noise of the suppressor at high core jet velocities.

#### 4.1.2.3 Influence of the Kinematic Ratios ( $V_r$ , $CV_r$ and $T_r^S$ ) on the Acoustic Characteristics of the 32 Chute Suppressor Nozzle

Salient results of a sensitivity study of the shield to core jet velocity ratio ( $V_r$ ), thermal acoustic shield velocity ratio ( $CV_r$ ) and combined influence of  $V_r$  and  $CV_r$  at a constant static temperature ratio ( $T_r^S$ ) for the 32 chute suppressor nozzle with 180° shield of 0.97" thickness (TAS-8) are presented in this subsection. For this study, the core jet conditions were maintained at a typical cutback condition and the partial shield was in the community orientation. The conditions of the partial shield were varied within the operating domain defined in Subsection 3.2.1 and Figure 3.3.

Figure 4.1.2-10 shows the influence of varying the shield to core jet velocity ratio ( $V_r$ ), keeping the thermal acoustic shield velocity ratio ( $CV_r$ ) approximately constant, on PNL directivity and spectral content for simulated flight condition. Note that the PNL values in the aft quadrant are lower for  $V_r = 0.6$  compared to  $V_r = 0.34$ , whereas, in the front quadrant, the PNL values are slightly higher for  $V_r = 0.6$  compared to  $V_r = 0.34$ . The spectral data are shown at  $\theta_i = 60^\circ$  and  $140^\circ$  in Figures 4.1.2-10b and 4.1.2-10c respectively. The influence of  $V_r$  in the front and aft quadrants are noted at high frequencies indicating that the  $V_r$  effect is significant for the high frequency noise sources located close to the nozzle exit plane. The higher velocity ratio shield yields lower high-frequency noise in the aft quadrant and higher high-frequency noise in the front quadrant, compared to the lower velocity ratio shield. This is another indication that different physical mechanisms dominate in the front and aft quadrants.

Test Point	Core Jet			Shield Jet			Mixed Conditions			$\frac{v^{sj}}{v^j}$	$\frac{(C+V)^{sj}}{(C+V)^j}$	$\frac{T_s^{sj}}{T_s^j}$
	$v^j$ , fps	$T_T^{j OR}$	$P_r^j$	$v^{sj}$ fps	$T_T^{sj OR}$	$P_r^{sj}$	$v^{mix}$ fps	$T_T^{mix OR}$	$P_r^{mix}$			
866	1858	1522	2.066	1122	954	1.502	1577	1305	1.824	.60	.71	.68
886	1855	1514	2.070	635	1285	1.097	1622	1470	1.751	.34	.66	1.00

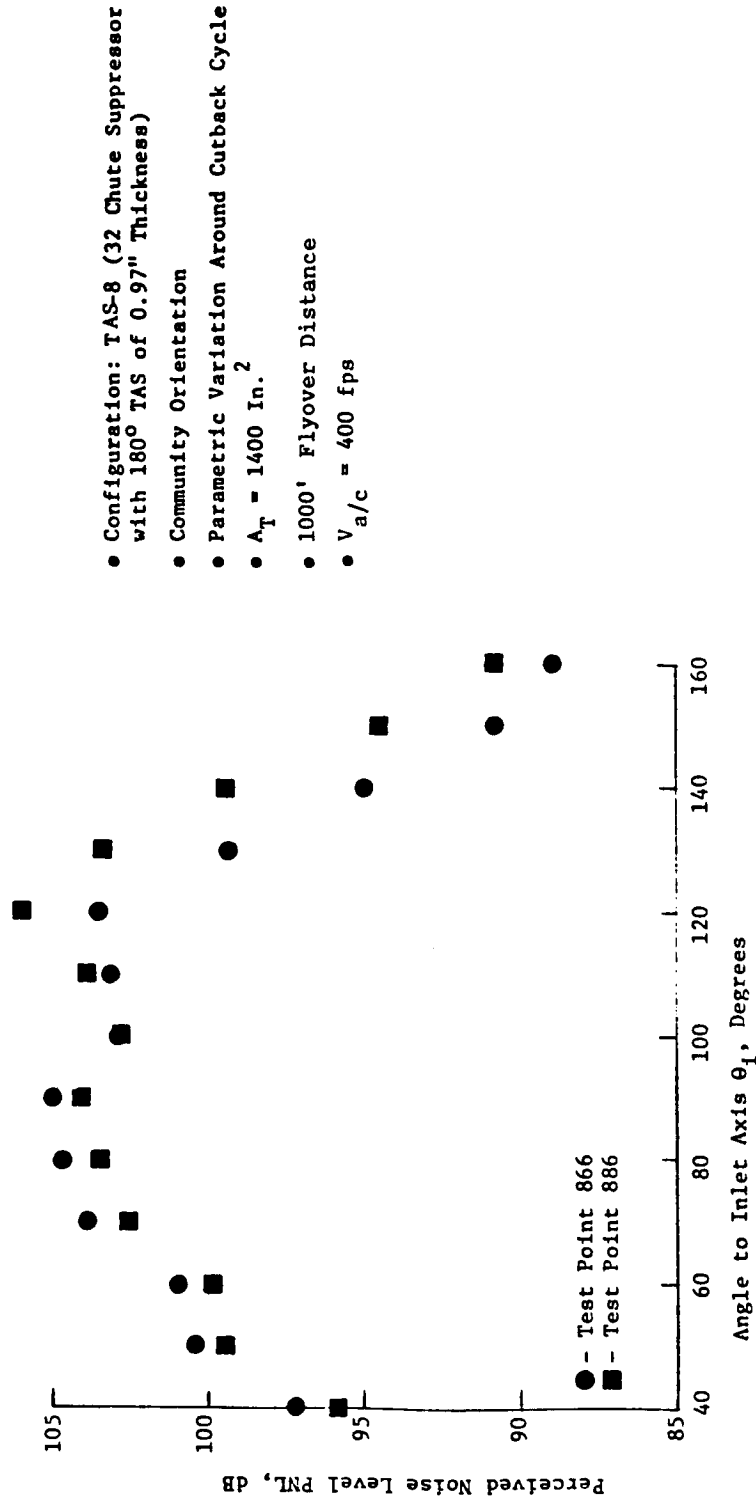


Figure 4.1.2-10a. Influence of Shield to Core Jet Velocity Ratio ( $v_r$ ) on PNL Directivity of Configuration TAS-8 at a Constant  $CV_r$ .



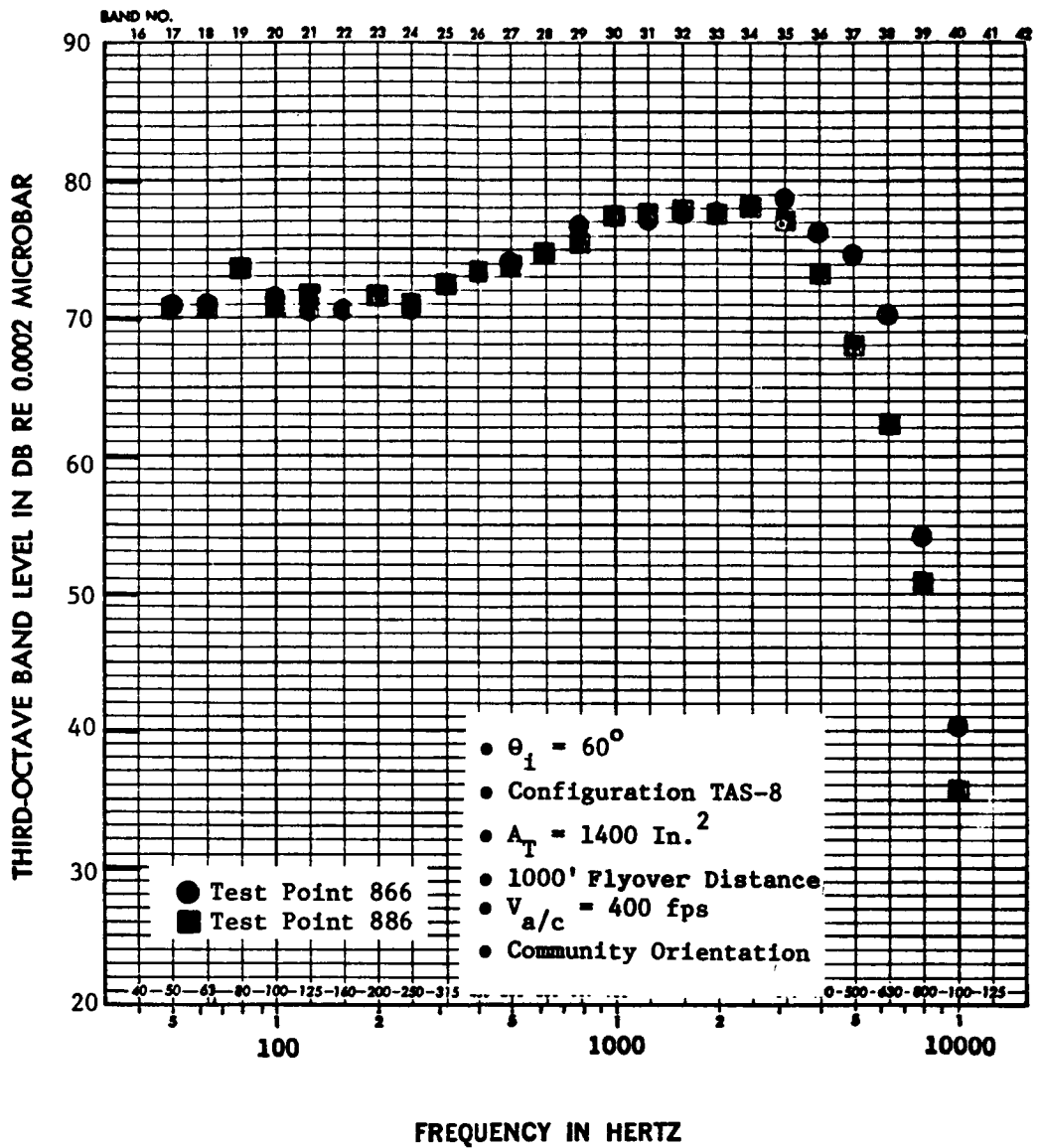


Figure 4.1.2-10b. Influence of Shield to Core Jet Velocity Ratio ( $V_s$ ) on Spectral Content at  $\theta_1 = 60^\circ$  of Configuration TAS-8 at a Constant  $CV_r$ .

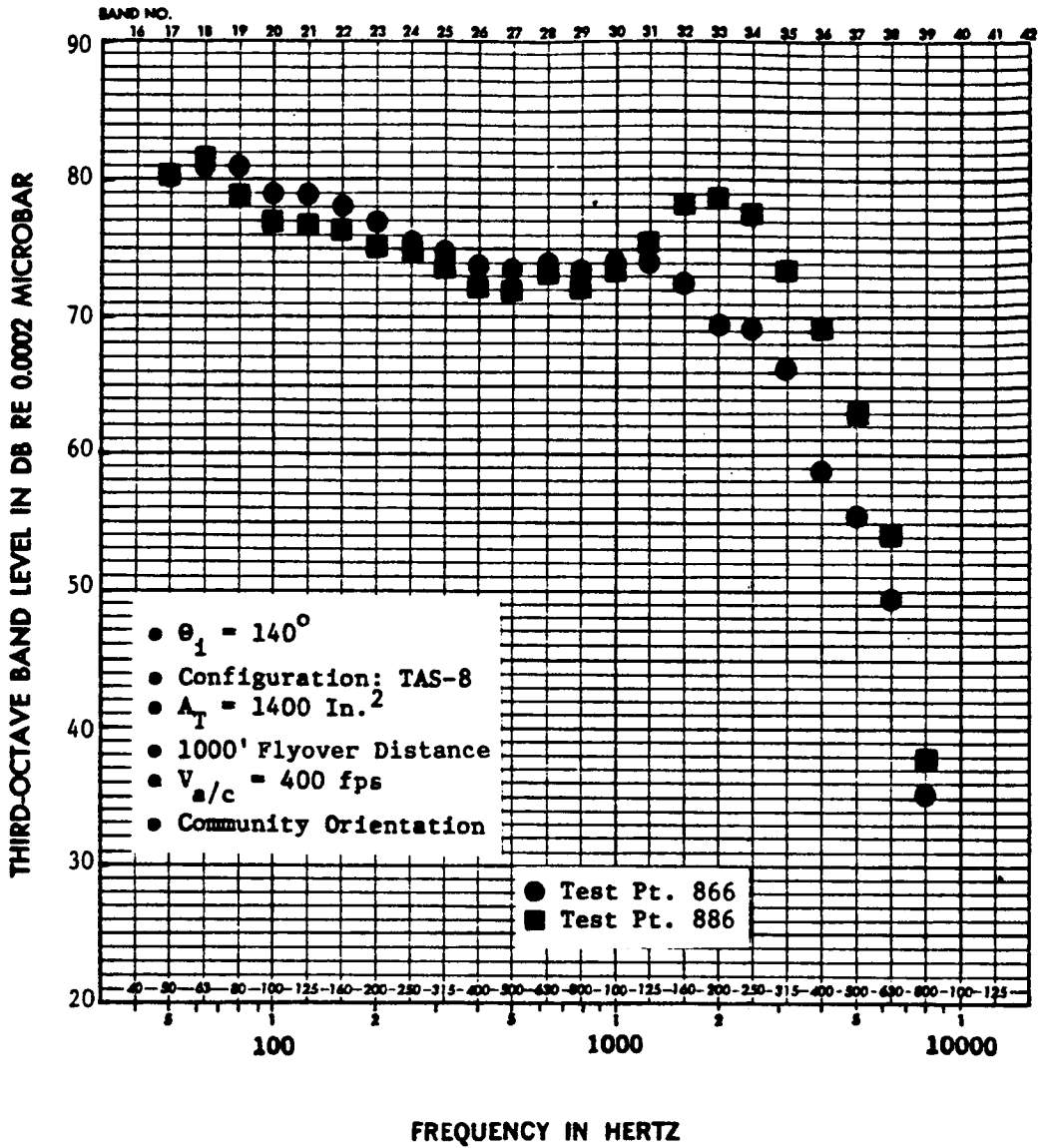


Figure 4.1.2-10c. Influence of Shield to Core Jet Velocity Ratio ( $V_r$ ) on Spectral Content at  $\theta_1 = 140^\circ$  of Configuration TAS-8 at a Constant  $CV_r$ .

Next, the influence of  $CV_r$  (holding  $V_r$  constant) on the PNL and spectral content are analyzed (see Figure 4.1.2-11). One notices that the PNL values reduce with an increase in  $CV_r$  up to  $\theta_i = 120^\circ$ . Spectral distributions are shown in Figures 4.1.2-11b and 4.1.2-11c at directivity angles  $60^\circ$  and  $140^\circ$ . At  $\theta_i = 60^\circ$ , as  $CV_r$  increases, the high frequency noise reduces; whereas such a trend is not observed at  $\theta_i = 140^\circ$ . Based on pure ray acoustic considerations, higher values of  $CV_r$  imply greater refracting effect of the thermal acoustic shield. However, for the limited variation of the  $CV_r$  parameter explored significant noise variation with  $CV_r$  has not been observed for the 32 chute suppressor nozzle with the thermal acoustic shield.

Next, the combined influence of  $V_r$  and  $CV_r$  holding the static temperature ratio ( $T_r^S$ ) approximately constant is analyzed. Figure 4.1.2-12 shows the PNL directivity and spectral data at  $\theta_i = 60^\circ$  and  $140^\circ$  for two test points with about the same  $T_r^S$ , but different values of  $V_r$  and  $CV_r$ . The PNL and spectra are not significantly different indicating that for the range of  $V_r$  and  $CV_r$  considered, their combined influence holding  $T_r^S$  constant on the acoustic characteristics of the 32 chute suppressor with thermal acoustic shield is minimal.

#### 4.1.3 COMPARISON OF ACOUSTIC INFLUENCE OF THERMAL ACOUSTIC SHIELDS ON UNSUPPRESSED ANNULAR PLUG AND 32 CHUTE SUPPRESSOR NOZZLES

A comparative study of the thermal acoustic shield influence on the unsuppressed annular plug and 32 chute suppressor nozzles was carried out to evaluate the following:

- A. Influence of the partial thermal acoustic shield of 0.97" thickness, on the directivity of 1/3 octave band frequencies of the unsuppressed annular plug and the 32 chute suppressor nozzles;
- B. Impact of the sideline distance on the PNL reduction due to the partial thermal acoustic shield of 0.97" thickness for the unsuppressed annular plug and the 32 chute suppressor nozzles; and,

Test Point	Core Jet			Shield Jet			Mixed Conditions			$\frac{V^{sj}}{V^j}$	$\frac{(C+V)^{sj}}{(C+V)^j}$	$\frac{T_s^{sj}}{T_s^j}$
	$V^j$ , fps	$T_{T,R}^j$	$P_r^j$	$V^{sj}$ fps	$T_{T,R}^{sj}$	$P_r^{sj}$	$V^{mix}$ fps	$T_{T,R}^{mix}$ or $P_r^{mix}$	$P_r^{mix}$			
866	1858	1522	2.066	1122	954	1.502	1577	1305	1.824	.60	.71	.68
872	1856	1513	2.073	1122	1651	1.257	1672	1548	1.761	.60	.85	1.25

- Configuration: TAS-8 (32 Chute Suppressor with 180° TAS of 0.97" Thickness)
- Community Orientation
- Parametric Variation Around Outback Cycle
- $A_T = 1400 \text{ In.}^2$
- 1000' Flyover Distance
- $V_{a/c} = 400 \text{ fps}$

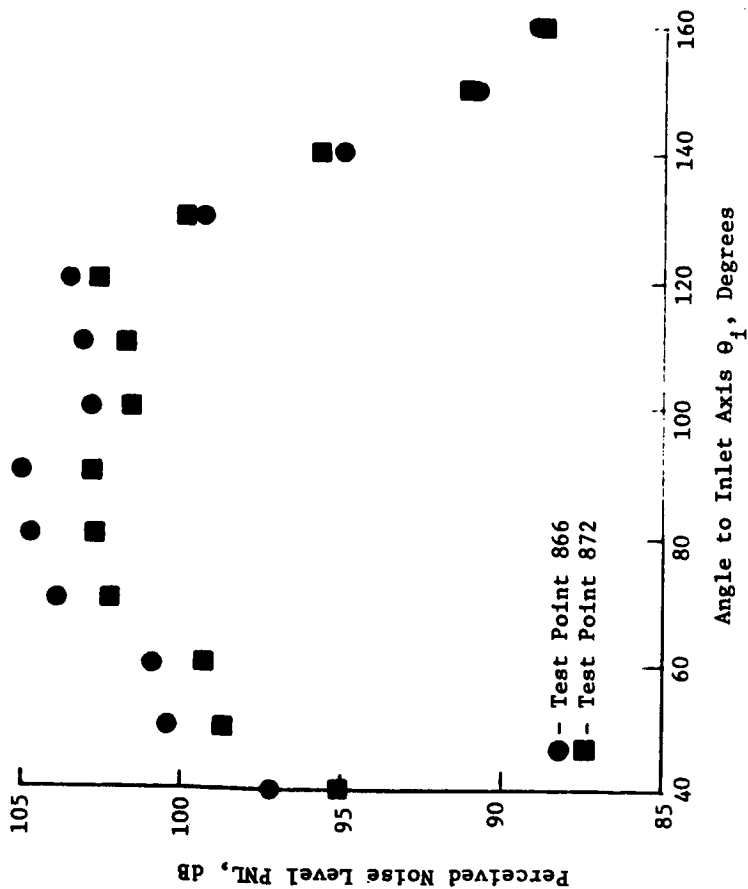


Figure 4.1.2-11a. Influence of  $CV_r$  on PNL Directivity of Configuration TAS-8 at a Constant Shield to Core Jet Velocity Ratio ( $V_r$ ).

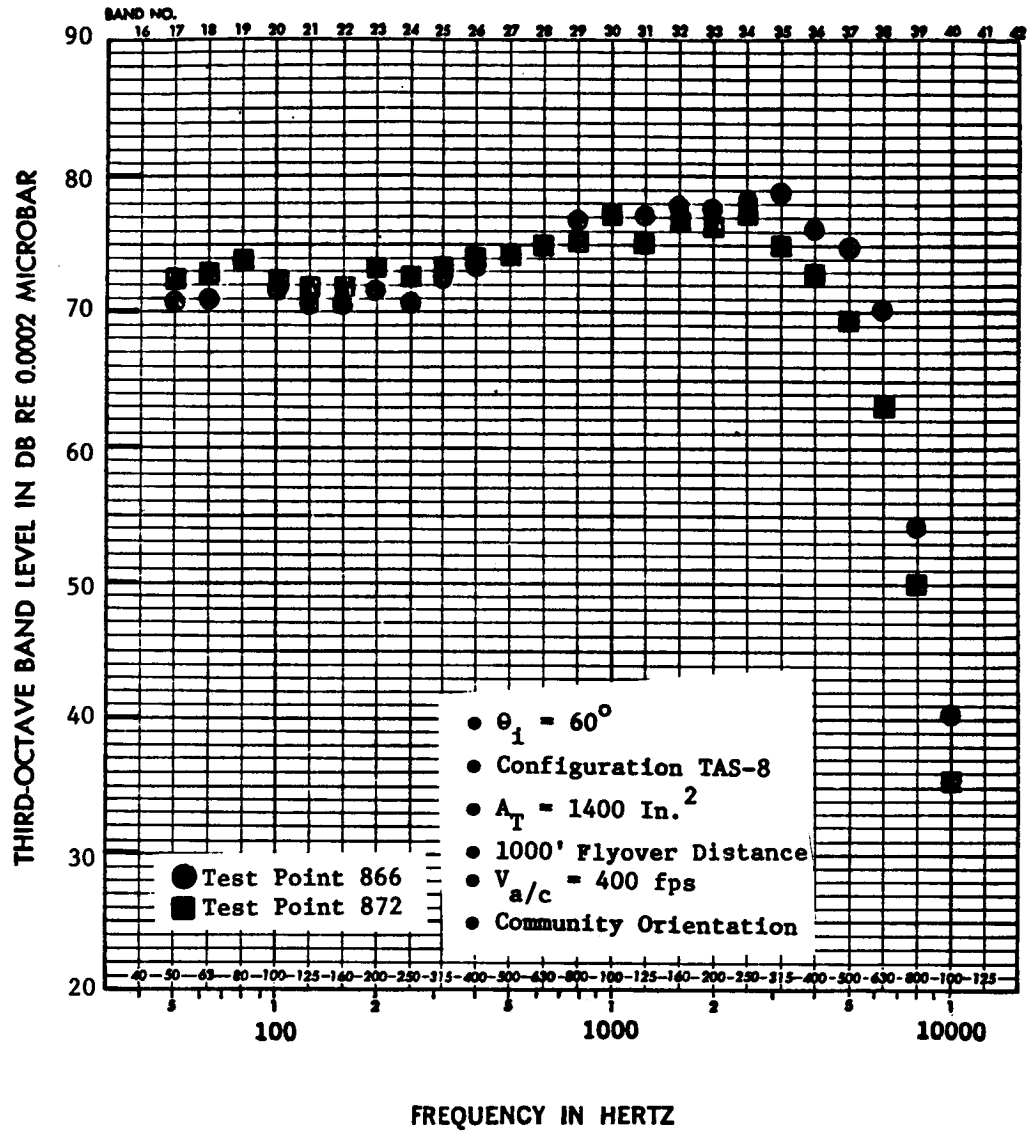


Figure 4.1.2-11b. Influence of  $CV_r$  on Spectral Content at  $\theta_1 = 60^\circ$  of Configuration TAS-8 at a Constant Shield to Core Jet Velocity Ratio ( $V_r$ ).

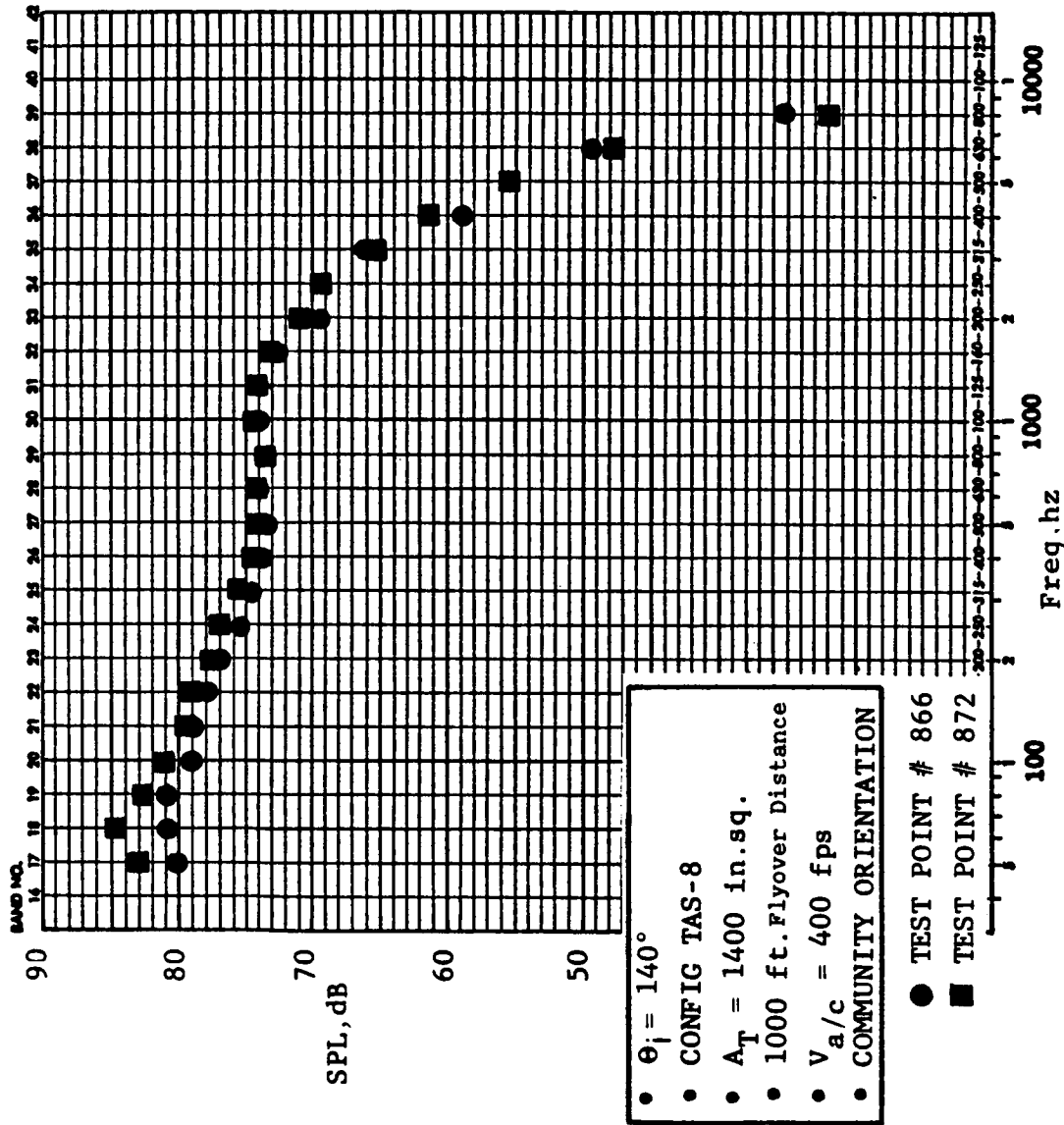


Figure 4.1.2-11C INFLUENCE OF  $V_r$  ON SPECTRAL CONTENT AT  $\theta_j = 140^\circ$  of CONFIGURATION TAS-8 AT A CONSTANT SHIELD TO CORE JET VELOCITY RATIO ( $V_r$ )

Test Point	Core Jet			Shield Jet			Mixed Conditions				$\frac{V^{sj}}{V^j}$	$\frac{(C+V)^{sj}}{(C+V)^j}$	$\frac{T_s^{sj}}{T_s^j}$
	$V^j$ , fps	$T_{T,R}^j$	$P_r^j$	$V^{sj}$ fps	$T_{T,R}^{sj}$	$P_r^{sj}$	$V^{mix}$ fps	$T_{T,R}^{mix}$	$P_r^{mix}$				
872	1856	1513	2.073	1122	1651	1.257	1672	1548	1.761	.60	.85	1.25	
884	1853	1513	2.066	1481	1654	1.502	1735	1558	1.838	.80	.94	1.19	

- Configuration: TAS-8 (32 Chute Suppressor with 180° TAS of 0.97" Thickness)
- Community Orientation
- Parametric Variation Around Outback Cycle
- $A_T = 1400 \text{ In.}^2$
- 1000' Flyover Distance
- $V_{a/c} = 400 \text{ fps}$

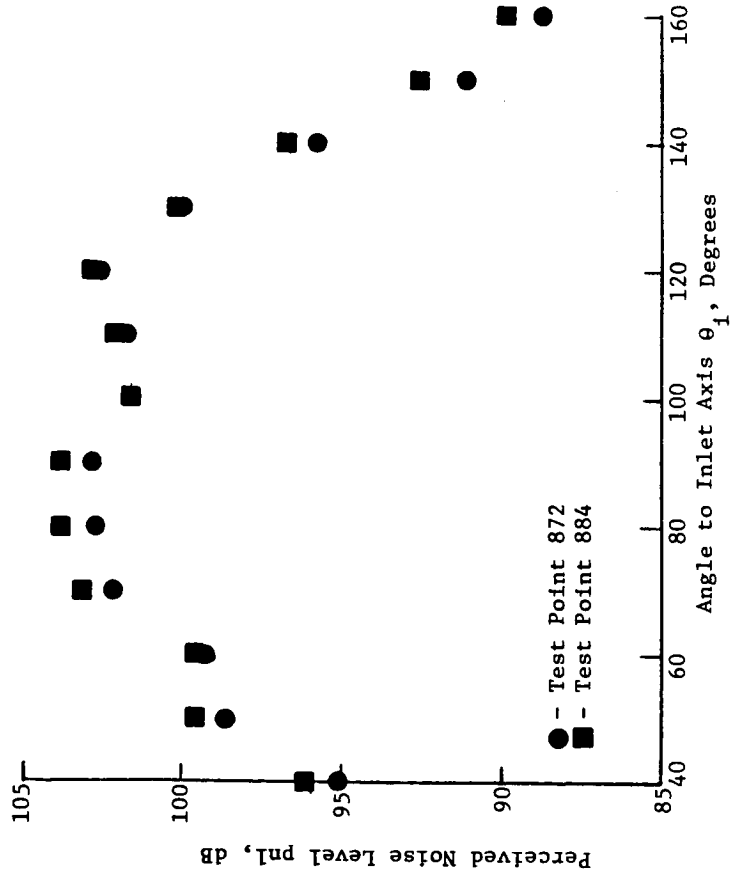


Figure 4.1.2-12a. Combined Influence of  $V_r$  and  $CV_r$ , Holding the Shield to Core Jet Static Temperature Ratio ( $T_s^j$ ) Constant, on PNL Directivity of Configuration TAS-8.

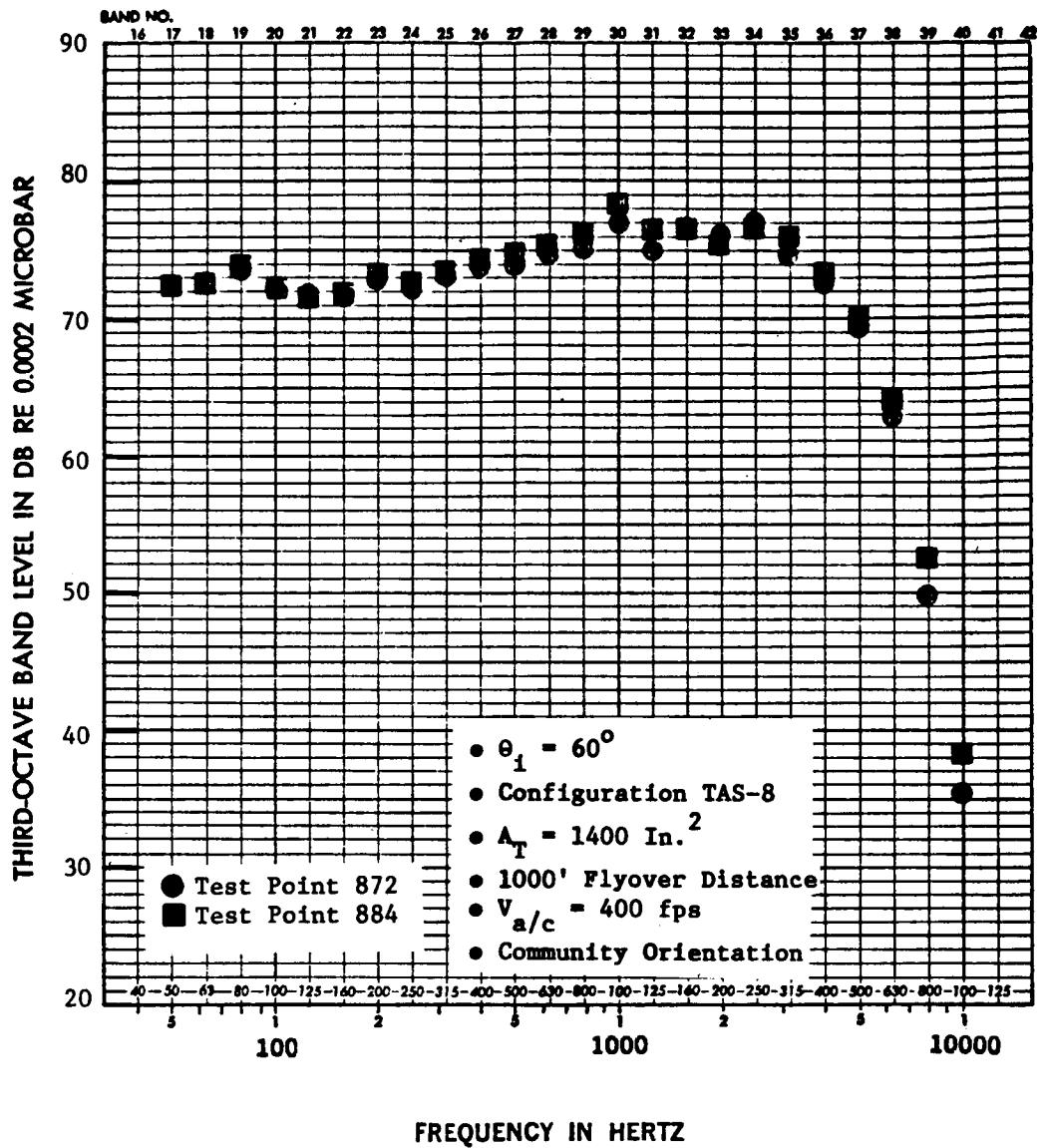


Figure 4.1.2-12b. Combined Influence of  $V_r$  and  $CV_r$  Holding  $T_r^S$  Constant on Spectral Content at  $\theta_i = 60^\circ$  of Configuration TAS-8.



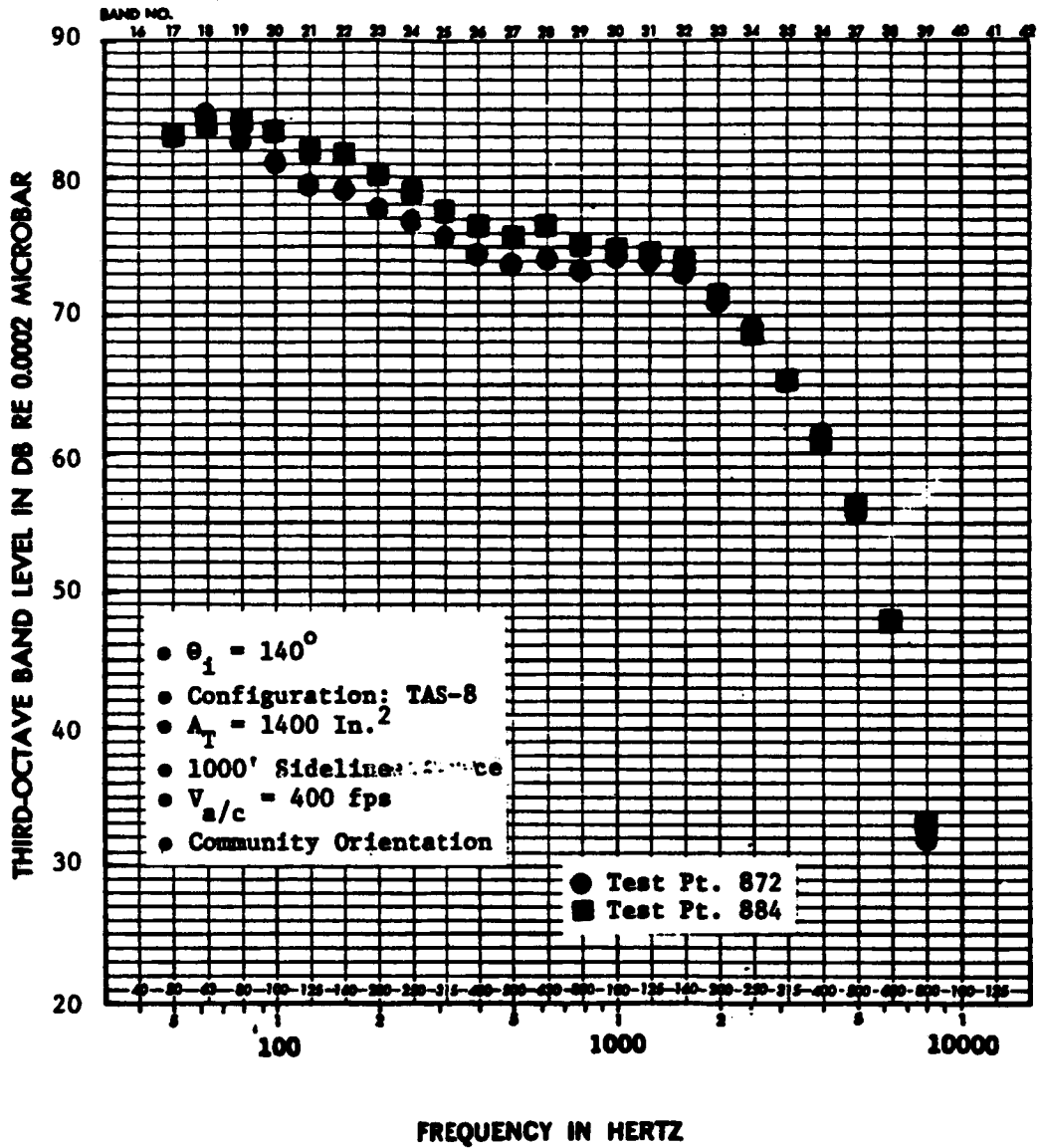


Figure 4.1.2-12c. Combined Influence of  $V_r$  and  $CV_r$  Holding  $T_r^S$  Constant on Spectral Content at  $\theta_1 = 140^\circ$  of Configuration TAS-8.

C. Asymmetric acoustic characteristics of the unsuppressed annular plug and 32 chute suppressor nozzles with the partial thermal acoustic shield of 0.97" thickness.

4.1.3.1 Influence of the Partial Thermal Acoustic Shield of 0.97" Thickness on the Directivity of 1/3 Octave Band Frequencies of the Unsuppressed Annular Plug and the 32 Chute Suppressor Nozzles

An evaluation of the differences in noise suppression effectiveness of the 180° shield of 0.97" thickness on the unsuppressed annular plug and the 32 chute suppressor nozzles in terms of the directivity of various 1/3 octave band frequencies was carried out to diagnose the importance of different physical mechanisms.

For this study, the static data of configurations TAS-1, TAS-3, TAS-6 and TAS-8 (scaled to a total flow area of 1400 in<sup>2</sup>) were used to calculate the shield effectiveness directivity patterns at various 1/3-octave frequencies. Figure 4.1.3-1 shows the influence of the 180° shield of 0.97" thickness on the directivity of the various 1/3 octave band frequencies of unsuppressed annular plug and 32 chute suppressor nozzles at a typical approach cycle condition. Note the high levels of suppression of the high frequency bands due to the partial shield in the aft quadrant for both the unsuppressed and 32 chute suppressor nozzles. For the 4000 HZ band, the maximum suppression is about 19-20 dB at  $\theta_i = 140^\circ$  for both the unsuppressed and 32 chute suppressor nozzles. For the unsuppressed nozzle, as the frequency increases so does the suppression in the aft quadrant. However, such a clear trend is observed for the 32 chute suppressor nozzle only at two (2) aft quadrant angles (viz.,  $\theta_i = 140^\circ$  and  $150^\circ$ ). The rapid increase in the suppression of the high frequency noise in the aft quadrant is attributed to the fluid shielding which results for angles aft of the (theoretical) critical angle for total internal reflection. Based on the aerodynamic conditions of the shield and core jets, the critical angle for total internal reflection can be calculated by the following theoretical relationship (Reference 4.4):

Sym.	Frequency, Hz
○	250
□	500
◇	1000
△	2000
▽	4000

$A_T = 1400 \text{ In.}^2$  for TAS-1 and TAS-3

Static

Approach Cycle

Conf.	Test Point	Core Jet			Shield Jet			Mixed Cond.		
		$v^j$ , fps	$T_T^j$ , °R	$P_r^j$	$v^{sj}$ , fps	$T_T^{sj}$ , °R	$P_r^{sj}$	$v^{mix}$ , fps	$T_T^{mix}$ , °R	$P_r^{mix}$
TAS-1	101	1340	1252	1.558	---	NO SHIELD	---	1340	1252	1.558
TAS-3	317	1341	1256	1.556	793	1246	1.162	1185	1253	1.407

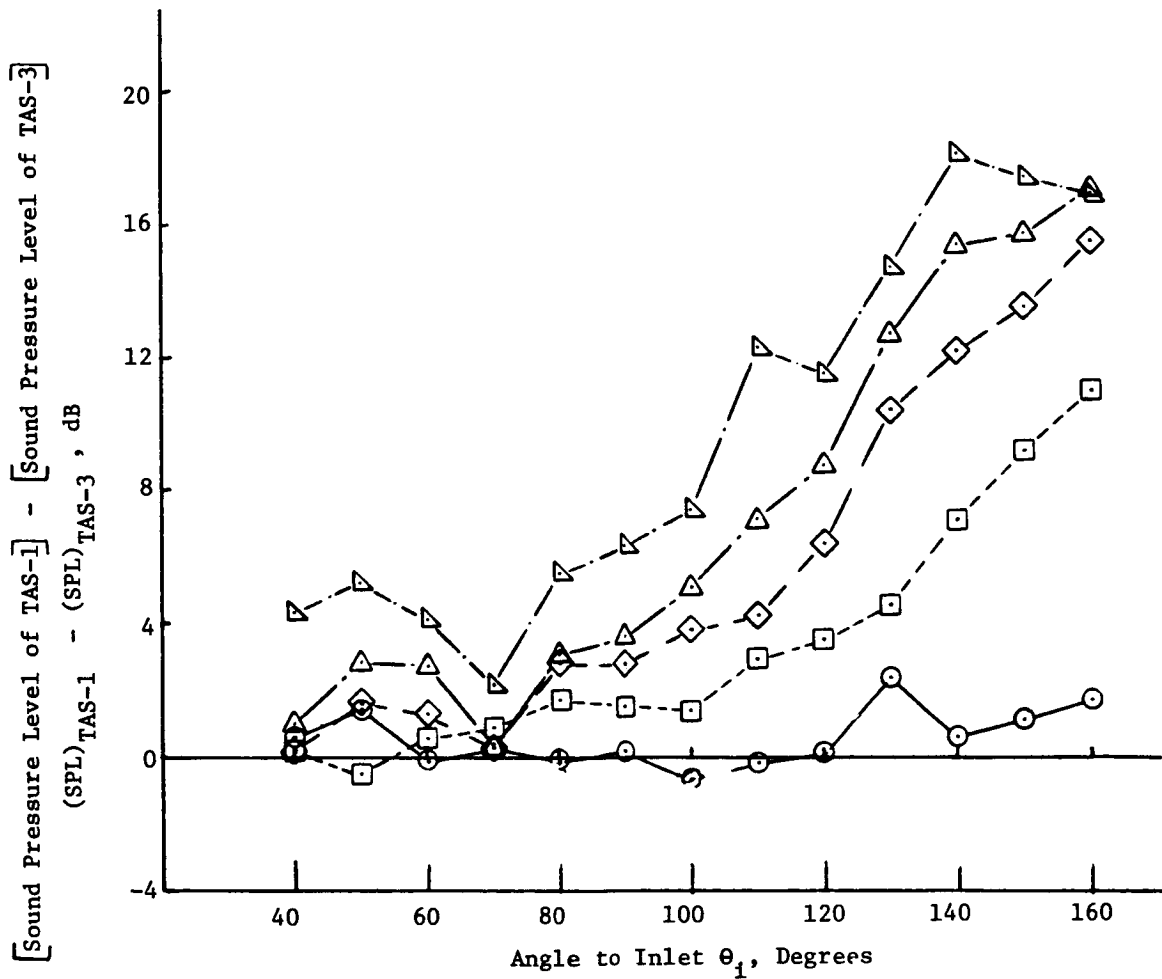


Figure 4.1.3-1a. Influence of  $180^\circ$  Shield of 0.97" Thickness on the Directivity of Various One-Third Octave Band Frequencies of Unsuppressed Annular Plug Nozzle at Approach Condition (Static).

Sym.	Frequency, Hz
○	250
□	500
◇	1000
△	2000
▽	4000

$A_T = 1400 \text{ In.}^2$  for TAS-6 and TAS-8

Static

Approach Cycle

Conf.	Test Point	Core Jet			Shield Jet			Mixed Cond.		
		$v^j$ , fps	$T_T^j$ , °R	$P_r^j$	$v^{sj}$ , fps	$T_T^{sj}$ , °R	$P_r^{sj}$	$v^{mix}$ , fps	$T_T^{mix}$ , °R	$P_r^{mix}$
TAS-6	601	1341	1267	1.550	---	NO SHIELD	---	1341	1267	1.550
TAS-8	817	1323	1240	1.546	801	1244	1.166	1176	1241	1.405

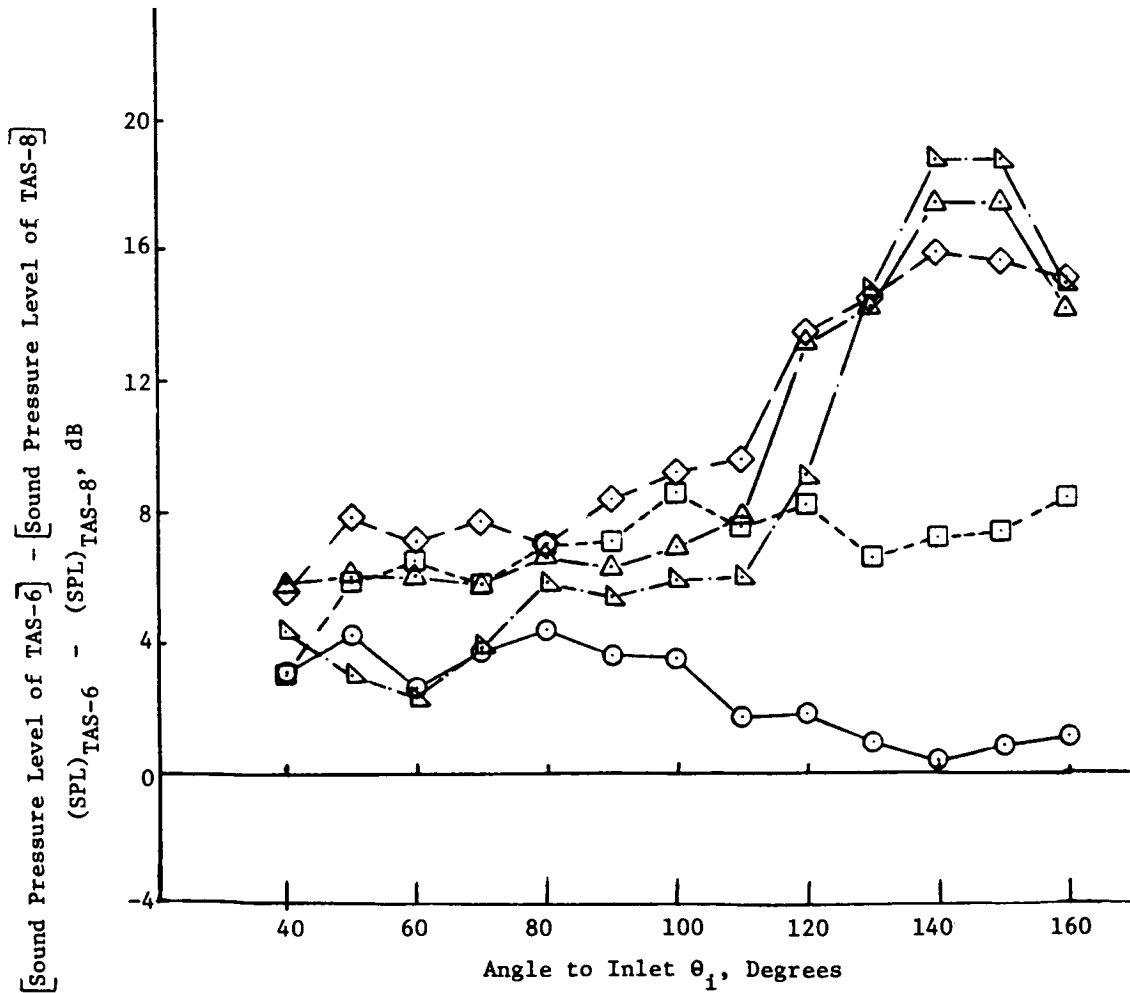


Figure 4.1.3-1b. Influence of 180° Shield of 0.97" Thickness on the Directivity of Various One-Third Octave Band Frequencies of 32 Chute Suppressor Nozzle at Approach Condition. (Static).

$$\cos(\theta_1)_{cr} = \frac{1}{M_c + (c/c_{amb})} \quad (4.1.1)$$

where

$M_c$  is the noise source (eddy) convection Mach number,  $c$  is the local sonic speed through which the eddy is convecting, and,  $c_{amb}$  is the ambient sonic speed.

The above relationship is based on ray acoustic considerations and assumes a plug flow model for the jets. The eddy convection Mach number ( $M_c$ ) is calculated empirically. Typical empirical correlations for the eddy convection Mach number utilized in Reference 4.4 are as follows:

For unsuppressed nozzles:

$$M_c = \frac{1}{2} \left[ 0.55 + \frac{0.39}{v_{sj}/v_j} \right] \frac{v_j}{c_{amb}} \quad (4.1.2)$$

For mechanical suppressor nozzles:

$$M_c = \frac{1}{2} \left[ 0.4 + \frac{0.2}{v_{sj}/v_j} \right] \frac{v_j}{c_{amb}} \quad (4.1.3)$$

Utilizing equations (4.1.1) through (4.1.3) the critical angle for total internal reflection for the approach case for the unsuppressed annular plug nozzle is calculated to be 117.4°, and 122.2° for the 32 chute suppressor nozzle. The measured data does indicate that, for  $\theta_1 > 120^\circ$ , the partial shield produces large amounts of suppression for the high frequency waves which behave like acoustic rays, implying that the internal reflection is one of the dominating mechanisms at shallow angles to the jet axis. However, there is no abrupt onset of the noise cutoff mechanism in real jets for the high frequency waves as is implied by the ray concept of total internal reflection, due to the distributed nature of sources and spatially varying flow fields.

The noise reduction in the front quadrant and at  $\theta_i = 90^\circ$  is attributed to the source modifications due to changes in the velocity and temperature gradients by the partial shield. The partial shield reduces the velocity and temperature gradients of the core jet near the jet exit plane and thereby reduces the source strength of the eddies close to the exit plane. However, the reduction in gradients of velocity by the shield results in lengthening of the jet in the axial direction which in turn raises the contribution of the low frequency noise. One notes in Figure 4.1.3-1 that for frequencies greater than or equal to 250 Hz, the partial shield is able to reduce the noise in the front quadrant for both the unsuppressed annular plug and 32 chute suppressor nozzles.

The above analysis was repeated for the cutback, takeoff and maximum thrust cycle conditions (see Figures 4.1.3-2 through 4.1.3-4). The shield suppression characteristics in the aft quadrant for the unsuppressed annular plug nozzle for the cutback case (see Figure 4.1.3-2a) resemble that of the annular plug nozzle for the approach case, namely, as frequency increases so does the suppression and the 4000 Hz frequency shows a peak suppression of about 22 dB at  $\theta_i = 150^\circ$  and  $160^\circ$ . Compared to the approach case, the cut-off mechanism seems to set in more abruptly and there is smaller amount of source reduction in the front quadrant; both indicating a reduced mixing of the shield and core jets for the cutback case. In the case of the 32 chute suppressor at the cutback case (see Figure 4.1.3-2b), the 4000 HZ 1/3 octave band frequency yields about the same maximum value of suppression in the aft quadrant as in the approach case, namely 19 dB. The 250 HZ and 500 HZ 1/3 octave bands show amplification due to the shield in the aft quadrant for the cutback case, unlike the approach case. The partial shield is seen to yield larger values of source reduction in the front quadrant for the suppressor nozzle (cf., Figures 4.1.3-2a and 4.1.3-2b) attributable to the differences in the mixing characteristics between the 32 chute suppressor and unsuppressed annular plug nozzles. For the 32 chute suppressor nozzle with the partial shield, only two highest frequencies examined (viz., 2000 HZ and 4000 HZ) show features of total internal reflection, whereas, in the case of the unsuppressed annular plug nozzle, all the frequencies considered except the lowest frequency show features of total internal reflection in the aft quadrant. This observation again confirms that source modification is more significant for the 32 chute suppressor nozzle than for the unsuppressed annular plug nozzle with the partial thermal acoustic shield.

Sym.	Frequency, Hz
○	250
□	500
◇	1000
△	2000
▽	4000

$A_T = 1400 \text{ In.}^2$  for TAS-1 and TAS-3

Static

Cutback Cycle

Conf.	Test Point	Core Jet			Shield Jet			Mixed Cond.		
		$V^j$ , fps	$T_T^j$ , °R	$P_r^j$	$V^{sj}$ , fps	$T_T^{sj}$ , fps	$P_r^{sj}$	$V^{mix}$ , fps	$T_T^{mix}$ , °R	$P_r^{mix}$
TAS-1	105	1851	1504	2.074	---	NO SHIELD	---	1851	1504	2.074
TAS-3	321	1852	1507	2.073	1112	1504	1.280	1649	1506	1.760

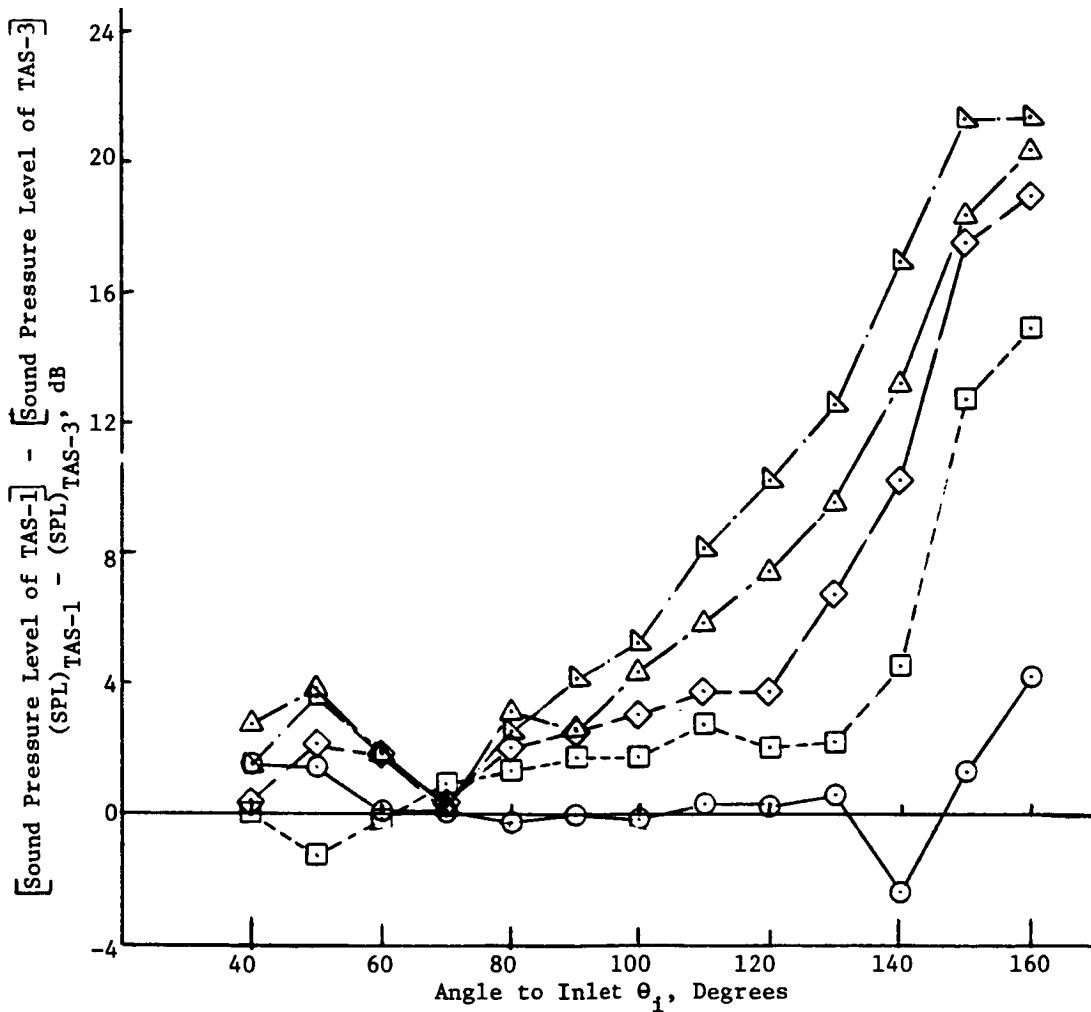


Figure 4.1.3-2a. Influence of 180° Shield of 0.97" Thickness on the Directivity of Various One-Third Octave Band Frequencies of Unsuppressed Annular Plug Nozzle at Cutback Condition (Static).

Sym.	Frequency, Hz
○	250
□	500
◇	1000
△	2000
▽	4000

$A_T = 1400 \text{ In.}^2$  for TAS-6 and TAS-8

Static

Cutback Cycle

Conf.	Test Point	Core Jet			Shield Jet			Mixed Cond.		
		$v^j$ , fps	$T_T^j$ , °R	$P_r^j$	$v^{sj}$ , fps	$T_T^{sj}$ , fps	$P_r^{sj}$	$v^{mix}$ , fps	$T_T^{mix}$ , °R	$P_r^{mix}$
TAS-6	605	1847	1508	2.061	-----	NO SHIELD	---	1847	1508	2.061
TAS-8	821	1842	1491	2.072	1115	1495	1.284	1647	1492	1.768

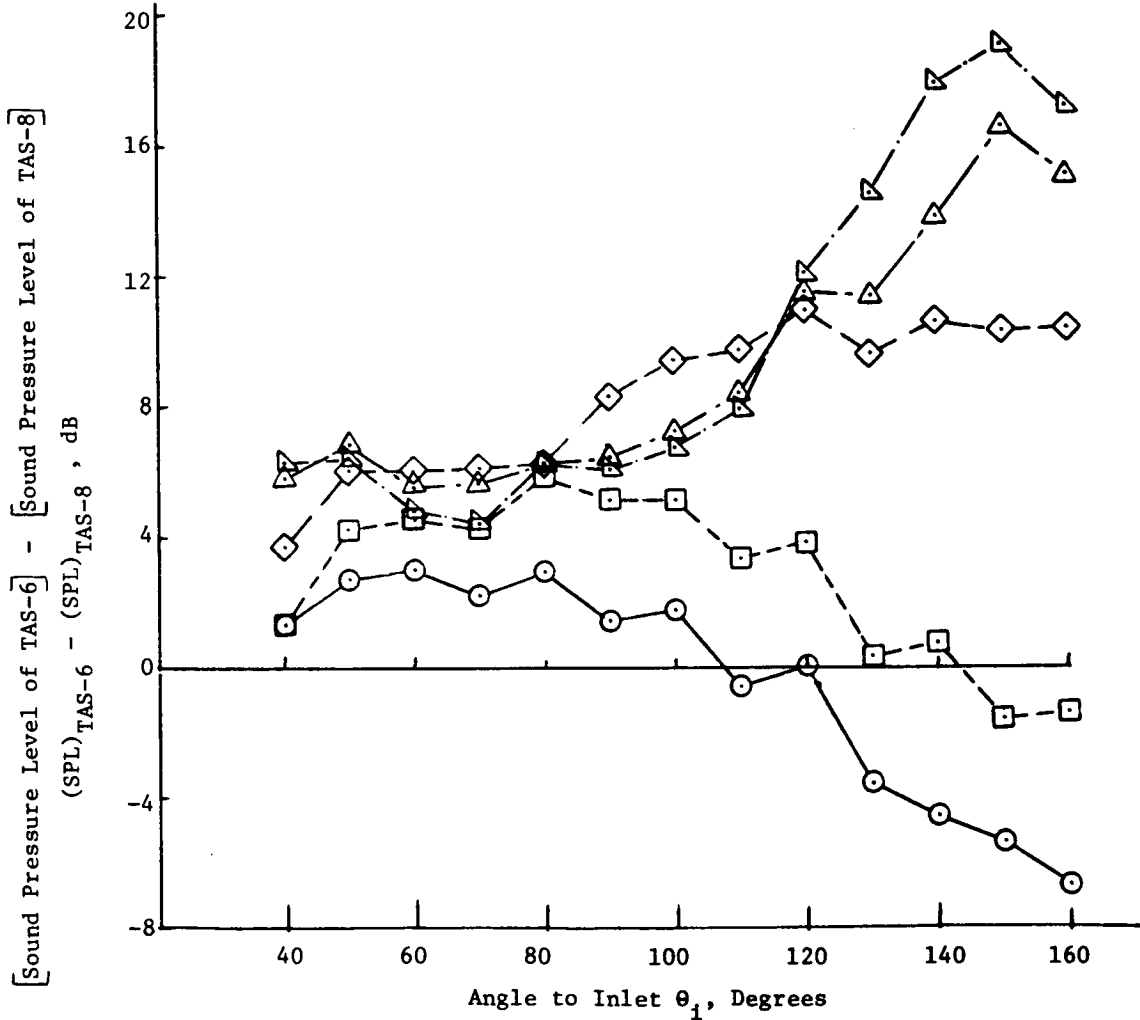


Figure 4.1.3-2b. Influence of 180° Shield of 0.97" Thickness on the Directivity of Various One-Third Octave Band Frequencies of 32 Chute Suppressor Nozzle at Cutback Condition (Static).



Sym.	Frequency, Hz
○	250
□	500
◇	1000
△	2000
▽	4000

$A_T = 1400 \text{ In.}^2$  for TAS-1 and TAS-3

Static

Takeoff Cycle

Conf.	Test Point	Core Jet			Shield Jet			Mixed Cond.		
		$v^j$ , fps	$T_T^j$ , °R	$P_r^j$	$v^{sj}$ , fps	$T_T^{sj}$ , °R	$P_r^{sj}$	$v^{mix}$ , fps	$T_T^{mix}$ , °R	$P_r^{mix}$
TAS-1	109	2210	1631	2.693	---	NO SHIELD	---	2210	1631	2.693
TAS-3	325	2221	1644	2.700	1319	1642	1.379	1994	1643	2.178

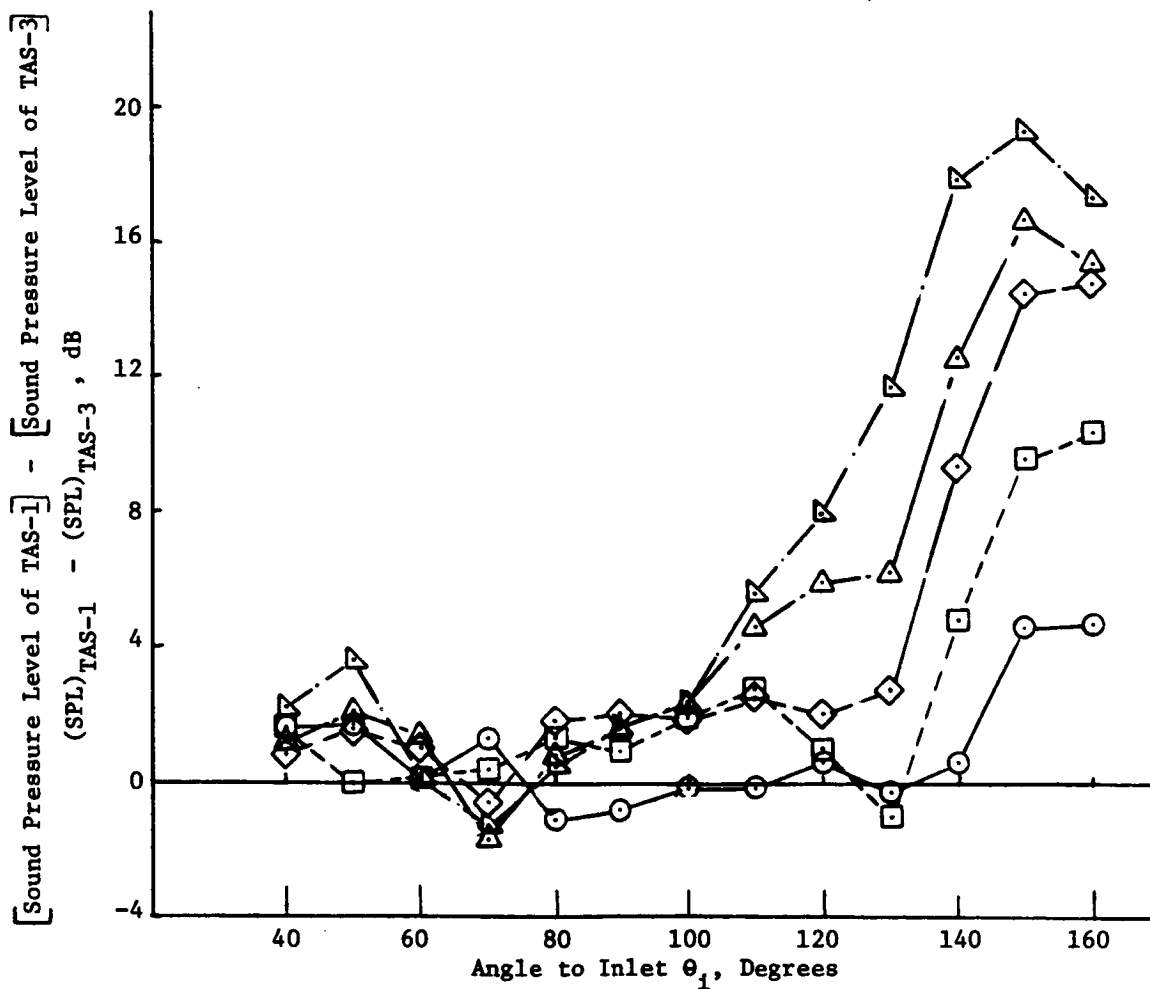


Figure 4.1.3-3a. Influence of 180° Shield of 0.97" Thickness on the Directivity of Various One-Third Octave Band Frequencies of Unsuppressed Annular Plug Nozzle at Takeoff Condition (Static).

Sym.	Frequency, Hz
○	250
□	500
◇	1000
△	2000
▽	4000

$A_T = 1400 \text{ In.}^2$  for TAS-6 and TAS-8

Static

Takeoff Cycle

Conf.	Test Point	Core Jet			Shield Jet			Mixed Cond.		
		$v^j$ , fps	$T_T^j$ , °R	$P_r^j$	$v^{sj}$ , fps	$T_T^{sj}$ , fps	$P_r^{sj}$	$v^{mix}$ , fps	$T_T^{mix}$ , °R	$P_r^{mix}$
TAS-6	609	2234	1662	2.701	---	NO SHIELD	---	2234	1662	2.701
TAS-8	825	2211	1631	2.695	1323	1619	1.388	1990	1628	2.188

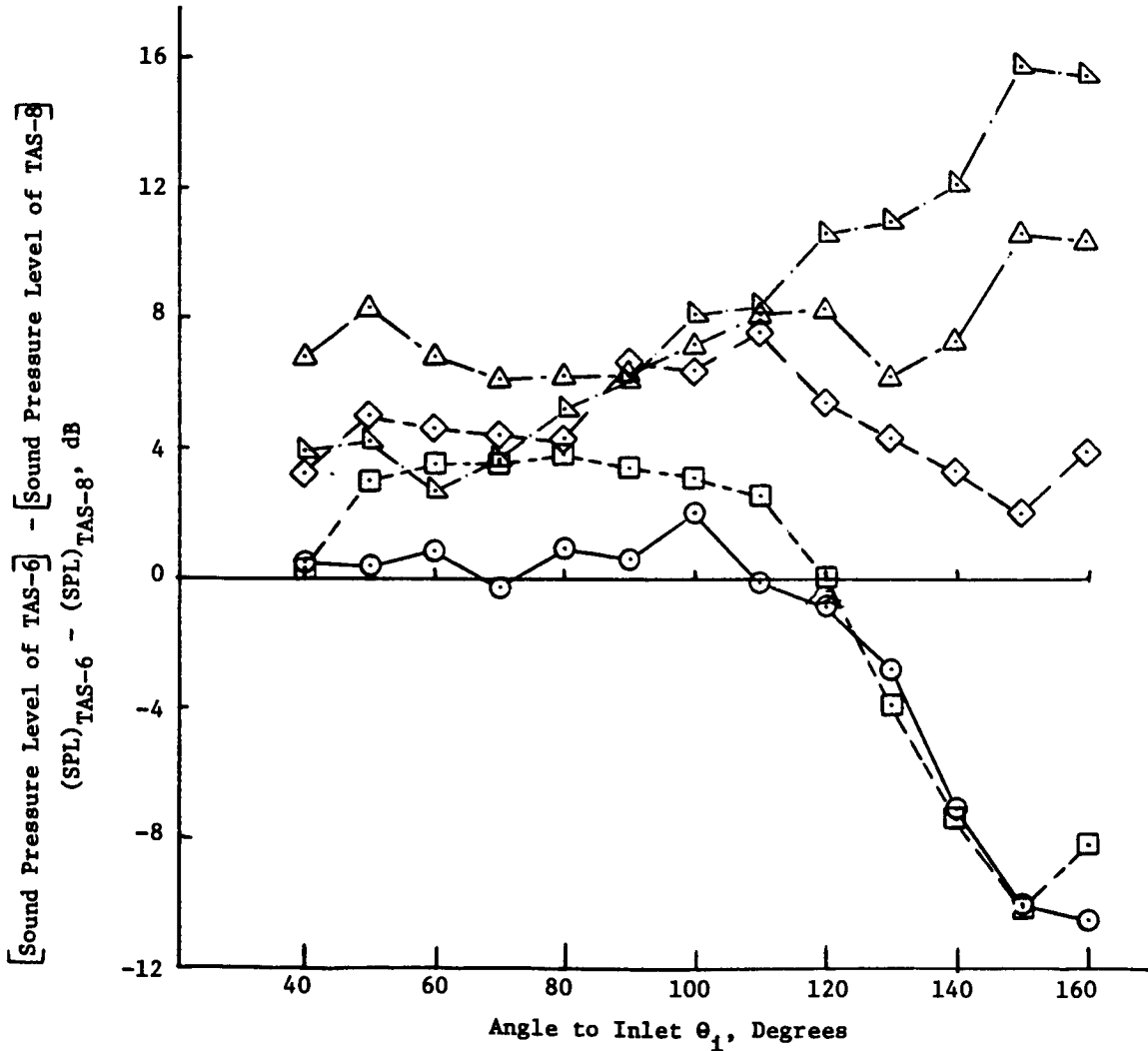


Figure 4.1.3-3b. Influence of 180° Shield of 0.97" Thickness on the Directivity of Various One-Third Octave Band Frequencies of 32 Chute Suppressor Nozzle at Takeoff Condition (Static).

Sym.	Frequency, Hz
○	250
□	500
◇	1000
△	2000
▽	4000

$A_T = 1400 \text{ In.}^2$  for TAS-1 and TAS-3

Static

Max Thrust

Conf.	Test Point	Core Jet			Shield Jet			Mixed Cond.		
		$V^j$ , fps	$T_T^j$ , °R	$P_r^j$	$V^{sj}$ , fps	$T_T^{sj}$ , fps	$P_r^{sj}$	$V^{mix}$ , fps	$T_T^{mix}$ , °R	$P_r^{mix}$
TAS-1	115	2583	1730	3.788	---	NO SHIELD	---	2583	1730	3.788
TAS-3	331	2513	1727	3.491	1567	1738	1.544	2290	1729	2.727

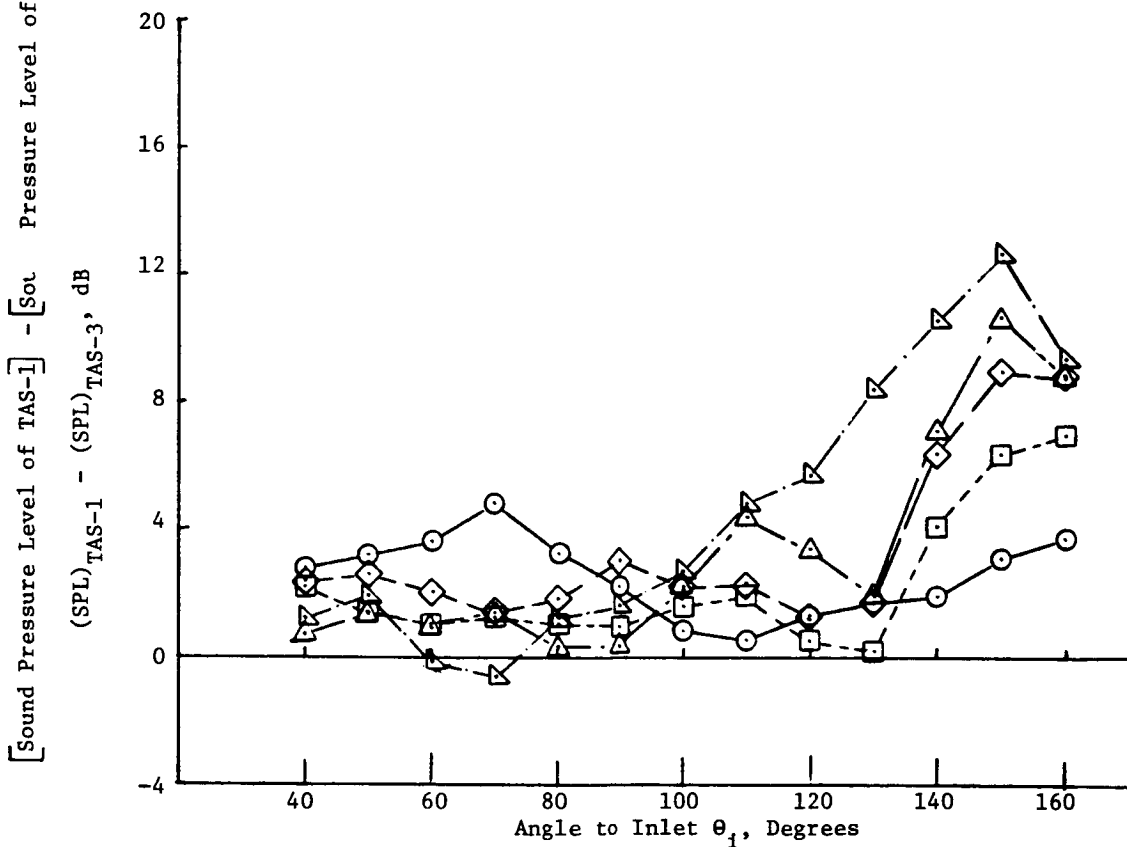


Figure 4.1.3-4a. Influence of 180° Shield of 0.97" Thickness on the Directivity of Various One-Third Octave Band Frequencies of Unsuppressed Annular Plug Nozzle (Static).

Sym.	Frequency, Hz
○	250
□	500
◇	1000
△	2000
▽	4000

$A_T = 1400 \text{ In.}^2$  for TAS-6 and TAS-8

Static

Max Thrust

Conf.	Test Point	Core Jet			Shield Jet			Mixed Cond.		
		$v^j$ , fps	$T_T^j$ , °R	$P_r^j$	$v^{sj}$ , fps	$T_T^{sj}$ , fps	$P_r^{sj}$	$v^{mix}$ , fps	$T_T^{mix}$ , °R	$P_r^{mix}$
TAS-6	615	2587	1716	3.861	---	NO SHIELD	---	2587	1716	3.861
TAS-8	831	2567	1693	3.853	1552	1699	1.547	2350	1694	2.980

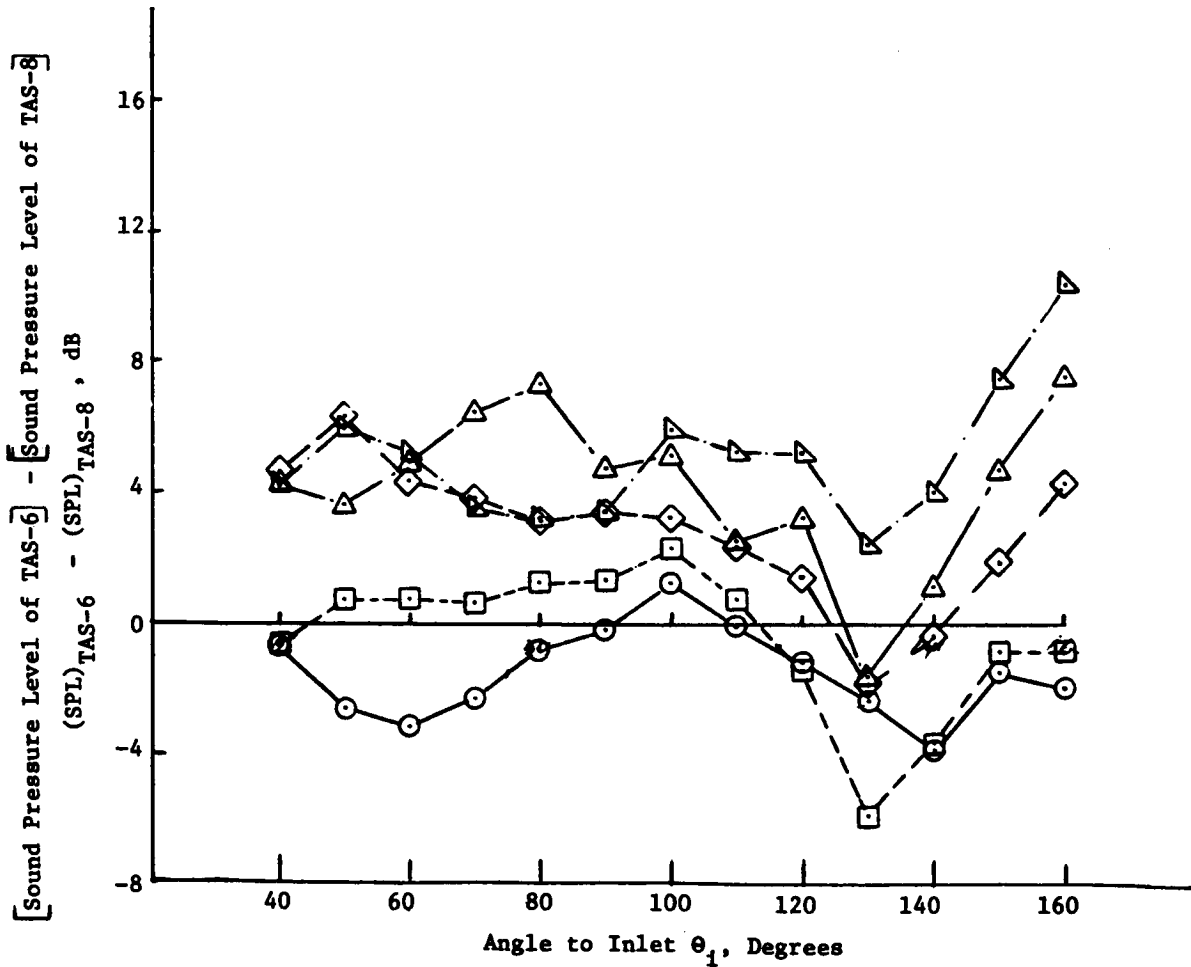


Figure 4.1.3-4b. Influence of 180° Shield of 0.97" Thickness on the Directivity of Various One-Third Octave Band Frequencies on 32 Chute Suppressor Nozzle (Static).

The influence of the partial thermal acoustic shield on the directivity of various one-third octave band frequencies of unsuppressed annular plug and 32 chute suppressor nozzles at a takeoff condition is shown in Figure 4.1.3-3. The noise suppression features of the partial shield on the unsuppressed annular plug nozzle closely resemble those at the cutback condition. However, in the case of the 32 chute suppressor nozzle, only the 4000 HZ frequency shows features of total internal reflection, and the source modification seems to be the dominant feature in the takeoff case. There is considerable amount of amplification of the 250 HZ and 500 HZ frequencies in the aft quadrant by the partial thermal acoustic shield for the 32 chute suppressor nozzle, and such amplifications are not observed in the case of the unsuppressed annular plug nozzle at 250 HZ and 500 HZ. This is yet another manifestation of the significantly different mixing features of the unsuppressed annular plug and the 32 chute suppressor nozzles with the partial thermal acoustic shield.

The influence of the partial shield of 0.97" thickness on the directivity of various 1/3 octave band frequencies of unsuppressed annular plug and 32 chute suppressor nozzles at maximum thrust conditions are shown in Figure 4.1.3-4. For both the nozzles, the maximum suppression for 4000 HZ frequency has reduced noticeably at the maximum thrust condition which indicates that the potential of the thermal acoustic shield to suppress the noise reduces as the core jet velocity increases. As at other cycle conditions, the suppression effectiveness of the partial shield increases as the frequency increases and the total internal reflection seems to be the dominant mechanism in the aft quadrant for the unsuppressed annular plug nozzle for the maximum thrust case. However, in the case of the 32 chute suppressor nozzle, the noise reductions in the front quadrant are at about the same level or slightly lower than those in the aft quadrant implying that source modification plays a major role in the noise suppression effectiveness of the partial shield on a mechanical suppressor nozzle.

#### 4.1.3.2 Impact of the Sideline Distance on the PNL Reduction Due to the Partial Thermal Acoustic Shield of 0.97" Thickness on the Unsuppressed Annular Plug and the 32 Chute Suppressor Nozzles

The sideline distances for typical aircraft noise monitoring locations for approach, cutback and takeoff conditions are different (see Subsection 4.1.1.1). As has been shown in the previous sections, the thermal acoustic

shields yield mid and high frequency noise reductions. As the sideline or propagation distance increases, the high frequency noise attenuates faster than the low frequency noise, since, atmospheric absorption of sound increases with frequency. Hence, the contribution of the high frequency noise component to the perceived noise level decreases as the sideline distance increases. Hence, the effectiveness of the thermal acoustic shield in terms of the PNL reductions is expected to be a function of the sideline distance. Thus, it is important to evaluate the acoustic effectiveness of the thermal acoustic shield at the sideline distances appropriate for the cycle conditions. With the above objective in mind, the acoustic effectiveness of the partial shield of 0.97" thickness on the unsuppressed annular plug and the 32 chute suppressor nozzles over the entire AST/VCE operating line is evaluated in this subsection.

Figure 4.1.3-5 shows the influence of sideline distance on thrust and jet-density-normalized peak PNL and spectral reduction by the 180° thermal acoustic shield of 0.97" thickness on the unsuppressed annular plug nozzle. Figure 4.1.3-5a shows the dependence of normalized peak PNL reduction along an engine operating line on the sideline distance for the simulated flight condition. One notices that, as the core jet velocity ( $V^J$ ) increases, the extent of noise reduction by the thermal acoustic shield diminishes. Also, at high core velocities, there is a noise amplification. The normalized PNL reduction by the thermal acoustic shield is seen to be dependent on the sideline distance.

Spectral content at the peak noise angle ( $\theta_1 = 130^\circ$ ) for the cutback case, which has a core jet velocity of approximately 1850 fps is shown at 370 ft., 1000 ft. and 2400 ft. sideline distances in Figures 4.1.3-5b, 4.1.3-5c and 4.1.3-5d, respectively. There is a significant amount of high frequency noise of configuration TAS-1 contributing to the PNL at 370 ft. sideline distance. As the sideline distance increases, the contribution of the high frequency noise to PNL decreases due to the dissipation of the high frequency noise by air attenuation (see Figures 4.1.3-5c and 4.1.3-5d). Since the thermal acoustic shield is quite effective in suppressing the high frequency noise, its effectiveness on PNL reduction is more noticeable at 370 ft. sideline distance than at 1000 ft. or 2400 ft. However, the sound pressure level reduction at any one-third octave band by the thermal acoustic shield is the same irrespective of the sideline distance chosen.

Symb.	Distance, ft.
●	2400
■	1000
▲	370

- $V_{a/c} = 400$  fps
- $A_T = 1400 \text{ in.}^2$  for TAS-1 and TAS-3

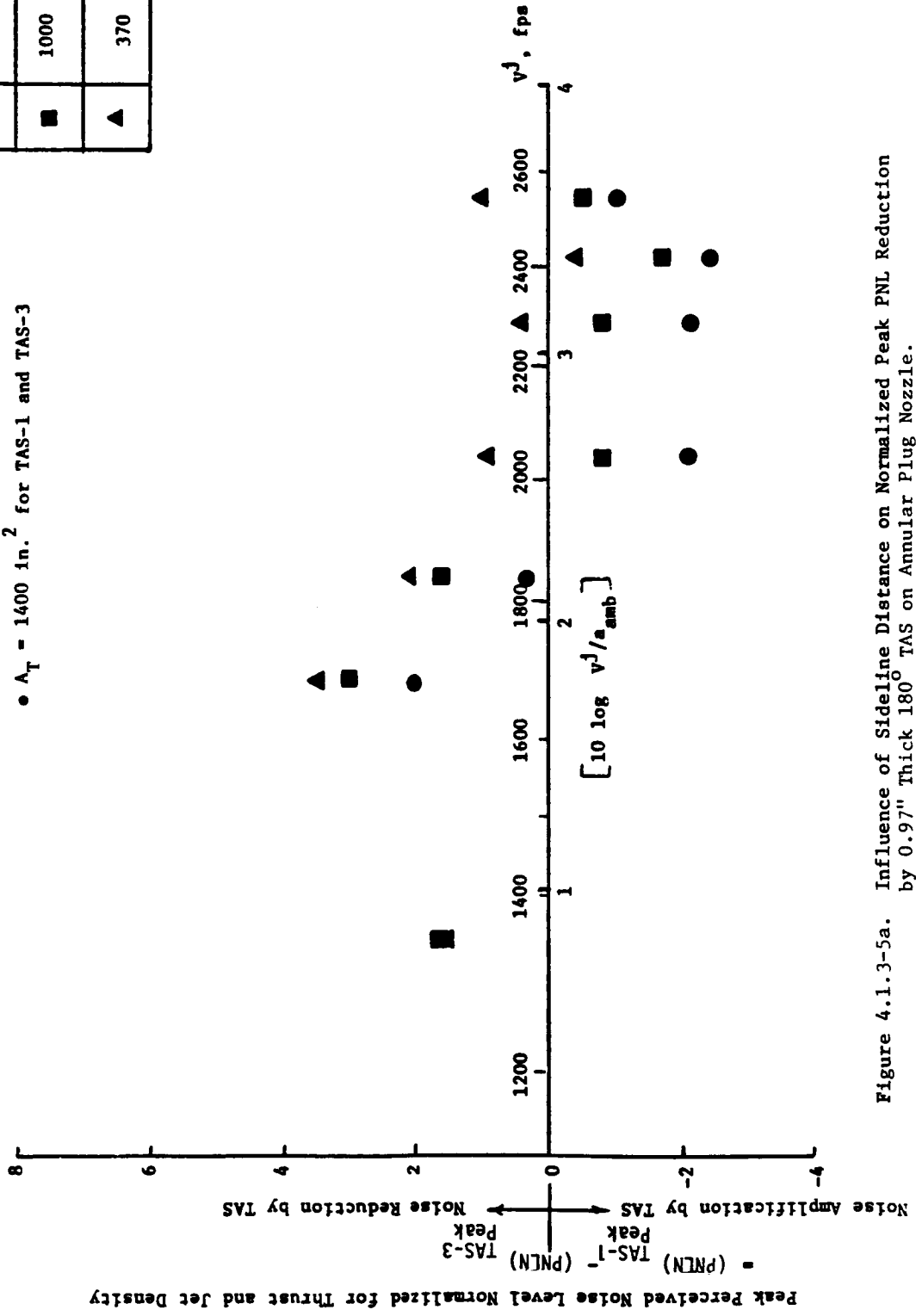


Figure 4.1.3-5a. Influence of Sideline Distance on Normalized Peak PNL Reduction by 0.97" Thick 180° TAS on Annular Plug Nozzle.

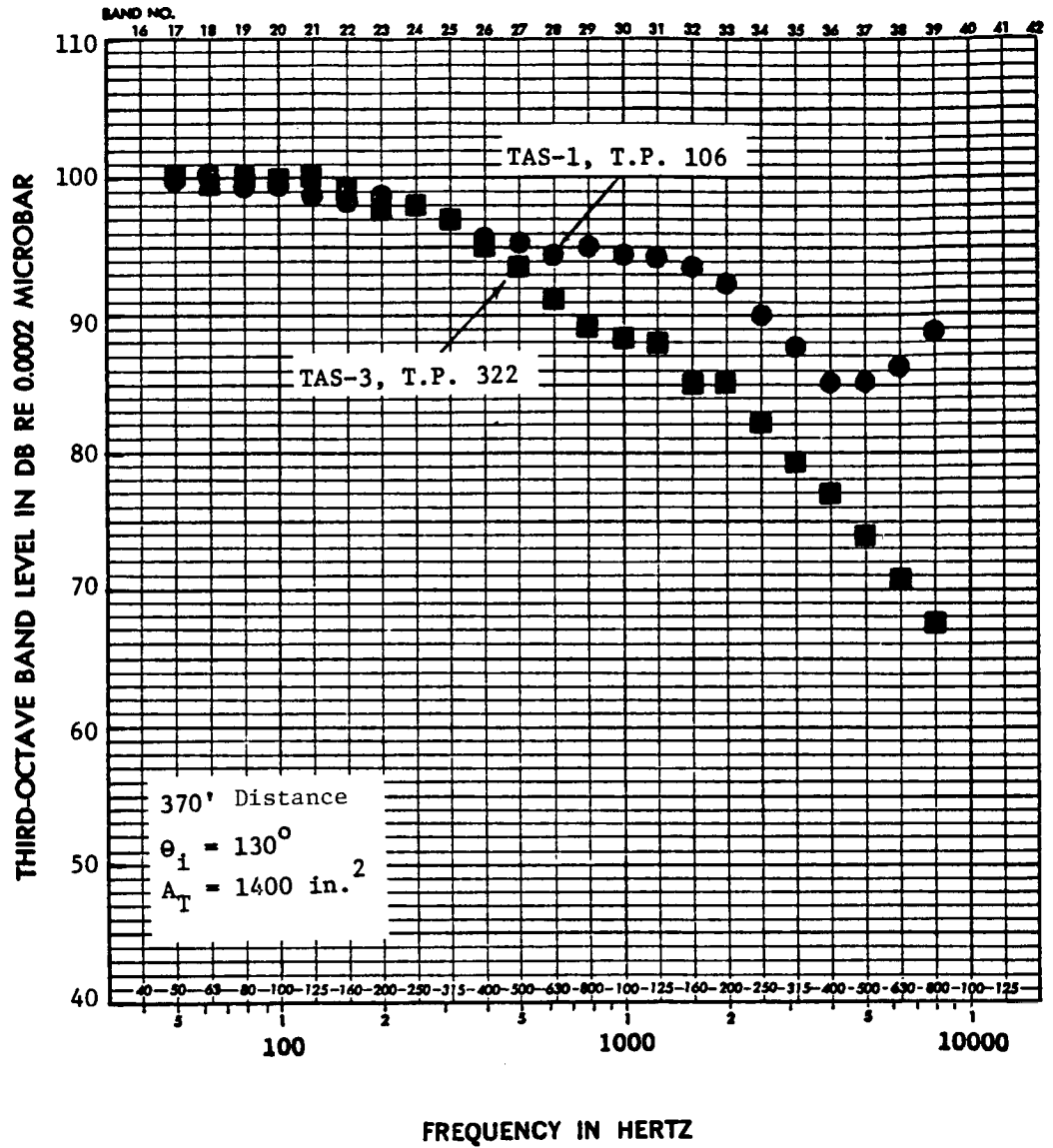


Figure 4.1.3-5b.

Spectral Comparison of Configuration TAS-1 and TAS-3 at 370' Flyover Distance (Flight).



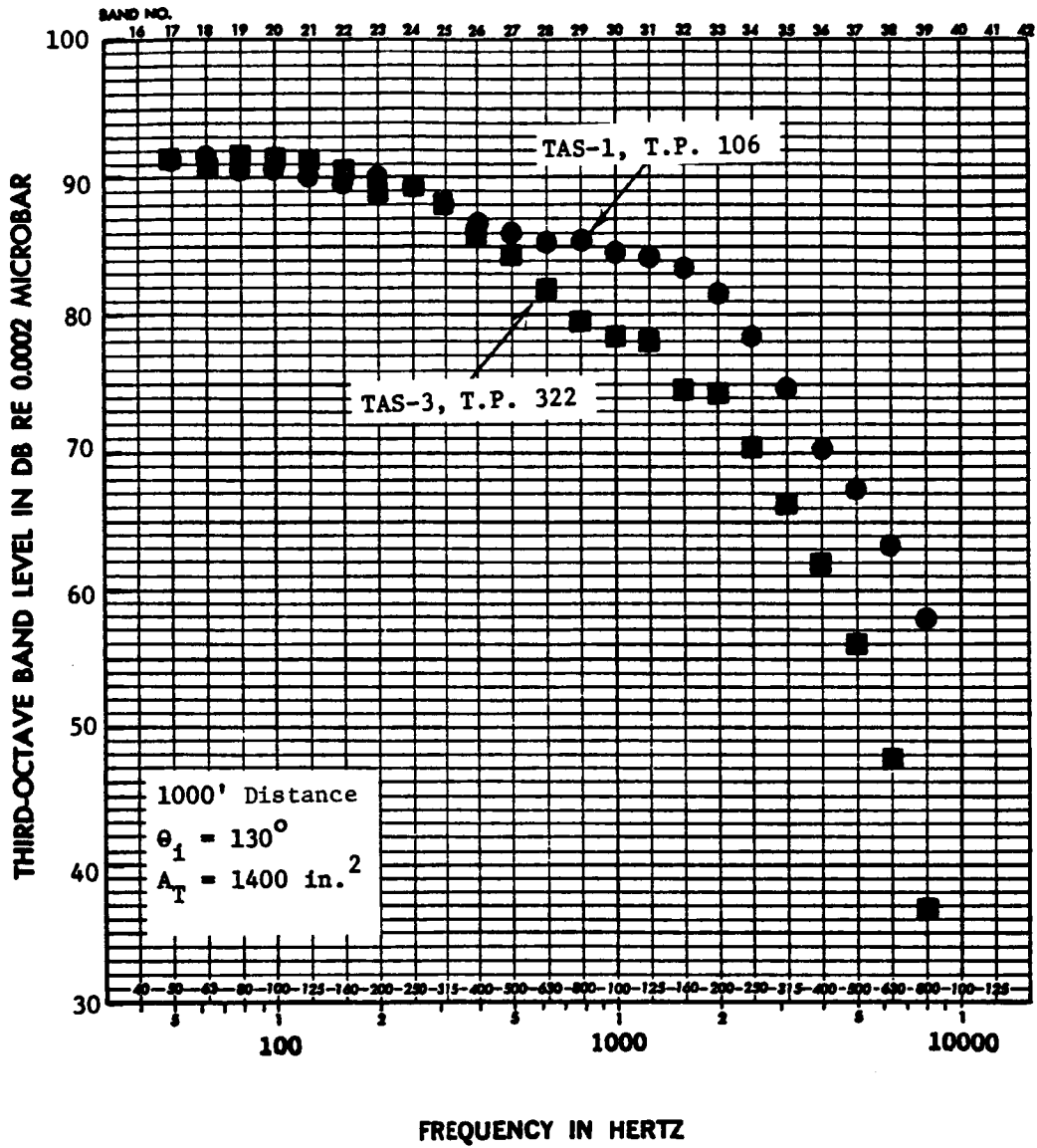


Figure 4.1.3-5c. Spectral Comparison of Configuration TAS-1 and TAS-3 at 1000' Flyover Distance (Flight).

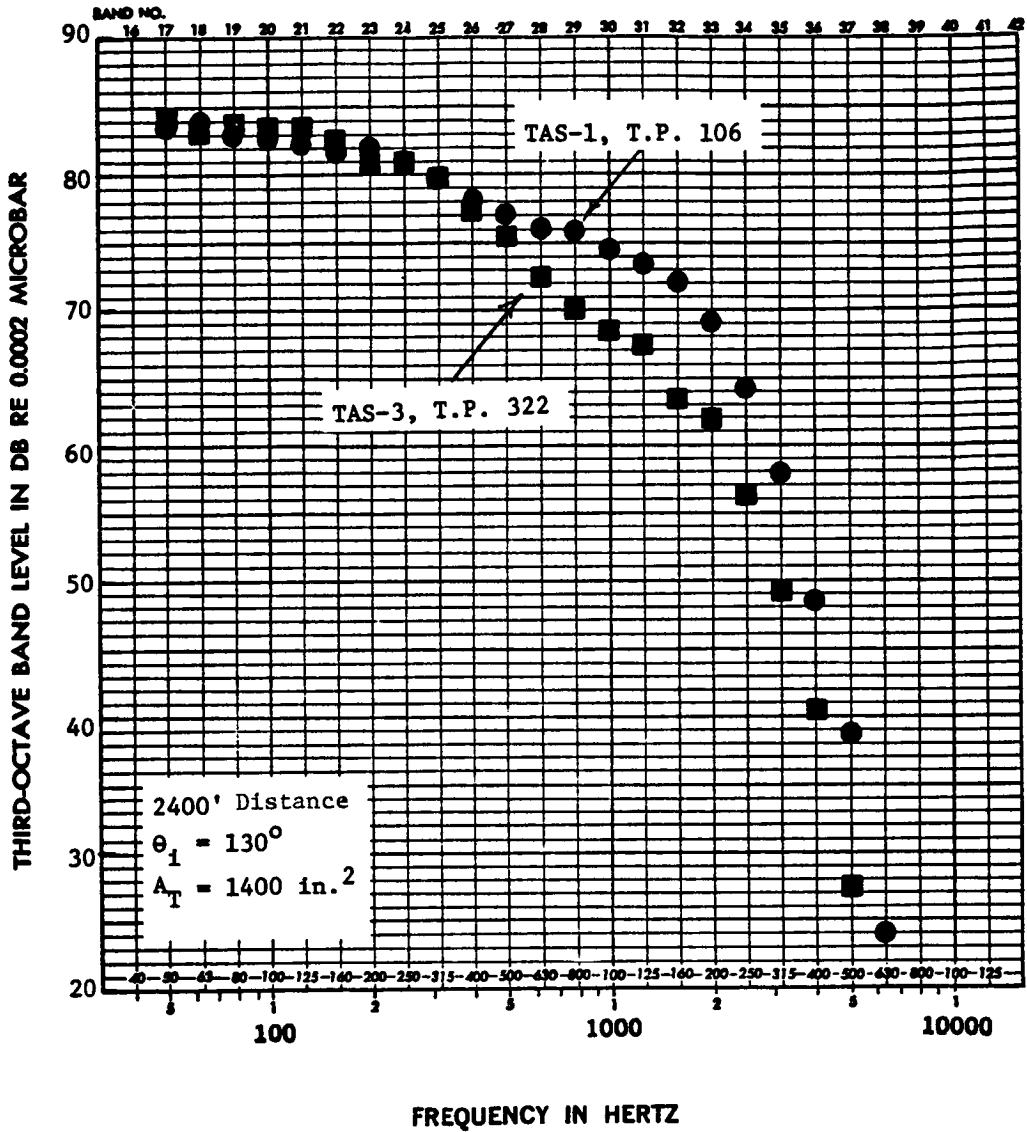


Figure 4.1.3-5d. Spectral Comparison of Configuration TAS-1 and TAS-3 at 2400' Flyover Distance (Flight).

Figure 4.1.3-6 shows the influence of sideline distance on thrust and jet-density-normalized peak PNL and spectral reduction by the 180° T.A.S. of 0.97" thickness on the 32-chute suppressor nozzle. Figure 4.1.3-6a shows the dependence of normalized peak PNL reduction along an engine operating line on the sideline distance for the simulated flight condition. One notices a maximum normalized PNL reduction of 8 dB at a core jet velocity of approximately 1850 fps. The thermal acoustic shield on the 32-chute suppressor nozzle yields significantly higher PNL reductions over the entire engine operating line compared to the unsuppressed annular plug nozzle (see Figures 4.1.3-5a and 4.1.3-6a). This can be attributed to the relatively larger high frequency noise content of a mechanical suppressor nozzle compared to an unsuppressed nozzle, accompanied by the effective suppression of the high frequency noise by the thermal acoustic shield.

Figures 4.1.3-6b, 4.1.3-6c and 4.1.3-6d respectively show the spectral content at the peak noise angle ( $\theta_i = 120^\circ$ ) for the cutback case which has a core jet velocity of approximately 1850 fps at 370 ft., 1000 ft. and 2400 ft. sideline distances. Note that even at a sideline distance of 2400 ft. (see Figure 4.1.3-6d), the 32 chute-suppressor nozzle (Configuration TAS-6) has a pronounced high frequency content. Due to its ability to reflect and refract the high frequency noise, the thermal acoustic shield is seen to yield large PNL reductions on a nozzle which generates more high frequency noise. Also note that, at the cutback case under study for the 32 chute suppressor, the sideline distance does not have as much influence on PNL reductions as it had for the unsuppressed plug nozzle (see Figure 4.1.3-6a). Unlike the unsuppressed plug nozzle (Configuration TAS-1), the 32-chute suppressor (TAS-6) has a significant amount of high frequency noise content even at 2400 ft. sideline distance. Thus, the high frequency noise reduction by the thermal acoustic shield has a similar impact on PNL reductions at 370 ft., 1000 ft. and 2400 ft. sideline distance.

#### 4.1.3.3 Asymmetric Acoustic Characteristics of the Unsuppressed Annular Plug and 32 Chute Suppressor Nozzles with the Partial Thermal Acoustic Shield of 0.97" Thickness

Figure 4.1.3-7 shows the azimuthal variation in the PNL directivity of configurations TAS-3 (annular plug) and TAS-8 (32 chute suppressor) at the cutback condition. Both the configurations show noticeable azimuthal

SYMB.	Distance, ft
●	2400
■	1000
▲	370

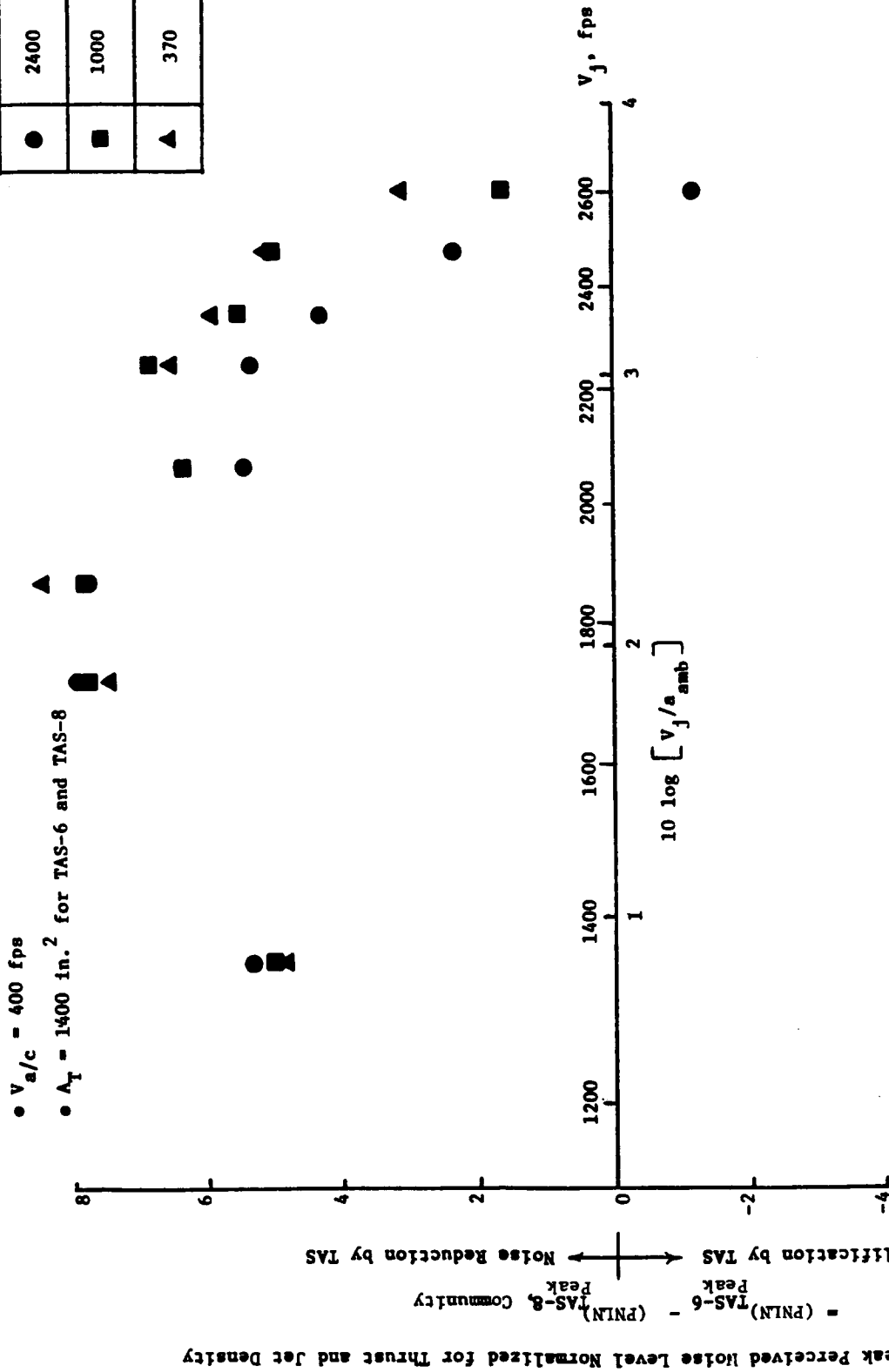


Figure 4.1.3-6a. Influence of Sideline Distance on Normalized Peak PNL Reduction by 0.97" Thick 180° TAS on 32 Chute Suppressor Nozzle (Flight).

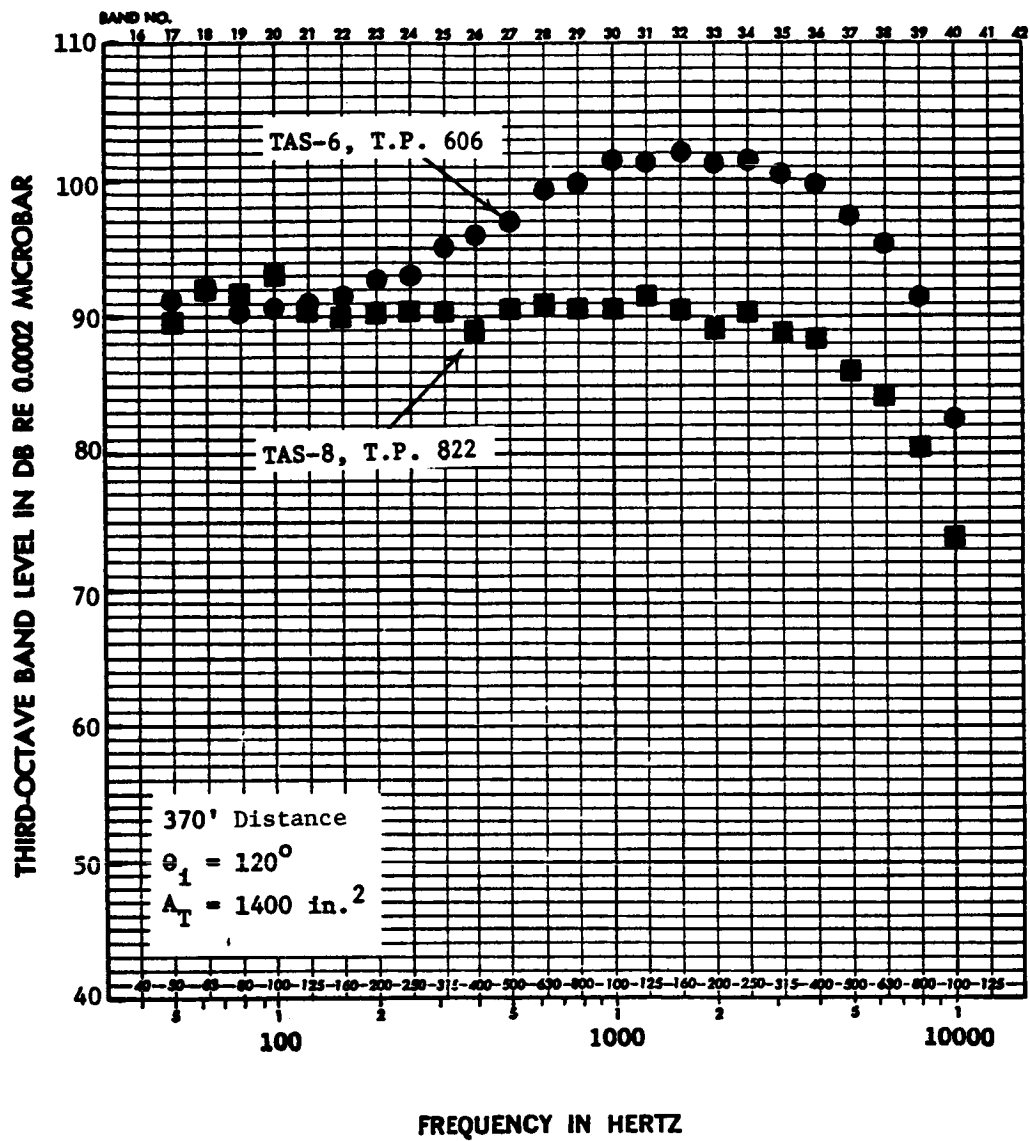


Figure 4.1.3-6b. Spectral Comparison of Configuration TAS-6 and TAS-8 at 370' Flyover Distance (Flight).

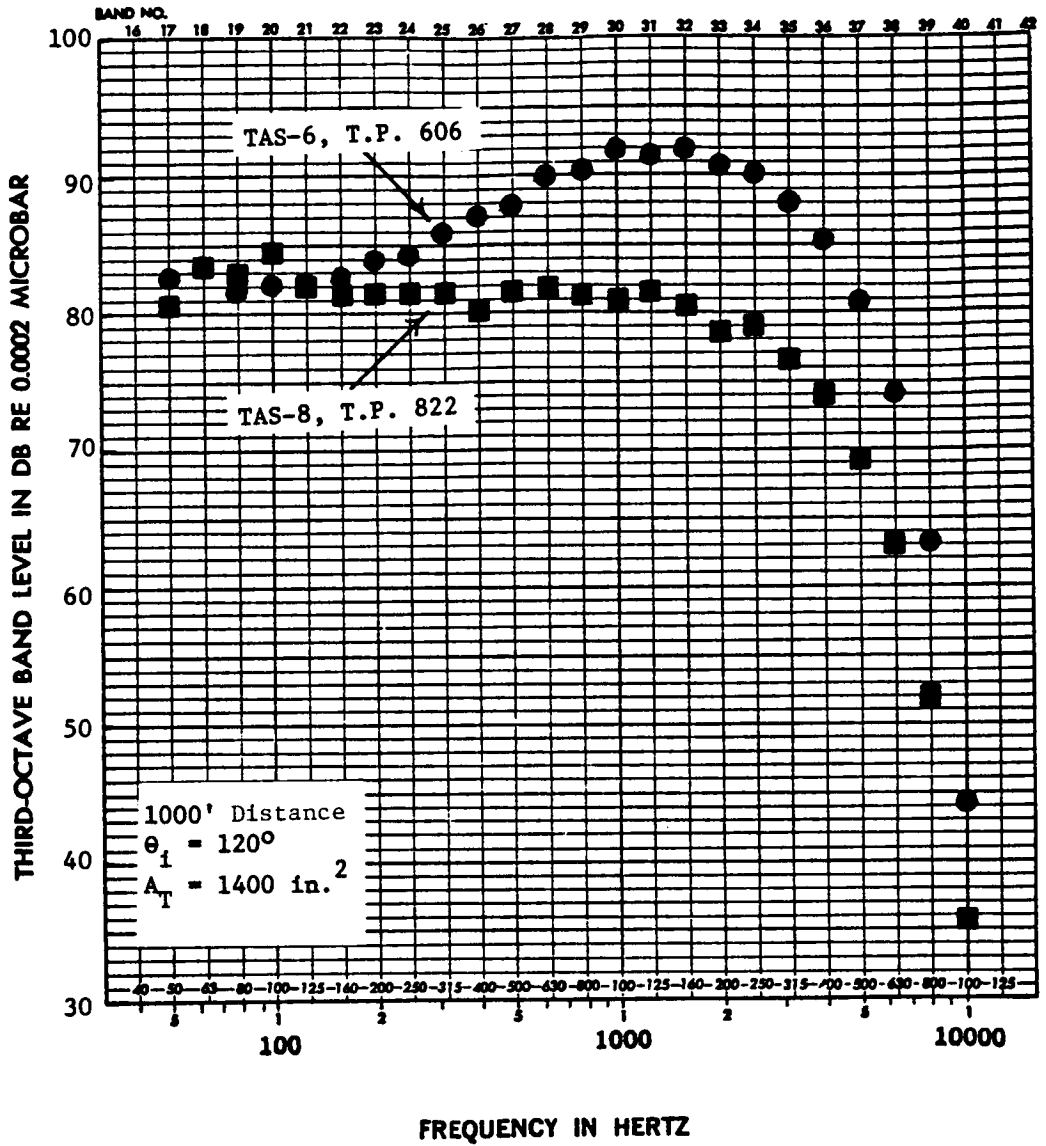


Figure 4.1.3-6c. Spectral Comparison of Configuration TAS-6 and TAS-8 at 1000' Flyover Distance (Flight).

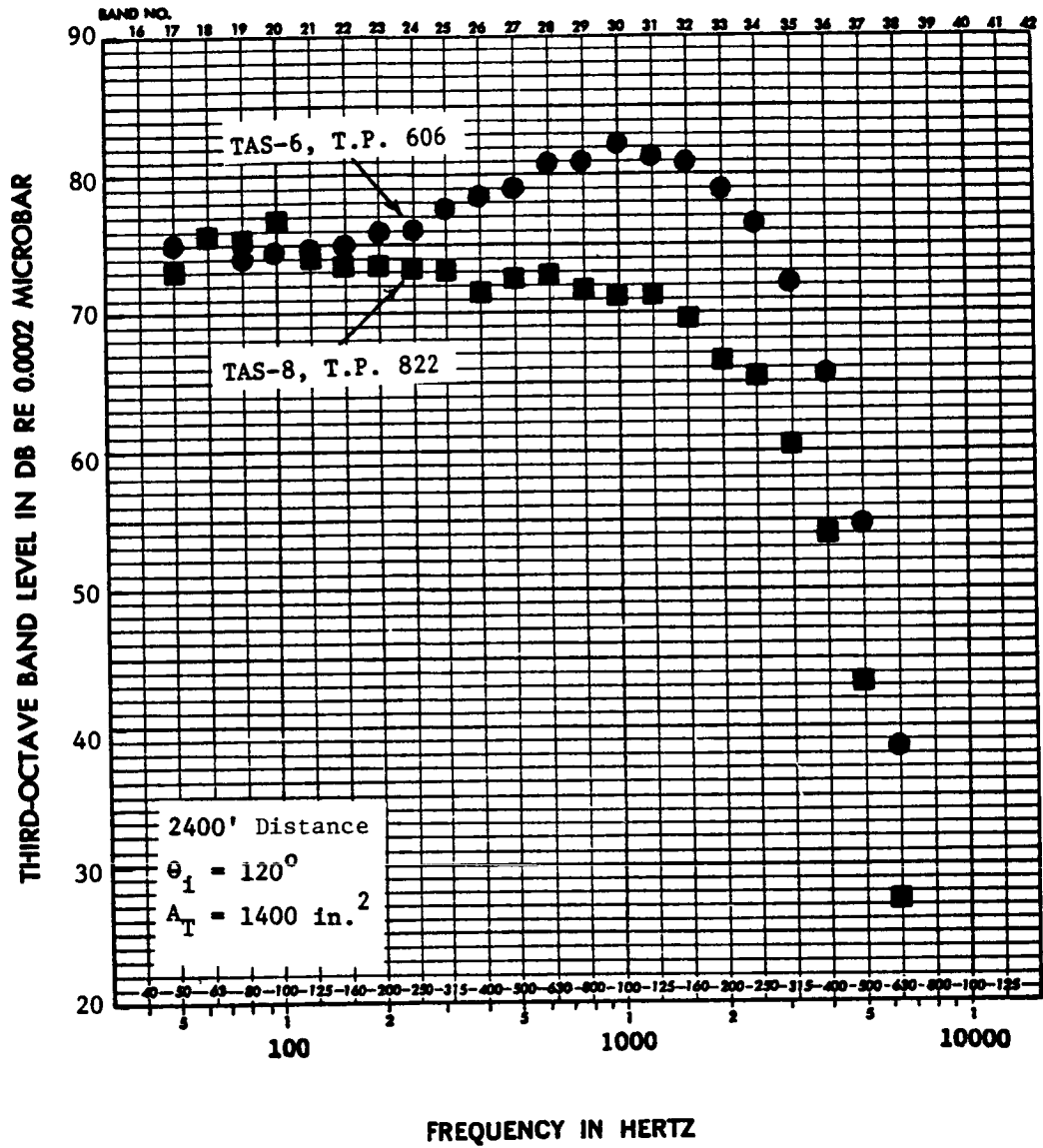


Figure 4.1.3-6d. Spectral Comparison of Configuration TAS-6 and TAS-8 at 2400' Flyover Distance (Flight).

Configuration TAS-3

Sym	Point	Orientation
□	305	Sideline, $\theta = 70^\circ$
○	321	Community, $\theta = 0^\circ$

$A^T = 1400 \text{ In.}^2$   
 1000' Distance  
 Static  
 Outback Cycle

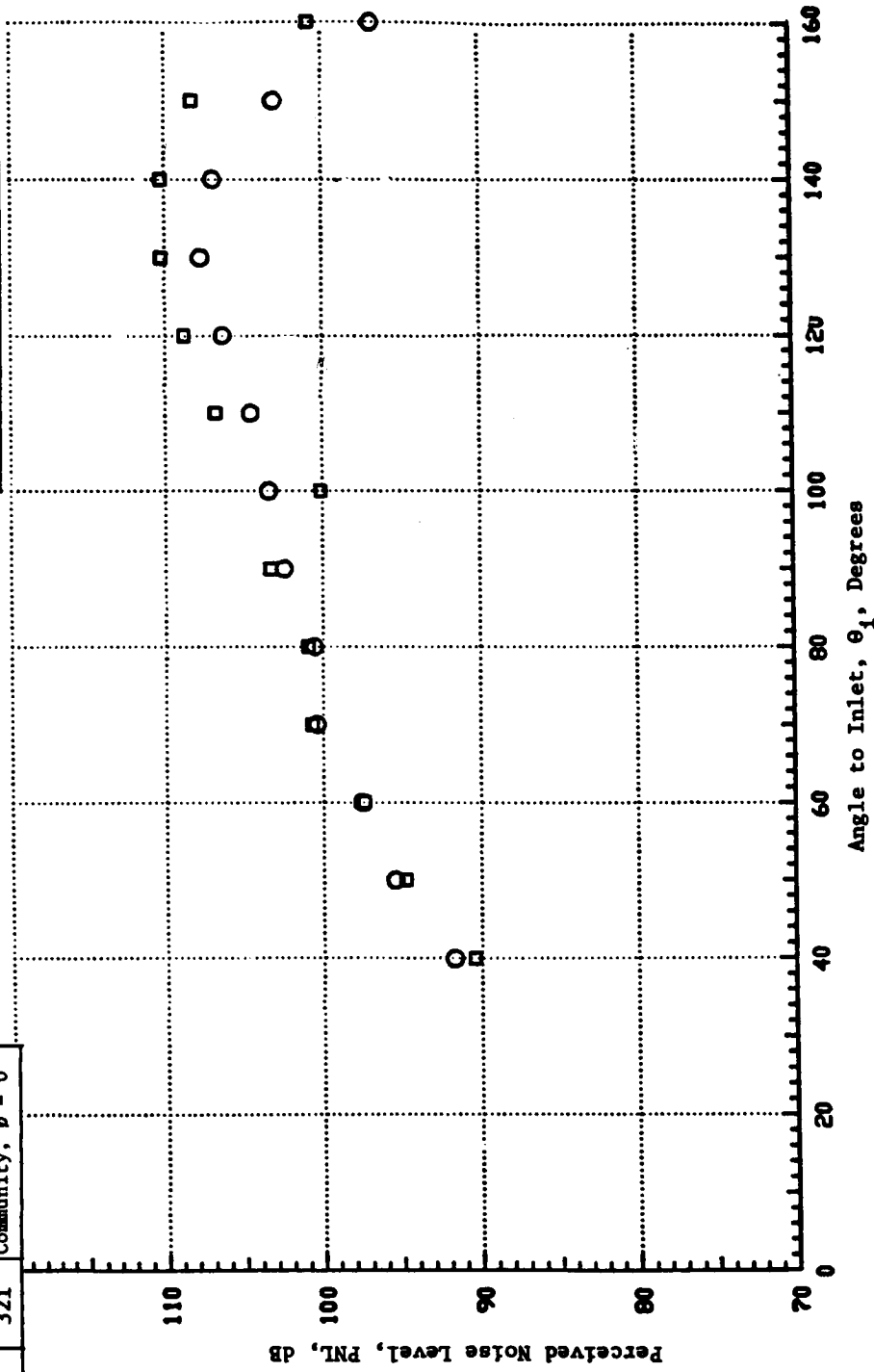


Figure 4.1.3-7a. Azimuthally Asymmetric Acoustic Influence of  $180^\circ$  Shield of 0.97" Thickness on the PNL Directivity of Unsuppressed Annular Plug Nozzle at a Cutback Cycle (Static).



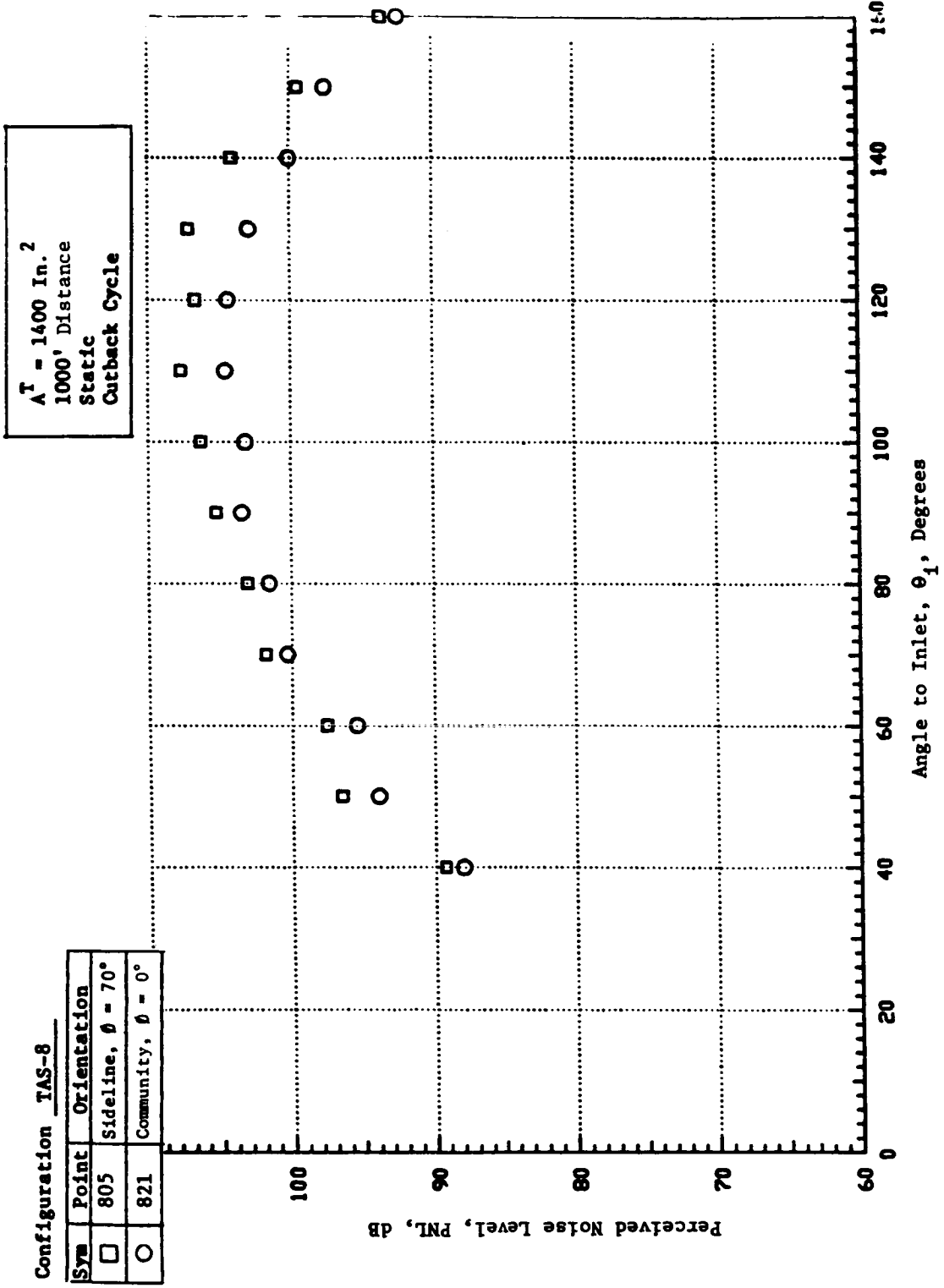


Figure 4.1.3-7b. Azimuthally Asymmetric Acoustic Influence of 180° Shield of 0.97" Thickness on the PNL Directivity of 32 Chute Suppressor Nozzle at a Outback Cycle (Static).

asymmetry in the aft quadrant. Configuration TAS-8 shows some azimuthal variation in the front quadrant whereas TAS-3 shows negligible azimuthal variation in the front quadrant. Figures 4.1.3-8, 4.1.3-9 and 4.1.3-10 respectively, compare the azimuthal variation in the spectral content at  $\theta_i = 60^\circ$ ,  $90^\circ$  and  $140^\circ$  of configurations TAS-3 and TAS-8. The spectral data at  $\theta_i = 60^\circ$  and  $90^\circ$  shows that the presence of the partial shield creates more azimuthal asymmetry for the 32 chute suppressor nozzle compared to the unsuppressed annular plug nozzle, which is another indication that the partial shield seems to modify the source characteristics to a greater extent for the 32 chute suppressor nozzle than the unsuppressed annular plug nozzle. The spectral data at  $\theta_i = 140^\circ$  indicates that the spectral asymmetry (i.e., SPL differences at each 1/3 octave band) due to the partial shield in the case of the unsuppressed annular plug nozzle are higher than the corresponding spectral asymmetry in the case of the 32 chute suppressor nozzle, which again implies lesser mixing of the jets in the case of the unsuppressed annular plug nozzle compared to the 32 chute suppressor nozzle. However, due to the reduced contribution of the high frequency noise to the total noise for the unsuppressed annular plug nozzle, the noted higher asymmetric spectral distribution of the unsuppressed annular plug nozzle with the partial shield in the aft quadrant does not result in higher asymmetric PNL directivity compared to the 32 chute suppressor nozzle with the same partial shield (see Figures 4.1.3-7a and 4.1.3-7b).

#### 4.2 LASER VELOCIMETER TEST RESULTS

The discussion of the laser velocimeter (LV) test results is grouped under the following headings:

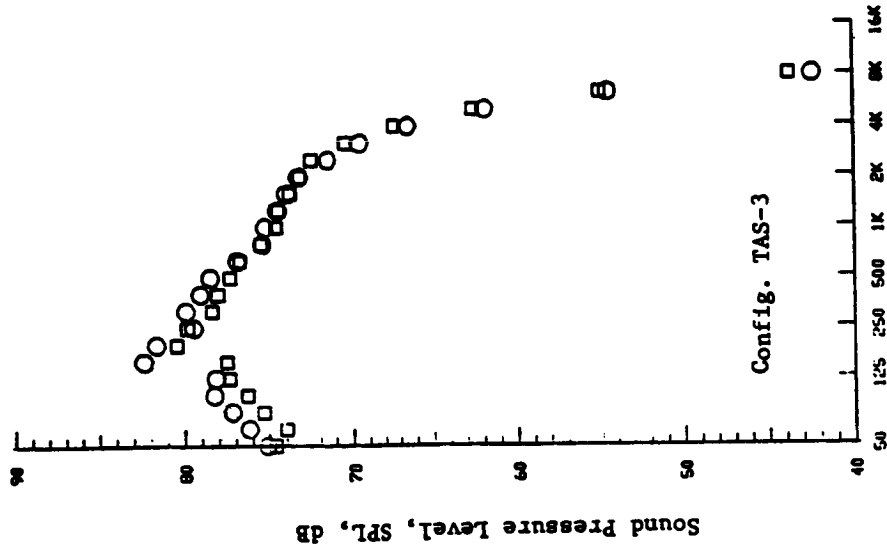
- A. Plume characteristics of unsuppressed annular plug nozzle with thermal acoustic shield under static and simulated flight conditions; and
- B. Plume characteristics of 32 chute suppressor nozzle with thermal acoustic shield under static and simulated flight conditions.

The deployment of the laser velocimeter in measuring the mean and turbulent velocity descriptions of the nozzles with the full and partial

$A^T = 1400 \text{ In.}^2$   
 1000' Distance  
 Cutback Cycle  
 Static  
 $\theta_1 = 60^\circ$

Configuration TAS-3

Sym	Point	Orientation
□	305	Sideline, $\beta = 70^\circ$
○	321	Community, $\beta = 0^\circ$



Configuration TAS-8

Sym	Point	Orientation
□	805	Sideline, $\beta = 70^\circ$
○	821	Community, $\beta = 0^\circ$

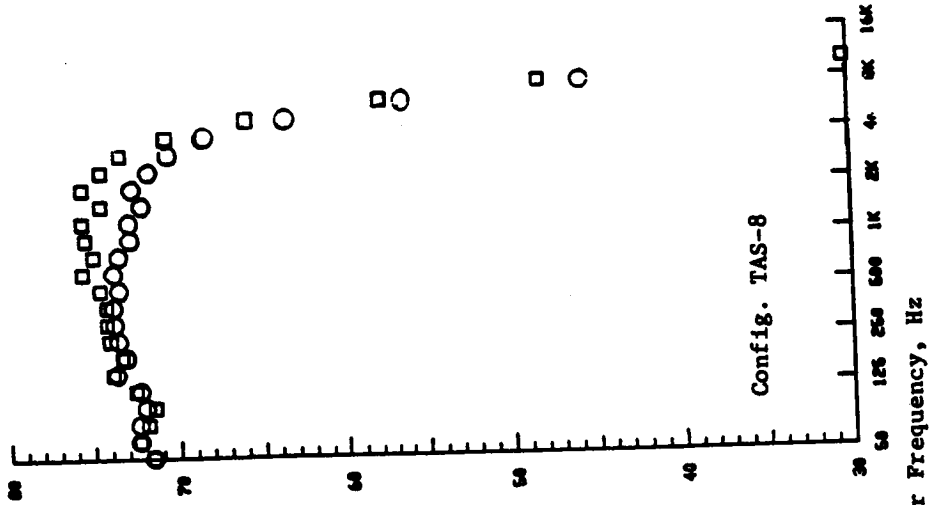
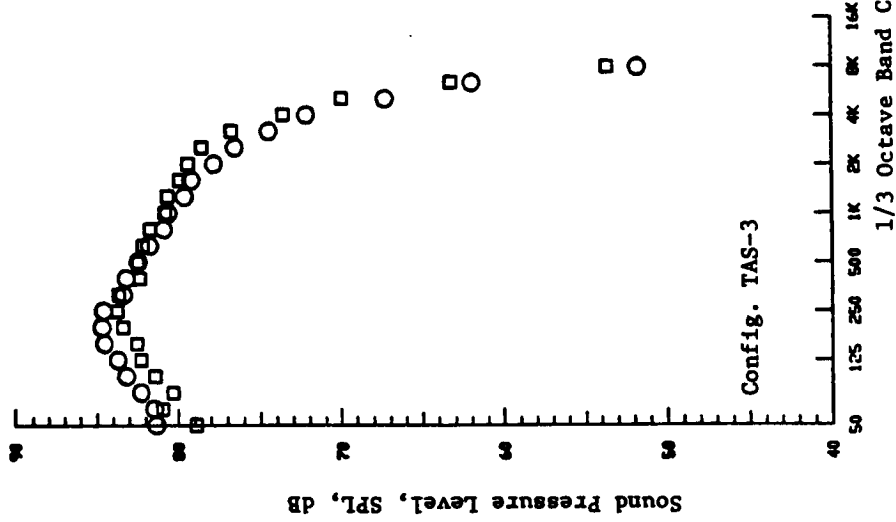


Figure 4.1.3-8. Comparison of the Asymmetric Acoustic Influence of 180° Shield of 0.97" Thickness on the Spectral Content of Unsuppressed Annular Plug and the 32 Chute Chute Suppressor Nozzle at  $\theta_1 = 60^\circ$  for a Cutback Cycle (Static).

$T = 1400$  In. <sup>2</sup>  
 1000' Distance  
 Cutback Cycle  
 Static  
 $\theta_1 = 90^\circ$

Configuration TAS-3

Sym	Point	Orientation
□	305	Sideline, $\theta = 70^\circ$
○	321	Community, $\theta = 0^\circ$



Configuration TAS-8

Sym	Point	Orientation
□	805	Sideline, $\theta = 70^\circ$
○	821	Community, $\theta = 0^\circ$

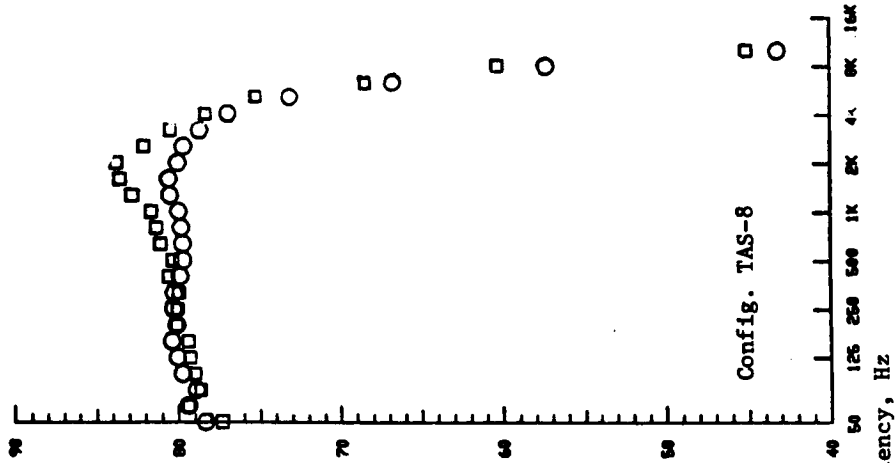
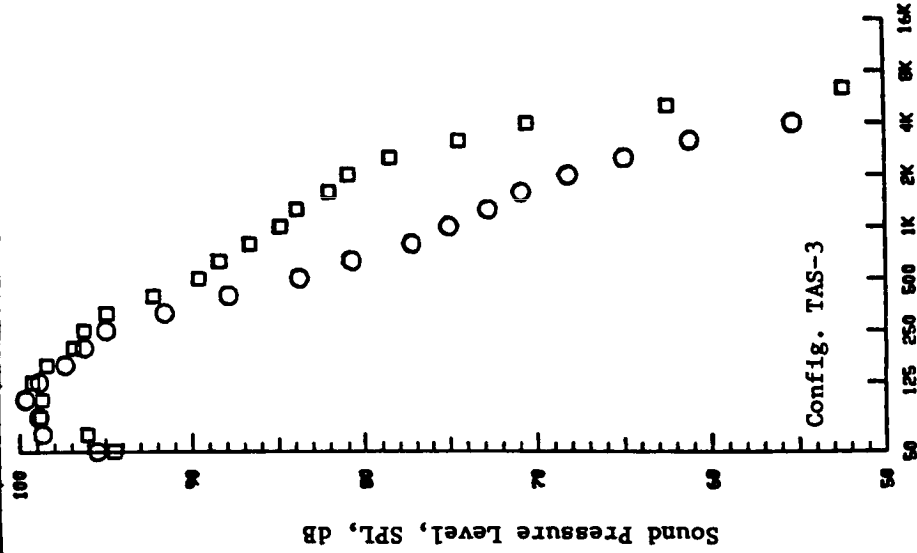


Figure 4.1.3-9. Comparison of the Asymmetric Acoustic Influence of  $180^\circ$  Shield of 0.97" Thickness on the Spectral Content of Unsuppressed Annular Plug and the 32 Chute Suppressor Nozzle at  $\theta_1 = 90^\circ$  for a Cutback Cycle (Static).

$A^T = 1400 \text{ In.}^2$   
 1000' Distance  
 Outback Cycle  
 Static  
 $\theta_1 = 140^\circ$

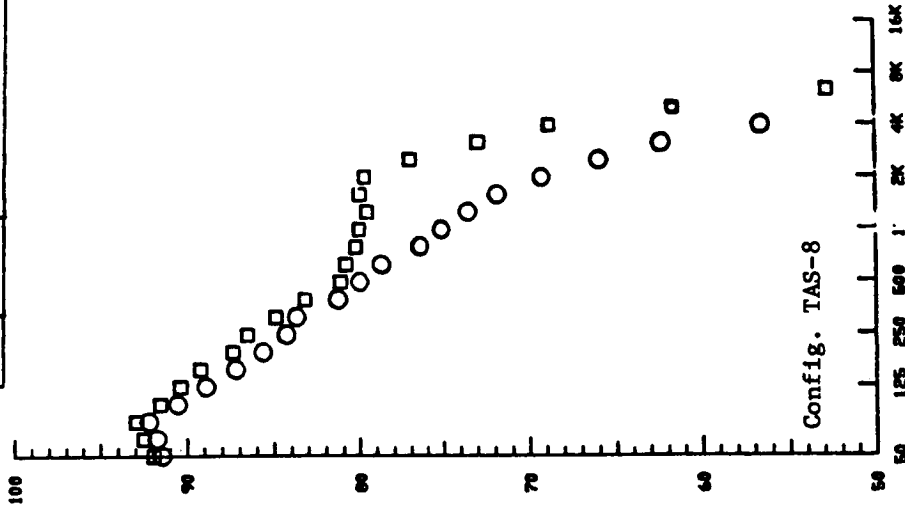
Configuration TAS-3

Sym	Point	Orientation
□	305	Sideline, $\theta = 70^\circ$
○	321	Community, $\theta = 0^\circ$



Configuration TAS-8

Sym	Point	Orientation
□	805	Sideline, $\theta = 70^\circ$
○	821	Community, $\theta = 0^\circ$



1/3 Octave Band Center Frequency, Hz

Figure 4.1.3-10. Comparison of the Asymmetric Acoustic Influence of 180° Shield of 0.97" Thickness on the Spectral Content of Unsuppressed Annular Plug and the 32 Chute Suppressor Nozzle at  $\theta_1 = 140^\circ$  for a Cutback Cycle (Static).

thermal acoustic shields has yielded valuable information on the relative mixing characteristics of these nozzles. Certain salient results of these measurements are discussed in this subsection.

Two (2) new features have been incorporated in the LV measurements to enhance its diagnostic capability and they are:

- A. A fine traverse along a line parallel to the plug surface to detect and characterize plug shock cell structure and mean velocity decay along the flow path (see Figure 4.2.1).
  
- B. A point-by-point calculation and automatic plotting of the mean velocity along a traverse (axial or radial or slant), to be hence-forth called "Mini-Histograms". The particle sampling with mini-histograms is just enough to give a good estimate (accuracy:  $\pm 5\%$ ) of the mean velocity. The advantage of mini-histograms relative to the usual pen traverse is that the data shows less scatter. However, a traverse with mini-histograms takes about 4-5 times the amount of time required for a pen traverse. Figure 4.2.2 shows the comparison of the laser velocimeter velocity measurements by the pen traverse and mini-histograms for configuration TAS-4. A one-to-one correspondence of both the methods is noted.

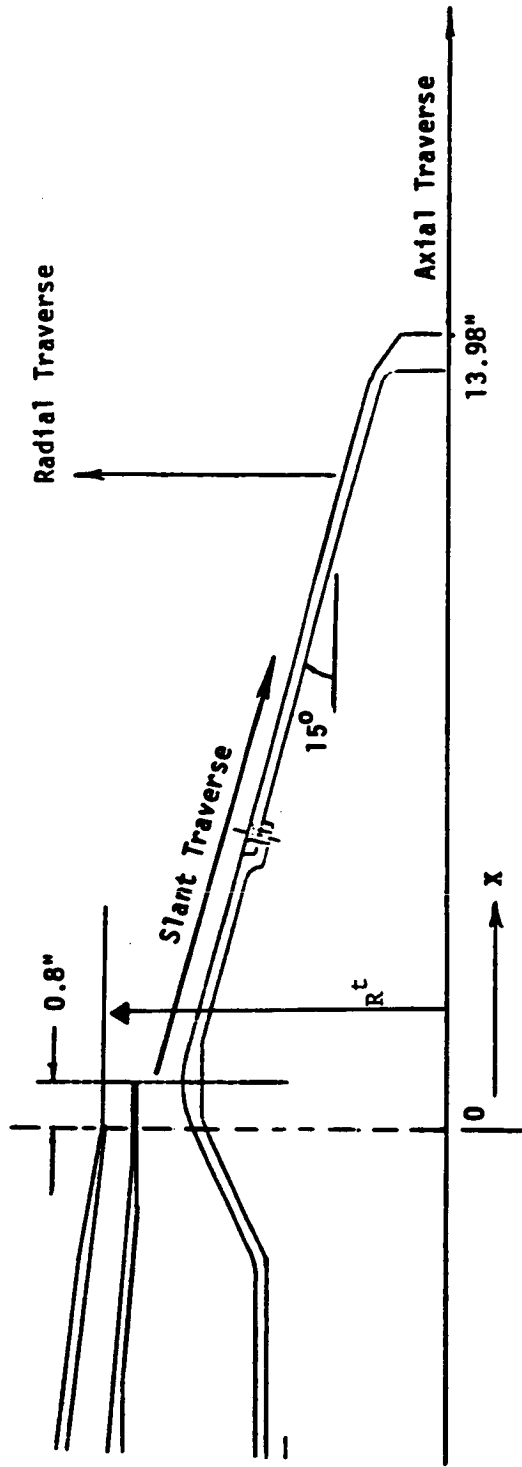


Figure 4.2.1. Sketch of Configuration TAS-4 (Annular Plug Nozzle With 360° Thermal Acoustic Shield) Nozzle Along With Typical LV Traverses.

- LV Plume #6
- Test Point 410
- Flight,  $V_{a/c} = 400$  fps
- $R^t = 5.99$  inches
- $D_{eq} = 5.67$  inches (Based on Core Jet Area of  $25.28 \text{ in}^2$  only)

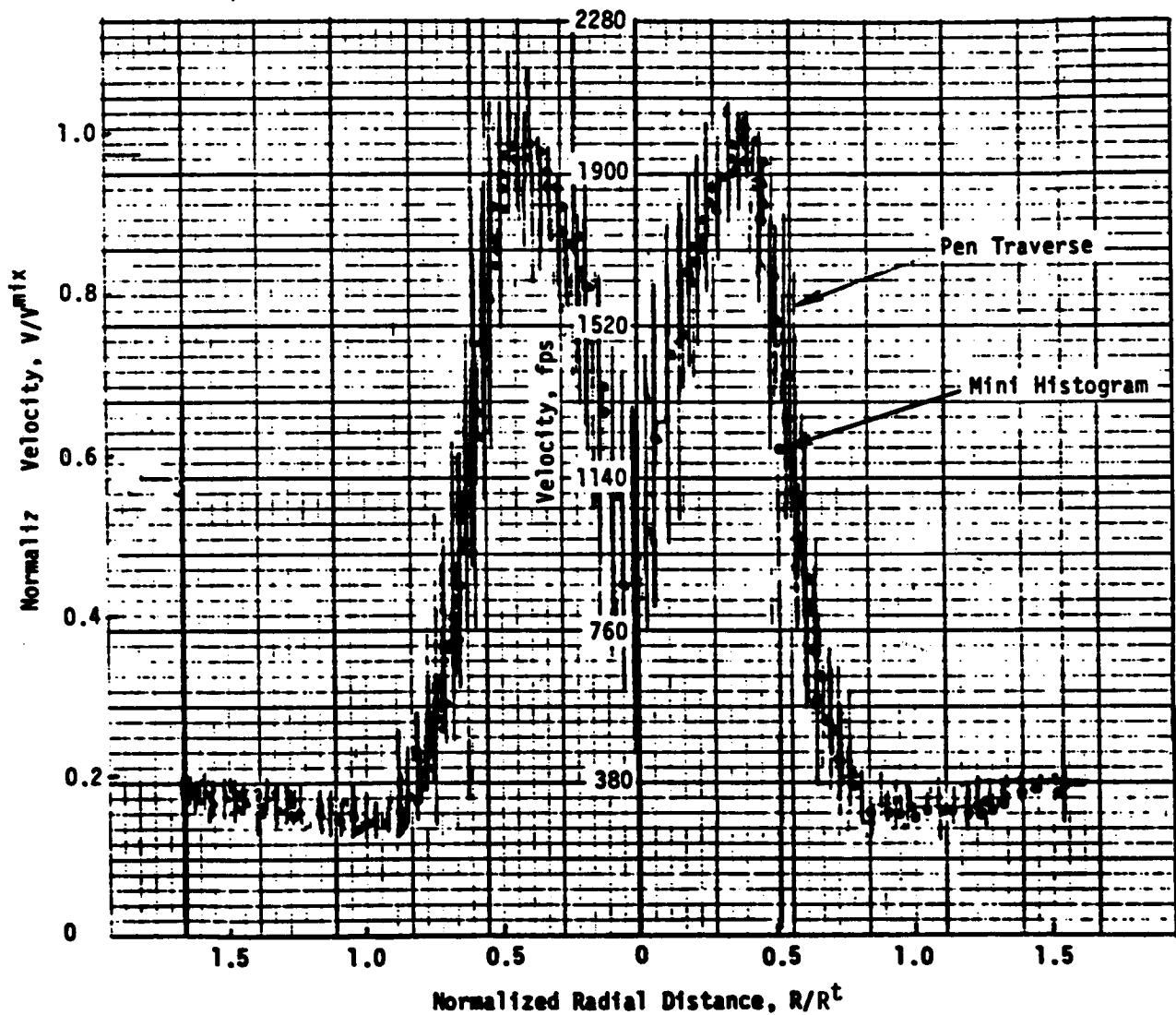


Figure 4.2.2. Radial Velocity Profile of TAS-4 (Annular Plug Nozzle with  $360^\circ$  Shield) @  $X/D_{eq} = 3$  As Measured by Pen Traverse and Mini-Histograms Showing the One-to-One Correspondence of Both Methods.



#### 4.2.1 PLUME CHARACTERISTICS OF UNSUPPRESSED ANNULAR PLUG NOZZLE WITH THERMAL ACOUSTIC SHIELD UNDER STATIC AND SIMULATED FLIGHT CONDITIONS

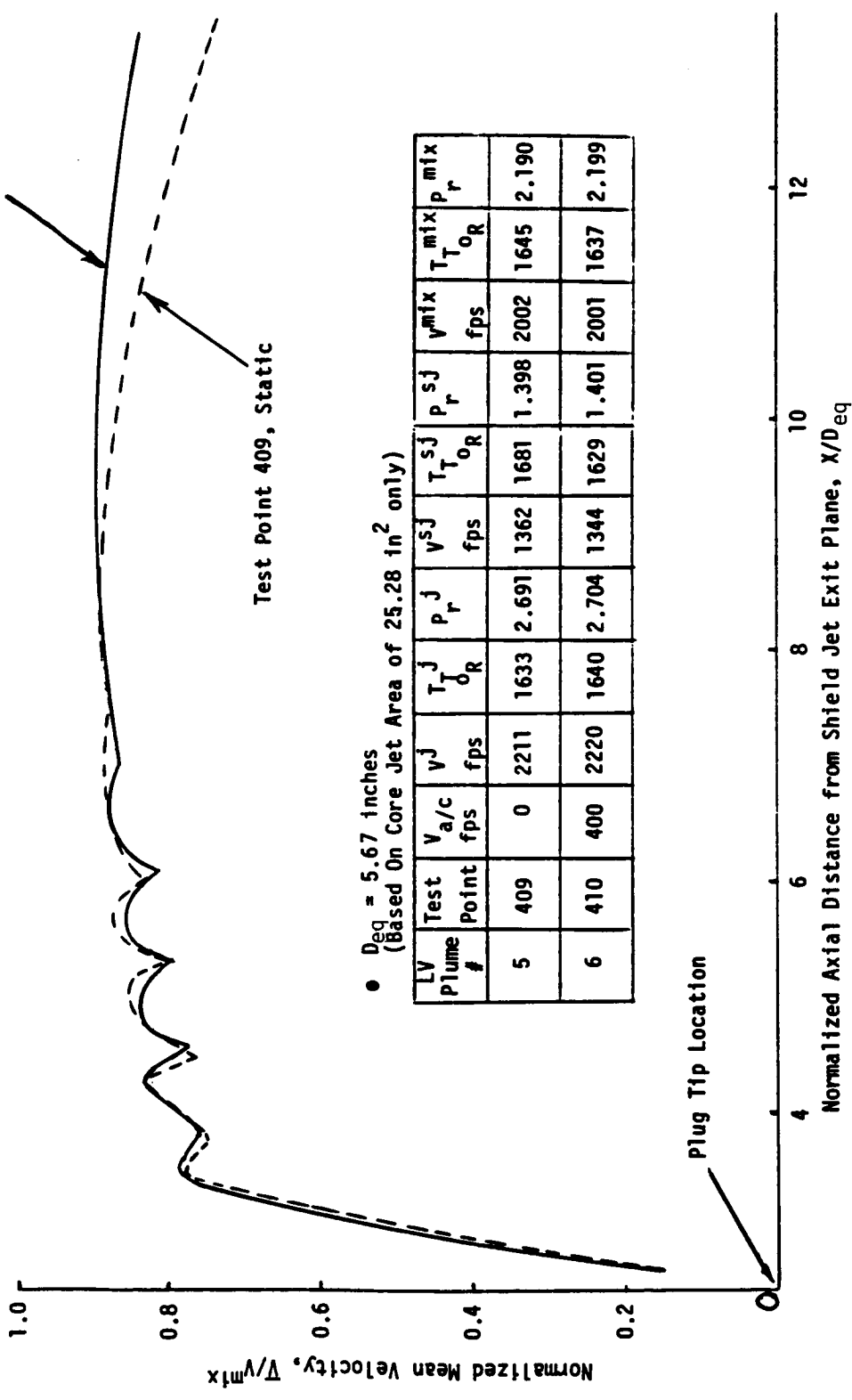
Figure 4.2.3 compares the mean and turbulent velocity variations along the center line of configuration TAS-4 for static and simulated flight conditions at takeoff. Due to the flow separation upstream of the plug tip, the mean velocity reduces just downstream of the plug tip. The mean velocity variation exhibits four (4) shock cells for both static and simulated flight cases without any significant changes in the shock structure, thus indicating that these shock cells are imbedded in the potential core of the jet and thus are not noticeably affected by the simulated flight velocity. The mean velocity decay for the static case is seen to be faster than the flight case for  $X/D_{eq} > 8$ , which can be attributed to the reduction in shear by the ambient air when there is a simulated flight velocity. Note that the simulated flight velocity has no significant effect on turbulence along the center line for  $X/D_{eq} < 6$  (the potential core region). For  $X/D_{eq} > 6$ , the turbulent velocities for the static case are higher than the simulated flight case reaffirming the reduction of shear stress by the simulated flight velocity. Recall that turbulent shear stress is proportional to the square of turbulent velocity.

Next, Figure 4.2.4 shows the mean velocity variation along a line parallel to the plug surface beginning at the middle of the shielding jet (see Figure 4.2.1 also). One distinctly notes the existence of the thermal acoustic shield at a velocity ratio of  $\approx 0.6$ . As the slant traverse progresses, the core jet appears and exhibits two (2) shocks. Note the steep rise in velocity indicating no appreciable mixing of the TAS and core jets at these locations. However, to diagnose the existence of the TAS, an axial traverse beginning at the middle of the shield jet has to be studied. Figure 4.2.5 shows the axial velocity variation beginning at the middle of the TAS. One observes that the TAS jet maintains its identity for about  $1.4 D_{eq}$  from its exit plane. The non-zero mean velocity measured downstream corresponds to the freejet velocity.

Figure 4.2.2 shows the radial mean velocity profile on configuration TAS-4 at a normalized axial location ( $X/D_{eq}$ ) of  $\approx 3$ , which is slightly

Test Point 410, Flight ( $V_{a/c} = 400$  fps)

Test Point 409, Static



•  $D_{eq} = 5.67$  inches  
(Based On Core Jet Area of 25.28 in<sup>2</sup> only)

LV Plume #	Test Point	$V_{a/c}$ fps	$v_j$ fps	$T_{OR}^j$	$P_r^j$	$v_{sj}$ fps	$T_{OR}^{sj}$	$P_r^{sj}$	$v_{mix}$ fps	$T_{OR}^{mix}$	$P_r^{mix}$
5	409	0	2211	1633	2.691	1362	1681	1.398	2002	1645	2.190
6	410	400	2220	1640	2.704	1344	1629	1.401	2001	1637	2.199

FIGURE 4.2.3a. Influence of Flight On Nozzle Center Line Mean Velocity Distribution of TAS-4 (Annular Plug Nozzle With 360° Thermal Acoustic Shield) At a Typical Takeoff Condition.

o  $D_{eq} = 5.67$  inches (Based on Core  
Jet Area of 25.28 in<sup>2</sup> only)

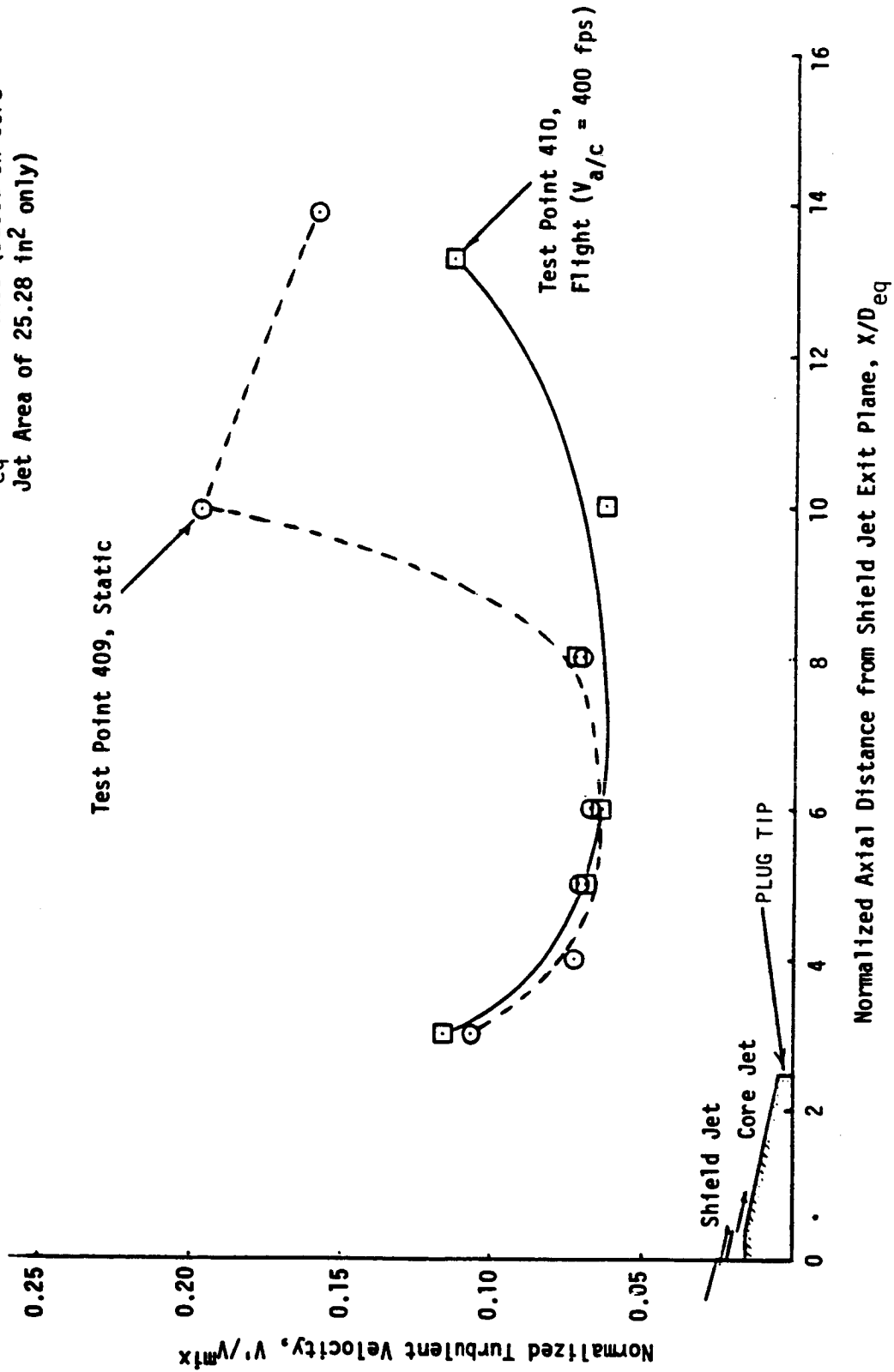


FIGURE 4.2.3b. Influence of Flight On Nozzle Centerline Turbulent Velocity Distribution of TAS-4 (Annular Plug Nozzle With 360° Thermal Acoustic Shield) At a Typical Takeoff Condition.

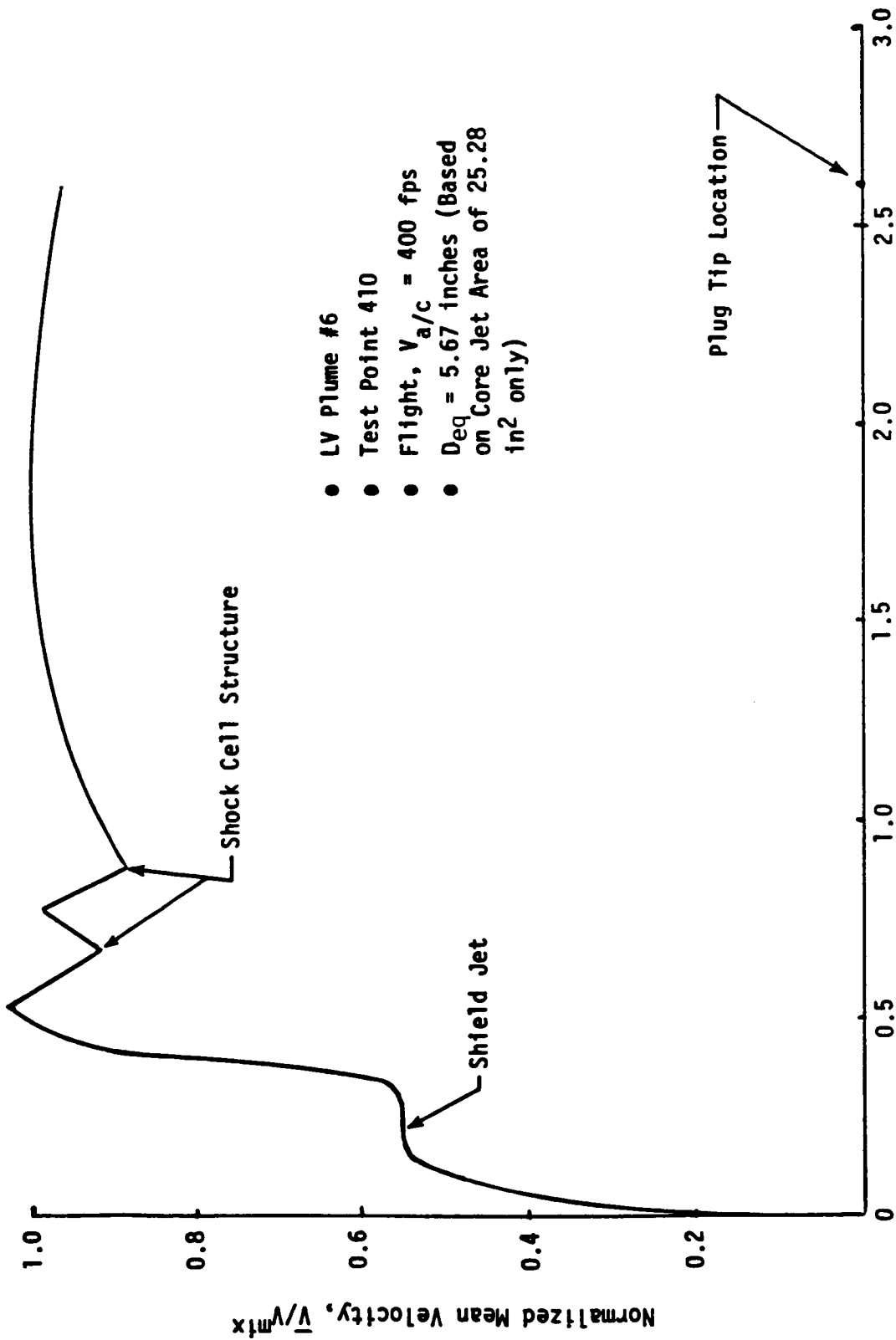
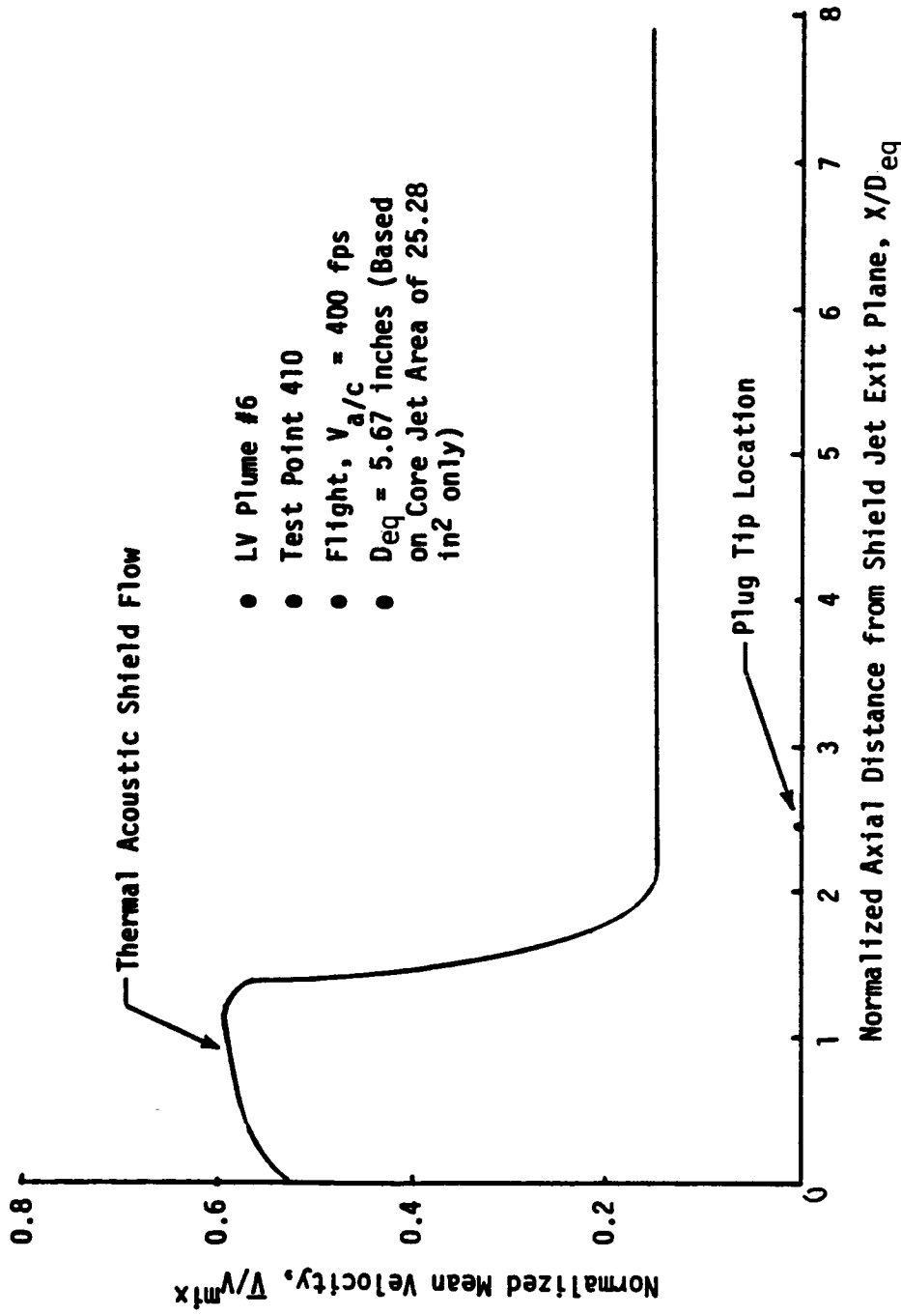


FIGURE 4.2.4. Mean Velocity Variation along Plug from Shield Jet Exit Plane,  $S/D_{eq}$  Jet Flow And Shock Cell Structure of The Core Jet.



- LV Plume #6
- Test Point 410
- Flight,  $V_{a/c} = 400$  fps
- $D_{eq} = 5.67$  inches (Based on Core Jet Area of 25.28 in<sup>2</sup> only)

FIGURE 4.2.5. Axial Mean Velocity Variation of The Thermal Acoustic Shield Indicating The Existence of The Shielding Jet For  $\approx 1.4 D_{eq}$  From The TAS Exit Plane.

downstream of the plug. Note the excellent symmetry of the velocity profile indicating an excellent geometric centering of the nozzle. The dip in the velocity near the jet axis is due to the flow separation zone existing downstream of the plug. The velocity for large values of radius reaches the simulated flight velocity of 400 fps.

Next, the plume characteristics of the unsuppressed annular plug nozzle in the presence of a partial shield of 0.48" thickness (i.e., configuration TAS-2) are discussed. The aerodynamic conditions of the measured plumes correspond to typical takeoff and cutback conditions.

Figure 4.2.6 shows the axial variation of mean and turbulent velocities along the nozzle centerline, on the shield and opposite to the shield sides for a typical cutback case in flight. One notes an asymmetric variation of the mean and turbulent velocities on the shield and the opposite shield side. The mean velocity decay rate and the turbulent velocity on the shield side are seen to be lower compared to the opposite shield side, which can be attributed to the reduction of shear stress by the shield. The core nozzle center line mean velocity increases just downstream of the plug tip and remains constant, indicating the existence of the potential core for about ten (10) equivalent diameters based on core jet area only. The turbulent velocity along the nozzle center line remains at about 7% reaffirming the existence of the potential core.

Figure 4.2.7 compares the axial mean velocity variation at radial locations corresponding to the middle of the core jet on the shield side and opposite to the shield side at a cutback case in simulated flight. The existence of the shield at about  $X/D_{eq} \approx 2$  and the slower decay on the shield side are clearly noticeable.

Figure 4.2.8 shows the radial variation of mean and turbulent velocities at  $X/D_{eq} \approx 4$ . One notices asymmetric mean and turbulent velocity variations on either side. Also, note that the turbulent velocity reaches a peak at  $R/R^t \approx 0.5$ , where the mean velocity gradient is the steepest and also is the shear layer region. Within the jet core (i.e.,  $R/R^t < 0.3$ ) one notes a low level of turbulence.

STREAM	V, fps	T <sub>p</sub> , °R	P <sub>T</sub>
CORE JET	1880	1512	2.117
SHIELD	1150	1518	1.300
MIXED	1765	1513	1.921

- NOZZLE : TAS-2
- TEST POINT: 222
- LV PLUME NO. 4
- V<sub>a/c</sub> = 400. fps
- D<sub>eq</sub> = 5.67 in.

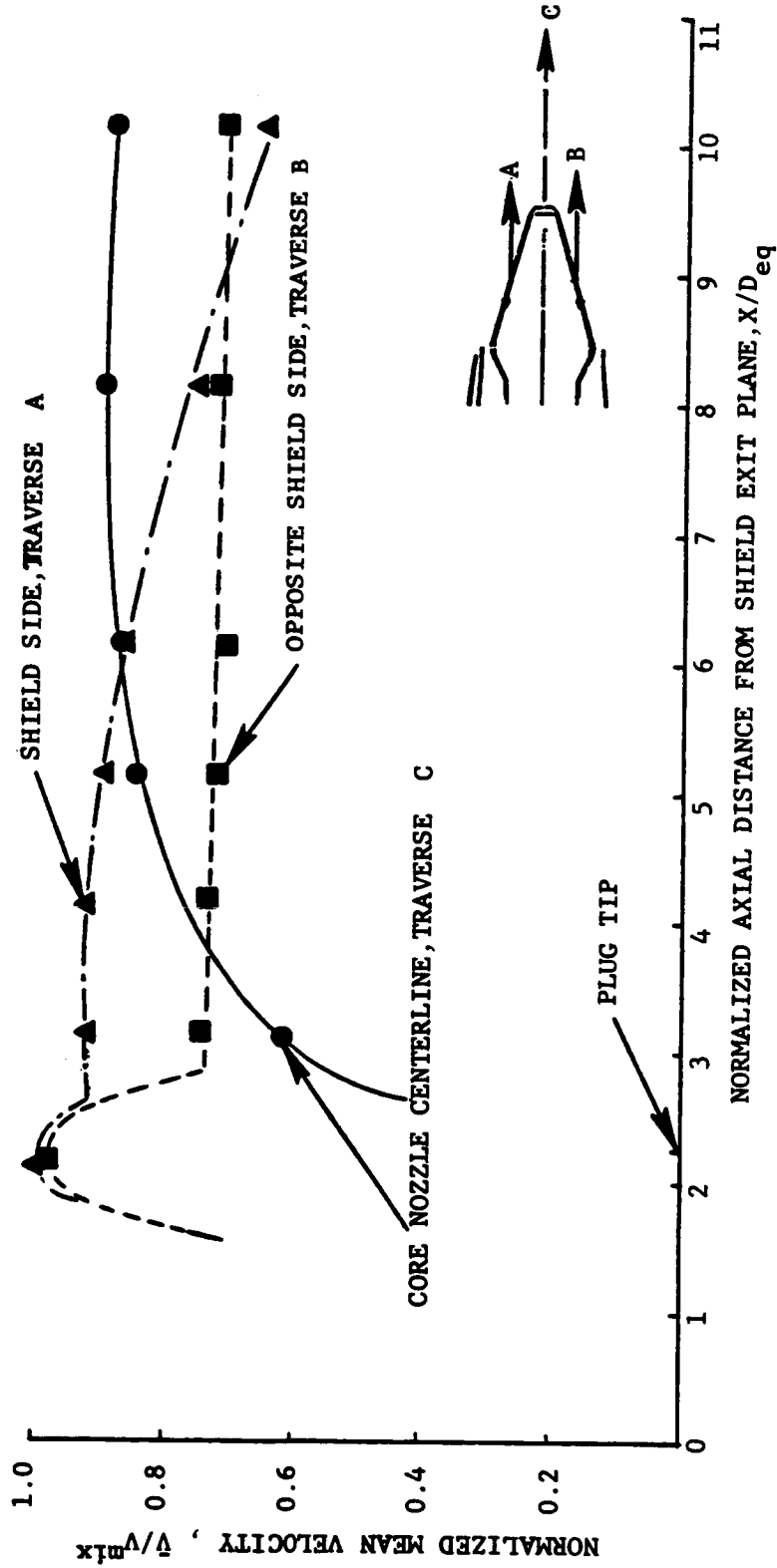


FIGURE 4.2-6A ASSYMETRIC AXIAL MEAN VELOCITY DISTRIBUTION DUE TO THE PARTIAL SHIELD AT A TYPICAL CUTBACK CASE ( FLIGHT )

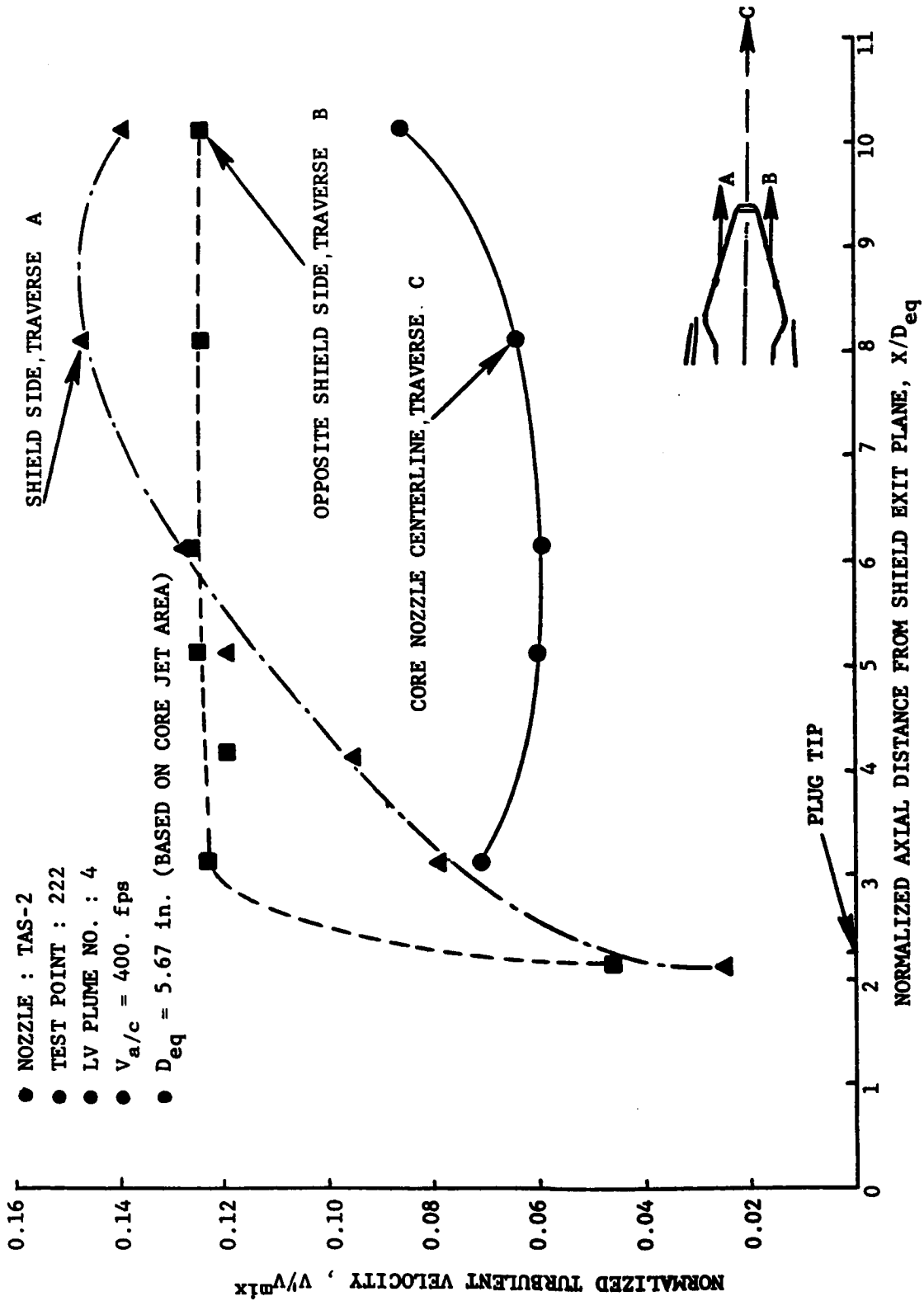


FIGURE 4.2.6b ASYMMETRIC TURBULENT VELOCITY DISTRIBUTION DUE TO THE PARTIAL SHIELD AT A TYPICAL CUTBACK CASE ( FLIGHT )



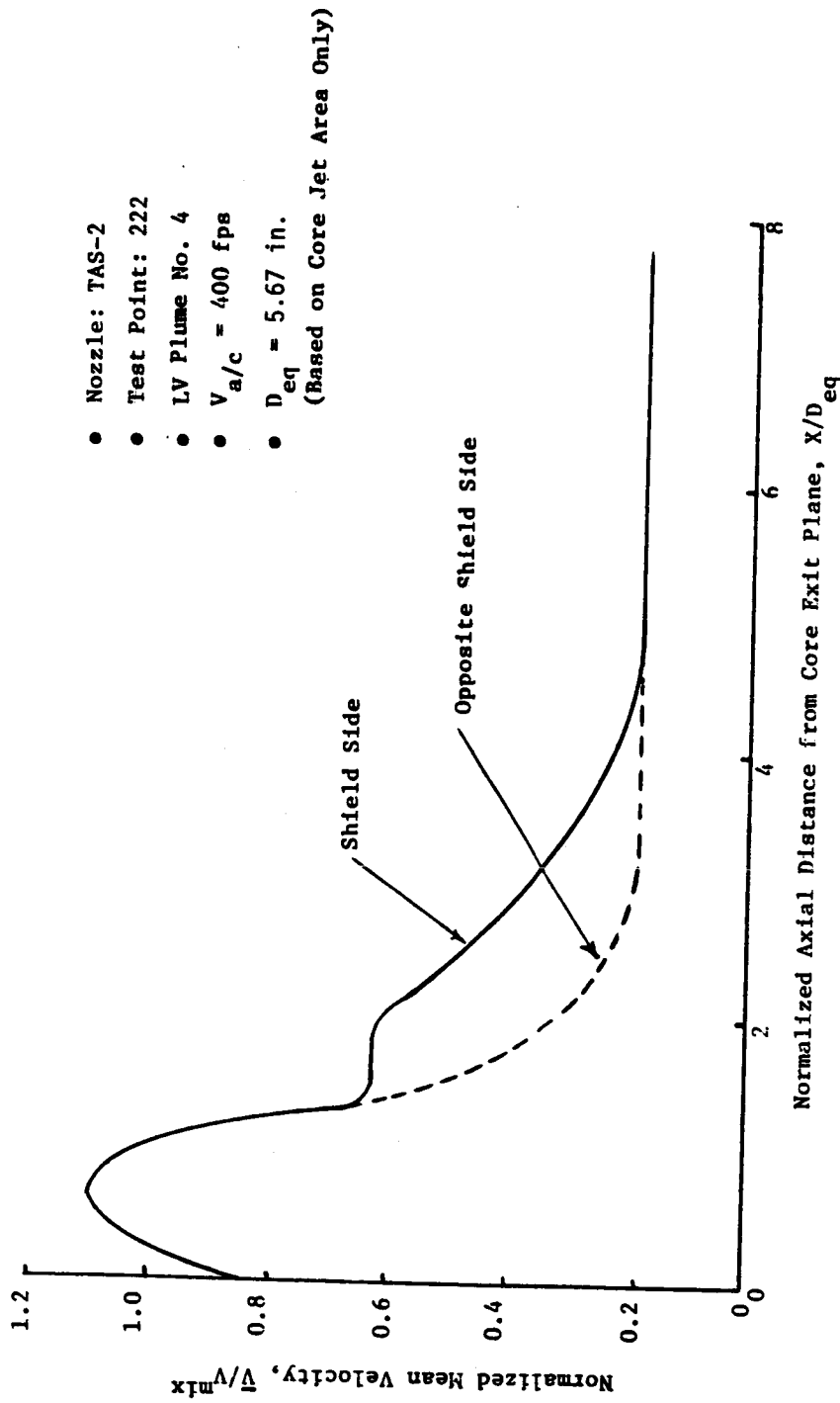


Figure 4.2.7. Comparison of Axial Mean Velocity Distribution at Radial Locations Corresponding to the Middle of Core Jet on the Shield Side and Opposite to the Shield Side at a Cutback Case (Flight).

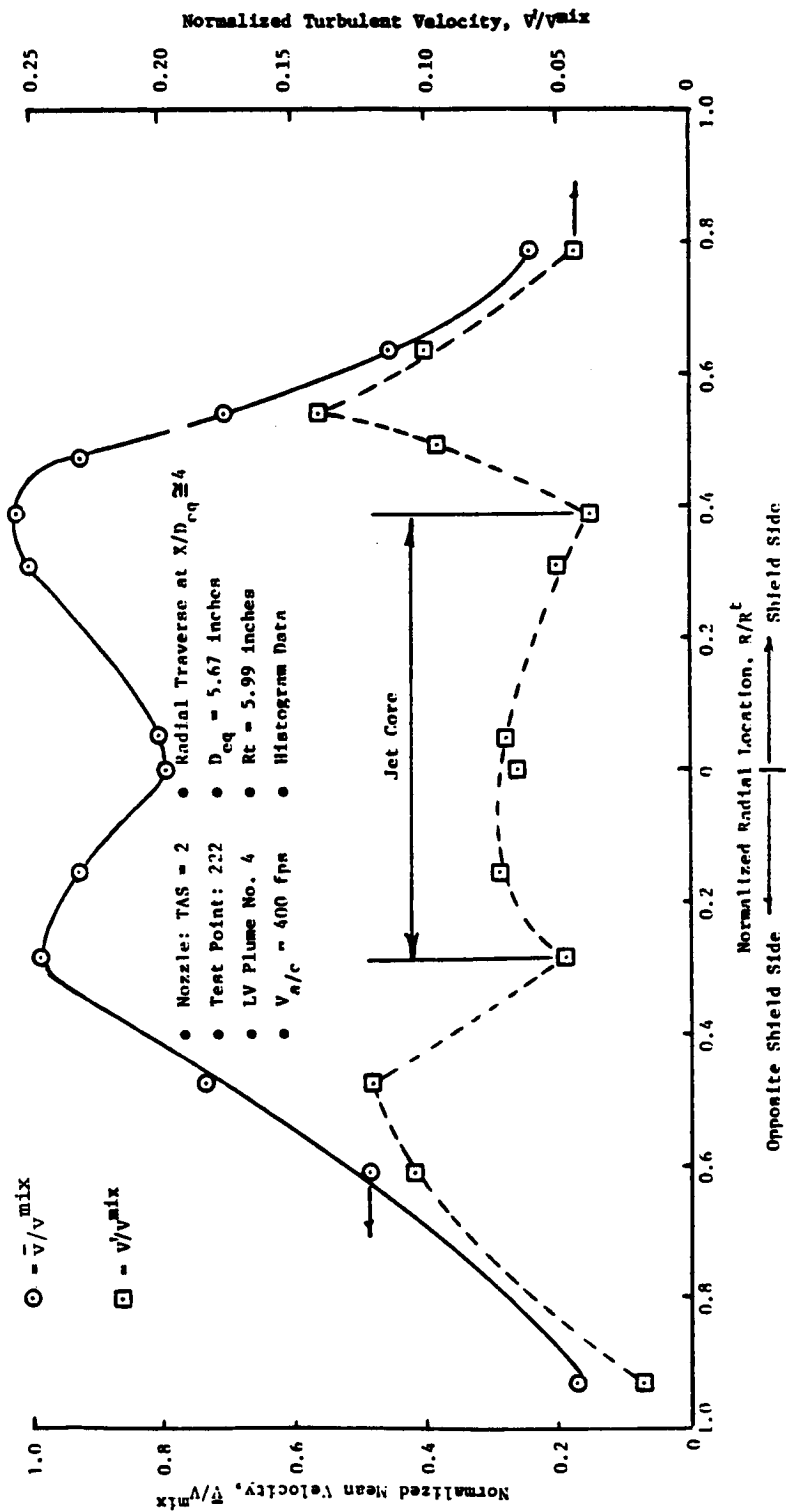


Figure 4.2.8. Radial Variation of Normalized Mean and Turbulent Velocities on the Shield and Opposite Shield Sides at a Typical Outback Case (Flight).

Figure 4.2.9 shows the axial variation of mean and turbulent velocities along the nozzle center line, on the shield and opposite to the shield sides for a typical takeoff case in flight. The normalized mean and turbulent velocity profiles for the takeoff and cutback cases in flight are similar (cf., Figures 4.2.6 and 4.2.9).

Figure 4.2.10 compares the axial mean velocity distribution at radial locations corresponding to the middle of the core jet on the shield and opposite to the shield sides at a typical takeoff case in flight. Unlike the cutback case, one does not note a clear indication of the presence of the shield. However, the mean velocity decay rates are different.

Figure 4.2.11 compares the mean velocity variation along a streamline parallel to the plug surface (utilizing the recently developed slant traverse mechanism) for typical takeoff and cutback cases in flight. Due to the higher core pressure ratio for the takeoff case, one notices the presence of two (2) shock cells.

#### 4.2.2 PLUME CHARACTERISTICS OF 32 CHUTE SUPPRESSOR NOZZLE WITH THERMAL ACOUSTIC SHIELD UNDER STATIC AND SIMULATED FLIGHT CONDITIONS

Plume characteristics of the 32 chute suppressor nozzle with 360° shield of 0.48" thickness (i.e., configuration TAS-9) and with 180° shield of 0.97" thickness (i.e., configuration TAS-8) at a typical takeoff cycle are discussed in this subsection.

Figures 4.2.12 compares the axial plume decay and turbulent velocity distributions of the 32-chute suppressor with 180° and 360° shields for a typical takeoff case in simulated flight. One notes that at mid shield radial location, the 180° shield has higher mean velocities than the 360° shield for  $x/D_{eq} < 6$ . The 180° shield has a thickness of 0.97" whereas the 360° shield has a thickness of 0.48". The thicker partial shield has reduced the mean velocity decay for  $x/D_{eq} < 6$ . However, for  $x/D_{eq} > 6$ , the mean velocity decay for the 180° shield is seen to be faster than the full 360° shield. The mean velocity distribution along the core nozzle center line is not significantly different for the 360° and 180° shields implying that the shields do not significantly influence the core nozzle center line mean

Stream	V, fps	T <sub>T</sub> , °R	P <sub>r</sub>
Core Jet	2242	1654	2.736
Shield	1374	1661	1.413
Mixed	2115	1655	2.417

- Nozzle: TAS-2
- Test Point: 226
- LV Plume No. 2
- V<sub>a/c</sub> = 400 fps
- D<sub>eq</sub> = 5.67 inches  
(Based on Core Jet Area Only)

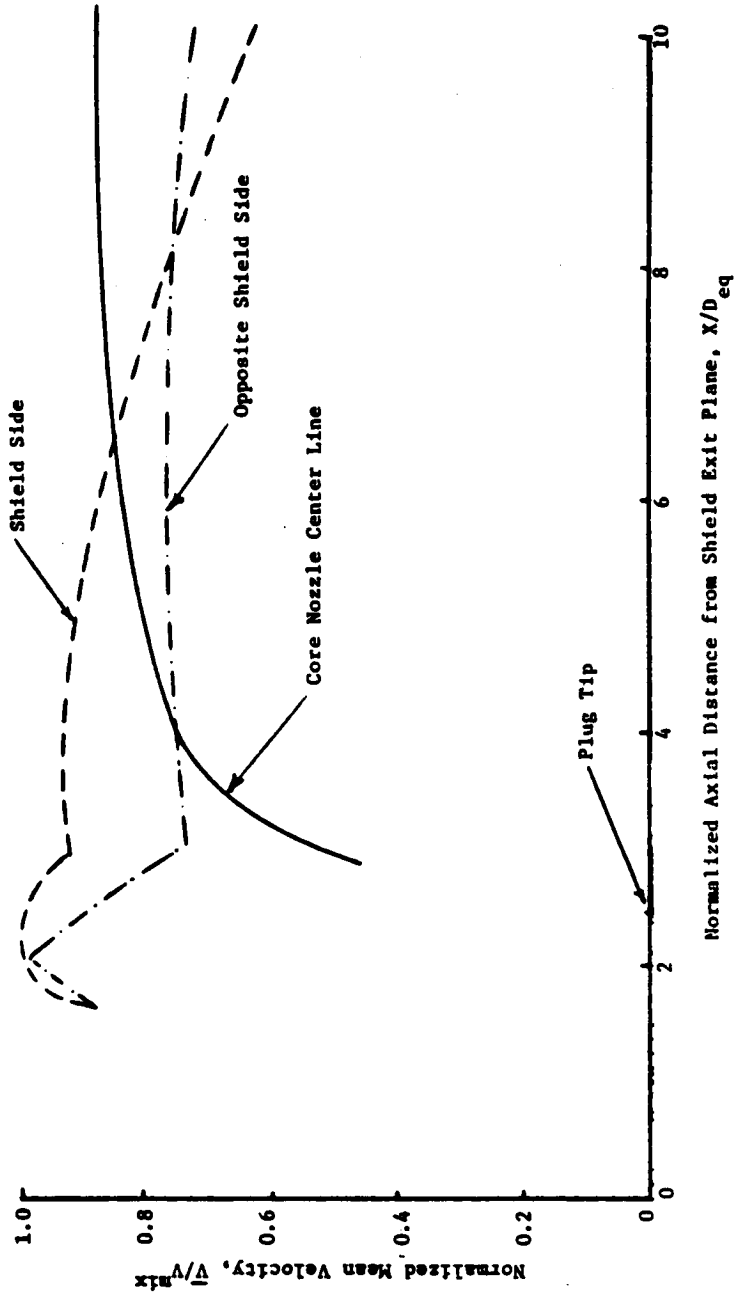


Figure 4.2.9a. Assymmetric Axial Mean Velocity Distribution Due to the Partial Shield at a Typical Takeoff Case (Flight).

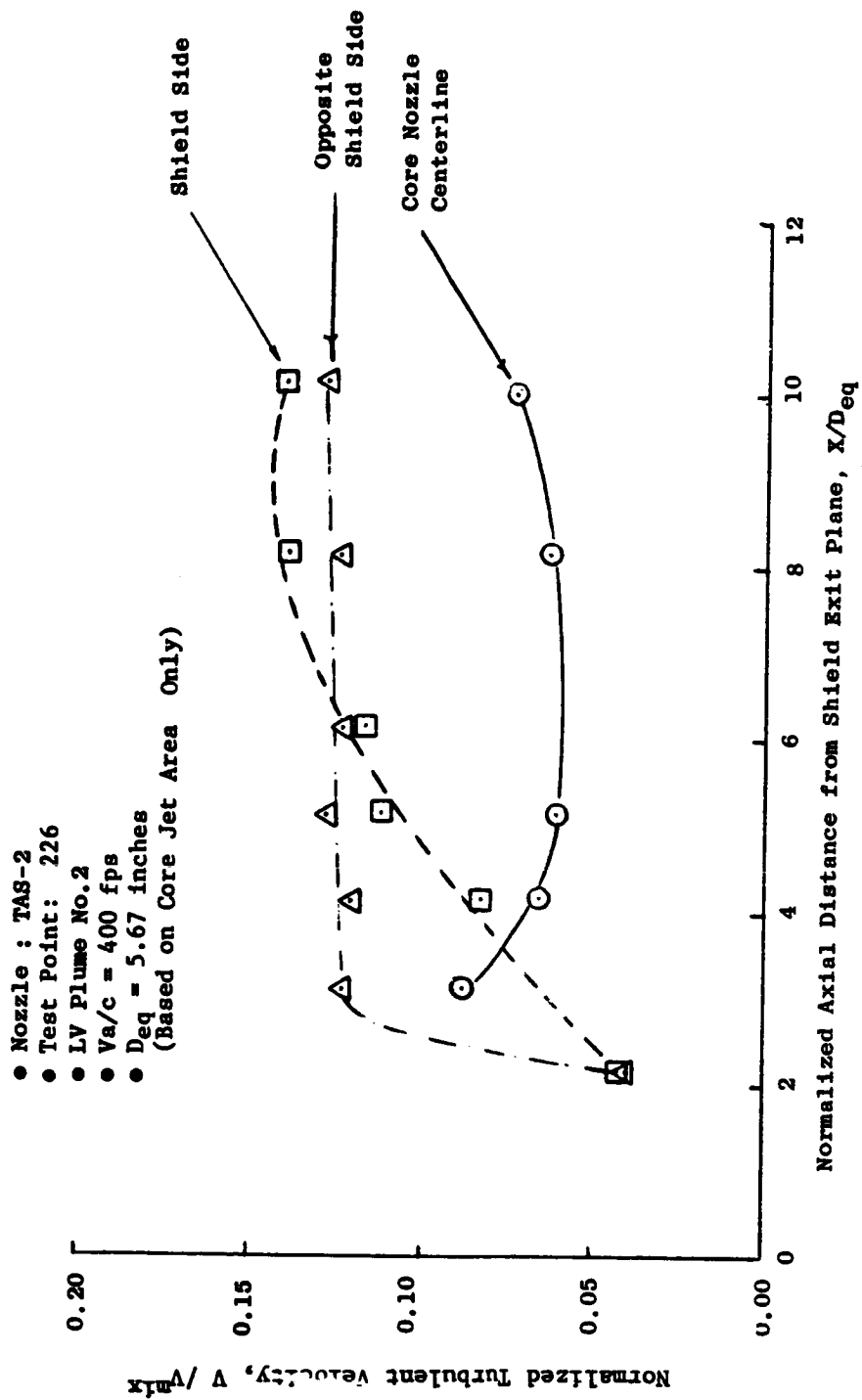
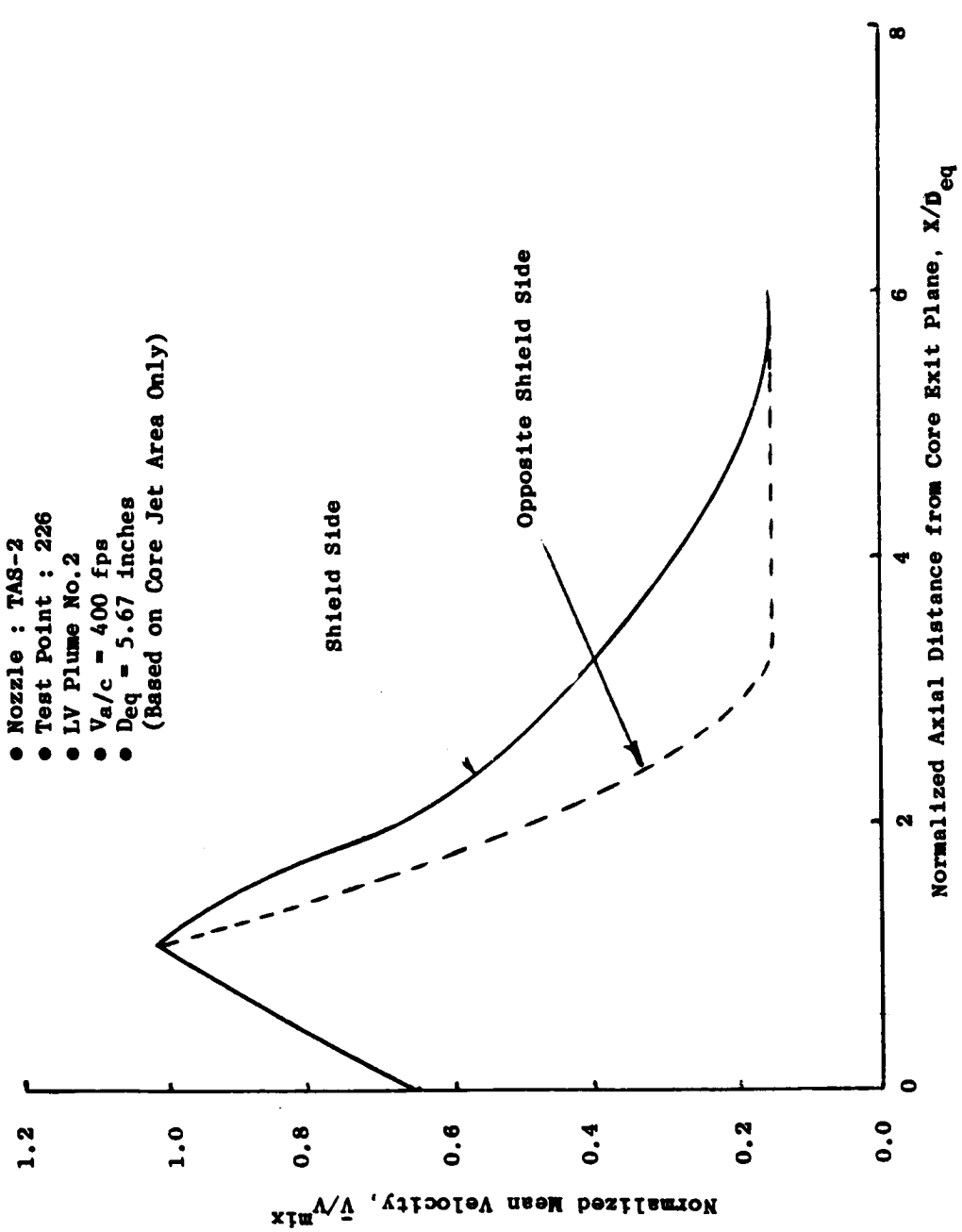


Figure 4.2.9b. Asymmetric Turbulent Velocity Distribution Due to the Partial Shield at a Typical Takeoff Case (Flight).



- Nozzle : TAS-2
- Test Point : 226
- LV Plume No.2
- $V_a/c = 400$  fps
- $D_{eq} = 5.67$  inches
- (Based on Core Jet Area Only)

Figure 4.2.10. Comparison of Axial Mean Velocity Distribution at Radial Locations Corresponding to the Middle of Core Jet on the Shield and Opposite Sides at a Takeoff Case (Flight).

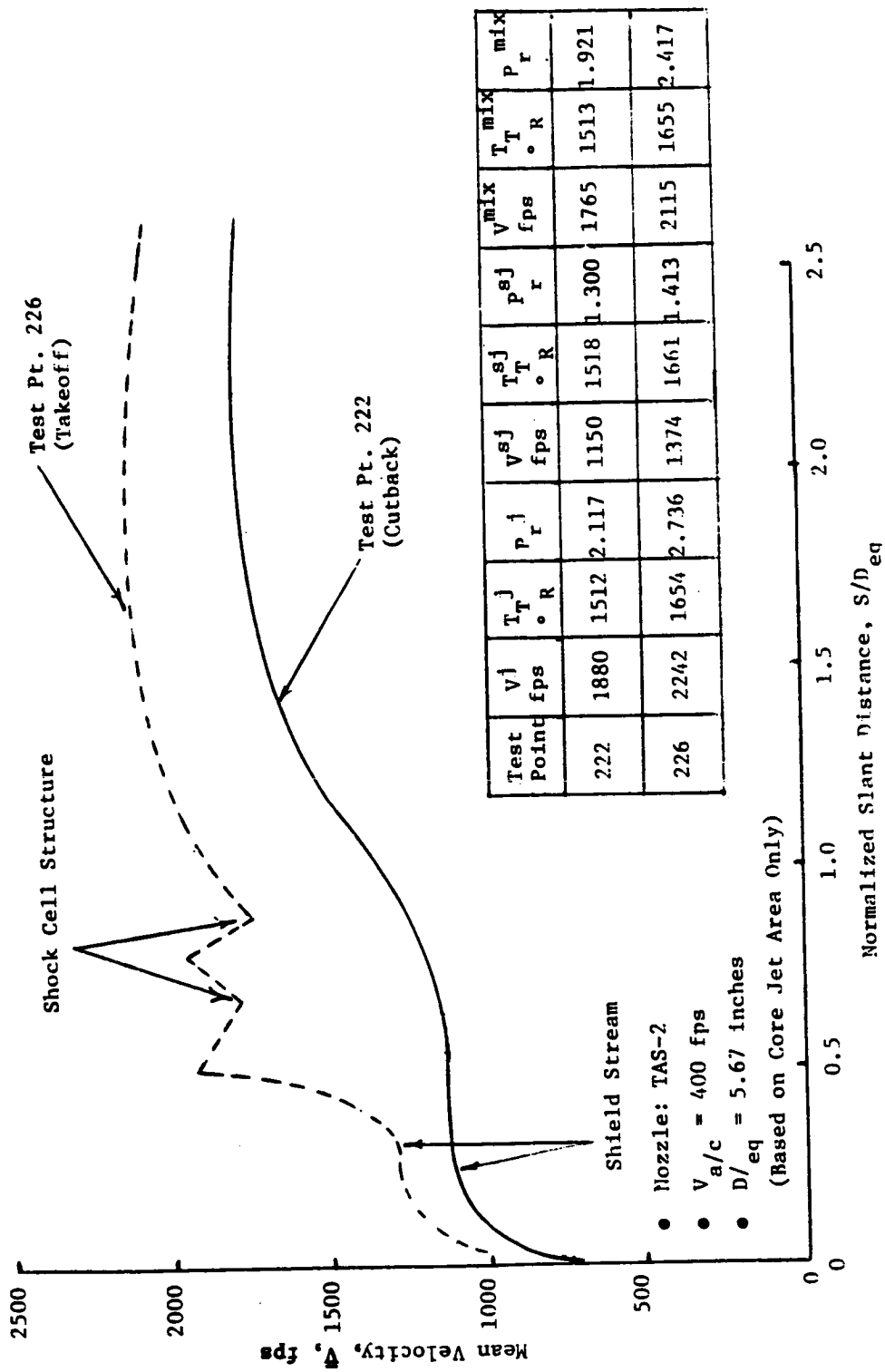


Figure 4.2.11. Mean Velocity Variation Along a Streamline Parallel to the Plug Surface for Typical Takeoff and Cutback Cases (Flight).

NOZZLE IDENT.	LV PLUME NO.	MATCHING ACOUSTIC TEST PT.	CORE JET			SHIELD JET			MIXED CONDITIONS		
			$v^j$ , fps	$T_T^j$ , °R	$P_R^j$	$v^{sj}$ , fps	$T_T^{sj}$ , °R	$P_R^{sj}$	$v^{mix}$ , fps	$T_T^{mix}$ , °R	$P_R^{mix}$
TAS-8	8	894	2218	1640	2.696	1325	1606	1.394	1993	1632	2.190
TAS-9	10	910	2235	1667	2.693	1352	1707	1.381	2026	1678	2.197

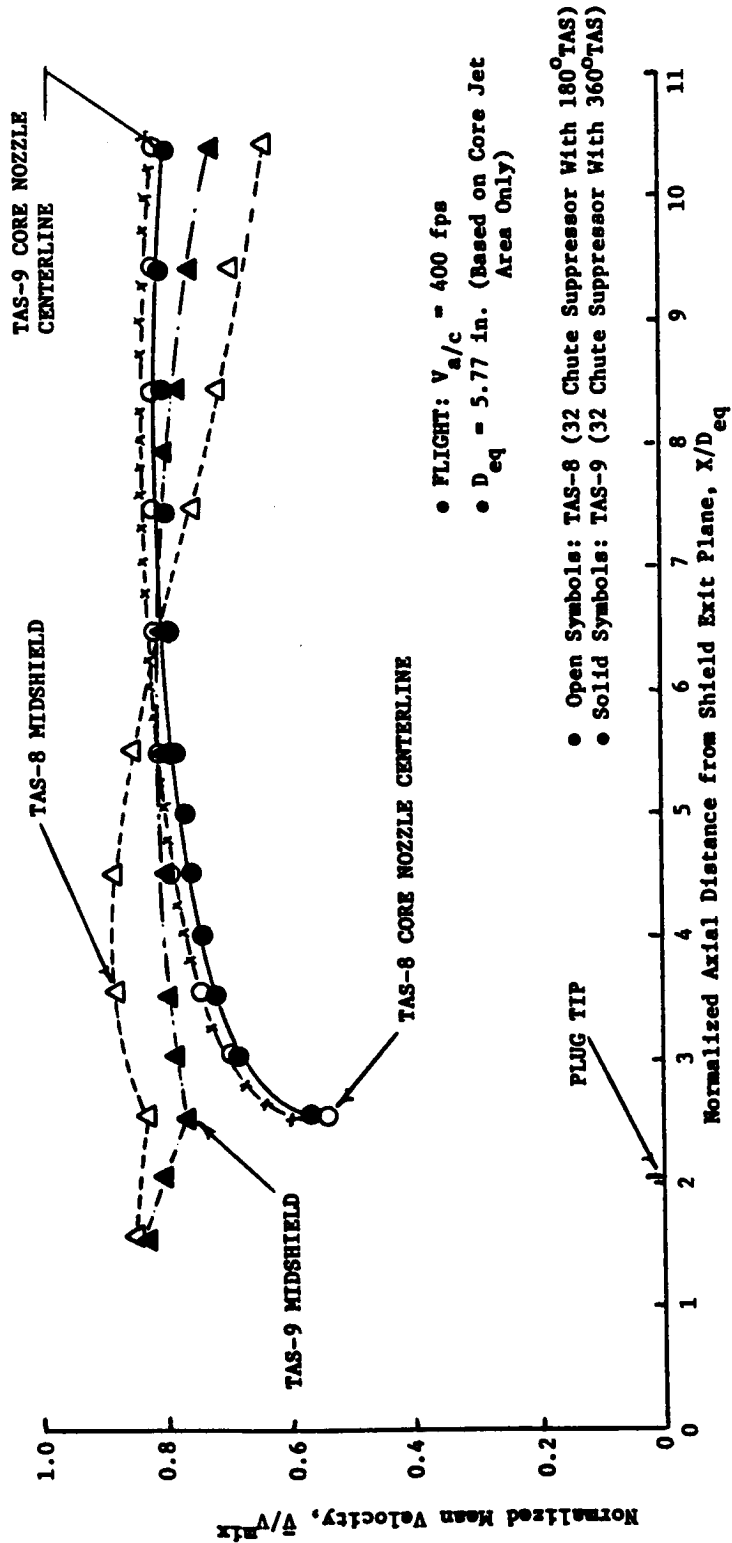


FIGURE 4.2.12a. COMPARISON OF THE PLUME DECAY OF THE 32 CHUTE SUPPRESSOR NOZZLE WITH A PARTIAL (180°) AND A FULL (360°) TAS AT TWO (2) RADIAL LOCATIONS (HISTOGRAM DATA).



- FLIGHT,  $V_{a/c} = 400 \text{ fps}$
- $D_{eq} = 5.77 \text{ In.}$  (Based on Core Jet Area Only)
- Open Symbols: TAS-8 (32 Chute Suppressor with  $180^\circ$  TAS)
- Solid Symbols: TAS-9 (32 Chute Suppressor with  $360^\circ$  TAS)

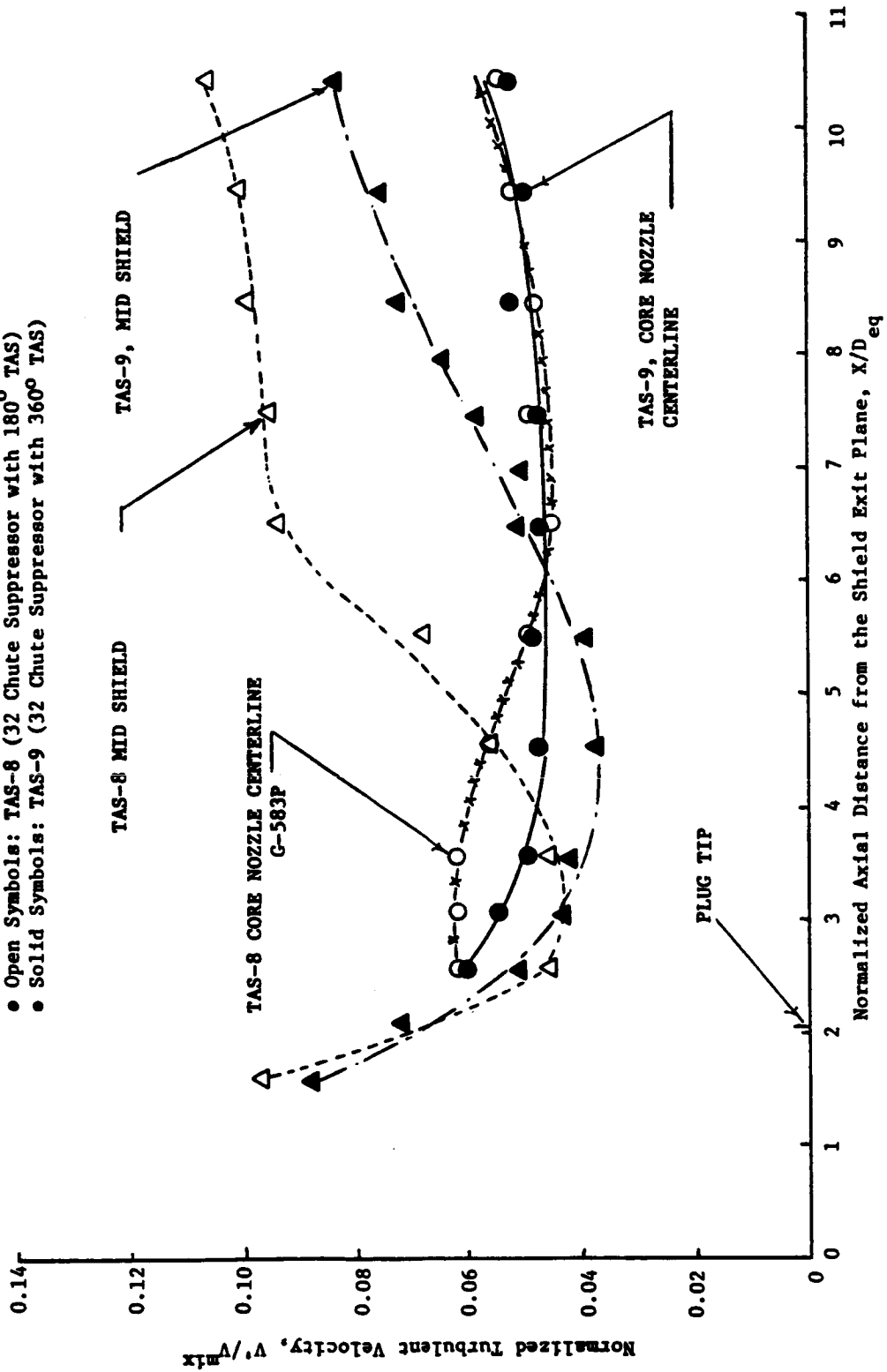


FIGURE 4.2.12b. COMPARISON OF THE TURBULENT VELOCITY DISTRIBUTION OF THE 32 CHUTE SUPPRESSOR NOZZLE WITH A PARTIAL ( $180^\circ$ ) AND A FULL ( $360^\circ$ ) TAS AT TWO (2) RADIAL LOCATIONS (HISTOGRAM DATA)

velocities. The turbulent velocities for the partial shield are larger than those of the full shield at a mid-shield location for  $X/D_{eq} > 3$ . The turbulent velocities along the core nozzle centerline for the partial shield are larger than those of the full shield for  $X/D_{eq} < 5$ , thus indicating that the suppressor jet flow with partial shield is more turbulent than with the full shield.

Figure 4.2.13 shows the asymmetric axial mean and turbulent velocity distributions due to the partial shield on the 32-chute suppressor for a takeoff case in simulated flight. The mean velocity on the shield side is seen to be higher than the opposite shield side for  $X/D_{eq} > 3$ . The high values of turbulent velocities in the plug region (i.e.,  $X/D_{eq} < 3$ ) are due to the highly turbulent flow issuing out of the chutes.

Figure 4.2.14 shows the influence of simulated flight velocity on the plume decay and turbulent velocity distribution of the 32-chute suppressor with 180° shield. Note that the influence of the simulated flight velocity is to reduce the plume decay rate and the turbulent velocities. The influence of simulated flight velocity on the mean velocity at mid-shield location occurs when  $X/D_{eq} > 4$ . Along the core nozzle centerline, it occurs at  $X/D_{eq} > 6.5$  indicating the reduced shearing influence of the simulated flight velocity at the nozzle centerline. The turbulent velocities with simulated forward flight velocity are seen to be lower at both mid-shield and core nozzle centerline which could be attributed to the streamlining of the jet flow by the simulated forward flight velocity.

Figure 4.2.15 similarly shows the influence of simulated flight velocity on the plume decay and turbulent velocity distribution of the 32-chute suppressor with 360° shield. As in the case of the partial shield (see Figure 4.2.14) the simulated flight velocity has reduced the plume decay rate and smoothed the jet flow for the full shield case also.

Stream	V, fps	T <sub>T</sub> , °R	P <sub>r</sub>
Core Jet	2218	1640	2.696
Shield	1325	1606	1.394
Mixed	1993	1632	2.190

- NOZZLE: TAS-8 (32 CHUTE SUPPRESSOR WITH 180° TAS OF 0.97" THICKNESS)
- LV PLUME NO. 8
- MATCHING ACOUSTIC TEST POINT 894
- V<sub>a/c</sub> = 400 fps
- D<sub>eq</sub> = 5.77 INCHES (BASED ON CORE JET AREA ONLY)

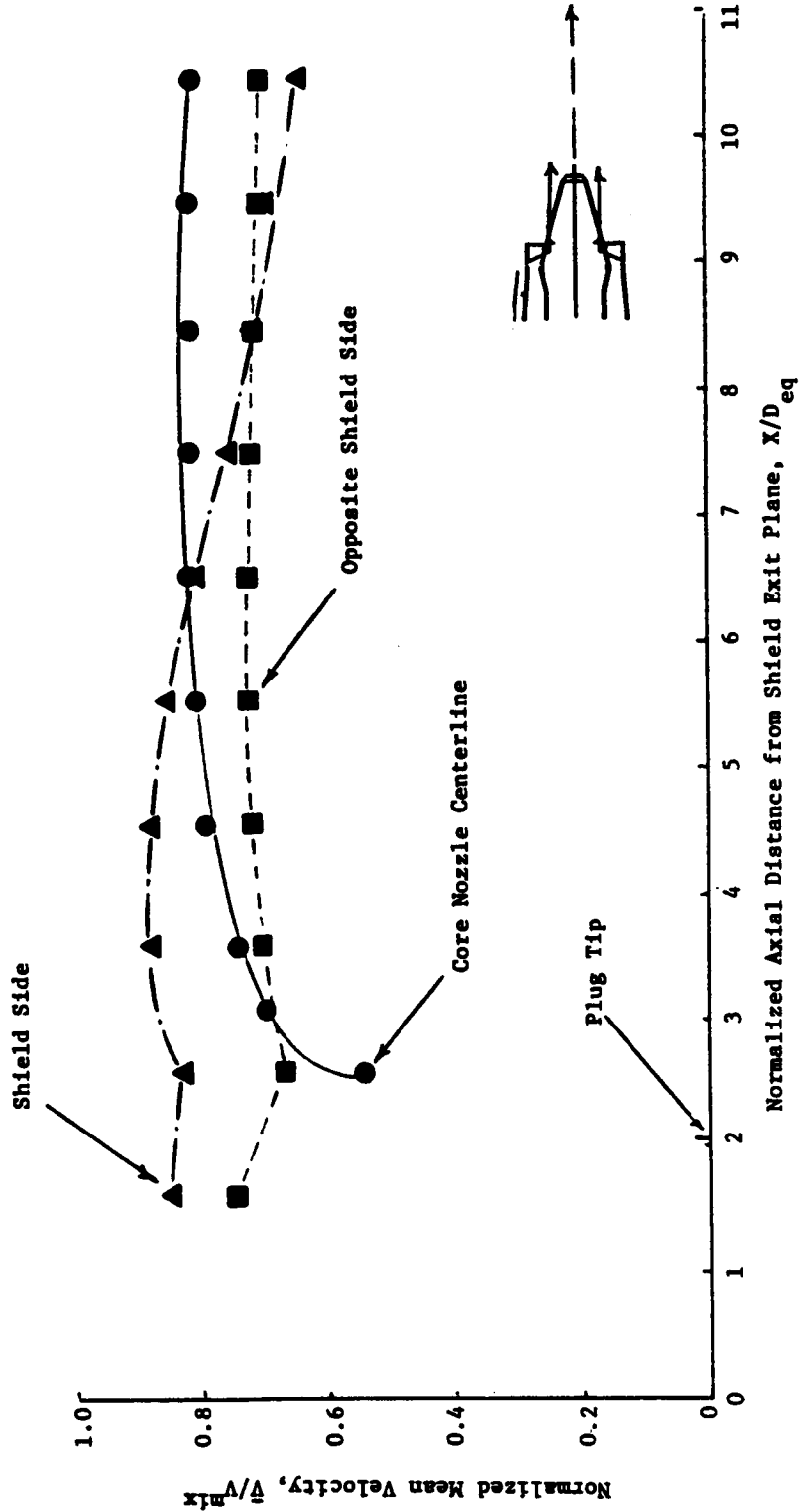


FIGURE 4.2.13a. ASYMMETRIC AXIAL MEAN VELOCITY DISTRIBUTION DUE TO THE PARTIAL SHIELD ON THE 32 CHUTE SUPPRESSOR NOZZLE FOR A FLIGHT CASE (HISTOGRAM DATA)

- NOZZLE: TAS-8 (32 CHUTE SUPPRESSOR WITH 180° TAS OF 0.97" THICKNESS)
- LV PLUME NO. 8
- MATCHING ACOUSTIC TEST POINT 894
- $v_{a/c} = 400$  fps
- $D_{eq} = 5.77$  INCHES (BASED ON CORE JET AREA ONLY)

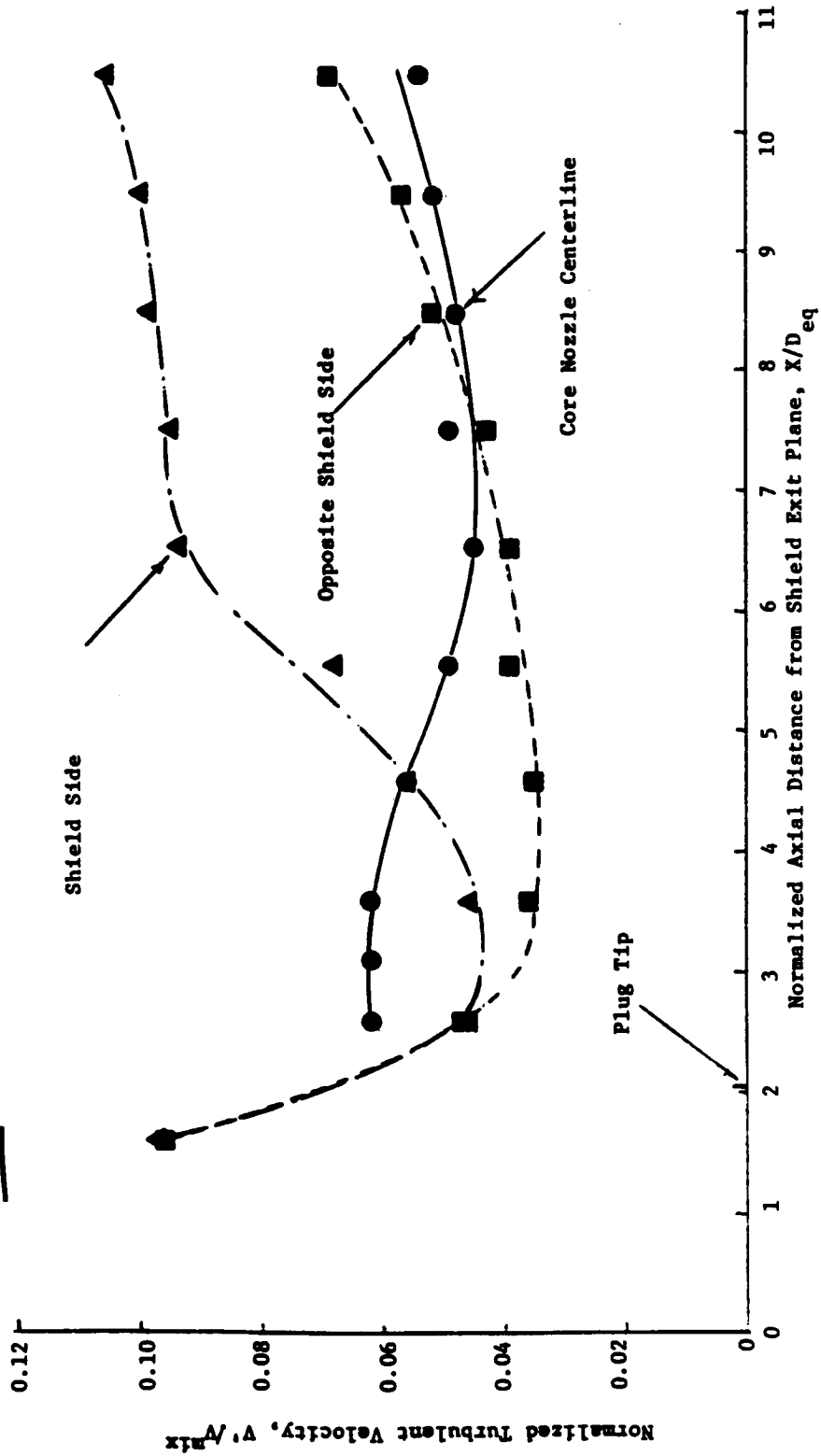
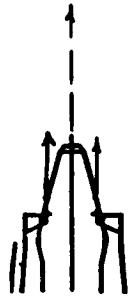


FIGURE 4.2.13b. ASYMMETRIC TURBULENT VELOCITY DISTRIBUTION DUE TO THE PARTIAL SHIELD ON THE 32 CHUTE SUPPRESSOR NOZZLE FOR A FLIGHT CASE (HISTOGRAM DATA)

LV PLUME NO.	MATCHING ACOUSTIC TEST PT.	$V_{a/c}$ , fps	CORE JET			SHIELD JET			MIXED CONDITIONS		
			$V^j$ , fps	$T_T^j$ , °R	$P_I^j$	$V^{sj}$ , fps	$T_T^{sj}$ , °R	$P_I^{sj}$	$V^{mix}$ , fps	$T_T^{mix}$ , °R	$P_I^{mix}$
7	893	0	2211	1631	2.695	1323	1619	1.388	1990	1628	2.188
8	894	400	2218	1640	2.696	1325	1606	1.394	1993	1632	2.190

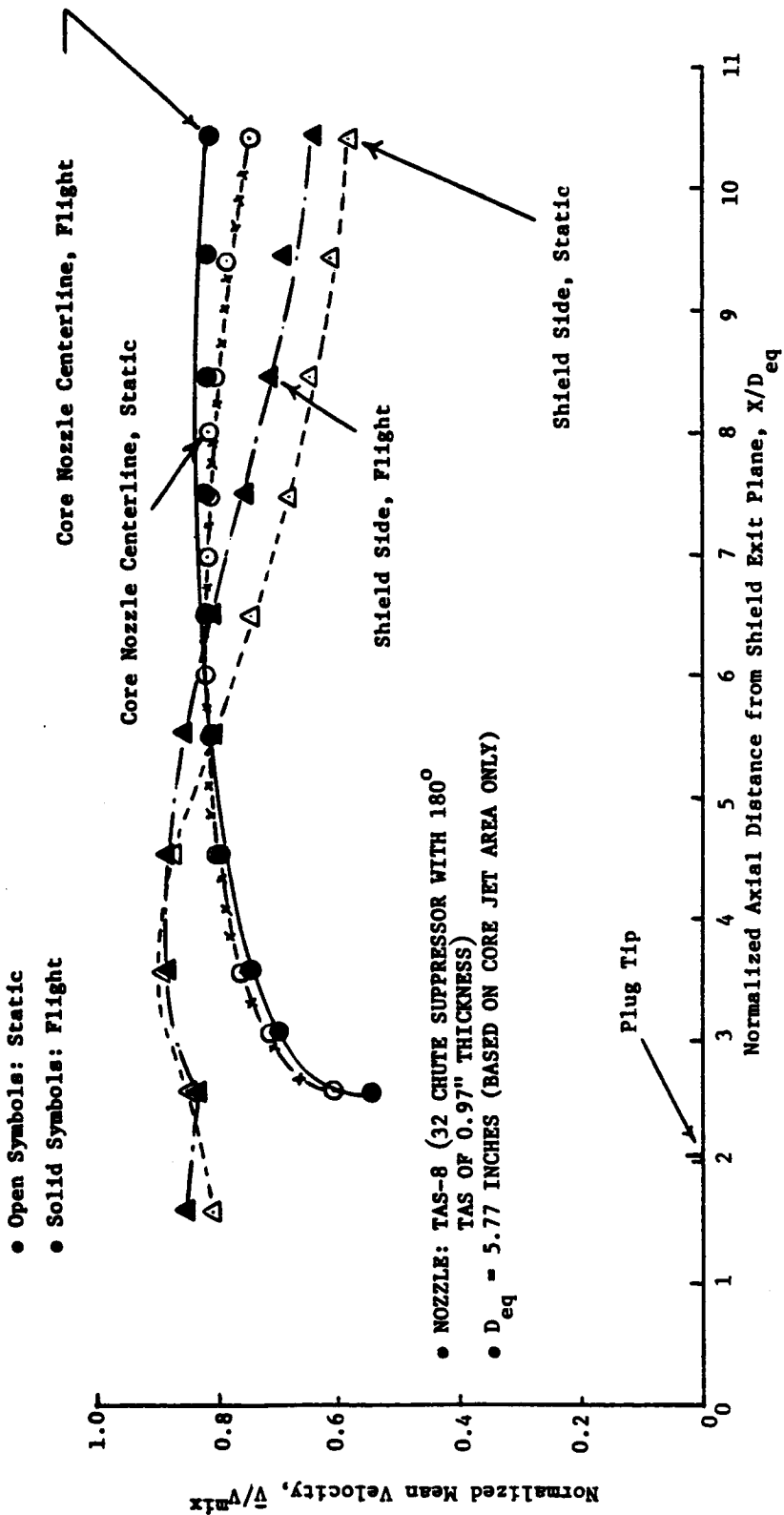


FIGURE 4.2.14a. INFLUENCE OF FLIGHT VELOCITY ON THE PLUME DECAY OF THE 32 CHUTE SUPPRESSOR WITH 180° TAS OF 0.97" THICKNESS AT TWO (2) RADIAL LOCATIONS (HISTOGRAM DATA)

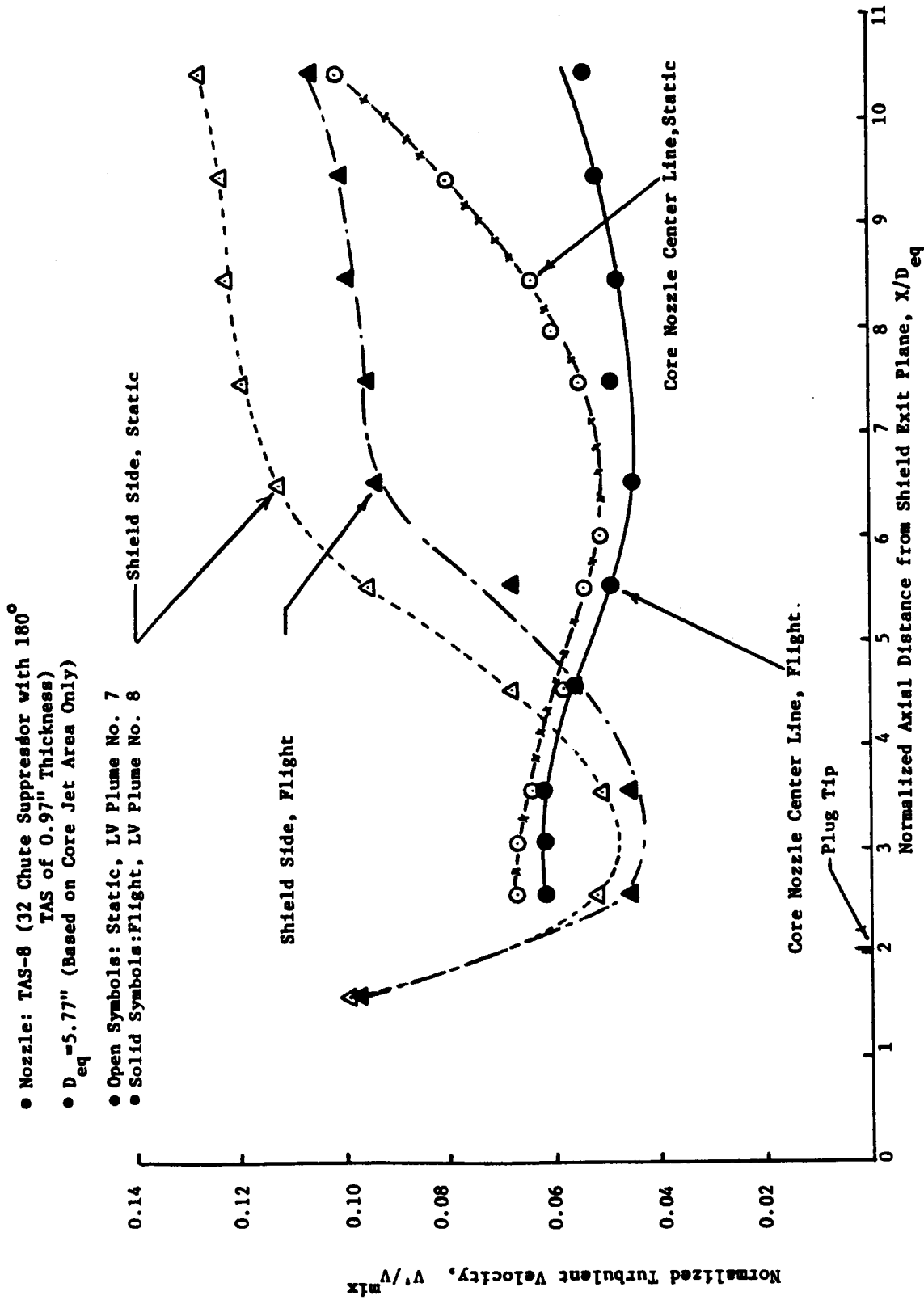


FIGURE 4.2.14b. INFLUENCE OF FLIGHT VELOCITY ON THE TURBULENT VELOCITIES OF THE 32 CHUTE SUPPRESSOR WITH 180° T.A.S. OF 0.97" THICKNESS AT TWO(2) RADIAL LOCATIONS (HISTOGRAM DATA).

LV PLUME MATCHING ACOUSTIC TEST PT. NO.	$V_{a/c}$ , fps	CORE JET			SHIELD JET			MIXED CONDITIONS		
		$V_j$ , fps	$T_j$ , °R	$P_j$ , $\frac{lb}{in^2}$	$V^{sj}$ , fps	$T^{sj}$ , °R	$P_r^{sj}$	$V^{mix}$ , fps	$T^{mix}$ , °R	$P_r^{mix}$
9	0	2226	1649	2.701	1348	1675	1.390	2016	1655	2.205
10	400	2235	1667	2.693	1352	1717	1.381	2026	1678	2.197

- Open Symbols: Static
- Solid Symbols: Flight
- NOZZLE: TAS-9 (32 CHUTE SUPPRESSOR WITH 360° TAS OF 0.48" THICKNESS)
- $D_{eq} = 5.77$  INCHES (BASED ON CORE JET AREA ONLY)

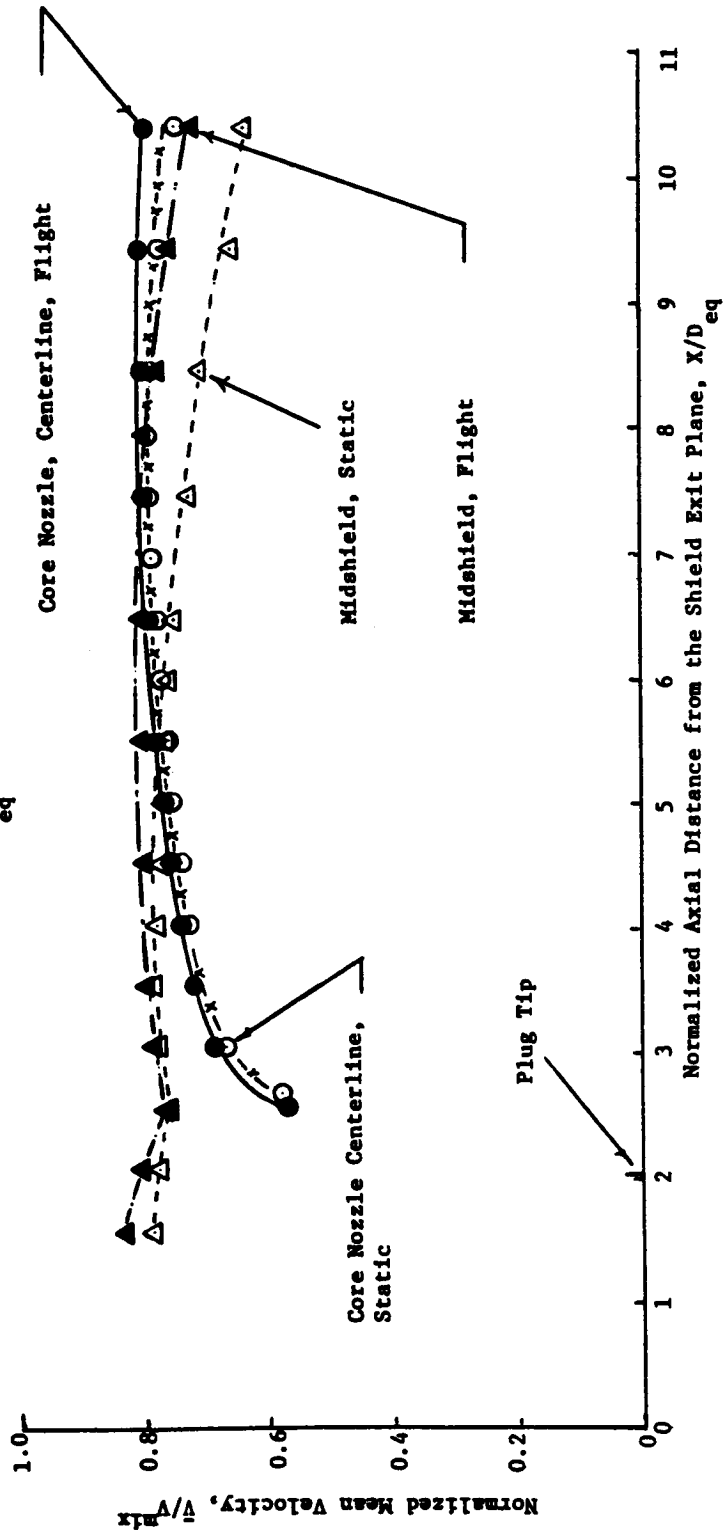


FIGURE 4.2.15a. INFLUENCE OF FLIGHT VELOCITY ON THE PLUME DECAY OF THE 32 CHUTE SUPPRESSOR WITH 360° TAS OF 0.48" THICKNESS AT TWO (2) RADIAL LOCATIONS (HISTOGRAM DATA)

- NOZZLE: TAS-9 ( 32 CHUTE SUPPRESSOR WITH 360° TAS OF 0.48" THICKNESS)
- $D_{eq} = 5.77"$  ( BASED ON CORE JET AREA ONLY )
- OPEN SYMBOLS: STATIC, LV PLUME NO. 9
- SOLID SYMBOLS: FLIGHT, LV PLUME NO. 10

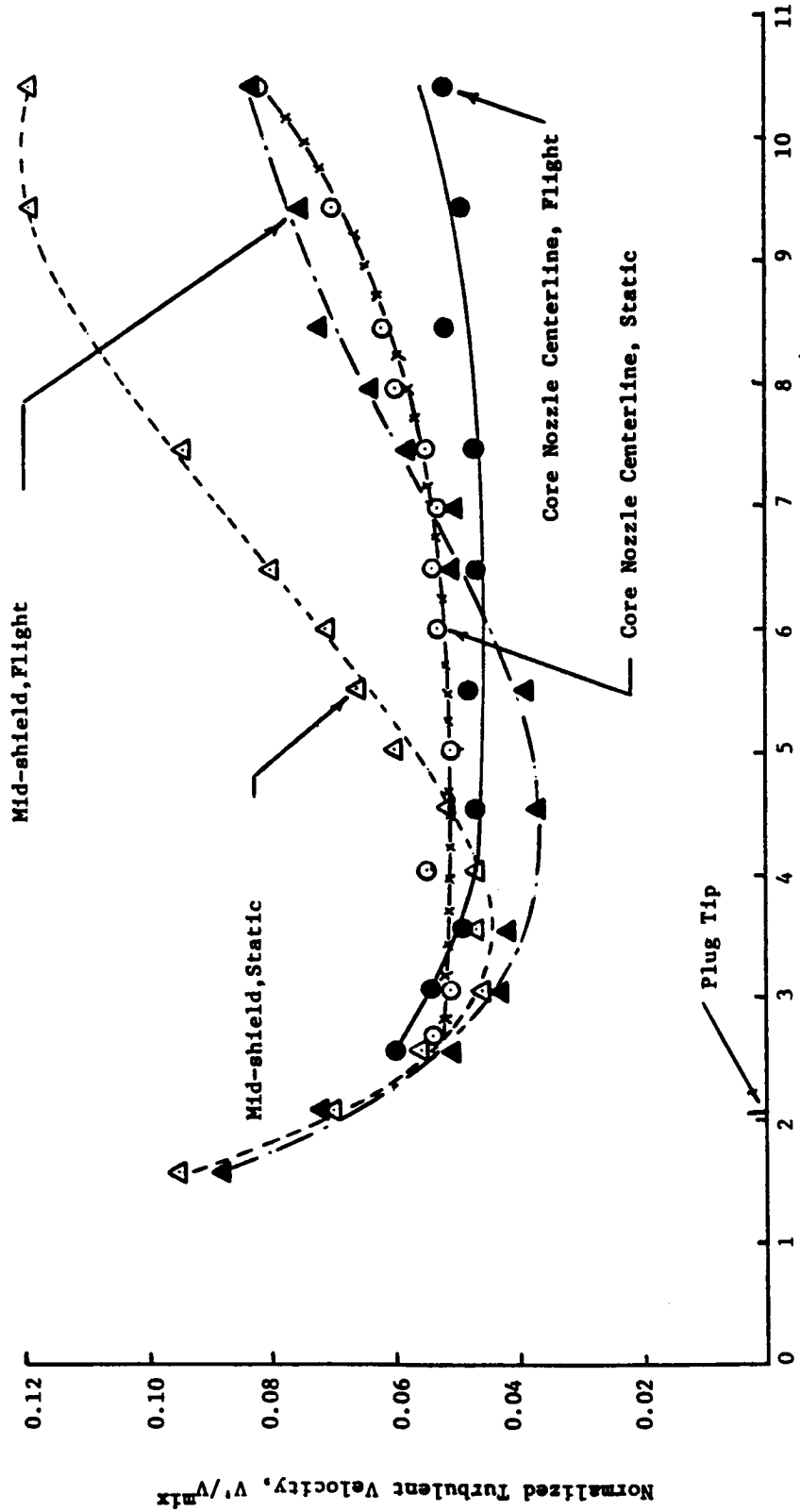


FIGURE 4.2.15b. INFLUENCE OF FLIGHT VELOCITY ON THE TURBULENT VELOCITIES OF THE 32 CHUTE SUPPRESSOR WITH 360° T.A.S. OF 0.48" THICKNESS AT TWO(2) RADIAL LOCATIONS (HISTOGRAM DATA).



#### 4.3 AERODYNAMIC CALIBRATION AND DIAGNOSTIC TEST RESULTS

The discussion of the aerodynamic calibration and diagnostic test results is grouped under the following headings:

- A. Stagnation pressure calibration of full and partial thermal acoustic shield streams;
- B. Measured and predicted pressure field interactions of core and shield streams; and
- C. Influence of the thermal acoustic shields on the base drag of the 32 chute suppressor nozzle under heated, simulated flight and static conditions.

##### 4.3.1 STAGNATION PRESSURE CALIBRATION OF FULL AND PARTIAL THERMAL ACOUSTIC SHIELD STREAMS

As noted in Subsection 3.2.3, aerodynamic calibration of the thermal acoustic shield exit plane with respect to the upstream test facility charging station was conducted on the 360° shield of 0.48" thickness of configuration TAS-4 (see Table 3-XXII) and on the 180° shield of 0.48" thickness of configuration TAS-2 (see Table 3-XXI).

The total pressure calibration results of the 360° shield of 0.48" thickness on configuration TAS-4 are summarized in Figure 4.3.1 wherein the  $(P_T/P_{amb})$  data as measured by three (3) total pressure rakes located at the exit of the thermal acoustic shield are plotted versus  $(P_T/P_{amb})$  data measured by the facility rakes that are located upstream of the exit. The data include the series of measurements taken with the total temperature of the shield jet at 550°R and 1730°R. From the measured data, the percent loss in total pressure of the shield flow relative to facility-rake measured data is calculated as:

$$\Delta P_T = \left[ 1 - \frac{(P_T^{Rake}/P_{amb})}{(P_T^{Facility}/P_{amb})} \right] \times 100 \quad (4.3.1)$$

Figure 4.3.1 contains the calibration data as well as the percent loss in total pressure. The following conclusions may be drawn from these measurements:

- A. The associated loss in total pressure of the 360° shield jet is within 1% and, hence, facility measured total pressures have been employed to set the necessary aerodynamic conditions on the 360° shield stream; and
- B. The total temperature of the stream has no noticeable effect on these measurements.

As there is no flow turning with 360° shield as compared to 180° shield, no significant pressure loss is anticipated. The total pressure measurements on the 360° shield serves as the baseline case to measure  $P_T$  losses of 180° shield.

Next, results of the flow calibration tests conducted on the 180° shield of 0.48" thickness of configuration TAS-2 are discussed. Total pressure data measured by each of the three rakes located at different azimuthal locations in the shield jet stream at shield total temperatures of 550°R and 1730°R respectively are presented in Figures 4.3.2 and 4.3.3. The total pressure at each of the rakes was obtained from an area weighted average of the measurements taken by the four (4) elements of that rake. For each of the test cases, the corresponding total pressure data obtained from the facility rakes that are mounted upstream, before the annular flow is turned through the 180° partial shield are indicated also in the figures. An examination of the figures indicates that the total pressure at the shield exit is uniform over most of the mid-regions of the partial shield and approximately equal to the upstream-facility measured data. However, there exists a loss in total pressure at the extremities of the 180° shield.

To determine the effect of the above observed angular dependence of the total pressure at the shield exit, a representative average value of the total pressure was calculated from the individual rake readings. For this

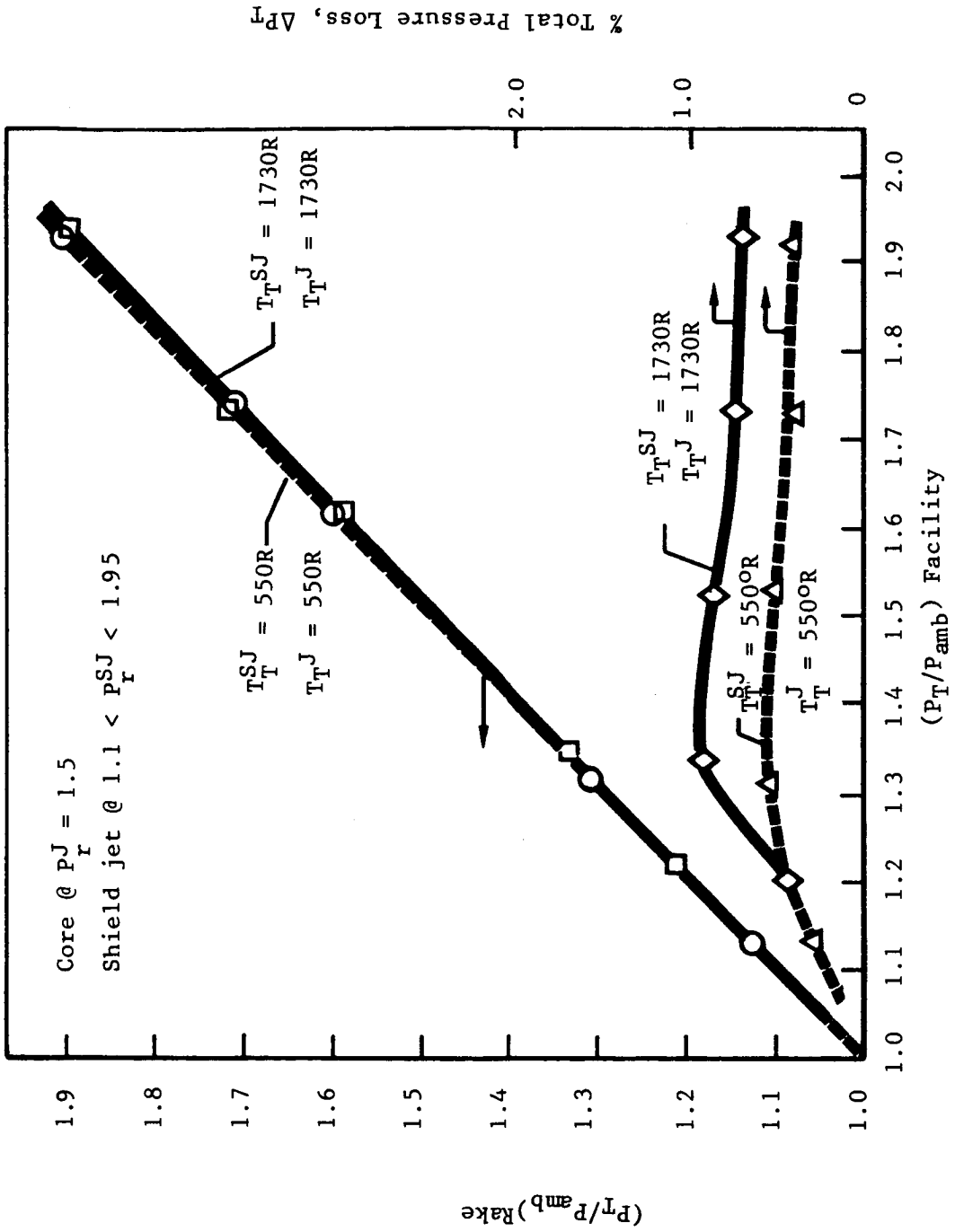


Figure 4.3.1. Total Pressure Calibration of 360° Thermal Acoustic Shield of 0.48" Thickness on Configuration TAS-4 at 550°R and 1730°R

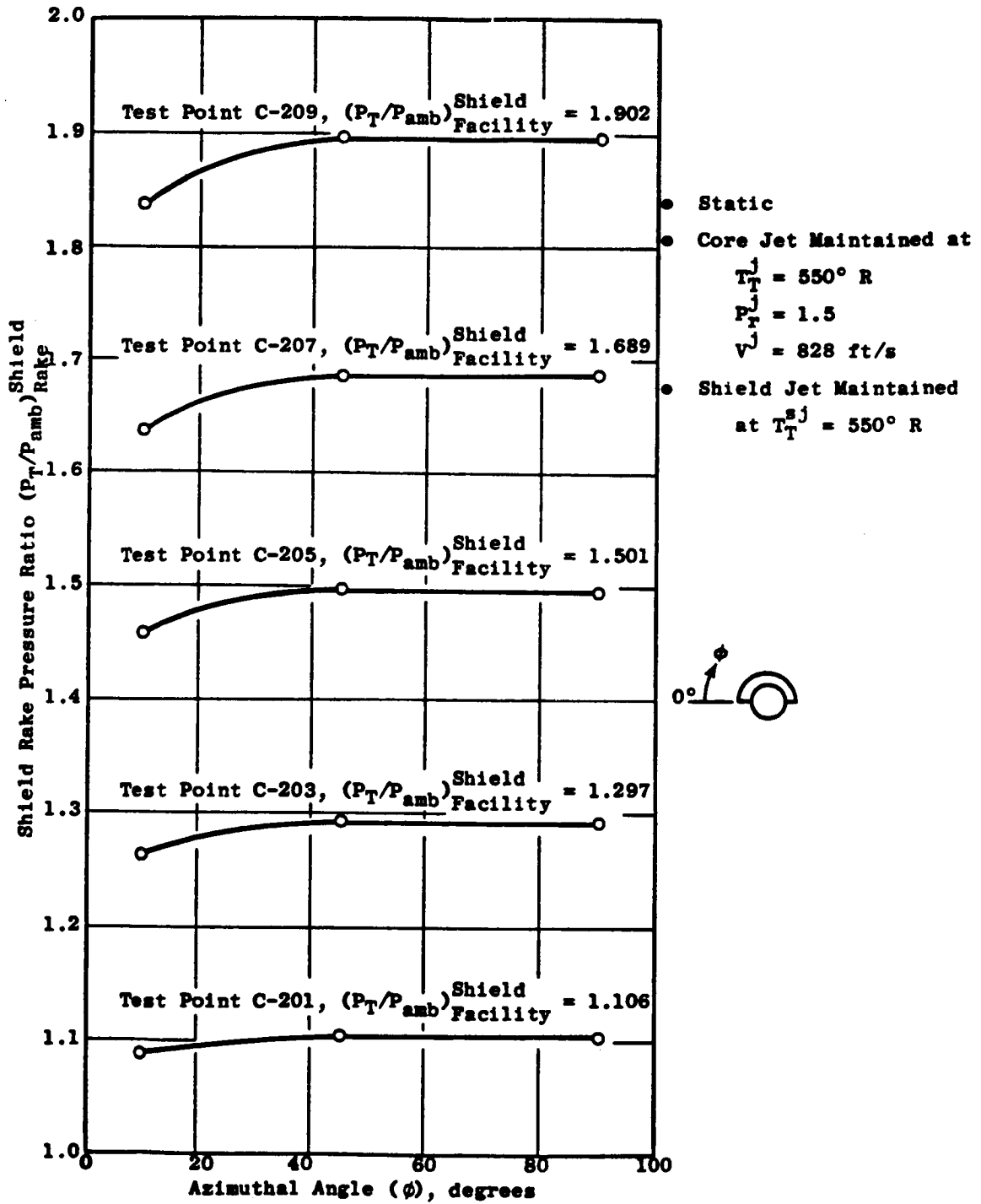


Figure 4.3.2. Azimuthal Variation of Pressure Ratio Measured by the  $P_T$  Rakes at the Shield Exit Plane - Indicating the Loss in Total Pressure Near the Edges of the Shield Jet.

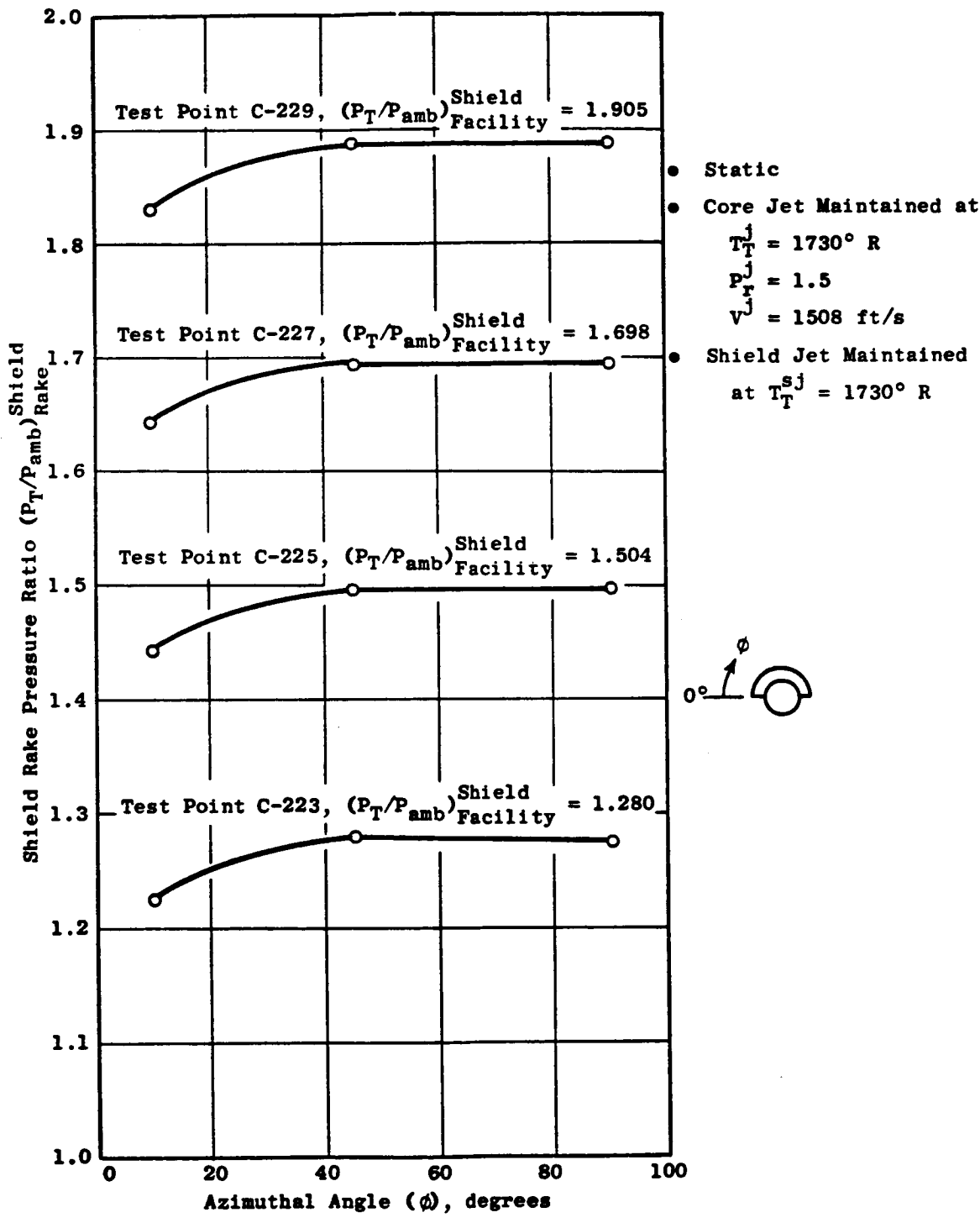
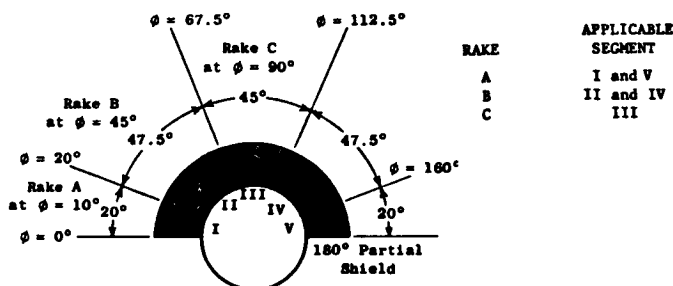


Figure 4.3.3. Azimuthal Variation of Pressure Ratio Measured by the  $P_T$  Rakes at the Shield Exit Plane - Indicating The Loss in Total Pressure Near the Edges of the Shield Jet.

calculation, the shield exit area was suitably distributed into five segments as shown in the sketch below:



and, for a given test point, each of the three rake measurements was assumed to be a representative average total pressure that is applicable to one of these segments. An area weighted average total pressure at the shield exit was calculated next, using the following expression:

$$\frac{P_T^{\text{rake}}}{P_{\text{amb}}} = \frac{1}{180} \left[ \frac{2 \times 20 \times P_T^{\text{rake A}} + 2 \times 47.5 \times P_T^{\text{rake B}} + 45 \times P_T^{\text{rake C}}}{P_{\text{amb}}} \right] \quad (4.3.2)$$

$$= \frac{0.222 P_T^{\text{rake A}} + 0.528 P_T^{\text{rake B}} + 0.250 P_T^{\text{rake C}}}{P_{\text{amb}}}$$

The  $P_T$  calibration data so calculated for shield temperatures of  $T_T^{\text{SJ}} = 550^\circ\text{R}$  and  $1730^\circ\text{R}$  are presented in Figure 4.3.4 and are plotted as a function of the facility measured ( $P_T/P_{\text{amb}}$ ) data. An examination of this figure indicates: 1) no significant effect of the shield temperature on the total pressure measurements; and 2) the calibration data is linear on a line close to 45° slope. In addition, the associated percent loss,  $\Delta P_T$  (see Equation 4.3.1), in shield exit total pressure relative to the facility-measured upstream  $P_T$  (also presented in Figure 4.3.4) is observed to be in the vicinity of 1%. Based on these calibration data, the facility measured  $P_T$  has been employed to set the required aerodynamic conditions of the 180° thermal acoustic shield streams during the acoustic tests.

#### 4.3.2 MEASURED AND PREDICTED PRESSURE FIELD INTERACTIONS OF CORE AND SHIELD STREAMS

For aerodynamic flowpath development for the shield, the General Electric Stream Tube Curvature (S.T.C.) aerodynamic analysis program has been

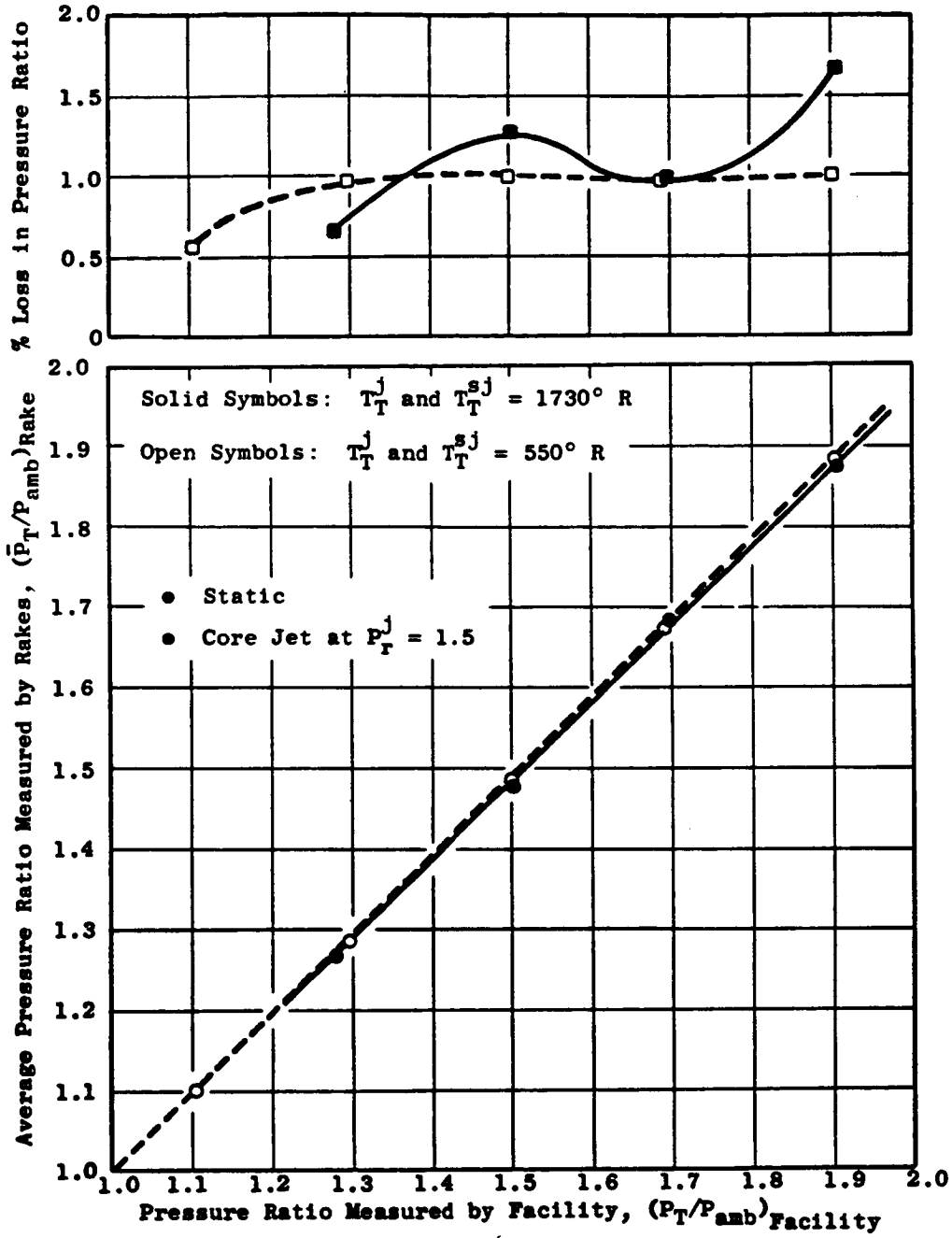


Figure 4.3.4. Total Pressure Calibration of 180° Thermal Acoustic Shield of 0.48-in. Thickness (TAS-2) at 550° R and 1730° R.

utilized (Reference 4.5). S.T.C. predicts the inviscid pressure distribution and flowfield about or inside an arbitrary axisymmetric or planar ducted body at transonic speeds. This prediction technique provides means for conducting parametric studies so that design criteria can be analytically evaluated to select configurations for experimental investigation.

The S.T.C. program solves equations of fluid motion along streamlines,  $\psi = \text{constant}$ , and along lines orthogonal to the streamlines,  $\xi = \text{constant}$  lines. The variable  $\xi$  is introduced to avoid conflict with the velocity potential  $\phi$  which is only valid when the flow is irrotational. Thus, this enables STC to solve rotational flow problems.

S.T.C. is, therefore, capable of handling complexities that arise when two coincident streamlines with different velocities and stagnation properties converge. A good example is the thermal acoustic shield problem.

S.T.C. analysis of a shield configuration with coplanar shield and core nozzle exit planes indicated the presence of an adverse pressure gradient generated on the shield inner flowpath near its exit plane. The local overpressurization thus lowered the pressure drop across the duct and reduced the mass flow, thus degrading the shield discharge coefficient. Figures 4.3.5 and 4.3.6 show the S.T.C. flowfield solution as a graphic representation of the streamlines and variation of static pressure throughout the flowfield, respectively. The overpressure phenomenon at the shield exit plane is the result of communication between the higher static pressure region at the choked convergent core nozzle exit and the subsonic flowfield of the shield duct.

Subsequent S.T.C. modeling of a setback shield nozzle indicated no overpressurization in the shield throat plane region. Examples of this flowfield solution are shown in Figures 4.3.7 and 4.3.8. The setback shield nozzle was thus selected for the final model design.

As an illustration of the validity of the S.T.C. predictions, a one-to-one comparison of the static pressure distribution on the plug surface of configuration TAS-1 is presented next. Figure 4.3.9 shows good agreement



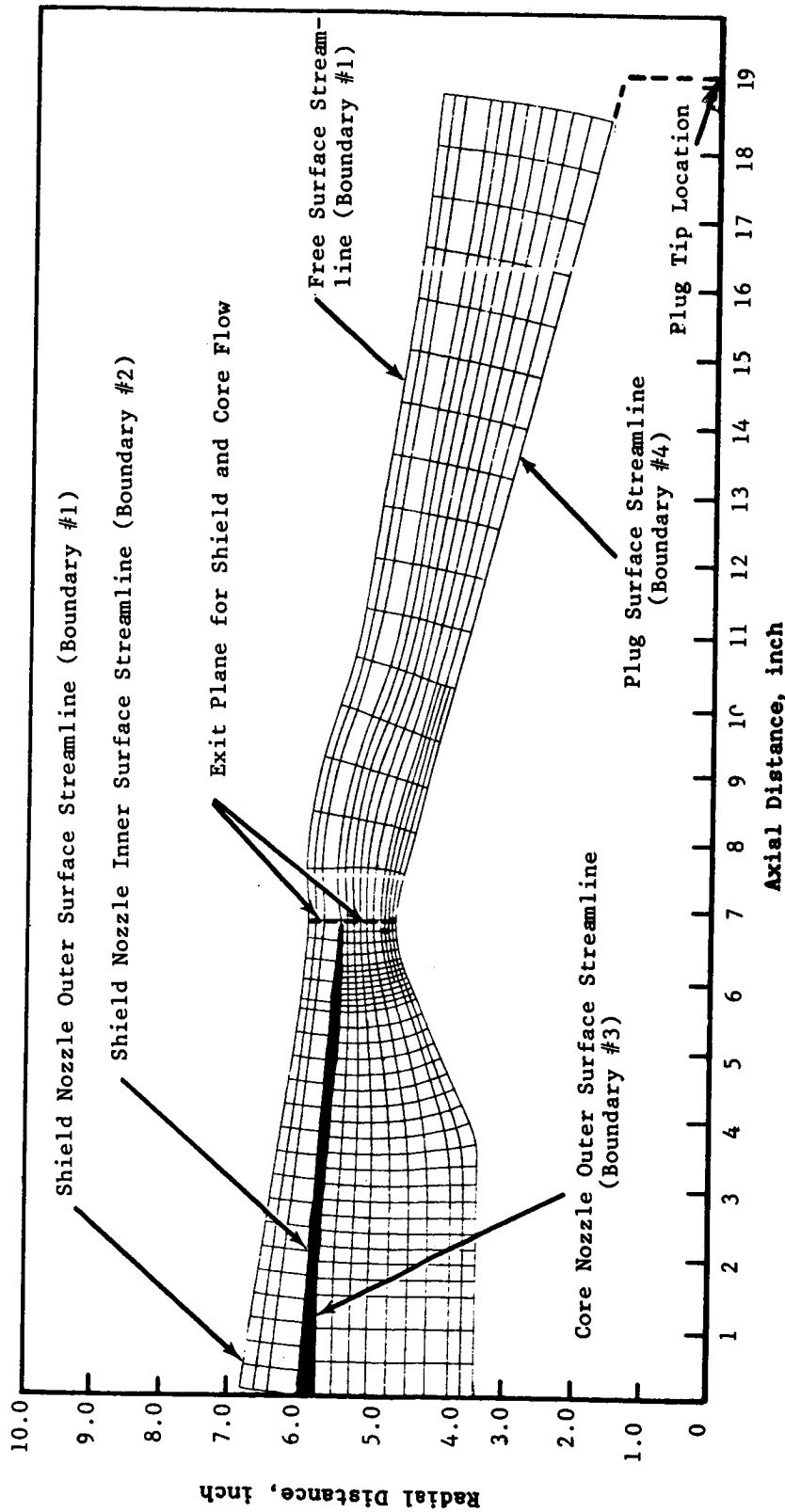


Figure 4.3.5. Streamline Distribution for the Shield and Core Nozzles with Coplanar Exits.

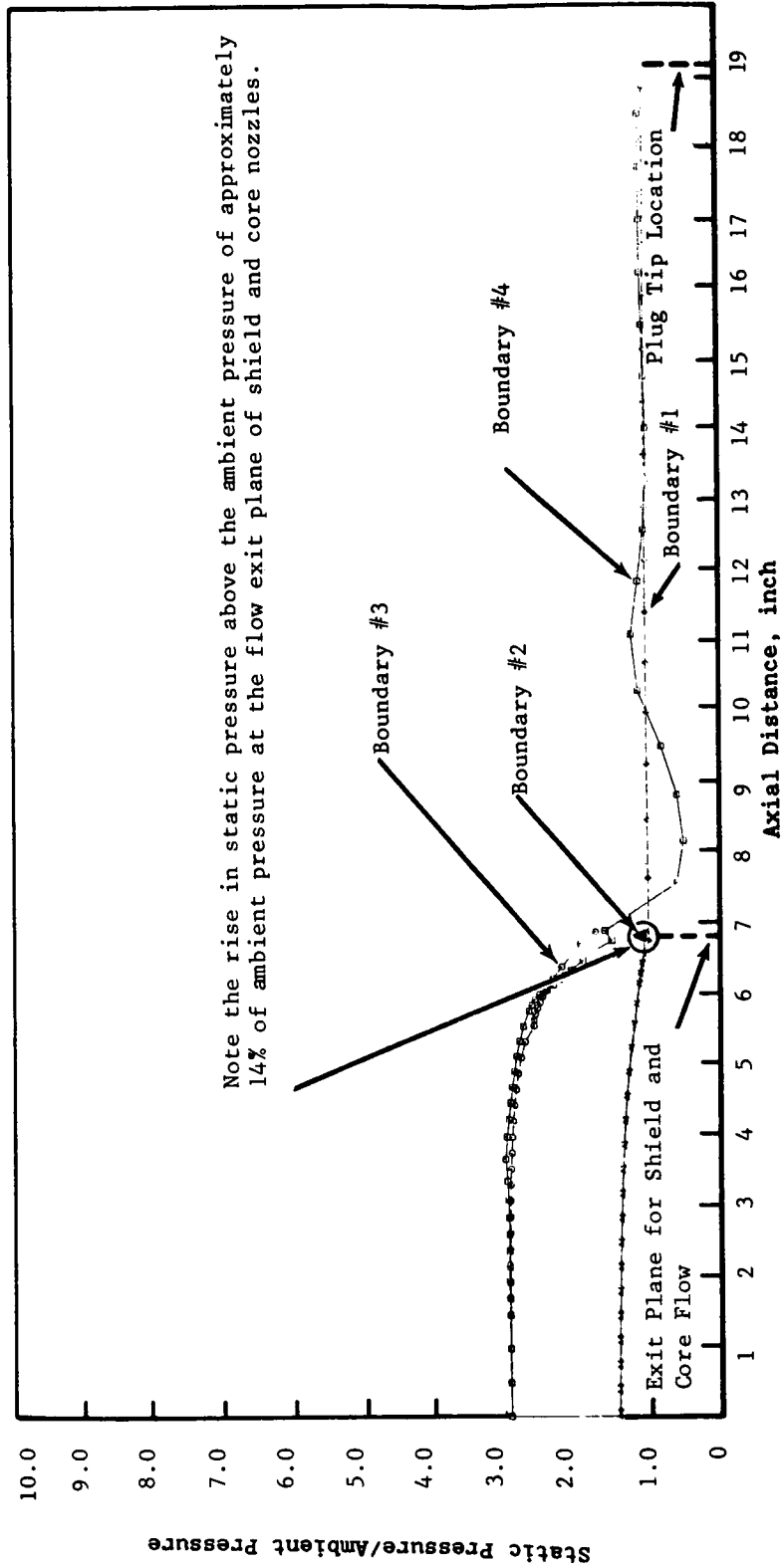


Figure 4.3.6. Static Pressure Distribution Along the Various Boundaries (see Figure 4.3.5 the Definition of the Boundaries) of the Shielded Nozzle.

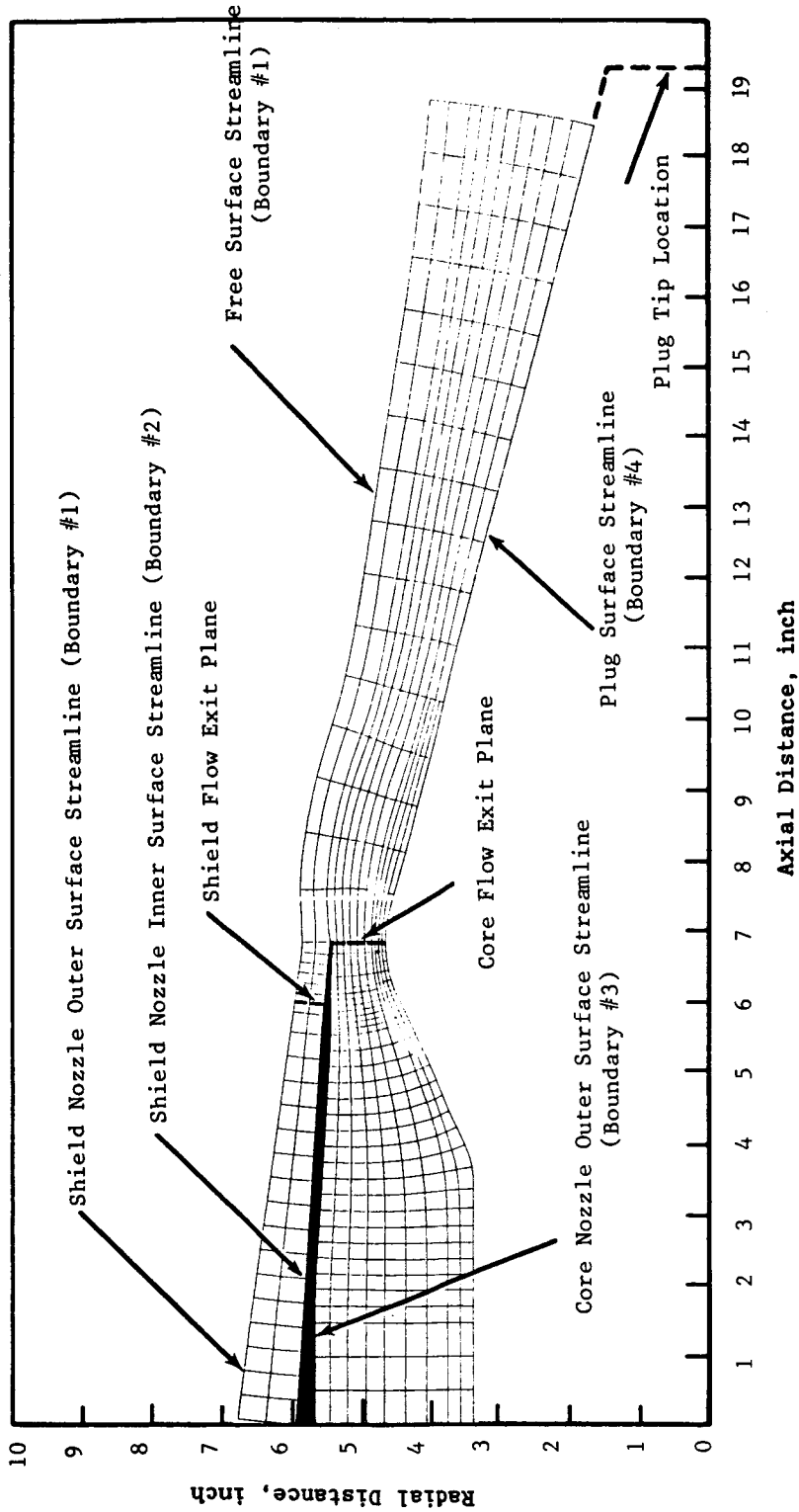


Figure 4.3.7. Streamline Distribution for the Shield and Core Nozzles with a Stagger of Approximately One Core Annulus Height.

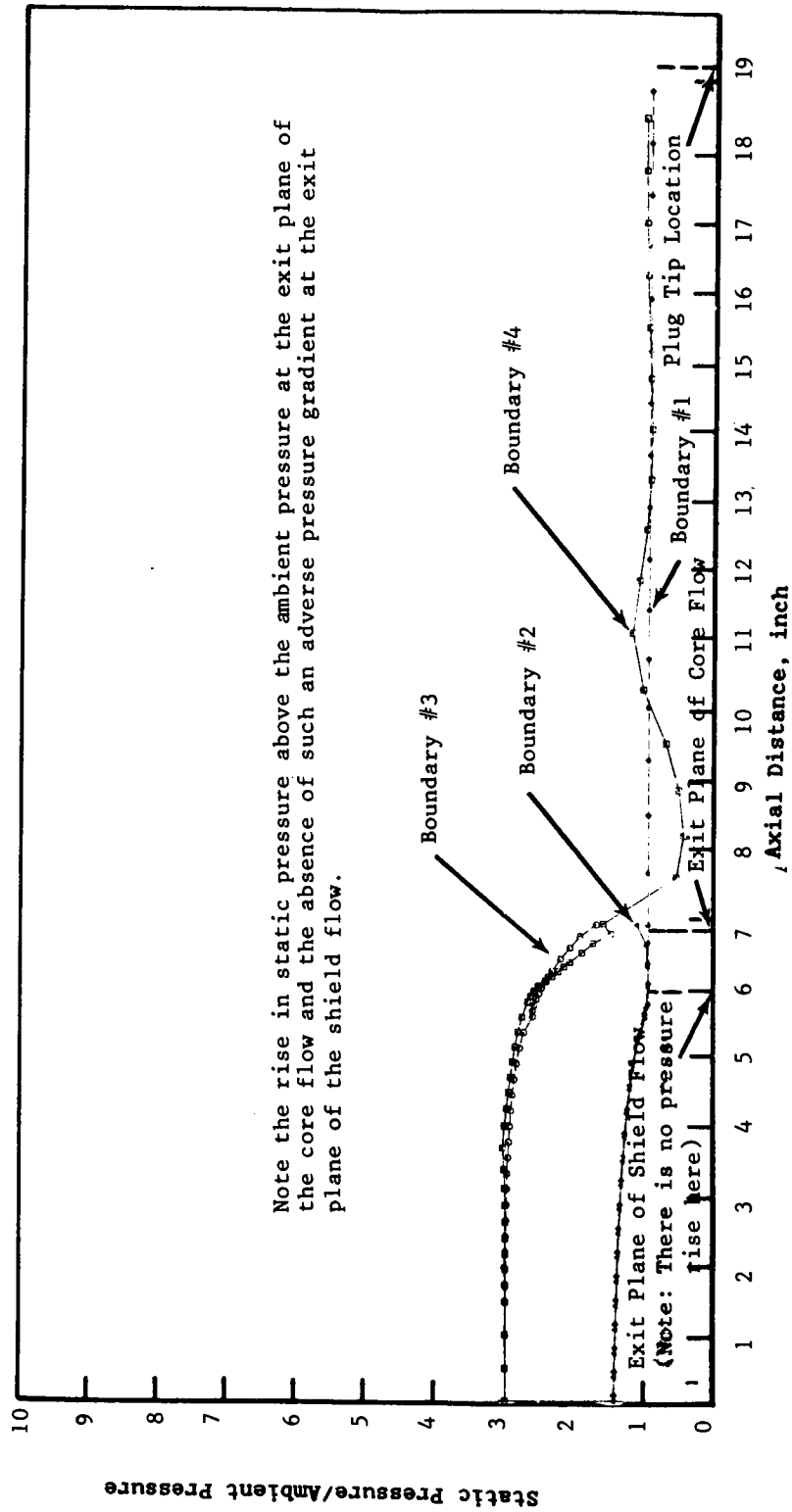


Figure 4.3.8. Static Pressure Distribution Along the Various Boundaries (see Figure 4.3.7 for the Definition of the Boundaries) of the Shielded Nozzle.

— Predictions of GE STC Computer Program at  
 Typical Takeoff Conditions

○ Measured Data

Configuration TAS-1, Test Point 111,  $V_J = 2319$  ft/sec,  $P_T^J = 2.9$ ,  $T_T^J = 1683^\circ$  R,  $V_a/c = 0$

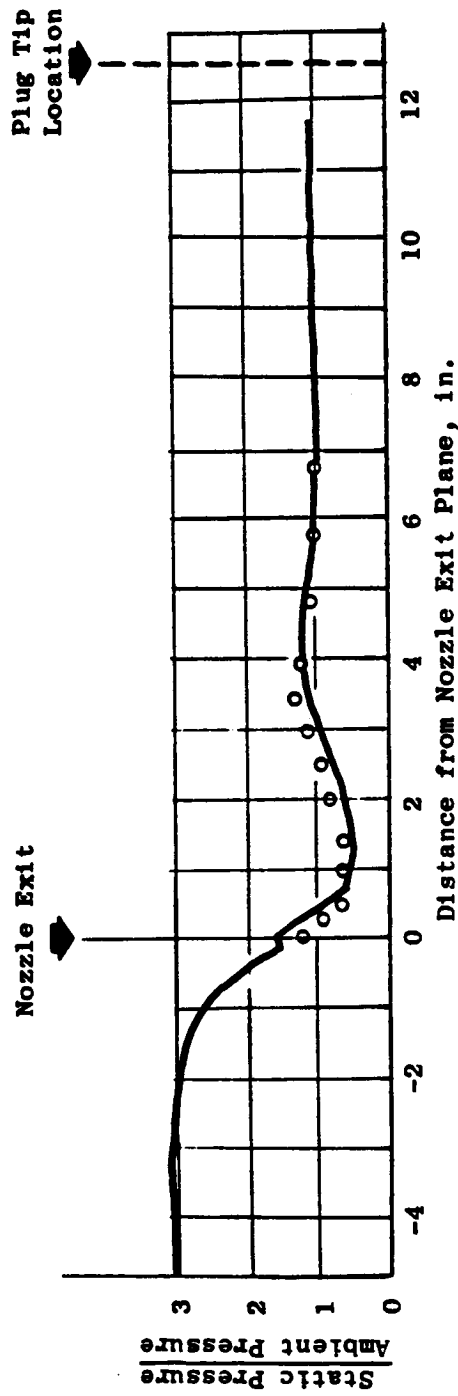


Figure 4.3.9. Comparison of Measured and Predicted Static Pressure Distribution on the Plug Surface.

between the predictions by the S.T.C. program and the measured static pressure distribution on the plug surface of configuration TAS-1 at a typical takeoff condition. The plug surface static pressure just downstream of the throat plane falls below the ambient pressure which indicates flow expansion around the crown of the plug. A rise above the ambient pressure further downstream indicates the presence of a shock.

Next, the measured interactions between the core and shield streams are discussed. Static pressure data were measured on the sleeves of the 180° shield of 0.48" thickness and the 360° shield of 0.48" thickness between the core and shield jet exit planes. Figures 4.3.10 and 4.3.11 respectively show the static pressure distribution in the vicinity of the shield exit for a supersonic core jet for configurations TAS-2 and TAS-4. For both the configurations, a static pressure rise in the shield jet flow is noted close to the core jet exhaust, confirming the predictions of the S.T.C. program. This overpressurization in the shield jet is not expected to affect the flow rates since the shield jet in each of the test cases is fully expanded upstream of the overpressurization location.

Static pressure data were measured on the sleeve of the 180° shield of 0.48" thickness for a range of shield conditions (viz.,  $T_T^{sj} \approx 1730^\circ R$  and  $115 \leq Pr^{sj} \leq 1.9$ ) keeping the core jet subsonic in order to pinpoint the cause of the overpressurization noted above. Figure 4.3.12 shows that the static pressure continues to expand below the ambient pressure when the core jet is subsonic indicating that the overpressurization of the shield flow was due to the static pressure feedback from the supersonic core jet to the subsonic shield jet. An interesting feature in the case of the subsonic core jet is that the static pressure of the shield jet falls below ambient pressure, instead of remaining uniformly at ambient pressure level. A physical explanation for the above noted observation can be given by examining the static pressure distribution on the plug surface of configuration TAS-1 for a subsonic flow condition (see Figure 4.3.13). The static pressure just past the crown of the plug (i.e., the throat plane) falls below the ambient condition for the subsonic core jet due to rapid acceleration of the flow around the plug crown and then monotonically reaches the ambient level for

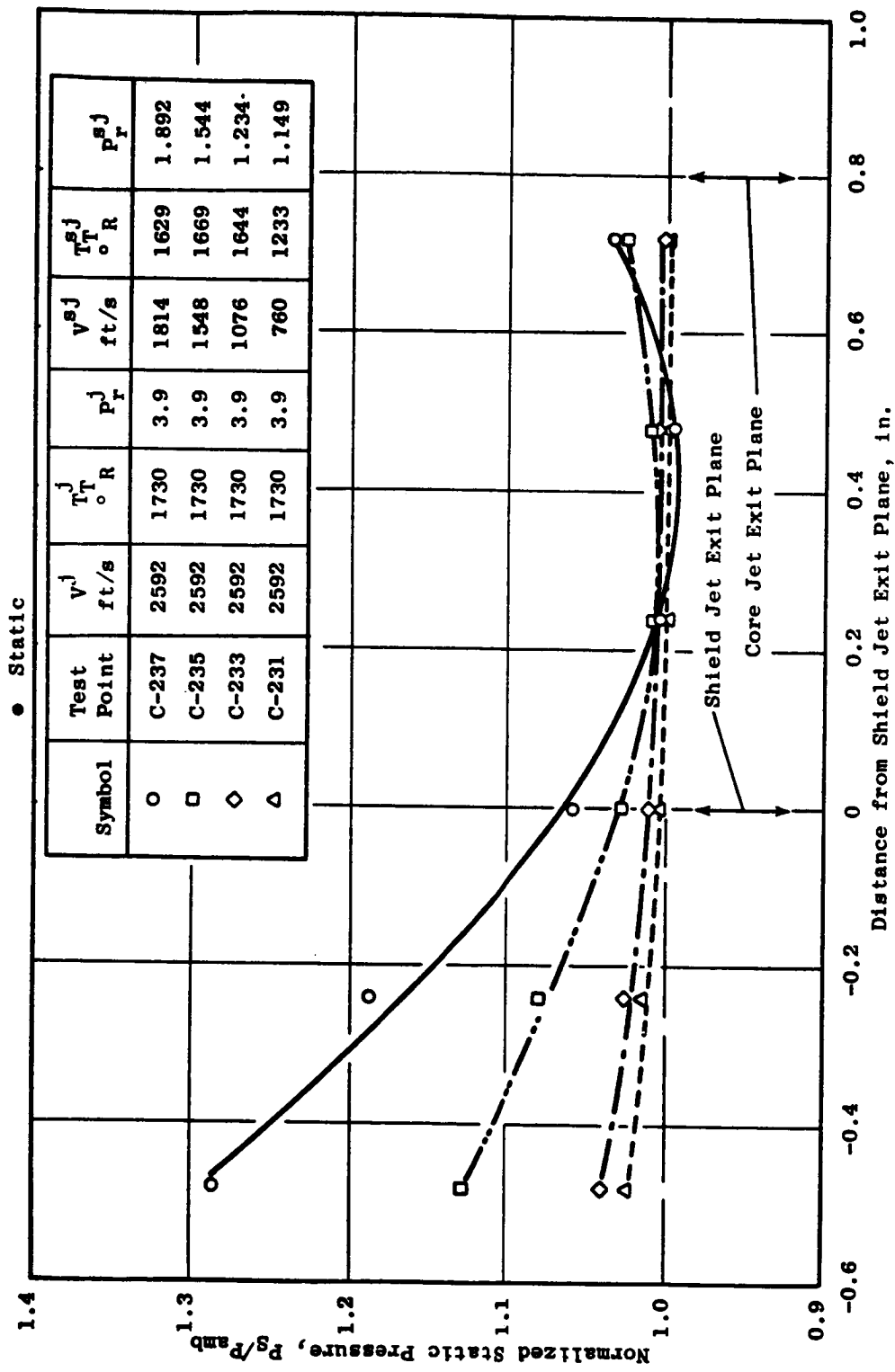


Figure 4.3.10. Static Pressure Distribution in the Vicinity of the Shield Exit for a Supersonic Core Jet for Configuration TAS-2.

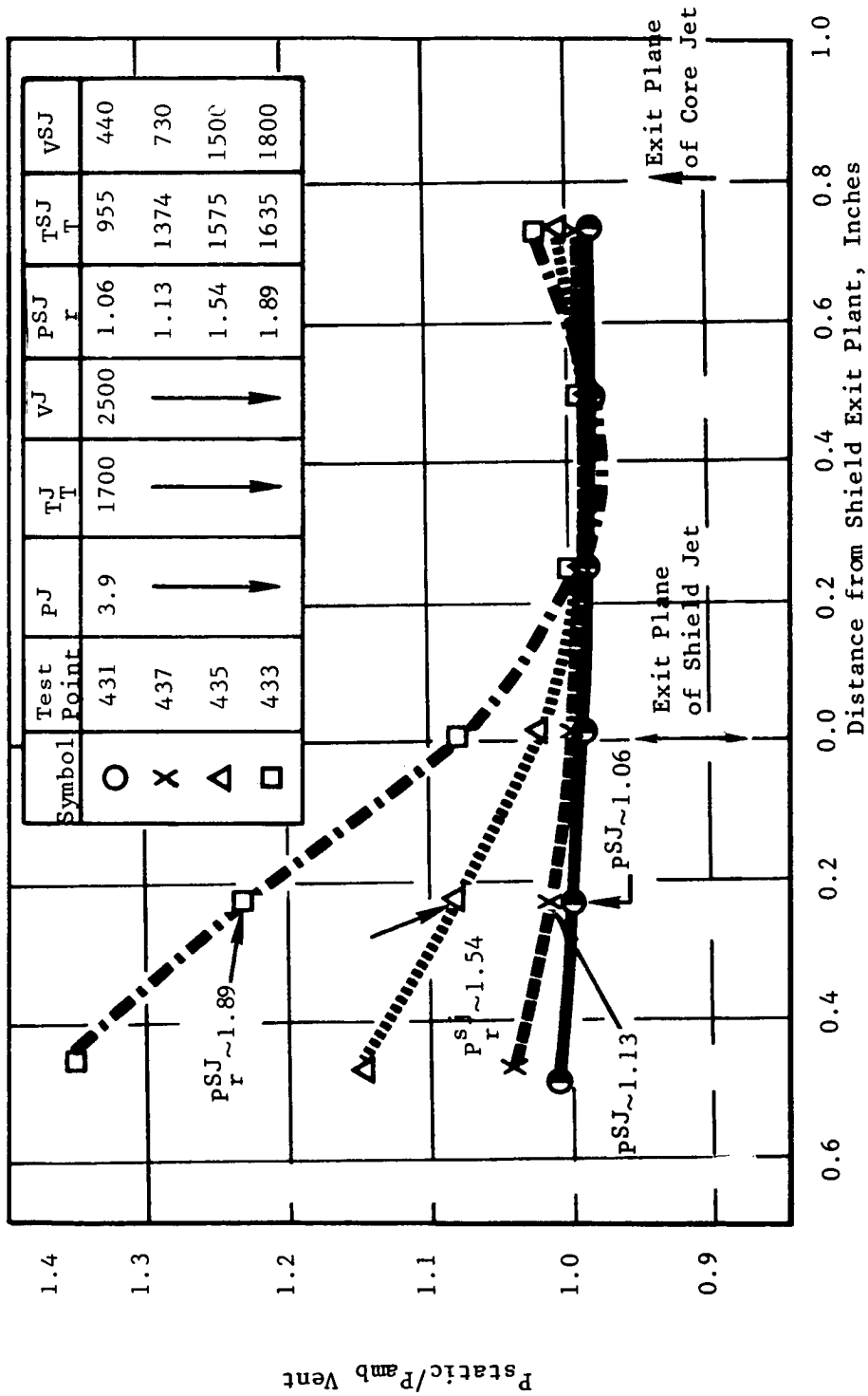


Figure 4.3.11. Static Pressure Distribution in the Vicinity of the Shield Exit for a Supersonic Core Jet for Configuration TAS-4.



• Static

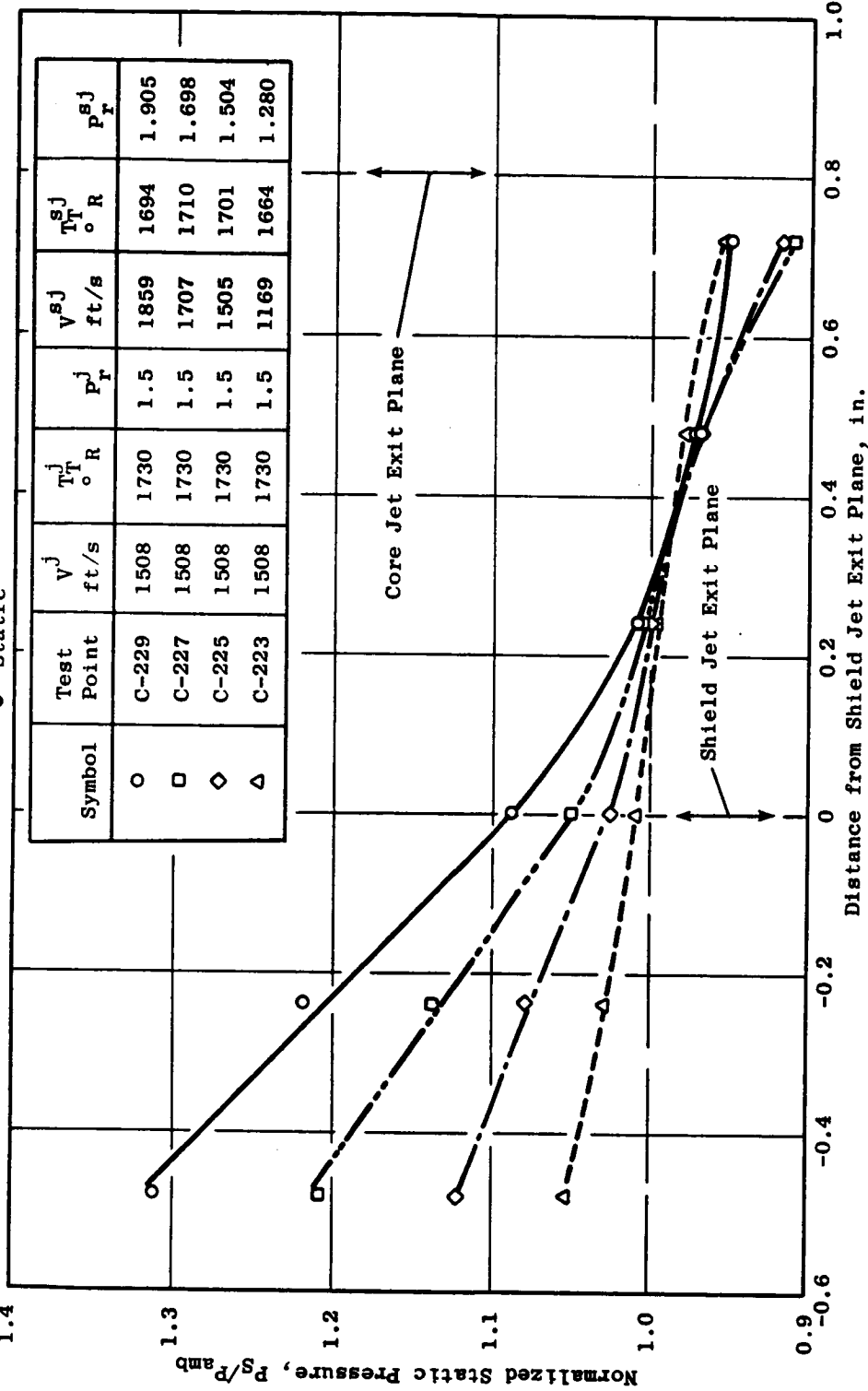


Figure 4.3.12. Static Pressure Distribution in the Vicinity of the Shield Exit for a Subsonic Core Jet for Configuration TAS-2.

Test Point	$v_j$ ft/sec	$P_T^j$	$T_T^j, \text{ } ^\circ\text{R}$	$V_a/c$
101 (Subsonic Case)	1340	1.558	1253	0

Plug Length = 13.31 in. (2.35 Deq)

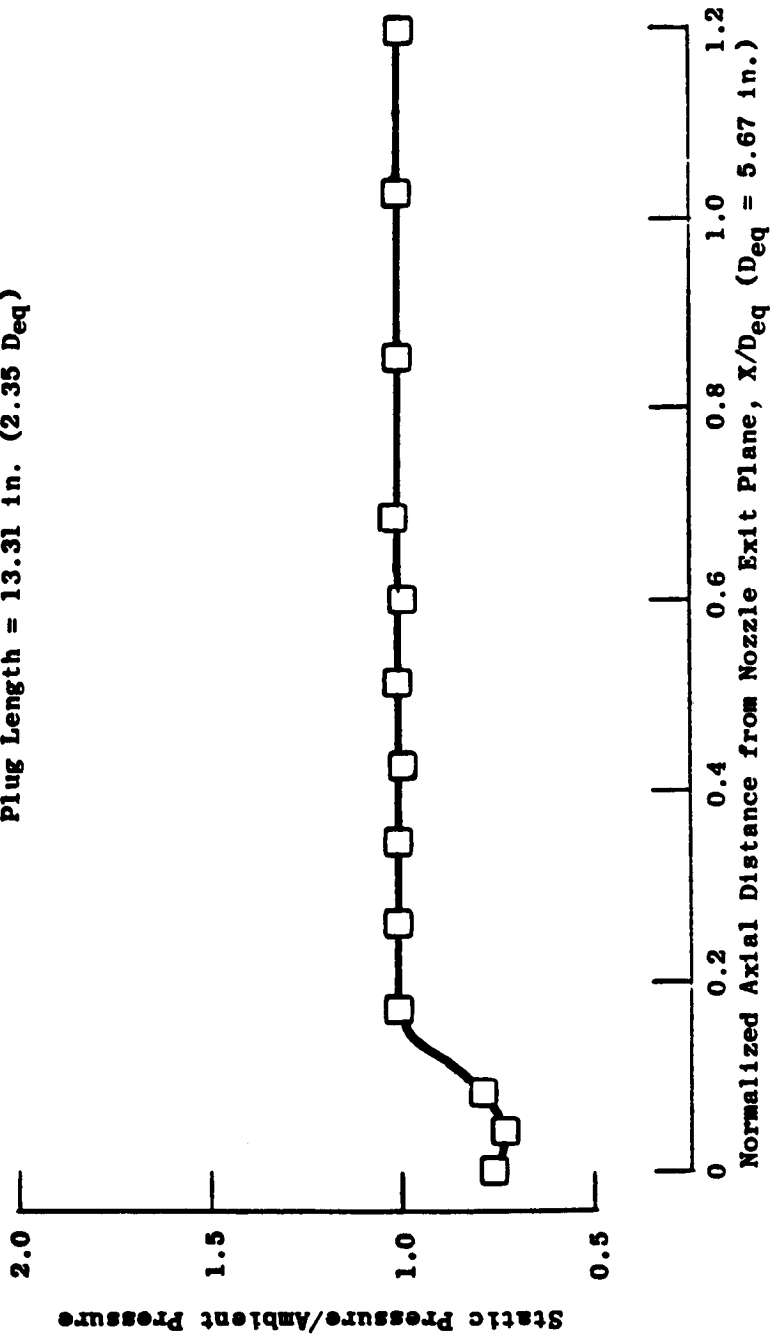


Figure 4.3.13. Static Pressure Distribution on the Plug Surface of Configuration TAS-1 for Subsonic Flow Condition.

$X/D_{eq} \approx 0.2$ . The influence of the subambient pressure region near the crown of the plug can be felt upstream of the core and shield jet flows as both are subsonic flows, and this leads to the noted expansion of the shield jet below the ambient pressure.

#### 4.3.3 INFLUENCE OF THERMAL ACOUSTIC SHIELDS ON THE BASE DRAG OF 32 CHUTE SUPPRESSOR NOZZLE UNDER HEATED, SIMULATED FLIGHT AND STATIC CONDITIONS

One of the significant considerations in employing a thermal acoustic shield flow on a mechanical suppressor nozzle with chutes is the increase in base drag of the suppressor due to the presence of a shield flow over the chutes. The presence of a flow over the chutes reduces ventilation in the base region of the chutes, leading to a reduction in base pressure and consequent increase in the base drag. In order to evaluate the influence of the thermal acoustic shield on the base drag of the 32 chute suppressor, static pressure measurements were made in the chute base region during the engine operating line studies of configurations TAS-6, TAS-7, TAS-8 and TAS-9, for both static and simulated flight conditions. This subsection briefly describes the method of estimating the percent thrust loss due to base drag and discusses the salient results obtained from the base pressure measurements.

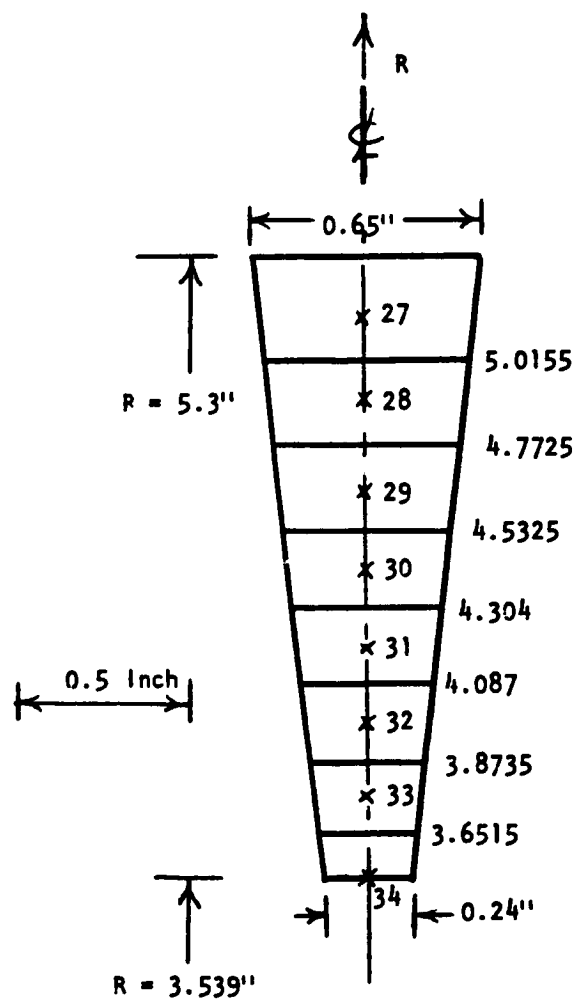
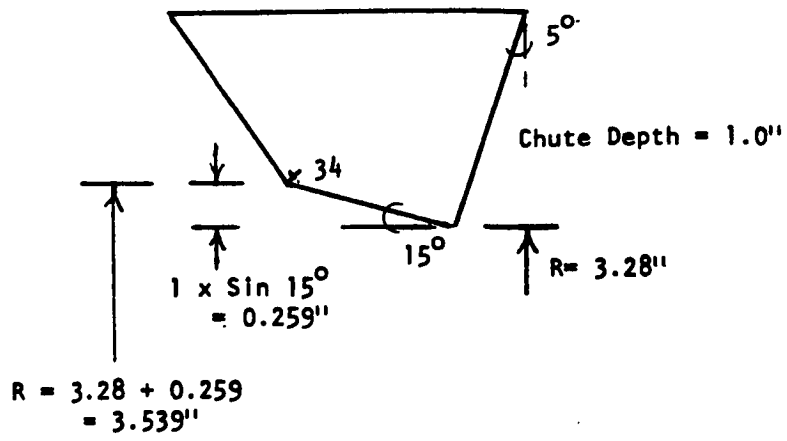
Figure 4.3.14 shows the location of static pressure instrumentation in the chute region of the 32 chute suppressor nozzle and other pertinent dimensions. Each of the static pressure taps has an area associated with it over which the static pressure is assumed to be constant. An area-weighted average chute base pressure is determined by the following equation:

$$\bar{P} = \frac{\sum_{i=1}^{N^e} P_i A_i}{\sum_{i=1}^{N^e} A_i} \quad (4.3.3)$$

where  $N^e$  is the total number of elements within the chute

$A_i$  is the elemental area and

$P_i$  is the static pressure over the  $i^{\text{th}}$  element.



Ps Tap #	Radius, Inch
27	5.134
28	4.897
29	4.648
30	4.417
31	4.191
32	3.983
33	3.764
34	3.539

FIGURE 4.3.14. SKETCH SHOWING THE LOCATION OF STATIC PRESSURE TAPS ON A CHUTE OF THE 32 CHUTE SUPPRESSOR NOZZLE.

The base drag per chute is given by:

$$F_d = (P_{amb} - \bar{P}) A^e \quad (4.3.4)$$

where  $A^e = \sum_{i=1}^{N^e} A_i$

The total base drag is given by:

$$F_D = NF_d \quad (4.3.5)$$

where N is the number of chutes.

The ideal thrust of the suppressor is given by:

$$F_S = \dot{W}_S V_S / g \quad (4.3.6)$$

where

$\dot{W}_S$  is the weight flow rate of the suppressor,  $V_S$  is the ideally expanded jet velocity of the suppressor, and  $g$  is the gravitational constant. Hence, the percent thrust loss coefficient due to chute base drag is:

$$\Delta C_{FGS} = \frac{F_D}{F_S} \times 100 \quad (4.3.7)$$

For the configurations TAS-7 and TAS-8 which employ partial shields, the base pressure measurements are made on the shield side. The base pressures on the side without the shield are assumed to be the same as in Configuration TAS-6. Hence, the total base drag for configuration TAS-7 is calculated as:

$$(F_D)_{TAS-7} = 16 \left[ P_{amb} - (\bar{P})_{TAS-6} \right] A^e + 16 \left[ P_{amb} - (\bar{P})_{TAS-7} \right] A^e \quad (4.3.8)$$

where  $(\bar{P})_{TAS-6}$  is the area weighted static pressure for configuration TAS-6 and  $(\bar{P})_{TAS-7}$  is the area weighted static pressure for configuration TAS-7, measured on the shield side. Similarly, the base pressure for configuration TAS-8 is calculated as:

$$(F_D)_{TAS-8} = 16 \left[ P_{amb} - (\bar{P})_{TAS-6} \right] A^e + 16 \left[ P_{amb} - (\bar{P})_{TAS-8} \right] A^e \quad (4-3-9)$$

where  $(\bar{P})_{TAS-8}$  is the area weighted static pressure for configuration TAS-8, measured on the shield side.

Figures 4.3.15 and 4.3.16 respectively show the radial variation of normalized chute base pressure for 32 chute suppressor nozzle (configuration TAS-6) and 32 chute suppressor nozzle with 360° shield of 0.48" thickness (configuration TAS-9) over a range of core jet pressure ratios typical of an engine operating line. The influence of simulated flight for both the configurations can be seen to be a reduction of base pressures compared to the static case, due to the reduced penetration of the chute by the ambient air. This results in lesser chute ventilation and hence larger base drag. Note that for the same core jet condition, the influence of the thermal acoustic shield has been to reduce the base pressure which again can be attributed to the reduction of the ventilation of the chutes when there is a flow over the chutes. It should also be pointed out that the simulated flight velocity reduces the base pressure of the 32 chute suppressor alone to a larger extent compared to the 32 chute suppressor with a shield, since the chutes with a shield are to some extent insulated, from the simulated flight velocity by the thermal acoustic shield flow.

Figure 4.3.17 shows the variation of  $\Delta C_{FGS}$  with suppressor pressure ratio for the 32 chute suppressor (configuration TAS-6) for static and simulated flight cases. Since the chute base pressure radial distribution is not significantly influenced by the suppressor pressure ratio (see Figure 4.3.15) and since the ideal thrust of suppressor increases with pressure ratio,  $\Delta C_{FGS}$  is found to decrease with an increase in the suppressor pressure ratio. Also, note that the base drag coefficient increases when there is a simulated flight velocity. Figures 4.3.18, 4.3.19 and 4.3.20 similarly show the variation of  $\Delta C_{FGS}$  with the suppressor pressure ratio for configurations TAS-7, TAS-8 and TAS-9, respectively.

Symbol	$P_r^j$
○	1.55
□	2.06
◇	2.70
△	3.86

○  $V_{a/c} = 0$  for Open Symbols  
 ○  $V_{a/c} = 400$  fps for Solid Symbols

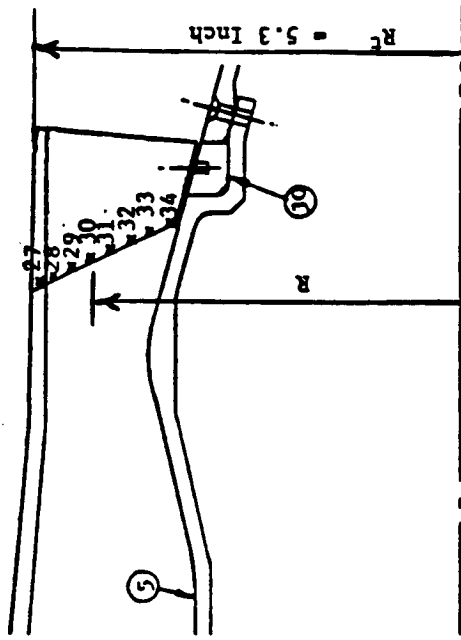
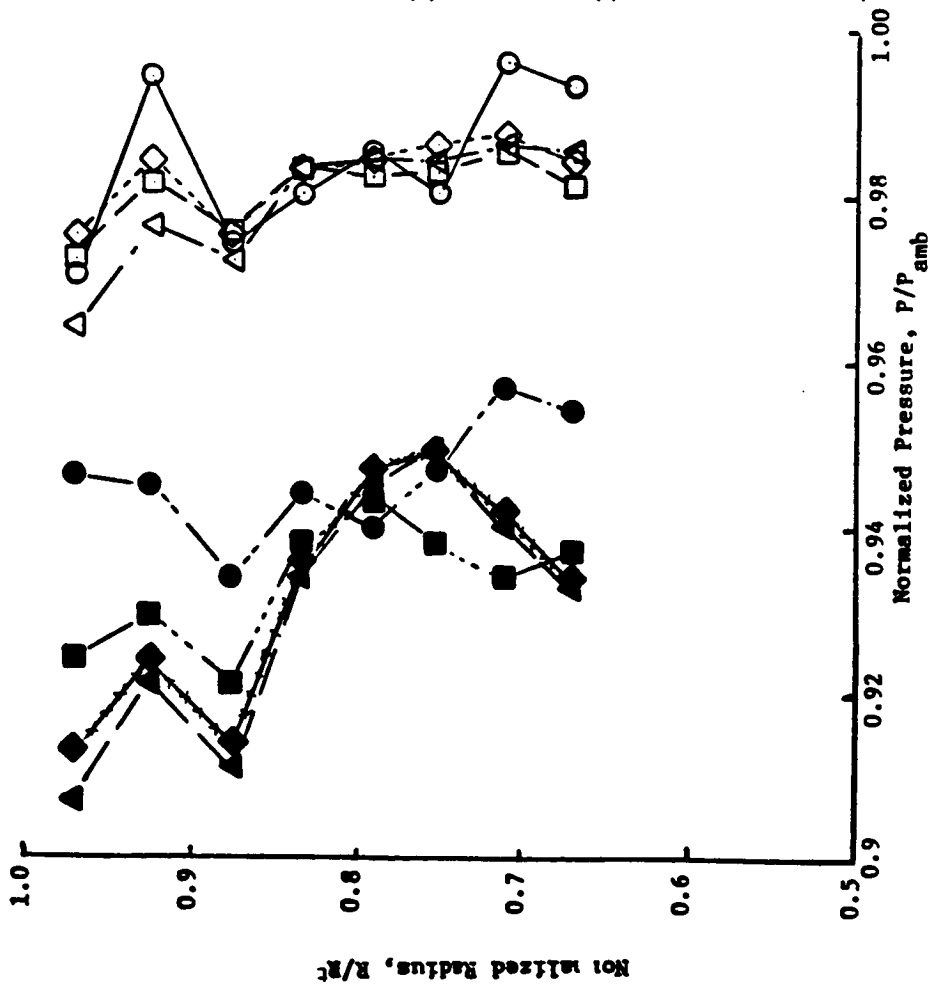


FIGURE 4.3.15. RADIAL VARIATION OF NORMALIZED CHUTE BASE PRESSURE FOR 32-CHUTE SUPPRESSOR NOZZLE FOR STATIC AND FLIGHT POINTS.

SYMBOL	$r_j$
○	1.56
□	2.07
◇	2.70
△	3.87

● 32-CHUTE SUPPRESSOR WITH 360° SHIELD OF 0.48" THICKNESS  
(TAS-9) @  $v^s_j/v^j = 0.6$  KEEPING  $T^s_j = T^s_j$

○  $V_a/c = 0$  FOR OPEN SYMBOLS

●  $V_a/c = 400$  fps FOR SOLID SYMBOLS

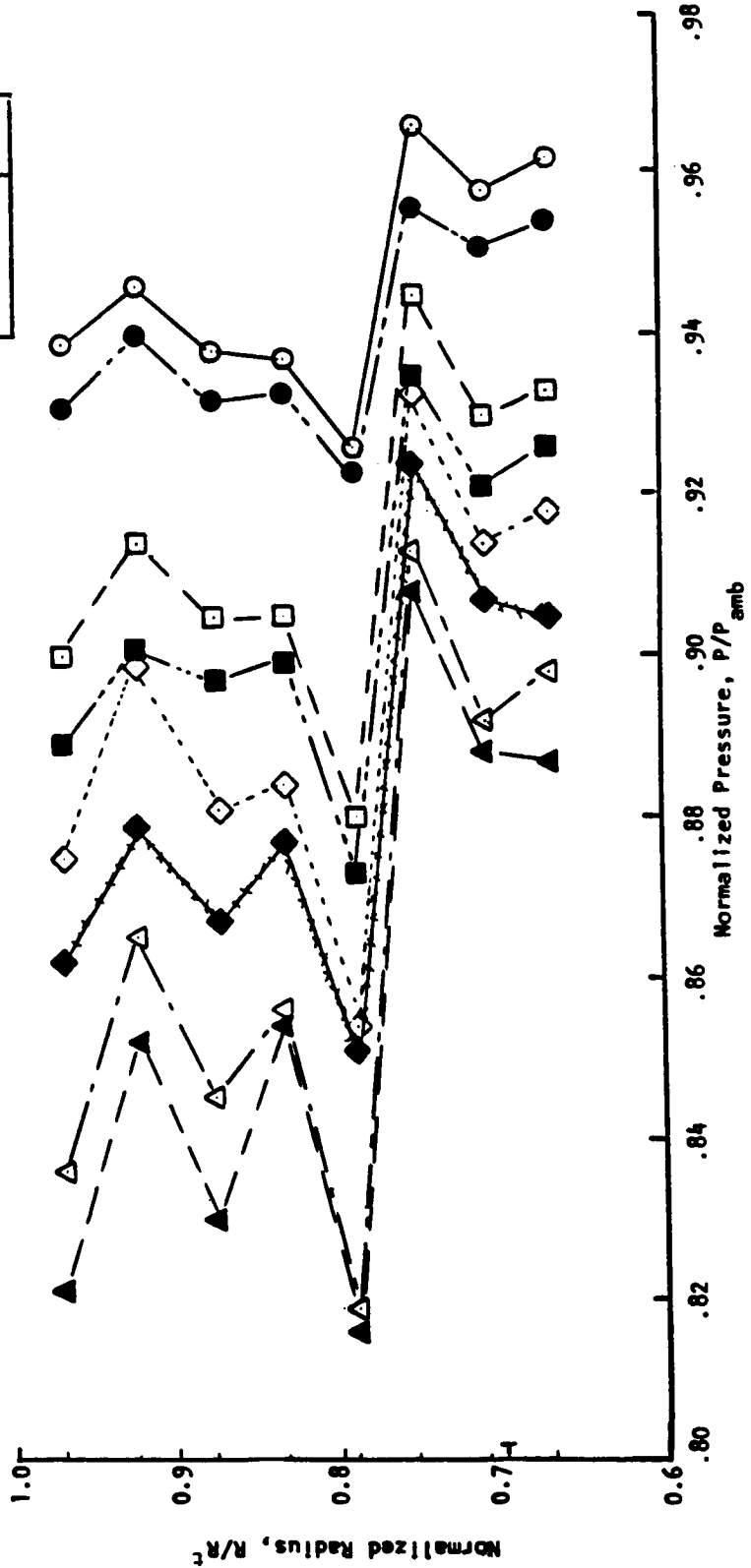


FIGURE 4.3.16. RADIAL VARIATION OF NORMALIZED CHUTE BASE PRESSURE FOR 32-CHUTE SUPPRESSOR NOZZLE WITH 360° SHIELD OF 0.48" THICKNESS FOR STATIC AND FLIGHT POINTS.



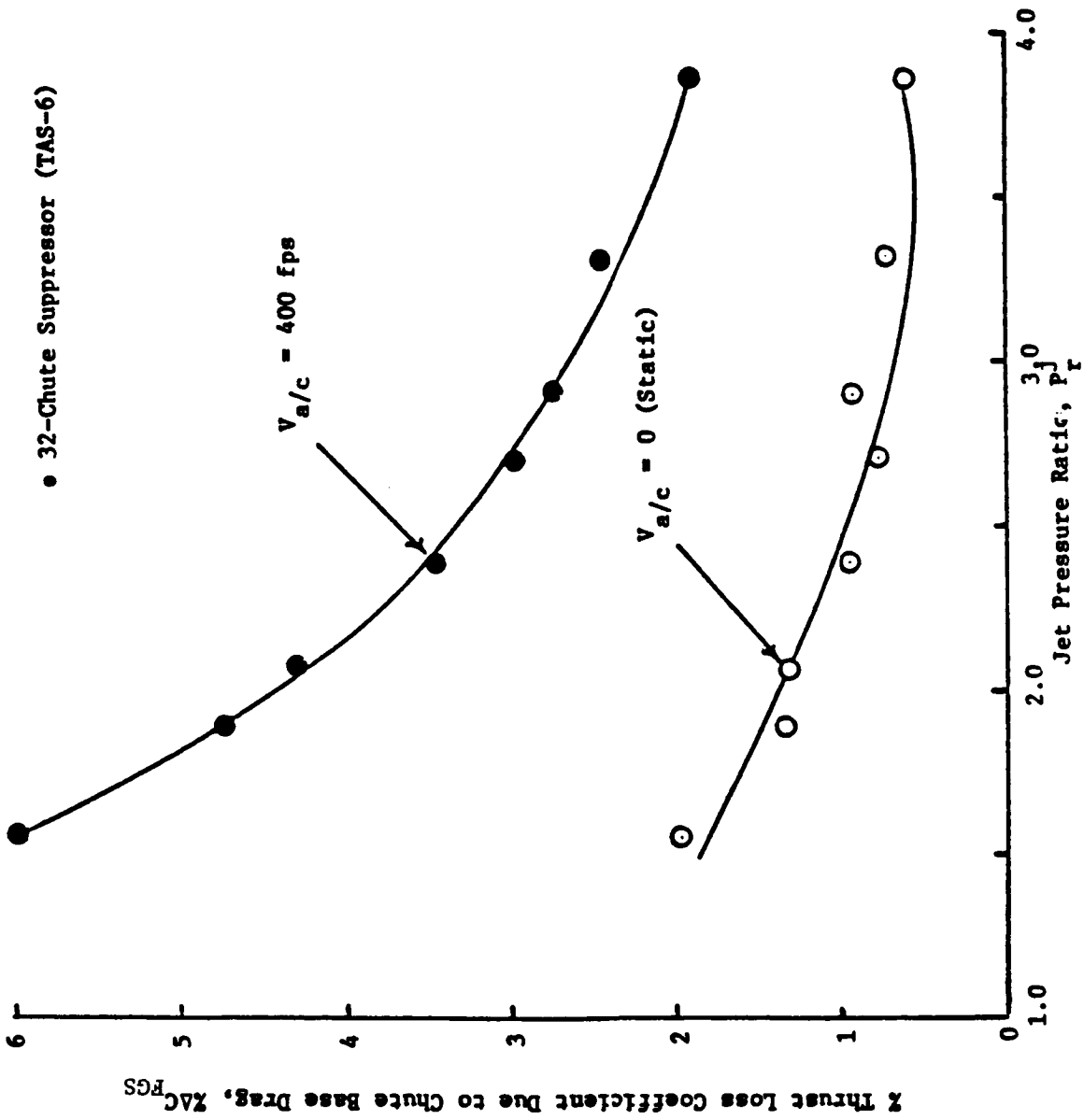


FIGURE 4.3.17. VARIATION OF  $Z$  THRUST LOSS COEFFICIENT DUE TO CHUTE BASE DRAG AS A FUNCTION OF JET PRESSURE RATIO FOR 32-CHUTE SUPPRESSOR NOZZLE (TAS-6) FOR STATIC AND FLIGHT TESTS.

● 32-Chute Suppressor with 180° Shield  
of 0.48" Thickness (TAS-7)

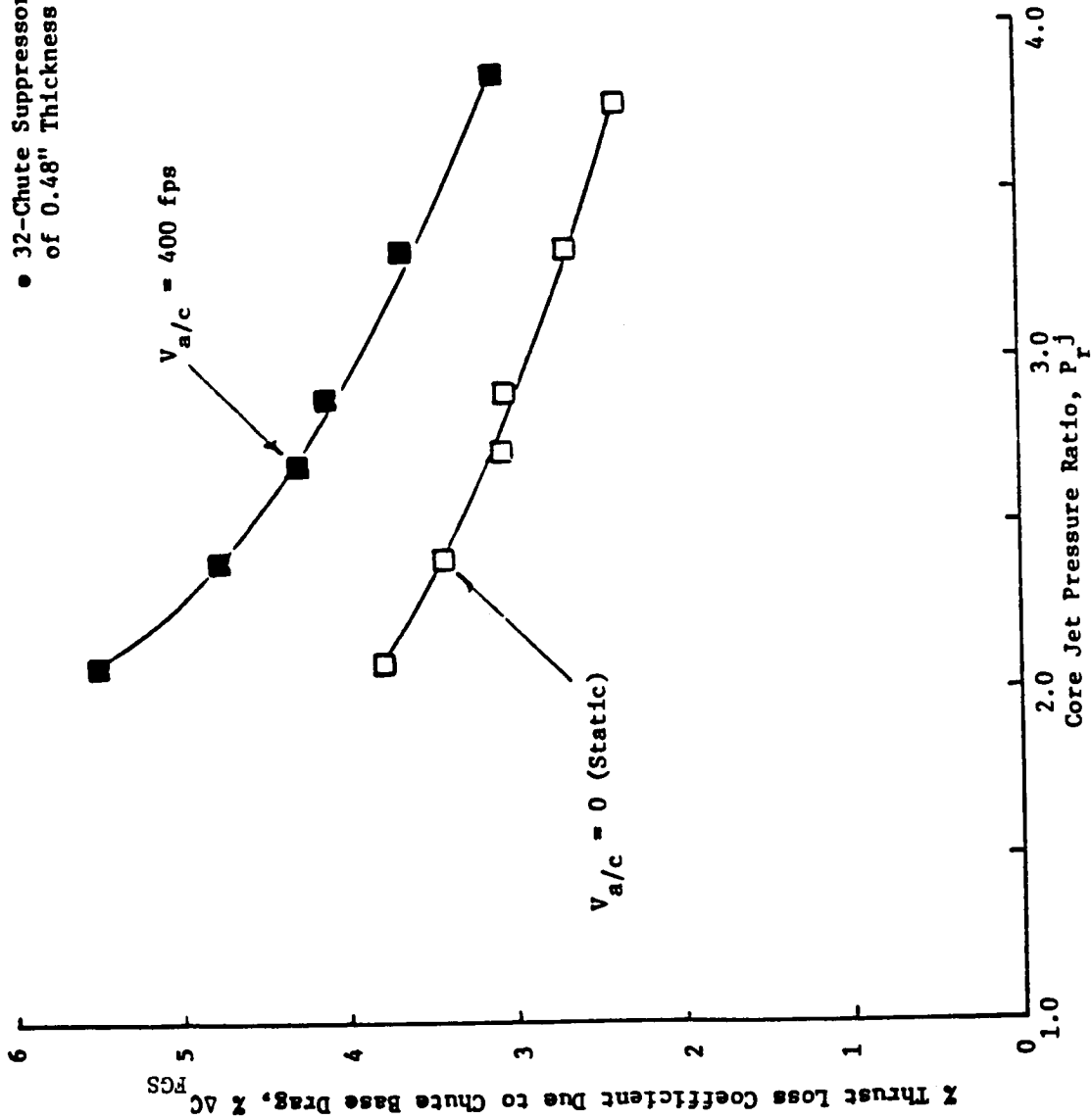


FIGURE 4.3.18. VARIATION OF  $\%$  THRUST LOSS COEFFICIENT DUE TO CHUTE BASE DRAG AS A FUNCTION OF CORE JET PRESSURE RATIO FOR 32-CHUTE SUPPRESSOR NOZZLE WITH 180° THERMAL ACOUSTIC SHIELD OF 0.48" THICKNESS (TAS-7) FOR STATIC AND FLIGHT TESTS.

- 32 Chute Suppressor with 180° Shield of 0.97" Thickness (TAS-8)

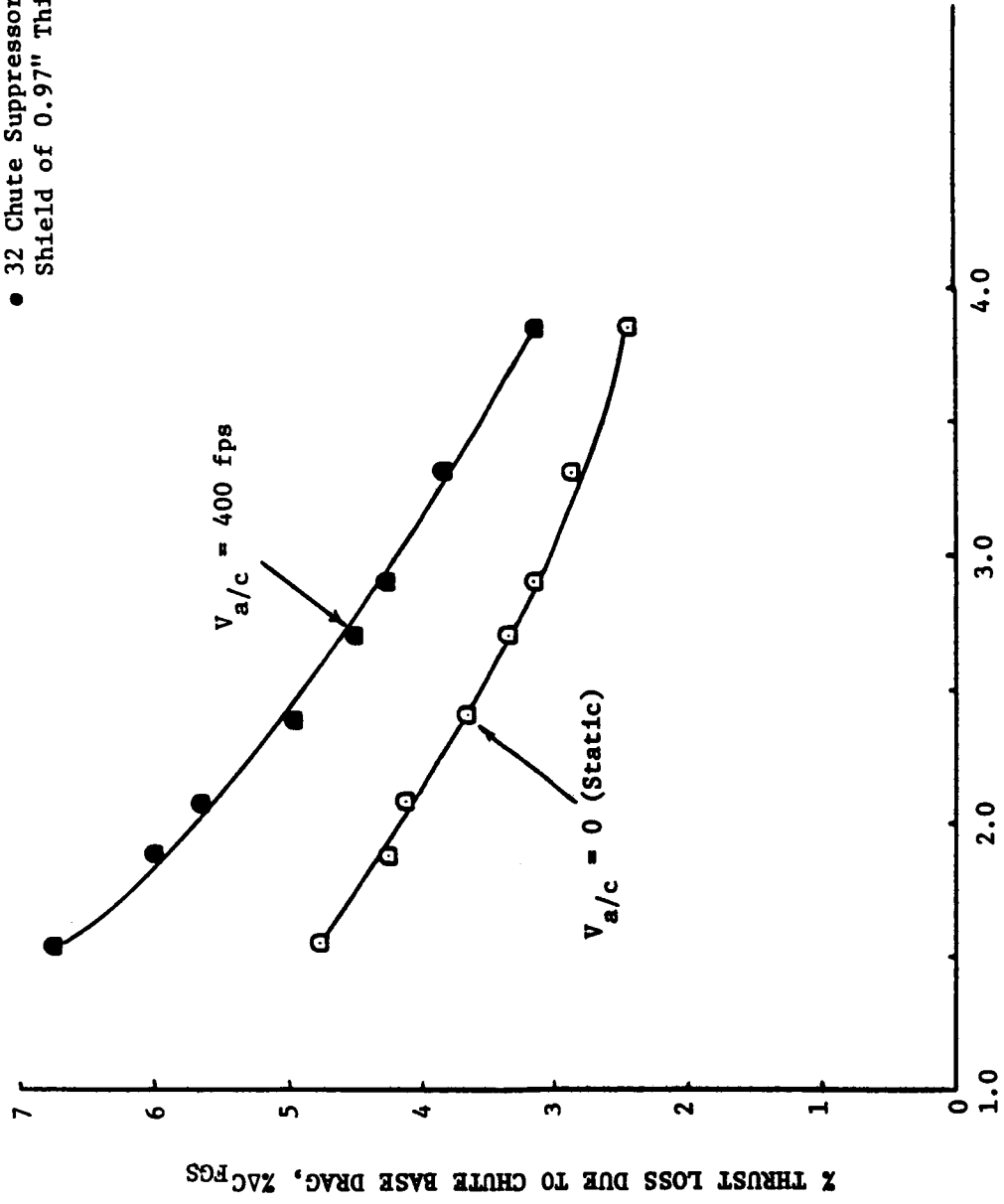
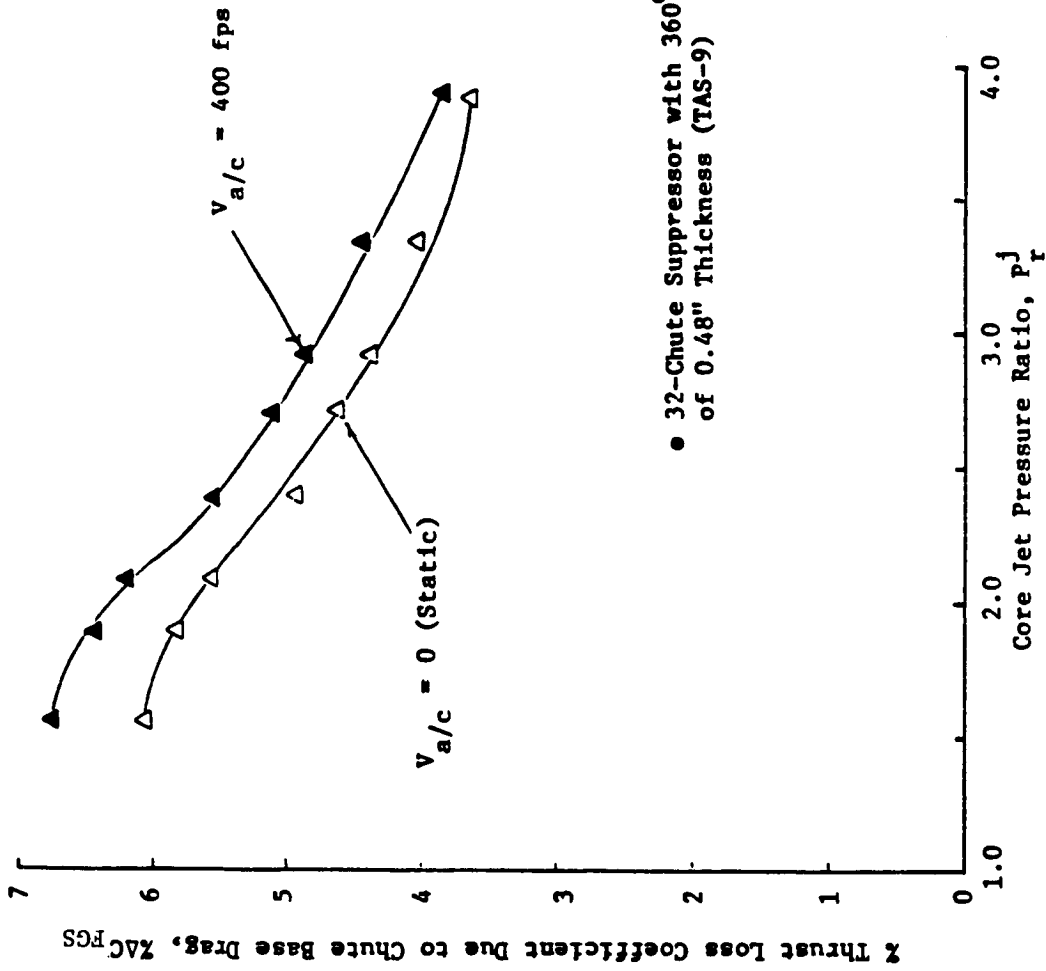


FIGURE 4.3.19. VARIATION OF % THRUST LOSS COEFFICIENT DUE TO CHUTE BASE DRAG AS A FUNCTION OF SUPPRESSOR PRESSURE RATIO FOR 32 CHUTE SUPPRESSOR WITH 180° THERMAL ACOUSTIC SHIELD OF 0.97" THICKNESS (TAS-8) FOR STATIC AND FLIGHT TESTS.



● 32-Chute Suppressor with 360° shield of 0.48" Thickness (TAS-9)

FIGURE 4.3.20. VARIATION OF % THRUST LOSS COEFFICIENT DUE TO CHUTE BASE DRAG AS A FUNCTION OF CORE JET PRESSURE RATIO FOR 32-CHUTE SUPPRESSOR NOZZLE WITH 360° SHIELD OF 0.48" THICKNESS (TAS-9) FOR STATIC AND FLIGHT TESTS.

Figures 4.3.21 and 4.3.22 compare the  $\Delta C_{FGS}$  variation with suppressor pressure ratio for configurations TAS-6, TAS-7, TAS-8 and TAS-9 for static and simulated flight conditions, respectively. Note that the chute base drag in the presence of 180° or 360° shields increases for both static and simulated flight cases, since the presence of the shield flow over the chutes reduces ventilation of the chutes. However, the relative increase in chute base drag due to the shield for simulated flight cases is smaller than the static case since, in simulated flight, configuration TAS-6 also suffers from reduced ventilation as do configurations TAS-7, TAS-8 and TAS-9. In the case of configuration TAS-9, the increase in chute base drag due to simulated flight is less than 1% indicating that the simulated flight velocity has no significant effect on the ventilation of the chutes in the presence of the 360° shield (see Figure 4.3.20). In the case of configuration TAS-6, the simulated flight velocity has a significant effect in reducing ventilation and results in a substantial increase in the chute base drag (see Figure 4.3.17). In the case of configuration TAS-7, since half of the 32 chutes are simulated by the shield, the  $\Delta C_{FGS}$  variation for configuration TAS-7 seems to be an average of the  $\Delta C_{FGS}$  variation of configurations TAS-6 and TAS-9 (see Figures 4.3.21 and 4.3.22). Also, note that the chute base drag is not sensitive to the shield thickness (i.e., compare configurations TAS-7 and TAS-8 in Figures 4.3.21 and 4.3.22) for both static and simulated flight cases. This indicates that the reduction in ventilation of the chutes by the 0.97" thick 180° shield is not significantly more than that of the 180° shield 0.48" thick.

Thus, in summary, the thermal acoustic shields noticeably increase the chute base drag of the 32 chute suppressor for both the static and simulated flight cases.

#### 4.3.4 AERODYNAMIC AND ACOUSTIC PERFORMANCE EVALUATION OF THE THERMAL ACOUSTIC SHIELD ON THE 32 CHUTE SUPPRESSOR NOZZLE

An aerodynamic performance and acoustic evaluation of the thermal acoustic shield on the 32-chute suppressor is included in this subsection. One of the methods for the implementation of the thermal acoustic shield is to extract the shield flow from the core jet flow and throttle it through a choke plate system to obtain a desired shield-to-core jet velocity ratio. One of

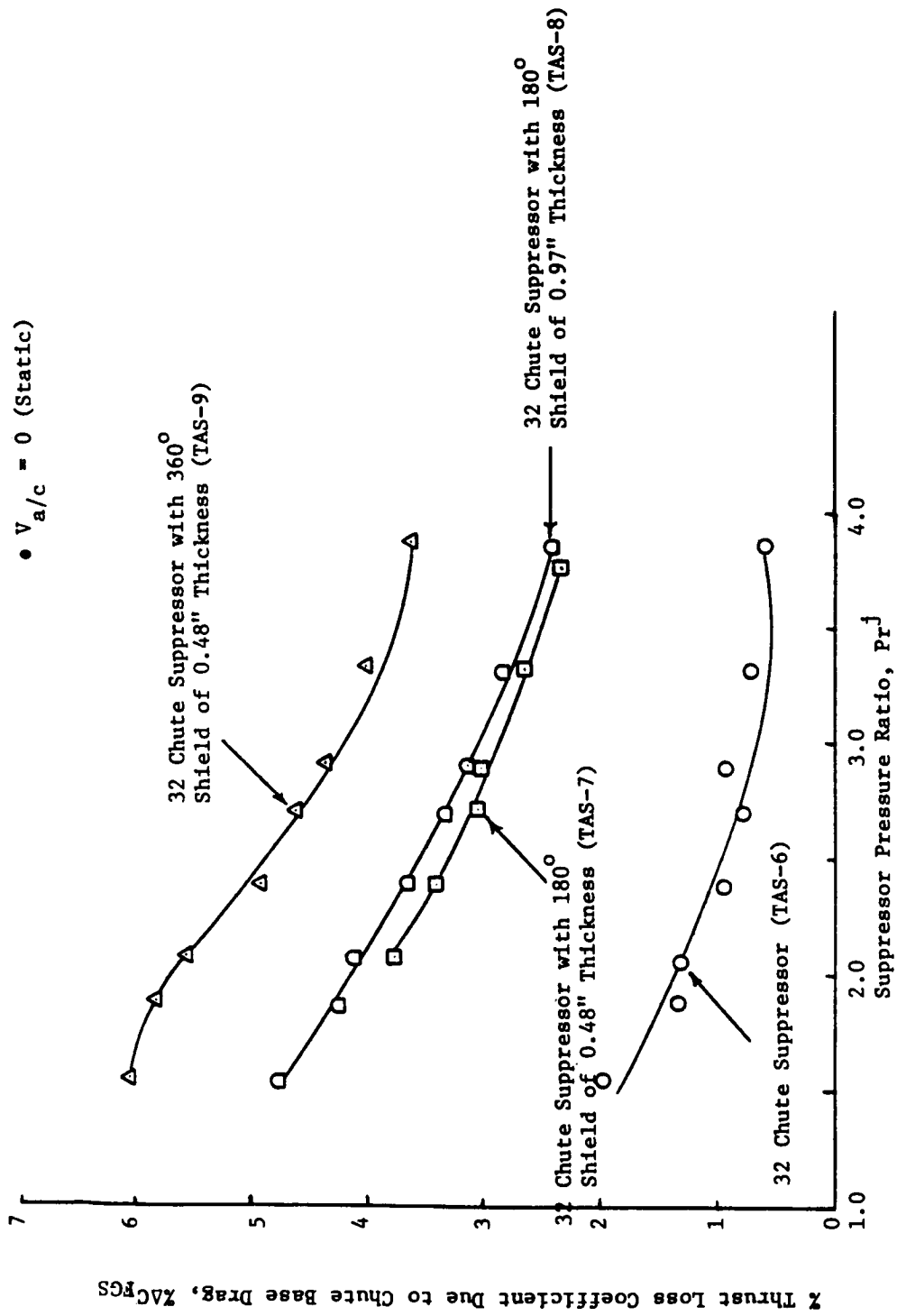


FIGURE 4.3.21. COMPARISON OF % THRUST LOSS COEFFICIENT DUE TO CHUTE BASE DRAG OF 32 CHUTE SUPPRESSOR WITH AND WITHOUT THERMAL ACOUSTIC SHIELDS (STATIC).

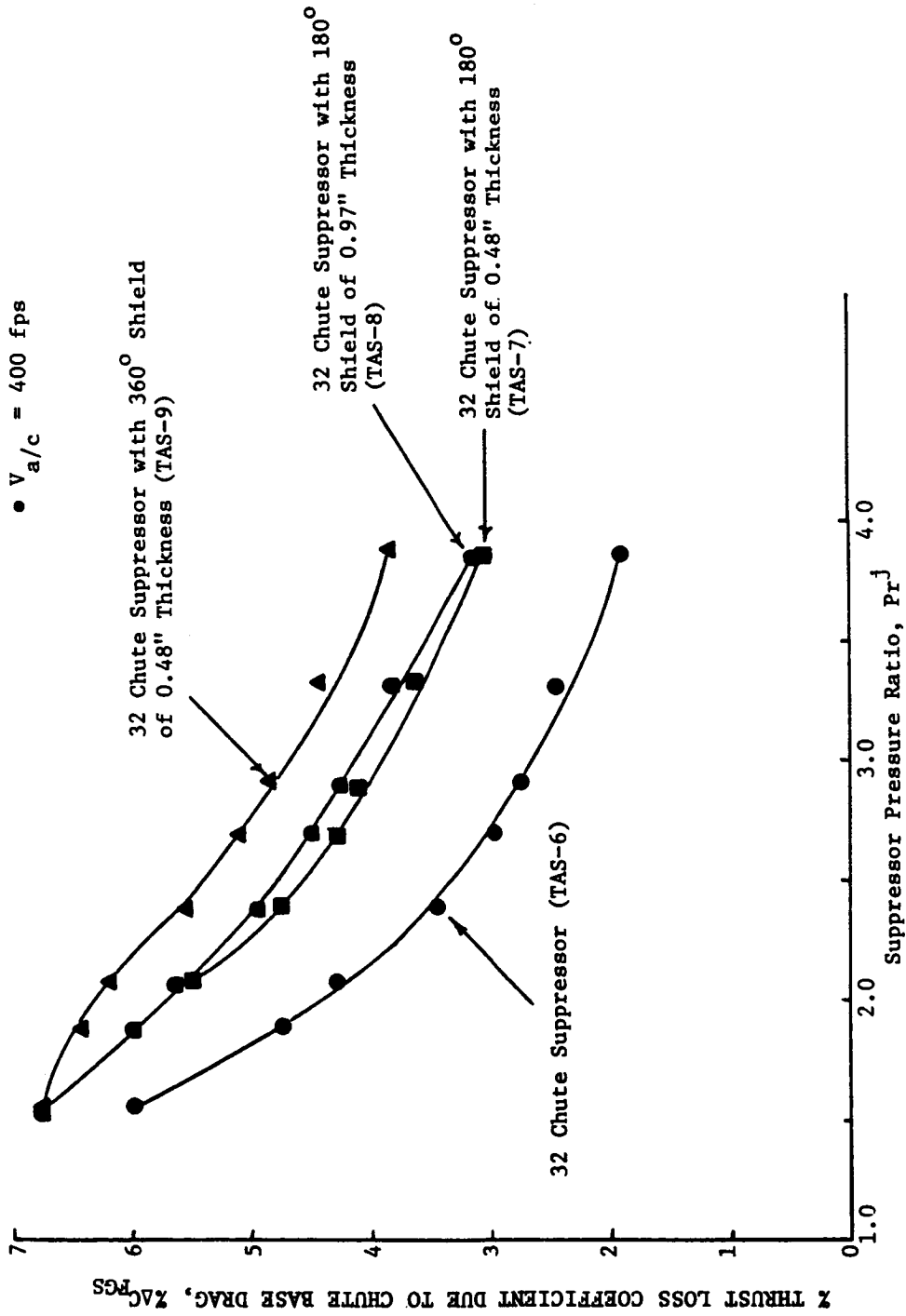


FIGURE 4.3.22. COMPARISON OF % THRUST LOSS COEFFICIENT DUE TO CHUTE BASE DRAG OF 32 CHUTE SUPPRESSOR WITH AND WITHOUT THERMAL ACOUSTIC SHIELDS (FLIGHT).

the chief concerns of such a throttling device is the associated thrust loss. A combined analysis of the acoustic data and the thrust loss estimates of a choke plate system has yielded valuable insight into a method of improving the aerodynamic performance while maintaining the acoustic benefit of the thermal acoustic shield device.

Figure 4.3.23 shows the measured variation of the peak perceived noise levels (normalized for jet density and thrust) with respect to shield-to-core jet velocity ratios ( $V_r$ ) for the 32-chute suppressor with 180° shield of 0.97" thickness. During these parametric studies, the core jet conditions were maintained at typical take-off cycle and cutback cycle. Different shield-to-core jet velocity ratios were obtained by independently varying the shield conditions. It is noted from the figure that the peak PNL, normalized for thrust and jet density, does not vary significantly with shield-to-core jet velocity ratios for  $0.5 < V_r < 0.8$  for both takeoff and cutback cycle conditions. Next, Figures 4.3.24 and 4.3.25 show the PNL directivities and spectral content of a reference conic nozzle (Reference 4.6) and the 32-chute suppressor with 180° shield of 0.97" thickness at two velocity ratios for the takeoff and cutback cycles, respectively. The data for the reference conic nozzle is included to yield an estimate of the total noise benefit that can be obtained relative to a conic nozzle by employing a mechanical suppressor with a partial thermal acoustic shield. It is noted that the shield-to-core jet velocity ratio variation, at both takeoff and cutback cycles, does not have a noticeable influence on PNL directivities and spectra of the 32-chute suppressor with the 180° shield of 0.97" thickness. Due to the relatively small area ratios (defined as  $A^{sj}/A^j$ ) employed in the thermal acoustic shield nozzles (as compared to a typical commercial high bypass turbofan engine such as the CF6-50 engine), the momentum flux of the shield flow is small compared to that of the core flow. The velocity ratio between the two streams essentially determines the velocity gradient. However, the magnitude of the turbulent shear stress is determined by the differences in the momentum fluxes between the two streams. For small values of area ratio, the shield stream is not able to significantly alter the mixing characteristics of the core stream by virtue of its low momentum flux. Hence, the velocity ratio does not significantly influence the jet mixing and associated acoustic characteristics. Gliebe and Balsa have done extensive data-theory comparisons of dual flow exhaust nozzles and have presented the influence of velocity ratio on the acoustic behavior of dual flow exhaust



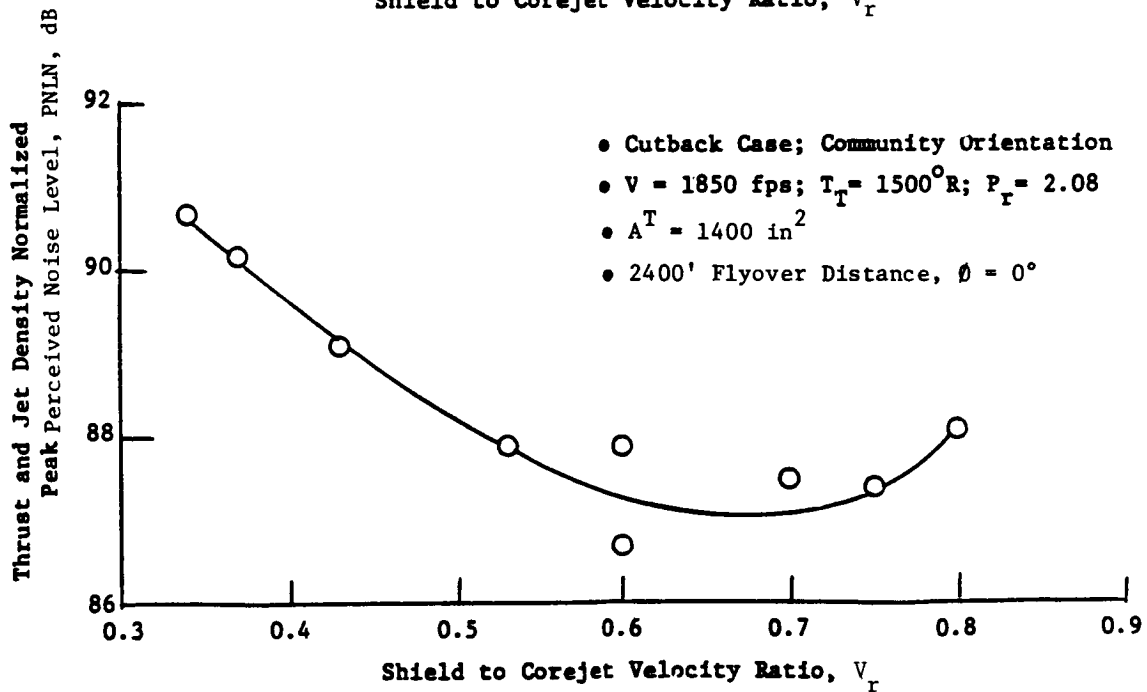
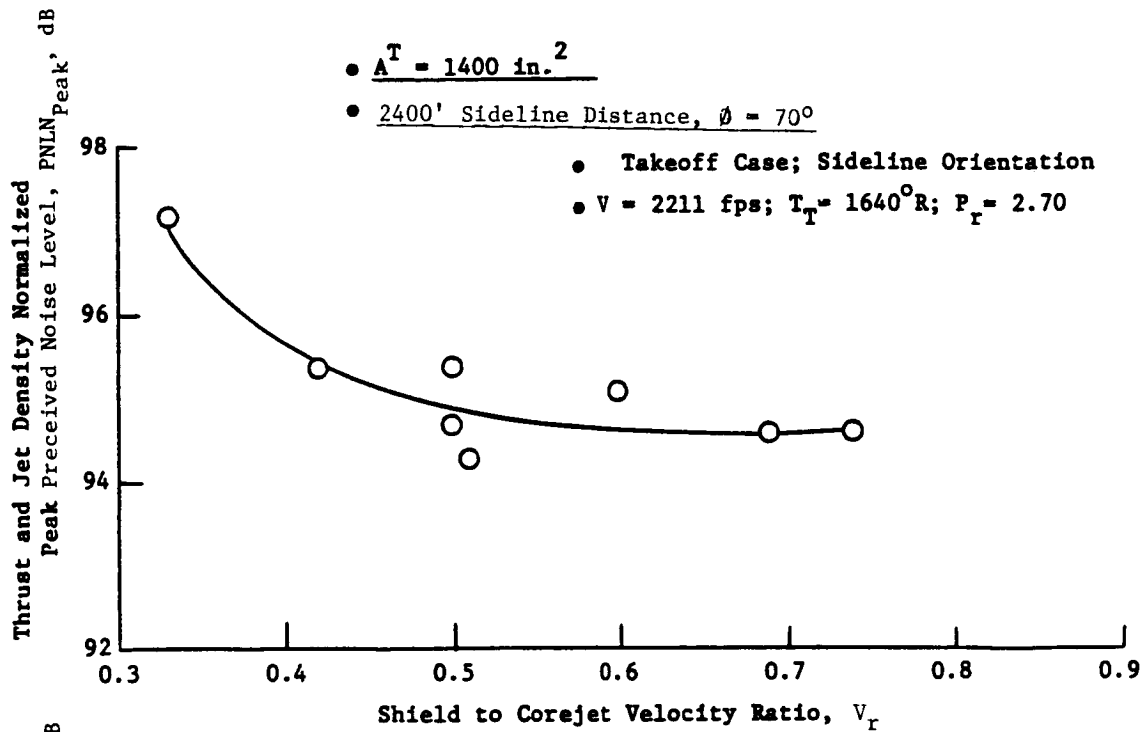


Figure 4.3.23. Influence of Shield to Corejet Velocity Ratio on Normalized Peak PNL of 32 Chute Suppressor with  $180^\circ$  Shield of 0.97" Thickness at Takeoff and Cutback Cases in Simulated Flight ( $V_{a/c} = 400 \text{ fps}$ ).

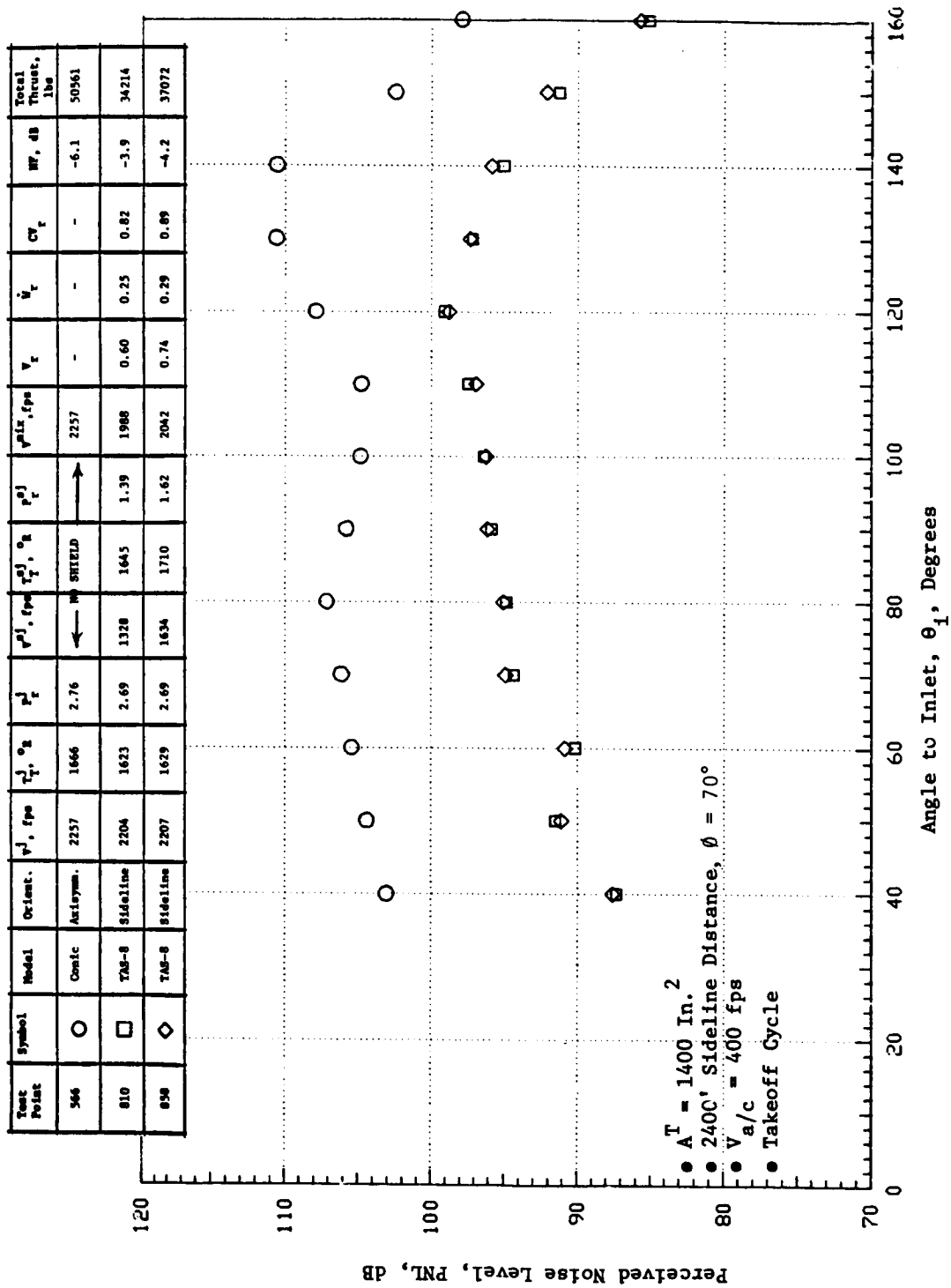


Figure 4.3.24a. Comparison of the Perceived Noise Level Directivities of 32 Chute Suppressor with 0.97" Thick 180° T.A.S. at Two Velocity Ratios with That of the Conic Nozzle at a Typical Takeoff Case in Simulated Flight.

- $T = 1400$  In. <sup>2</sup>
- 2400' Sideline Distance,  $\theta = 70^\circ$
- $V_{a/c} = 400$  fps
- Takeoff Cycle

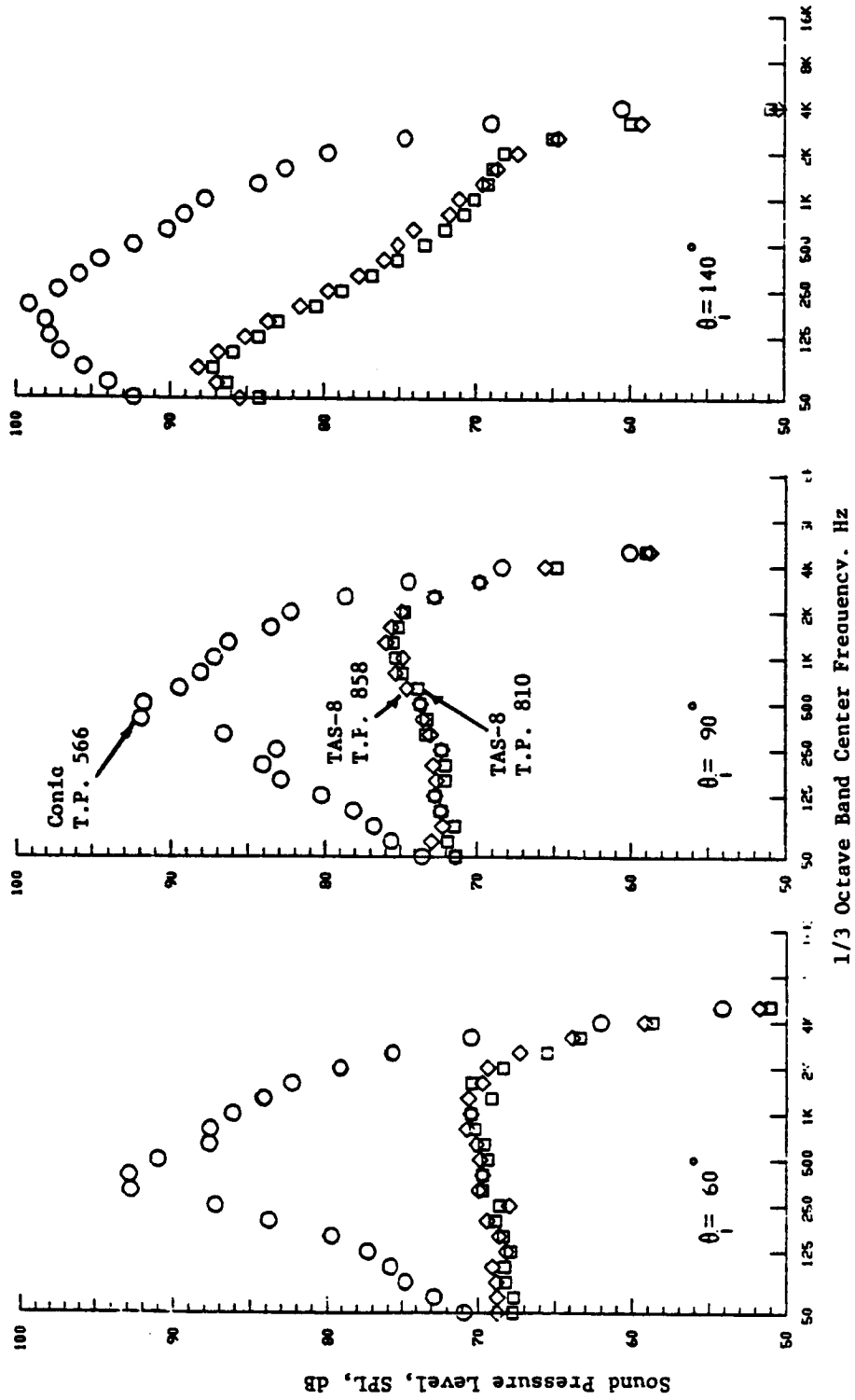


Figure 4.3.24b. Comparison of the Spectral Content of 32 Chute Suppressor with 0.97" Thick 180° T.A.S. at Two Velocity Ratios with That of the Conic Nozzle at a Typical Takeoff Case in Simulated Flight.

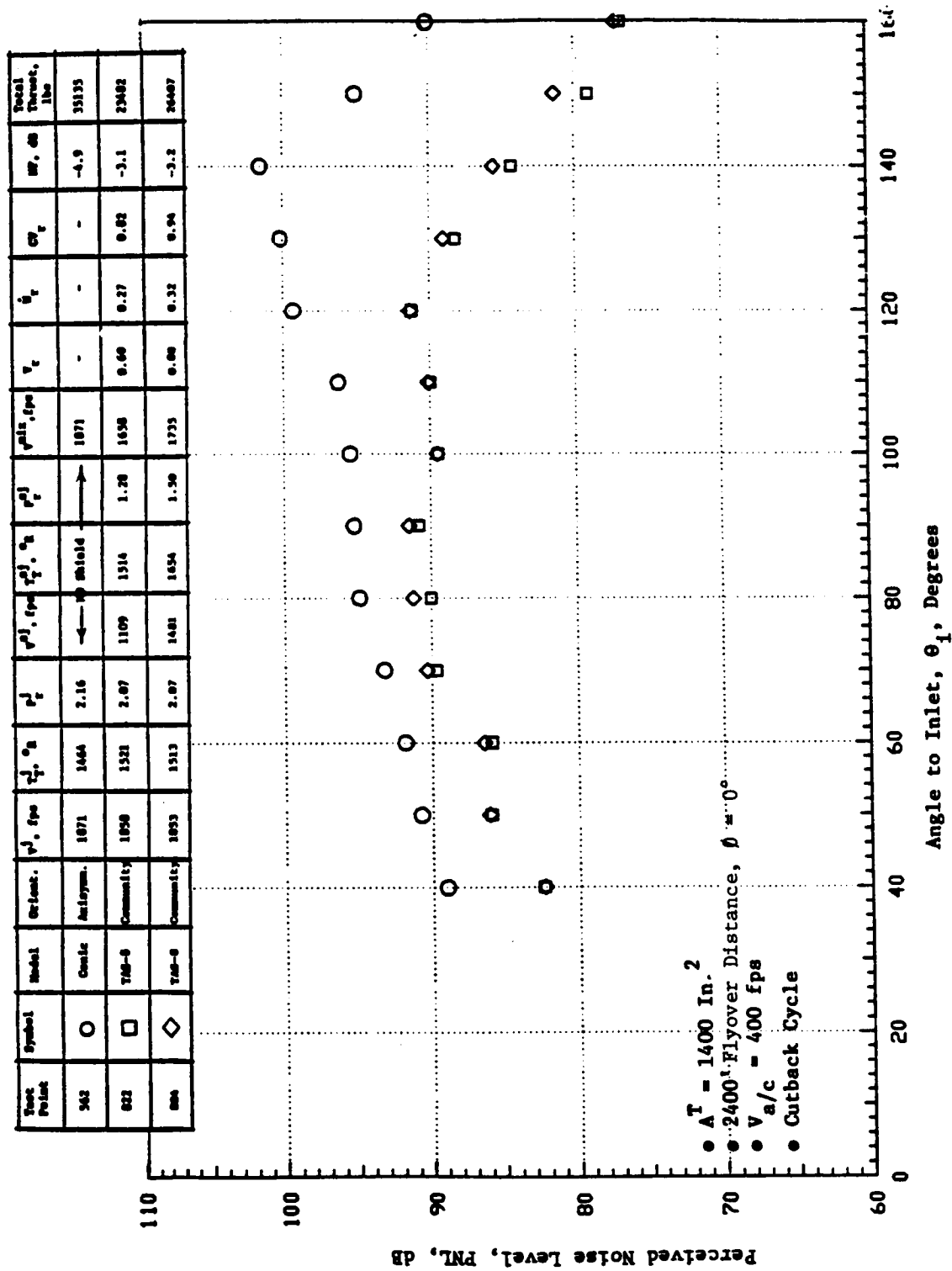


Figure 4.3.25a. Comparison of the Perceived Noise Level Directivities of 32 Chute Suppressor with 0.97" Thick 180° T.A.S. at Two Velocity Ratios with That of the Conic Nozzle at a Typical Cutback Case in Simulated Flight.

- $A_T = 1400$  In. <sup>2</sup>
- 2400' Flyover Distance,  $\theta = 0^\circ$
- $V_{a/c} = 400$  fps
- Cutback Cycle

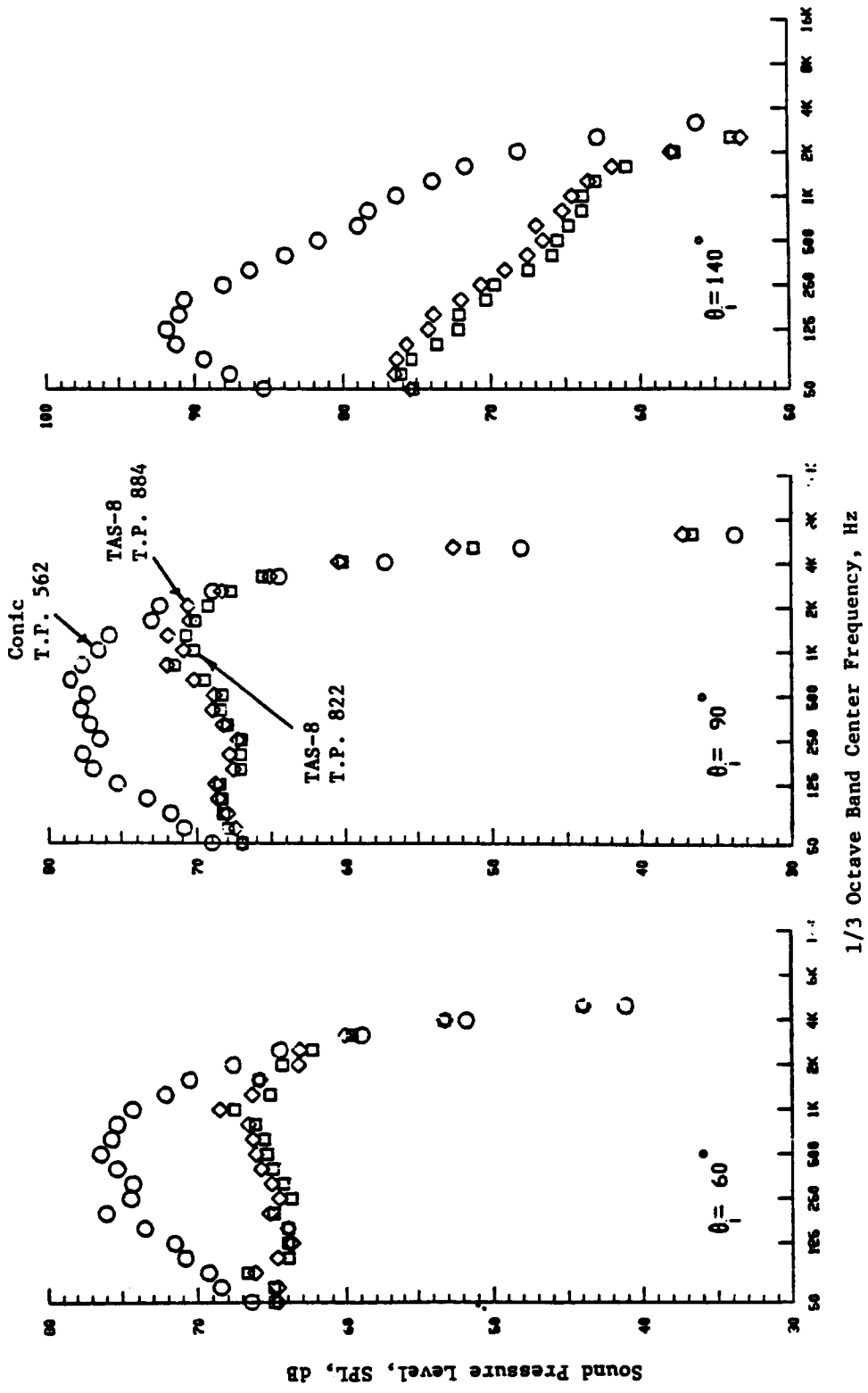


Figure 4.3.25b. Comparison of the Spectral Content of 32 Chute Suppressor with 0.97" Thick 180° T.A.S. at Two Velocity Ratios with That of the Conic Nozzle at a Typical Cutback Case in Simulated Flight.

nozzles at different outer-to-inner area ratios (see References 4.7 and 4.8). Both the data and theory in their work indicate clearly that as the outer-to-inner area ratio decreases, the influences of outer-to-inner velocity ratio on the OASPL directivity and spectral content decreases. The acoustic data of the 32-chute suppressor with 180° T.A.S. of 0.97" thickness that is presented in this report confirms the above observations.

Next, the thrust loss due to throttling of the core stream to obtain the shield flow is evaluated. Let  $\dot{W}^J$  and  $\dot{W}^{SJ}$  be the weight flow rates through the core jet and shield jet, respectively. The corresponding core jet and shield jet velocities are  $V^J$  and  $V^{SJ}$ . The total ideal gross thrust that will result is given by:

$$F_1 = \frac{\dot{W}^J V^J + \dot{W}^{SJ} V^{SJ}}{g} \quad (4.3.10)$$

where  $g$  is the gravitational constant. If no throttling was performed, the weight flow through the shield jet would be discharged at a velocity of  $V^J$  rather than  $V^{SJ}$ , in which case the total gross thrust will be given by:

$$F_2 = \frac{(\dot{W}^J + \dot{W}^{SJ}) V^J}{g} \quad (4.3.11)$$

Hence, the thrust loss coefficient due to throttling can be given by:

$$\Delta F_{\text{Throttling}} = \frac{F_2 - F_1}{F_2} \quad (4.3.12)$$

Defining shield bypass ratio as:

$$\beta = \frac{\dot{W}^{SJ}}{\dot{W}^{SJ} + \dot{W}^J} \quad (4.3.13)$$

and shield-to-core velocity ratio as:

$$V_r = \frac{V^{SJ}}{V^J} \quad (4.3.14)$$

equation (4.3.12) can be rewritten as:

$$\Delta F_{\text{Throttling}} = \beta [1 - V_r] \quad (4.3.15)$$

Thrust loss calculations due to throttling have been performed using the above expressions for the 32-chute suppressor with 180° T.A.S. of 0.48" (TAS-7) and 0.97" thickness (TAS-8) with the core maintained at a typical takeoff cycle. Figure 4.3-16 shows the variation of the thrust coefficient, CFG, with the shield bypass ratio,  $\beta$ , for a range of shield-to-core velocity ratios,  $V_r$ , for both TAS-7 and TAS-8 configurations. The thrust coefficient for the 32-chute suppressor, by itself, is measured to be  $\approx 0.94$  for the takeoff cycle, under simulated flight conditions (see Reference 4.9). The presence of the thermal acoustic shield over the chutes reduces ventilation and hence increases the chute base drag. The chute base drag measurements presented in Section 4.3.3 indicate that the 180° shield of 0.97" and 0.48" thickness exhibited an extra 1.25% thrust loss due to chute base drag compared to an unshielded 32-chute suppressor at a takeoff cycle in simulated flight. The above information has been utilized in the evaluation of the thrust coefficient of the 32-chute suppressor with the partial shields.

In Figure 4.3.26, lines of constant  $V_r$  and lines of constant shield-to-core flow area ratios are shown. Along a  $V_r = \text{constant}$  line, the shield flow area increases as the shield bypass ratio  $\beta$  increases. Along a  $\beta = \text{constant}$  line, the shield flow area decreases as  $V_r$  increases to satisfy continuity. The lines of constant shield-to-core flow area ratios are essentially parabolas with minima in the neighborhood of  $V_r \approx 0.4-0.5$ . One notices that a significant aerodynamic performance improvement in terms of increased thrust coefficient, CFG, can be obtained by employing higher shield to core jet velocity ratios for a fixed  $A^{sj}/A^j$  ratio.

Thus, in summary, higher shield-to-core jet velocity ratios are shown to decrease the thrust loss due to throttling while maintaining the acoustic benefit of the thermal acoustic shield.

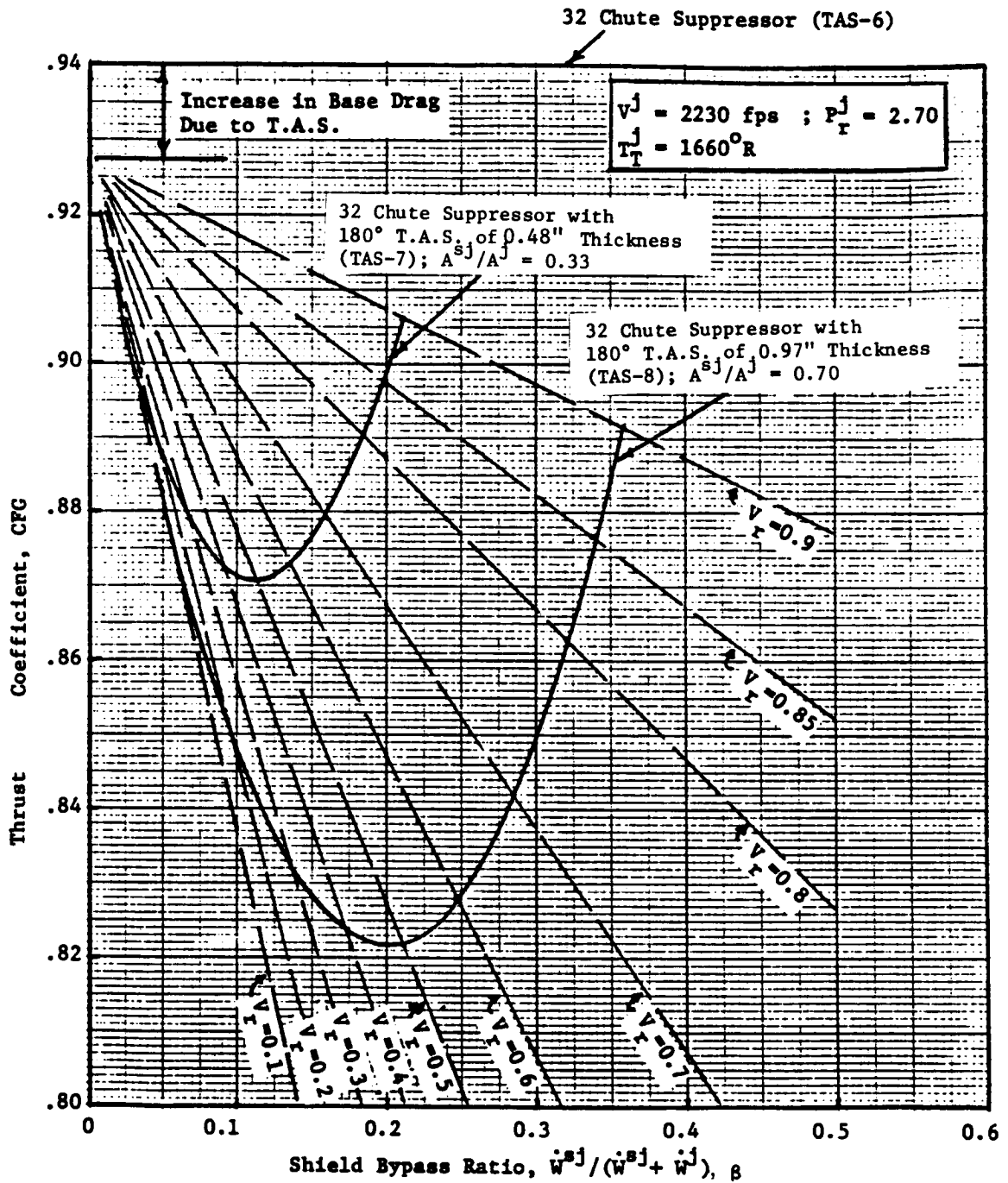


Figure 4.3.26. Aerodynamic Performance of 32 Chute Suppressor Nozzle With and Without Thermal Acoustic Shields at a Typical Takeoff Cycle.



#### REFERENCES FOR SECTION 4.0

- 4.1 "Federal Aviation Regulations." Vol. III Part 36, Noise Standards: Aircraft Type Certification, Published by the Department of Transportation, Federal Aviation Administration, December 1969.
- 4.2 Shields, F.D. and Bass, H.E., "Atmospheric Absorption of High Frequency Noise and Application to Fractional Octave Bands", NASA CR-2760, June 1977.
- 4.3 Knott, P.R., Janardan, B.A. and Majjigi, R.K., "Free-Jet Investigation of Mechanically Suppressed High-Radius-Ratio Coannular Plug Model Nozzles", Final Report Draft, NAS3-21608, October 1981.
- 4.4 Majjigi, R.K., "A Unique Spectral Acoustic Prediction Method for Jet and Shock Cell Noise of Mechanical Suppressor Nozzles", General Electric Technical Information Series Report Number R81AEG363, May 1981.
- 4.5 Keith, J.S., Ferguson, D.R., Merkle, C.L., Heck, P.H. and Lahti, D.J., "Analytical Method for Predicting the Pressure Distribution About a Nacelle at Transonic Speeds", NASA CR-2217, July 1973.
- 4.6 Janardan, B.A., Brausch, J.F., Hoerst, D.J., Selmeier, J.P. and Knott, P.R., "Free-jet Investigation of Mechanically Suppressed, High-Radius-Ratio Conannular Plug Model Nozzles". Comprehensive Data Report Vol. I for Contract NAS3-21608, General Electric Technical Information Series Report Number R81AEG484, May 1981.
- 4.7 Balsa, T.F. and Gliebe, P.R., "Aerodynamics and Noise of Coaxial Jets", AIAA Journal, Vol. 15, No. 11, November 1977, pp. 1550-1558.
- 4.8 Gliebe, P.R. and Balsa, T.F., "Aeroacoustics of Axisymmetric Single-and-Dual-Flow Exhaust Nozzles", Journal of Aircraft, Vol. 15, No. 11, November 1978, pp. 743-749.
- 4.9 Brausch, J.F. Stringas, E.J., Mani, R., et al, "High Velocity Jet Noise Source Location and Reduction, Task 5 - Investigation of 'In-Flight' Aeroacoustic Effects on Suppressed Exhausts", General Electric Company Contractor Final Report No. FAA-RD-76-79, V, January 1979.

## 5.0 THEORETICAL AEROACOUSTIC PREDICTION METHOD FOR THERMAL ACOUSTIC SHIELDS

### 5.1 BACKGROUND

The aeroacoustic prediction methodology selected for the theoretical modeling of thermal acoustic shields is the General Electric's Mani\*Gliebe\*Balsa (M\*G\*B) model (see Reference 5.1 for complete details).

This is a unified aerodynamic/acoustic prediction technique for assessing the noise characteristics of arbitrary shaped nozzles. The technique utilizes an extension of Reichardt's method to provide predictions of the jet plume field (velocity, temperature and turbulence intensity distributions). The turbulent fluctuations produced in the mixing regions of the jet are assumed to be the primary source of noise generation, as in the classical theories of jet noise. The alteration of the generated noise by the jet plume itself as it propagates through the jet to the far-field observer (sound/flow interaction or fluid shielding) is modelled utilizing the high-frequency shielding theory based on Lilley's equation.

These basic modelling elements (flow field prediction, turbulent mixing noise generation, and sound/flow interaction) have been coupled together in a discrete volume-element formulation. The jet plume is divided into elemental volumes, each roughly the size of a representative turbulence correlation volume appropriate to that particular location in the plume. Each volume element is assigned its own characteristic frequency, spectrum, and acoustic intensity. The sound/flow interaction effects for each volume element are evaluated from the flow environment of the element. The individual volume elements are assumed to be uncorrelated with each other, so that the total contribution to the far-field is simply the sum of the individual volume element contributions.

The M\*G\*B model described in Reference 5.1 predicts the flow field and turbulent mixing noise generation for arbitrary nozzle shapes and azimuthally averages the flow field and noise source characteristics to predict the far-field noise distribution. In the case of partial thermal acoustic shield surrounding the unsuppressed annular plug nozzle, the measured acoustic and flow field data (see Sections 4.1 and 4.2) have shown azimuthally asymmetric

characteristics, an anticipated feature. Hence, it was necessary to modify the M\*G\*B model to reflect the asymmetric flow field and acoustic features of the partial thermal acoustic shield.

The following two (2) methodologies were developed to predict the acoustic characteristics of axially asymmetric thermal acoustic shields:

- I. An analytical model for the acoustic field of a quadropole convecting above a planar (i.e., two-dimensional) thermal acoustic shield of finite thickness;
- II. Analytical/computational modifications of the M\*G\*B method for partial thermal acoustic shields.

The principal output of the first methodology is a closed form analytical evaluation of the influence of certain key parameters on the acoustic characteristics of a thermal acoustic shield. The principal output of the second methodology is the prediction of the azimuthally varying acoustic characteristics of the partial thermal acoustic shield and some selective data-theory comparisons. Details of the above two (2) methodologies are discussed in the following section.

## 5.2 METHODOLOGIES FOR AXIALLY ASYMMETRIC THERMAL ACOUSTIC SHIELDS

### 5.2.1 A THEORY FOR PLANAR (2-D) THERMAL ACOUSTIC SHIELDS

#### 5.2.1.1 Introduction

About ten years ago it was realized, primarily through the work of Lilley<sup>(5.2)</sup>, Mani<sup>(5.3)</sup>, and Tester<sup>(5.4)</sup> that the mean velocity and temperature of a jet have significant impact on the sound field radiated by the convecting turbulence in the jet. As a result of this and other work, it became obvious that the fluid shielding afforded by the mean flow can be used to suppress the noise of jets. Considerable experimental activity along these directions has taken place, for example, in the area of noise generated by dual flow jets with "inverted" velocity and temperature profiles. Here the

high velocity and temperature outer flow does indeed provide an effective shielding of the noise sources, although there may be other mechanisms that are partly responsible for the overall noise reduction.

In all of the early theoretical work, the shielding of an axial source by an axially symmetric mean flow was investigated (Reference 5.5). Later Balsa<sup>(5.6)</sup> examined the acoustic field of a convecting point quadrupole at an arbitrary location in a round jet, however, as recently pointed out by Goldstein<sup>(5.7)</sup>, this analysis is strictly valid only when the source is not too far from the axis of the jet. Balsa found, roughly speaking, that the amount of acoustic shielding in the zone of silence is proportional (in dB) to  $(f\delta/c_\infty)$  where  $f$  is the source frequency,  $c_\infty$  is the speed of sound at infinity and  $\delta$  is an effective distance which characterizes how far the source is embedded in the jet. Note that here we are using the term "acoustic shielding" (or fluid shielding) in a technical sense as it describes the behavior of the sound field in the classical cone of silence.

More recently, Goldstein<sup>(5.7)</sup> used a high frequency theory to investigate the radiation field of sources in arbitrary parallel shear flows; for the first time the assumption of axial symmetry of the mean flow is completely relaxed. His analysis, in the present form, describes the sound field outside the cone of silence and there is speculation that this work could be extended into the cone of silence. Goldstein's work clearly shows how the acoustic field becomes increasingly distorted as the observer approaches the cone of silence and how the radiation from the acoustic sources is reflected upward by the thermal acoustic shield.

In order to understand how a typical thermal acoustic shield affects the radiation field of a primary jet at all emission angles, a model problem is solved in this section. The shielding jet is assumed to be planar with velocity and temperature profiles depending only on the vertical transverse coordinate (Figure 5.1). The solution of this problem, together with the axially symmetric cases and Goldstein's results, can provide semi-quantitative information on the effects of thermal acoustic shields.

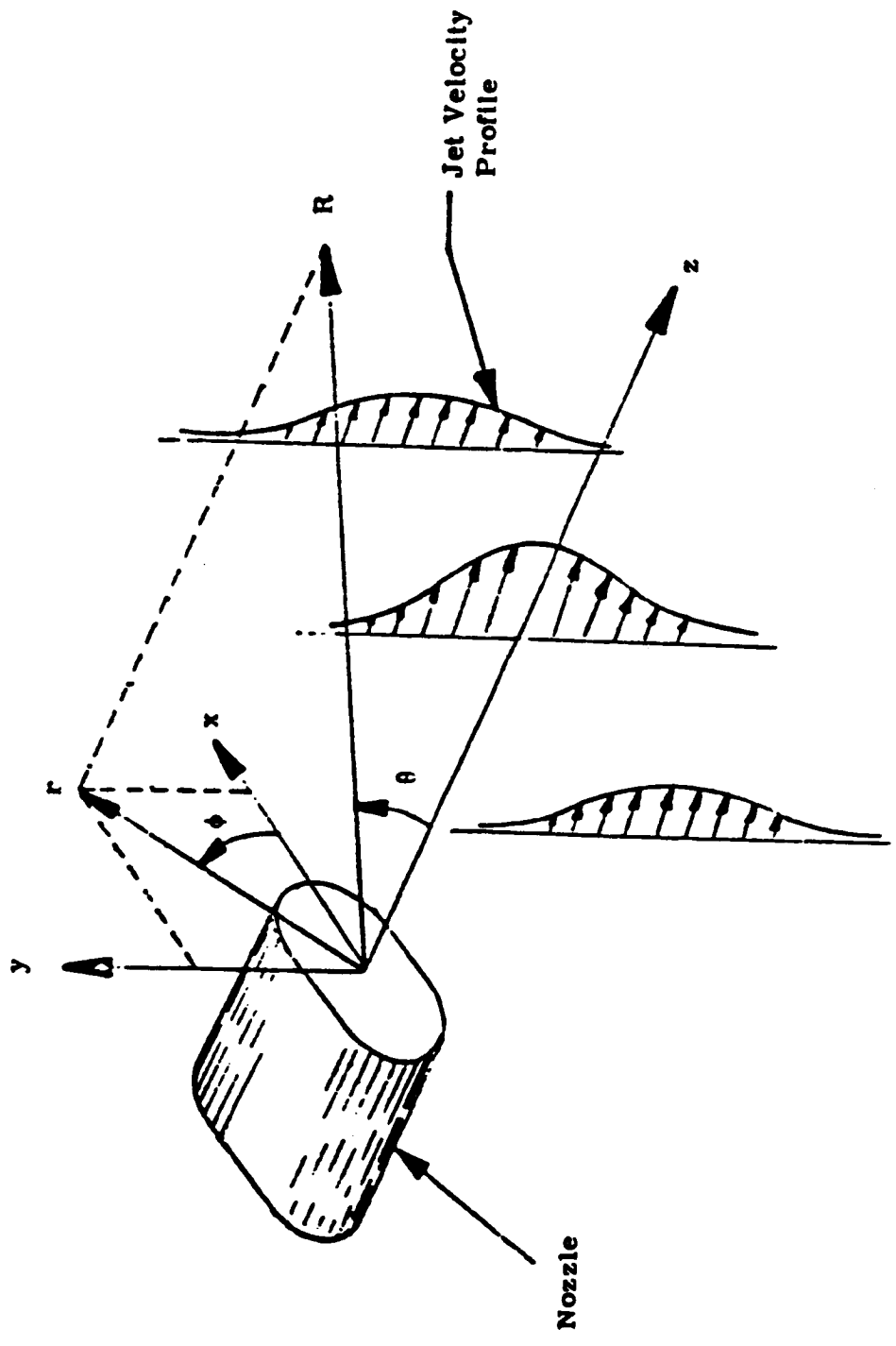


Figure 5.1. Geometry of Jet Flow Field.

### 5.2.1.2 The Lilley Equation for Arbitrary Parallel Shear Flows

The original form of the Lilley equation is given for axially symmetric mean flows which occur in round jets (Reference 5.2). The purpose of this section is to generalize the Lilley equation for arbitrary parallel shear flows in order to provide a new interpretation and a systematic derivation. The derivation itself was suggested, in the absence of heat addition, by M.E. Goldstein of the NASA Lewis Research Center (private communication).

Under the generally accepted assumption that viscous and thermal dissipation are unimportant in the generation and propagation of sound through a turbulent jet, the starting point for our derivation is the Euler equations

$$\frac{Dp}{Dt} + c^2 \rho \nabla \cdot \mathbf{q} = \frac{pQ}{C_v} \quad (5.1a)$$

$$\frac{D\mathbf{q}}{Dt} + \mathbf{q} \cdot \nabla \mathbf{q} = - \frac{\nabla p}{\rho} \quad (5.1b)$$

$$\frac{DS}{Dt} = Q \quad (5.1c)$$

$$p = p(\rho, S) = \text{Const } \rho^K \exp. (S/C_v) \quad (5.1d)$$

where  $p$ ,  $\rho$ ,  $S$ ,  $\mathbf{q}$  are the fluid pressure, density, entropy and velocity respectively,  $c = [(\partial p / \partial \rho)_S]^{1/2}$  is the speed of sound in the fluid and  $D/Dt = \partial/\partial t + \mathbf{q} \cdot \nabla$  is the convective derivative. Time is denoted by  $t$  and the gradient operator by  $\nabla = \partial/\partial \underline{x}$  where  $\underline{x} = (x, y, z)$  are Cartesian space coordinates (Figure 5.1).

The fluid is assumed to consist of a single gas obeying thermally and calorically perfect equations of state. Thus, the specific heat capacity at constant volume,  $C_v$ , and the ratio of specific heats,  $K$ , are constants. The time rate of entropy addition, which may be due to combustion, is denoted by  $Q$ . Roughly speaking,  $Q$  is proportional to the local heat addition. In supersonic flows where shocks may be present, the entropy equation (5.1c) is valid only in the regions between the shocks. In other words, eq. (5.1c) is not valid across shocks. In the present report, we do not discuss shock

associated noise which is generally considered to be a statistically independent addition to turbulent mixing noise in the synthesis of the overall noise from jets.

Equations (5.1) represent the usual forms of mass continuity, momentum and energy conservation and thermodynamic state with the exception that in the continuity equation, the convective derivative of the density has been eliminated in favor of  $Dp/Dt$  by the use of Eq. (5.1c) and the equation of state, Eq. (5.1d). Since the above equations do not contain volume source terms, we do not include explicitly the effects of mass and momentum additions in our analysis. However, combustion noise, characterized by energy addition, is included in the present derivation.

Following Lilley<sup>(5.2)</sup> and Goldstein<sup>(5.7)</sup>, we expand each of our dependent variables,  $p$ ,  $\rho$ ,  $S$ ,  $c^2$ ,  $q$ , and  $Q$  in a small parameter, say  $\epsilon$ , which characterizes the magnitude of the unsteady disturbances that are superimposed on the mean flow of the jet. The typical form of this expansion is

$$P = P_0 + \epsilon P_1 + \epsilon^2 P_2 + \dots \quad (5.2a)$$

$$c_0^2 = c_0^2 + \epsilon c_1^2 + \epsilon^2 c_2^2 + \dots \quad (5.2b)$$

$$Q = Q_0 + \epsilon Q_1 + \epsilon^2 Q_2 + \dots \quad (5.2c)$$

After substituting this expansion into Eqs. (5.1), and collecting like powers of  $\epsilon$ , we obtain equations for the mean flow (denoted by subscript 0) and the first and second order perturbations (denoted by subscripts 1 and 2).

In the parallel shear flow approximation, we assume that the undisturbed pressure,  $p_0$ , is a constant throughout the jet and the ambient, the undisturbed velocity has a single component along the axis of the jet (which is chosen to be the  $z$ -axis), say  $q_0 = u_0 e_z$ , and  $\rho_0$ ,  $S_0$ ,  $c_0$  and  $w_0$  are functions of the cross plane variables  $x$  and  $y$  only. The first order perturbations  $p_1$ ,  $q_1$  and  $S_1$  satisfy

---

\* $e_z$  denotes the unit vector in the  $Z$  direction.

$$\frac{D_0 p_1}{Dt} + \rho_0 c_0^2 \nabla \cdot \underline{q}_1 = \frac{\rho_0 Q_1}{C_v} \quad (5.3a)$$

$$\frac{D_0 \underline{q}_1}{Dt} + \underline{q}_1 \cdot \nabla \underline{q}_0 + \frac{\nabla p_1}{\rho_0} = 0 \quad (5.3b)$$

$$\frac{D_0 S_1}{Dt} + \underline{q}_1 \cdot \nabla S_0 = Q_1 \quad (5.3c)$$

where  $D_0/Dt = \partial/\partial t + w_0 \partial/\partial z$  is the convective derivative based on the mean velocity. The second order perturbations  $p_2$ ,  $\underline{q}_2$  and  $S_2$  satisfy the following equations:

$$\frac{D_0 p_2}{Dt} + \rho_0 c_0^2 \nabla \cdot \underline{q}_2 = - \underline{q}_1 \cdot \nabla p_1 - (\rho_0 c_1^2 + c_0^2 \rho_1) \nabla \cdot \underline{q}_1 + \frac{\rho_0 Q_2 + \rho_1 Q_1}{C_v} \quad (5.4a)$$



$$\frac{D_0 \underline{q}_2}{Dt} + \underline{q}_2 \cdot \nabla \underline{q}_0 + \frac{\nabla p_2}{\rho_0} = - \underline{q}_1 \cdot \nabla \underline{q}_1 + \frac{\rho_1}{\rho_0} \nabla p_1 \quad (5.4b)$$

$$\frac{D_0 s_2}{Dt} + \underline{q}_2 \cdot \nabla s_0 = - \underline{q}_1 \cdot \nabla s_1 + Q_2 \quad (5.4c)$$

The first order perturbations satisfy homogeneous equations (5.3) in the absence of heat addition. Since the left hand side of (5.3) is equivalent to the inviscid Orr-Sommerfeld operator (this will become clearer later in this section), the first order perturbations represent the entire family of permissible instability waves. These instability waves and the energy terms  $Q_1$  and  $Q_2$  form the inhomogeneous terms for the second order perturbations (5.4), therefore, these terms may be regarded as the source of the perturbations. We now claim, following Lilley<sup>(5.2)</sup>, that the second order perturbations give the unsteady field associated with aerodynamic sound (again this will become clearer later in this section). The present analysis reveals that noise is indeed a by-product of the instability (or turbulence) which exists in jets and the acoustic field is driven by this instability.

In order to obtain a Lilley-like equation for the second order pressure  $p_2$ , we eliminate the velocity  $\underline{q}_2$  from the governing equations (5.4a, 5.4b). The procedure is standard and may be found in Reference 5.2. The final result is:

$$L \left[ \frac{p_2}{K p_0} - \frac{K-1}{2} \left( \frac{p_1}{K p_0} \right)^2 \right] = \frac{D_0}{Dt} \nabla \cdot \underline{F} - 2(\nabla \cdot \underline{v}_0) \cdot \frac{\partial \underline{F}}{\partial z} + \frac{D_0^2}{Dt^2} \left( \frac{Q_1}{K C_v} \frac{p_1}{K p_0} \right) + \frac{D_0^2}{Dt^2} \frac{Q_2}{K C_v} \quad (5.5a)$$

where the Lilley operator is

$$L = \frac{D_0}{Dt} \left[ \frac{D_0^2}{Dt^2} - \nabla \cdot c_0^2 \nabla \right] + 2c_0^2 (\nabla w_0) \cdot \nabla \frac{\partial}{\partial z} \quad (5.5b)$$

and

$$\underline{F} = \nabla \cdot (\underline{q}_1 \underline{q}_1) + c_1^2 \frac{\nabla p_1}{\kappa p_0} - \frac{Q_1 \underline{q}_1}{\kappa c_v} \quad (5.5c)$$

The Lilley operator (5.5b) is a third order operator in the convective derivative  $D_0/Dt$ ;  $c_0 = c_0(x, y)$  and  $w_0 = w_0(x, y)$  are the undisturbed speed of sound and jet velocity, respectively. This operator expresses the convection of the acoustic pressure fluctuations by the mean flow and the interaction between these fluctuations and the velocity and temperature gradients of the jet. (Since the undisturbed static pressure  $p_0$  is a constant, the mean speed of sound  $c_0$  describes completely the thermodynamic state of the jet.) The axis of the jet is along the  $z$  coordinate (Figure 5.1). Strictly speaking, the operator  $L$  is also recognized as the inviscid Orr-Sommerfeld operator of classical stability theory. This operator arises from the left hand side of Eq. (5-3) or Eq. (5.4). Thus our previous remark that the solution to equations (5.3) contains a family of instability waves is confirmed. Since solutions to Eq. (5.4) represent the aerodynamic sound field (which is finite), the instability waves arising in Eq. (5.4) are ignored. This assumption is related to causality (see Reference 5.8).

In the absence of heat addition,  $Q_1 = Q_2 = 0$ , the source  $\underline{F}$  consists of the divergence of the velocity tensor ( $\underline{q}_1 \underline{q}_1$ ) where, strictly speaking,  $\underline{q}_1$  represents the velocity fluctuations in the instability wave. Because of the similarity of this source term with the Lighthill source term (see Reference 5.9), we now assume that  $\underline{q}_1$  represents the instantaneous velocity of the turbulence; we thereby acknowledge that the turbulence in a jet is triggered by the instability waves; this instability does not persist, but in fact, it degenerates into turbulence. The second term on the right hand side of Eq. (5.5c) is quadratic, and represents a noise source due to the

interaction between temperature and pressure fluctuations in turbulence. This source is usually unimportant for jets at reasonable temperatures and at high velocities. We emphasize that the assumption that the second order perturbations describe the aerodynamic sound field is based on the similarity of the source term to that of Lighthill and physical intuition.

The dependent variable in the argument of the Lilley operator in Eq. (5.5) is not simply the second order (i.e., acoustic) pressure  $p_2$ . An additional term, quadratic in the turbulent pressure fluctuations  $p_1$ , also appears. Since this term is proportional to a small factor,  $(K - 1)/2$ , and turbulence is convected by the flow, this term will be ignored.

In this section we have derived a generalization to Lilley's equation for arbitrary parallel shear flows. Under certain reasonable approximations, the acoustic pressure,  $p_2$ , ( $p_0$  = undisturbed or ambient pressure,  $K$  = isentropic exponent of gas) obeys a Lilley-like equation in which the mean speed of sound  $c_0$  and jet velocity  $w_0$  (along the  $z$ -axis) are arbitrary functions of the cross plane variables,  $x$  and  $y$  (Figure 5.1). The source of sound is expressible in terms of the divergence of the turbulent velocity tensor ( $\underline{q}_1 \underline{q}_1$ ). The interpretation for the additional sources of noise in the case of heat addition is straightforward. Thus the relevant, but approximate, equations for sound generation and propagation are, in the absence of combustion,

$$L \left( \frac{p_2}{\rho p_0} \right) = \frac{D_0}{Dt} \nabla \cdot \underline{F} - 2 (\nabla w_0) \cdot \frac{\partial F}{\partial z} \quad (5.5d)$$

where

$$\underline{F} = \nabla \cdot (\underline{q}_1 \underline{q}_1) \quad (5.5e)$$

$L$  is defined by Eq. (5.5b) and  $D_0/Dt = \partial/\partial t + w_0 \partial/\partial z$ .

### 5.2.1.3 The Green's Function

The solution to Lilley's equation (5.5b, 5.5d) may be written down, at least in principle, if the Green's function  $G$  is known. This is because equation (5.5d) is linear and the method of superposition is valid. In other words, the acoustic field generated by an extended source, such as the right hand side of Eq. (5.5d) is just the sum of that generated by point sources; the strength of each point source being defined appropriately. Thus we will obtain the solution for

$$\frac{1}{c^2} \frac{D^3 G}{Dt^3} - \frac{D}{Dt} \Delta G - (\nabla \log c^2) \cdot \frac{D}{Dt} \nabla G + 2 (\nabla w) \cdot \nabla \frac{\partial G}{\partial z} = e^{-i\omega t} \times \delta(x - x_0) \delta(y - y_0) \delta(z - U_c t) \quad (5.6)$$

where the left hand side of Eq. (5.6) is obtained from the Lilley operator  $L$  by performing the indicated differentiations and by dividing by  $c_0^2$ . Note that in Eq. (5.6) we write  $c$  and  $w$  for  $c_0$  and  $w_0$  in order to avoid the use of unnecessary subscripts. Therefore, the mean speed of sound and velocity of the jet are denoted by  $c = c(x, y)$  and  $w = w(x, y)$  and the convective derivative is  $D/Dt = \partial/\partial t + w \partial/\partial z$ . This new notation will be adhered to in the rest of this report.

The right hand side of Eq. (5.6) represents a harmonically oscillating point source which is convecting along the  $z$  direction (which is the axis of the jet). The circular frequency of the source in the convecting reference frame is  $\omega \geq 0$  and its convection velocity is  $U_c \geq 0$ . Of course,  $\nabla$  is the gradient operator,  $\Delta$  is the Laplacian,  $\delta$  denotes the delta function and  $(x_0, y_0)$  denote the position of the source in the cross plane. From the Green's function we can obtain the acoustic field of a convecting dipole or quadrupole by differentiation.

Since the coefficients of Eq. (5.6) are independent of the axial variable,  $z$ , it is natural to extract the  $z$  dependence by a Fourier transform

$$G^+(x, y, t) = \frac{1}{(2\pi)^{1/2}} \int_{-\infty}^{\infty} \exp(-isz) G(\underline{x}, t) dz \quad i = (-1)^{1/2} \quad (5.7a)$$

where  $\underline{X} = (x, y, z)$  and whose inverse is

$$G(\underline{X}, t) = \frac{1}{(2\pi)^{1/2}} \int_{-\infty}^{\infty} \exp(isz) G^+(x, y, t) ds \quad (5.7b)$$

where  $s$  is the Fourier transform variable associated with  $z$ .  $G^+$  depends, of course, on  $s$ ; this dependence is not shown explicitly. Introducing a new dependent variable

$$G(x, y) = \frac{e^{i\omega(1+M_c\sigma)t}}{F} G^+(x, y, t) \quad (5.8a)$$

we find

$$\Delta_t G + \left\{ k^2 \left[ \frac{(1-N\sigma)^2}{(c/c_\infty)^2} - \sigma^2 \right] + F \nabla_t \cdot \frac{\nabla_t F}{F^2} \right\} G \quad (5.8b)$$

$$= - \frac{i}{(2\pi)^{1/2}} \frac{c}{c_\infty^2} \frac{1}{k^2} \frac{\delta(x-x_0) \delta(y-y_0)}{(1-N\sigma)^2}$$

where  $c_\infty = \text{const}$  is the speed of sound in the ambient,  $k = \omega/c_\infty$ ,  $\sigma = s/k$ ;  $M(x, y) = w(x, y)/c_\infty$  and  $M_c = U_c/c_\infty$  are the jet and convective Mach numbers,  $c = c(x, y)$  is the speed of sound in the jet

$$N = N(x, y) = M(x, y) - M_c \quad (5.8c)$$

$$F = F(x, y) = k \frac{1 - N\sigma}{c/c_\infty} \quad (5.8d)$$

Note that  $\sigma$  plays the role of the Fourier transform variable  $s = (k\sigma)$  and that  $G$  is independent of time since the source is oscillating harmonically and the coefficients of the Lilley operator  $L$  are also independent of time. Thus  $G$  depends on the cross-plane coordinates  $(x, y)$  and on the Fourier transform variable  $\sigma$ . The gradient operator in the transverse plane is denoted by  $\nabla_t = (\partial/\partial x, \partial/\partial y)$  and  $\Delta_t$  is the corresponding Laplacian ( $\Delta_t = \nabla_t \cdot \nabla_t$ ).

We may combine Eq. (5.8a) and Eq. (5.7b) in order to obtain directly an expression for  $G(\underline{X}, t)$  in terms of  $G(x, y)$ . After some straightforward algebra, we arrive at

$$G(\underline{X}, t) = \frac{k^2}{(2\pi)^{1/2}} e^{-i\omega t} \int_{-\infty}^{\infty} e^{ik\sigma(z - U_c t)} \frac{1 - N\sigma}{(c/c_\infty)} G(x, y) d\sigma \quad (5.9)$$

where  $G$  depends, of course, parametrically on the Fourier transform variable  $G = s/k$ . Thus once the modified Green's function  $G$  is known, the actual Green's function  $G(\underline{X}, t)$  can be recovered by quadrature Eq. (5.9).

Note that  $G$  satisfies a Helmholtz-like equation (5.8b) in the cross plane; this equation has variable coefficients because of the presence of  $N$ ,  $c$  and  $F$ . However, outside the jet, as  $r = (x^2 + y^2)^{1/2} \rightarrow \infty$ , the coefficient in the curly bracket of Eq. (5.8b) reduces to a constant; more precisely Eq. (5.8b) simplifies to

$$\Delta_t G + k^2 \frac{c_\infty^2}{c^2} G = 0 \text{ as } r \rightarrow \infty \quad (5.10a)$$

where  $g_\infty^2 = (1 + M_c \sigma)^2 - \sigma^2 > 0$ . It is assumed that the jet velocity vanishes at infinity. The outgoing wave solution of Eq. (5.10a) is

$$G \sim e^{ikg_\infty r} \text{ as } r \rightarrow \infty \quad (5.10b)$$

where the factor of proportionality in Eq. (5.10b) involves an amplitude (which may be complex) that depends on  $r$  and the azimuthal angle. However, Eq. (5.10b) gives the entire unbounded phase (in the sense of geometrical acoustics) of  $G$  as  $r \rightarrow \infty$ .

These remarks suggest that we multiply and divide the integrand of Eq. (5.9) by  $\exp(ikg_\infty r)$  in order to obtain

$$G(\underline{x}, t) = \frac{k^2}{(2\pi)^{1/2}} e^{-i\omega t} \int_{-\infty}^{\infty} \frac{1 - M_c \sigma}{(c/c_\infty)} \hat{G}(x, y) e^{ik[g_\infty r + \sigma(z - U_c t)]} d\sigma \quad (5.11a)$$

where

$$\hat{G}(x, y) = G(x, y) e^{-ikg_\infty r} \quad (5.11b)$$

For large distances away from the jet, Eq. (5.11a) may be evaluated by the method of stationary phase (see Reference 5.10, pp 274). This is because the rapidly oscillating part of the integrand in Eq. (5.11a) is entirely contained in the exponential factor  $\exp ik[\dots]$ . The dominant contribution comes from the point of stationary phase\*

$$\sigma = \sigma_* = \frac{\cos\theta}{1 - M_c \cos\theta} \quad (5.12a)$$

---

\*From this we see that  $g_\infty^2$  at  $\sigma_*$  is indeed positive as stated below in Eq. (5.10a).  $g_\infty$  is the positive square root of  $g_\infty^2$ .

where  $\theta$  is the angle with respect to the jet axis and  $M_c < 1$  is the convective Mach number of the source. After applying the method of stationary phase, we find that in the far field

$$G(\underline{X}, t) = k^2 e^{-i\omega t} \hat{G}_* \frac{e^{ikR}}{(kR)^{1/2}} \frac{\sin\theta}{(1 - M_c \cos\theta)^{5/2}} e^{-i\pi/4} \quad (5.12b)$$

where  $R \rightarrow \infty$  is the distance from the jet,  $k = \omega/c_\infty$ ,  $\hat{G}_*$  is the value of  $G$  at the point of stationary phase  $\sigma = \sigma_*$ . The phase factor  $\exp(-i\pi/4)$  arises from the stationary phase calculation. Strictly speaking  $R$  and  $\theta$  represent the "retarded" distance from the source and the "retarded" angle that the observation vector makes with the  $z$ -axis (see Ref. 5.11, pp 723).

In this section we have shown the actual Green's function  $G(\underline{X}, t)$  (see Eq. (5.6)) is expressible in terms of the modified Green's function  $\hat{G}(x, y)$  (see Eq. (5.12b)). The latter is evaluated at the point of stationary phase  $\sigma = \sigma_*$  (see Eq. (5.12a) and is obtained by solving a Helmholtz-like equation in the transverse plane Eq. (5.8b). The coefficients in that equation are also evaluated at  $\sigma = \sigma_*$ . Thus, the procedure for obtaining  $G(\underline{X}, t)$  is greatly simplified.

#### 5.2.1.4 The Modified Green's Function - Unshielded Case

The modified Green's function,  $G$ , obeys Eq. (5.8b). Unfortunately, it is extremely difficult to obtain closed form solutions for  $G$  since the coefficients of the governing equation depend on the coordinates  $(x, y)$ , in the cross plane. At high frequencies ( $k = \omega/c_\infty \rightarrow \infty$ ) the first term in the curly bracket of Eq. (5.8b) is much larger than the second term and certain analytic procedures are available\*. In the rest of this report, we restrict the discussion to high frequencies. In this case Eq. (5.8b) may be written as

$$A_t G + k^2 G = - \frac{i}{(2\pi)^{1/2}} \frac{c}{c_\infty^2} \frac{1}{k^2} \frac{\delta(x - x_0) \delta(y - y_0)}{(1 - M\sigma)^2} \quad (5.13a)$$

\*Strictly speaking, the first term in the curly bracket of Eq. (5.8b) is much larger than the second term when  $F$  changes slightly in one wave length.



where

$$g^2 = g^2(x, y) = \frac{\left[ \frac{(1 - M \cos\theta)^2}{(c/c_\infty)^2} - \cos^2\theta \right]}{(1 - M_c \cos\theta)^2} \quad (5.13b)$$

In Eq. (5.13b), the point of stationary phase  $\sigma^*$  has been substituted for  $\sigma$  in accordance with our previous remarks at the end of the last section,  $M = M(x, y)$  and  $M_c$  are the jet and convective Mach numbers respectively and  $c = c(x, y)$  is the speed of sound in the jet. The angle to the jet axis is denoted by  $\theta$ . At infinity,

$$g^2 \rightarrow g_\infty^2 = \frac{\sin^2\theta}{(1 - M_c \cos\theta)^2} \geq 0 \quad (5.13c)$$

provided that  $M \rightarrow 0$  and  $c/c_\infty \rightarrow 1$ . This implies that there is no jet flow at infinity and the ambient temperature is a constant there.

When the acoustic shielding function,  $g^2$ , is positive, the left hand side of Eq. (5.13a) is formally equivalent to classical wave propagation in a medium with variable index of refraction. In this case, a high frequency theory provides the lowest order solution in the frequency (see Reference 5.12). Goldstein<sup>(5.7)</sup> has applied this procedure for obtaining some idea of the acoustic shielding properties of asymmetric jets. In order to have some idea of the three-dimensionality of the acoustic field and the effectiveness of thermal shields at all emission angles, we solve the governing equation (5.13a) for an infinite planar shield. In this case, the jet velocity (or Mach number) and speed of sound are independent of the x-coordinate, specifically,

$$M = w(y)/c_\infty = M(y) \quad (5.14a)$$

$$= c(y) \quad (5.14b)$$

and we may obtain closed form solutions using various forms of the WKBJ procedure.

These solutions are obtained by first taking Fourier transforms in the x-direction. Define the transform of G as

$$\tilde{G}(y) = \frac{1}{(2\pi)^{1/2}} \int_{-\infty}^{\infty} e^{-ivx} G(x, y) dx \quad (5.15a)$$

with inverse

$$G = \frac{1}{(2\pi)^{1/2}} \int_{-\infty}^{\infty} e^{+ivx} \tilde{G}(y) dv \quad (5.15b)$$

where v is the transform variable. Applying this transformation to Eq. (5.13a) and setting  $x_0 = 0$ , we find

$$\frac{\partial^2 \tilde{G}}{\partial y^2} + k^2 (s^2 - v^2) \tilde{G} = \frac{A_0}{(2\pi)^{1/2}} \delta(y - y_0) \quad (5.15c)$$

where  $k = \omega/c_0$ ,

$$v = v/k \quad (5.15d)$$

$$A = A_0 = \frac{-i}{(2\pi)^{1/2}} \frac{c_0}{c_\infty^2} \frac{1}{k^2} \frac{1}{(1 - N_0 \sigma_0)^2} = \text{const} \quad (5.15e)$$

and now the subscript 0 means that a quantity is evaluated at the location of the source,  $y = y_0$  (e.g.,  $c_0 = c(y_0)$ ). Note that in the coefficient of the delta function on the right hand side of Eq. (5.15c) we may replace y by  $y_0$ .

The ordinary differential equation (5.15c) for  $\tilde{G}$  still has a variable coefficient, namely

$$\Gamma^2 = \Gamma^2(y) = g^2 - v^2 \quad (5.16)$$

which we call the extended shielding function. However, Eq. (5.15c) is readily solved by the WKBJ procedure.

Before we do this, we discuss the inverse transform in Eq. (5.15b). At infinity,  $\Gamma^2 \rightarrow \Gamma_\infty^2$  where  $\Gamma_\infty^2 = (g_\infty^2 - v^2)$  is a constant, so that

$$\tilde{G} \rightarrow B e^{\pm ik\Gamma_\infty y} \text{ as } y \rightarrow \pm \infty \quad (5.17)$$

for a suitable amplitude function  $\tilde{B}$  (which we will find momentarily). The upper and lower signs go together in Eq. (5.17). In order to have propagating waves at infinity, we require  $\Gamma_\infty^2 > 0$ , and  $\Gamma_\infty$  denotes the positive square root of  $\Gamma_\infty^2$ . After combining Eqs. (5.15b) and (5.17), we obtain

$$G = \frac{k}{(2\pi)^{1/2}} \int_{-\infty}^{\infty} \tilde{B} e^{ikr(\nu \cos\phi \pm \Gamma_\infty \sin\phi)} d\nu \quad (5.18)$$

where  $r = (x^2 + y^2)^{1/2}$  and  $\phi = \tan^{-1} (y/x)$  are the distance from the jet axis and the azimuthal angle respectively (Figure 5.1). As  $r \rightarrow \infty$ , the rapidly varying phase of the integrand in Eq. (5.18) is entirely contained in the exponential factor  $\exp ikr (\dots)$ . Thus, we may apply the method of stationary phase in order to evaluate Eq. (5.18) as  $r \rightarrow \infty$  (see Ref. 5.10, pp. 274). The result is

$$G = \left(\frac{k g_0}{r}\right)^{1/2} \tilde{B}_0 |\sin \theta| e^{i k g_0 r} e^{-\frac{i\pi}{4}} \quad (5.19a)$$

where  $B_*$  is evaluated at the point of stationary phase

$$\sigma = \sigma_0 = \frac{\cos \theta}{1 - M_c \cos \theta} \quad \text{and} \quad V = V_0 = g_0 \cos \theta \quad (5.19b)$$

Note from Eqs. (5.11b) and (5.19a) that

$$\hat{G}_0 = G_0 e^{-i k g_0 r} = \left(\frac{k g_0}{r}\right)^{1/2} \tilde{B}_0 |\sin \theta| e^{-\frac{i\pi}{4}} \quad (5.19c)$$

so that  $G(\underline{X}, t)$  is directly expressible in terms of Eqs. (5.12b) and (5.19c).

We next solve Eq. (5.15c) in order to obtain an explicit representation for the amplitude function  $B$ . At first, this will be done under the assumption that  $\Gamma^2 > 0$  everywhere; later we shall permit  $\Gamma^2$  to change its algebraic sign somewhere in the jet. The latter case happens when  $\theta$  is within the zone of silence. In the former case, the WKBJ solutions to Eq. (5.15c) are

$$\tilde{G} = \frac{e^{\pm i k \int \Gamma dy}}{\Gamma^{1/2}} \quad (5.20)$$

where  $\Gamma$  is the positive square root of  $\Gamma^2$  (see Ref. 5.10, pp. 291). On either side of the source  $y = y_0$ , we, therefore, have

$$\tilde{G} = \begin{cases} \frac{\alpha e^{ik \int_{y_0}^y \Gamma dy}}{\Gamma^{1/2}} & y > y_0 \\ \frac{\beta e^{-ik \int_{y_0}^y \Gamma dy}}{\Gamma^{1/2}} & y < y_0 \end{cases} \quad (5.21a)$$

$$\tilde{G} = \begin{cases} \frac{\alpha e^{ik \int_{y_0}^y \Gamma dy}}{\Gamma^{1/2}} & y > y_0 \\ \frac{\beta e^{-ik \int_{y_0}^y \Gamma dy}}{\Gamma^{1/2}} & y < y_0 \end{cases} \quad (5.21b)$$

for suitable constants  $\alpha$  and  $\beta$ . Note that Eqs. (5.21a, 5.21b) represent outgoing waves as  $y \rightarrow \pm \infty$  with time factor  $\exp(-i\omega t)$ .

The constants  $\alpha, \beta$  are determined by requiring  $\tilde{G}$  to be continuous across  $y = y_0$  and by allowing  $(\alpha G/\partial y)$  to jump by  $\Delta/(2\pi)^{1/2}$  across the source. This provides two linear equations for  $(\alpha, \beta)$  which can be solved easily in the limit as  $k \rightarrow \infty$ . For  $y \rightarrow -\infty$ , that is for an observation point below the acoustic shield.

$$\tilde{B} = \frac{\Delta}{2 (2\pi)^{1/2} ik \Gamma_0^{1/2} \Gamma_-^{1/2}} \cdot \left[ - ik \int_{y_0}^{\infty} (\Gamma - \Gamma_-) dy + ik \Gamma_- y_0 \right] \quad (5.22)$$

where  $\Gamma_0$  denotes the value of  $\Gamma$  at the source.

We next combine Eqs. (5.22), (5.19c) and (5.12b) to obtain

$$G(\underline{x}, t) = \frac{i}{4\pi k R c_\infty} \frac{c_0}{c_\infty} \frac{e^{-i\omega t} e^{ikR}}{(1 - M_0 \cos\theta)^2} \times \left(\frac{\Gamma_\infty}{\Gamma_0}\right)^{1/2} \exp ik \left[ \Gamma_\infty y_0 - \int_0^y (\Gamma - \Gamma_\infty) dy \right] \quad (5.23a)$$

where  $R$  and  $\theta$  denote the distance from the jet and the emission angle respectively, the subscripts 0 and  $\infty$  indicate the values of a variable at the source and infinity,

$$\Gamma = \Gamma(y) = \frac{\left[ \frac{(1 - M \cos\theta)^2}{(c/c_\infty)^2} - \cos^2\theta - \sin^2\theta \cos^2\phi \right]^{1/2}}{1 - M_c \cos\theta} \quad (5.23b)$$

$M_c = U/c_\infty$  is the source convection Mach number and  $\phi$  is the azimuthal angle.

The Green's function Eq. (5.23a) represents an outgoing wave whose strength is explicitly proportional to the speed of sound at the source. A convective amplification factor  $(1 - M_0 \cos\theta)^{-2}$  appears because of jet (rather than source) convection effects. This factor determines one part of the directivity; the other part is contained in  $(\Gamma_\infty/\Gamma_0)^{1/2}$  which depends on both the emission and azimuthal angles,  $\theta$  and  $\phi$ . Note that the Green's function also depends implicitly on the jet velocity and temperature through the factor  $(\Gamma/\Gamma_0)^{1/2}$ .

From the Green's function, we can readily obtain the solutions for various convecting dipoles and quadrupoles. Define the Lilley operator (actually the original operator  $L$  divided by the square of the mean speed of sound) as (see also Eq. (5.6))

$$M = -\frac{1}{c^2} \frac{D^3}{Dt^3} - \frac{D}{Dt} \Delta - (\nabla \log c^2) \cdot \frac{D}{Dt} \nabla + 2 (\nabla w) \cdot \nabla \frac{\partial}{\partial z} \quad (5.24a)$$

and a convecting disturbance

$$R = e^{-i\omega t} \delta(x - x_0) \delta(y - y_0) \delta(z - z_0 - U_c t) \quad (5.24b)$$

where  $z_0$  is the  $z$  location of the source at  $t = 0$ . The source, dipole and quadrupole solutions of Lilley's equation satisfy

Source

$$M [S] = \frac{D}{D_t} R \quad (5.25a)$$

(m) Dipole:

$$M [D_m] = - \frac{D}{D_t} \frac{\partial R}{\partial \xi_{0m}} \quad m = 1, 2, 3 \quad (5.25b)$$

(m - n) Quadrupole:

$$M [Q_{mn}] = \frac{D}{D_t} \frac{\partial^2 R}{\partial \xi_{0m} \partial \xi_{0n}} \quad m = 1, 2, 3 \quad n = 1, 2, 3 \quad (5.25c)$$

where  $\xi_{0m}$  stands for the source coordinates  $x_0, y_0, z_0$  respectively as  $m$  takes on values 1, 2, and 3. After the space derivatives have been evaluated in Eqs. (5.25b, 5.25c)  $x_0$  and  $z_0$  are set to zero. This implies no loss in generality since the planar shield problem is invariant under a coordinate translation in the  $x$  and  $z$  directions.

After carrying out the indicated differentiations in Eq. (5.25), we obtain the pressure to first order in the frequency ( $k = \omega/c_\infty \rightarrow \infty$ ) in the far field below the thermal shield ( $y \rightarrow -\infty$ )

Source:

$$S(\underline{X}, t) = \frac{1}{4\pi R} \frac{c_0}{c_m} \frac{e^{-i\omega t} e^{ikR}}{(1 - M_0 \cos\theta)(1 - M_c \cos\theta)} \times \left(\frac{\Gamma_m}{\Gamma_0}\right)^{1/2} \exp ik \left[ \Gamma_m y_0 - \int_{y_0}^{\infty} (\Gamma - \Gamma_m) dy \right] \quad (5.26a)$$

Dipoles:

$$D_x = ik \frac{\sin\theta \cos\phi}{1 - M_c \cos\theta} S(\underline{X}, t) \quad (5.26b)$$

$$D_y = - ik \frac{\hat{\Gamma}_0}{1 - M_c \cos\theta} S(\underline{X}, t) \quad (5.26c)$$

$$D_z = ik \frac{\cos\theta}{1 - M_c \cos\theta} S(\underline{X}, t) \quad (5.26d)$$



Quadrupoles:

$$\rho_{xx} = -k^2 \frac{\sin^2 \theta \cos^2 \phi}{(1 - M_c \cos \theta)^2} S(\underline{X}, t) \quad (5.26e)$$

$$\rho_{yx} = \rho_{xy} = k^2 \frac{\hat{\Gamma}_0 \sin \theta \cos \phi}{(1 - M_c \cos \theta)^2} S(\underline{X}, t) \quad (5.26f)$$

$$\rho_{zx} = \rho_{xz} = -k^2 \frac{\sin \theta \cos \theta \cos \phi}{(1 - M_c \cos \theta)^2} S(\underline{X}, t) \quad (5.26g)$$

$$\rho_{yy} = -k^2 \frac{\hat{\Gamma}_0^2}{(1 - M_c \cos \theta)^2} S(\underline{X}, t) \quad (5.26h)$$

$$\rho_{zy} = \rho_{yz} = k^2 \frac{\cos \theta}{(1 - M_c \cos \theta)^2} \hat{\Gamma}_0 S(\underline{X}, t) \quad (5.26i)$$

$$\rho_{zz} = -k^2 \frac{\cos^2 \theta}{(1 - M_c \cos \theta)^2} S(\underline{X}, t) \quad (5.26j)$$

where

$$\hat{\Gamma} = (1 - M_c \cos \theta) \Gamma \quad (5.26k)$$

and  $\Gamma$  is defined by Eq. (5.23b). Note that we have written  $D_x$  for  $D_1$ ,  $D_y$  for  $D_2$ , etc. As before, the subscripts 0 and  $\infty$  indicate that a quantity is evaluated at the source ( $y = y_0$ ) and infinity respectively,  $c = c(y)$  is the speed of sound in the plane thermal shield,  $M = M(y)$  is the

corresponding Mach number and  $\theta$  and  $\phi$  are the emission and azimuthal angles respectively (Figure 5.1). The subsonic source convective Mach number is denoted by  $M_c$ . In the Lighthill theory ( $M = 0$ ,  $c/c_\infty = 1$ ,  $\hat{\Gamma} = \hat{\Gamma}_0$ ,  $\sin\theta = \sin\phi$ ).

The source function  $S(\underline{x}, t)$  contains two Doppler factors of convective amplification; one is based on the jet Mach number at the source, the other on the source convection Mach number. An additional far field directivity arises because of the presence of the factor  $(\Gamma_\infty/\Gamma_0)^{1/2}$ . The magnitude of the acoustic pressure in the far field is explicitly proportional to the speed of sound at the source although there is also implicit dependence on the jet velocity and temperature through the  $\Gamma$  factor.

The dipole and quadrupole solutions are proportional to the first and second powers of the frequency (actually  $k = \omega/c_\infty$ ) as expected from the corresponding classical results. Furthermore, they carry the usual factors of the source convective amplification,  $(1 - M_c \cos\theta)$ . Note, however, that the dipoles and quadrupoles (e.g.,  $D_Y$  and  $Q_{xy}$ ) depend in a fairly complicated manner on the jet Mach number and temperature through the terms  $\Gamma_0$  and  $\Gamma_\infty$ . This additional dependence represents some of the interaction between the mean flow and the aerodynamic sound field. Observe that when  $\Gamma_0 = \Gamma_\infty$  (i.e., the source is well above the shielding jet), the magnitude of the acoustic field of the source is omnidirectional except for convective effects Eq. (5.26a). This result may be confirmed by geometrical acoustics.

#### 5.2.1.5 The Modified Green's Function - Shielded Case

By far the most important effect of the thermal acoustic shield is called acoustic shielding. This occurs when the extended shielding function  $\Gamma^2(y)$  (see Eq. (5.23b) changes its algebraic sign somewhere in the jet. In this report, we consider one of the simplest\* possibilities, namely, when  $\Gamma^2$  vanishes at two points  $y_1$  and  $y_2$  with  $y_1 \leq y_2$ . Note that the zeros of  $\Gamma^2$  must occur in pairs since  $\Gamma^2 \rightarrow \Gamma_\infty^2 > 0$  as  $y \rightarrow \pm \infty$  (Figure 5.2).

---

\*A consideration of all the other possibilities is beyond the scope of this effort.

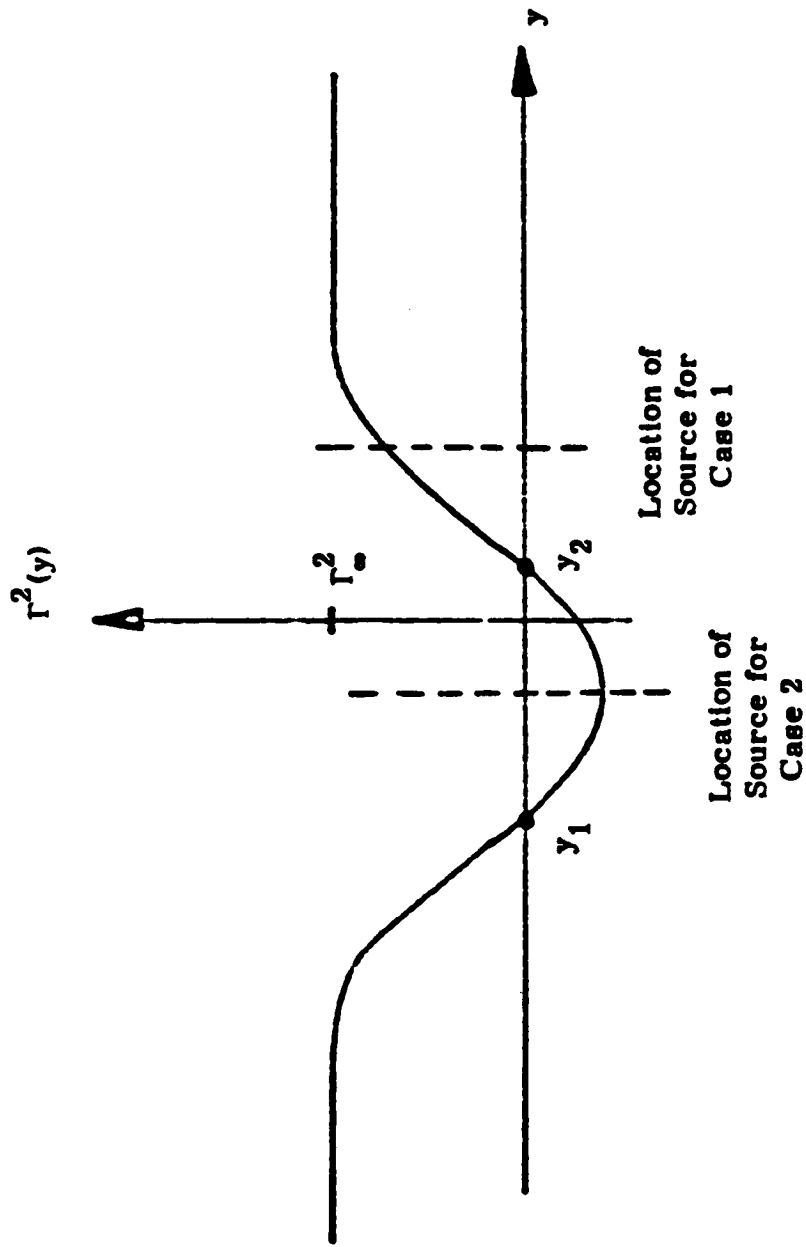


Figure 5.2. The Behaviour of the Extended Shielding Function and Turning Points.

We shall now treat briefly two of the most important cases: (1) when the source lies above [or to the right of (see Figure 5.2)] the region in which  $\Gamma^2 < 0$ ;  $y_0 > y_2$  and (2) when the source lies in the region where  $\Gamma^2$  is negative;  $y_1 < y_0 < y_2$ . The third possibility ( $y_0 < y_1$ ) is of little practical interest for an observer below the jet ( $y \rightarrow -\infty$ ) since in this case the source is not "shielded" by the secondary jet.

We can build on the ideas developed in the previous section. For  $y > y_2$  and  $y < y_1$ , a solution of the type given by Eq. (5.20) is valid. Across the turning points or the zeroes of  $\Gamma^2$ , we must match these oscillating solutions to (real) exponential solutions according to the WKBJ formulas (see Reference 5.10, pp. 295). The analysis is straightforward and details will be omitted. Note that across the source,  $y = y_0$ ,  $\tilde{G}$  is continuous and  $(\partial\tilde{G}/\partial y)$  jumps by an amount  $\Delta/(2\pi)^{1/2}$ .

With these remarks in mind, the solutions for the source function,  $S(\underline{X}, t)$  are in the far field below the jet ( $y \rightarrow -\infty$ ).

Case 1:  $y_0 > y_2$  (completely shielded source)

$$S(\underline{X}, t) = \frac{1}{4\pi R} \frac{c_0}{c_\infty} \frac{e^{-i\omega t} e^{ikR}}{(1 - M_0 \cos\theta)(1 - M_c \cos\theta)}$$

$$\times \left(\frac{\Gamma_\infty}{\Gamma_0}\right)^{1/2} e^{-k \int_{y_1}^{y_2} \gamma dy} \exp ik \left[ \Gamma_\infty (y_1 - y_2) + \Gamma_{J_0} - \int_{y_0}^{\infty} (\Gamma - \Gamma_\infty) dy \right] \quad (5.27a)$$

where  $\int$  denotes integration omitting the interval  $(y_1, y_2)$ . Note the appearance of the real exponential factor whose integrand is defined by

$$\gamma^2 = -\Gamma^2 > 0 \quad (5.27b)$$

and  $\gamma$  is the positive square root of  $\gamma^2$ .

Case 2:  $y_1 < y_0 < y_2$  (partially shielded source)

$$S(\underline{X}, t) = \frac{1}{4\pi R} \frac{c_0}{c_\infty} \frac{e^{-i\omega t} e^{ikR}}{(1 - M_0 \cos\theta)(1 - M_c \cos\theta)} e^{-\frac{i\pi}{4}}$$

$$\times \left(\frac{\Gamma_\infty}{\Gamma_0}\right)^{1/2} e^{-k \int_{y_1}^{y_0} \gamma dy} \exp ik \left[ \Gamma_{J_1} - \int_{y_1}^{\infty} (\Gamma - \Gamma_\infty) dy \right] \quad (5.27c)$$

These solutions look very similar to Eq. (5.26a) except for the appearance of a real exponential and a slight modification in the complex phase. The appearance of the real exponential factor is caused by acoustic shielding; the amount of shielding is roughly proportional to a suitably weighted distance between the source and observer with the understanding that no shielding occurs when  $\Gamma^2 > 0$  over this distance. The pressure in the far field for dipoles and quadrupoles for Case 1 is given by expressions Eqs. (5.26b

through 5.26j), where, of course, (5.27a) is used for  $S(\underline{X}, t)$ . On the other hand, the corresponding pressures for Case 2 are also given by Eqs. (5.26b) through (5.26j) provided that  $(i\hat{\gamma}_0)$  is substituted for  $\hat{\Gamma}_0$  where

$$\hat{\gamma} = \gamma (1 - M_c \cos\theta) \quad (5.28)$$

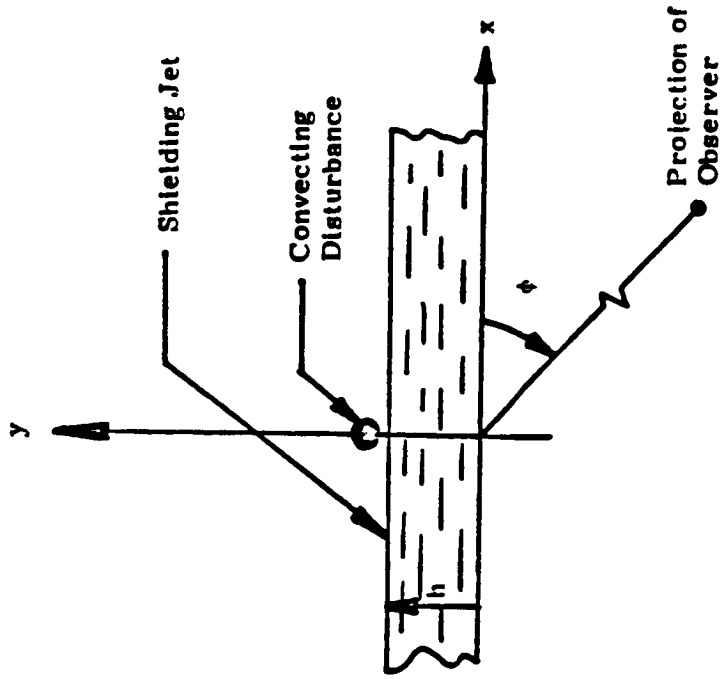
and Eq. (5.27c) is used for  $S(\underline{X}, t)$ . Recall that the subscript 0 designates the value of a variable at the source.

#### 5.2.1.6 Discussion of Results

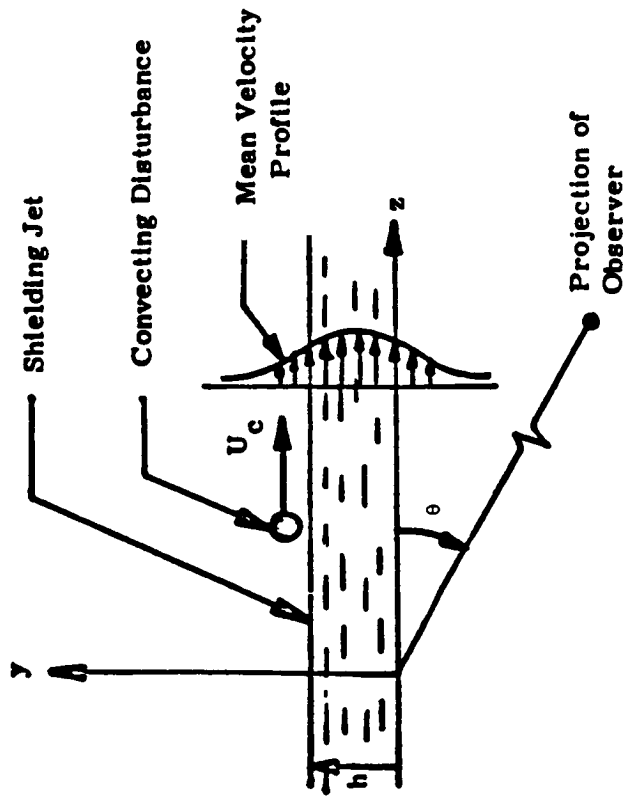
We have derived expressions for the acoustic field of convecting disturbances (sources, dipoles and quadrupoles) placed anywhere in a parallel jet (i.e., in a thermal acoustic fluid shield) whose mean velocity and temperature profiles are independent of the transverse coordinate,  $x$ . The idealized geometry of this problem is shown in Figure 5.3. The convecting disturbance represents, roughly speaking, the noise generated by the primary jet of an engine and the acoustic field below the shield ( $y \rightarrow -\infty$ ) is given by equations (5.26). When acoustic shielding is present, which occurs for certain values of  $\theta$  and  $\phi$ , Eqs. (5.27a) and (5.27c) are used in place of Eq. (5.26a). This problem sheds light on the noise reduction due to asymmetric fluid shields.

The influence of shield velocity and temperature are evaluated herein. The jet velocity and temperature profiles are taken to be uniform (i.e., slug profiles) for simplicity. Thus the present results may be thought of as an extension of Mani's (5.5) work on axially symmetric jets to asymmetric jets.

In Figures 5.4 through 5.9, we plot the acoustic pressure in the far field below the thermal acoustic shield for certain typical values of shield fluid velocity, temperature, source Strouhal number, etc. The quantity which is plotted on the vertical axis is



Cross Section in  $(x-y)$  Plane



Cross Section in  $(y-z)$  Plane

Figure 5.3. Geometry of Planar Shield.

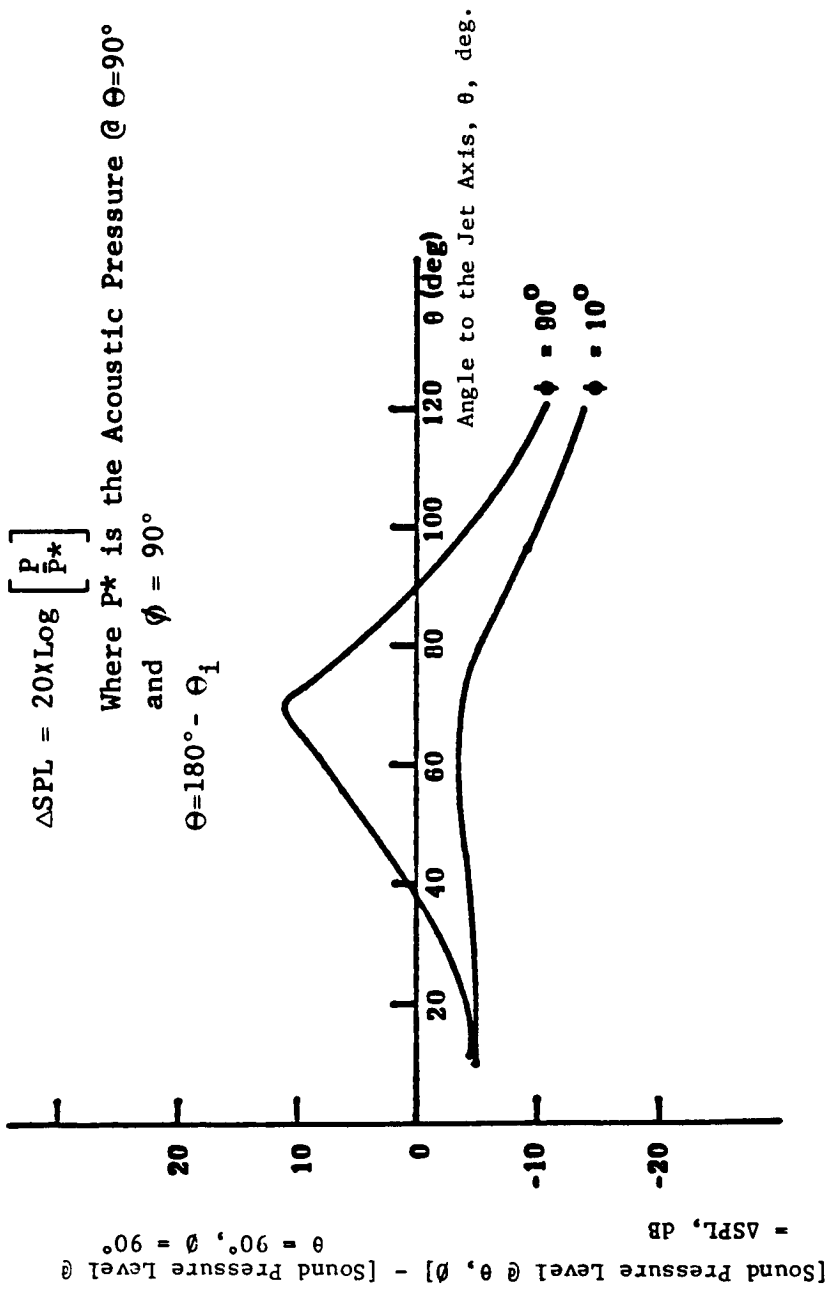


Figure 5.4. Effect of Azimuthal Angle  $\phi$  on Directivity. Shield Mach Number,  $M = 1$  and Temperature,  $(c/c_\infty)^2 = 3$ ; Primary Jet Convective Mach Number  $M_c = 1.5$ ; Primary Jet is Located Above the Shield  $M_0 = 0$ ,  $c_0/c_\infty = 1$ ,  $y_0/h = 1$ ; Strouhal Number Based on Shield Velocity and Primary Jet Characteristic Frequency is  $St = 0.2$ .



[Sound Pressure Level @  $\theta, \theta$ ] - [Sound Pressure Level @  $\theta = 90^\circ, \theta = 90^\circ$ ]  
 =  $\Delta$ SPL, dB

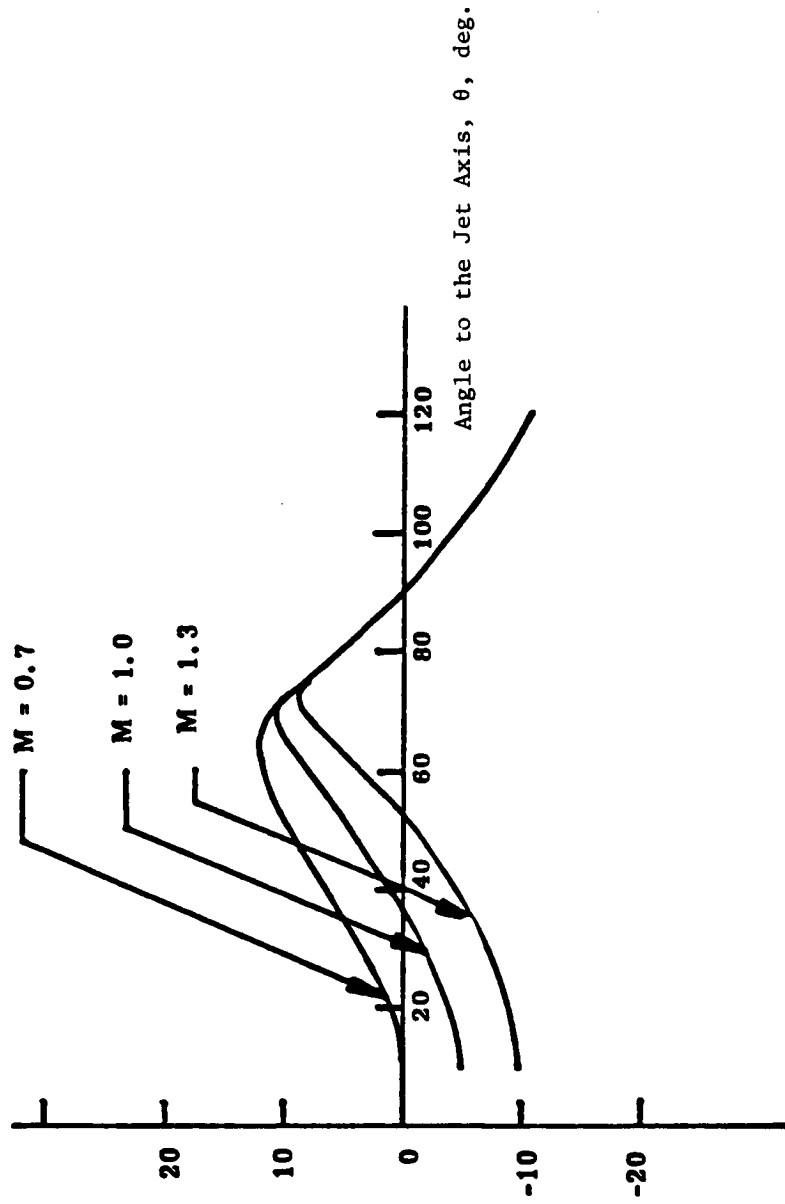


Figure 5.5. Effect of Shield Mach Number on Directivity at Azimuthal Angle of  $\phi = 90^\circ$ . (For Values of Other Parameters, see Figure 5.4).

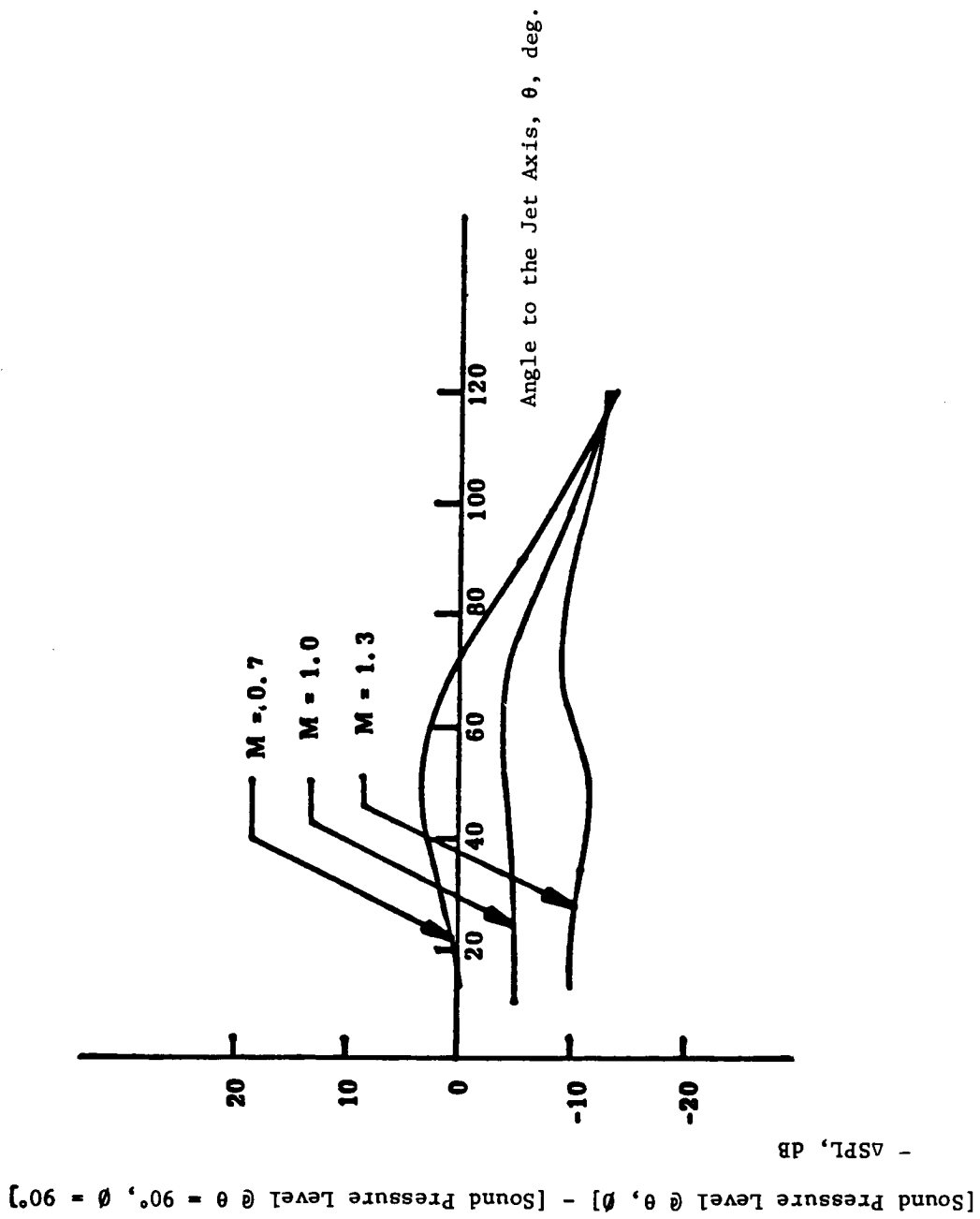


Figure 5.6. Effect of Shield Mach Number on Directivity at Azimuthal Angle of  $\theta = 10^\circ$ . (For Values of Other Parameters, see Figure 5.4).

[Sound Pressure Level @  $\theta, \theta$ ] - [Sound Pressure Level @  $\theta = 90^\circ, \theta = 90^\circ$ ]

= ASPL, dB

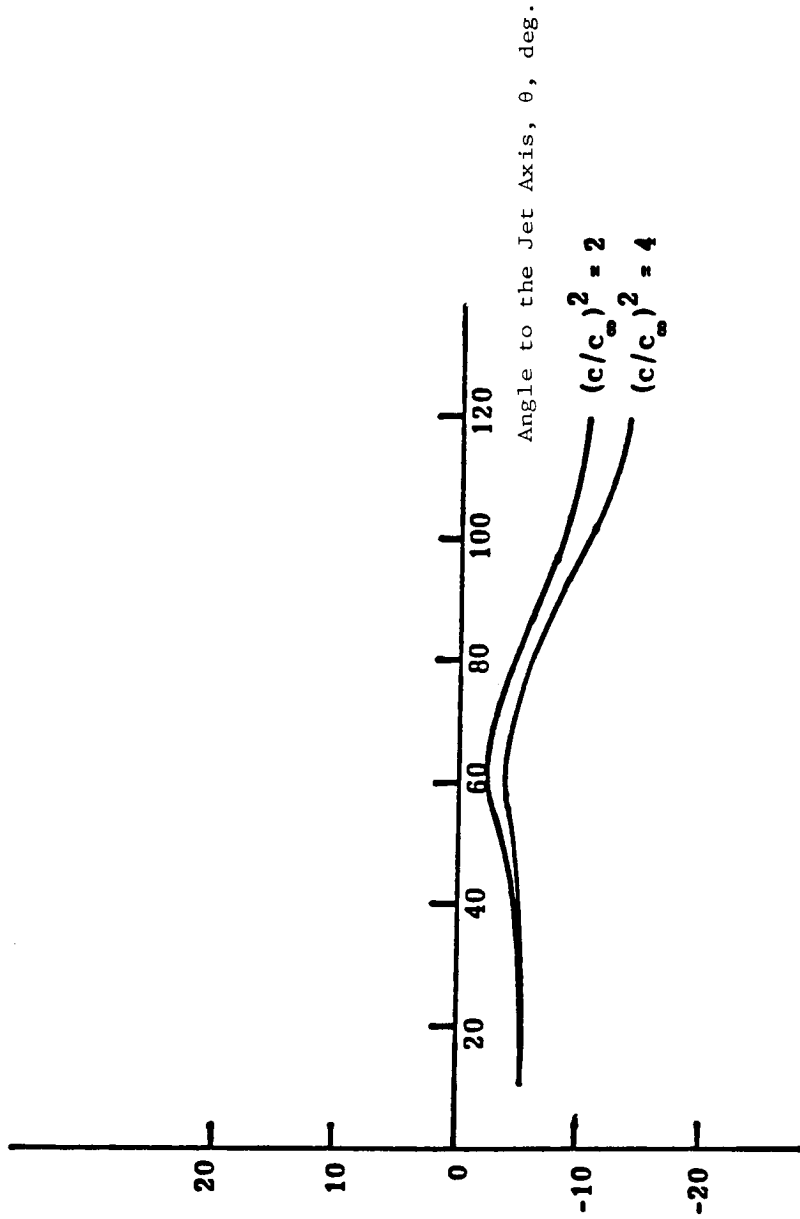


Figure 5.7. Effect of Shield Temperature on Directivity at Azimuthal Angle of  $\phi = 10^\circ$ . (For Values of Other Parameters, see Figure 5.4).

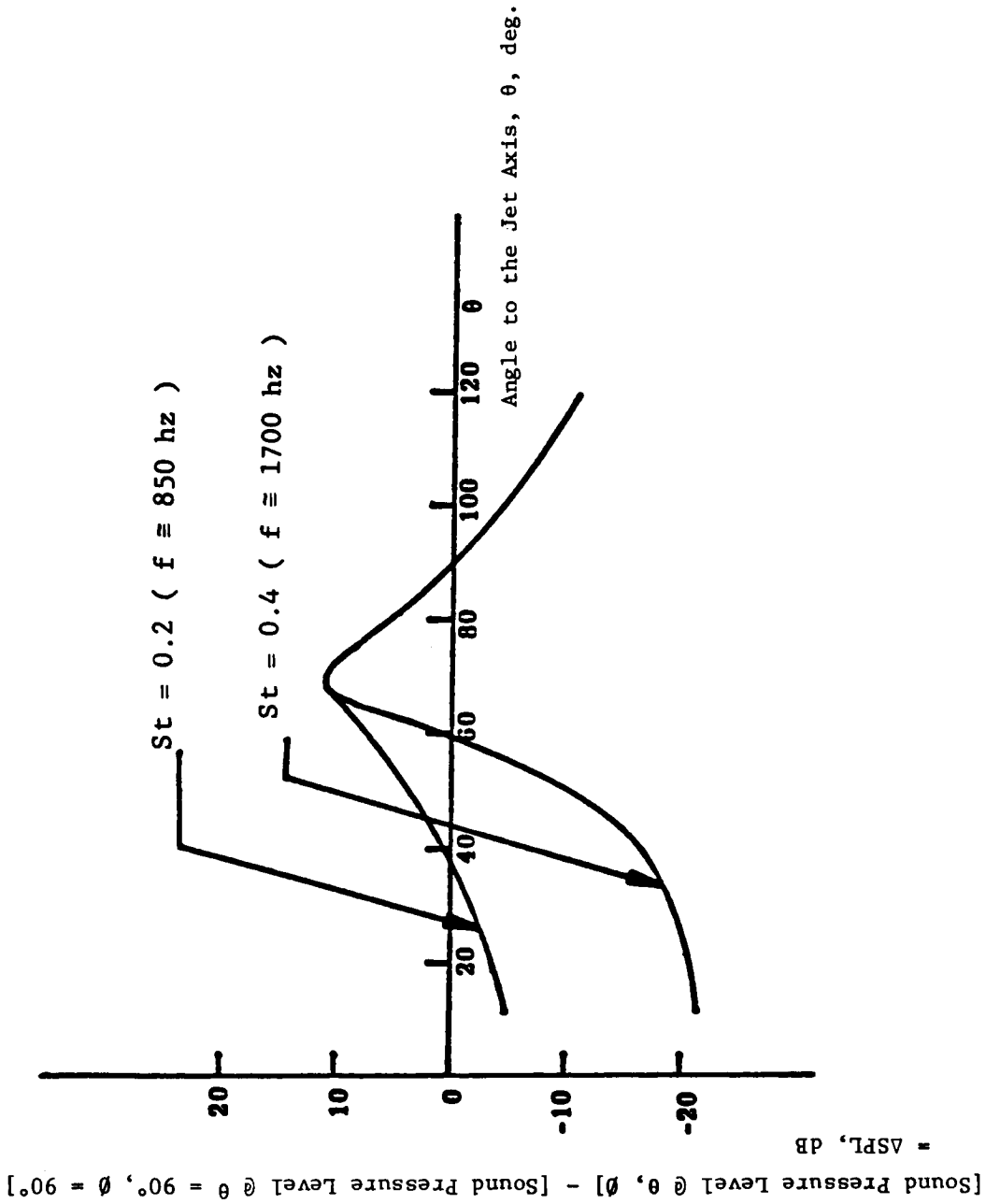


Figure 5.8. Effect of Primary Jet Strouhal Number on Directivity at Azimuthal Angle of  $\phi = 90^\circ$ . (For Values of Other Parameters, see Figure 5.4).

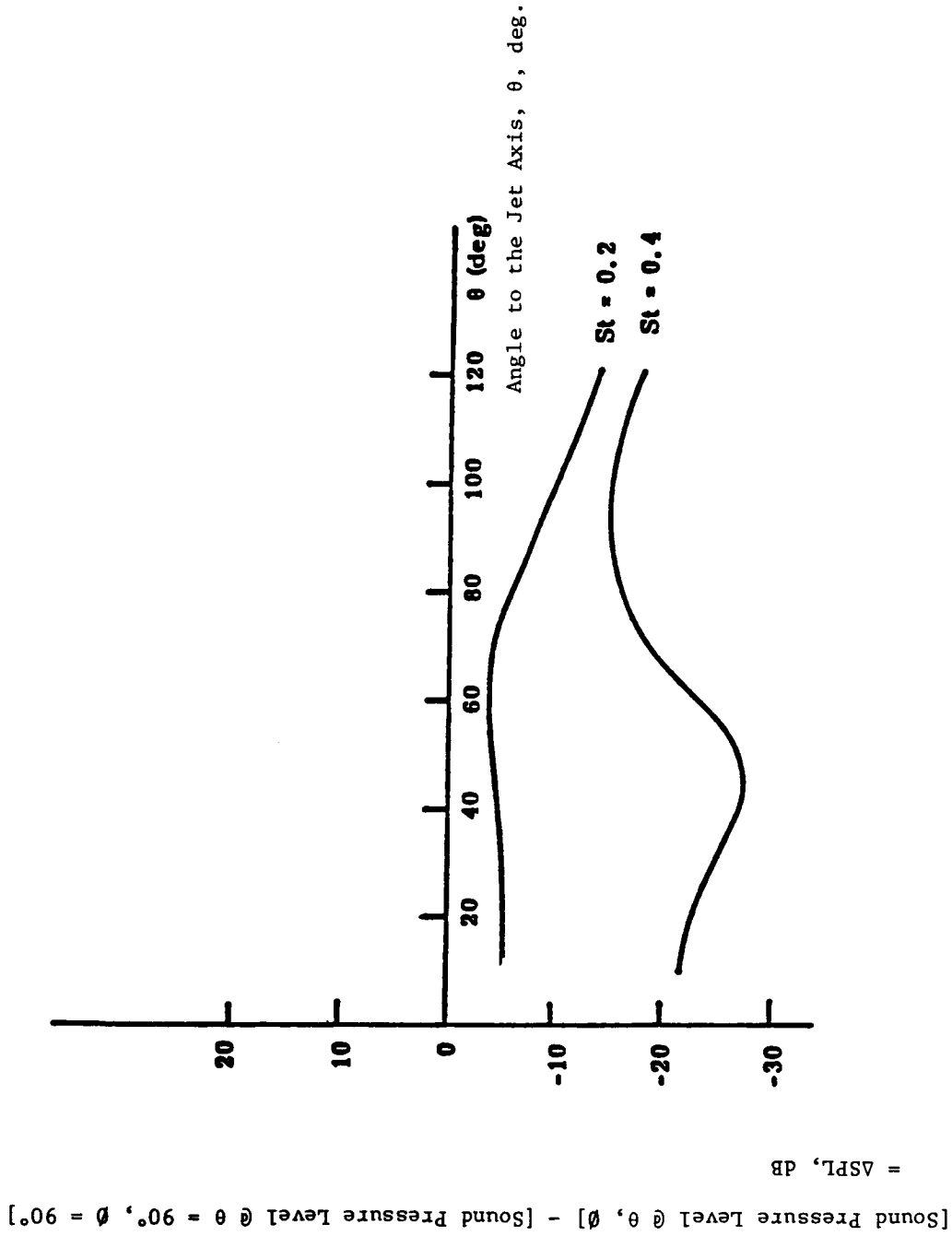


Figure 5.9. Effect of Primary Jet Strouhal Number on Directivity at Azimuthal Angle of  $\emptyset = 10^\circ$ . (For Values of Other Parameters, see Figure 5.4).

$$\Delta\text{SPL} = 10 \log_{10} (p/p_*)^2 \quad (5.29a)$$

where  $p_*$  is the value of  $p$  at  $\theta = \phi = 90^\circ$ . On the other hand,  $p$  is obtained from a superposition of uncorrelated quadrupoles of equal strength, namely,

$$p^2 = \sum_{i,j} |Q_{ij}|^2 \quad (5.29b)$$

where we have used an obvious notation and written  $Q_{11}$  for  $Q_{xx}$ , etc. The primary jet, which is now represented by a set of quadrupoles in the sense of Eq. (5.29b), has a velocity of 2500 fps. This corresponds to a primary jet convection Mach number of  $M_c = 1.5$ .

The primary jet is placed just above the thermal shield so that the shield velocity there is approximately zero and the shield temperature is very nearly the same as that in the ambient; this permits us to set  $M_0 \approx 0$ ,  $c_0/c_\infty \approx 1$  and  $y_0/h \approx 1$  where  $h$  is the thickness of the shield. Unless otherwise stated, the velocity and temperature of the shield will be respectively taken as 1100 fps and 1380°R (corresponding to  $M \approx 1$  and  $c/c_\infty \approx 1.7$ ).

In Figure 5.4, we show the sound field as a function of emission angle  $\theta$  for two values of the azimuthal angle  $\phi$ . When the observer is directly below the jet ( $\phi = 90^\circ$ ), the directivity looks very much like that of classical jet noise: the noise first increases as the angle to the jet axis decreases because of convective amplification. However, at smaller angles to the jet axis, the noise is greatly reduced because of acoustic shielding. On the other hand, on the sideline ( $\phi = 10^\circ$ ), the noise is 5-10 dB less than the noise directly below the jet. The principal reason for this is that the noise emitted toward the sidelines propagates through a thicker effective thermal acoustic shield and, therefore, its intensity is reduced. In fact, a zone of silence appears for small values of  $\phi$  even when the emission angle is quite large, say  $\theta \sim 90^\circ$ . This is easily seen from the extended shielding function Eq. (5.23b) which becomes imaginary when  $\phi < \phi_c$  where  $\phi_c = \cos^{-1}(c_\infty s/c)$ . Thus for a planar shield, we have zones of silence not only at small angles to the jet axis, but also at small azimuthal angles even when the emission angle is quite large.

The dependence of the directivity on the shield velocity is shown in Figures 5.5 and 5.6 for two values of the azimuthal angle  $\phi$ . As expected, an increase in the shield velocity will result in a decrease of the noise. Recall that in this calculation, the self noise of the thermal acoustic shield is neglected. This effect is fairly dramatic and we estimate that several decibels in noise reduction is possible by the proper choice of the velocity. Of course, the present slug flow calculations probably exaggerate the effects of velocity, Strouhal number, etc., as in the axially symmetric case (see Ref. 5.5).

The effect of shield temperature is shown in Figure 5.7. This effect is surprisingly modest and arises only when the extended shielding function, Eq. (5.23b) is imaginary. It is interesting to note that temperature effects are the most important when  $(1 - M \cos\theta)$  is large; this occurs when the emission angle  $\theta$  is large. We reiterate that velocity effects are the most important at small emission angles whereas temperature effects are most important at large emission angles. This implies that by a suitable combination of shield velocity and temperature, it is possible to reduce the noise for a range of angles.

Finally, the effects of source frequency are shown in Figures 5.8 and 5.9. As expected, a thermal acoustic shield is most effective at high frequencies.

#### 5.2.1.8 Conclusions

The present analysis shows that thermal acoustic shields are effective in reducing the noise of jet engines. Several decibels in noise reduction is possible. This reduction can be achieved by a proper choice of shield velocity and temperature; velocity effects are most important in the rearward quadrant whereas temperature effects are most pronounced in the forward quadrant. In relative terms, velocity effects are more important than temperature effects. The present work also shows that for a planar shield, little noise is radiated to the sidelines because of the appearance of a secondary zone of silence.

### 5.2.2 ANALYTICAL/COMPUTATIONAL MODIFICATIONS OF THE M\*G\*B METHOD FOR PARTIAL THERMAL ACOUSTIC SHIELDS AND SELECTIVE DATA THEORY COMPARISONS

This subsection summarizes the modifications performed on the M\*G\*B method to account for the azimuthal variations associated with partial thermal acoustic shields and shows some selective data theory comparisons.

A full three dimensional calculation of the acoustic field of partial thermal acoustic shields is beyond the scope of present work. The application of an extension of the Reichardt's method has yielded predictions of the jet flow field in terms of velocity, temperature and turbulence intensity distributions in a three dimensional space. In the M\*G\*B version described in Ref. 5.1, the noise source characteristics (viz., eddy source strength, source frequency, etc.) and the flow field characteristics (i.e., velocity, temperature, etc.) were circumferentially averaged and the acoustic problem was converted from a 3-D problem to an axisymmetric problem. The modifications of the M\*G\*B method incorporated to convert the full 3-D problem into a quasi-3D problem are:

- (1) Utilize the local jet velocity and static temperature along the line of sight of the observer, which vary azimuthally;
- (2) Utilize an eddy convection Mach number which is weighted by the azimuthally varying eddy source strength and circumferentially averaged; and,
- (3) Utilize an eddy source frequency which is weighted by the azimuthally varying eddy source strength and circumferentially averaged.

The above modifications yield an "ad-hoc" acoustic solution to the problem of partial thermal acoustic shield. The principal factor which yields azimuthal variation in the acoustic results is the velocity and static temperature profiles along the line of sight used in calculating the fluid



shielding effects. The rationale for choosing the line of sight approach for calculating the fluid shielding effects is that, the fluid shielding effects have been found to be significant at high frequencies and acoustic waves at high frequencies behave like rays. In order to account for the azimuthal variation in eddy convection Mach number and source frequency, a source strength weighted, circumferentially averaging procedure was adopted for them, instead of the simple circumferential averaging adopted in Ref. 5-1. The above modifications have been incorporated into the M\*G\*B computer code and calculations have been performed on configuration TAS-2 (i.e., annular plug nozzle with 180° shield of 0.48" thickness) and TAS-1 (i.e., baseline annular plug nozzle).

Figure 5-10 shows the sketch of configuration TAS-2 (Annular plug nozzle with 180° TAS of 0.48" thickness) on an AST size for performing the M\*G\*B predictions. Figure 5-11 shows the description of the partial shield geometry in terms of the nodes. The nodes are prescribed at 10° intervals on the inner and outer edges of the partial shield to form a closed boundary for the shield jet. Only one node is sufficient for prescribing the axially symmetric core jet.

M\*G\*B calculations have been performed for both TAS-1 (Baseline annular plug nozzle) and TAS-2 (Annular Plug nozzle with 180° TAS) configurations. The cycle conditions corresponds to a sonic core jet with shield jet at a 0.6 velocity ratio. Figure 5-12 shows the influence of the asymmetric shield on normalized maximum and circumferentially, radially averaged mean velocity axial distribution as predicted by the M\*G\*B program for the annular plug nozzle. Note that the decay of the plume with the partial shield is slower compared to without the shield for both the maximum and averaged mean velocities. This could be attributed to reduced shearing stresses in the presence of the shield. Figure 5-13 shows the azimuthal variation of the normalized mean and turbulent velocities at three (3) axial stations (viz.,  $X/D_{eq} = 1.6, 4, \text{ and } 10.2$ ) at a normalized radial location  $R/D_{eq} \approx 0.5$  as predicted by the M\*G\*B program. Note that at  $R/D_{eq} \approx 0.5$  and  $X/D_{eq} = 1.6$ , there is an azimuthal variation for  $60^\circ < \phi < 120^\circ$  (see sketch on

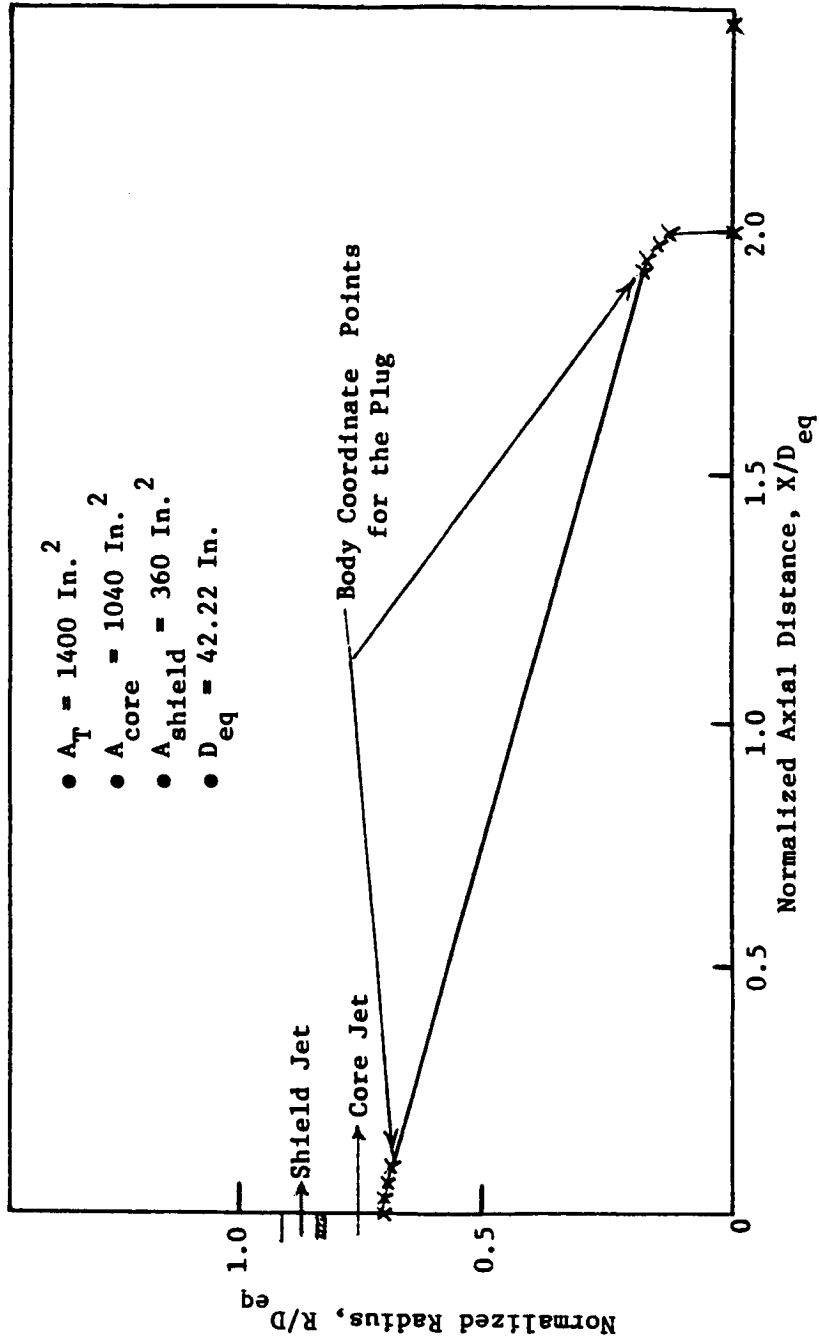


FIGURE 5.10. SKETCH OF CONFIGURATION TAS-2 (ANNULAR PLUG NOZZLE WITH  $180^\circ$  THERMAL ACOUSTIC SHIELD) FOR M\*G\*B PREDICTIONS.

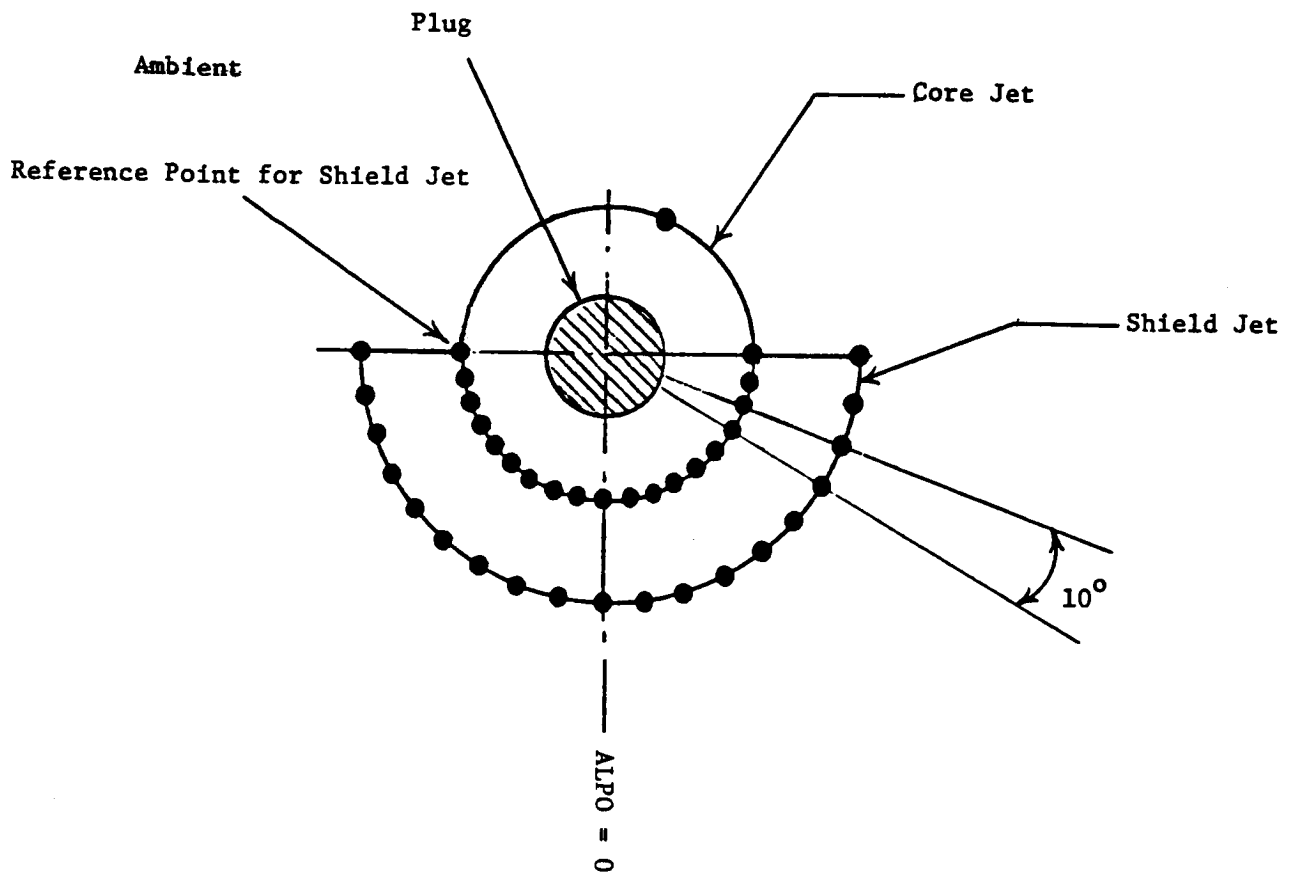


Figure 5.11. PRESCRIPTION OF THE NODAL GEOMETRY OF CONFIGURATION TAS-2 (ANNULAR PLUG NOZZLE WITH 180° TAS) FOR M\*G\*B PREDICTIONS.

- $A_T = 1400 \text{ In.}^2$  for TAS-2
- $v^j = 1867 \text{ fps}$ ,  $T_T^j = 1730^\circ\text{R}$ ,  $P_T^j = 1.89$
- $1040 \text{ In.}^2$  for TAS-1
- $v^{sj} = 1121 \text{ fps}$ ,  $T_T^{sj} = 1730^\circ\text{R}$ ,  $P_T^{sj} = 1.24$
- $D_{eq} = 42.22 \text{ In.}$  Based on  $A_T$  of TAS-2
- Static,  $V_{a/c} = 0$

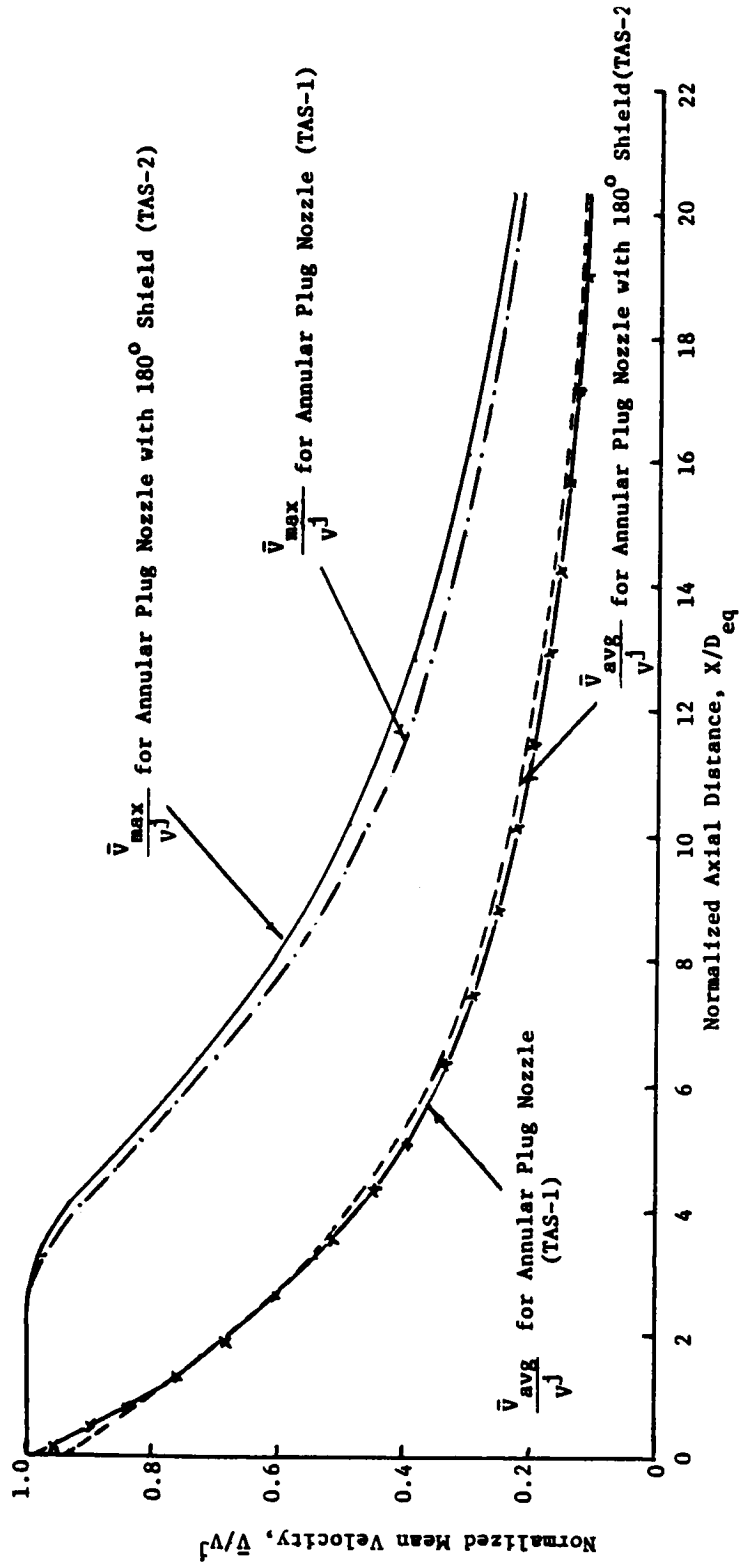


FIGURE 5.12. INFLUENCE OF THE 180° SHIELD ON NORMALIZED MAXIMUM AND AVERAGED MEAN VELOCITY AXIAL DISTRIBUTION AS PREDICTED BY M\*G\*B FOR AN ANNULAR PLUG NOZZLE.

- o  $V^j = 1867$  fps
- o  $D_{eq} = 42.22$  In.

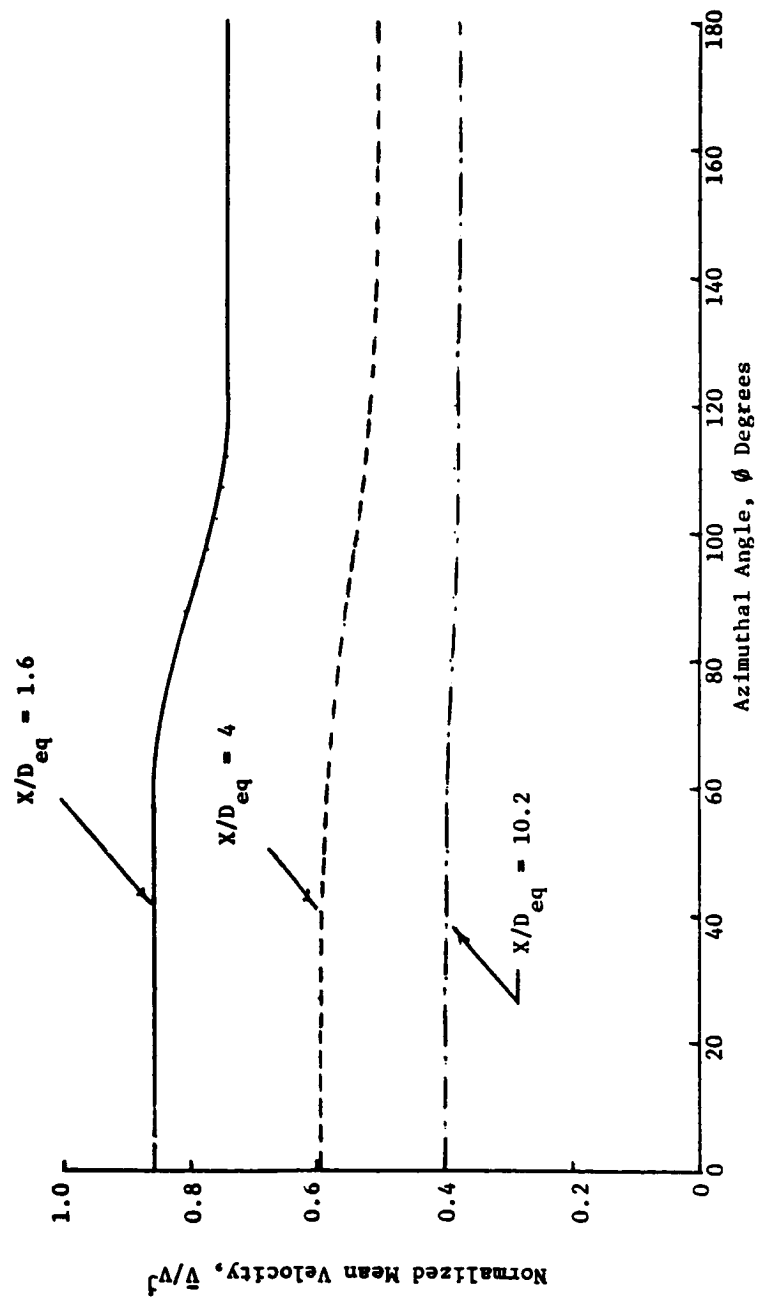
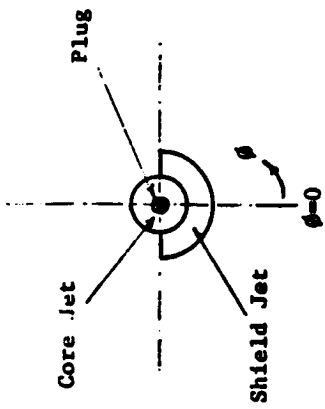


FIGURE 5.13a. AZIMUTHAL VARIATION OF THE MEAN VELOCITY AS PREDICTED BY M\*G\*B FOR ANNULAR PLUG NOZZLE WITH 180° SHIELD AT THREE (3) AXIAL STATIONS AT  $R/D_{eq} \approx 0.5$ .

- o  $v^j = 1867$  fps
- o  $D_{eq} = 42.22$  In.

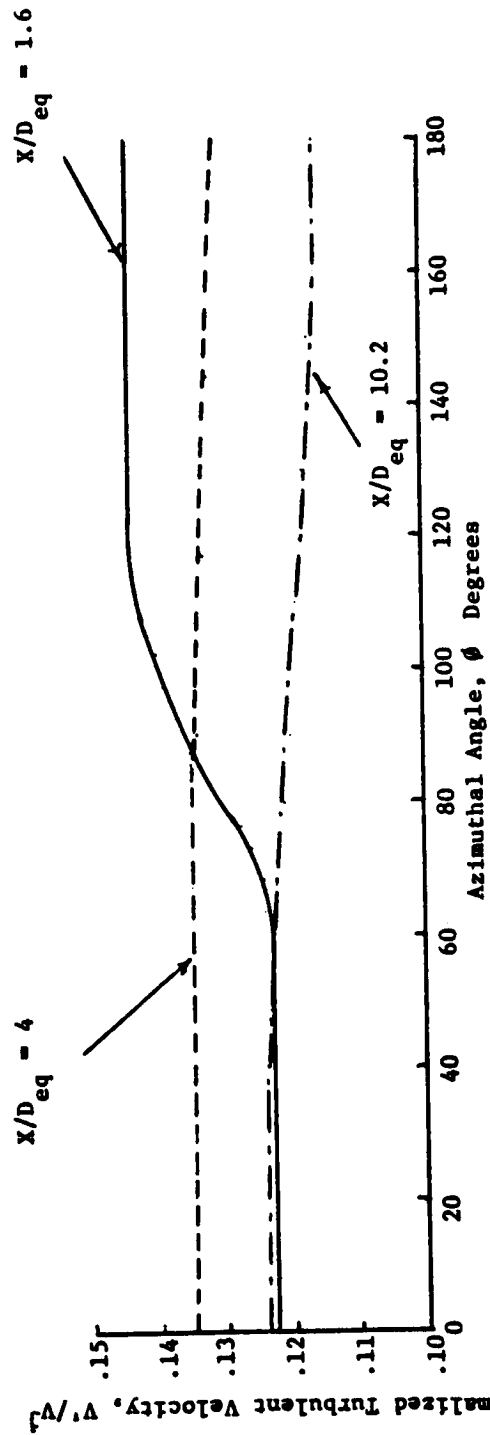
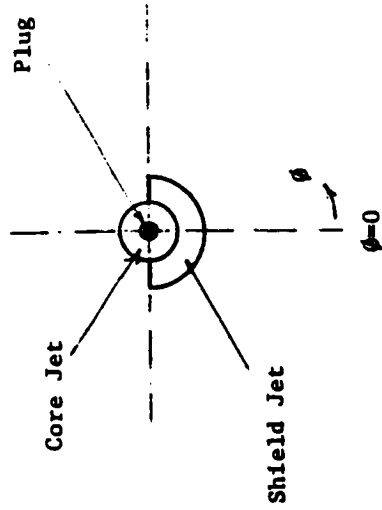


FIGURE 5.13b. AZIMUTHAL VARIATION OF THE TURBULENT VELOCITY AS PREDICTED BY M\*G\*B FOR ANNULAR PLUG NOZZLE WITH 180° SHIELD AT THREE (3) AXIAL STATIONS AT  $R/D_{eq} = 0.5$ .

Figure 5.13) for both mean and turbulent velocities. For  $\phi < 60^\circ$  and  $\phi > 120^\circ$ , there is no azimuthal variation. The extent of azimuthal variation at  $R/D_{eq} = 0.5$  for downstream axial locations is seen to reduce, indicating the mixing of the partial shield with the core jet.

Figure 5.14 shows the PNL directivities and spectra at  $\theta_i = 140^\circ$ ,  $90^\circ$  and  $60^\circ$  for TAS-1 and TAS-2 at community and opposite community locations at a 2400 ft. sideline distance, as predicted by the modified M\*G\*B program. One notes that the perceived noise levels of TAS-2 at community and opposite community orientations are on either side of TAS-1 indicating that the partial shield is a good reflector of noise (see Figure 5.14a). The influence of the partial shield in the aft quadrant is seen to be larger than in the front quadrant. Figure 5.14b compares the azimuthally asymmetric spectral content of TAS-2 with the axisymmetric spectral content of TAS-1 at the peak noise angle,  $\theta_i = 140^\circ$ . Note the significant mid and high frequency noise reduction by the partial shield in the community orientation and also the corresponding mid and high frequency noise amplification in the opposite community orientation compared to the baseline annular plug nozzle. Also, note that the low frequency noise increases in the presence of the partial shield which can be attributed to the slower decay of the jet in the presence of the shield. The low frequency noise of TAS-2 in community and opposite orientations is almost the same indicating that the low frequency noise sources are located in zones where the flow field has almost lost all of its azimuthal asymmetry.

Figure 5.14c shows the azimuthally asymmetric spectral content of TAS-2 in comparison with the axisymmetric spectral content of TAS-1 at  $\theta_i = 90^\circ$ . Note that the asymmetry exists in mid and high frequency regions. Also, since the spectrum at  $\theta_i = 90^\circ$  corresponds to source spectrum where eddy convection and mean flow shrouding effects are minimal, the spectral distribution at  $\theta_i = 90^\circ$  yields valuable insight into relative source strengths. The reduced shear stresses close to the nozzle exit plane by the thermal acoustic shield imply reduced source strengths close to the nozzle exit plane where the high and mid frequency noise sources are located. Figure 5.14d compares the spectral content of TAS-2 at community and opposite community orientations with that of TAS-1 at  $\theta_i = 60^\circ$ . In the front

• 2400' Sideline Distance •  $V_{a/c} = 0$  (Static) •  $A_T = 1400 \text{ In.}^2$  for TAS-2  
 •  $A_T = 1040 \text{ In.}^2$  for TAS-1

Configuration	Core Jet			Shield Jet			Mixed Conditions		
	$V_j$ , fps	$T_T^j$ , °R	$P_T^j$	$V_{sj}$ , fps	$T_T^{sj}$ , °R	$P_T^{sj}$	$v_{mix}$ , fps	$T_T^{mix}$ , °R	$p_r^{mix}$
TAS-1	1867	1730	1.89	NO SHIELD	---	---	1867	1730	1.89
TAS-2	1867	1730	1.89	1121	1730	1.24	1749	1730	1.74

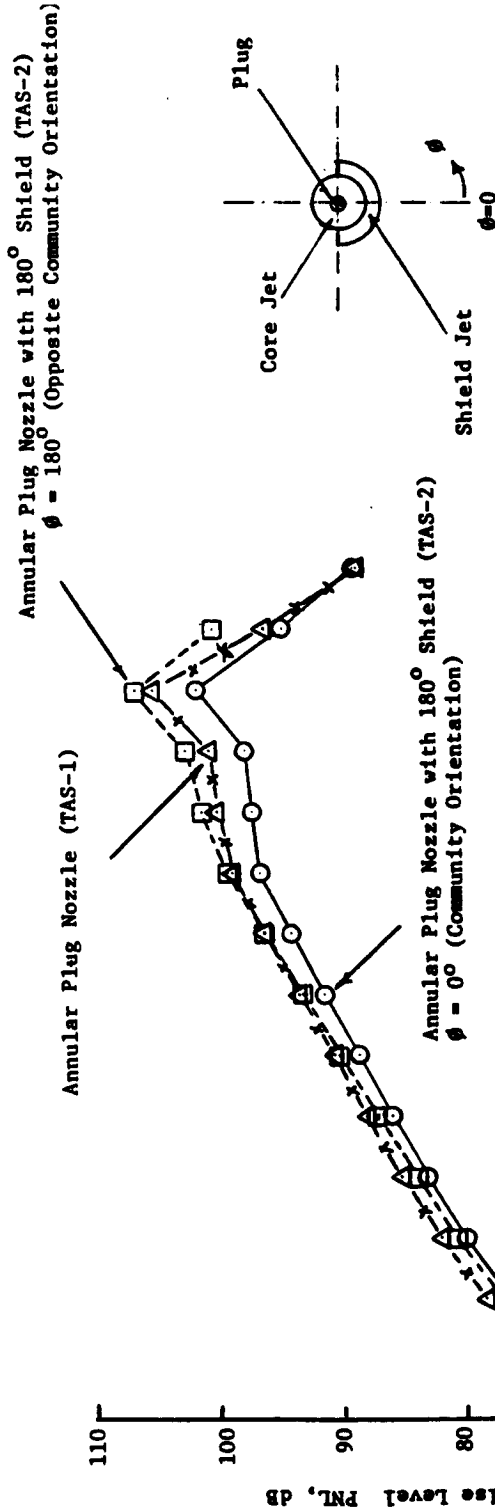


FIGURE 5.14a. AZIMUTHALLY ASYMMETRIC PNL DIRECTIVITIES AS PREDICTED BY M\*G\*B PROGRAM FOR A PLUG NOZZLE WITH THE PARTIAL SHIELD IN COMPARISON WITH THAT OF THE PLUG NOZZLE WITHOUT THE SHIELD.



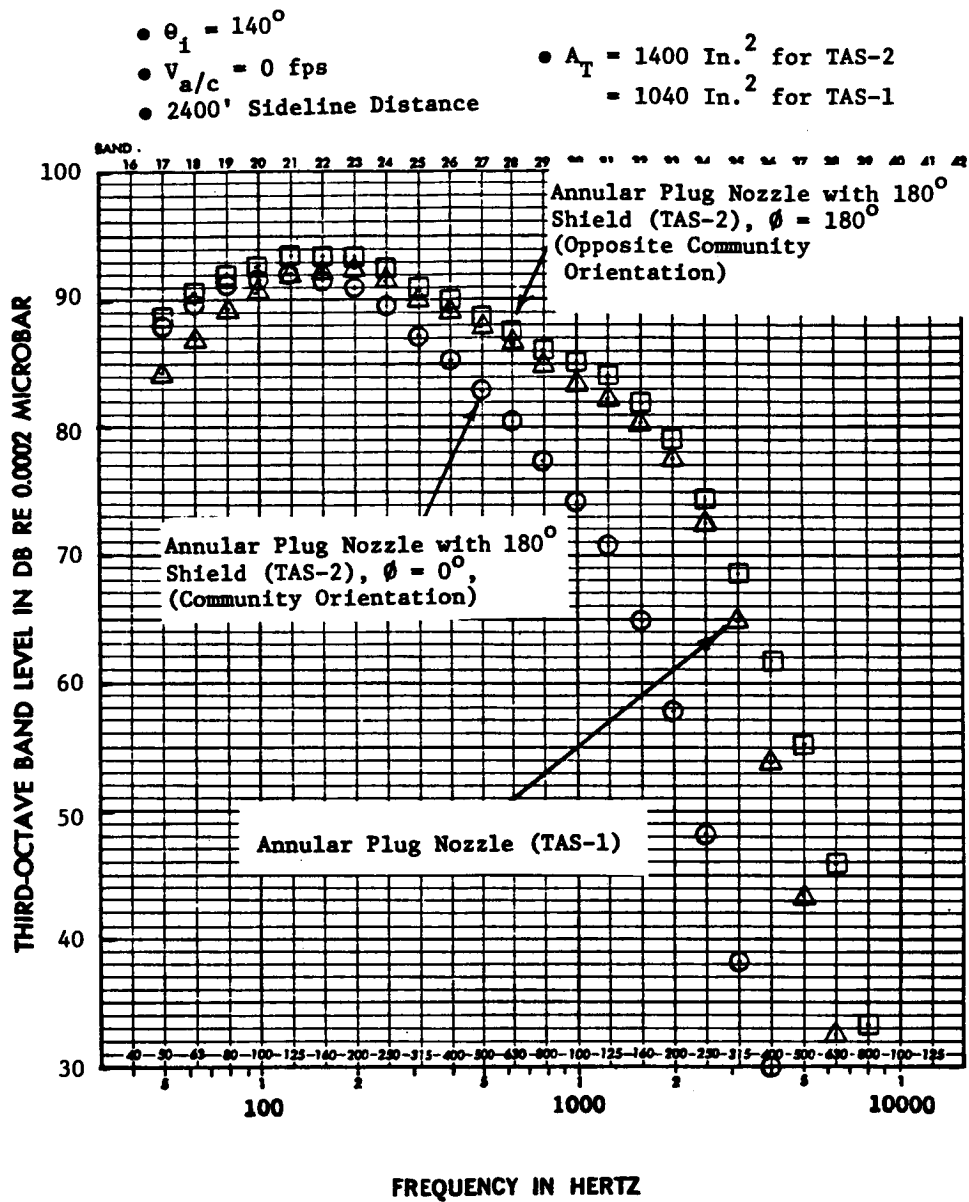


FIGURE 5.14b. AZIMUTHALLY ASYMMETRIC SPECTRAL CONTENT OF A PLUG NOZZLE WITH PARTIAL SHIELD AS PREDICTED BY M\*G\*B PROGRAM AT  $\theta_1 = 140^\circ$  IN COMPARISON WITH THAT OF THE PLUG NOZZLE WITHOUT THE SHIELD.

- $\theta_i = 90^\circ$
- $V_{a/c} = 0$  fps
- 2400' Sideline Distance
- $A_T = 1400$  In.<sup>2</sup> for TAS-2
- $A_T = 1040$  In.<sup>2</sup> for TAS-1

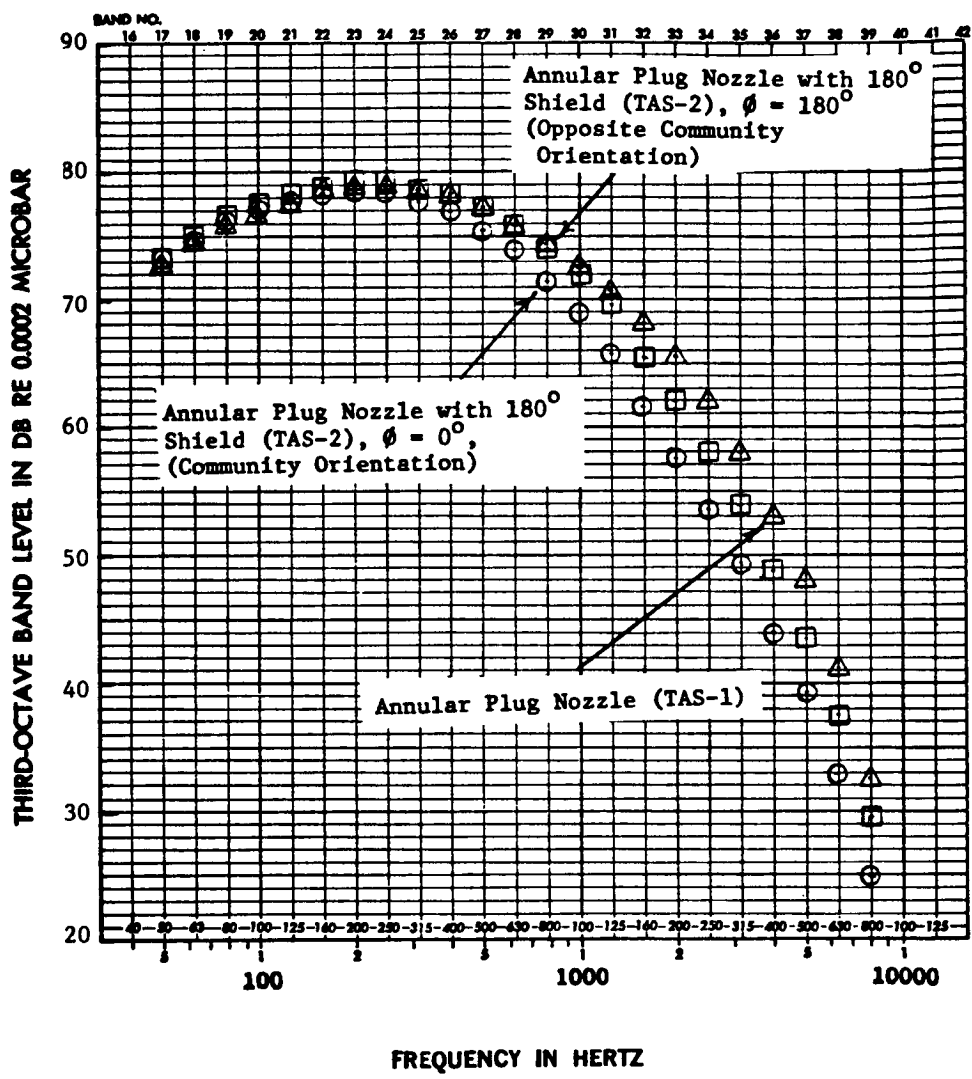


FIGURE 5.14c. AZIMUTHALLY ASSYMMETRIC SPECTRAL CONTENT OF A PLUG NOZZLE WITH PARTIAL SHIELD AS PREDICTED BY M\*G\*B PROGRAM AT  $\theta_i = 90^\circ$  IN COMPARISON WITH THAT OF THE PLUG NOZZLE WITHOUT THE SHIELD.

- $\theta_1 = 60^\circ$
- $V_{a/c} = 0$  fps
- 2400' Sideline Distance
- $A_T = 1400 \text{ In.}^2$  for TAS-2
- $A_T = 1040 \text{ In.}^2$  for TAS-1

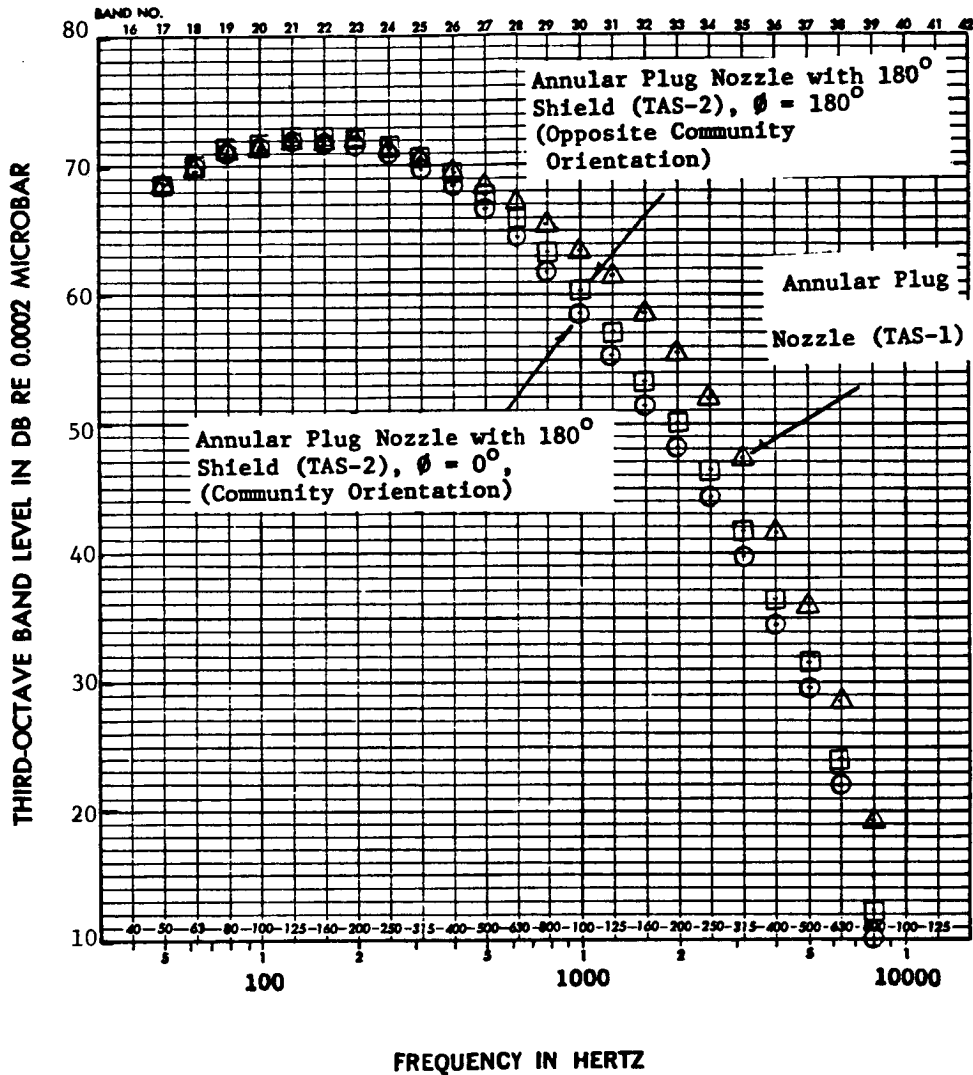


FIGURE 5.14d. AZIMUTHALLY ASSYMMETRIC SPECTRAL CONTENT OF A PLUG NOZZLE WITH PARTIAL SHIELD AS PREDICTED BY M\*G\*B PROGRAM AT  $\theta_1 = 60^\circ$  IN COMPARISON WITH THAT OF THE PLUG NOZZLE WITHOUT THE SHIELD.

effects exist. However, since the front quadrant is outside of the zone of silence, there are no fluid shrouding effects. One notes similar relative spectral distribution in the front quadrant to that at  $\theta_i = 90^\circ$ .

Next, a comparison of the measured and predicted azimuthal asymmetry in terms of spectral differences for configuration TAS-2 were examined. Acoustic data for configuration TAS-2 measured in community and opposite community orientations have been scaled to a total flow area of 1885 in<sup>2</sup> and extrapolated to 2400 ft sideline distance. Algebraic spectral differences between the above two orientations at three angles to inlet (viz.,  $\theta_i = 60^\circ, 80^\circ$  and  $140^\circ$ ) were calculated. Predictions were made utilizing the modified M\*G\*B procedure for identical geometry and cycle conditions at community and opposite community orientations, and the predicted spectral differences between the two (2) orientations at the above three (3) angles to inlet were compared with the measured spectral differences in Figure 5.15. Note that at  $\theta_i = 60^\circ$  and  $80^\circ$ , there is a good agreement between the measured and predicted spectral differences at all the frequencies. Both the data and predictions indicate that, for unsuppressed annular plug nozzle with  $180^\circ$  thermal acoustic shield, there is very little azimuthal asymmetry in the front quadrant, indicating that reflection and refraction effects of a partial thermal acoustic shield are not dominant in the front quadrant. The measured and predicted algebraic spectral differences due to azimuthal asymmetry at  $\theta_i = 140^\circ$  are shown in Figure 5-15c. Both the data and predictions indicate that for unsuppressed annular plug nozzle with a partial shield, significant amount of spectral azimuthal asymmetry can be observed in the aft quadrant. Though the predicted spectral asymmetry is higher than the measured asymmetry, both data and predictions indicate a similar trend, namely, as the frequency increases the azimuthal asymmetry in the sound pressure level increases. The observer angle,  $\theta_i = 140^\circ$  is in the zone of silence where reflection/refraction effects of the partial shield are the dominant mechanisms. As the frequency increases, the behavior of the sound waves asymptotically approaches that of rays. The rays get totally internally reflected by the partial shield in the zone of silence and are anticipated to yield maximum acoustic asymmetry between the community and opposite community orientations. Both the predictions and the data indicate a flattening trend at frequencies greater than 3150 Hz indicating that one may be asymptotically approaching the acoustic ray limit at these frequencies.

- Config. TAS-2
- Test Pt. for Community Orientation: 221
- Test Pt. for Opposite Community Orientation: 287
- $A^T = 1885 \text{ In.}^2$
- 2400' Sideline Distance
- Cutback Cycle
- Static

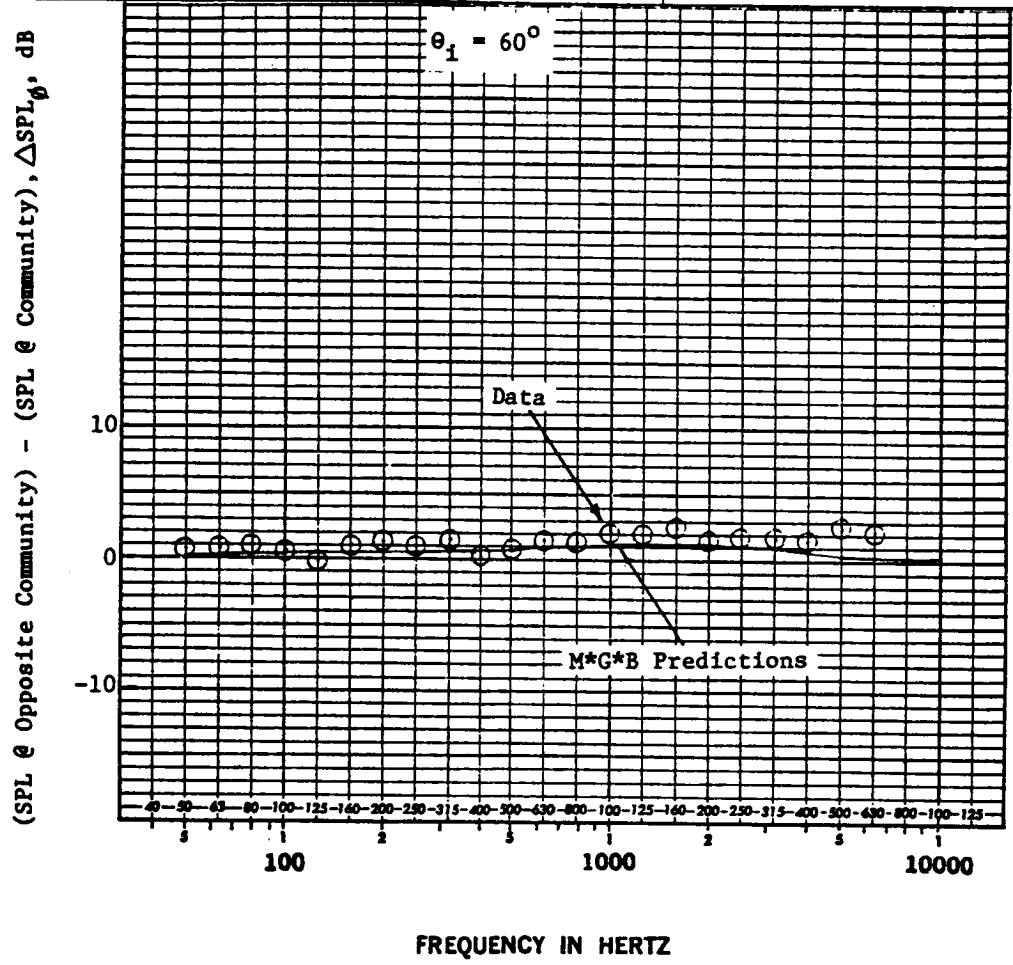


Figure 5-15a. Comparison of the Predicted and Measured Differences in SPL at  $\theta_1 = 60^\circ$  for Community and Opposite Community Orientations for Configuration TAS-2 at a Typical Cutback Case (Static).

- Config. TAS-2
- Test Pt. for Community Orientation: 221
- Test Pt. for Opposite Community Orientation: 287

- $A^T = 1885 \text{ In.}^2$
- 2400' Sideline Distance
- Cutback Cycle
- Static

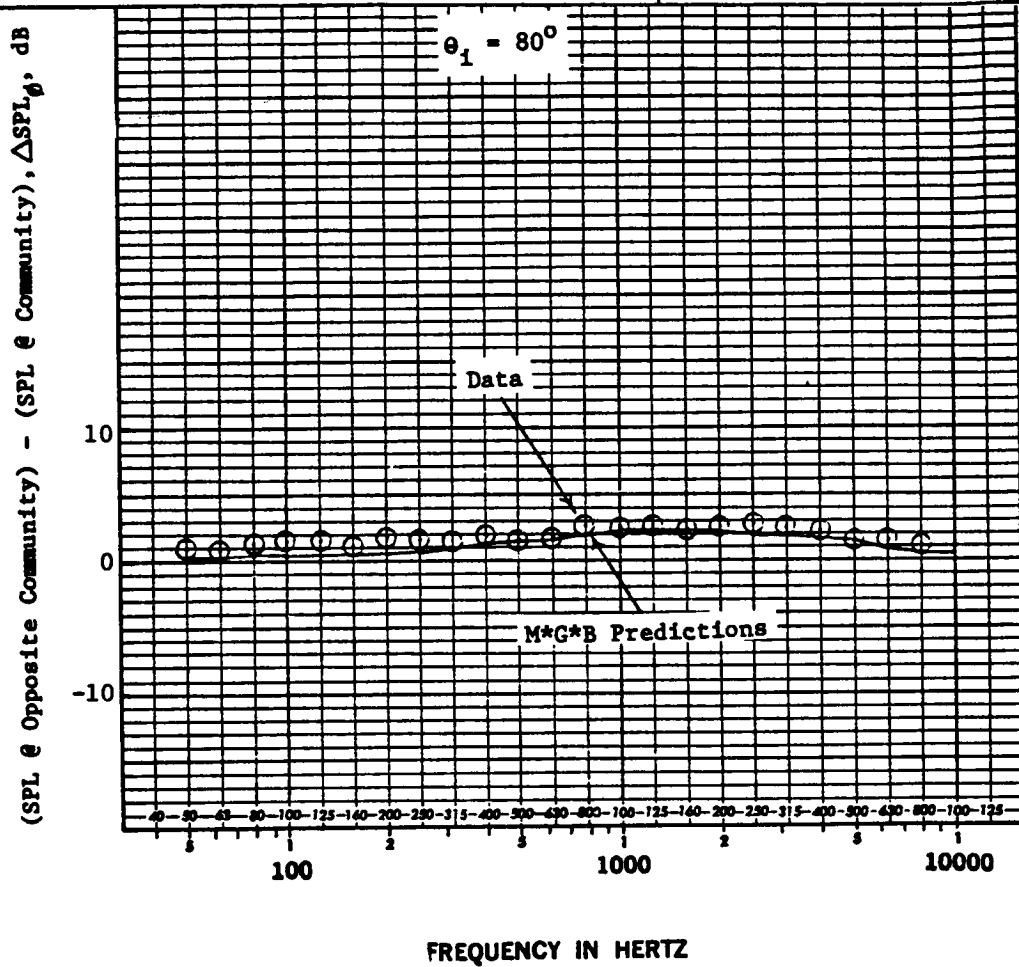


Figure 5-15b. Comparison of the Predicted and Measured Differences in SPL at  $\theta_i = 80^\circ$  for Community and Opposite Community Orientations for Configuration TAS-2 at a Typical Cutback Case (Static).

- |  |   |
|--|---|
| <ul style="list-style-type: none"> <li>• Config. TAS-2</li> <li>• Test Pt. for Community Orientation: 221</li> <li>• Test Pt. for Opposite Community Orientation: 287</li> </ul> | <ul style="list-style-type: none"> <li>• <math>A^T = 1885 \text{ In.}^2</math></li> <li>• 2400' Sideline Distance</li> <li>• Cutback Cycle</li> <li>• Static</li> </ul> |
|--|---|

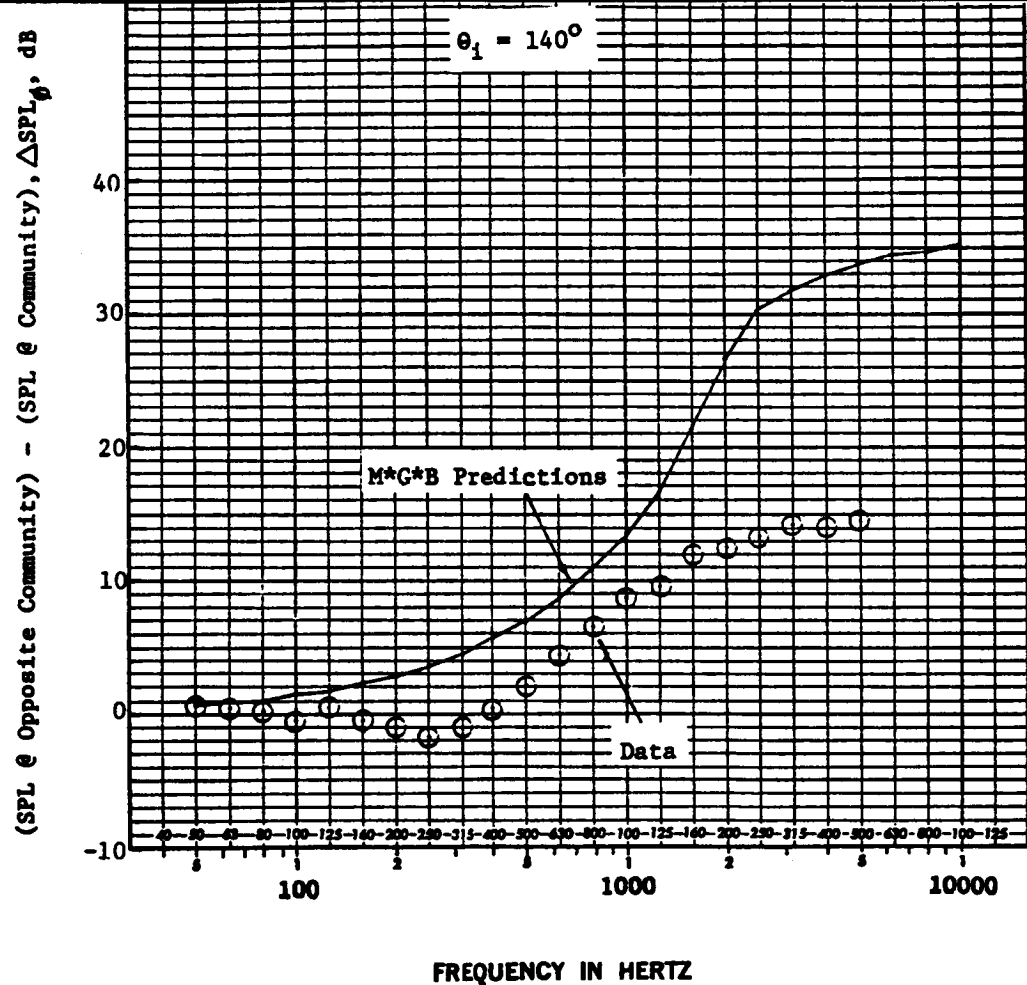


Figure 5-15c. Comparison of the Predicted and Measured Differences in SPL at  $\theta_1 = 140^\circ$  for Community and Opposite Community Orientations for Configuration TAS-2 at a Typical Cutback Case (Static).

## REFERENCES FOR SECTION 5.0

- 5.1 Mani, R., Gliebe, P.R., Balsa, T.F., Stringas, E.J., et al, "High Velocity Jet Noise Source Location and Reduction, Task II - Theoretical Developments and Basic Experiments", General Electric Company Contractor Final Report Number FAA-RD-76-79, II, 1976.
- 5.2 Lilley, G.M., Plumblee, H.E., Strahle, W.C., Ruo, S.Y., Doak, P.E., "Theory of Turbulence Generated Noise, Noise Radiation from Upstream Sources and Combustion Noise", Volume IV. The Generation and Radiation of Supersonic Jet Noise, AFAPL-TR-72-53, 1972.
- 5.3 Mani, R., "A Moving Source Problem Relevant to Jet Noise", J. Sound and Vibration, 25, Page 337, 1972.
- 5.4 Tester, B.J. and Morfey, C.L., "Developments in Jet Noise Modeling, Theoretical Predictions and Comparisons with Measured Data", J. of Sound and Vibration, 46, Page 79, 1976.
- 5.5 Mani, R., "The Influence of Jet Flow on Jet Noise, Parts 1 and 2", J. Fluid Mech., 73, Page 753, 1976.
- 5.6 Balsa, T.F., "The Acoustic Field of Sources in Shear Flow with Application to Jet Noise: Convective Amplification", J. Fluid Mech., 79, Page 33, 1977.
- 5.7 Goldstein, M.E., "High Frequency Sound Emission from Moving Point Multipole Sources Embedded in Arbitrary Transversely Sheared Mean Flows" J. Sound and Vibration, 80, Page 499, 1982.
- 5.8 Jones, D.S. and Morgan, J.D., "The Instability of a Vortex Sheet on a Subsonic Stream Under Acoustic Radiation", Proc. Camb. Phil. Soc., 72, Page 465, 1972.
- 5.9 Lighthill, M.J., "On Sound Generated Aerodynamically", Proc. Roy. Soc., 211A, Page 564, 1952.



- 5.10 Carrier, G.F., Krook, M., Pearson, C.E., Functions of a Complex Variable, McGraw-Hill, 1966.
- 5.11 Morse, P.M. and Ingard, U.K., Theoretical Acoustics, McGraw-Hill, 1968.
- 5.12 Avila, G.S. and Keller, J.B., "The High-Frequency Asymptotic Field of a Point Source in an Inhomogeneous Medium", Comm. Pure and Appl. Math., 16, Page 363, 1963.

## 6.0 AN INSTALLED NOISE ANALYSIS OF THERMAL ACOUSTIC SHIELD DATA

### 6.1 INTRODUCTION

This section contains the results of work performed by The Boeing Company under sub-contract to the General Electric Company as part of its work under NASA Contract NAS3-22137. The objective of this task is to quantify the effects of flight on the generation, propagation and shielding of noise for the configurations tested. To perform the task, The Boeing Company has made use of data supplied by the General Electric Company.

A TAS could be implemented in many different ways, the end requirement being a stream of heated gas or air to shroud the noisy jet. (Note that in some experiments higher temperature air streams have been successfully simulated by helium mixtures. Hence use of lighter gases cannot be ruled out). The simplest method of implementation is that depicted in Figure 6.1 where the TAS is derived by bleeding gas from the main jet through choke plates to reduce velocity. This removes energy from the main jet so that the "throttle has to be opened" to make up the lost thrust. This is possible in an SST engine since in most cases the engine is sized by requirements of operations other than takeoff or approach (e.g., cruise). A design study (Reference 6.1) has established the feasibility of an engine that implements a bleed system TAS. The feasibility of other implementations, such as a TAS from an independent source, has not been established at this time.

There is no specific community noise rule that an advanced design of SST must meet at this time. Working Group E of the Committee for Aircraft Noise (CAN) of the International Civil Aviation Organization (ICAO) has studied the definition of a rule for an SST for several years, but has not arrived at firm recommendations for a rule. The sideline distance used in these studies, 650m, is in line with recommendations that have been made by the above working group.

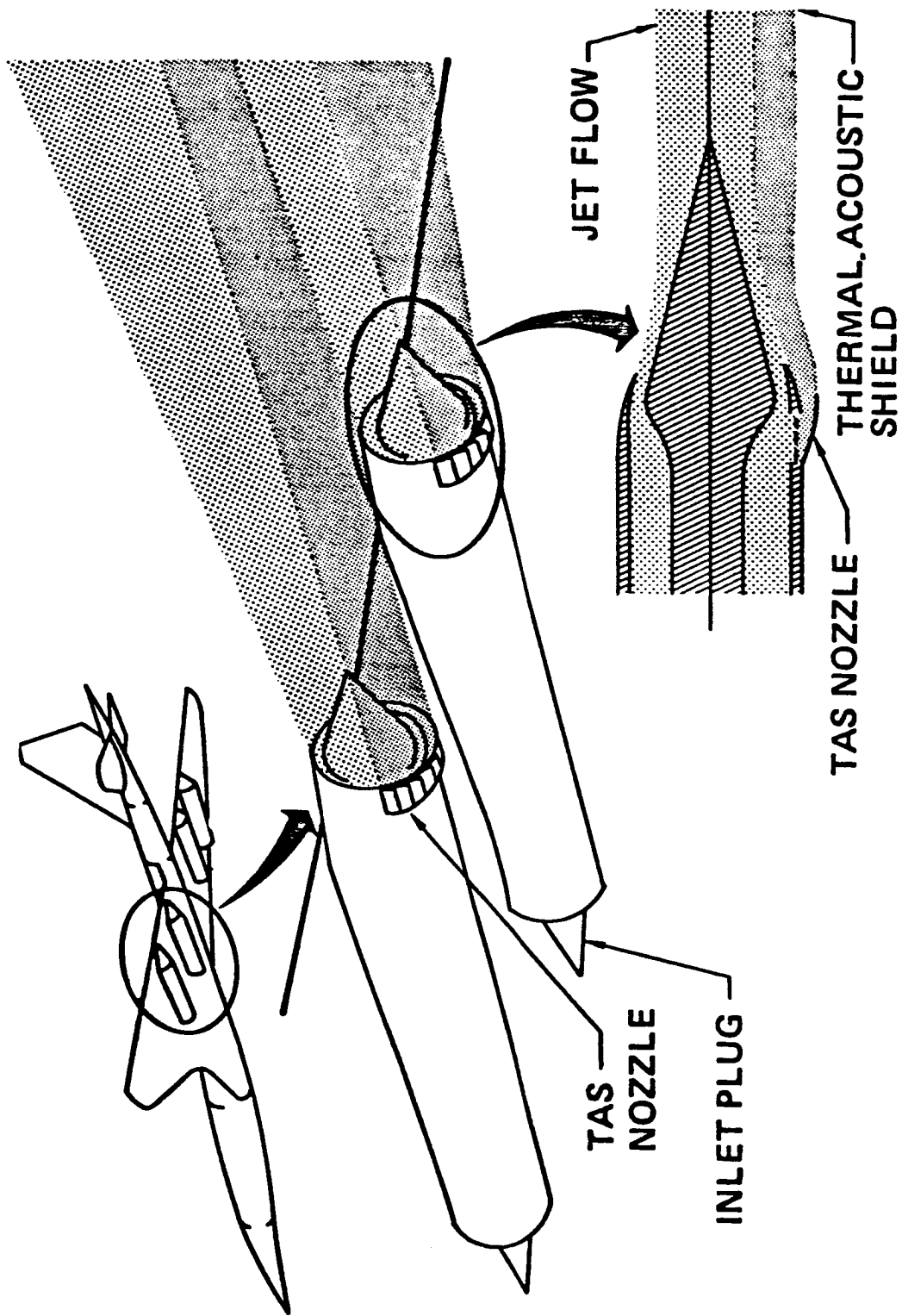


Figure 6.1. Application of Thermal Acoustic Shield Utilizing Engine Bleed Concept.

The noise levels that a comparably sized subsonic transport (4 engines, 340,200 Kg (750000 lb)) are required to meet are:

Takeoff	105.3 EPNdB
Sideline	102.4 EPNdB
Approach	105.0 EPNdB

A practical design would require lower predicted noise levels than these to assure sufficient margin to achieve certification. These values could be used to judge the value of noise suppression devices such as a TAS.

## 6.2 DATA SOURCES

The data used in the analysis is comprised of three parts. The first is the jet noise obtained from the model test, scaled to an equivalent full scale engine. The second is the details of the airplane's flight profile which relates position with thrust and airplane speed and attitude. The third is a description of an engine to permit analytical prediction or other, non-jet, noise components when estimating total noise. This section describes these data parts and their sources.

### 6.2.1 JET NOISE TEST DATA

Acoustic test data simulating an engine throttle line and the corresponding aerodynamic test conditions were supplied by General Electric to The Boeing Company for configurations TAS-1, TAS-3, TAS-6 and TAS-8. This data was scaled to a total equivalent nozzle area of 9033 square centimeters (1400 square inches), with relative velocity data having the necessary flight transformations for an aircraft speed of 122 m/sec (400 ft/sec).

Test data for a simple Round Convergent (RC) nozzle was not included. To provide this reference point that noise was predicted using standard ARP-876 (Reference 6.2) for jet mixing and shock-cell noise.

### 6.2.2 FLIGHT PROFILES

The flight profiles used in this study were developed in support of the NASA Supersonic Cruise Research (SCR) program. From the large number of profiles studied during that program, three takeoff cases were chosen for this study. These are:

- A. An advanced operating procedure that takes advantage of an Advanced SST's flight management system (Reference 6.3). This is shown in Figure 6.2.
- B. A standard takeoff following FAR-36 rules using cutback. This is shown in Figure 6.3.
- C. A takeoff following FAR-36 rules without cutback, as shown in Figure 6.4.

These profiles are generated by a computer program which "flies" the airplane taking into account such factors as drag, fuel burn, engine spin-down rate, angle of attack, etc., and how they vary with time. The program provides outputs integrated with other programs used to predict airport community noise.

Note that at this level of study, it is assumed that the engine differences implicit in the inclusion of a suppression device do not affect the takeoff flight profile. Differences would be reflected in the airplane payload range as exemplified in Reference 6.1.

### 6.2.3 NON-JET NOISE COMPONENTS

Because jet noise has been such a dominating problem for an SST, it has become customary to ignore other noise components. These other components can represent a noise floor which reduces the effectiveness of jet noise reduction success. It was therefore considered desirable to include these components in the study to determine how they might affect a TAS equipped airplane.

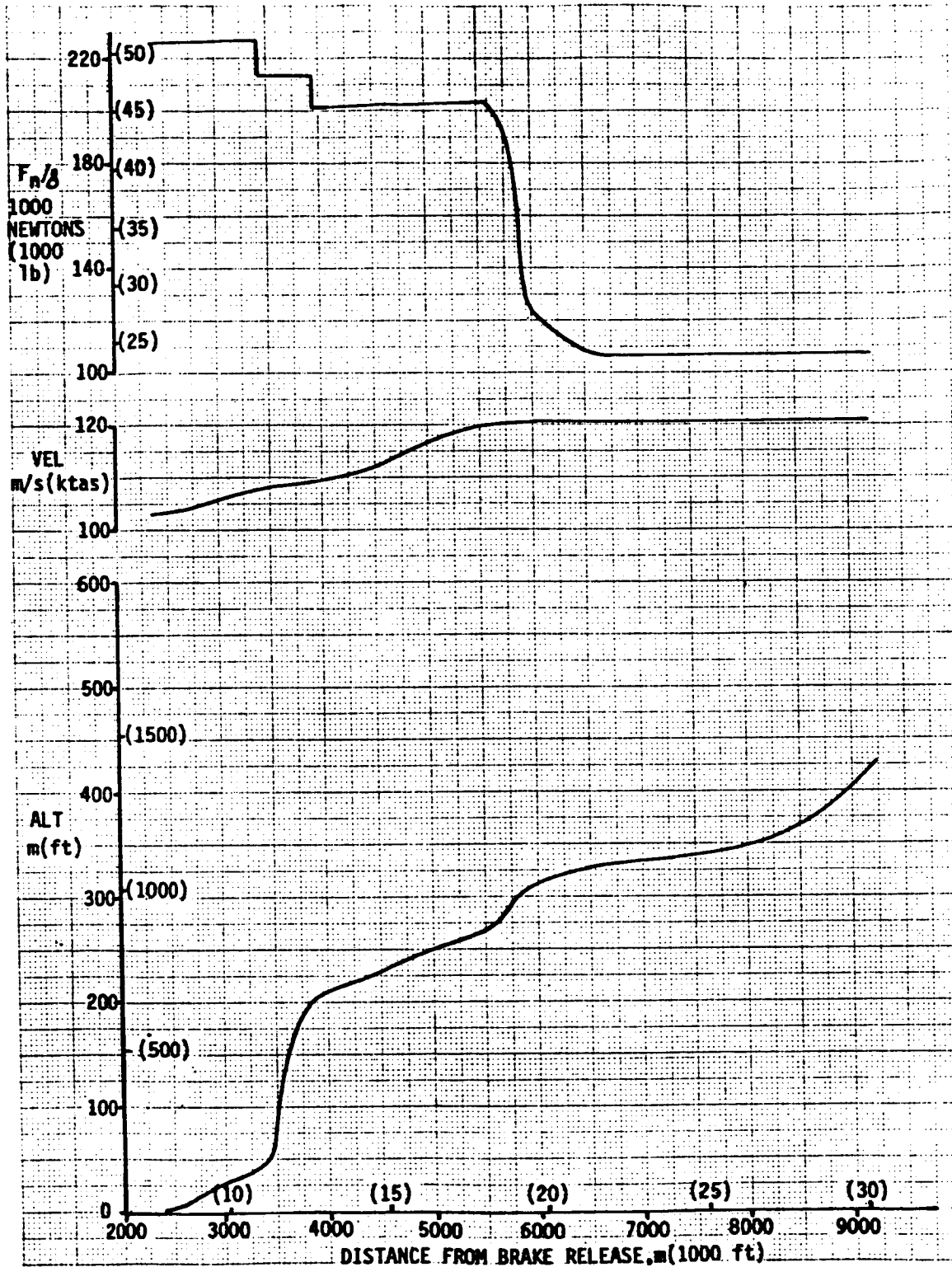


Figure 6.2. Advanced Procedure Takeoff Trajectory

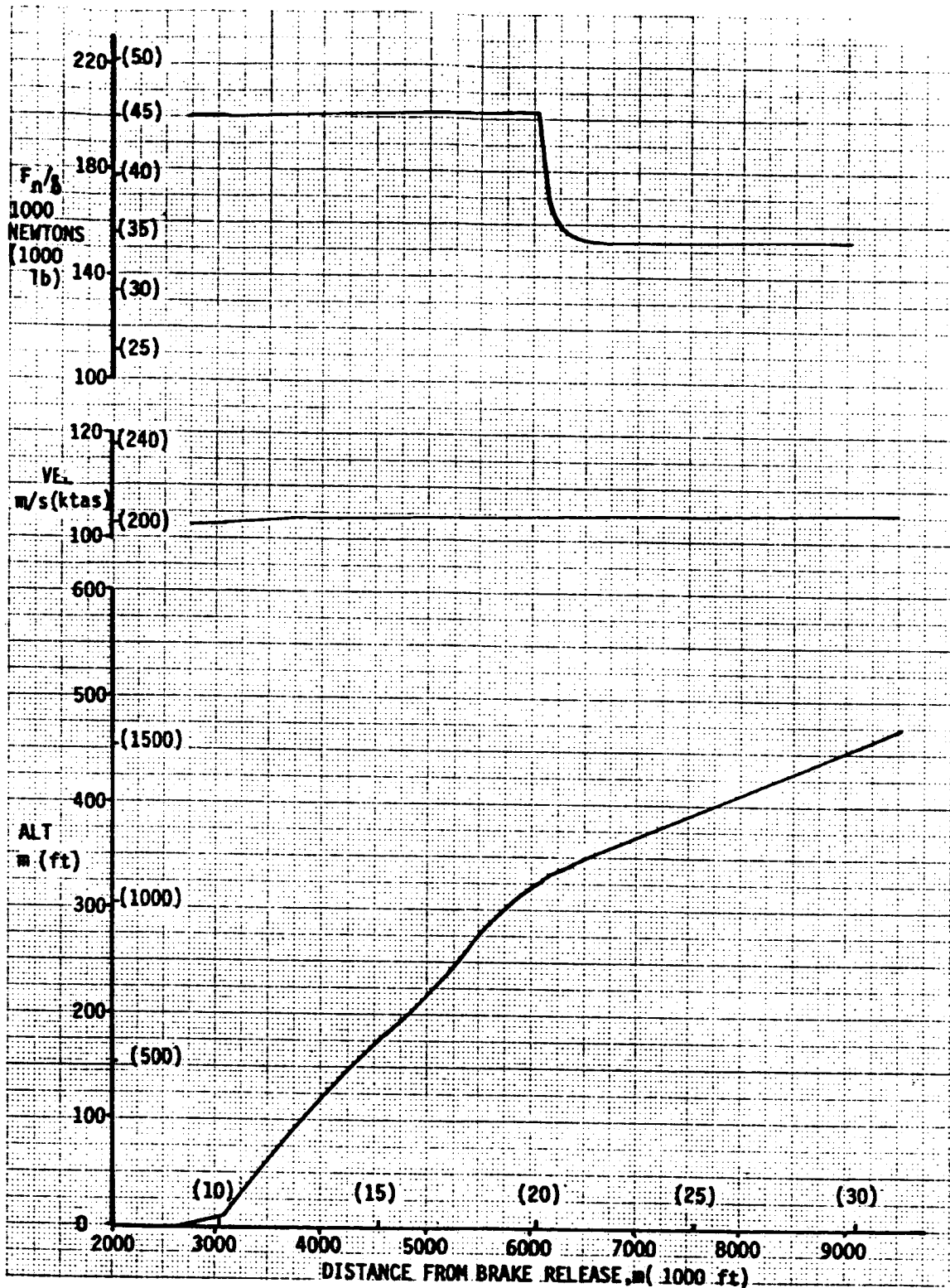


Figure 6.3. FAR36 with Outback Takeoff Trajectory

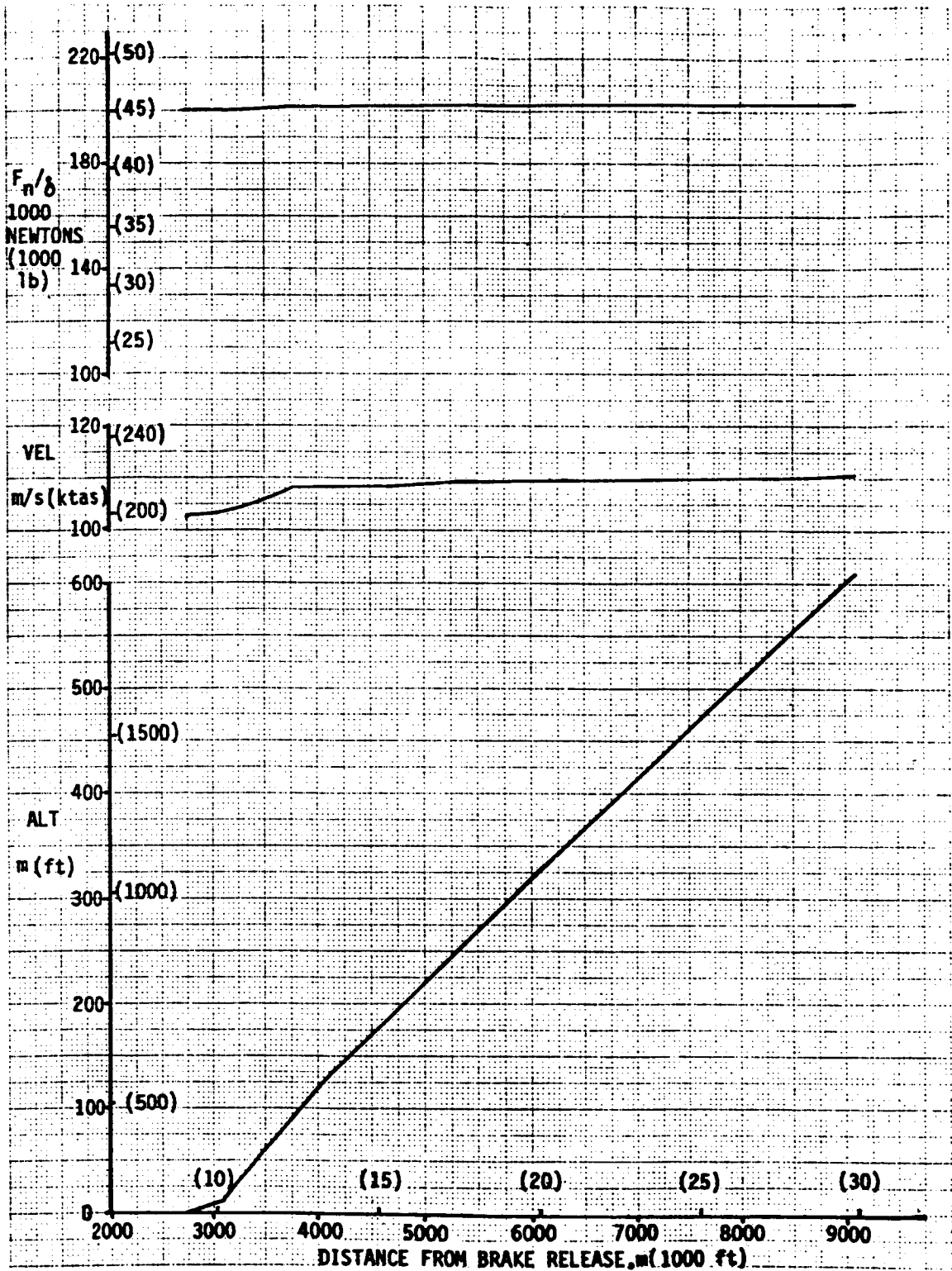


Figure 6.4. FAR36 No-Cutback Takeoff Trajectory



The scaling of the data selected by General Electric, a 9033 sq. cm. (1400 sq. in.) total nozzle area led to the selection of the GE21/J11-B15B study engine as the model for other engine noise components. Data for this engine was supplied to Boeing by General Electric to support the inlet studies of Reference 6.4.

Although engine thrust is not directly used in the noise prediction, it is needed to correlate the specific airplane operating condition with the noise produced. The normalized thrust  $F_n/\delta$  is required. This is estimated from:

$$F_n/\delta = \left\{ \left( \frac{100 - \Delta CFG}{100} \right) V_{j\_ideal} - V_{flight} \right\} \frac{\dot{W}_{meas}}{g} \frac{14.7}{P_{meas}}$$

where:

$V_{j\_ideal}$  is the ideal jet velocity

$\dot{W}_{meas}$  is the scaled measured jet weight flow rate

$P_{meas}$  is the model test ambient pressure

$V_{flight}$  is the model test relative velocity

$g$  is the acceleration due to gravity

$\Delta CFG$  is the percentage thrust loss due nozzle base drag, etc.

$\delta$  is the ratio of ambient pressure to ISA pressure  
( $P_{amb}/P_{std}$ )

The  $\Delta CFG$  values for the 32 chute suppressor nozzles (TAS-6 and TAS-8) are obtained from Section 4.3.3. For the Baseline plug nozzle (TAS-1),  $\Delta CFG$  is taken to be 0%, while for TAS-3 a value of 1% is used.

The test flight velocity was used as more accurately representing the noise generated. Use of the slightly lower flight profile airplane velocity would have given approximately 2% higher thrust and by implication slightly lower noise (in the order of 0.2 to 0.3 EPNdB). The choice of flight velocity for thrust calculation does not of course affect the relative values.

### 6.3 METHOD OF ANALYSIS

The analysis was performed using existing Boeing proprietary computer programs. A program identified as N394C takes flight profile data (Section 6.2.2), tabulations of noise/power/distance sound pressure level data, and observer locations to derive the noise time history and resulting EPNL value. The noise tabulations are generated by the program FSPP (Full Standards Prediction Program) which has the capability of combining measured data with predictions of other noise components.

The processing of data is described below. It was also found desirable to perform analysis with the TAS data rescaled to represent a different mode of derivation. The rescaling is also discussed.

#### 6.3.1 GENERAL DESCRIPTION

The geometry related to the evaluation of community noise is shown in Figure 6.5. The data relating to the flight profile (Section 6.2.2) provide the altitude, distance from brake release,  $F_n/\delta$ , time from brake release,  $V_{tas}$ , body angle and gradient. Additional inputs to the evaluation are the observer X and Y locations (relative to the brake release point), the receiver (microphone) height, ground reflection properties, and the engine/airframe noise characteristics. A flyover noise evaluation program (with a version control code reference of N394C) takes this data to derive the sound propagation path distance and direction, taking into account the time for the sound to propagate, and determines the moment by moment (0.2 to 0.5 sec) interval noise spectrum and from this PNLT at the observer location. The type of procedure is shown in Figure 6.6. The resulting PNLT-time history is then used to compute the EPNL (Effective Perceived Noise Level) value.

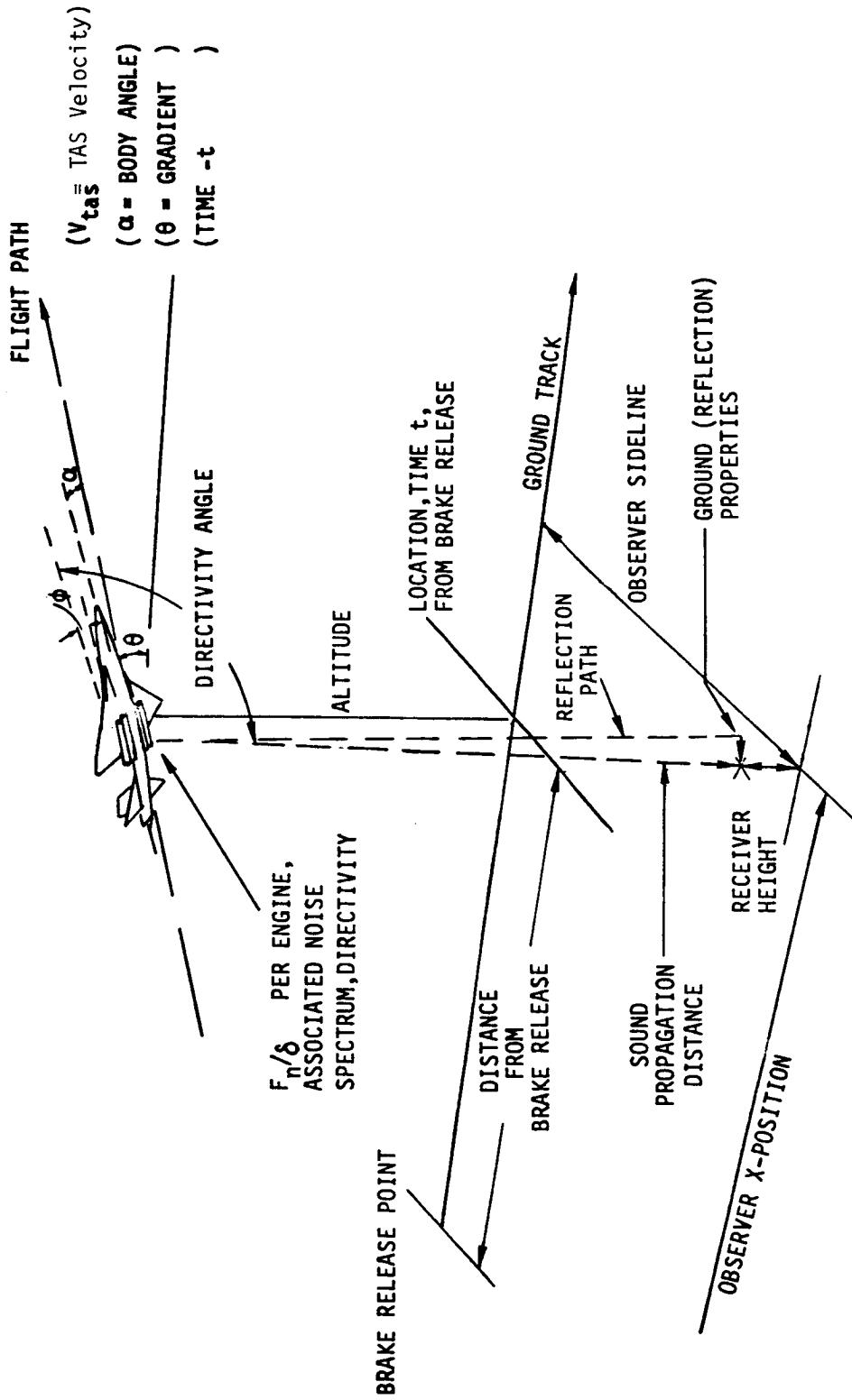


Figure 6.5. Flyover Evaluation Geometry

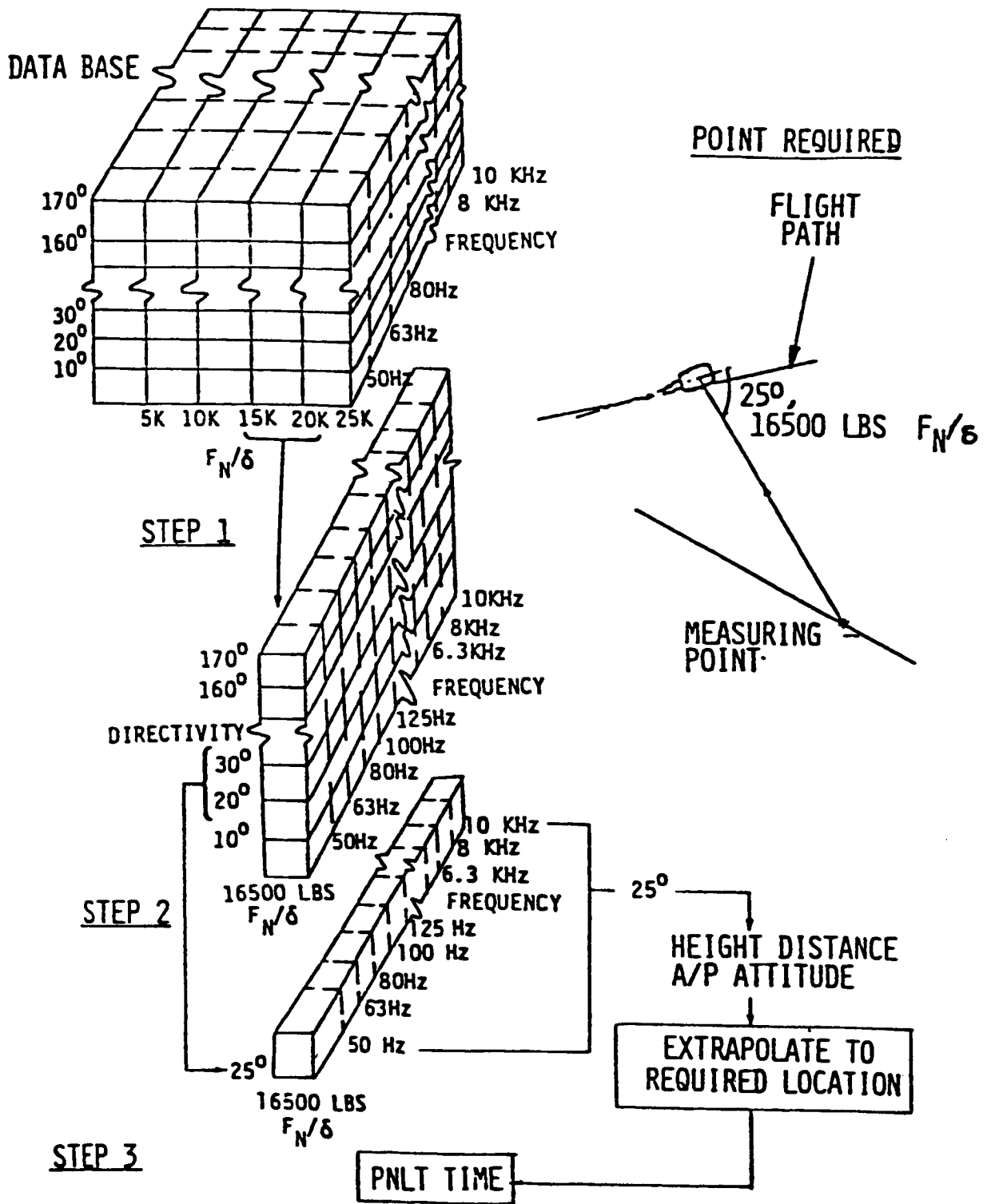


Figure 6.6. Flyover Noise Calculation Procedure

The engine/airframe noise characteristic tables are generated by a general purpose noise prediction computer program known as FSPP (version control reference N266G). FSPP also provides the total and component EPNL values derived for a level flyover that are given later. FSPP can compute the EPNL for simple fixed flight profiles, but cannot account for transient changes in operating conditions. Past evaluations have shown that the large changes in thrust, and associated changes in inlet operating conditions, can result in large errors in EPNL (as much as 5 EPNdB) if not properly accounted for. This is the reason for N394C. (The flight profiles used here have been developed to reduce the effect of thrust changes, and hence errors would in fact be fairly small  $\approx 1$  EPNdB).

The resulting overall analysis scheme is shown in Figure 6.7 with the conversion process given in Figure 6.8. Note that the conversion program was used to perform the rescaling discussed in the next section.

#### 6.3.2 RESCALE OF JET TEST DATA

As will be seen later, the analysis results using the test data as supplied were disappointing. This is because the data was scaled to represent a system in which the TAS is obtained by removing the necessary gas from main (primary) jet stream and reducing its velocity by bleed plates. Details of the design implementation study for this system are given in Reference 6.1. While, as shown in Reference 6.1, this is a practical and feasible method of implementation, it does carry the penalty of creating a significant loss of thrust by the removal of velocity energy (total pressure) from the overall jet. For an SST, the loss of thrust by itself is not serious since there is in most designs an excess of thrust available for takeoff (since the engine is sized for the high speed segments of the flight envelope). The problem arises in the increase in noise that accompanies opening the throttle to compensate for the lost thrust. This is the classic suppressor dilemma that can (and does in the case of TAS-3) result in the airplane with a suppressor being noisier than without.

The TAS is unusual among suppression devices in that there are application concepts that can overcome the thrust loss dilemma. In fact the TAS can,

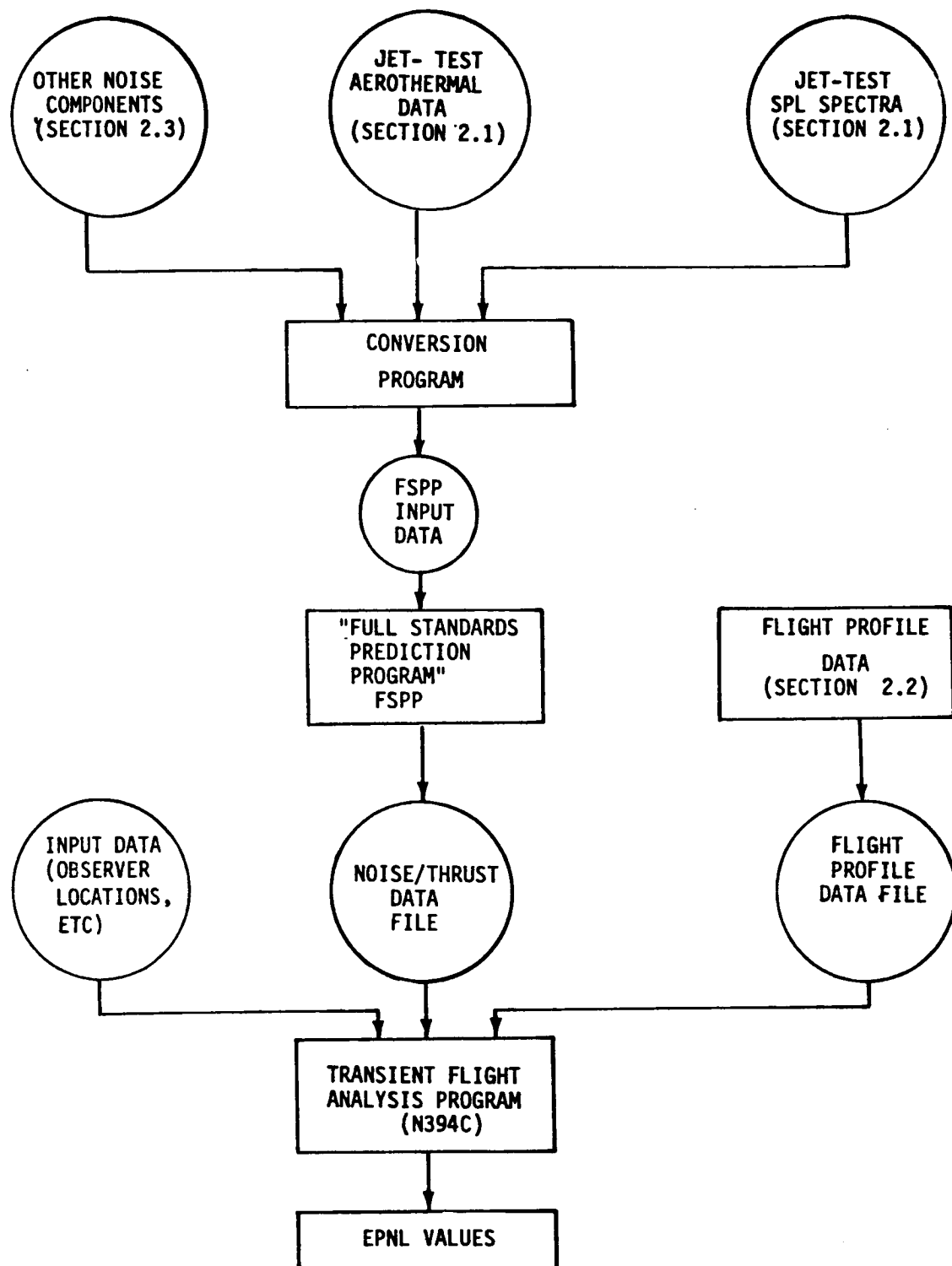


Figure 6.7. Analysis Schematic

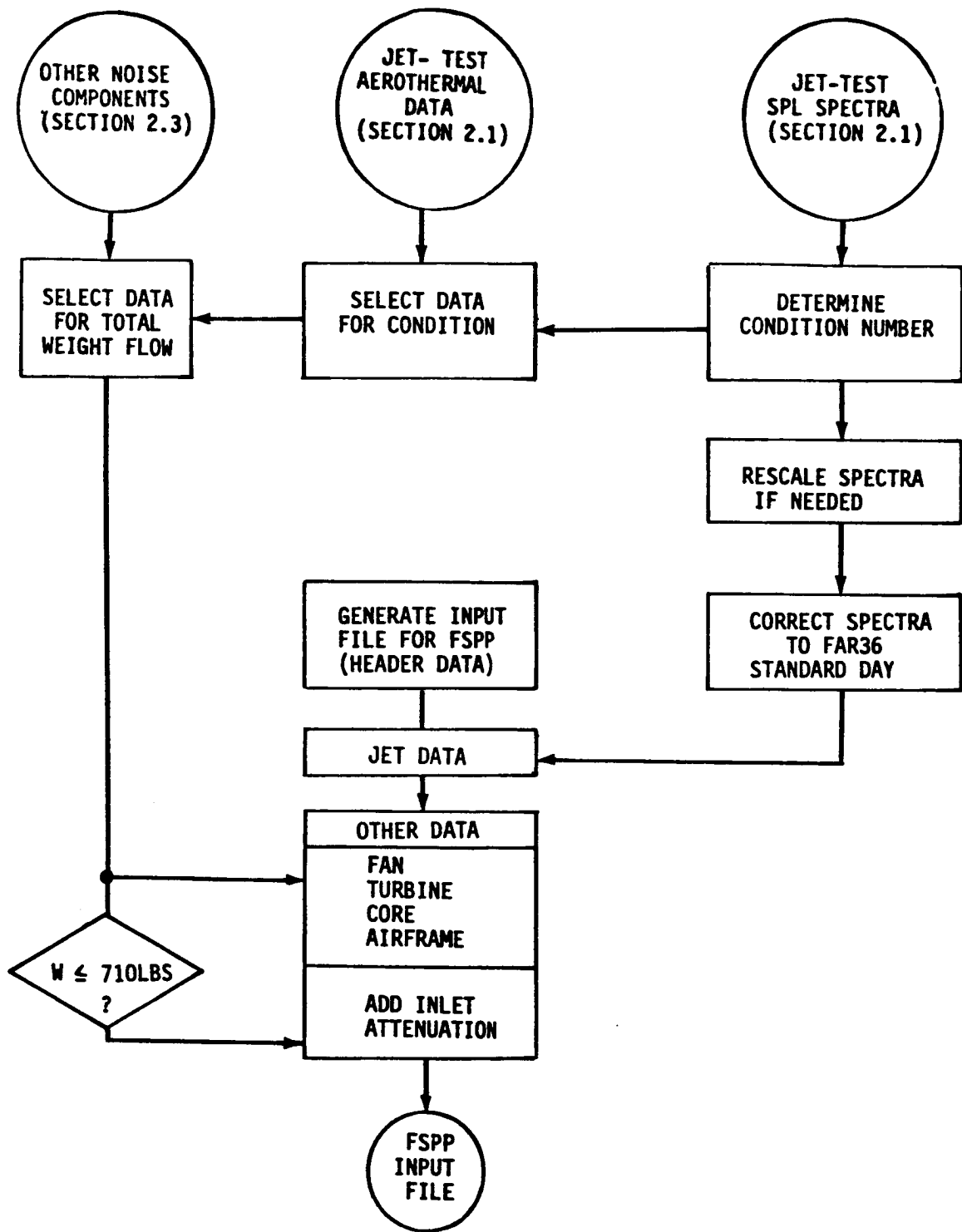


Figure 6.8. Conversion Process

by actually adding thrust, enhance its noise reduction capability. One concept is to use a separate gas generator that is not used propulsively during the cruise or similar condition that sizes the main engine. This gas generator might function as an APU supplying electric, hydraulic, air-conditioning and cooling services during the critical cruise condition (relieving the main engine). During takeoff when these services are less demanding it could be used to generate the TAS. Other concepts include using only a small amount of bleed to drive an ejector system with its own burners to provide an even hotter shielding system.

These alternate systems are more difficult to implement and have their own problems. The needed trade and implementation studies are beyond the scope of this study. However, by rescaling the test data, it is possible to obtain an assessment of the acoustic value of an alternate, additive system. In this the primary jet with the TAS is the same size as the baseline primary jet so that the TAS is additive. The rescaled scale factors and gas weight flows are given in Table 6.1 and Table 6.2.

The steps in rescaling the SPL spectra are as follows:

- Step 1. Remove the effects of atmospheric absorption, since this is frequency dependent.

$$SPL_{f_1} = SPL_{f_1} + \alpha_{f_1 d}$$

where  $SPL_f$  is the sound pressure level at frequency  $f_1$  and  $\alpha_{f_1 d}$  is the SPL increment at frequency  $f_1$  for the reference distance  $d$  (46m or 150 ft). (Note that we use the computer type of expression which means that the new value of  $SPL_{f_1}$  is the old value with  $\alpha_{f_1 d}$  added to it.)

- Step 2. Adjust the level for the new scale:

$$SPL_{f_1} = SPL_{f_1} - 20 \log_{10} \frac{\text{Old Scale}}{\text{New Scale}}$$

- Step 3. Transform the frequency spectrum for the change in scale:

$$f_x = f_1 \frac{\text{Old Scale}}{\text{New Scale}}$$



TABLE 6.1. TAS-3 RESCALING

WEIGHT-FLOW      LB/SEC

TEST POINT	OLD SCALE		NEW SCALE	
	PRIMARY	SECONDARY	PRIMARY	SECONDARY
318	262.6	107.5	452.1	185.1
320	311.0	120.4	535.5	207.3
322	334.7	125.3	576.3	215.7
324	374.8	136.3	645.3	234.7
326	413.7	139.1	712.3	239.5
328	434.4	144.3	747.9	248.5

OLD SCALE:  $\left( \frac{1400}{25.28+18.21} \right)^{1/2} = 5.67$

NEW SCALE:  $\left( \frac{1400}{25.28} \right)^{1/2} = 7.44$

TABLE 6.2. TAS-8 RESCALING

WEIGHT-FLOW      LB/SEC

TEST POINT	OLD SCALE		NEW SCALE	
	PRIMARY	SECONDARY	PRIMARY	SECONDARY
818	262.5	98.4	445.3	166.9
820	311.4	116.5	528.3	197.6
822	333.8	121.9	566.3	206.8
824	377.4	130.4	640.3	221.2
826	418.2	140.4	709.5	238.2
828	441.7	139.6	749.3	236.8

OLD SCALE:  $\left( \frac{1400}{26.15+18.2} \right)^{1/2} = 5.62$

NEW SCALE:  $\left( \frac{1400}{26.15} \right)^{1/2} = 7.32$

This gives a new spectrum for which the frequency band may now have non-standard values.

Step 4. Convert spectrum to standard frequency base (e.g., by interpolation).

Step 5. Re-apply the effects of atmospheric absorption to the new spectrum.

$$SPL_{f2} = SPL_{f1} - \alpha_{f1d}$$

#### 6.4 RESULTS OF ANALYSIS

The analysis has used only the test data for which relative velocity of 122 m/s (400 ft/s) was applied. In addition, the data was that measured in a community orientation, or central to the shield jet. Since the analytical methods used assume a symmetrical noise source, it should be understood that reference to sideline has limitations applied to the TAS. Sideline here is that of noise as measured with the community oriented shield observed at the sideline. This result is optimistic for a shield orientated optimally for the community locations and gives a lower limit for sideline noise. A partial shield has reduced effectiveness to the sideline.

There are two types of analysis:

- A. Noise-Thrust-Altitude characteristic
- B. Certification point noise

In each case both jet noise only, and total airplane noise characteristics were obtained.

Noise-Thrust-Altitude (NTA) data is the variation in EPNL at a fixed location when the airplane is flown over in level flight, at various constant thrusts and at various heights. These are useful for appraising the general characteristics of the airplane and in "what-if" studies. Caution should be used in applying this data to certification point values since other factors not included, such as airplane attitude have an effect.

#### 6.4.1 TAS OBTAINED BY A BLEED SYSTEM

EPNL values for various thrusts at three level flyover heights are given in Tables 6.3 and 6.4. Those in Table 6.3 are for jet noise only while those in Table 6.4 are for total noise.

Values for the 305m (1000 ft) flyover are plotted comparatively in Figures 6.9 through 6.12. The plug nozzle with and without TAS are compared in Figure 6.9 for jet noise only and Figure 6.10 for total noise. The 32 chute suppressor with and without TAS are compared in Figure 6.11 and Figure 6.12 for jet only and total noise respectively. In each figure the predicted RC nozzle result is included for reference.

It will be noted that adding the TAS to the plug nozzle (TAS-3) not only adds no benefit, but negates the benefit of the plug nozzle relative to the RC. This is due to the thrust loss incurred by the bleed system (in the order of 33%). This result while following similar trends is not entirely consistent with earlier work (Reference 6.5). Those earlier, static only tests, showed less benefit for a plug nozzle relative to the RC, while showing greater suppression for the TAS than the present analysis. The result then was that there remained some small net benefit for the TAS even with the bleed thrust loss (e.g., Figure 12 of Reference 6.5).

Adding the TAS to the 32 chute suppressor retains some advantage, even with the thrust loss, at the lower thrust levels. It loses advantage at the higher thrust levels however. Note, however, that both TAS-6 and TAS-8 are inferior to the baseline plug nozzle (TAS-1) at the lower thrust levels. The 32 chute suppressor (TAS-6) has a small advantage over the baseline at high thrust levels, whereas with the TAS (TAS-8) they become approximately equal.

FAR-36 noise levels for the various nozzle configurations are given for the community point in Table 6.5 and the sideline location in Table 6.6. Note that the sideline noise assumes an axisymmetric noise source. Both jet only and total noise for the three flight profiles are included in the tables. Also tabulated are suppression values relative to the predicted RC nozzle.

TABLE 6.3. LEVEL FLYOVER EPNL VALUES - JET NOISE ONLY

TAS-1 BASELINE PLUG NOZZLE			
THRUST - $F_n/6$		ALTITUDE meters (feet)	
NEWTONS	lbs	91(300)	305 (1000) 914 (3000)
98100	22054	108.3	97.7 87.7
116900	26282	110.2	101.4 91.3
150400	33814	116.1	107.1 97.0
181200	40743	119.6	110.8 101.0
201200	45227	122.3	113.6 103.8
245300	55151	125.3	116.6 107.0

TAS-3 PLUG NOZZLE WITH 180° 1 in. SHIELD			
THRUST - $F_n/6$		ALTITUDE meters (feet)	
NEWTONS	lbs	91(300)	305 (1000) 914 (3000)
101400	22797	113.2	104.9 95.6
121700	27359	117.5	109.5 100.4
135700	30509	119.8	111.8 102.8
164100	36887	123.6	115.6 106.6
177800	39971	125.2	117.2 108.2

TAS-6 32- CHUTE SUPPRESSOR			
THRUST - $F_n/6$		ALTITUDE meters (feet)	
NEWTONS	lbs	91(300)	305 (1000) 914 (3000)
90200	20277	112.2	103.1 90.9
109600	24636	114.6	105.5 93.1
140700	31634	117.3	107.9 95.2
173600	39036	120.1	110.5 97.7
195300	43916	121.6	112.0 98.9
237100	53312	123.5	114.1 101.2

TAS-8 32- CHUTE WITH 180° 1 in. SHIELD			
THRUST - $F_n/6$		ALTITUDE meters (feet)	
NEWTONS	lbs	91(300)	305 (1000) 914 (3000)
95700	21512	109.7	100.6 88.9
117200	26341	112.7	103.2 92.3
130800	29405	114.7	105.4 94.8
158600	35661	118.0	109.0 98.7
195600	43971	121.3	112.6 102.9

EQUIVALENT RC TURBOJET			
THRUST - $F_n/6$		ALTITUDE meters (feet)	
NEWTONS	lbs	91(300)	305 (1000) 914 (3000)
98100	22054	111.3	104.1 96.2
116900	26282	117.4	109.8 101.2
150400	33814	121.7	114.3 106.3
181200	40743	124.5	117.3 109.5
201200	45227	125.8	118.7 111.0
245300	55151	128.0	120.9 113.3

FLYOVER VELOCITY  
122 m/s (400 ft/s)

TABLE 6.4. LEVEL FLYOVER EPNL VALUES - TOTAL NOISE

TAS-1 BASELINE PLUG NOZZLE			
THRUST - $F_n/6$		ALTITUDE meters (feet)	
NEWTONS	lbs	91(300)	305 (1000) 914 (3000)
98100	22054	110.9	101.5 91.4
116900	26282	113.2	103.9 93.8
150400	33814	117.4	108.4 98.5
181200	40743	120.4	111.6 101.9
201200	45227	123.7	114.7 104.4
245300	55151	125.9	117.0 107.2

TAS-3 PLUG NOZZLE WITH 180° 1in SHIELD			
THRUST - $F_n/6$		ALTITUDE meters (feet)	
NEWTONS	lbs	91(300)	305 (1000) 914 (3000)
101400	22797	114.8	106.5 97.2
121700	27359	118.7	110.6 101.7
135700	30509	120.6	112.6 103.5
164100	36887	124.1	116.1 107.1
177800	39971	125.6	117.7 108.6

TAS-6 32- CHUTE SUPPRESSOR			
THRUST - $F_n/6$		ALTITUDE meters (feet)	
NEWTONS	lbs	91(300)	305 (1000) 914 (3000)
90200	20277	113.8	104.5 92.7
109600	24636	115.9	106.6 94.3
140700	31634	118.4	108.9 96.4
173600	39036	120.8	111.3 98.4
195300	43916	122.8	113.2 100.0
237100	53312	124.2	114.7 101.9

TAS-8 32- CHUTE WITH 180° 1 in SHIELD			
THRUST - $F_n/6$		ALTITUDE meters (feet)	
NEWTONS	lbs	91(300)	305 (1000) 914 (3000)
95700	21512	112.1	102.8 91.6
117200	26341	114.8	105.2 94.6
130800	29405	116.4	107.1 96.7
158600	35661	119.4	110.3 100.3
195600	43971	122.9	114.1 104.2

EQUIVALENT RC TURBOJET			
THRUST - $F_n/6$		ALTITUDE meters (feet)	
NEWTONS	lbs	91(300)	305 (1000) 914 (3000)
98100	22054	113.9	106.3 97.9
116900	26282	118.3	110.6 102.4
150400	33814	122.7	115.3 107.2
181200	40743	125.2	118.1 110.1
201200	45227	127.1	119.8 111.8
245300	55151	128.6	121.4 113.5

FLYOVER VELOCITY  
122 m/s (400 ft/s).

305M (1000FT) LEVEL FLYOVER AT 122M/S (400FT/S)

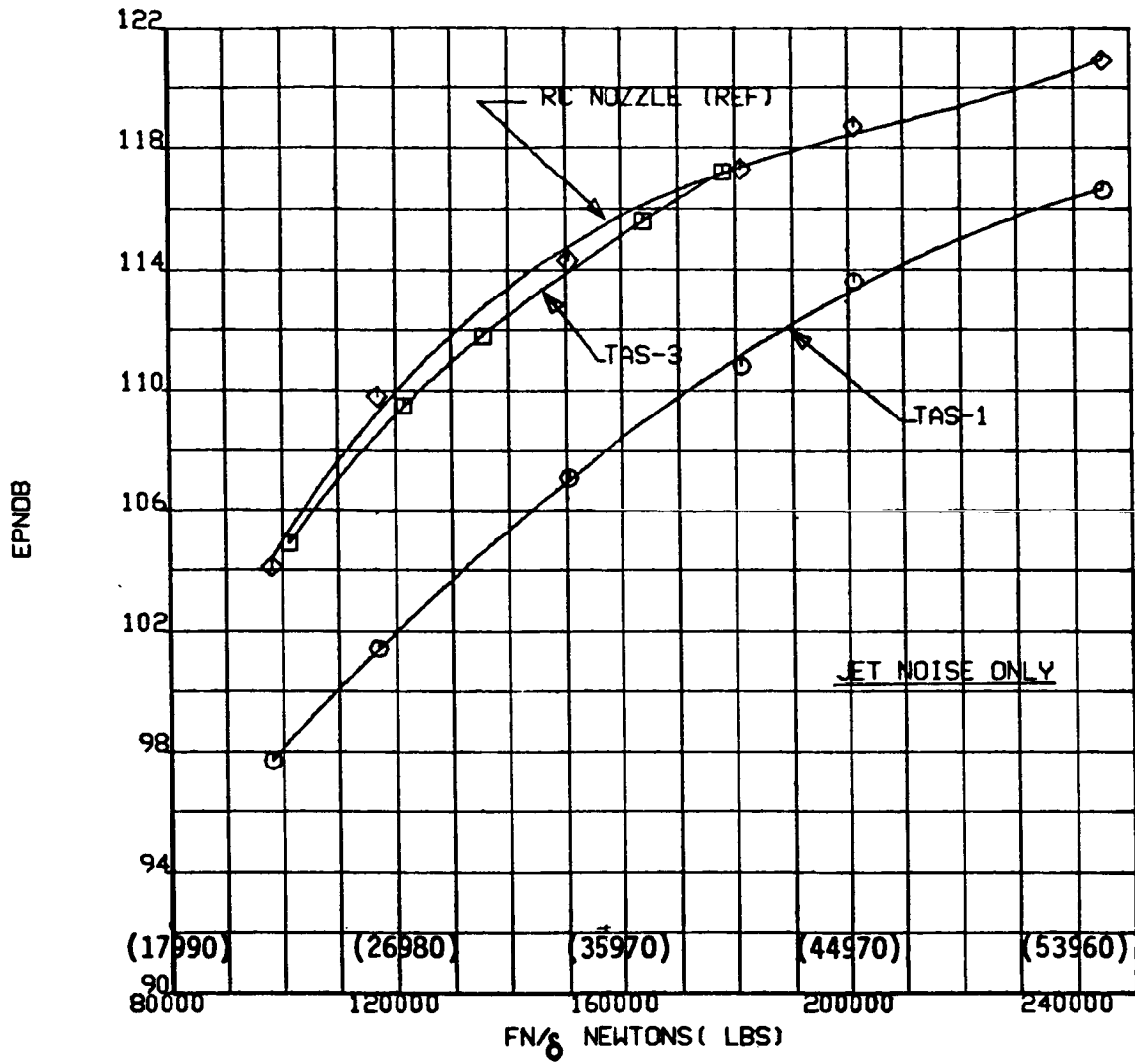


Figure 6.9. Plug Nozzles Compared Jet Noise Only

305M (1000FT) LEVEL FLYOVER AT 122M/S (400FT/S)

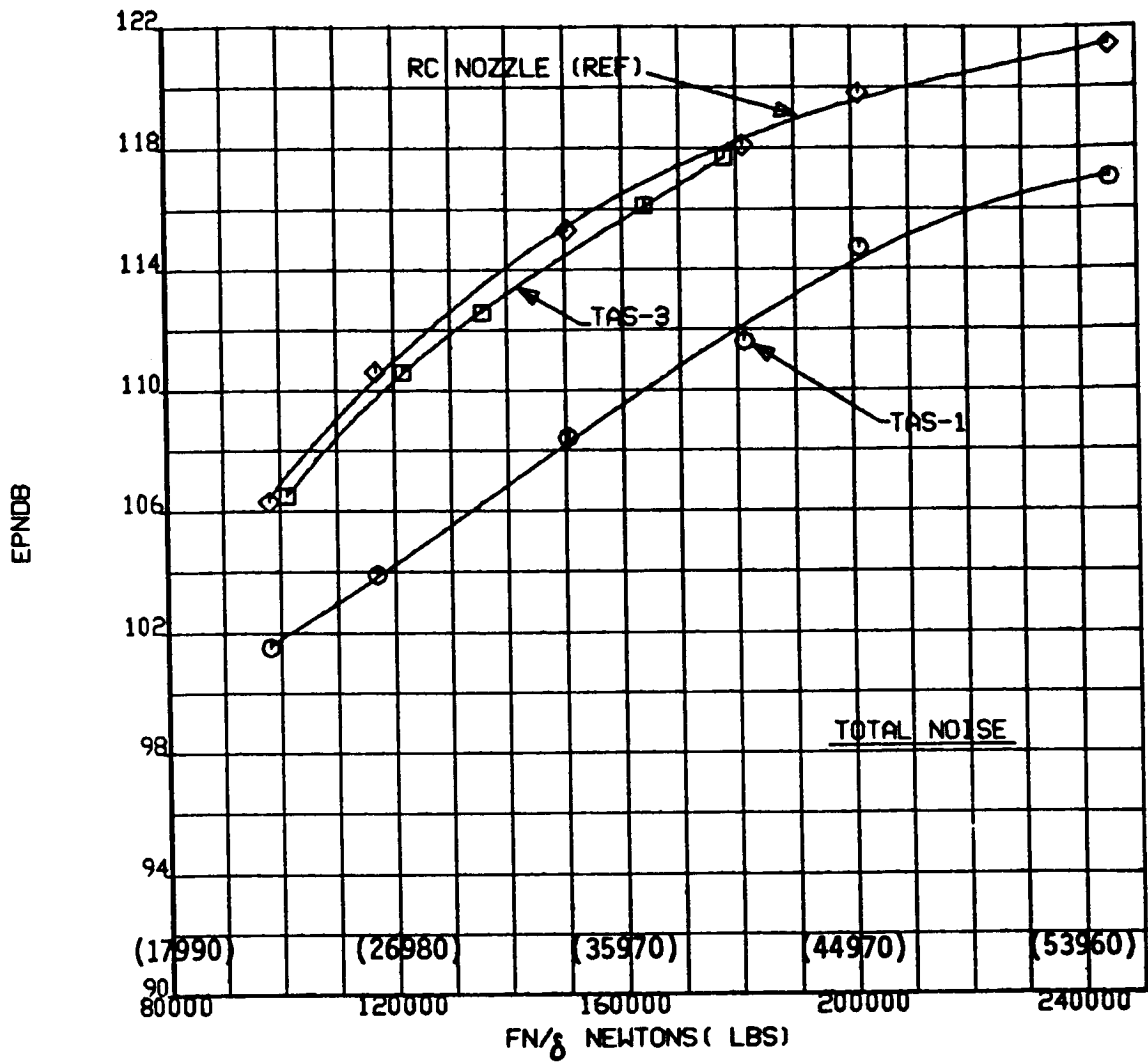


Figure 6.10. Plug Nozzles Compared Total Noise



305M (1000FT) LEVEL FLYOVER AT 122M/S (400FT/S)

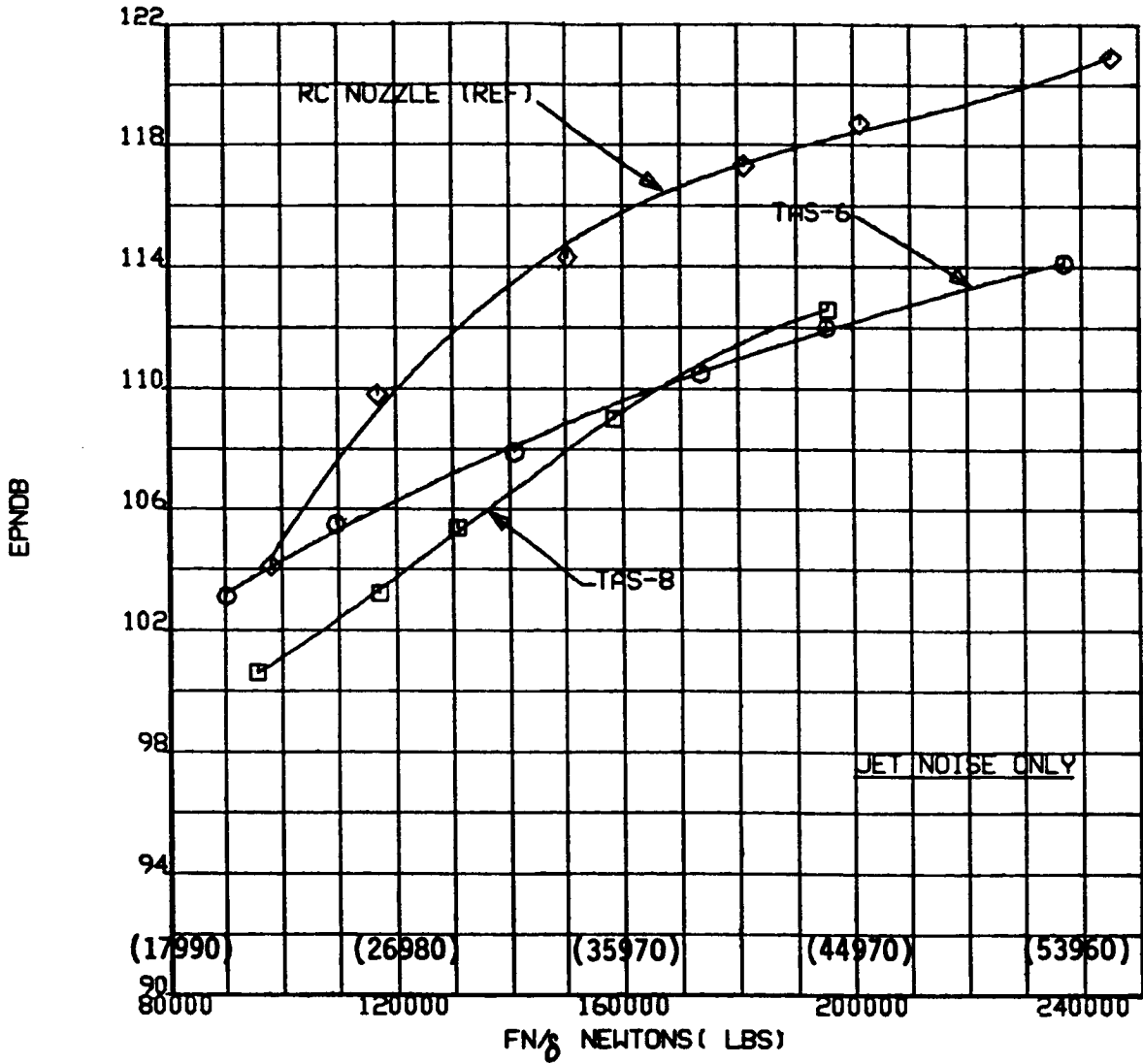


Figure 6.11. 32-Chute Suppressor Nozzles Compared Jet Noise Only

305M (1000FT) LEVEL FLYOVER AT 122M/S (400FT/S)

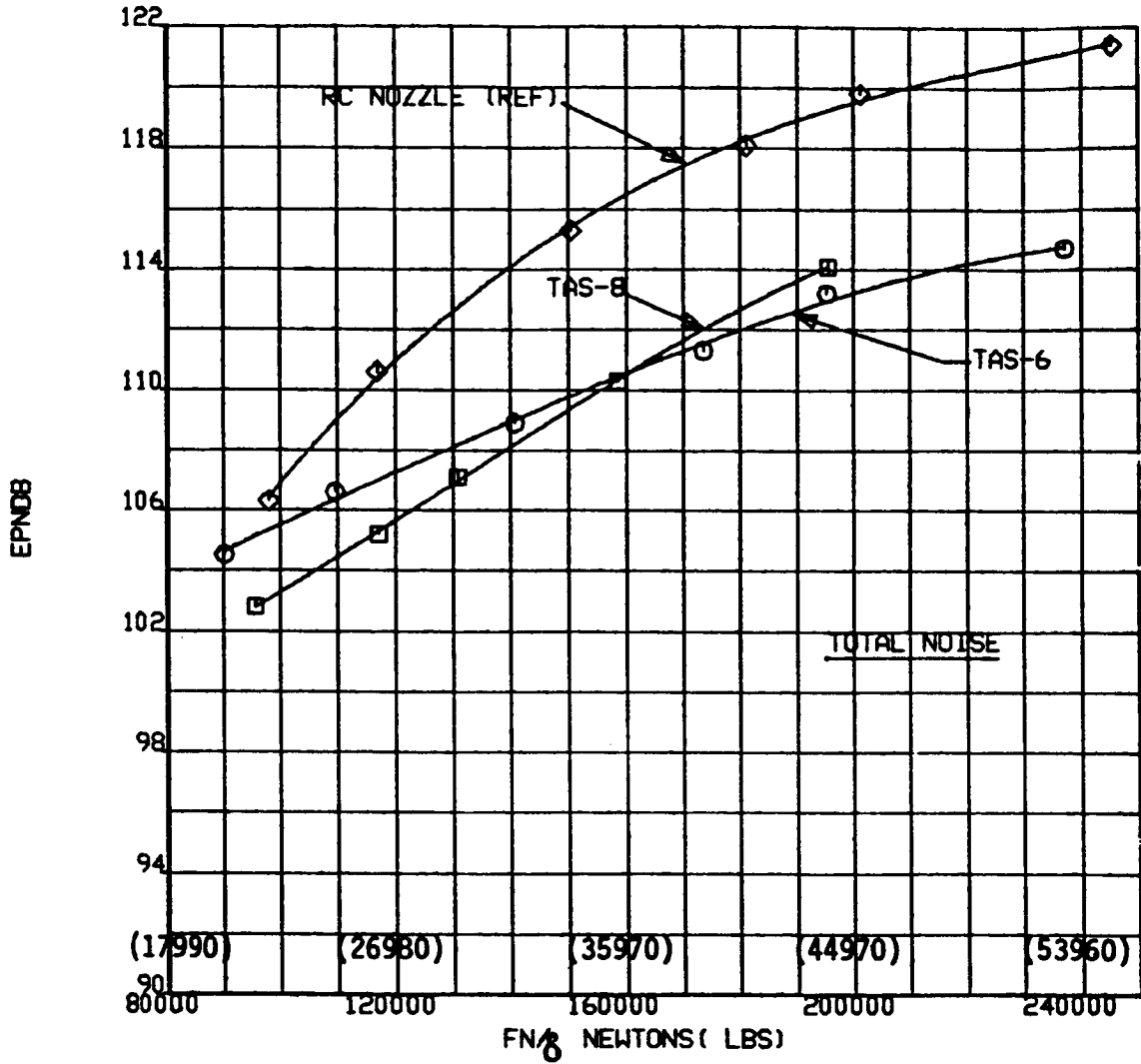


Figure 6.12. 32-Chute Suppressor Nozzles Compared Total Noise

TABLE 6.5. FAR-36 NOISE LEVELS FOR THE COMMUNITY POINT

BLEED SYSTEM ~ 0.6 VELOCITY RATIO

COMMUNITY POINT	ADVANCED PROCEDURE		FAR-36 CUTBACK		FAR-36 FULL-POWER	
	JET ONLY	TOTAL	JET ONLY	TOTAL	JET ONLY	TOTAL
EQUIVALENT R.C.	110.0	111.7	117.7	118.6	121.3	121.9
TAS-1 BASELINE PLUG NOZZLE	103.3	106.2	110.9	112.2	116.2	116.9
TAS-3 BASLINE WITH TAS	110.1	111.4	117.4	117.9	121.8	122.1
TAS-6 32-CHUTE SUPPRESSOR	108.0	109.7	111.6	112.9	114.2	115.0
TAS-8 32-CHUTE WITH TAS	104.7	107.4	111.4	113.0	116.0	117.0

SUPPRESSION RELATIVE TO RC NOZZLE

TAS-1	6.7	5.5	6.8	6.4	5.1	5.0
TAS-3	-0.1	0.3	0.3	0.7	-0.5	-0.2
TAS-6	2.0	2.0	6.1	5.7	7.1	6.9
TAS-8	5.3	4.3	6.3	5.6	5.3	4.9

TABLE 6.6. FAR-36 NOISE LEVELS FOR THE SIDELINE LOCATION

BLEED SYSTEM ~ 0.6 VELOCITY RATIO

SIDELINE *	ADVANCED PROCEDURE		FAR-36 CUTBACK		FAR-36 FULL-POWER	
	JET ONLY	TOTAL	JET ONLY	TOTAL	JET ONLY	TOTAL
EQUIVALENT R.C.	112.4	113.2	112.8	113.7	113.7	114.6
TAS-1 BASELINE PLUG NOZZLE	106.1	106.8	106.4	107.0	107.1	107.7
TAS-3 BASLINE WITH TAS	112.5	112.8	112.5	112.9	113.2	113.5
TAS-6 32-CHUTE SUPPRESSOR	102.6	103.6	102.7	103.6	102.7	103.7
TAS-8 32-CHUTE WITH TAS	106.1	107.3	105.6	106.9	106.9	108.0

SUPPRESSION RELATIVE TO RC NOZZLE

TAS-1	6.3	6.4	6.4	6.7	6.6	6.9
TAS-3	-0.1	0.4	0.3	0.8	0.5	1.1
TAS-6	9.8	9.6	10.1	10.1	11.0	10.9
TAS-8	6.3	5.9	7.2	6.8	6.8	6.6

\* ASSUMES AN OMNI-DIRECTIONAL TAS  
BY USING CENTERLINE DATA.

The Community Point location (6500m from brake release) noise levels are shown in bar-chart form in Figure 6.13 (jet noise only) and Figure 6.14 (total noise). It will be seen that the trends indicated by the NTA curves are followed.

These results suggest that a bleed type of TAS has no merit when compared with a simple baseline plug nozzle. It is possible that optimization of velocity ratio (to reduce thrust loss) may be beneficial with the 32 chute suppressor, e.g., an increase in velocity ratio to 0.75 would increase thrust by the order of 10% (for TAS-8) with a potential improvement in the order of 1 to 1.5 EPNdB. This is however only a small improvement and would still leave the TAS at a disadvantage relative to the plug baseline at low thrusts. Therefore, optimization of a bleed type system may be of limited value.

#### 6.4.2 TAS OBTAINED FROM AN INDEPENDENT SOURCE

An alternate possibility to a bleed system is an independent source of hot gas that would add thrust to the overall system instead of subtracting from it. The main jet in this case is the same as the respective baseline, delivering the same thrust. Since the shield thrust adds to this, the engine will be throttled back, further improving the noise characteristic. Additional discussion related to rescaling is given in Section 6.3.2. To differentiate between the original and rescaled data the rescaled cases are designated as TAS-3RS and TAS-8RS.

The NTA results for rescaling of TAS-3RS and TAS-8RS are given in Table 6.7, with the baseline results in Tables 6.3 and 6.4 still applicable. Plots of the 305m (1000 ft) level flyover are given in Figures 6.15, 6.16, 6.17 and 6.18.

Now both TAS-3RS and TAS-8RS show strong positive benefit, particularly in the case of TAS-8RS. However, as predicted (see Section 6.4.3 for additional discussion), other noise components strongly erode the benefit in jet noise reduction showing the need for their consideration.

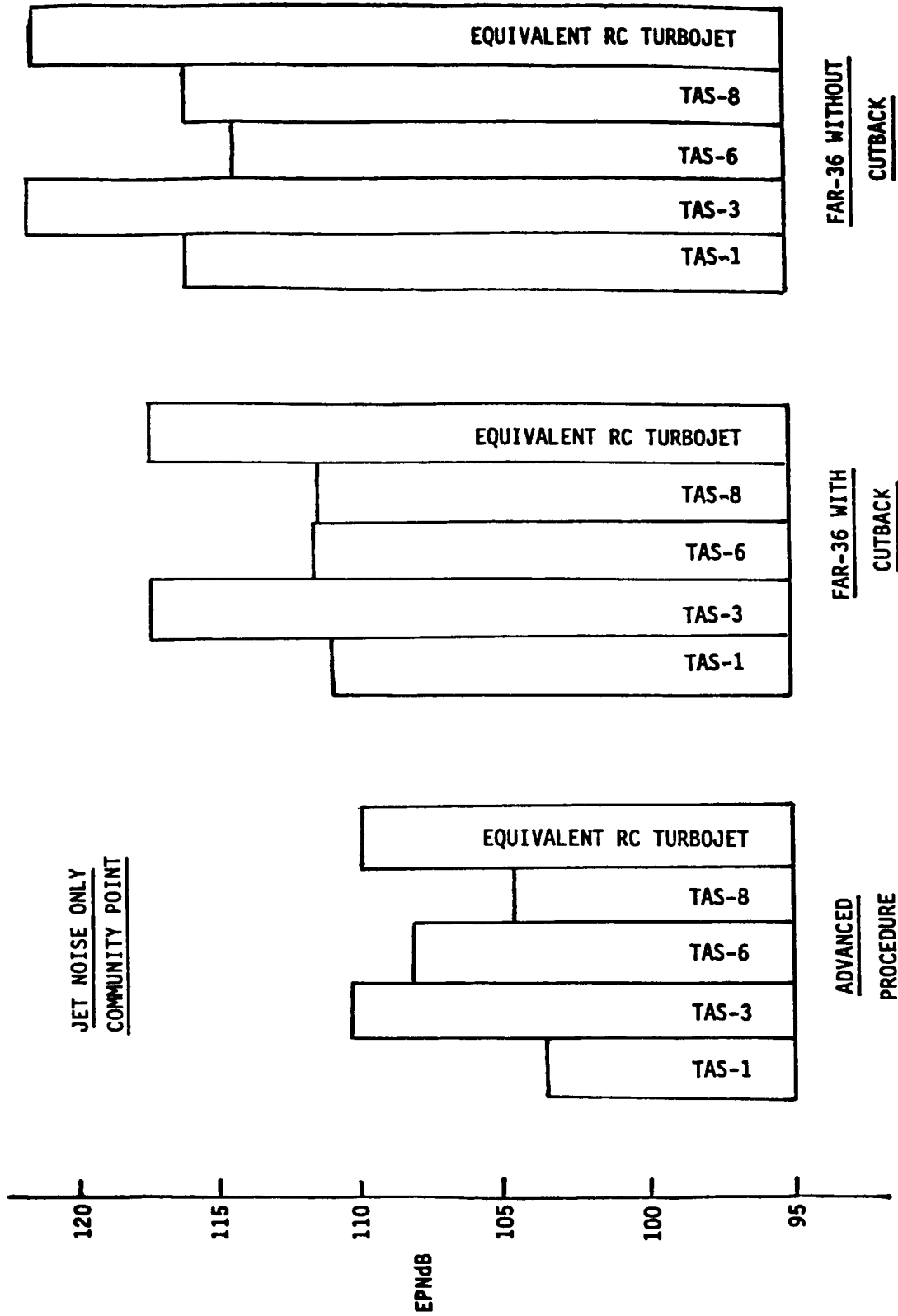


Figure 6.13. Jet Noise Levels of the Various Nozzles at the Community Point Location.

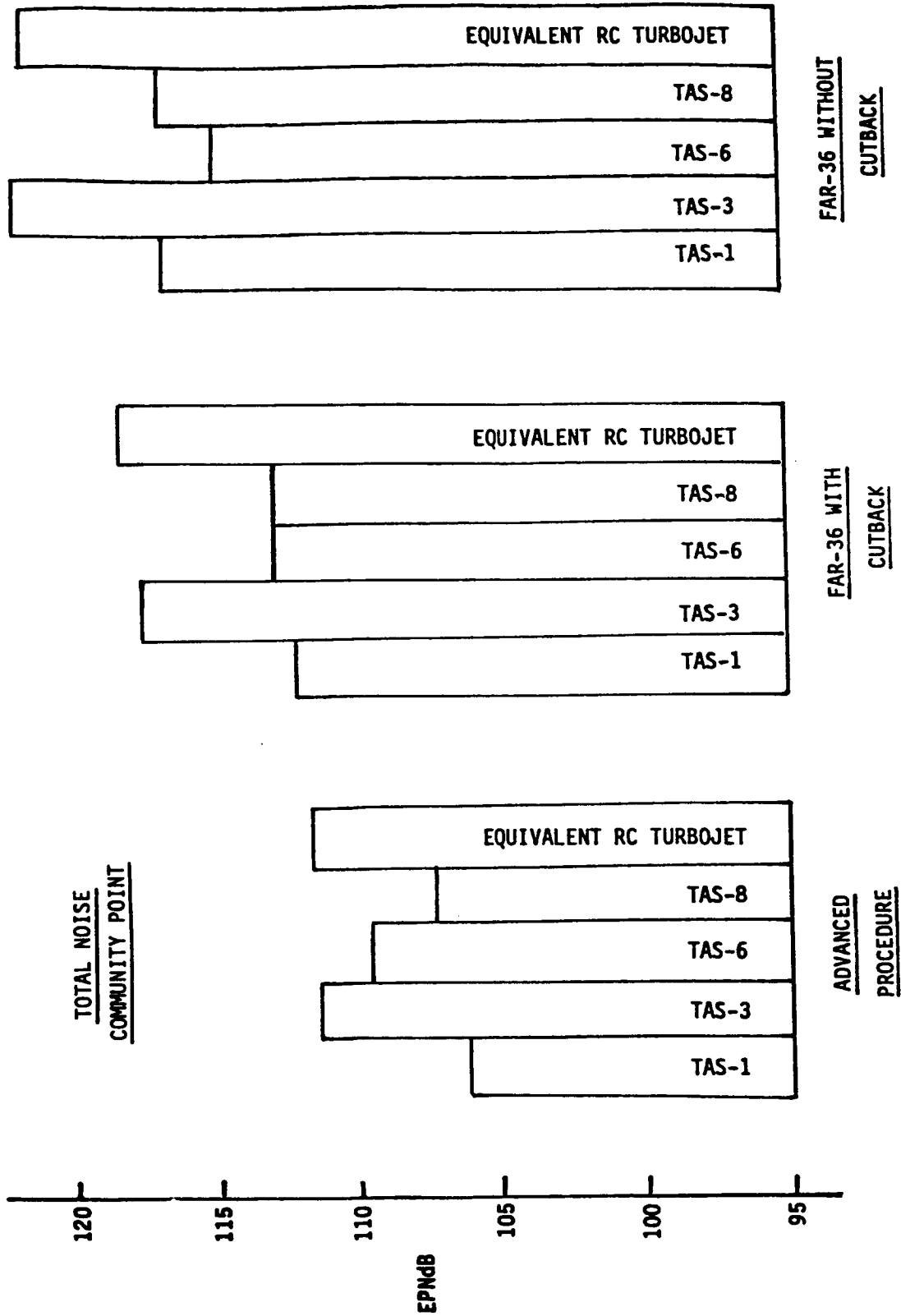


Figure 6.14. Total Noise Levels of the Various Nozzles at the Community Point Location

TABLE 6.7. LEVEL FLYOVER AT 122 M/S (400 FT/S) EPNL FOR THE RESCALED CONFIGURATIONS

<u>MODEL:</u> TAS-8RS		<u>CASE:</u> JET NOISE ONLY	
THRUST - $F_n/\delta$		ALTITUDE meters (feet)	
NEWTONS	1bs	91(300)	305 (1000) 914 (3000)
103600	23300	106.8	97.8 85.6
125500	28218	109.1	100.0 88.1
162600	36557	112.4	103.2 91.7
198300	44570	115.5	106.1 94.8
221600	49813	117.4	108.1 97.1

<u>MODEL:</u> TAS-8RS		<u>CASE:</u> TOTAL NOISE	
THRUST - $F_n/\delta$		ALTITUDE meters (feet)	
NEWTONS	1bs	91(300)	305 (1000) 914 (3000)
103600	23300	110.8	101.4 89.7
125500	28218	112.7	103.2 91.6
162600	36557	115.6	106.0 94.6
198300	44570	117.9	108.3 97.3
221600	49813	120.9	111.2 99.9

<u>MODEL:</u> TAS-3RS		<u>CASE:</u> JET NOISE ONLY	
THRUST - $F_n/\delta$		ALTITUDE meters (feet)	
NEWTONS	1bs	91(300)	305 (1000) 914 (3000)
113200	25457	104.0	95.6 86.1
136100	30605	108.8	100.5 90.8
174700	39264	115.2	106.8 97.4
209600	47130	119.5	111.4 102.2
233500	52486	121.8	113.7 104.6

<u>MODEL:</u> TAS-3RS		<u>CASE:</u> TOTAL NOISE	
THRUST - $F_n/\delta$		ALTITUDE meters (feet)	
NEWTONS	1bs	91(300)	305 (1000) 914 (3000)
113200	25457	110.2	100.8 90.4
136100	30605	113.1	104.0 93.9
174700	39264	117.6	108.9 99.5
209600	4713	122.2	113.7 104.2
233500	52486	123.6	115.2 105.6



305M (1000FT) LEVEL FLYOVER AT 122M/S (400FT/S)

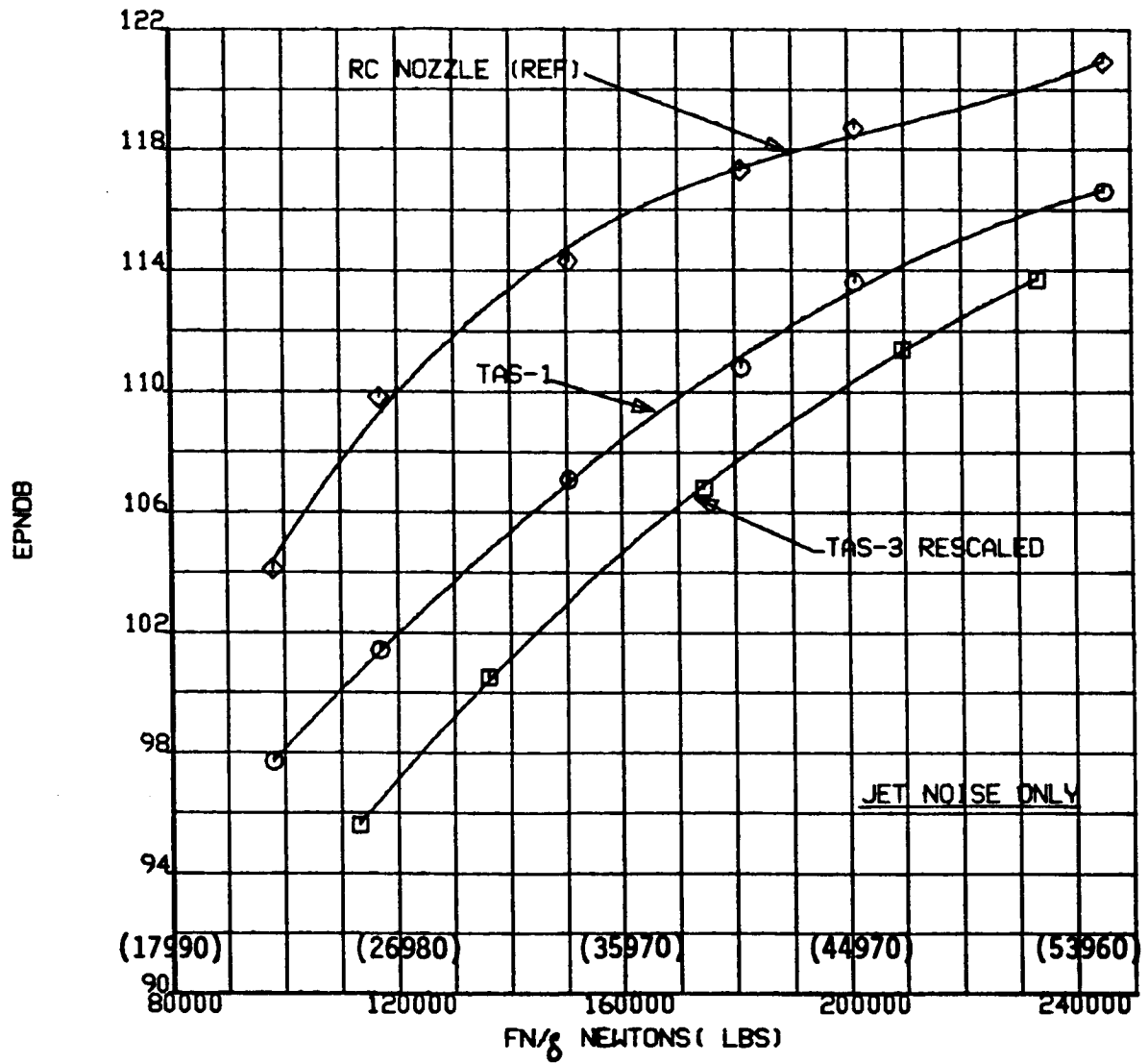


Figure 6.15. Plug Nozzles Compared Jet Noise Only.

305M (1000FT) LEVEL FLYOVER AT 122M/S (400FT/S)

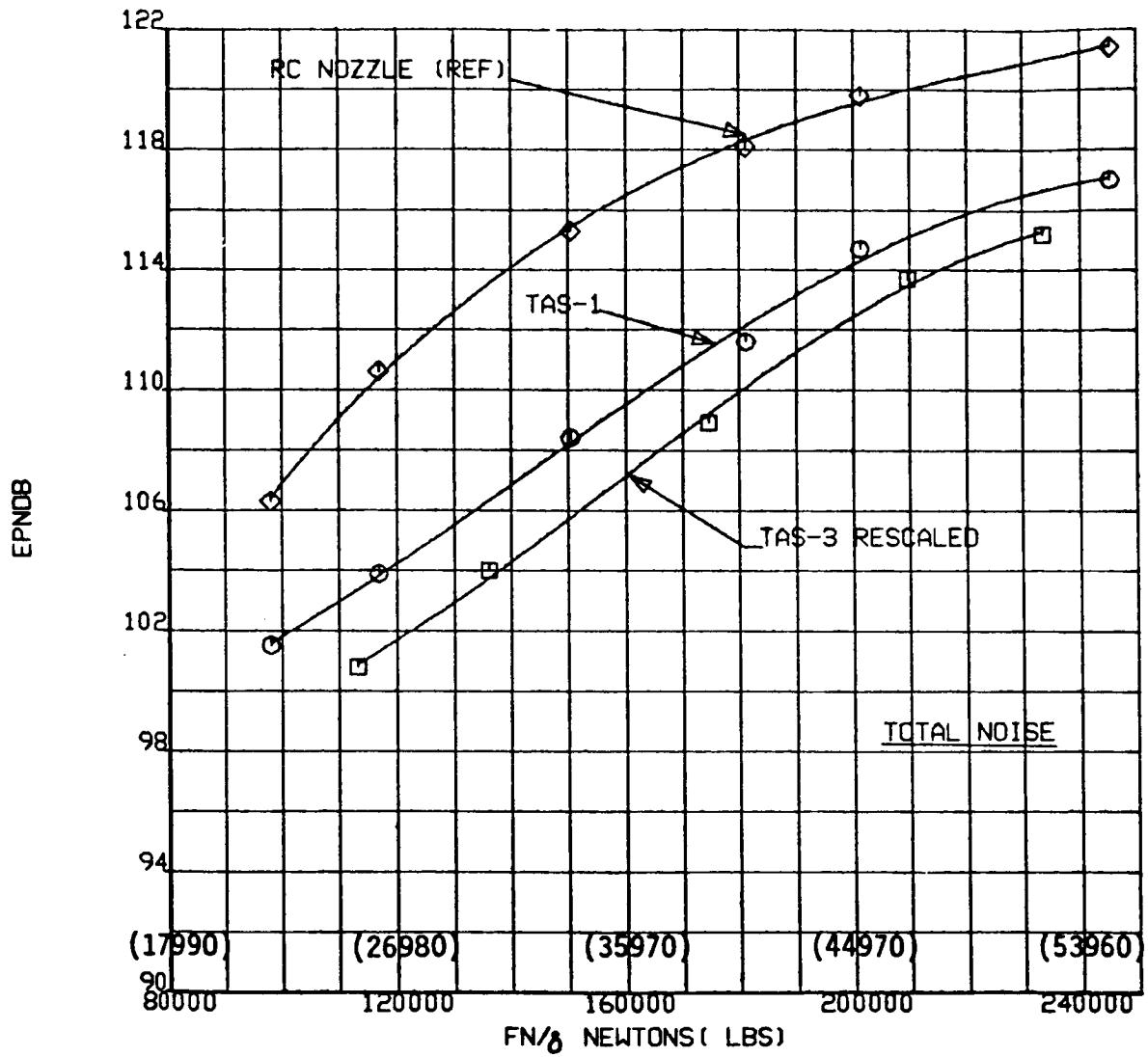


Figure 6.16. Plug Nozzles Compared Total Noise

305M (1000FT) LEVEL FLYOVER AT 122M/S (400FT/S)

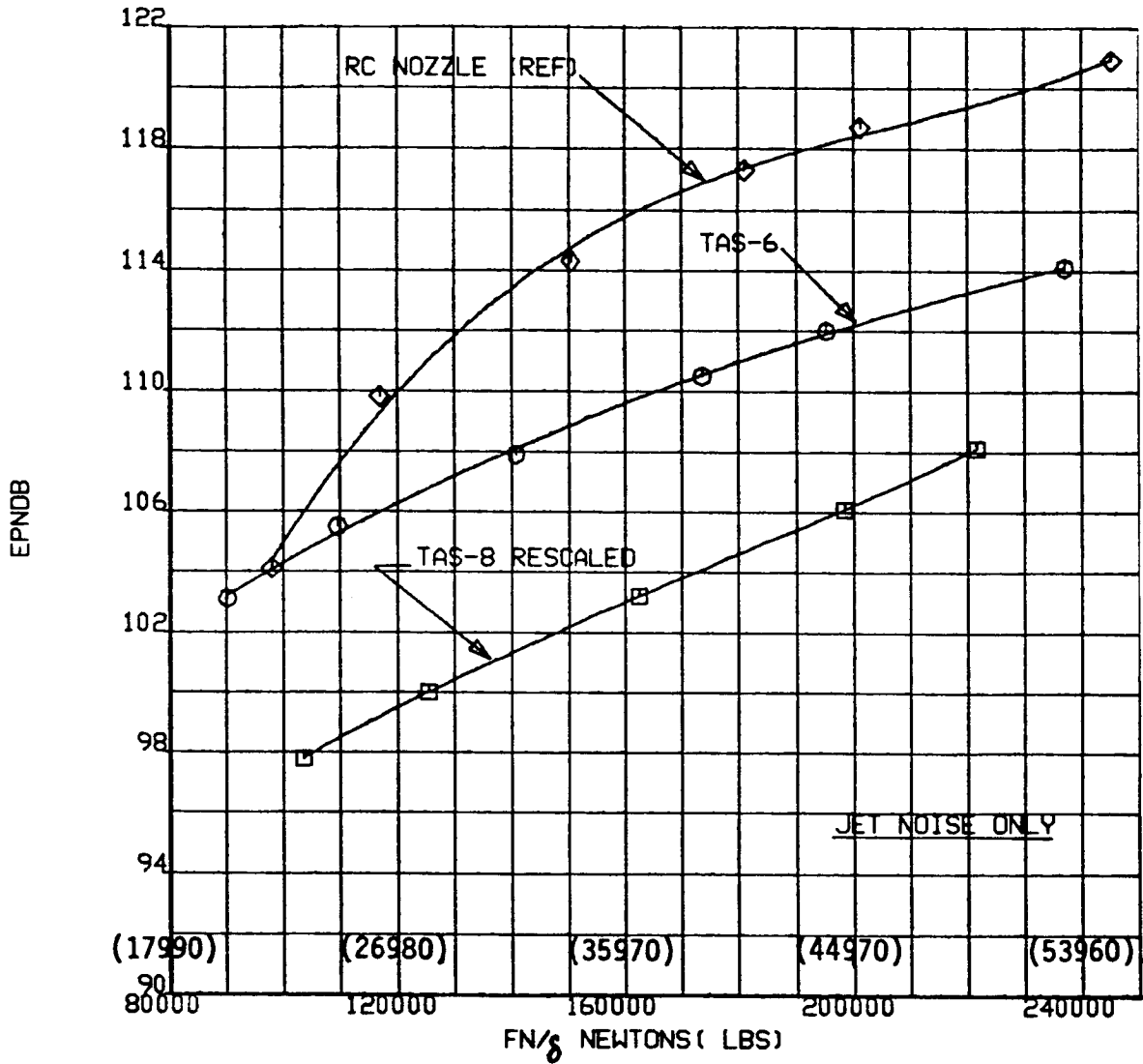


Figure 6.17. 32-Chute Suppressor Nozzles Compared Jet Noise Only.

305M (1000FT) LEVEL FLYOVER AT 122M/S (400FT/S)

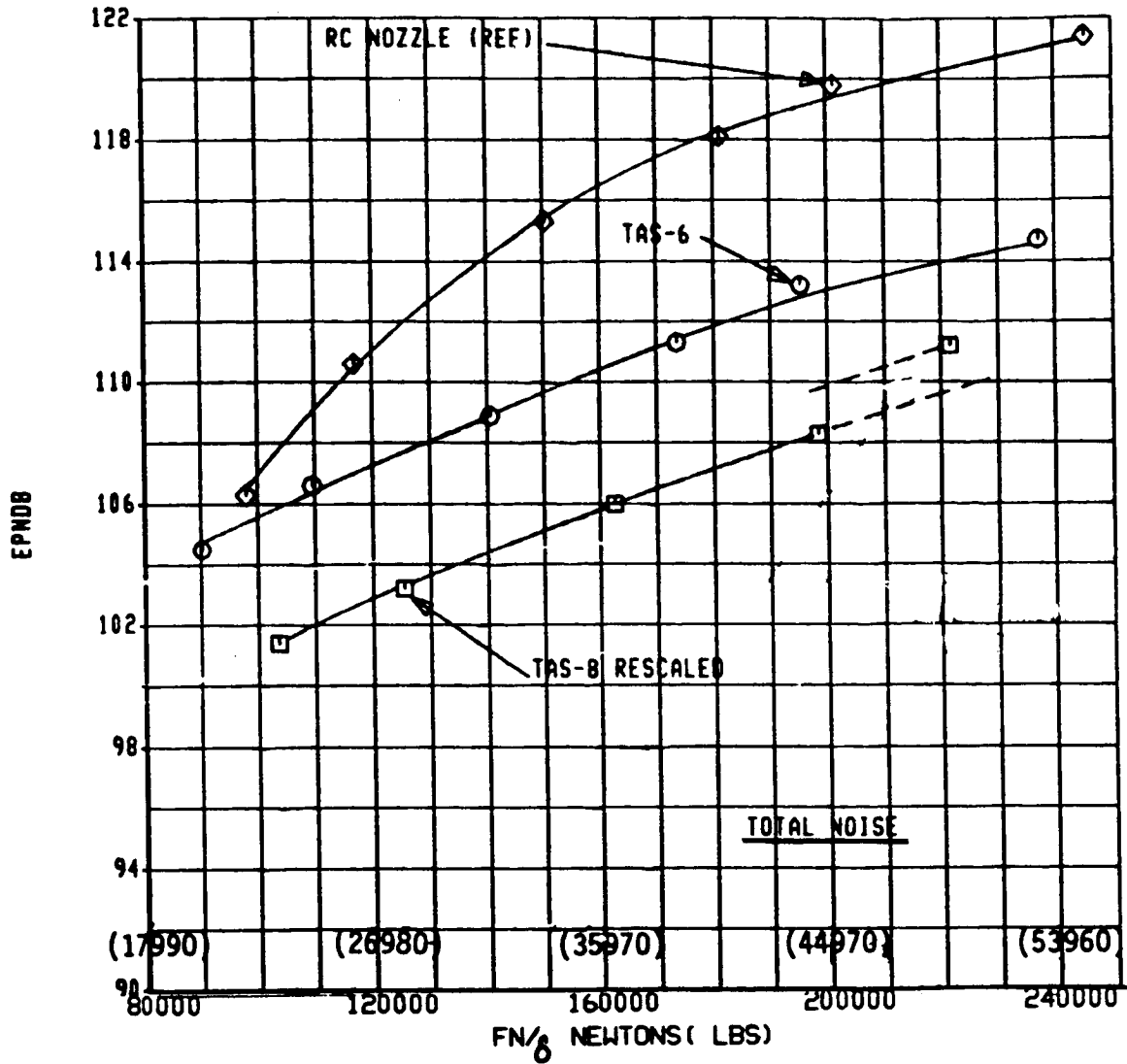


Figure 6.18. 32-Chute Suppressor Nozzles Compared Total Noise.

Results for the FAR-36 Community Point location (6500m from brake release) are given in Table 6.8 and for the sideline location (650m sideline) in Table 6.9. As before the sideline noise values assume an omni-directional source. Community Point location results are given in bar-graph form for jet noise only in Figure 6.19 and total noise in Figure 6.20. In these figures the bleed system results are shown dashed for comparison.

The substantial improvement in TAS-3RS result is most notable, this becoming the best for an Advanced Procedure Community point. TAS-8RS appears better for sideline and more conventional takeoff profiles. Note however that even in these cases, achievement of Stage 3 noise levels with conventional flight profiles remains questionable, whereas with an advanced procedure this appears more practical.

#### 6.4.3 OTHER ANALYSIS RESULTS

Relative noise components as predicted are shown in Figure 6.21 in bar-graph form. As predicted the second strongest component after jet noise over most of the power range is turbine noise, with core noise a strong component. Those predictions should be tempered by there being no acoustic treatment included. Furthermore, there is no credit taken for attenuation of these components by the thermal acoustic shield since the current test data does not address these types of noise source. Both core and turbine noise tend to peak at 120 degrees to the engine axis, and thus should experience attenuation through a TAS so that levels should in practice be lower than depicted in Figure 6.21.

The fan of the SST engine is predicted to be an IGV type with very close rotor/stator spacings, and hence very noisy. This shows in Figure 6.21 for an APR type of takeoff application (note that with a more representative engine size it would show with the FAR-36 full power takeoff case). Note however that this high relative level shows where a high level of jet noise suppression exists, as with the rescaled TAS-8, and is less apparent with higher levels of jet noise.

TABLE 6.8. FAR-36 NOISE LEVELS AT THE COMMUNITY POINT LOCATION FOR THE  
CASE WHEN TAS IS FROM A SEPARATE SOURCE

RE-SCALED TO TAS FROM SEPARATE SOURCE

COMMUNITY POINT	ADVANCED PROCEDURE		FAR-36 CUTBACK		FAR-36 FULL-POWER	
	JET ONLY	TOTAL	JET ONLY	TOTAL	JET ONLY	TOTAL
EQUIVALENT R.C.	110.0	111.7	117.7	118.6	121.3	121.9
TAS-1 BASELINE PLUG NOZZLE	103.3	106.2	110.9	112.2	116.2	116.9
TAS-3 BASLINE WITH TAS	98.7	104.0	107.0	109.8	112.7	114.4
TAS-6 32-CHUTE SUPPRESSOR	108.0	109.7	111.6	112.9	114.2	115.0
TAS-8 32-CHUTE WITH TAS	100.9	105.4	105.0	108.3	108.3	110.5

SUPPRESSION RELATIVE TO RC NOZZLE

TAS-1	6.7	5.5	6.8	6.4	5.1	5.0
TAS-3	11.3	7.7	10.7	8.8	8.6	7.5
TAS-6	2.0	2.0	6.1	5.7	7.1	6.9
TAS-8	9.1	6.3	12.7	10.3	13.0	11.4

TABLE 6.9. FAR-36 NOISE LEVELS AT THE SIDELINE LOCATION FOR THE CASE WHEN TAS IS FROM A SEPARATE SOURCE

RE-SCALED TO TAS FROM SEPARATE SOURCE

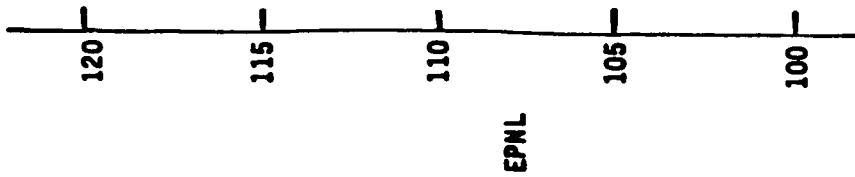
SIDELINE*	ADVANCED PROCEDURE		FAR-36 CUTBACK		FAR-36 FULL-POWER	
	JET ONLY	TOTAL	JET ONLY	TOTAL	JET ONLY	TOTAL
EQUIVALENT R.C.	112.4	113.2	112.8	113.7	113.7	114.6
TAS-1 BASELINE PLUG NOZZLE	106.1	106.8	106.4	107.0	107.1	107.7
TAS-3 BASLINE WITH TAS	103.4	105.4	102.9	105.2	101.3	106.0
TAS-6 32-CHUTE SUPPRESSOR	102.6	103.6	102.7	103.6	102.7	103.7
TAS-8 32-CHUTE WITH TAS	98.7	101.2	98.0	100.9	98.7	101.2

SUPPRESSION RELATIVE TO RC NOZZLE

TAS-1	6.3	.64	6.4	6.7	6.6	6.9
TAS-3	9.0	7.8	9.9	8.5	12.4	8.6
TAS-6	9.8	9.6	10.1	10.1	11.0	10.9
TAS-8	13.7	12.0	14.8	12.8	15.0	13.4

\*ASSUMES AN OMNI-DIRECTIONAL TAS BY USING CENTER-LINE DATA.

NOISE AT COMMUNITY POINT



JET NOISE ONLY

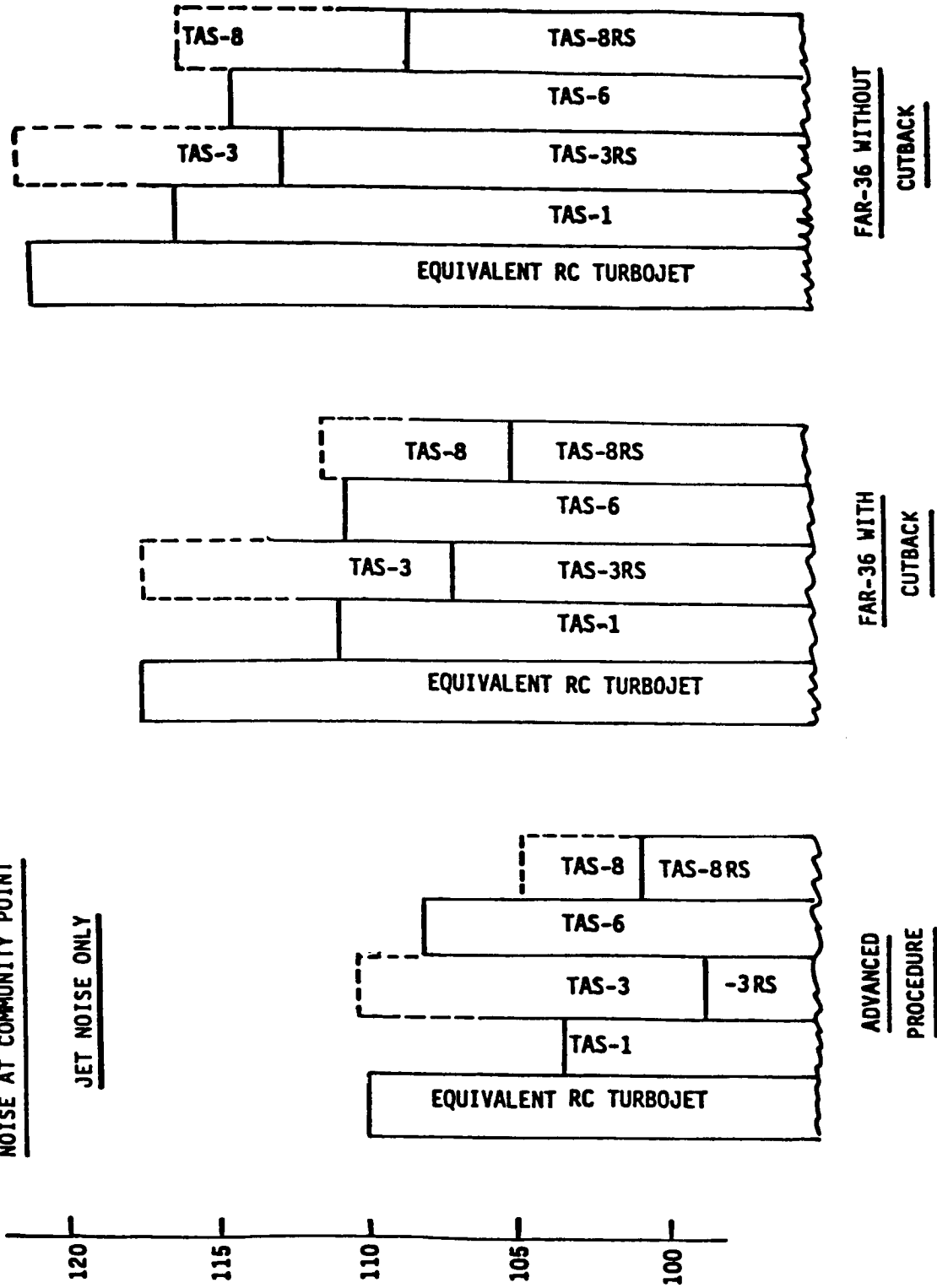


Figure 6.19. Jet Noise Levels of the Various Nozzles at the Community Point Location.



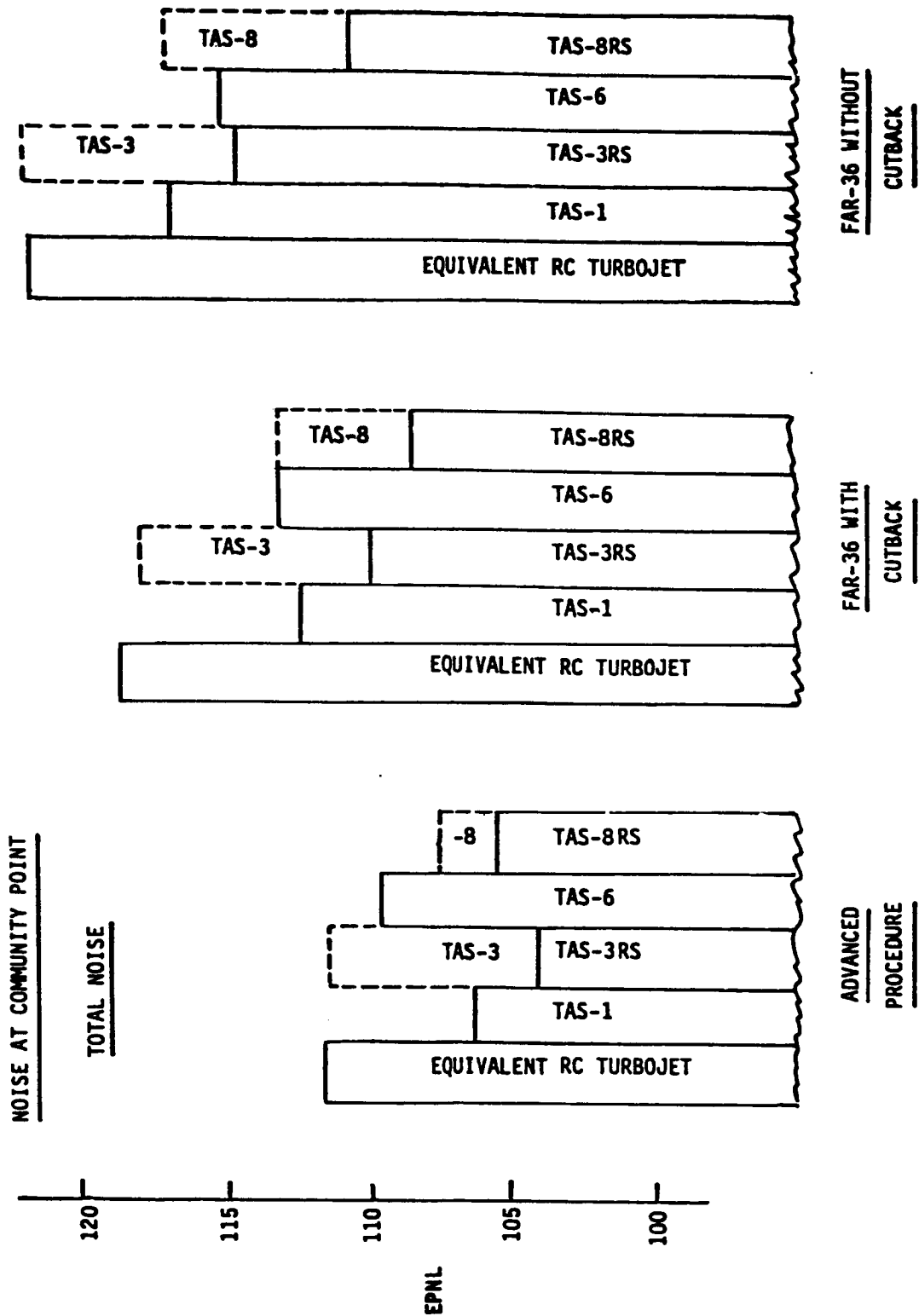
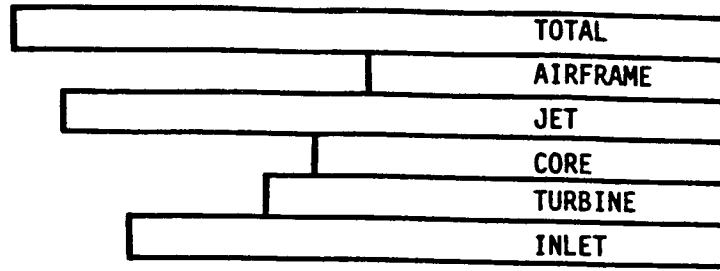


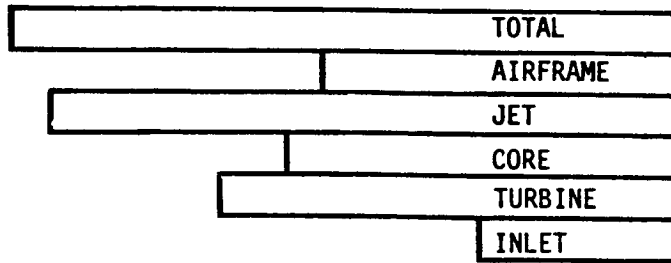
Figure 6.20. Total Noise Levels of the Various Nozzles at the Community Point Location.

**TYPICAL RELATIVE NOISE COMPONENT LEVELS**

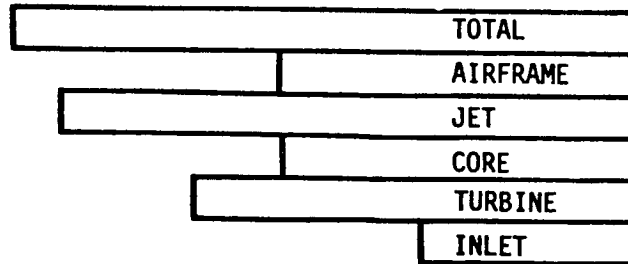
**TAS-8 RESCALED**



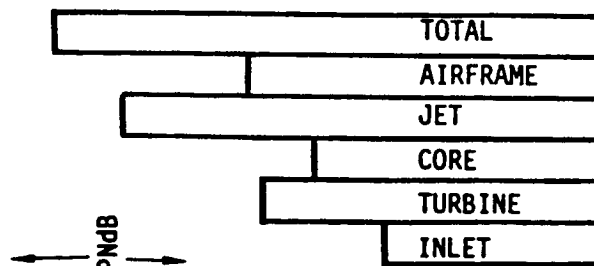
**APR TAKEOFF  
(MAX-POWER)**



**FAR-36  
(FULL-POWER)**



**FAR-36  
(CUTBACK)**



**ADVANCED PRECEDURE  
(CUTBACK)**

10 EPNdB

Figure 6.21. Typical Relative Noise Component Levels of TAS-8 Rescaled

In some cases the benefit of a suppression device derives from a change in spectrum shape and how this affects sideline propagation. In Figure 6.22 are shown a sideline distance attenuation comparison between the simple RC nozzle and the rescaled 32 chute suppressor with a TAS. Note that these calculations assume an omni-directional source (i.e., the community orientation TAS noise source). They do include the effects of EGA (Extra-ground-attenuation) and ground reflections as well as inverse square law and atmospheric attenuation.

## 6.5 CONCLUSIONS AND RECOMMENDATIONS

### A. Conclusions

The bleed type system implementation of a TAS, as evaluated in Reference 6.1, does not hold promise of being a significant noise control tool for an advanced SST. While improvements due to optimization of operating conditions and design are feasible, it is probable that these will not be substantial.

On the other hand when used in a configuration where the TAS is obtained from a separate source that does not detract from the main propulsion system it holds great promise. In fact it seems likely that it may be possible to meet subsonic airplane noise levels, when used with advanced operating procedures, with the device.

A substantial effort will be needed to implement an independent source TAS that does not impose excessive weight or drag penalties. However, while details of such a device have not been addressed here, such an implementation appears possible.

These analyses confirm the need to consider net installed system thrust when considering the acoustic benefit of noise suppression systems.

SIDELINE\* NOISE ATTENUATION CHARACTERISTICS  
 FAR-36 WITH CUTBACK  
 TOTAL NOISE

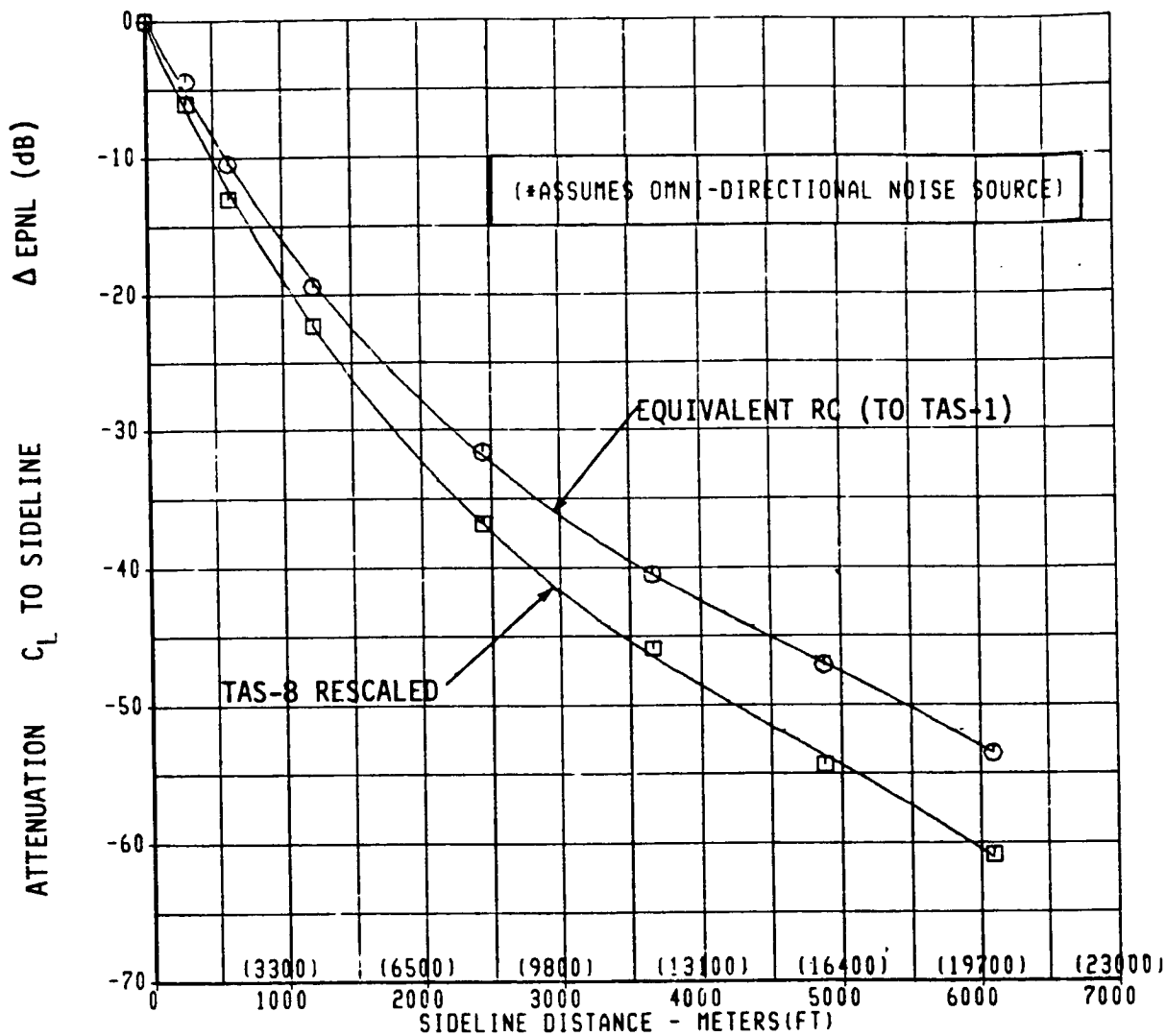


Figure 6.22. Sideline Noise Attenuation Characteristics.

## B. Recommendations

Studies should be initiated to derive practical implementations of Thermal Acoustic Shields from sources independent of the SST main propulsion system. The implementation should consider other uses of the source, such as auxiliary power unit use, which might enhance the efficiency of the main propulsion system. The studies should consider the effects on overall airplane performance and should also consider availability (or lack of) of competing suppression systems (e.g., the penalty might be significant but still less than that of the competing system).

The test programs underway should be continued in order to establish TAS characteristics of the dual flow systems.

### REFERENCES FOR SECTION 6.0

- 6.1 P.E. Johnson, G.W. Klees, "Acoustic Shield Design Study," Section 12, "Advanced Concept Studies for Supersonic Vehicles," NASA CR-165881, October 1981.
- 6.2 Society of Automotive Engineers, Inc., "Gas Turbine Jet Exhaust Noise Prediction," ARP 876A, September 1980.
- 6.3 J.D. Vachal, D. Cosley, "Operational Procedures for Reduced Noise Using the Flight Management System" Section 10, "Advanced Concept Studies for Supersonic Vehicles," NASA CR-159028, April 1979.
- 6.4 D. Gunnarson, "Inlet Technology - Variable Diameter Centerbody," Section 13, "Advanced Concept Studies for Supersonic Vehicles," NASA CR-159028, April 1979.
- 6.5 N. Pickup, R.A. Mangiarotty, J.V. O'Keefe, "Tests of a Thermal Acoustic Shield with a Supersonic Jet," AIAA 81-2021R, Journal of Aircraft, November 1982.

## 7.0 CONCLUSIONS AND RECOMMENDATIONS

The primary objective of this investigation was to develop a technology base for the thermal acoustic shield concept as a noise suppression device for nozzles employing a single core flow. To achieve the above objective, the following tasks were performed:

- Acoustic data for three hundred and fourteen (314) test points on nine (9) scale model nozzles were obtained. The effects of simulated flight and selected geometric and aerodynamic flow variables on the acoustic behavior of the thermal acoustic shield were determined through static and simulated flight model-scale acoustic tests.
- Laser velocimeter data in terms of mean and turbulent velocities for ten (10) plumes of four (4) scale model nozzles were obtained to aid in understanding of the underlying aerodynamic mechanisms of the jet plumes of the nozzles with thermal acoustic shields.
- Aerodynamic diagnostic data were obtained to determine the impact of the thermal acoustic shield on base drag of the 32 chute mechanical suppressor nozzle, the pressure field interactions between the core and the shield streams.
- An existing theoretical aeroacoustic prediction method (M\*G\*B model) was modified to predict the acoustic characteristics of partial thermal acoustic shields and selective data theory comparisons were performed.

The significant conclusions drawn from analyses of the measured acoustic data are as follows:

- For a given shield flow rate, a 180° partial thermal acoustic shield yields larger noise reductions than a full 360° shield for the 32 chute mechanical suppressor nozzle at all observer angles.

For the unsuppressed annular plug nozzle, the partial shield yields larger noise reductions than the full shield in the aft quadrant only.

- Shield thickness has a significant bearing on the noise reduction potential of a thermal acoustic shield; the larger the thickness, higher the noise suppression.
- A thermal acoustic shield yields larger PNL reductions for a mechanical suppressor nozzle than for an unsuppressed annular plug nozzle. Whereas the fluid shielding effect of a thermal acoustic shield is the dominant effect for the unsuppressed annular plug nozzle, both fluid shielding and source alteration effects are important for a mechanical suppressor nozzle.
- Noise suppression effectiveness of the thermal acoustic shield in terms of PNL reductions is dependent on the observer sideline distance. The 180° shield of 0.97" thickness has been shown to yield a maximum peak noise reduction of 8.0 dB in PNL at 1000 ft sideline distance, on a thrust and jet density normalized basis for the 32 chute suppressor nozzle at a core jet velocity 1850 fps, typical of cutback cycle under simulated flight conditions, and the same shield has been shown to yield a maximum of 3.5 dB reduction in PNL at 1000 ft sideline distance on a thrust and jet density normalized basis for the unsuppressed annular plug nozzle at a cutback cycle.
- The noise reduction potential of a thermal acoustic shield decreases as the core jet and corresponding shield jet velocities increase.
- The three (3) significant physical mechanisms of a thermal acoustic shield are:

- A. Mid and high frequency noise reduction at shallow angles to jet axis due to the total internal reflection of sound waves from the core jet;
- B. Mid and high frequency noise reduction in the front quadrant and at  $\theta_i = 90^\circ$  due to source strength reduction by the thermal acoustic shield; and,
- C. Low frequency noise amplification due to an elongation of the jet plume by the thermal acoustic shield.
- The overall benefit of the thermal acoustic shield in terms of PNL or EPNL reductions is determined by the relative dominance of the high and low frequency domains of a jet noise spectrum.
  - Partial thermal acoustic shields create azimuthally asymmetric acoustic fields for both chute suppressor and unsuppressed annular plug nozzles in the mid and high frequency ranges, whereas the low frequency noise is fairly axisymmetric in nature. The azimuthal asymmetry reduces at very high core jet velocities (viz.,  $V^J > 2200$  fps).
  - Within the domain of practical interest, the kinematic ratios, velocity ratio ( $V_r$ ), thermal acoustic shield velocity ratio ( $CV_r$ ) and static temperature ratio ( $T_r^S$ ) show some influence on the high frequency noise. Of the above three kinematic ratios, velocity ratio influences the high frequency noise most.
  - A thermal acoustic shield does not significantly reduce the PNL values of the unsuppressed annular plug nozzle with a convergent-divergent (C-D) flowpath for the supersonic core nozzle due to the high core jet velocities at which the C-D nozzle is operating. The axial stagger between shield and core jet exit planes does not have a noticeable influence on the acoustic behavior of the unsuppressed annular plug nozzles at high core jet velocities.



- For an unsuppressed annular plug nozzle with a partial thermal acoustic shield, the shield maintains its identity for about 1.5 nozzle equivalent diameters. However, it is shown to create azimuthally asymmetric mean and turbulent velocity fields up to ten (10) nozzle equivalent diameters.
- A partial thermal acoustic shield is observed to create higher levels of turbulence compared to a full thermal acoustic shield on a suppressor nozzle, indicating the different mixing and noise generation characteristics of a partial and a full thermal acoustic shield.
- The influence of simulated flight velocity for both the unsuppressed annular plug and the 32 chute suppressor nozzles with thermal acoustic shields is to streamline the flow, thereby reducing the mean velocity decay and the turbulence levels.
- Though the partial thermal acoustic shield exhibited loss of total pressure at the shield extremities, on an area weighted basis, the total pressure loss compared to the facility measurement is less than 1.5%. The loss of total pressure for the full thermal acoustic shield is less than 1%.
- The static pressure measurements and predictions in the vicinity of the shield exit plane showed a pressure rise in the presence of a supersonic core jet due to a static pressure feedback. The adverse influence of this static pressure rise on shield flow discharge can be avoided by utilizing staggered shield and core jet exit planes.
- The thermal acoustic shields reduce ventilation of the chutes of the 32 chute mechanical suppressor nozzle and thereby increase the chute base drag. However, the relative increase in chute base drag due to the shields for simulated flight cases is smaller than the static case since the suppressor nozzle with or without thermal acoustic shields suffers reduced ventilation in the presence of a simulated flight velocity.

- The M\*G\*B model, modified to predict the azimuthally asymmetric acoustic characteristics of nozzles with partial thermal acoustic shields, predicts significant asymmetry for both acoustic and flow field characteristics for an unsuppressed annular plug nozzle with partial thermal acoustic shield. Selective data theory comparisons indicate that the predictions and experimental data show good spectral agreement in the front quadrant and in the aft quadrant they show similar spectral trends.

This investigation has resulted in a strong technology base for the thermal acoustic shield concept as a noise suppression device for nozzles employing single core flow. Some recommendations for future work which will broaden the scope of the technology base and improve the understanding of the physical mechanisms of a thermal acoustic shield concept are suggested below:

- An acoustic evaluation of the thermal acoustic shield concept for nozzles employing dual flows.
- Acoustic power level calculations of nozzles with partial thermal acoustic shields will answer the question whether partial shields yield any power level reductions or simply redirect sound energy. To determine acoustic power of azimuthally asymmetric sound fields due to partial thermal acoustic shields, acoustic measurements need to be made at various azimuthal locations and suitably numerically integrated.

## 8.0 REFERENCES

### REFERENCES FOR SECTION 2.0

- 2.1 Vdoviak, J.W., Knott, P.R. and Ebacker, J.J., "Aerodynamic/Acoustic Performance of YJ101/Double Bypass VCE with Coannular Plug Nozzle", NASA CR-159869, January 1981.
- 2.2 Fitzsimmons, R.D., McKinnon, R.A., Johnson, E.S. and Brooks, J.R., "Flight and Wind Tunnel Test Results of a Mechanical Jet Noise Suppressor Nozzle", AIAA Paper Number 80-0165, January 1980.
- 2.3 Stringas, E.J., Clapper, W.S., Brausch, J.F., et al, "High Velocity Jet Noise Source Location and Reduction, Task 3 - Experimental Investigation of Suppression Principles, Volume II - Parametric Testing and Source Measurements", General Electric Company Contractor Final Report Number FAA-RD-76-79, . III-II, December 1978.
- 2.4 Knott, P.R., Janardan, B.A. and Majjigi, R.K., "Free-Jet Investigation of Mechanically Suppressed, High-Radius-Ratio Coannular Plug Model Nozzles", Final Report Draft for Contract NAS3-21608, October 1981.
- 2.5 Vijayaraghavan, A. and Parthasarathy, S.P., "Noise Shielding by a Hot Subsonic Jet", AIAA Paper Number 81-2018, October 1981.
- 2.6 Ahuja, K.K. and Dosanjh, D.S., "Heated Fluid Shroud as an Acoustic Shield for Noise Reduction - An Experimental Study", AIAA Paper Number 77-1286, October 1977.
- 2.7 Goodykoontz, J., "Effect of a Semi-Annular Thermal Acoustic Shield on Jet Exhaust Noise", NASA TM 81615, Prepared for the One-Hundredth Meeting of the Acoustical Society of America, November 1980.
- 2.8 Pickup, N., Mangiarotty, R.A. and O'Keefe, J.V., "Tests of a Thermal Acoustic Shield with a Supersonic Jet", AIAA Paper Number 81-2021, October 1981.

- 2.9 Majjigi, R.K., Janardan, B.A., Brausch, J.F., Hoerst, D.J., Price, A.O., and Knott, P.R., "Free-Jet Feasibility Study of a Thermal Acoustic Shield Concept for AST/VCE Application - Single Flow," General Electric Technical Information Series Report Number R82AEB493, Vol. I, also, NASA CR-168302, July 1983.
- 2.10 Majjigi, R.K., Janardan, B.A., Brausch, J.F., Hoerst, D.J., Price, A.O., and Knott, P.R. "Free-Jet Feasibility Study of a Thermal Acoustic Shield Concept for AST/VCE Application - Single Flow," General Electric Technical Information Series Report Number R82AEB493, Vol. II, also, NASA CR-168303, July 1983.

#### REFERENCES FOR SECTION 3.0

- 3.1 Brausch, J.F., Majjigi, R.K. and Bediako, E.D., "Model Hardware Design Report for a Thermal Acoustic Shield Concept for AST/VCE Application - Single Stream Nozzle Designs", General Electric Technical Information Series Report Number R891AEG575, July 1981.
- 3.2 Yamamoto, K., et al., "Experimental Investigation of Shock-Cell Noise Reduction for Single Stream Nozzles in Simulated Flight," General Electric Technical Information Series Report No. R82AEB492, September 1983.
- 3.3 Vdoviak, J.W., Knott, P.R. and Ebacker, J.J., "Aerodynamic/Acoustic Performance of YJ101/Double Bypass VCE with Coannular Plug Nozzle", NASA CR-159869, January 1981.
- 3.4 Majjigi, R.K., Janardan, B.A., Brausch, J.F., Hoerst, D.J., Price, A.O. and Knott, P.R., "Freejet Feasibility Study of a Thermal Acoustic Shield Concept for AST/VCE Application - Single Flow", General Electric Technical Information Series Report Number R82AEB493, Vol. I., also: NASA CR-168302, July 1983.
- 3.5 Majjigi, R.K., Janardan, B.A., Brausch, J.F., Hoerst, D.J., Price, A.O., and Knott, P.R., "Free-Jet Feasibility Study of a Thermal Acoustic Shield Concept for AST/VCE Application - Single Flow," General Electric Technical Information Series Report Number R82AEB493, Vol. II, also, NASA CR-168303, July 1983.

REFERENCES FOR SECTION 4.0

- 4.1 "Federal Aviation Regulations", Volume III, Part 36, Noise Standards: Aircraft Type Certification, Published by the Department of Transportation, Federal Aviation Administration, December 1969.
- 4.2 Shields, F.D. and Bass, H.E., "Atmospheric Absorption of High Frequency Noise and Application to Fractional Octave Bands", NASA CR-2760, June 1977.
- 4.3 Knott, P.R., Janardan, B.A. and Majjigi, R.K., "Free-Jet Investigation of Mechanically Suppressed High-Radius-Ratio Coannular Plug Model Nozzles", Final Report Draft, NAS3-21608, October 1981.
- 4.4 Majjigi, R.K., "A Unique Spectral Acoustic Prediction Method for Jet and Shock Cell Noise of Mechanical Suppressor Nozzles", General Electric Technical Information Series Report Number R81AEG363, May 1981.
- 4.5 Keith, J.S., Ferguson, D.R., Merkle, C.L., Heck, P.H. and Lahti, D.J., "Analytical Method for Predicting the Pressure Distribution About a Nacelle at Transonic Speeds", NASA CR-2217, July 1973.

REFERENCES FOR SECTION 5.0

- 5.1 Mani, R., Gliebe, P.R., Balsa, T.F., Stringas, E.J., et al, "High Velocity Jet Noise Source Location and Reduction, Task II - Theoretical Developments and Basic Experiments", General Electric Company Contractor Final Report Numbr FAA-RD-76-79, II, 1976.
- 5.2 Lilley, G.M., Plumblee, H.E., Strahle, W.C., Ruo, S.Y., Doak, P.E., "Theory of Turbulence Generated Noise, Noise Radiation from Upstream Sources and Combustion Noise", Volume IV. The Generation and Radiation of Supersonic Jet Noise, AFAPL-TR-72-53, 1972.

- 5.3 Mani, R., "A Moving Source Problem Relevant to Jet Noise", J. Sound and Vibration, 25, Page 337, 1972.
- 5.4 Tester, B.J. and Morfey, C.L., "Developments in Jet Noise Modeling, Theoretical Predictions and Comparisons with Measured Data", J. of Sound and Vibration, 46, Page 79, 1976.
- 5.5 Mani, R., "The Influence of Jet Flow on Jet Noise, Parts 1 and 2", J. Fluid Mech., 73, Page 753, 1976.
- 5.6 Balsa, T.F., "The Acoustic Field of Sources in Shear Flow with Application to Jet Noise: Convective Amplification", J. Fluid Mech., 79, Page 33, 1977.
- 5.7 Goldstein, M.E., "High Frequency Sound Emission from Moving Point Multi-pole Sources Embedded in Arbitrary Transversely Sheared Mean Flows", J. Sound and Vibration, 80, page 499, 1982.
- 5.8 Jones, D.S. and Morgan, J.D., "The Instability of a Vortex Sheet on a Subsonic Stream Under Acoustic Radiation", Proc. Camb. Phil. Soc., 72, Page 465, 1972.
- 5.9 Lighthill, M.J., "On Sound Generated Aerodynamically", Proc. Roy. Soc., 211A, Page 564, 1952.
- 5.10 Carrier, G.F., Krook, M., Pearson, C.E., Functions of a Complex Variable, McGraw-Hill, 1966.
- 5.11 Morse, P.M. and Ingard, U.K., Theoretical Acoustics, McGraw-Hill, 1968.
- 5.12 Avila, G.S. and Keller, J.B., "The High-Frequency Asymptotic Field of a Point Source in an Inhomogeneous Medium", Comm. Pure and Appl. Math., 16, Page 363, 1963.

REFERENCES FOR SECTION 6.0

- 6.1 P.E. Johnson, G.W. Klees, "Acoustic Shield Design Study," Section 12, "Advanced Concept Studies for Supersonic Vehicles," NASA CR-165881, October 1981.
- 6.2 Society of Automotive Engineers, Inc., "Gas Turbine Jet Exhaust Noise Prediction," ARP 876A, September 1980.
- 6.3 J.D. Vachal, D. Cosley, "Operational Procedures for Reduced Noise Using the Flight Management System," Section 10, "Advanced Concept Studies for Supersonic Vehicles," NASA CR-159028, April 1979.
- 6.4 D. Gunnarson, "Inlet Technology - Variable Diameter Centerbody," Section 13, "Advanced Concept Studies for Supersonic Vehicles," NASA CR-159028, April 1979.
- 6.5 N. Pickup, R.A. Mangiarotty, J.V. O'Keefe, "Tests of a Thermal Acoustic Shield with a Supersonic Jet," AIAA 81-2021R, Journal of Aircraft, November 1982.

## 9.0 NOMENCLATURE

A	Area, in <sup>2</sup>
AST	Advanced Supersonic Transport
c	Sonic Speed, fps
C <sub>D</sub>	Discharge Coefficient
C-D	Convergent - Divergent
CFG	Thrust Coefficient, defined as (actual thrust/ideal gross thrust)
AC <sub>FGS</sub>	% Thrust Loss Coefficient due to Chute Base Drag
CV <sub>r</sub>	Thermal Acoustic Shield Velocity Ratio, defined as $(C^{SJ} + V^{SJ}) / (C^J + V^J)$
D	Diameter, inch
F	Thrust, lbs
ΔF <sub>Throttling</sub>	Thrust Loss Coefficient Due to Throttling
g	Gravitational constant, ft/sec <sup>2</sup>
h	Annular passage height, inch
LBM	Shock Strength Parameter, defined as $10 \log \sqrt{M_j^2 - 1}$
LV	Laser velocimeter
LVM	Velocity normalization factor, defined as $10 \log (V/c_{amb})$
M	Mach number
M*G*B	Mani*Gliebe*Balsa Theoretical Model
N	Number of Chutes
NF	Thrust and jet density normalization factor defined as $-10 \log \left[ \frac{F}{F_{ref}} \left( \frac{\rho_j}{\rho_{amb}} \right)^{\omega-1} \right], \text{ dB}$
P	Pressure, psi
PNL	Perceived Noise Level, dB
PNLN	Normalized Perceived Noise Level, defined as PNL+NF, dB
R	Radius, inch
RH	Relative Humidity
R <sub>r</sub>	Radius Ratio



S	Slant Distance along the plug surface
SPL	Sound Pressure Level, dB
S.T.C.	Stream Tube Curvature Program
T	Temperature, °R
TAS	Thermal Acoustic Shield
$T_r^s$	Ratio of Shield to Core Jet Static Temperature
V	Velocity, fps
VCE	Variable Cycle Engine
W	Weight flow rate, lbs/sec
X	Axial Distance from the Shield Exit Plane, inch

#### GREEK SYMBOLS

$\alpha$	Air Attenuation Factor, dB/ft
$\beta$	Shield bypass ratio, defined as $\dot{w}^{sj}/(\dot{w}^j + \dot{w}^{sj})$
$\gamma$	Specific Heat Ratio
$\delta$	Ratio of ambient pressure to ISA pressure ( $P_{amb}/P_{std}$ )
$\theta$	Model Hardware Flow Path Angle; also Angle of Observer Relative to Jet Axis, Degree
$\theta_i$	Angle of Observer Relative to Inlet Axis, Degree
$\Delta$	Difference
$\psi$	Stream Function
$\phi$	Velocity Potential Function; also Azimuthal Angle, Degree
$\zeta$	Pseudo Velocity Potential Function for Rotational Flows
$\omega$	Jet density exponent

#### SUPERSCRIPTS

e	Effective
Facility	Refers to Test Facility Measurement Station
h	Hub
j	Core Jet Condition
mix	Mass Averaged Condition
Rake	Refers to Total Pressure Rake at Shield Exit Plane
sj	Shield Jet Condition
T	Total
t	Tip

TAS	Thermal Acoustic Shield
th	Throat
	Average Quantity

SUBSCRIPTS

a/c	Aircraft
amb	Ambient Condition
D, d	Drag
e	Exit
eq	Equivalent
i	Inner
o	Outer
r	Ratio
s	Static Condition, Suppressor
T	Total Condition
TAS	Thermal Acoustic Shield
th	Throat

APPENDIX A-I

This appendix contains the acoustic test matrices of configurations TAS-1 thru TAS-9 in SI units.



TABLE A-II. TEST MATRIX FOR CONFIGURATION TAS-2 SIMULATING ENGINE OPERATING LINE IN SIDELINE, COMMUNITY, AND OPPOSITE COMMUNITY ORIENTATIONS.

\*\*\*\*\* S.I. UNITS \*\*\*\*\*

NOZZLE - MODEL TAS2 AREA [MODEL SIZE - INNER = 0.0163 OUTER = 0.0056 FULL SIZE - TOTAL = 0.0031] sq m

TEST POINT	V ac	s_j V	s_j T	s_j T	s_j P	s_j W	s_j W	s_j F	s_j V	J T	J T	J T	J P	J W	J W	J F	J V	mix T	mix T	mix P	mix W	T F	s_j V/V
	m/s	m/s	O K	O K	O K	kg/s	kg/s	N	m/s	O K	O K	O K	N	m/s	O K	O K	N	kg/s	kg/s	kg/s	kg/s	N	
205	0	341.7	839.4	787.3	1.2841	35.2	750	573	1.843	3.693	2.2	1.113	195.0	6984	537.8	462.3	711.2	1.9156	230	7735	0.60		
206	122	345.0	856.1	803.4	1.2841	34.8	750	573	0.855	8.706	4.2	2.0846	191.0	6841	537.9	469.6	724.9	1.8950	226	7591	0.60		
207	0	380.4	886.7	822.6	1.3431	37.4	889	631.8	882.3	700.3	2.4174	218.0	8606	594.9	484.4	722.6	2.1613	255	9496	0.60			
208	122	380.7	893.9	830.1	1.3407	37.1	884	633.0	890.3	707.9	2.4046	215.9	8541	595.9	488.7	730.2	2.1510	253	9425	0.60			
209	0	418.2	923.9	846.9	1.4113	39.9	1043	673.3	905.3	698.4	2.6927	239.0	10056	636.8	498.1	724.2	2.23857	279	11099	0.62			
210	122	408.4	921.1	847.7	1.3891	38.7	988	682.7	925.1	713.3	2.7097	236.7	10099	644.1	507.2	737.2	2.23957	275	11088	0.60			
211	0	434.3	944.4	861.8	1.4391	40.7	1104	708.4	936.7	708.4	2.9145	254.1	11250	670.5	514.5	734.7	2.25634	295	12355	0.61			
212	122	428.5	950.6	870.4	1.4216	39.9	1068	717.2	960.2	727.4	2.9116	251.2	11259	677.6	526.1	752.4	2.25886	291	12328	0.60			
213	0	471.2	948.3	851.1	1.5381	44.8	1318	749.7	954.3	697.8	3.3036	285.3	13365	711.9	525.2	726.5	2.28918	330	14713	0.60			
214	122	454.2	968.3	878.3	1.4761	41.9	1189	752.0	955.8	697.7	3.3246	287.8	13524	714.1	525.2	726.5	2.28918	330	14683	0.63			
215	0	475.5	953.3	854.4	1.5467	45.0	1335	788.0	958.0	672.6	3.8220	329.2	16213	750.5	525.3	700.7	3.2974	374	17548	0.60			
216	122	477.0	962.8	863.5	1.5444	44.7	1333	787.5	973.3	681.7	3.8699	331.1	16505	759.4	533.3	709.7	3.3355	376	17638	0.60			
221	0	377.7	847.2	796.7	1.2735	34.5	727	552.4	826.2	688.5	2.0200	189.1	6529	519.3	456.0	708.4	1.8435	224	7257	0.61			
222	122	343.8	841.1	788.4	1.2876	35.3	758	566.8	825.7	678.2	2.1102	197.1	6981	532.9	454.3	698.4	1.9153	232	7739	0.61			
223	0	370.0	862.2	801.4	1.3325	37.4	865	617.1	852.2	677.4	2.3902	219.6	8471	581.2	468.4	699.6	2.1387	257	9337	0.60			
224	122	376.7	879.4	816.8	1.3384	37.3	879	630.7	883.4	702.2	2.4058	216.9	8547	593.4	484.4	723.3	2.1516	254	9426	0.60			
225	0	395.9	877.8	808.1	1.3831	39.7	981	664.9	880.6	677.7	2.7028	244.0	10138	627.3	482.9	700.7	2.3894	284	11120	0.60			
226	122	399.3	896.7	826.3	1.3807	39.1	976	668.1	889.6	685.1	2.7003	242.4	10124	630.8	488.6	709.6	2.3872	282	11101	0.60			
227	0	425.8	938.3	859.0	1.4216	40.3	1072	706.3	936.9	710.1	2.8925	253.7	11201	667.8	514.1	735.7	2.5435	294	12274	0.60			
228	122	420.3	920.0	842.5	1.4184	40.4	1061	699.8	920.5	696.9	2.8917	255.1	11156	661.6	505.0	722.1	2.5424	295	12217	0.60			
229	0	445.6	944.4	857.5	1.4682	42.2	1175	748.6	950.0	693.9	3.3123	288.3	13492	709.9	520.8	720.8	2.8810	331	14668	0.60			
230	122	444.4	931.1	844.7	1.4733	42.6	1183	737.9	926.5	676.4	3.2982	290.0	13374	700.3	508.7	703.7	2.8705	333	14557	0.60			
231	0	469.4	946.1	849.5	1.5340	44.7	1311	777.7	935.5	656.1	3.8113	333.1	16192	741.2	514.0	685.1	3.2868	378	17504	0.60			
232	122	467.0	931.7	835.8	1.5376	45.3	1320	780.0	942.6	662.1	3.7992	331.0	16135	742.3	516.4	689.2	3.2778	376	17456	0.60			
287	0	335.9	847.2	796.9	1.2701	34.4	722	569.0	842.9	695.0	2.0873	194.3	6911	533.9	462.8	714.0	1.8952	229	7633	0.59			
288	122	376.8	842.2	791.8	1.2737	34.7	730	563.0	842.6	697.9	2.0524	191.3	6724	528.2	462.3	715.9	1.8686	226	7455	0.60			
289	0	376.4	887.8	825.6	1.3338	37.2	874	629.2	881.3	700.8	2.4005	218.1	8582	592.4	484.1	723.3	2.1469	255	9457	0.60			
290	122	375.2	882.8	820.7	1.3339	37.3	875	629.0	880.7	700.2	2.4007	218.5	8587	592.0	483.4	722.2	2.1471	256	9462	0.60			
291	0	411.5	922.2	848.2	1.3956	39.6	1018	678.4	915.8	706.3	2.7022	240.8	10210	640.7	503.0	731.1	2.3908	280	11228	0.61			
292	122	408.1	916.7	843.8	1.3904	39.5	1006	664.1	920.6	720.6	2.5624	227.9	9457	626.2	504.7	743.3	2.2812	267	10464	0.61			
293	0	423.1	952.2	874.3	1.4075	39.5	1044	713.0	949.8	719.2	2.9101	254.3	11333	674.1	521.3	745.6	2.5554	294	12378	0.59			
294	122	424.9	944.4	865.7	1.4159	40.1	1063	712.8	950.3	719.8	2.9065	254.1	11319	673.6	520.9	745.1	2.5537	294	12383	0.60			
295	0	449.0	955.0	866.8	1.4706	42.2	1185	751.7	955.4	697.5	3.3233	289.5	13603	713.1	524.1	725.0	2.8900	332	14788	0.60			
296	122	452.0	951.7	862.6	1.4807	42.8	1207	752.4	953.7	695.2	3.3404	291.3	13700	713.9	523.1	722.5	2.9050	334	14908	0.60			
297	0	474.0	962.8	864.5	1.5354	44.7	1324	792.8	962.9	674.1	3.8654	335.3	16615	755.3	528.2	702.9	3.3305	380	17940	0.60			
298	122	475.2	961.7	862.9	1.5396	44.7	1335	796.2	971.7	680.9	3.8662	333.6	16602	756.1	532.5	709.0	3.3271	379	17938	0.60			

Sideline  
 Community  
 Opposite  
 Community

TABLE A-II. (CONT'D) TEST MATRIX FOR CONFIGURATION TAS-2 SIMULATING ENGINE OPERATING LINE IN SIDELINE, COMMUNITY, AND OPPOSITE COMMUNITY ORIENTATIONS.

TEST POINT	T amb DISC K Pascal	P amb Pascal	RH %	NF dB	LVM LEM	PWL (FULL SIZE 731 m SIDE LINE) ANGLE RELATIVE TO INLET DEGREES	dB				s <sub>j</sub> j T <sub>S</sub> /T <sub>S</sub> CV / CV	s <sub>j</sub> j W / W	TEST CONFIG				
							50	60	70	120							
205	270.9	100091.	36	-3.3	2.12	-10.00	86.5	87.9	91.2	93.5	98.9	101.2	101.1	0.93	0.82	0.15	SL
206	273.8	100078.	82	-3.2	2.10	-10.00	87.8	88.4	91.0	91.7	94.6	96.3	95.5	0.94	0.82	0.15	SL
207	270.8	100064.	36	-4.0	2.56	-3.34	91.0	92.9	95.9	97.7	103.3	106.5	106.4	0.93	0.82	0.15	SL
208	274.2	100112.	82	-3.9	2.54	-3.42	93.1	93.8	96.4	96.1	99.0	101.2	101.8	0.93	0.82	0.15	SL
209	271.5	99832.	36	-4.6	2.85	-2.03	92.2	94.2	98.1	99.7	105.0	109.4	107.4	0.94	0.83	0.14	SL
210	272.4	99388.	86	-4.6	2.89	-2.00	95.5	97.0	99.8	98.7	102.3	105.2	106.2	0.92	0.81	0.14	SL
211	271.3	99856.	36	-5.1	3.08	-1.41	93.3	95.5	99.5	101.2	106.7	111.9	108.9	0.92	0.82	0.14	SL
212	274.2	100102.	82	-5.0	3.10	-1.43	97.8	99.0	101.6	101.1	103.8	108.0	107.6	0.91	0.81	0.14	SL
213	271.2	99856.	36	-5.9	3.34	-0.64	97.0	98.9	102.7	104.1	109.0	114.9	110.5	0.89	0.82	0.14	SL
214	275.1	100182.	82	-5.9	3.32	-0.64	102.4	102.9	105.9	104.8	106.3	111.0	110.6	0.92	0.81	0.13	SL
215	270.3	99812.	34	-6.8	3.57	-0.01	99.9	102.0	105.9	107.3	111.5	117.8	112.6	0.89	0.81	0.12	SL
216	276.9	99987.	82	-6.9	3.57	0.03	105.7	106.5	108.9	108.4	109.7	114.8	112.5	0.89	0.80	0.12	SL
221	269.5	100502.	88	-3.1	1.98	-10.00	85.5	87.5	89.0	90.5	97.9	101.2	100.8	0.96	0.83	0.15	CC
222	270.7	100088.	49	-3.4	2.08	-10.00	86.2	88.0	89.0	87.9	93.5	95.4	95.1	0.95	0.83	0.15	CC
223	270.7	100139.	74	-4.0	2.46	-3.54	90.0	92.5	93.6	93.8	101.2	106.2	107.7	0.94	0.82	0.15	CC
224	271.5	100102.	49	-3.9	2.54	-3.42	91.6	93.4	93.9	93.8	98.0	101.1	101.4	0.92	0.81	0.15	CC
225	271.2	100071.	74	-4.8	2.79	-2.03	92.1	94.9	96.4	99.0	104.4	109.7	106.8	0.92	0.81	0.14	CC
226	270.8	100075.	49	-4.7	2.81	-2.04	95.5	97.1	97.5	98.0	100.8	104.8	105.8	0.93	0.81	0.14	CC
227	270.7	100479.	74	-5.0	3.06	-1.48	93.1	95.8	97.7	100.6	106.8	112.1	109.7	0.92	0.81	0.14	CC
228	270.9	100195.	74	-5.1	3.02	-1.48	97.2	99.2	99.6	100.6	102.6	107.4	107.9	0.92	0.81	0.14	CC
229	270.9	100481.	74	-5.9	3.33	-0.67	97.0	99.6	101.3	104.2	109.1	114.6	109.4	0.90	0.80	0.13	CC
230	271.1	100112.	74	-5.9	3.27	-0.68	101.2	103.0	103.5	103.7	105.8	111.0	110.6	0.91	0.81	0.13	CC
231	271.2	100031.	74	-6.9	3.51	-0.03	99.5	102.6	104.4	107.3	111.4	117.3	112.5	0.91	0.81	0.12	CC
232	271.3	100102.	74	-6.8	3.52	-0.04	104.7	106.7	107.7	107.9	109.9	114.5	112.1	0.89	0.80	0.12	CC
287	265.5	100870.	52	-3.1	2.13	-10.00	86.2	89.1	91.9	94.9	100.2	102.0	102.1	0.95	0.82	0.15	CC
288	265.7	100870.	52	-3.0	2.09	-10.00	88.2	89.7	92.1	93.0	95.5	97.3	95.5	0.94	0.82	0.15	CC
289	265.5	100843.	52	-3.9	2.59	-3.47	90.9	93.8	96.9	98.6	103.4	106.7	109.1	0.94	0.82	0.15	CC
290	267.3	100877.	52	-3.9	2.57	-3.47	94.3	95.8	97.7	97.7	100.3	102.2	101.7	0.93	0.81	0.15	CC
291	265.7	100857.	52	-4.6	2.92	-2.02	92.8	95.9	99.1	101.0	105.4	109.8	109.8	0.93	0.82	0.14	CC
292	268.5	100919.	52	-4.2	2.80	-2.53	96.7	98.6	101.0	100.7	103.2	106.3	105.8	0.92	0.82	0.14	CC
293	264.2	100822.	52	-4.9	3.15	-1.45	94.0	97.2	100.6	102.5	106.8	112.4	111.1	0.92	0.81	0.13	CC
294	264.5	100870.	52	-4.9	3.12	-1.45	99.0	100.5	102.4	102.4	104.9	108.4	108.0	0.91	0.81	0.14	CC
295	264.5	100822.	52	-5.8	3.40	-0.65	98.0	100.8	103.7	105.6	109.6	115.4	112.1	0.91	0.81	0.13	CC
296	266.5	100843.	52	-5.9	3.39	-0.62	102.8	105.3	106.9	106.1	107.8	112.2	110.3	0.90	0.81	0.13	CC
297	264.9	100801.	52	-6.8	3.65	0.03	101.0	103.8	106.9	108.5	111.8	117.8	112.3	0.90	0.80	0.12	CC
298	265.8	100905.	52	-6.7	3.65	0.02	106.3	108.5	110.4	109.4	110.4	115.0	112.1	0.89	0.80	0.12	CC

Sideline

Community

Opposite Community











TABLE A-V. TEST MATRIX FOR CONFIGURATION TAS-3 SIMULATING ENGINE OPERATING LINE IN SIDELINE AND COMMUNITY ORIENTATIONS.

\*\*\*\*\* S.I UNITS \*\*\*\*\*

NOZZLE - MODEL TAS3 AREA [MODEL SIZE - INNER = 0.0163 , OUTER = 0.0117 ; FULL SIZE - TOTAL = 0.9031] sq m

TEST POINT	V ac	sj T	sj T	sj P	sj P	sj W	sj W	sj F	sj F	J T	J T	J P	J P	J R	J W	J W	J F	J F	mix V	mix V	mix T	mix T	mix P	mix P	mix R	.T W	.T W	T F	sj J V/V
	m/s	kg/s	kg/s	kg/s	kg/s	kg/s	kg/s	kg/s	kg/s	N	N	kg/s	kg/s	kg/s	kg/s	kg/s	kg/s	kg/s	m/s	m/s	m/s	m/s	m/s	m/s	m/s	kg/s	kg/s	kg/s	kg/s
301	0.	250.5	713.9	685.2	1.1692	48.7	762	415.4	711.3	631.0	1.5658	121.7	3160	368.3	390.7	649.3	1.4153	3160	368.3	390.7	649.3	1.4153	170.	3923	0.60	N			
302	122.	240.2	687.8	661.2	1.1606	48.4	726	401.2	707.5	632.6	1.5204	117.3	2941	354.2	385.0	643.6	1.3841	2941	354.2	385.0	643.6	1.3841	166	3667	0.60	N			
303	0	303.6	826.1	784.8	1.2206	51.5	977	519.8	814.2	690.7	1.8722	139.2	4522	461.4	448.5	720.8	1.6207	4522	461.4	448.5	720.8	1.6207	191.	5499	0.58	N			
304	122.	302.4	800.6	759.3	1.2268	53.0	1002	516.2	802.2	680.0	1.8737	140.3	4527	457.6	439.9	706.4	1.6233	4527	457.6	439.9	706.4	1.6233	193	5530	0.59	N			
305	0	343.5	851.1	798.6	1.2831	57.4	1231	566.1	849.0	702.9	2.0580	149.9	5302	504.5	466.1	734.6	1.7521	5302	504.5	466.1	734.6	1.7521	207	6534	0.61	N			
306	122	334.7	831.1	781.2	1.2740	57.2	1195	560.3	831.6	687.9	2.0584	151.6	5307	498.5	456.2	718.7	1.7499	5307	498.5	456.2	718.7	1.7499	209	6503	0.60	N			
307	0.	383.7	907.2	842.4	1.3410	60.6	1454	629.9	889.1	708.6	2.3848	169.2	6662	565.0	490.4	750.3	1.9703	6662	565.0	490.4	750.3	1.9703	230	8117	0.61	N			
308	122	379.2	887.2	823.7	1.3404	61.4	1454	631.9	892.3	710.7	2.3912	169.6	6697	564.8	488.8	747.3	1.9742	6697	564.8	488.8	747.3	1.9742	231.	8152	0.60	N			
309	0	408.4	920.6	847.6	1.3896	64.1	1638	679.6	921.4	711.4	2.6937	187.6	7965	610.5	505.4	753.8	2.1767	7965	610.5	505.4	753.8	2.1767	252	9603	0.60	N			
310	122.	411.5	925.6	851.6	1.3941	64.4	1655	683.1	933.2	721.7	2.6854	185.8	7931	613.2	511.0	762.7	2.1728	7931	613.2	511.0	762.7	2.1728	250	9586	0.60	N			
311	0.	429.8	960.0	879.8	1.4187	65.0	1745	711.5	950.8	721.3	2.8905	198.0	8803	641.8	522.9	768.8	2.3087	8803	641.8	522.9	768.8	2.3087	263	10549	0.60	N			
312	122.	429.5	960.0	879.6	1.4185	65.1	1748	712.8	954.3	724.1	2.8907	198.0	8821	642.7	524.3	770.9	2.3088	8821	642.7	524.3	770.9	2.3088	263	10570	0.60	N			
313	0.	450.5	966.7	878.5	1.4675	68.3	1922	752.5	958.9	700.7	3.3154	226.0	10627	682.4	527.1	751.3	2.5925	10627	682.4	527.1	751.3	2.5925	294	12550	0.60	N			
314	122	452.9	965.6	876.2	1.4744	68.8	1947	753.9	962.2	703.2	3.3161	225.8	10637	683.5	528.3	753.0	2.5949	10637	683.5	528.3	753.0	2.5949	295	12584	0.60	N			
315	0	476.4	960.6	861.3	1.5442	73.6	2191	790.1	962.9	676.3	3.8222	259.9	12836	720.9	528.0	727.2	2.9410	12836	720.9	528.0	727.2	2.9410	334	15028	0.60	N			
316	122	478.2	961.1	861.2	1.5489	74.0	2211	790.9	964.2	677.1	3.8257	260.4	12872	721.7	528.6	727.8	2.9445	12872	721.7	528.6	727.8	2.9445	334	15083	0.60	N			

TEST POINT	T amb DEG	P amb K Pascal	RH %	NF db	LVM	LBM	PML ANGLE RELATIVE TO INLET DEGREES	731 m SIDE LINE) db	70	90	120	130	140	sj J TsA1s CV /CV	sj J W /W	sj T TEST CONFIG
301	269.8	101098.	65	-4.1	0.49	-10.00	76.0	78.2	81.9	84.6	89.2	90.0	85.3	0.96	0.84	SL
302	271.2	101098	67	-4.2	0.31	-10.00	75.7	77.4	80.7	79.5	82.5	82.3	78.8	0.93	0.83	SL
303	270.3	101091.	65	-2.9	1.46	-10.00	81.2	83.0	86.5	89.4	95.6	97.1	97.3	0.96	0.82	SL
304	271.2	101043	67	-3.1	1.42	-10.00	82.1	83.6	86.3	86.9	90.2	90.8	80.9	0.95	0.82	SL
305	270.2	101215.	65	-2.8	1.85	-10.00	83.7	85.7	89.0	91.8	98.1	100.6	100.7	0.94	0.82	SL
306	271.0	101243.	67	-2.9	1.79	-10.00	85.2	87.3	89.7	90.0	94.0	94.8	94.2	0.94	0.82	SL
307	270.1	101050	65	-3.1	2.34	-6.54	88.3	90.7	93.9	95.8	102.1	105.3	107.2	0.95	0.82	SL
308	270.8	101174.	67	-3.2	2.34	-6.41	90.9	92.6	94.8	94.6	98.2	100.6	100.7	0.92	0.81	SL
309	270.4	101022.	65	-3.8	2.68	-3.28	92.9	96.4	98.3	105.1	108.4	107.7	107.7	0.92	0.81	SL
310	270.8	101056	67	-3.8	2.69	-3.31	94.0	95.6	98.0	97.9	101.4	104.0	104.9	0.91	0.81	SL
311	270.0	101043	60	-4.1	2.90	-2.45	91.9	94.6	98.1	99.6	106.4	110.6	108.8	0.93	0.81	SL
312	270.7	101243.	67	-4.1	2.90	-2.45	95.8	97.4	100.1	99.3	103.6	106.1	106.2	0.92	0.81	SL
313	270.0	100994.	60	-5.0	3.16	-1.39	96.2	98.2	101.1	102.6	108.3	113.8	111.3	0.92	0.81	SL
314	270.8	101056	60	-5.0	3.16	-1.38	99.2	101.2	103.7	102.8	106.3	110.4	109.5	0.91	0.81	SL
315	270.4	100988	60	-5.9	3.40	-0.61	99.5	101.8	104.7	105.8	110.2	116.1	112.9	0.89	0.81	SL
316	271.0	101153.	60	-5.9	3.40	-0.60	103.9	105.7	107.6	106.7	108.8	112.9	111.6	0.89	0.81	SL



TABLE A-VI. TEST MATRIX FOR CONFIGURATION TAS-4 SIMULATING ENGINE OPERATING LINE.

NOZZLE - MORÉL TAS4 AREA [MODEL SIZE - INNER = 0.0163 OUTER = 0.0113 FULL SIZE - TOTAL = 0.9031] sq.m

TEST POINT	V ac	V m/s	P K	T K	sj T	sj P	sj W	sj F	sj V	j T	j T	j T	j P	j W	j F	j V	mix T	mix T	mix T	mix T	mix T	mix P	mix W	T F	sj V/V
401	0	262.1	698.3	666.6	1.1919	50.5	827	417.6	693.7	612.1	4.5935	126.6	3303	373.3	381.3	630.1	1.4430	177	4130	0.63					
402	122	269.1	691.1	657.4	1.2058	52.6	883	420.3	697.1	614.4	1.6001	127.0	3335	376.1	381.5	629.4	1.4511	180	4219	0.64					
403	0	285.9	787.8	751.3	1.2031	48.9	872	511.8	785.9	665.3	1.8784	142.8	4568	454.2	431.5	692.2	1.6271	192.	5441	0.56					
404	122	306.0	799.4	757.2	1.2334	51.9	992	510.8	789.4	669.4	1.8677	141.7	4522	455.9	434.6	697.2	1.6274	194.	5514	0.60					
405	0	341.4	849.4	797.8	1.2797	55.0	1172	561.3	826.3	681.9	2.0750	153.6	5389	503.3	456.7	717.5	1.7693	209	6562	0.61					
406	122	344.4	844.4	791.8	1.2875	55.8	1201	560.6	824.2	680.0	2.0759	153.8	5388	503.1	455.2	714.7	1.7720	210	6590	0.61					
407	0	372.8	874.4	813.1	1.3322	58.8	1368	623.2	872.6	695.2	2.3793	171.0	6660	559.1	479.0	731.8	1.9747	230	8029	0.60					
408	122	372.8	870.6	809.1	1.3343	59.1	1377	620.0	860.7	684.6	2.3880	173.0	6703	557.0	473.6	722.6	1.9807	232	8081	0.60					
409	0	415.1	933.9	858.3	1.3985	62.1	1610	674.1	907.7	700.4	2.6914	189.6	7985	610.2	501.5	746.4	2.1903	252	9596	0.62					
410	122	409.7	905.0	830.9	1.4009	63.3	1620	676.8	911.2	702.4	2.7041	190.1	8041	610.1	499.0	741.8	2.1992	253	9662	0.61					
411	0	426.1	950.0	870.6	1.4159	62.8	1673	708.1	936.9	708.8	2.9105	201.6	8922	641.1	515.7	755.3	2.3351	264	10595	0.60					
412	122	425.5	939.4	859.9	1.4204	63.5	1690	703.5	933.9	708.7	2.8763	199.7	8781	636.4	513.1	753.1	2.3144	263	10471	0.60					
413	0	452.0	947.2	858.1	1.4834	67.5	1906	748.3	943.7	687.4	3.3407	230.3	10769	681.1	518.2	735.1	2.6312	298	12676	0.60					
414	122	456.3	965.6	875.1	1.4837	66.9	1908	748.3	946.1	689.9	3.3281	229.3	10723	682.3	521.5	740.6	2.6230	296	12632	0.61					
415	0	478.2	967.8	868.2	1.5437	70.7	2112	785.4	944.1	659.4	3.8761	267.5	13131	721.2	520.7	742.7	2.9981	338.	15244	0.61					
416	122	474.9	953.3	854.4	1.5451	71.3	2116	788.1	950.8	664.6	3.8722	266.1	13107	721.9	521.9	744.6	2.9962	337	15223	0.60					

TEST POINT	T amb DEG K	P amb Pascal	RH %	NF dB	LVM LBM	LBM	PML (FULL SIZE 731 m SIDE LINE) dB	ANGLE RELATIVE TO INLET DEGREES						T <sub>S</sub> /T <sub>S</sub> CV /CV	s <sub>j</sub> T TEST		
								50	60	70	90	120	130			140	W /W
401	296.2	99717.	59	-4.6	0.34	-10.00	74.5	76.2	78.0	82.3	87.0	87.8	86.5	0.96	0.85	0.29	AX
402	300.4	99765	50	-4.7	0.34	-10.00	75.3	75.9	75.7	78.0	80.0	80.3	79.3	0.94	0.85	0.29	AX
403	296.5	99795.	59	-3.8	1.19	-10.00	80.3	81.7	83.7	87.9	93.1	95.4	95.2	0.96	0.81	0.25	AX
404	300.7	99772	50	-3.9	1.18	-10.00	81.9	82.3	82.8	85.0	88.5	89.8	89.0	0.96	0.83	0.27	AX
405	297.4	99785	59	-3.6	1.63	-10.00	83.8	85.1	86.7	90.6	96.3	98.4	99.3	0.97	0.83	0.26	AX
406	301.3	99697	50	-3.7	1.60	-10.00	84.8	85.2	85.7	87.7	92.2	93.6	93.3	0.96	0.83	0.27	AX
407	297.7	99664.	59	-3.7	2.09	-6.42	88.9	92.3	92.1	96.0	100.3	103.8	107.7	0.93	0.82	0.26	AX
408	300.6	99745.	50	-3.9	2.05	-6.21	90.1	91.0	90.9	92.6	96.3	98.3	99.4	0.94	0.82	0.25	AX
409	298.2	99708.	53	-4.3	2.46	-3.16	90.6	92.4	93.6	97.0	102.8	106.6	108.7	0.95	0.83	0.25	AX
410	301.0	99731.	50	-4.4	2.44	-3.10	93.0	94.4	94.6	95.7	99.6	102.9	105.1	0.91	0.81	0.25	AX
411	299.3	99717.	53	-4.7	2.67	-2.32	92.0	93.5	95.2	99.1	104.9	109.9	110.3	0.93	0.81	0.24	AX
412	301.0	99789	51	-4.7	2.62	-2.42	95.1	96.1	96.6	97.7	101.4	104.9	107.4	0.92	0.81	0.24	AX
413	299.2	99603	53	-5.6	2.93	-1.27	96.0	97.9	99.0	102.5	107.5	113.1	112.4	0.91	0.81	0.23	AX
414	300.4	99688	51	-5.6	2.93	-1.30	100.2	101.0	101.8	102.6	105.1	109.0	111.1	0.92	0.82	0.23	AX
415	299.8	99751.	53	-6.5	3.18	-0.50	101.2	103.2	104.3	107.2	109.4	115.6	113.6	0.92	0.82	0.21	AX
416	299.8	99697	51	-6.5	3.18	-0.51	107.2	107.2	106.8	107.6	108.8	113.1	113.6	0.90	0.81	0.21	AX



TABLE A-VIII. TEST MATRIX FOR CONFIGURATION TAS-6 SIMULATING ENGINE OPERATING LINE.

\*\*\*\*\* S.I UNITS \*\*\*\*\*

NOZZLE - MODEL TAS6 AREA [MODEL SIZE - INNER =0.0169 , OUTER = 0 FULL SIZE - TOTAL = 0.9031] sq.m

TEST POINT	V		T		P		r		.sj		W		.sj		F		V		J		T		F		T		V		/V				
	m/s	°K	°K	°K	°K	°K	°K	°K	m/s	N	kg/s	kg/s	kg/s	kg/s	N	kg/s	kg/s	kg/s	kg/s	kg/s	kg/s	kg/s	kg/s	kg/s	kg/s	kg/s	kg/s	kg/s	kg/s	kg/s			
601	0.	288.3	288.2	1.0000	0.	0	408.9	704.2	626.2	1.5503	205.3	5247	408.9	386.3	626.2	1.5503	205	5247	0	0	0	0	0	0	0	0	0	0	0	0	0		
602	122.	0	288.3	288.2	1.0000	0.	0	410.9	710.4	631.9	1.5507	204.4	5249	410.9	389.8	631.9	1.5507	204	5249	0	0	0	0	0	0	0	0	0	0	0	0		
603	0.	0	288.3	288.2	1.0000	0.	0	517.9	801.6	678.5	1.8831	240.0	7770	517.9	439.8	678.5	1.8831	240	7770	0	0	0	0	0	0	0	0	0	0	0	0		
604	122.	0	288.3	288.2	1.0000	0.	0	521.2	809.1	684.7	1.8871	239.3	7793	521.2	443.9	684.7	1.8871	239	7793	0	0	0	0	0	0	0	0	0	0	0	0		
605	0	0	288.3	288.2	1.0000	0.	0	563.0	838.2	693.4	2.0611	256.9	9039	563.0	459.9	693.4	2.0611	257	9039	0	0	0	0	0	0	0	0	0	0	0	0		
606	122.	0	288.3	288.2	1.0000	0.	0	567.2	844.4	697.6	2.0731	257.1	9111	567.2	463.3	697.6	2.0731	257	9111	0	0	0	0	0	0	0	0	0	0	0	0	0	
607	0	0	288.3	288.2	1.0000	0.	0	630.3	887.6	706.8	2.3913	288.9	11379	630.3	487.0	706.8	2.3913	289	11379	0	0	0	0	0	0	0	0	0	0	0	0	0	
608	122.	0	288.3	288.2	1.0000	0.	0	624.4	874.4	696.4	2.3834	290.2	11323	624.4	479.8	696.4	2.3834	290	11323	0	0	0	0	0	0	0	0	0	0	0	0	0	
609	0	0	288.3	288.2	1.0000	0.	0	681.1	923.3	712.5	2.7011	319.5	13600	681.1	506.6	712.5	2.7011	320	13600	0	0	0	0	0	0	0	0	0	0	0	0	0	
610	122	0	288.3	288.2	1.0000	0.	0	682.1	926.7	715.4	2.6989	318.6	13584	682.1	508.4	715.4	2.6989	319	13584	0	0	0	0	0	0	0	0	0	0	0	0	0	0
611	0	0	288.3	288.2	1.0000	0.	0	711.4	949.9	720.4	2.8935	337.7	15018	711.4	521.1	720.4	2.8935	338	15018	0	0	0	0	0	0	0	0	0	0	0	0	0	0
612	122.	0	288.3	288.2	1.0000	0.	0	710.5	944.1	714.8	2.9074	339.9	15096	710.5	518.0	714.8	2.9074	340	15096	0	0	0	0	0	0	0	0	0	0	0	0	0	0
613	0.	0	288.3	288.2	1.0000	0.	0	746.6	944.2	689.2	3.3166	387.5	18084	746.6	518.0	689.2	3.3166	388	18084	0	0	0	0	0	0	0	0	0	0	0	0	0	0
614	122.	0	288.3	288.2	1.0000	0.	0	751.0	957.4	700.2	3.3044	385.0	18071	751.0	525.3	700.2	3.3044	385	18071	0	0	0	0	0	0	0	0	0	0	0	0	0	0
615	0	0	288.3	288.2	1.0000	0.	0	788.6	953.7	667.3	3.8611	448.7	22116	788.6	523.2	667.3	3.8611	449	22116	0	0	0	0	0	0	0	0	0	0	0	0	0	0
616	122	0	288.3	288.2	1.0000	0.	0	790.2	957.9	670.7	3.8570	448.1	22127	790.2	525.5	670.7	3.8570	448	22127	0	0	0	0	0	0	0	0	0	0	0	0	0	0

TEST POINT	T amb DEG K	P amb Pascal	RH %	NF	LWM	LBM	PML (FULL SIZE 731 m SIDE LINE) dB				ANGLE RELATIVE TO INLET DEGREES			140	sj j sj j sj j		T TEST W /W CONFIG
							50	60	70	90	120	130	Ts /Ts		CV /CV	W /W	
601	280.2	99912.	58	-4.5	0.86	-10.00	80.6	81.6	86.2	90.0	93.5	90.8	86.4	0.41	0.38	0	AX
602	284.7	99891.	56	-4.6	0.84	-10.00	86.3	85.7	88.5	90.0	90.5	85.8	79.6	0.41	0.37	0	AX
603	281.5	99926	58	-3.9	1.88	-10.00	86.2	86.9	91.4	95.3	99.3	96.4	93.1	0.36	0.33	0	AX
604	285.5	99877.	56	-4.0	1.87	-10.00	91.8	91.8	94.7	96.3	97.9	93.8	88.3	0.36	0.33	0.	AX
605	282.5	100022	55	-4.1	2.23	-4.15	87.7	88.2	92.8	96.8	100.5	97.3	92.8	0.34	0.31	0	AX
606	285.3	99891.	56	-4.2	2.24	-4.01	92.8	92.5	96.1	97.6	100.0	95.7	91.0	0.34	0.31	0.	AX.
607	282.4	99912.	55	-5.0	2.72	-1.91	89.8	91.0	94.9	99.0	101.6	99.9	96.2	0.32	0.29	0.	AX.
608	285.3	99891.	56	-5.1	2.66	-1.95	94.5	93.7	97.1	99.6	101.3	98.2	93.5	0.33	0.30	0	AX
609	282.9	99877.	55	-5.8	3.05	-0.96	92.2	92.7	96.7	100.3	103.7	101.4	98.4	0.31	0.28	0.	AX
610	285.4	99877.	56	-5.8	3.04	-0.97	96.0	96.0	98.9	101.1	103.4	100.9	96.3	0.31	0.28	0	AX
611	283.3	100043.	55	-6.2	3.24	-0.56	94.1	93.9	97.8	100.8	104.6	102.3	100.0	0.30	0.27	0	AX
612	285.7	99884	56	-6.3	3.22	-0.53	98.0	97.7	100.1	102.0	104.7	101.8	100.0	0.30	0.28	0	AX
613	283.6	99829	56	-7.2	3.45	0.09	96.5	96.7	100.4	102.6	105.9	104.5	104.0	0.31	0.27	0.	AX.
614	285.4	100270.	56	-7.1	3.46	0.08	100.1	99.9	103.1	104.2	106.3	103.8	100.9	0.30	0.27	0.	AX
615	284	99809	56	-8.2	3.68	0.66	98.7	99.1	102.5	104.1	108.0	107.7	108.2	0.30	0.26	0.	AX
616	285.0	100002.	56	-8.2	3.68	0.66	102.4	102.2	105.0	105.8	107.7	105.9	103.8	0.30	0.26	0.	AX

TABLE A-IX. TEST MATRIX FOR CONFIGURATION TAS-7 SIMULATING ENGINE OPERATING LINE IN SIDELINE AND COMMUNITY ORIENTATIONS.

\*\*\*\*\* S.I. UNITS \*\*\*\*\*

NOZZLE - MODEL TAS7 AREA [MODEL SIZE - INNER = 0.0169 OUTER = 0.0056 FULL SIZE - TOTAL = 0.9031] sq.m

TEST POINT	V		T		P		F		M		W		J		T		K		O		K		T		P		M		T		F		V		V	
	m/s	kg/s	m/s	kg/s	m/s	kg/s	m/s	kg/s	m/s	kg/s	m/s	kg/s	m/s	kg/s	m/s	kg/s	m/s	kg/s	m/s	kg/s	m/s	kg/s	m/s	kg/s	m/s	kg/s	m/s	kg/s	m/s	kg/s	m/s	kg/s	m/s	kg/s	m/s	kg/s
705	0	339.5	836.7	785.1	1.2810	34.1	723	567.0	844.9	698.2	2.0715	192.5	6820	532.8	462.8	714.7	1.8893	227.	7543	0.60																
706	122.	342.6	845.6	793.1	1.2839	34.2	731	566.5	841.4	694.8	2.0752	193.6	6854	532.9	461.9	712.9	1.8925	228.	7586	0.60																
707	0	376.7	869.4	806.7	1.3434	36.8	866	626.0	875.6	696.7	2.3921	218.0	8531	590.0	479.9	716.7	2.1482	255.	9398	0.60																
708	122	378.3	873.9	810.8	1.3446	36.8	871	626.3	873.6	694.4	2.4002	219.5	8592	590.7	479.3	715.2	2.1547	256.	9463	0.60																
709	0	406.0	912.2	839.6	1.3880	38.1	966	677.1	913.8	705.0	2.6978	240.4	10173	640.0	501.2	728.2	2.3943	279.	11140	0.60																
710	122	405.7	906.1	833.4	1.3910	38.5	975	679.8	923.6	713.7	2.6880	238.8	10143	641.8	505.4	735.2	2.3871	277.	11118	0.60																
711	0	424.6	939.4	860.8	1.4179	38.9	1031	711.8	950.5	720.8	2.8949	252.7	11238	673.5	520.7	744.7	2.5540	292.	12269	0.60																
712	122	427.3	944.4	864.4	1.4220	39.0	1042	712.7	950.2	719.8	2.9057	254.1	11320	674.7	520.9	744.3	2.5631	293.	12362	0.60																
713	0	457.2	981.1	890.1	1.4766	40.5	1156	742.1	929.7	676.8	3.3349	294.4	13654	707.7	513.4	707.9	2.9108	335.	14811	0.62																
714	122.	449.6	946.1	857.7	1.4783	41.4	1163	747.9	947.6	691.9	3.3147	290.4	13574	710.6	519.8	718.3	2.8955	332.	14738	0.60																
715	0	475.8	942.8	843.6	1.5555	44.4	1320	779.8	933.4	652.3	3.8588	339.9	16563	744.6	512.7	680.2	3.3417	384.	17884	0.61																
716	122.	474.9	947.8	848.7	1.5496	44.2	1312	788.1	936.4	670.7	3.8341	334.4	16470	751.5	524.2	697.6	3.3212	379.	17782	0.60																
721	0	338.3	834.4	783.7	1.2793	33.8	714	563.1	832.2	687.1	2.0738	193.0	6793	529.6	456.8	704.9	1.8908	227.	7508	0.60																
722	122	342.3	841.1	789.1	1.2848	34.0	727	568.0	846.0	698.8	2.0747	191.4	6794	533.9	463.8	715.8	1.8923	225.	7521	0.60																
723	0	376.3	895.6	832.3	1.3349	35.5	840	630.1	889.0	708.4	2.3862	214.0	8426	594.2	488.2	730.2	2.1424	250.	9267	0.60																
724	122.	379.5	888.9	825.2	1.3405	36.0	854	627.2	879.5	700.1	2.3904	216.0	8467	591.8	483.3	722.1	2.1464	252.	9322	0.61																
725	0	407.5	915.0	841.8	1.3905	37.7	960	676.4	909.9	701.4	2.7041	238.7	10089	639.7	499.6	725.3	2.3996	276.	11049	0.60																
726	122	408.7	926.7	853.7	1.3871	37.5	958	675.8	914.3	706.3	2.6844	237.8	10046	639.4	502.6	731.1	2.3836	275.	11005	0.60																
727	0	424.6	938.9	860.1	1.4182	38.5	1021	706.2	937.9	711.2	2.8872	251.1	11081	668.7	514.7	736.2	2.5479	290.	12103	0.60																
728	122	427.3	921.1	840.7	1.4355	39.8	1063	709.0	944.6	716.3	2.8900	251.6	11149	670.5	516.5	738.4	2.5527	291.	12213	0.60																
729	0	447.4	946.7	859.2	1.4718	40.5	1133	746.4	943.4	688.6	3.3173	287.7	11393	709.4	517.4	745.3	2.8966	328.	14526	0.60																
730	122.	449.0	941.7	853.4	1.4791	41.2	1155	748.7	948.4	692.2	3.3216	288.5	13503	711.3	519.9	748.1	2.9011	330.	14659	0.60																
731	0	470.9	961.1	864.4	1.5273	42.4	1247	778.1	945.8	667.1	3.7478	323.8	15746	782.5	519.9	695.8	3.2486	366.	16993	0.61																
732	122	469.4	936.7	839.7	1.5410	43.9	1286	786.5	949.6	664.6	3.8556	335.4	16449	749.8	520.2	691.0	3.3374	379.	17775	0.60																

Sideline

Community



TABLE A-IX. (CONT'D) TEST MATRIX FOR CONFIGURATION TAS-7 SIMULATING ENGINE OPERATING LINE IN SIDELINE AND COMMUNITY ORIENTATIONS.

TEST POINT	T amb DEG K	P amb Pascal	RH %	NF dB	LVM	LEW	PWL (FULL SIZE 731 ■ SIDE LINE) dB							140	s <sub>j</sub> j T <sub>S</sub> A <sub>1</sub> S CV / CV	s <sub>j</sub> j W / M	TEST CONFIG
							ANGLE RELATIVE TO INLET DEGREES										
705	284.4	99920.	64	-3.5	1.97	-10.00	84.8	85.8	90.4	94.4	98.5	96.6	94.4	0.93	0.82	0.15	SL
706	286.0	100128.	64	-3.6	1.97	-10.00	89.8	89.4	92.9	94.5	96.6	92.7	87.7	0.94	0.82	0.15	SL
707	284.4	99896	64	-4.2	2.42	-3.44	87.6	88.2	92.6	96.1	100.7	99.2	97.4	0.92	0.81	0.14	SL
708	286.7	100095	64	-4.3	2.41	-3.39	91.3	91.0	94.5	96.5	99.5	96.2	91.7	0.93	0.82	0.14	SL
709	284.3	99869	64	-4.8	2.77	-2.00	90.5	90.8	95.2	98.0	102.9	101.7	101.4	0.92	0.81	0.14	SL
710	286.0	100105	49	-4.8	2.77	-2.03	93.0	92.8	96.2	98.4	101.6	99.3	95.5	0.90	0.81	0.14	SL
711	282.4	99853	45	-5.1	3.01	-1.44	92.6	93.2	97.4	99.5	104.7	103.8	104.2	0.91	0.81	0.13	SL
712	286.5	100055	49	-5.2	2.99	-1.42	94.1	94.3	97.3	99.3	103.6	100.7	97.9	0.91	0.81	0.13	SL
713	282.5	99835	45	-6.2	3.22	-0.60	95.2	95.9	100.0	101.4	106.4	106.3	107.8	0.96	0.83	0.12	SL
714	285.9	100088	49	-6.1	3.22	-0.63	97.0	97.0	99.9	101.0	105.1	102.8	101.1	0.91	0.81	0.12	SL
715	281.4	99822.	45	-7.1	3.45	0.05	96.5	97.6	101.4	103.2	108.7	110.3	110.8	0.90	0.81	0.12	SL
716	286.0	100115.	49	-7.1	3.46	0.02	99.6	99.7	102.3	103.8	107.3	105.6	105.6	0.89	0.80	0.12	SL
721	278.6	99326	82	-3.4	1.99	-10.00	85.7	86.5	90.8	94.7	98.1	97.2	93.9	0.94	0.82	0.15	CO
722	276.4	99291.	63	-3.3	2.05	-10.00	90.1	90.1	93.2	94.9	97.4	93.4	88.7	0.93	0.82	0.15	CO
723	276.8	99064.	84	-3.9	2.51	-3.50	88.1	88.8	93.3	97.2	100.3	100.2	96.7	0.94	0.82	0.14	CO
724	278.4	99264	88	-4.0	2.48	-3.46	93.0	92.0	95.0	97.0	99.4	96.6	92.0	0.94	0.82	0.14	CO
725	276.5	98705	84	-4.7	2.83	-1.98	91.1	91.4	96.1	98.7	102.1	102.1	100.4	0.93	0.81	0.14	CO
726	277.4	99326.	88	-4.7	2.82	-2.05	94.4	93.7	96.3	98.7	101.6	99.8	95.9	0.93	0.82	0.14	CO
727	276.6	98816.	84	-5.0	3.02	-1.46	92.5	91.1	97.5	99.9	103.6	104.0	103.2	0.92	0.81	0.13	CO
728	277.7	99291.	88	-5.1	3.03	-1.44	95.1	94.5	97.2	99.5	103.3	101.2	98.5	0.89	0.81	0.14	CO
729	276.2	98643.	84	-5.9	3.28	-0.63	95.4	95.6	100.0	101.6	105.8	106.9	106.7	0.91	0.81	0.12	CO
730	277.7	99285.	88	-6.0	3.28	-0.62	98.2	97.9	100.6	101.9	105.7	104.1	102.1	0.90	0.81	0.12	CO
731	277.0	98602.	84	-6.8	3.47	-0.08	96.6	97.3	101.3	102.9	107.6	109.3	110.2	0.91	0.81	0.12	CO
732	278.8	99491.	88	-7.0	3.50	0.04	100.4	100.3	103.1	103.5	107.1	106.7	106.5	0.88	0.80	0.12	CO

Sideline

Community

TABLE A-1. TEST MATRIX FOR CONFIGURATION TAS-7 FOR V<sub>c</sub>, CV<sub>r</sub>, AND T<sub>s</sub> PARAMETRIC STUDY FOR A TAKEOFF CASE IN SIDELINE ORIENTATION.

NOZZLE - MODEL TAS7 CONTINUED

\*\*\*\*\* S.I. UNITS \*\*\*\*\*

TEST POINT	V ac	m/s	T		P		F		W		J		J		V		T		mix		mix		mix		T		F		T		V/W	
			amb	o	o	k	o	k	o	k	o	k	o	k	o	k	o	k	o	k	o	k	o	k	o	k	o	k	o	k	o	k
737	0	353.0	509.4	447.5	1.5748	62.1	1370	677.2	915.1	706.3	2.6942	237.9	10153	610.5	456.3	0.59	6.2	3.983	302	11524	0.52											
738	122	346.6	506.1	446.6	1.5525	60.9	1318	678.7	919.6	710.1	2.6920	239.9	10090	611.0	458.3	0.59	6.3	3.915	249	11408	0.51											
739	0	341.4	631.7	576.7	1.3993	46.6	994	676.2	910.6	702.1	2.7009	241.1	10190	621.9	474.8	0.688	4	2.3898	288	11484	0.50											
740	122	349.9	634.4	576.3	1.4228	47.6	1041	681.0	920.4	709.4	2.7104	240.5	10195	626.1	478.9	0.693	4	2.4003	287	11236	0.51											
741	0	341.1	799.4	746.9	1.2997	36.0	766	679.2	918.2	708.3	2.7014	240.1	10190	635.1	495.2	0.719	7	2.3870	276	10957	0.50											
742	122	345.9	800.6	746.8	1.3094	36.3	785	682.2	932.6	721.6	2.6795	235.1	10026	637.2	502.0	0.731	4	2.3700	271	10811	0.51											
743	0	340.2	921.7	871.2	1.2521	30.8	653	677.6	914.2	705.1	2.7011	240.5	10187	639.4	502.0	0.730	1	2.3857	271	10841	0.50											
744	122	343.2	899.4	847.9	1.2648	32.0	685	679.7	920.4	710.4	2.6980	240.0	10194	640.1	503.7	0.732	8	2.3835	272	10879	0.50											
745	0	407.8	923.3	850.6	1.3864	37.8	962	678.8	917.6	708.3	2.6945	239.6	10157	641.4	501.9	0.732	5	2.3915	277	11120	0.60											
746	122	410.0	877.8	803.5	1.4167	40.3	1032	678.8	919.9	710.4	2.6920	239.6	10165	640.1	501.4	0.728	5	2.3940	280	11198	0.60											
747	0	406.9	748.9	672.8	1.5013	47.7	1212	677.6	915.8	706.8	2.6954	239.6	10160	632.8	487.3	0.705	8	2.4086	286	11373	0.60											
748	122	416.1	781.1	701.9	1.5023	46.4	1207	679.7	919.2	709.1	2.7028	238.9	10147	636.8	491.9	0.712	4	2.4156	285	11355	0.61											
749	0	413.3	666.7	586.0	1.6097	55.6	1437	676.1	912.3	704.1	2.6936	240.4	10144	637.7	475.2	0.686	3	2.4244	296	11592	0.61											
750	122	415.7	663.9	581.9	1.6229	56.0	1455	681.8	926.1	714.9	2.6984	237.6	10144	637.7	475.2	0.686	3	2.4244	296	11592	0.61											
751	0	413.9	514.4	429.3	1.8852	75.9	1964	675.3	910.9	703.1	2.6912	240.1	10133	637.7	475.2	0.686	3	2.4244	296	11592	0.61											
752	122	418.5	525.6	438.6	1.8862	74.8	1958	680.6	926.9	716.7	2.6844	236.3	10133	637.7	475.2	0.686	3	2.4244	296	11592	0.61											
753	0	477.6	961.7	862.2	1.5470	43.6	1302	677.4	915.1	706.2	2.6944	239.8	10153	637.7	475.2	0.686	3	2.4244	296	11592	0.61											
754	122	477.9	968.3	868.5	1.5434	43.5	1248	680.1	925.2	715.1	2.6858	238.3	10177	637.7	475.2	0.686	3	2.4244	296	11592	0.61											
755	0	476.4	834.4	731.6	1.6585	51.3	1529	676.4	911.4	702.9	2.6999	241.0	10189	641.3	492.6	0.710	8	2.4471	292	11718	0.70											
756	122	475.8	828.9	726.2	1.6617	51.3	1527	679.6	920.7	710.7	2.6967	238.2	10116	643.4	496.2	0.716	4	2.4451	290	11643	0.70											
757	0	502.9	976.1	865.4	1.6145	45.8	1438	676.5	913.2	704.8	2.6938	240.2	10153	648.7	506.5	0.733	1	2.4328	286	11592	0.74											
758	122	505.4	979.4	867.9	1.6198	46.0	1452	681.1	928.1	717.5	2.6850	237.9	10124	652.6	513.7	0.744	5	2.4274	284	11577	0.74											

TEST POINT amb P RH NF LVM LHM

ANGLE RELATIVE TO INLET DEGREES

731 70 90 120 130 140

T<sub>s</sub> ATTS CV / CV W/W CONFIC

0.49 0.65 0.21 SL

0.89 0.64 0.20 SL

0.63 0.68 0.16 SL

0.69 0.17 SL

0.81 0.73 0.13 SL

0.80 0.73 0.13 SL

0.95 0.76 0.11 SL

0.92 0.76 0.12 SL

0.93 0.81 0.14 SL

0.87 0.80 0.14 SL

0.76 0.76 0.17 SL

0.78 0.76 0.16 SL

0.75 0.75 0.19 SL

0.64 0.75 0.19 SL

0.63 0.74 0.19 SL

0.69 0.69 0.24 SL

0.47 0.69 0.24 SL

0.94 0.88 0.15 SL

0.94 0.87 0.15 SL

0.80 0.84 0.18 SL

0.79 0.84 0.18 SL

0.95 0.90 0.16 SL

0.94 0.94 0.16 SL







TABLE A-XII. (CONT'D) TEST MATRIX FOR CONFIGURATION TAS-8 SIMULATING ENGINE OPERATING LINE IN SIDELINE AND COMMUNITY ORIENTATIONS.

NOZZLE - MODEL TAS8 CONTINUED

\*\*\*\*\* S.I. UNITS \*\*\*\*\*

TEST POINT	T amb DEG K	P amb Pascal	RH %	NF dB	LVM	LEM	PWL (FULL SIZE, 731 m SIDE LINE) dB ANGLE RELATIVE TO INLET DIRECTION					140	sj j Ts/Ts CV / CV	sj j W / W	TEST CONFIG		
							50	60	70	90	120					130	
801	278.4	98512	85	-4.3	0.29	-10.00	77.2	78.3	82.9	86.2	86.5	85.2	82.3	0.97	0.84	0.27	SL
802	271.5	99506	70	-4.1	0.38	-10.00	80.2	80.2	83.9	85.9	85.9	81.3	74.9	0.98	0.84	0.27	SL
803	278.0	98445	85	-3.3	1.36	-10.00	82.4	83.3	88.1	91.5	93.2	93.4	89.5	0.95	0.82	0.27	SL
804	271.0	99495	70	-3.0	1.45	-10.00	86.6	86.3	90.6	91.2	91.8	84.4	83.5	0.96	0.83	0.27	SL
805	279.8	98499	85	-3.1	1.73	-10.00	84.3	85.3	89.8	93.4	95.3	95.7	93.3	0.93	0.82	0.27	SL
806	271.7	99482	70	-2.8	1.84	-10.00	88.5	87.8	91.7	92.8	93.9	91.0	87.0	0.96	0.83	0.26	SL
807	280.4	98371	86	-3.4	2.22	-6.13	86.1	87.1	91.6	95.1	98.0	98.3	97.2	0.93	0.82	0.26	SL
808	271.8	99492	70	-3.2	2.30	-6.24	88.9	88.3	92.1	94.2	96.5	94.4	90.3	0.93	0.82	0.26	SL
809	280.7	98354	86	-4.0	2.57	-3.23	88.6	89.0	93.3	96.7	100.0	101.3	101.6	0.94	0.82	0.25	SL
810	270.7	99495	70	-3.9	2.64	-3.23	91.5	90.2	94.4	95.9	99.1	97.1	95.1	0.93	0.82	0.25	SL
811	281.2	98301	86	-4.4	2.80	-2.33	90.1	90.3	94.7	97.9	102.2	103.6	104.4	0.94	0.82	0.24	SL
812	271.4	99429	70	-4.2	2.87	-2.39	93.0	91.7	95.6	97.2	100.5	99.1	98.0	0.91	0.81	0.24	SL
813	282.7	98305	81	-5.3	3.02	-1.32	93.7	93.9	97.4	99.5	105.0	106.9	108.1	0.93	0.82	0.23	SL
814	274.7	99498	70	-5.1	3.09	-1.35	95.1	93.8	97.2	99.0	103.0	102.4	102.1	0.91	0.81	0.23	SL
815	283.7	98278	81	-6.2	3.27	-0.53	96.3	96.6	100.2	101.1	107.1	110.0	111.7	0.92	0.81	0.21	SL
816	271.8	99443	70	-6.2	3.34	-0.51	98.2	97.6	101.0	100.9	105.2	105.7	106.4	0.90	0.81	0.22	SL
817	275.8	100119	46	-4.3	0.32	-10.00	75.1	77.1	81.4	85.2	85.7	83.1	78.3	0.96	0.84	0.28	CU
818	280.9	100142	68	-4.2	0.34	-10.00	78.6	79.0	82.8	84.8	83.7	78.3	71.9	0.98	0.84	0.27	CU
819	276.8	100166	46	-3.3	1.37	-10.00	79.7	81.3	86.0	89.6	91.2	90.2	85.7	0.97	0.83	0.27	CU
820	281.0	100102	68	-3.3	1.38	-10.00	84.1	84.4	88.5	89.3	88.9	85.4	80.6	0.94	0.82	0.27	CU
821	277.2	100102	46	-3.1	1.77	-10.00	81.9	83.3	88.2	91.5	94.2	93.3	90.7	0.94	0.82	0.27	CU
822	280.9	100112	68	-3.1	1.77	-10.00	85.9	85.9	89.7	90.9	91.2	88.2	84.3	0.94	0.82	0.27	CU
823	277.9	100068	46	-3.4	2.24	-6.12	84.2	85.5	90.3	93.5	97.6	96.3	95.5	0.95	0.82	0.26	CU
824	281.0	100139	60	-3.3	2.24	-6.27	87.9	88.1	91.6	93.1	94.1	92.3	89.1	0.93	0.81	0.26	CU
825	277.7	100062	46	-4.0	2.59	-3.20	86.6	87.6	92.1	95.6	100.2	100.4	100.6	0.91	0.81	0.25	CU
826	282.0	100105	60	-4.1	2.56	-3.18	89.3	89.7	93.1	94.5	96.4	95.4	94.3	0.90	0.81	0.25	CU
827	296.9	100028	38	-4.6	2.67	-2.37	88.5	89.4	93.8	96.7	102.0	102.4	103.3	0.93	0.81	0.24	CU
828	281.4	100064	60	-4.4	2.80	-2.37	90.3	90.7	94.0	95.4	98.5	97.8	97.4	0.93	0.82	0.24	CU
829	278.4	99991	38	-5.2	3.06	-1.35	91.6	92.4	96.1	98.4	104.8	106.7	106.9	0.92	0.81	0.23	CU
830	281.7	100132	60	-5.3	3.05	-1.34	92.9	92.8	96.2	97.2	100.6	101.4	102.2	0.92	0.81	0.23	CU
831	279.2	100004	38	-6.2	3.30	-0.53	94.3	95.2	99.1	100.4	107.3	109.9	109.4	0.90	0.81	0.21	CU
832	280.7	100085	60	-6.3	3.29	-0.54	96.0	95.9	98.9	100.0	103.4	105.5	107.0	0.89	0.81	0.21	CU

Sideline

Community









1. Report No. NASA CR-3758		2. Government Accession No.		3. Recipient's Catalog No.	
4. Title and Subtitle Free Jet Feasibility Study of a Thermal Acoustic Shield Concept for AST/VCE Application - Single Stream Nozzles				5. Report Date July 1984	
				6. Performing Organization Code	
7. Author(s) R. K. Majjigi, J. F. Brausch, B. A. Janardan, T. F. Balsa, P. R. Knott, and N. Pickup				8. Performing Organization Report No. R82AEB494	
				10. Work Unit No.	
9. Performing Organization Name and Address General Electric Company Aircraft Engine Business Group Cincinnati, Ohio 45215				11. Contract or Grant No. NAS3-22137	
				13. Type of Report and Period Covered Contractor Report	
12. Sponsoring Agency Name and Address National Aeronautics and Space Administration Washington, D.C. 20546				14. Sponsoring Agency Code 505-31-31 (E-2132)	
15. Supplementary Notes  Final report. Project Manager: Jack H. Goodykoontz, Fluid Mechanics and Instrumentation Division, NASA Lewis Research Center, Cleveland, Ohio 44135.					
16. Abstract  The objective of this investigation is to develop a technology base for the thermal acoustic shield concept as a noise suppression device for single stream exhaust nozzles. Acoustic data for 314 test points for 9 scale model nozzle configurations were obtained. Five of these configurations employed an unsuppressed annular plug core jet and the remaining four nozzles employed a 32 chute suppressor core nozzle. Influence of simulated flight and selected geometric and aerodynamic flow variables on the acoustic behavior of the thermal acoustic shield was determined. Laser velocimeter and aerodynamic measurements were employed to yield valuable diagnostic information regarding the flow field characteristics of these nozzles. An existing theoretical aeroacoustic prediction method was modified to predict the acoustic characteristics of partial thermal acoustic shields. From the results of this investigation, it was found that: the three significant physical influences of a thermal acoustic shield are: 1) mid and high frequency noise reduction at shallow angles to the jet axis due to total internal reflection; 2) mid and high frequency noise reduction in the front quadrant and at $\theta_1 = 90^\circ$ due to source strength reduction; and 3) low frequency noise amplification due to an elongation of the jet plume. Due to the larger high frequency noise content of the 32 chute suppressor nozzle, the thermal acoustic shield yields larger PNL and EPNL reductions due to the thermal acoustic shield are dependent on the observer sideline distance, and hence appropriate sideline distances must be utilized in determining the noise suppression at takeoff, cutback and approach cycle conditions. The shield thickness has a significant bearing on the noise reduction potential of a thermal acoustic shield. Partial thermal acoustic shields create significant amount of acoustic and flow asymmetry which is confirmed by the theoretical predictions. An increase in base drag of the 32 chute suppressor nozzle due to the shields was observed, but is smaller for the simulated flight case than the static case.					
17. Key Words (Suggested by Author(s))  Jet noise; Thermal acoustic shield; Annular nozzle; Suppressor nozzle; Shock cell noise; Variable cycle engine			18. Distribution Statement  Unclassified - unlimited STAR Category 71		
19. Security Classif. (of this report) Unclassified		20. Security Classif. (of this page) Unclassified-		21. No. of pages 353	22. Price* A16